TRANSPORTATION OF FERROMAGNETIC POWDER USING LINEAR MOTOR DEVICES

by

D. K. Gupta

A Doctoral Thesis

Submitted in partial fulfilment of the requirements
for the award of

Doctor of Philosophy of the Loughborough University of Technology

13 August 1994

Abstract

The travelling magnetic wave of a linear induction motor induces eddy currents in a secondary circuit (usually a sheet consisting at least partly of a non-magnetic metal, often aluminium), which cause the unrestrained member to move linearly in the direction of the travelling wave. A linear motor can also transport ferromagnetic powder, although this travels in the opposite direction to the travelling magnetic field. The motion is therefore due to a mechanism other than the eddy currents flowing in the sheet secondary.

Expressions for the forces acting on an iron particle due to a travelling magnetic field are derived in the thesis. Preliminary experiments support the assumptions made in the derivations of the force expressions and lead to the formation of an hypothesis. This is shown to be capable of predicting both linear and rotational particle speeds and, with greater accuracy, the distance travelled and the rotation experienced by the particles. Experiments conducted on tubular and transverse flux motors have enabled different linear motors to be identified as suitable for a number of powder transportation applications. The results obtained show also the importance of large flux density values, the tangential to normal flux density ratio and large pole-pitch winding arrangements, with the latter lending support to the original hypothesis.

The results of a finite element investigation of the tubular motor did not closely agree with the results from the experimental motor although similar trends were evident. Flux density values within particles were found to be considerably greater than those outside, as assumed in the hypothesis.

Acknowledgements

I would like to thank Professor Les Hobson and Mr John Lloyd for securing funding from SERC for the project and for their assistance during the first two years and Dr Gordon Kettleborough for acting as my supervisor during the writing of the thesis. Thanks are also due to Phil Atkinson for various photographs, and especially to Geoff Boyden for the high-speed photographs. The staff in the Chemical Engineering Laboratory kindly explained particle-sizing methods and produced the sizing results in Chapter 3. Construction of the experimental devices would not have been possible without the considerable assistance of Peter Barrington and his workshop.

I should also thank Davy McKee (Sheffield) Limited for several powder samples and for the loan of their powder cleaner, Linear Motors of Loughborough for initial discussions regarding powder transportation, and SERC, Rutherford-Appleton Laboratories and GEC at Stafford for use of their finite-element packages. I gratefully acknowledge the typing efforts of Tracy Finn without whom I would still be typing away. My thanks also go to Janet Redman who made many of my diagrams presentable. I am also grateful to my wife and family for the sacrifices they have had to make whilst I have been writing the thesis. I feel mostly indebted to Professor Ivor Smith, who has kindly and painstakingly guided me through the writing of the thesis, and without whom it would have been an extremely poor document.

Finally I wish to thank my friend Y'shua who has helped me through this project and has taught me perseverance, and to whom I dedicate this work.

Contents

Symbols and Abbreviations

Unless otherwise stated, the following symbols have the indicated meanings.

A	-	area
a, c, h, r, x, y	-	linear measures
B	-	flux density
B_x, B_y	-	x- and y- components of flux density
B_n, B_t	-	normal and tangential components of flux density
B_m	-	modulus of flux density
D	-	demagnetising factor
d	-	diameter
E	-	emf
F	-	force
F_p	-	packing factor
f	-	supply frequency
H	-	magnetic field intensity
I	-	current
J, j	-	current density
k_w	-	winding factor
M	-	dipole moment per unit volume (intensity of magnetisation)
m	-	pole strength or mass
$\dot{m}$, $\dot{m}_c$	-	mass and cumulative mass transport / flow rates
N_p	-	number of turns per phase
t	-	time
v	-	velocity
v_s	-	velocity of travelling field

κ_r	-	relative susceptibility
λ	-	wavelength
λ_p	-	pole-pitch
θ, ϕ	-	angular measure
μ_o	-	permeability of free space
μ, μ_r	-	permeability and relative permeability
ω	-	angular frequency ($\omega = 2\pi f$)
LIM	-	linear induction motor / machine
SLIM	-	single-sided LIM
DSLIM	-	double-sided LIM
TLIM	-	tubular LIM
TFLIM	-	transverse flux LIM
DSTFLIM	-	double-sided TFLIM
TFM	-	transverse flux motor/machine
LSM	-	linear synchronous motor/machine
LStM	-	linear stepping motor/machine
HSGT	-	high-speed ground transportation
MHD	-	magneto-hydrodynamics
f.e.	-	finite-element
LED	-	light emitting diode
SERC	-	Science and Engineering Research Council
rpm	-	revolutions per minute
rms	-	root mean square

1. Introduction

A linear induction motor (LIM) can be thought of as a conventional rotary motor that has been cut along an axial plane and "unrolled", as in Fig 1.1, to produce a flat structure capable of providing motion in a straight line. Both the LIM and the conventional machine have travelling airgap magnetic fields, but the magnetic similarity ends there since the rotary machine has a closed magnetic circuit whereas that of the LIM is open. This is an essential difference between the two devices and it is this "openness" that gives rise to what are commonly termed "end-effects".

Many different types of rotor (a better term being secondary, as the "rotor" in a LIM does not usually rotate) are used with linear machines and the majority of these consist partly, if not entirely, of a non-magnetic metal, usually aluminium but sometimes copper. The stator (or primary) travelling magnetic wave induces eddy currents in the secondary and interaction between these and the travelling magnetic field causes the unrestrained member (either the primary or secondary) to move linearly in the direction of the travelling wave.

The topic of this SERC funded research project is an investigation into the use of ferromagnetic powder as the secondary of different types of linear machines. Previous observations, described in Chapter 2, have already shown that, when under the influence of a travelling magnetic field, ferromagnetic powder travels in the opposite direction to a metal plate and, therefore, to that of the travelling magnetic flux wave. This study is concerned with attempting to obtain an understanding of the process, or processes, involved in this motion.

Applications of powder transportation

This movement of iron powder gives rise to a number of possible applications including:

a) the cleaning of ferromagnetic powder;

b) the cleaning of powder containing ferromagnetic impurities;

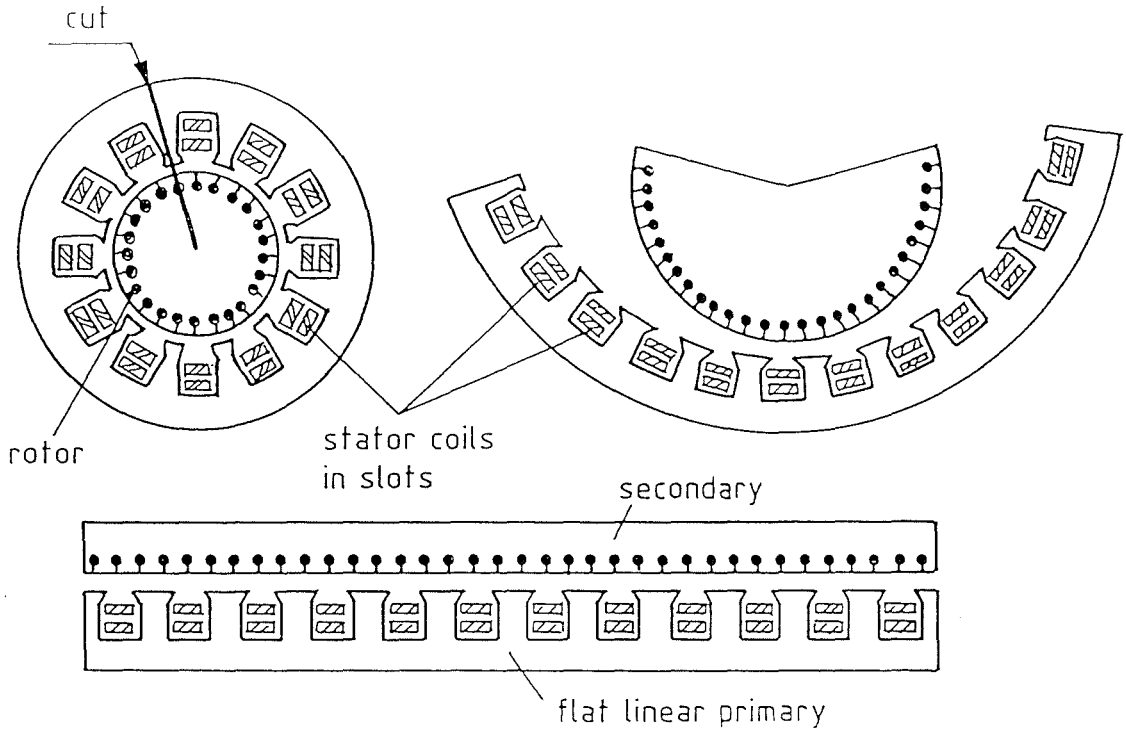

IMAGINARY PROCESS OF UNROLLING A CONVENTIONAL MOTOR TO OBTAIN A LINEAR MOTOR

Figure 1.1

c) the transportation of particulate materials without the intervention of either a conveying fluid or a mechanical conveying mechanism;

d) the classification and purification of powdered materials using their magnetic properties;

e) the recovery of expensive metals from industrial waste, e.g. grinding waste;

f) the enhancement of powder circulation and mixing within fluidised beds;

g) the sieving of magnetic powders in order to classify them into particle size.

The viability of these and other applications can only be assessed after studying both the electromagnetic phenomenon associated with the mechanisms involved and the transport characteristics of iron powder on linear machines.

The cleaning of ferromagnetic powder (see Chapter 2) would enable high quality steel to be manufactured from the powder. The powder itself could be produced from scrap iron by water or gas atomization, a technique well-known to powder metallurgists. Impurities in the powder may then be removed by transporting it using a linear motor and leaving the "rubbish" behind. The opposite application is also possible, i.e. the removal of iron powder from other powder by transporting out the ferromagnetic impurities. In addition, there is often a requirement to convey ferromagnetic powder from the end of one process to the start of another and linear machines would facilitate such a movement.

The size of ferromagnetic powder affects its motion (as will be seen later) giving rise to the possibility of sizing the powder (see Chapter 2) to provide particular particle size distributions. As the coercivity of ferromagnetic powder also affects its motion (discussed later), the powder may be classified as being either magnetically "soft" or magnetically "hard".

In a fluidised bed (that is, a bed of particles) air jets forced through the particles cause them to behave similarly to a fluid. This technique is used to increase the reaction rates within chemical reactors, since the agitation produces a good mixing of the chemical

agents. Enhancing both the circulation and mixing through the use of a linear motor could increase the reaction rates even further in fluidised beds containing ferromagnetic particles, whether the particles were one of the reactive agents or the catalyst for the reaction.

These briefly described applications indicate that numerous benefits may be achieved through the use of suitably designed linear devices for the motion or transportation of ferromagnetic powder.

Précis

This research project concentrated mainly on an experimental rather than a theoretical investigation, in order to have one or two experimental linear devices and associated results by the end of this work. After a brief historical introduction to linear machines, Chapter 2 describes various linear devices concentrating on those used in the present study, followed by a discussion of some applications of these machines. Other applications are also described where the application itself implies another method of transporting iron powder. By way of example, a trolley which contains iron powder may be moved via a linear motor. This thesis, however, studies the use of linear machines for directly transporting ferromagnetic powder. This application is therefore described in some detail, with particular reference to the cleaning of ferromagnetic powder due to the considerable previous work in this area.

Preliminary investigations are described in Chapter 3, including theoretical derivations of expressions for the forces on a ferromagnetic particle under the influence of a travelling magnetic field. The expressions (derived in detail in Appendix A) clearly imply that the particle is expected to move in the opposite direction to the travelling field, as observations have already shown. In addition, a hypothesis is developed, based upon initial experiments on a "powder cleaner" (see Chapters 2 and 3), in which both hypothesis and experiments concur with the force-expression. Particle velocity measurements were also made using high-speed photographic techniques and a specially designed electronic timer.

Following the preliminary study, two other classes of linear machine in addition to the LIM were investigated, namely the tubular linear induction machine (TLIM) and the transverse flux linear induction machine (TFLIM). It was hoped that the tubular device would increase powder transportation because of the increased surface area compared with a standard linear machine without the penalty of large losses in the end-turns (see Chapter 4). In addition, being an axial flux device (see Chapter 2), it was thought that the tubular device may "pump" the powder along its length. A finite-element analysis of both the tubular and linear machines was conducted alongside the design and construction of the tubular motor, in order to gain an understanding of the flux distribution and its likely effect on ferromagnetic particles, and this is described in Chapter 5.

Chapter 6 describes the design and construction of the transverse flux device and the associated experimental results. Various configurations of this machine were tried, in order to improve its performance at transporting powder. As with the powder cleaner arrangement, an inverted transverse flux device mounted on a suitable frame and two double-sided schemes were tried: a standard approach, with opposing magnetic poles facing each other, and an axial flux approach with like poles opposite each other (similar to a tubular machine).

Mass transport rate measurements of ferromagnetic powder were made for both the tubular and transverse flux devices and these give an indication of the machines' performance. A number of appendices provide detail on machine design and construction (including information concerning the finite-element models) and experimental results. Two published papers, describing some initial work detailed in Chapters 2 to 6, are included in the last appendix. The papers mainly discuss the background to the work and the initial high-speed photographs (see Chapters 2 and 3), and the design of the tubular and transverse flux motors (see Chapters 4 and 6).

The last chapter contains the conclusions that may be drawn from this work.

2. A Review of Previous Work

It is believed that the first linear motor, most probably a reluctance device, was built by Wheatstone during the early 1840's and that in the early 1850's Talbot patented the second linear motor[1]. Approximately forty years later the linear induction motor was developed, a few years after Tesla had invented the rotational induction motor. Despite this, some four decades elapsed before ideas for its practical application began to emerge; indeed it was only after World War II that developments of major significance were announced[2]. Between 1900 and 1940, the majority of work on linear machines was carried out by textile engineers, although their incorporation into looms was never commercialised as their cost was comparatively high when compared with the existing techniques[1]. Since the second world war there has been much interest in the application of linear machines to ground transportation and a wealth of published literature exists on this topic[3-30].

2.1 Topology

There are a large number of different types of linear machine[1,7,31,32]; the more common being single- or double-sided linear induction machines[33] with a short secondary (used for conveyors), and a tubular LIM with a short primary (used for short-stroke actuators)[34,35], with the most widely used being the single-sided LIM.

In addition there is the transverse flux LIM (TFLIM), the linear synchronous machine (LSM), the reluctance LIM (RLIM)[36], the linear stepping motor (LStM)[37], a LIM for helical motion[38,39], the dc LIM[40] and many others. If different secondary arrangements are used the resulting device behaves differently and becomes a new linear machine, increasing the variety of linear machines even further. For example, a single-sided LIM may have either a short or a long secondary (see below), comprising an aluminium plate, a mild steel plate, an aluminium plate attached to a steel plate (back-iron), or a "sandwich-type" secondary with aluminium strips attached to mild steel plates. (Where the secondary is of the sandwich type, the aluminium is between the stator core and the steel, thus tending to force the flux through the aluminium to produce the majority of the motive power.)

New forms of linear machine are still being invented[41] and a full description of these is outside the scope of this report. Nevertheless, a few of the more common varieties, including those relevant to the present work, are described in some detail below.

2.1.1 Single- and Double-sided Linear Induction Machines[7,33]

A simplified development of the LIM was given in Chapter 1 (see also Fig 1.1). If a conventional rotary machine is "unrolled" the rotor, or secondary, consists of conductors embedded in an iron structure on top of a flat stator. Such a machine would exert considerable magnetic pull on the secondary, which can be reduced by adding a second stator above the secondary with further conductors positioned along the top of the secondary. This arrangement produces a double-sided linear induction motor (DSLIM), with a magnetic pull now depending only on the inequality of the gaps on either side of the secondary.

As shown in Fig 2.1, the machine may be further developed by omitting the secondary iron and making the secondary purely a sheet of conducting material such as aluminium. In this case the two stators face each other with either a N-pole facing a S-pole or a N-pole facing a N-pole. The latter case must have a secondary containing iron, as the opposing fluxes are now forced axially along the secondary, and the continued development of this device leads to the tubular motors described below. In the former case, with opposing poles facing each other, the flux is forced through the sheet conductor and the magnetic pull is eliminated by the lack of iron in the secondary.

Removing one of the stators of the double-sided machine produces the "open-sided" or "single-sided" linear induction machine (SLIM), shown in Fig 2.1, in which the flux is forced through long air-paths. The magnetic circuit of these machines is poor and back-iron, which may or may not be laminated, is often added to the secondary to improve the magnetic circuit by providing a low reluctance path.

Both Fig 1.1 and Fig 2.1 show the stator and secondary of the motor as having equal lengths. Once motion has occurred, a part of the primary is no longer covered by the secondary and a corresponding length of secondary has run free of the primary at the other end. This results in a reduced force and, in order to prevent this condition, either

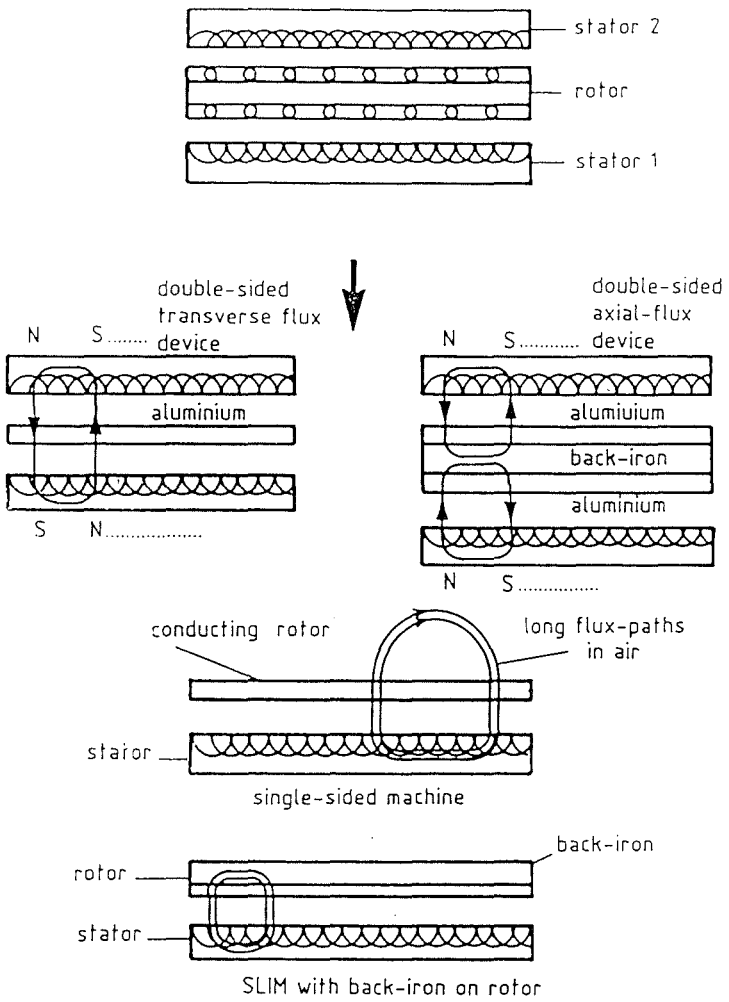

Comparison of flux paths in single and double-sided LIMs

Figure 2.1

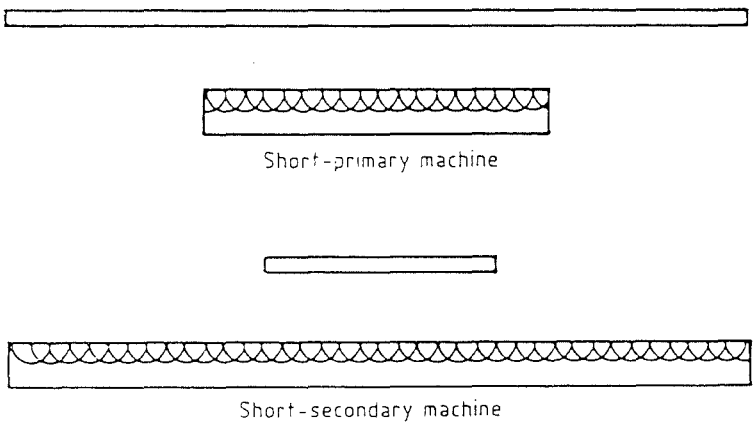

Classes of linear machine

Figure 2.2

the primary or the secondary must be extended. These extensions lead to the two main classes of linear machine shown in Fig 2.2, both of which suffer from transient effects at the edges of the shorter member of the machine. Firstly, there is the short-primary machine, in which the secondary is longer than the primary, and secondly there is the short-secondary machine, in which the primary is longer than the secondary.

2.1.2 Tubular Linear Induction Machine[7,33]

The tubular linear induction machine (TLIM) is a further development of the LIM and, as Fig 2.3 shows, is formed by `rolling' a LIM primary around an axis parallel to the direction of motion.

The TLIM primary, which is one of the easier linear machines to construct, has the advantage that the end connections are replaced by a single conductor which connects to the next pole. Although constructionally it is simpler to use circular laminations, longitudinal ones are often employed because the same laminations used for a flat LIM may then be used. The stator can be made up from packets of longitudinal laminations, just as if it had been constructed from a set of individual linear motors (see Fig 2.4). The TLIM secondary may be constructed in a number of ways: it may be laminated, as shown in Fig 2.4; it may consist of alternate rings of copper (or aluminium) and iron with an iron core[35]; it may simply be a solid copper or aluminium cylinder (but this would have a poor magnetic circuit), or it could be a solid steel cylinder[42].

It is possible to approximate to the tubular construction, as is necessary when using longitudinal laminations, by having a number of lamination stacks arranged around a circumference. For example, there may be four lamination stacks, in which case the secondary could be of rectangular cross-section[43]. Continuing the process further, and having only two stacks, results in a double-sided motor but with N-pole facing N-pole as opposed to N-pole facing S-pole (see Fig 2.5), thereby causing the flux to travel down the axis of the machine. For this reason members of the "tubular" motor family have been termed "axial-flux" machines, to distinguish them from other forms of linear motor. Although the secondary must contain iron[44], the construction of the primary may be further simplified by omitting all the stator iron. Once this is accomplished, the windings may be more distributed and the construction of the device becomes simpler. The

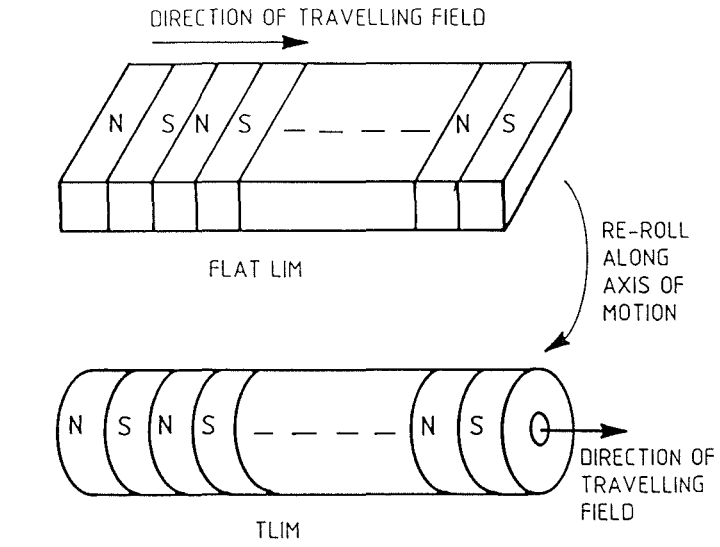

DEVELOPMENT OF THE TUBULAR MOTOR

Figure 2.3

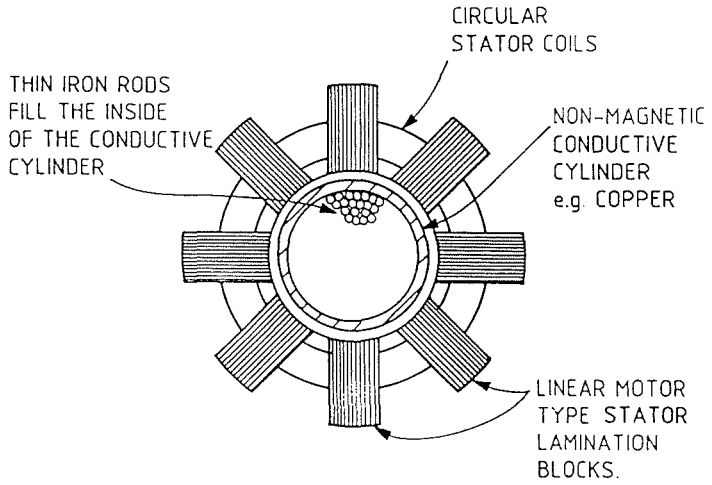

CROSS-SECTION THROUGH TUBULAR MOTOR CONSTRUCTED FROM PACKETS OF LONGITUDINAL LAMINATIONS

Figure 2.4

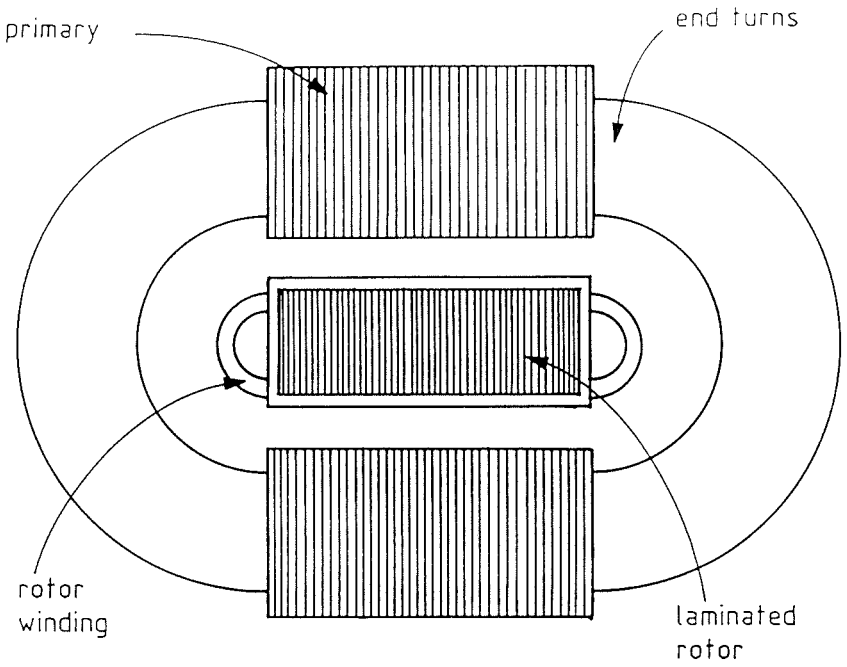

AN AXIAL FLUX MOTOR WITH A WOUND ROTOR

Figure 2.5

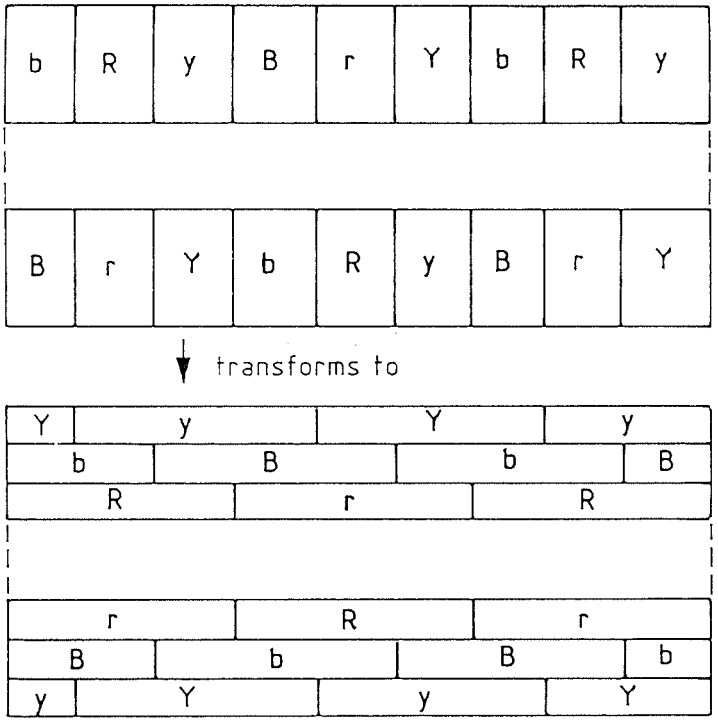

DISTRIBUTED WINDINGS FOR AN AIR-CORED TUBULAR MOTOR

Figure 2.6

windings are now layered, one phase on top of another, with the windings of each phase spread over a pole-pitch as shown in Fig 2.6. Such a winding has a loss of one-third of the effective ampere-turns over the non-distributed case, but this is balanced by the advantage of easier construction[43].

2.1.3 Transverse Flux Linear Induction Machine

These machines were originally studied with a view to improving the drive systems of high speed ground transportation (HSGT). The advantage of transverse flux linear machines (TFLIMs) is that an extension of the pole-pitch is possible without a corresponding increase in the core depth, and also without an increase in the reluctance of the magnetic circuit. The device is able to achieve this because the flux in each tooth of the transverse flux machine (TFM) is self-contained and independent of the pole-pitch, whereas in the longitudinal flux machine the flux in the primary teeth supplement each other in the core, as illustrated in Fig 2.7[45].

In transverse flux devices the flux is transverse to the direction of motion of the sheet secondary. Thus, referring to Fig 2.7[45], the direction of motion of the secondary is normal to the plane of the paper whereas, for a longitudinal flux machine, it is along a plane in the horizontal direction. If E-cores are used the windings may be placed almost anywhere on the cores, assuming that the phase relationship is such that the flux takes the path shown in the diagram; often the windings are placed around the centre-limb of the E-cores to make the primary simpler to construct. Alternatively C-cores may be employed with windings around both limbs or, more simply, a winding around the central portion. If in the case of E-cores, only the centre limbs are wound, then the mmf is required to drive the flux across the airgap twice, thereby halving the goodness factor[46] in comparison with the same current loading applied to the conventional longitudinal-flux machine[45]. An advantage is however gained in that the end-windings of an E-core machine are effectively embedded in the steel core. It will be remembered that, in the direction of motion of the TFLIM (see Fig 2.7[45]), the steel core is placed at regular intervals and is separated by spaces containing the primary winding. This break in the steel causes the flux to take a path transverse to the direction of motion.

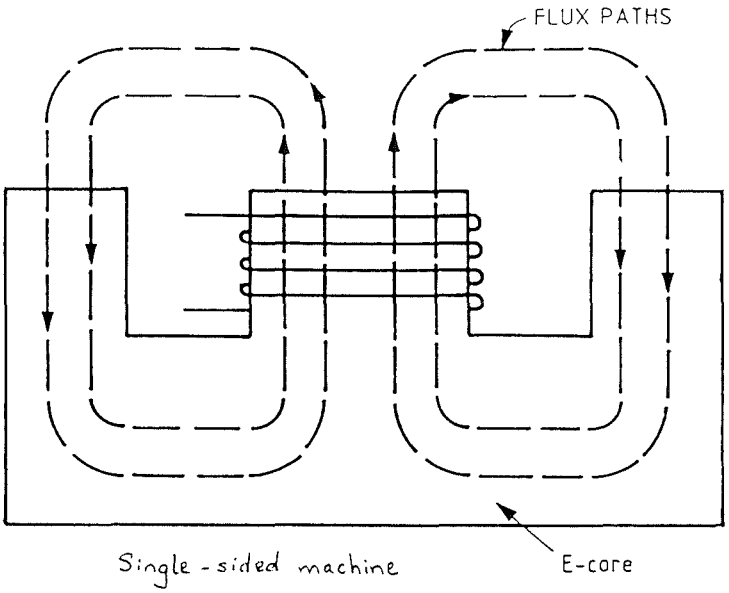

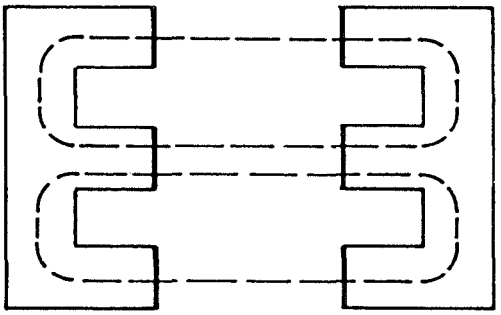

Transverse flux machine.

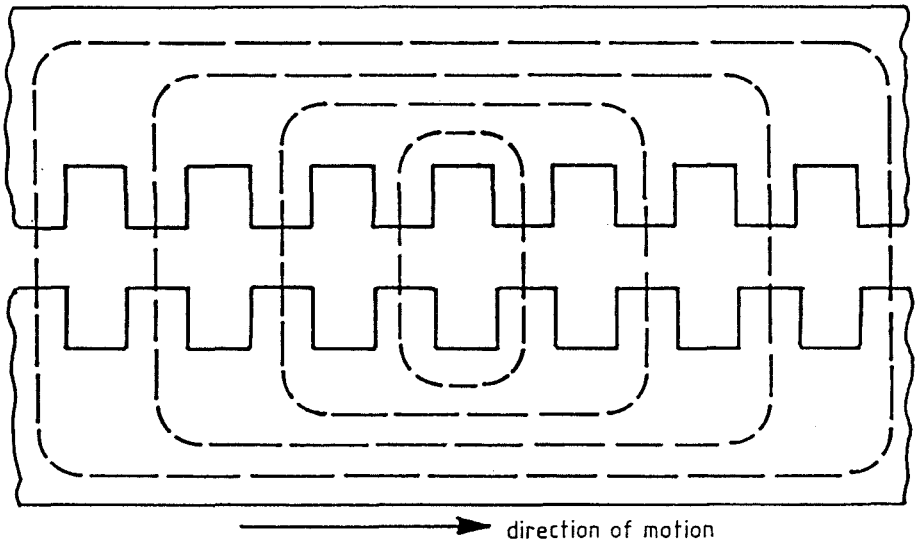

Longitudinal flux machine

Comparison of core flux between the transverse and longitudinal flux machines.

Figure 2.7

In addition to the flat transverse flux machine, transverse flux tubular motors have also been built[47,48], although their helical-shaped coils are difficult to construct. Their advantage is that they produce axial force only but this is only useful when they have few poles compared to the conventional tubular machine.

Further developments of linear machines have produced what have been termed "herringbone" motors because of the pattern followed by the pole faces of the device[49]. These machines tend to produce laterally inward travelling fields which aid lateral stability, for example, in the case of HSGT.

2.2 Winding Arrangements

In addition to there being different types of LIM each may also use different winding configurations, with the optimum arrangement being one that produces a pure sinusoidal travelling magnetic field along the whole length of the linear device. Due to the edges and ends of the motor such a travelling field is not practically realisable, but it can be approached when a double layer winding is used. The winding arrangement of Fig 2.8 shows a two layer winding which comes close to developing a sinusoidal travelling-wave field in the central zone of the motor, departing from this waveshape only at the edges and above the half-filled end slots.

Slot:	1	2	3	4	5	6	7	8	9	10	11	12	13	14	15	16	17	18
	R	y	B	r	Y	b	R	y	B	r	Y	b	R	y	B			
			r	Y	b	R	y	B	r	Y	b	R	y	B	r	Y	b	

Figure 2.8: Two layer winding, under-pitched with half-filled end slots

The 3-phase winding of Fig 2.8 repeats every 6 slots to produce a 1 slot/pole/phase winding with 3 slots/pole. The chording factor of an under-pitched arrangement may be calculated from a knowledge of the pole- and coil-pitches and for the arrangement of Fig 2.8 it is $^2/_3$. A winding is usually under-pitched to improve the shape of the flux wave[7,33], but for any pitch the shape with a 1 slot/pole/phase winding is inferior to that obtained from a winding with a larger number of slots per pole per phase[43].

The speed of the travelling field is related to the pole-pitch by the expression[43]

$$V_s = 2 \lambda_p f \qquad (2.1)$$

where V_s = field speed or synchronous speed,

λ_p = pole-pitch, and

f = frequency of supply.

This expression is arrived at by noting that the field moves by two pole-pitches in one cycle of the supply. Not only does a winding occupying a larger number of slots per pole per phase produce a better shaped flux wave, it also increases the speed of the travelling field since the pole-pitch is increased with an increased number of slots/pole. Unfortunately this is not without cost, because the lengthened end connections result in greater end-turn losses, to a larger or smaller extent depending upon the type of linear device. It is also possible to produce an accelerating field[80], especially with a tubular machine, as is described in Chapter 4.

2.3 Applications for Linear Machines

Before the advent of linear motors, rotary machines with some form of rotary-to-linear convertor were used to produce linear motion, in addition to any mechanical gearing that might be necessary. Linear machines do not need these mechanical devices, making them robust and more reliable than rotary motors used to produce linear motion. There are a number of other advantages in the use of linear motors; for example higher accelerations and decelerations are possible with a linear machine than with a drive through wheels which depends upon friction, mechanical and electrical protection. In addition, an ability to withstand hostile environments can be provided for the primary by encapsulating the whole unit in an epoxy-resin compound; ice and grease have no adverse effects when linear machines are used for driving; thrust on the secondary is provided without mechanical contacts; the existence of a normal force can be used to advantage in levitation machines, and they are easy to maintain, repair and replace[7,34].

Linear machines may be broadly classified into three areas of application[32], force, power and energy machines. Force machines are generally used for short-duty applications operating either at standstill or at low speeds. They are comparatively small in size and

efficiency is not a major consideration. Power machines are large and highly efficient devices operating continuously at speeds in excess of 10 m/s; their principal application is in high speed ground transportation. Another name for energy machines is accelerators which aptly describes their function. These devices can never have an efficiency greater than 50%, as half the input energy is lost in the secondary and, like force machines, they are short-duty devices.

A large number of applications exist for linear machines, ranging from artificial heart drivers[50] to high speed ground transportation (HSGT)[10]. A few applications are presented below to illustrate the great variety which exist, the choice being centred primarily on the use of LIMs, TLIMs and TFLIMs, all of which have been investigated for powder transportation in the present study.

i) *Ground transportation*

High speed ground transportation (HSGT) has been, and probably still is, the main topic of concern in the development of linear machines, and both the LIM and the LSM have been investigated in detail for this application. Both machines have 3-phase windings on the primary, with the LSM having either a d.c. field winding or a set of permanent magnets on the secondary. Both have been considered for the propulsion and guidance of Maglev (a vehicle carried on a magnetic cushion) but studies have indicated that the LSM is better suited to HSGT[32]. In addition, the use of superconducting field windings for the LSM has also been studied and an experimental model, recently constructed in Japan, has shown considerable promise[30].

The application of linear machines to ground transportation is outside the scope of this present work although many papers exist[3-32]. This application is certainly not new, with a system for urban transportation using a LIM being proposed at the beginning of this century[51,52], while in 1914 HSGT was proposed by Japolsky[53] using attractive Maglev. However, Japolsky failed to pursue the idea due to the development of aviation, believing that air traffic would solve the whole problem of passenger transport.

ii) *Overhead cranes*

In the area of mechanical handling single-sided motors with steel secondaries[54] are often used, which usually limits the acceleration to below 0.5 m/s^2 and the maximum speed to about 1.5 m/s. Such machines have a pronounced attractive force between the primary and secondary which can amount to ten times the thrust and can therefore be used to advantage e.g. in a steel trolley forming part of a travelling crane[34,55].

Linear disc motors[56,32] have also been used to provide traction motion for overhead cranes, where the crane-track configuration does not facilitate its use as a secondary for a standard linear primary. Briefly, the secondary of the motor comprises a sandwich type disc which produces rotary motion, with the aid of one or more primaries mounted radially on either side of the disc[56]. Despite rotary motors, there are advantages with this form of drive: in particular a flexibility to meet given conditions by varying the supply frequency and using different material for the disc to produce different resistivities; the use of more than one primary; and for ease of maintenance, a faulty primary may be rapidly replaced.

iii) *Transfer trolleys*

The transfer of material by trolley is common in many industries and accurate positioning of the trolley is often required, both at the end of the track and at intermediate points. A positioning accuracy of ± 5 mm may be achieved with the use of a tachogenerator and thyristor speed control unit, in conjunction with a pair of linear stators mounted on the sides of the trolley[34]. A particular application involving linear motor drive to trolleys occurs in the plating industry, where parts are transferred on a series of trolleys to plating vats. The facility of accurate positioning has enabled punched-tape programming to be used to control the sequence of movement and the plating times taken. This application, like the previous one, requires machines which are categorised as low-speed, force-producing devices.

iv) *Pile-drivers*

A further low-speed application is the use of linear machines as pile-drivers or forging hammers, first proposed in the early 1920's by Trombetta[57] and Japolsky[58-60]. Japolsky's invention, an 800lb forging hammer, was of considerable interest to the mining industry in South Africa[61,62] and is still of interest today. A successful method using two LIMs to drive a hammer has been used for several years for the production of refractory brick blanks[63], and a pile-driver using a tubular linear machine has been studied and found to have good mechanical properties[64].

v) *Hazardous areas*

A wheeled vehicle with an attached aluminium-steel secondary may be made to move inside a toxic or irradiated atmosphere such that it is close to a row of linear primaries. These are mounted outside the walls of the enclosed area and, with their associated control circuitry, they provide the motive power to the vehicles. The motors, the control gear and the associated maintenance are all outside the hazardous area, yet the necessary motion is still provided[34,65].

A LIM has also been considered for closing down a nuclear reactor in order to prevent runaway[66]. In this application balls of boron (a neutron absorber) would be propelled along a non-magnetic stainless steel tube using a travelling magnetic field. Separating the metallic components of spent nuclear reactor fuel elements is also of considerable interest and two systems have been studied (one using a d.c. and the other an a.c. field) in order to generate a travelling field[67].

vi) *Conveyors*[33,34,68-71]

Linear machines, which would be classed as force devices, have been used to transport coal, steel stock sections, production-line belts and passengers (e.g. escalators).

Conveyor tables with free-running rollers are usually inclined so that gravity provides the motive power. The insertion of linear primaries at intervals between rollers can provide a simple drive thrust, with variable speed if necessary. In addition, an inverted conveyor

with a linear primary can be used to lift steel plates and to transfer them horizontally; switching off the primary allows the plate to fall onto another conveyor for processing.

Another type of conveyor is an individually powered trolley running in a track which acts as the secondary. Each load carrying trolley is fitted with one or two linear primaries, with the power conducting system built into the track. A variation on this, which has been used for ore transportation, uses several linear primaries fixed to the ground between the rails on which the trolleys run, with each trolley being fitted with an aluminium-steel secondary. An additional method of transporting ore is to use a conveyor belt which, if the belt contains sufficient metal, may be driven by one or more pairs of double-sided linear motors.

vii) *Actuators and pumps*

These two applications are usually achieved by tubular induction motors which operate at standstill or low-speed, thus classifying them as force-devices[33,43]. Theoretically, when comparing the flux pattern and thrust of flat linear and tubular machines, it is found that the TLIM has a reduced performance, which is compensated for by mechanical and cost advantages, for short-stroke operation[44]. Since these devices have a low flux density, laminations may be omitted from their construction, further simplifying their manufacture. This is however only possible because, for axial-flux machines, it is necessary that the secondary contains iron especially when the stator laminations have been removed[35,72], as mentioned earlier.

Tubular machines have been used for relatively short-stroke applications such as the operation of valves for liquids or gases, parcel sorting and large hopper doors and sluice gates[34]. (Tubular machines powered from a variable frequency supply have also been studied for use as actuators[73].) Although the force:weight ratio of the tubular device is inferior to that of a comparable hydraulic or pneumatic actuator, the advantages which make the device attractive are the absence of piping, the readily available a.c. power supply and the flexibility of load and stroke[35].

Tubular motor actuators have also been used for providing thrust to a trolley: if the secondary comprises an aluminium, steel-cored cable which can be strained sufficiently

then the TLIM itself can travel along the cable providing thrust to whatever provides support to the TLIM[74].

A major application for linear devices is in the area of magneto-hydrodynamics (MHD), especially linear machines with tubular primaries. If the solid conducting secondary of a linear machine is replaced with an ionised gas (plasma) or a liquid metal, the resulting device is a linear motion MHD machine. Such devices are used in metallurgy and nuclear plants as liquid metal pumps[7]. As this highly complex subject involving electromagnetic and hydrodynamic problems is outside the scope of this thesis, only a very brief description will be presented; more information may be found in the literature[38,75-79].

The advantages of linear devices in MHD applications are the absence of moving parts, the simplicity of construction, good sealing and easy maintenance. Not only can they pump but they may also be used to stir liquid metal[78]. Two types exist: the linear induction pump and the dc conduction pump, which functions like a motor. In general induction pumps are used for higher conductivity liquid metals and conduction pumps for those of lower conductivity. Numerous physical configurations for linear induction pumps and stirrers are feasible and three representative structures are:

a) linear flat induction pumps with a double-sided primary with or without lateral end plates of high conductivity (Fig 2.9[7]).

b) linear flat induction pumps with single-sided primary and no secondary back iron (Fig 2.10[7]).

c) linear tubular pumps (Fig 2.11[7]).

The primaries of these pumps[7] closely resemble those of the linear flat single-and double-sided motors and the tubular induction motor. Use of a central laminated core in the tubular pump enables flux to be attracted into the bore of the machine and therefore through the whole of the molten secondary.

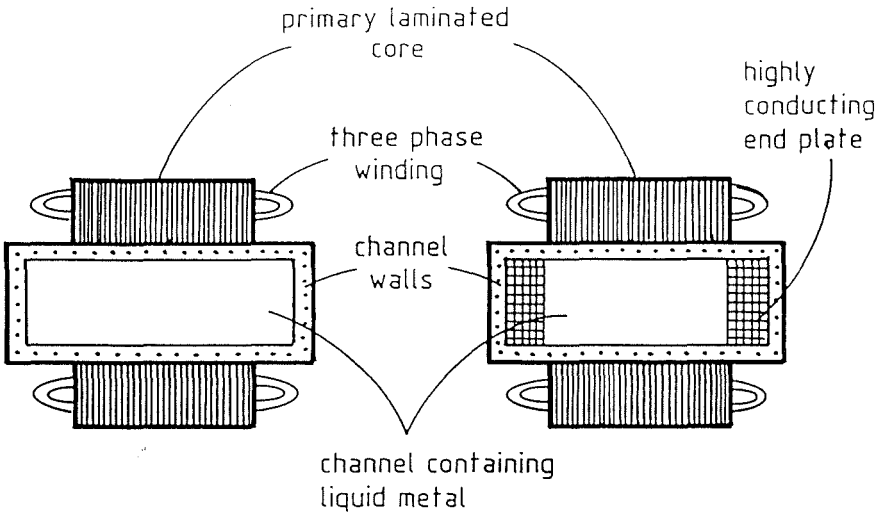

DOUBLE - SIDED LINEAR INDUCTION PUMP

Figure 2.9

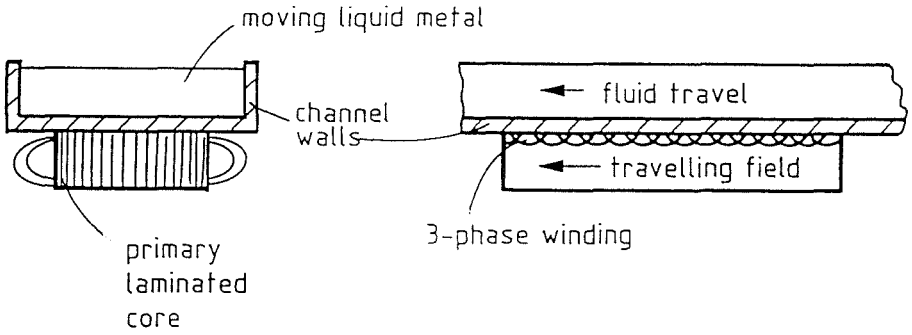

SINGLE - SIDED LINEAR INDUCTION PUMP

Figure 2.10

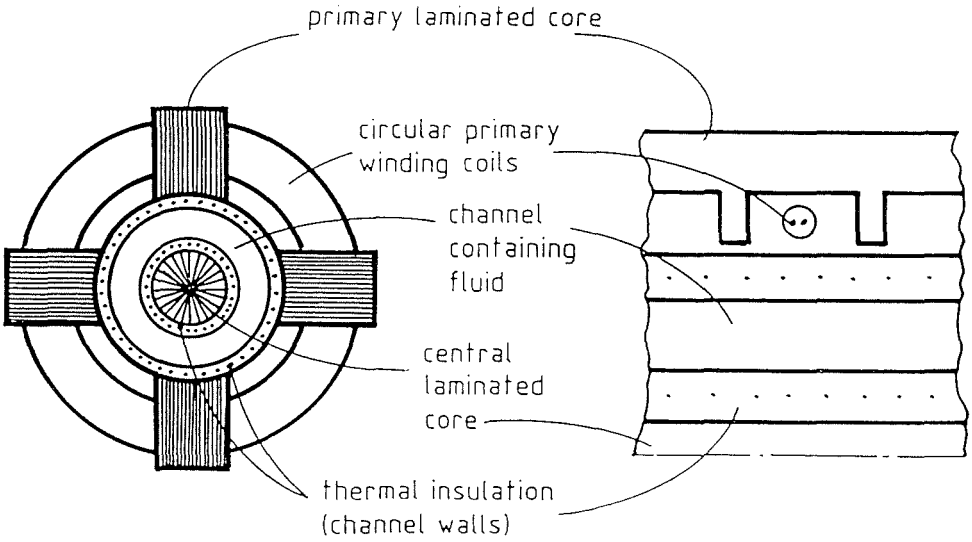

LINEAR TUBULAR PUMP

Figure 2.11

viii) *Accelerators*[33,80]

These short-duty machines are used to produce acceleration by imparting as much kinetic energy as possible to the moving member. One of the earliest applications was the Westinghouse aircraft launcher (Electropult[81]) built in 1946, where the primary was mounted on a carriage to which the aircraft was attached by means of a cable, and the secondary consisted of a slotted iron member carrying insulated windings. The primary was supplied with 700 A/phase and it was possible to accelerate a 5000 kg airplane to 50 m/s in a distance of 160 m in 4.2 s from rest.

The Motor Industry Research Association use a double-sided LIM for research into car-crash testing[82]. Mounted on a trolley which is automatically detachable from the vehicle, the DSLIM receives its power via rails running parallel to the test track and accelerates vehicles of 2500 kg mass up to 30 mph (13.4 m/s) in 4 s, over a distance of 80 feet (24.4 m).

Linear induction motors have also been used for impact-extrusion. A machine consisting of two double-sided motors was used to accelerate a mass to approximately 45 ft/s (13.7 m/s) with the mass acquiring 1000 lb-ft of energy[83].

ix) *Levitation*[33,84-88]

This is another major area to which linear machines have been applied, using either magnetic repulsion or magnetic attraction. The former machine is based on the principle that, if a magnet is moved over a non-magnetic conducting sheet, the eddy currents induced in the sheet give rise to a force of repulsion (due to Lenz's Law) between the magnet and the sheet.

An attraction-type levitation device is the 3-phase transverse flux machine, which consists of a set of E-cores, with the primary winding surrounding the centre-limb of each core. It is mounted on a non-magnetic frame but with a ferromagnetic secondary so that levitation occurs due to attractive forces. A feedback control system is usually required to stabilise the system.

The potential uses of levitators range from standstill applications such as active magnetic bearings and vibrating tables to the levitation and guidance of electrical vehicles. In addition, the normal forces developed in linear induction and linear synchronous machines are often used for levitation, especially in high-speed ground transportation applications[18,20-25].

Further applications of LIMs include sliding doors[89] (e.g. for warehouses and lifts) which may be operated via a linear primary attached to the door lintel and the secondary to the door itself. Such a system has the advantage that, in the event of a power failure, the doors may be hand operated. Small, high-speed goods lifts (e.g. in the construction industry) may be driven by LIMs to eliminate the need for a `motor house' at the top of the lift shaft[55,74]. Thin aluminium strip (between 0.5 and 1.4 mm) may be uniformly tensioned prior to coiling, using a bank of, for example, nine double-sided primaries to produce a constant flux over the full width of the strip[90,34]. Self-oscillating linear motors[91-95,33,43] have been considered for shuttle propulsion and package winding in the textile industry, and linear motor drives have also been developed for pen recorders[96] and personal computer printers[97].

2.4 The Application of Linear Devices to Powder Transport

It has become clear that there are a large number of applications for linear machines and that, in addition to these, a linear motor can move ferromagnetic powder, which travels in the opposite direction to the travelling magnetic field[98,99]. Although trolleys or conveyors could be used to transport iron powder, this thesis is concerned with using linear machines to transport directly the powder. Linear machines for this application do not fit readily into the categories of force, energy and power devices, since they are of low efficiency (similar to energy and force machines) and operate continuously (similar to power machines).

As much of the previous work in this area has primarily been concerned with the cleaning or separation of ferromagnetic powder from other material, the following discussion describes this application in some detail.

2.4.1 Background

The subject of cleaning magnetic materials has produced a number of patents[100-103], which relate to a range of particle sizes from metal chips to powders less than 200 mesh[104] (i.e. a particle having one of its physical dimensions no greater than an aperture of 75 micron as defined by a standard sieve[105]). Particle size analysis is often required by powder metallurgists and the application of a linear machine has been patented[106]. All the patents[100-103,106] describe the use of a travelling magnetic field to transport the particles, as other researchers[99,107-109] had discovered that the particles moved only when under the influence of such a field. The travelling field is generated in a variety of ways: by sequentially switching a set of coils energised from a single-phase supply, by rotating a set of bar magnets arranged in a radial fashion with alternating North-South polarity, or by energising a set of electromagnets using a 3-phase supply in what is effectively a simple form of linear motor[110].

Colloidal suspensions of single- or multi-domain particles behave as continuum ferromagnetic fluids and high rotation flow-rates are possible using rotating magnetic fields[107]. Having studied single-domain fluids, Moskowitz[107] suggested using such a fluid with a travelling field as a ferromagnetic pump. Shobair[111], who studied single- and multi-domain particles, found that the ferromagnetic fluid, and hence the magnetic particles, rotated in the opposite direction to the travelling field. Both authors suggest that every particle tends to behave like a permanent magnet (in the case of multi-domain particles) or a dipole (in the case of single-domain particles) trying to align itself with the applied field, thus producing torque. (This is also discussed in the next chapter, leading to the development of an hypothesis explaining the motion of a particle under the influence of a travelling field.)

Studies by Glazov[112] have shown that single-domain ferromagnetic suspensions can generate a "sizeable electrodynamic pressure head" due to the motion of the fluid under the influence of a linear motor, thus supporting the suggestion of their use as ferromagnetic pumps. His observations on ferrofluids set into motion by rotating magnetic fields have also shown that the fluid motion is counter to the rotational direction of the field[113]. It has been shown that, by using electromagnets and permanent magnets,

a ferromagnetic fluid can provide lift to a linear motor actuator, thus enabling the suspension and guidance of linear machines[114].

A powder cleaner[98] has been recently developed by Davy McKee (Sheffield) Ltd. in conjunction with Davy Linear Motors Ltd. As manufacturers of both water atomization and powder metallurgy extrusion plant, Davy McKee have an interest in reducing the inclusion content of their powders. By removing the refractory inclusions, the powder cleaner produces powder of sufficiently high quality from which commercially acceptable steel can be manufactured[115]. The cleaner consists of an inverted linear motor mounted on a rectangular framework as in Fig 2.12. A non-magnetic plate, along which the particles are made to move, aids in supporting the motor and this plate is contained within an enclosure having two outlets to which removable hoppers are fastened. A vibratory-feed device channels the powder deposited on it via another hopper into the magnetic field of the linear motor. Energising the motor from a 3-phase supply causes the particles to be attracted towards the non-magnetic plate. Most of the non-magnetic particles immediately fall into the first hopper, while a few are carried up with the magnetic particles. These particles are strongly agitated during their motion, causing more non-magnetic material (together with a very small amount of magnetic material) to be deposited into the first hopper. The remaining particles continue to travel towards the end of the motor, where they are dropped into the second hopper by having a separate winding on the last few teeth of the laminations which is energised independently of the main winding. Pulsing this winding "on" and "off" causes the magnetic powder to fall into the hopper.

2.4.2 Experimentation

Due to their interest in cleaning powder, Davy McKee initiated several research projects to study the phenomena involved and their experiments and findings are summarised below.

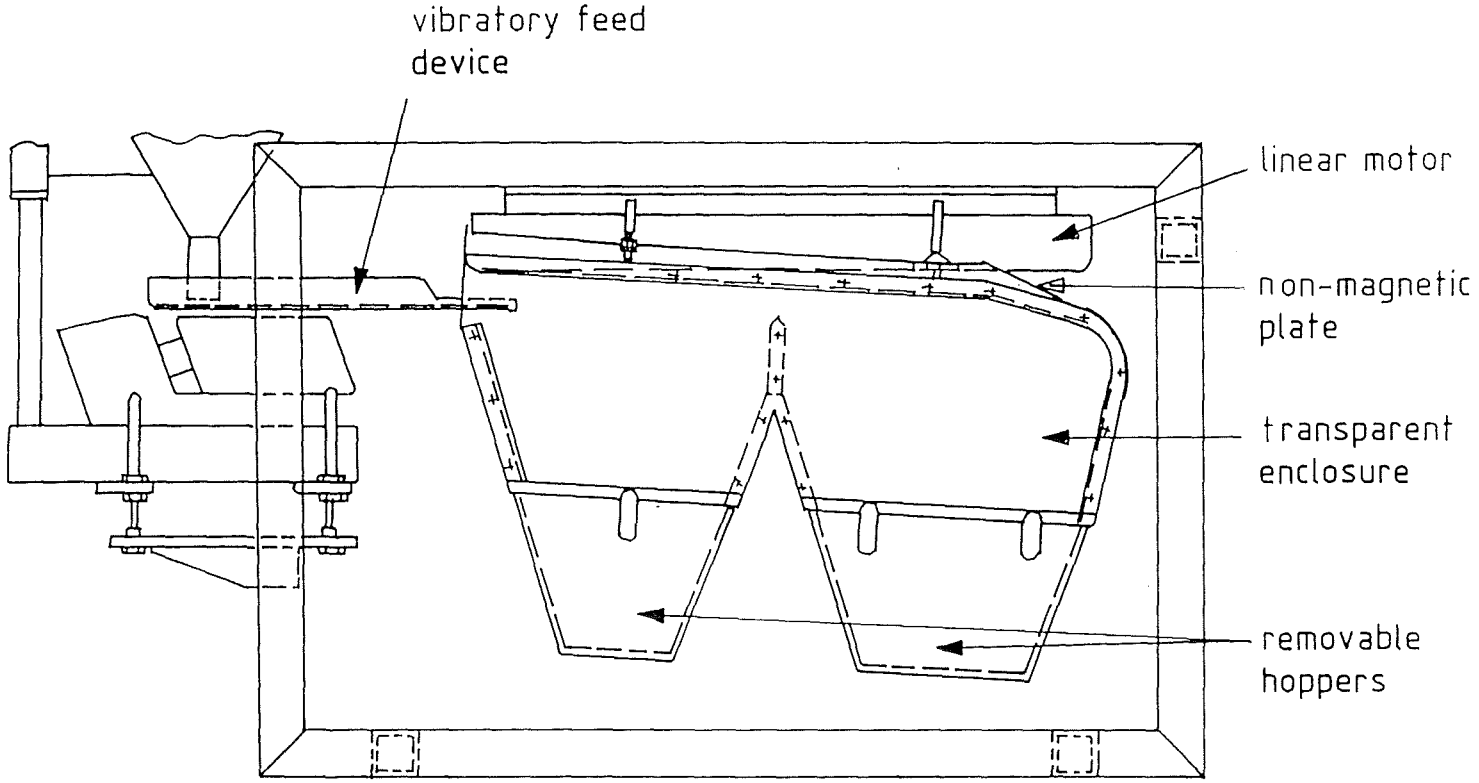

THE POWDER CLEANER

Figure 2.12

Particle Motion

During their investigations Davey McKee found that a number of factors influence the motion of the particles over the powder cleaner, including the mechanical configuration of the cleaner, e.g. the distance separating the vibratory-feed device from the motor; the feed rate of the powder into the motor's magnetic field; the powder characteristics (composition, inclusion content, particle size, etc.), and the electrical supply to the machine. It was observed that if the feed rate was too high, or if the transported powder was not discharged sufficiently quickly from the pulsed end, "blocking"[116] could occur predominantly at the two ends of the cleaner. Stationary ridges of powder, a few particle diameters deep, start to form at either or both ends of the cleaner and, as these grow steadily along the motor face, they hinder powder transport and eventually prevent it altogether. Some particles, however, traverse these ridges, as is shown schematically in Fig 2.13. Experiments carried out using a range of powders suggest that magnetically soft powders (such as of pure iron) are more susceptible to the formation of ridges. In order to discourage blocking, the vibratory feeder was fitted with a "diverter-plate" (see Fig 2.14). As the particles moved under this plate, they were attracted towards the motor and so collided with the plate. This hindered the particles being picked up in sheets, which was promoting blocking at the feed end. Measurements of transport rate against current (see Fig 2.15[116]) imply a quadratic relationship between the transport rate and the supply current; however the experimental conditions for the measurements were not provided.

Brown and Horsnell[99] discovered that, if a beaker containing ferromagnetic particles is placed inside the bore of an induction machine, the particles form thin layers (i.e. ridges, as described above) several millimetres apart when the applied voltage is low. If the voltage is increased and the layers are deliberately broken up, the authors observed a violently agitated cloud of particles having an ordered pattern corresponding to the instantaneous stator field distribution.

Glover and Minter[103] found the formation of ridges to be a hindrance, and their cure was to produce a discontinuity in the travelling field. They produced a travelling field by rotating a set of bar magnets arranged radially with alternating North-South polarity, with the repetitive pattern being disrupted at one point in the arrangement by a South pole

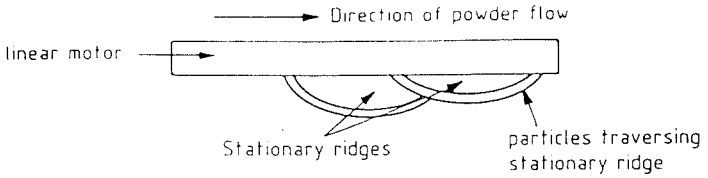

Figure 2.13 THE BUILD-UP OF POWDER ON THE MOTOR CAUSING BLOCKING

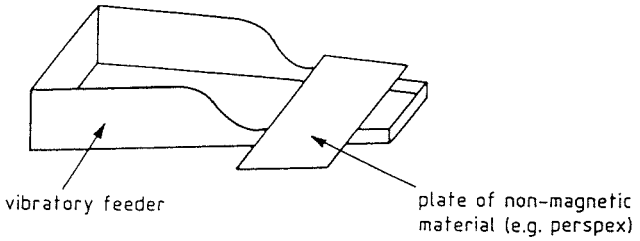

Figure 2.14 DIVERTER FIXED TO THE VIBRATORY FEEDER

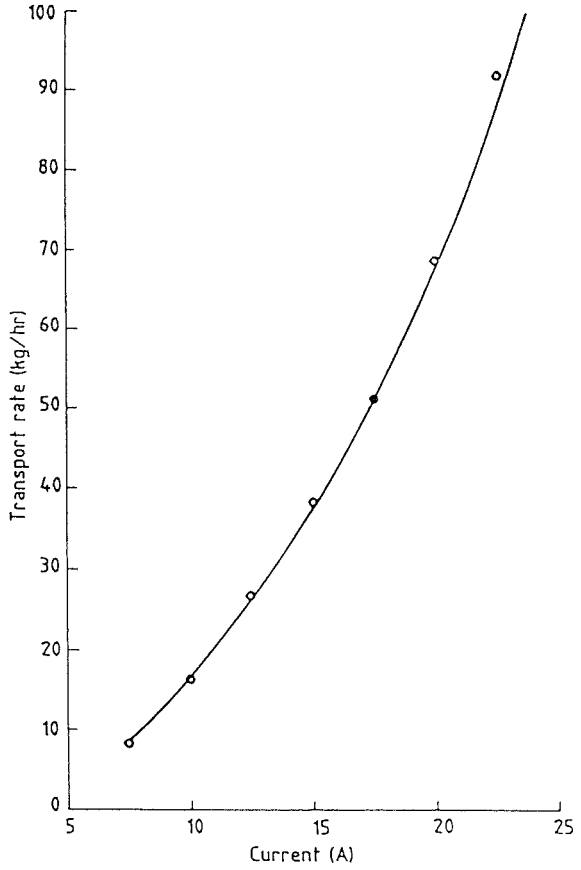

Figure 2.15 MASS TRANSPORT RATE AS A FUNCTION OF CURRENT

weaker than the other poles. This tended to break up, once every revolution, any ridges that had begun to form.

Rotating a permanent horse-shoe magnet under a tray of iron filings is one way of investigating a travelling field. Laithwaite[108] found that the particles spiralled inwards due to gyroscopic action and the shape of the field pattern. This was another problem that Glover encountered, which he resolved by positioning the bar magnets such that each had a slight angular displacement from a true radial alignment. This arrangement prevented the particles from migrating towards the centre of their tray, thus aiding the invention since the powder used was cleaned more efficiently.

Further experiments[117] were conducted by Davy McKee in order to determine whether the transport rate could be increased. By trying a number of powders having different particle size distributions, it was found that particles with a diameter greater than about 5 mm could not be transported. Such particles did not move parallel or anti-parallel to the travelling field but "tended to rotate round an axis parallel to the tooth to which they were attracted". However, no further information on the powder used or the speed of rotation of these particles was provided.

Magnetic Field

Using a 5 mm diameter, 40-turn search coil, the field profile along the linear motor was investigated. Readings for the horizontal and vertical components of the field were taken on and near tooth seven[118] (see Fig 2.16). It can be seen in Fig 2.17 that the horizontal component of the field was greatest across the gaps, and the vertical component was greatest across the teeth. Figures 2.18 and 2.19 indicate that, along the gaps and teeth, both the vertical and horizontal components of the field were strongest towards the edges of the motor, where the powder mostly travelled.

The field strength is a function of current and the transport rate was found to increase with current (Fig 2.15). Davy McKee developed a more powerful cleaner requiring currents of up to 1700A, with direct water cooling being necessary due to the considerable winding losses[117]. This prototype was an attempt to increase the mass transport rate by increasing the ampere-turns by 55% over the previous model. However

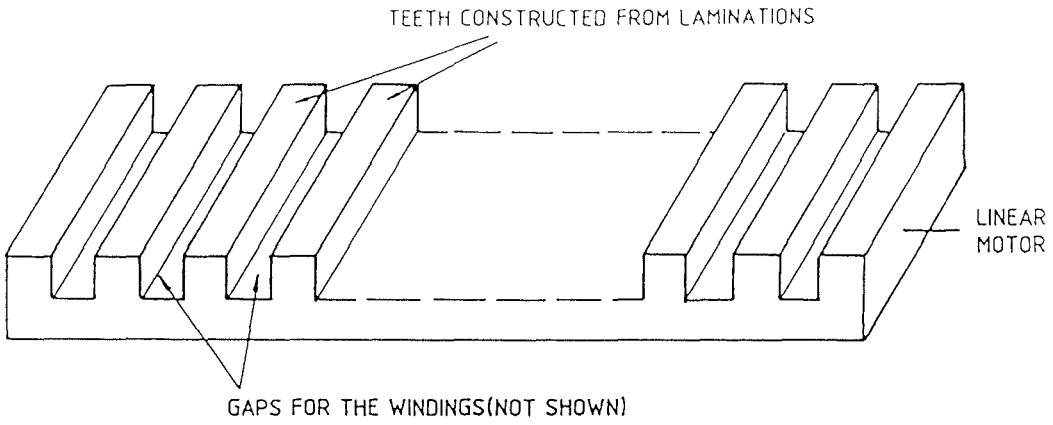

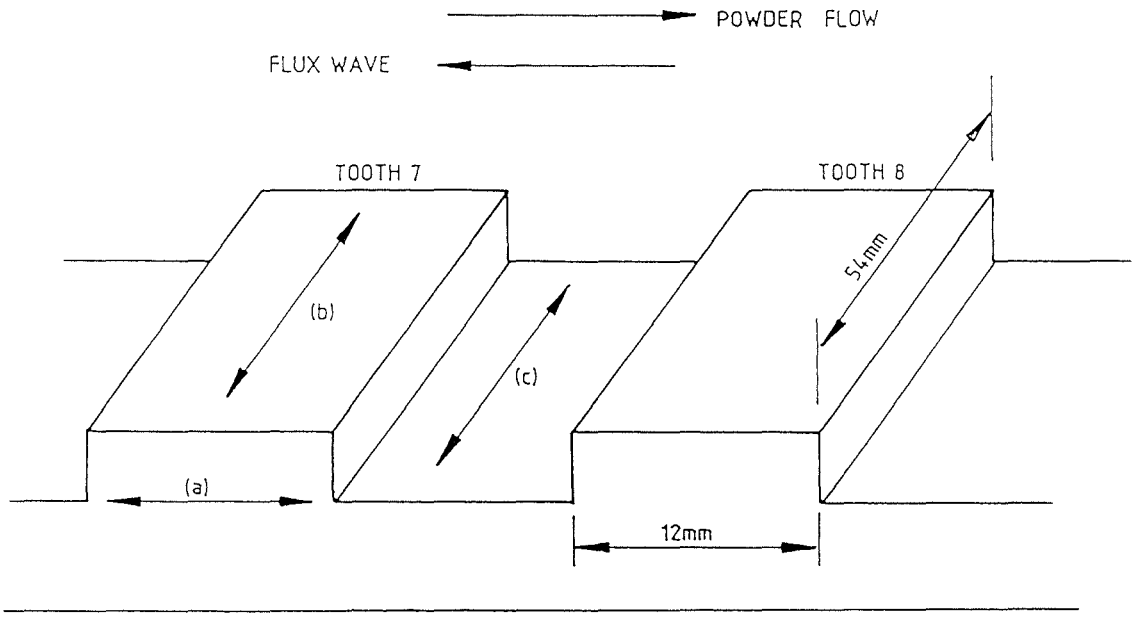

SCHEMATIC DIAGRAM SHOWING THE
AREA OF FIELD MEASUREMENTS ON THE ROTOR

(a), (b) Horizontal and vertical components of the field measured across a tooth
(c) Horizontal and vertical components of the field measured across a gap

Figure 2.16

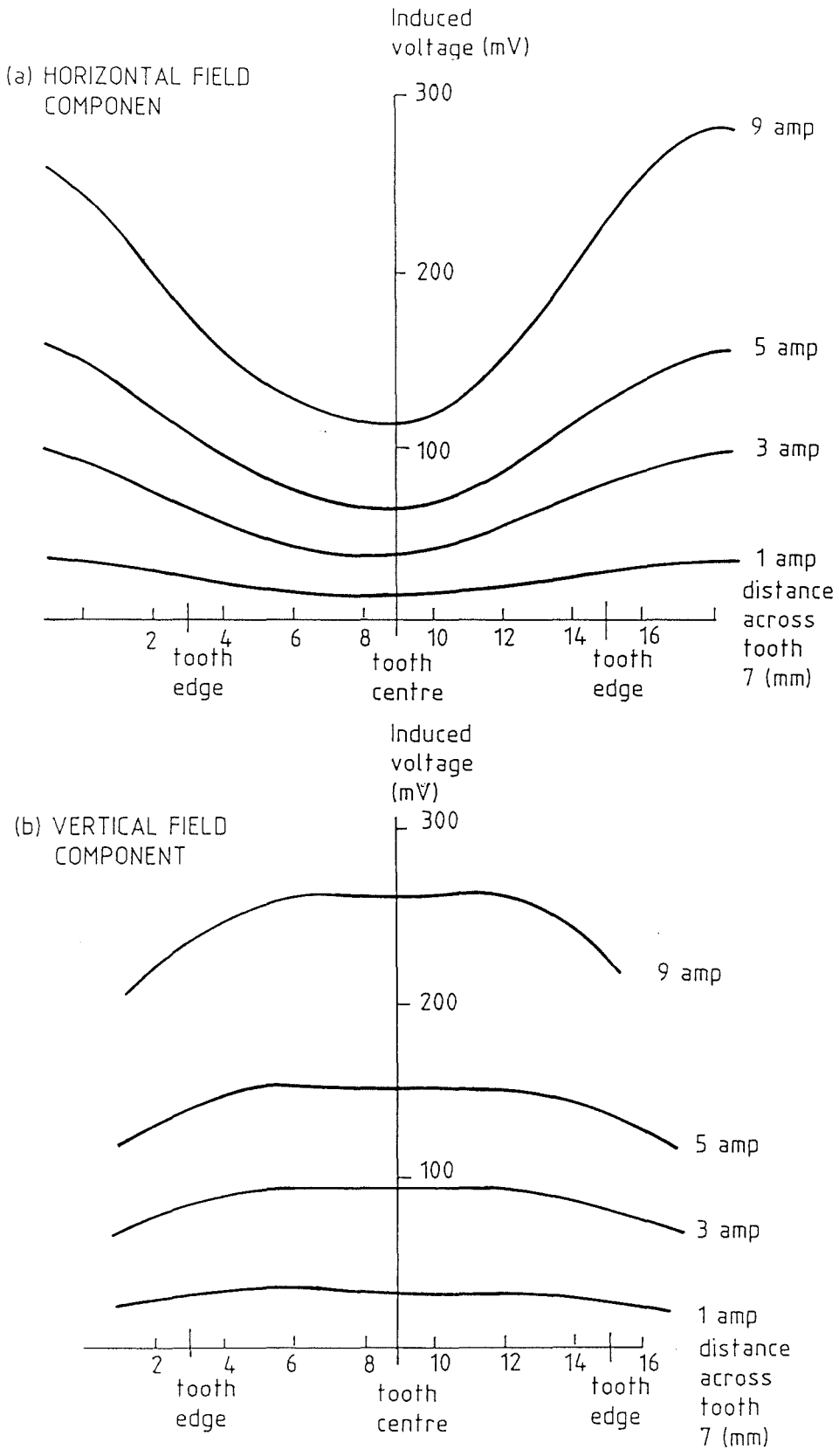

VARIATION OF THE FIELD ACROSS TOOTH 7

Figure 2.17

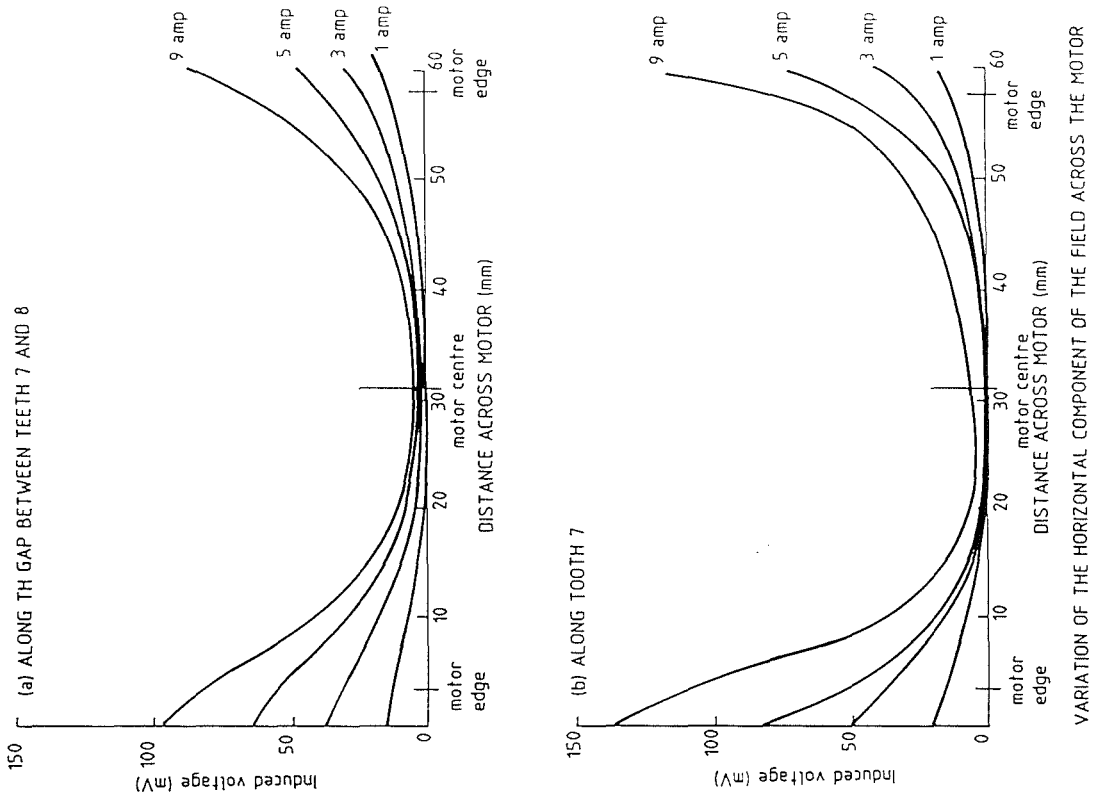

Figure 2.18

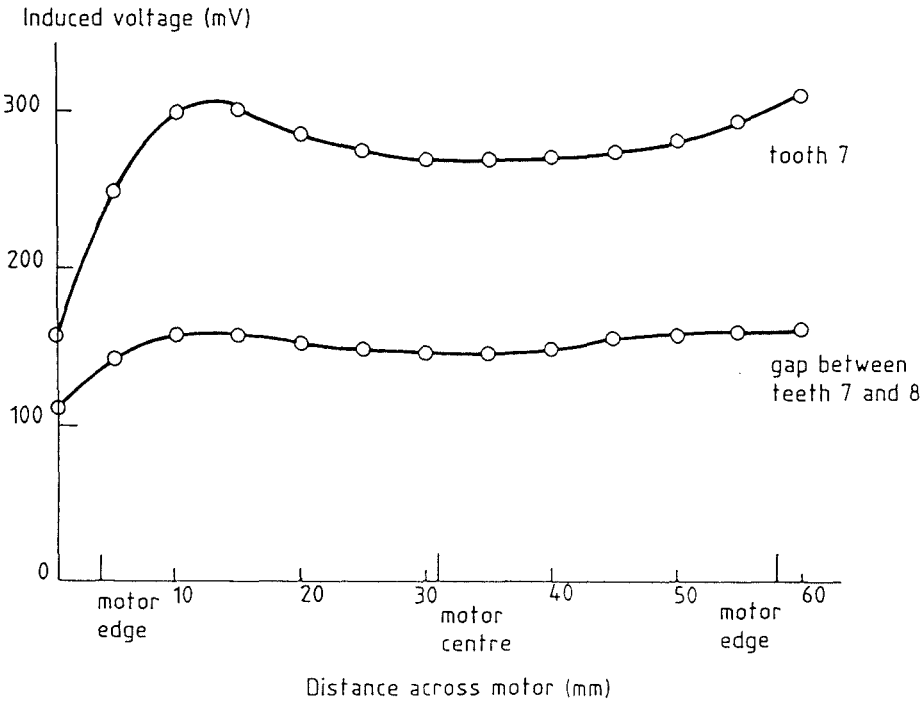

Variation of the vertical component of the field across the motor at 9A

Figure 2.19

the cleaner failed to perform as well as predicted. Due to the difficulties in winding the motor with copper pipes, it was wound under-pitched, whereas the previous motor was wound fully-pitched, and the tooth profile had been altered in order to accommodate the copper pipes. It appears that these factors had a detrimental effect on the transport rate.

Summary

Results from work carried out by Davy McKee give indications of the field profile of a LIM and that the transport rate increases with current (Figs 2.15, 2.17, 2.18 and 2.19). Their main interest was to discover whether the powder cleaner was capable of producing powder of sufficient quality with which commercially acceptable steel could be manufactured, and the cleaner was successful in this respect[115,116,118]. They then concerned themselves with attempting to increase the throughput of the cleaner by developing a new powder cleaner which failed to perform as expected[117] because other factors that could affect the transport rate were not considered.

2.4.3 Force on Ferromagnetic Particles

The difficult and complex problem of determining the force acting on ferromagnetic particles when under the influence of a travelling magnetic field has been studied[119-121]. Hesmondhalgh and Tipping[119] considered magnetic particles of different shape (block, cylinder and sphere) under the influence of the axial field produced by a DSLIM. They derived complicated expressions, requiring numerical integration for evaluation, for the force on the particles, and noted that the force on the different shapes were "very similar for the same overall dimensions". Unfortunately, their force-expressions are invalid for the present work, because the particle size in their study, although considerably less than a pole-pitch, is still much larger than the particles considered here.

Gopinath[120] also studied the force on ferromagnetic particles with shot-blasting applications in mind, using particles similar in size to the ones in the present investigation. Particles were accelerated along the axis of a set of coils connected to a 3-phase supply, i.e. a tubular linear machine. He found that, for ferromagnetic particles, reluctance forces predominate over conductance forces (which is also clear from the previous

discussion, since the iron particles travel in the opposite direction to the field) implying that the conductance forces may be neglected. (This may be shown by using non-magnetic powder, e.g. aluminium, which fails to move in either direction.) He derived an expression for the force on a spherical particle and Horsnell[121] extended this work to take into account the demagnetising effect[122] of an iron particle, thereby attaining closer agreement between predicted and experimental results.

2.5 Summary

This chapter has introduced and discussed some of the linear devices that are of relevance to the present investigation. It was noted that many linear machines exist, with new forms still being invented and further developments taking place through the study of different secondaries and winding arrangements. A number of applications were mentioned, culminating in a description of previous work connected with powder transport. Some characteristics of particle motion were described and applications such as cleaning (or sorting) ferromagnetic powder and the use of ferromagnetic fluids as pumps were discussed.

References

1. LAITHWAITE, E.R.: "A history of linear electric motors", (MacMillan Education Ltd, 1987, England).

2. LAITHWAITE, E.R.: "The development of linear electric motors - part 1", *Elec. Eng. (Australia)*, 1972, **49**, (4), pp.21-26.

3. LAITHWAITE, E.R. (Ed): "Transport without wheels", (Paul Elek (Scientific Books) Ltd, 1977, London).

4. LAITHWAITE, E.R. & BARWELL, F.T.: "Applications of linear induction motors to high-speed transport systems", *Proc. IEE*, 1969, **116**, (5), pp.713-724.

5. LAITHWAITE, E.R.: "The development of linear electric motors -part 2", *Elec. Eng. (Australia)*, 1972, **49**, (5), pp.14-18.

6. KLIMAN, G.B. & VON ZASTROW, E.E.: "Linear electric motors", *IAS Annual Meeting*, 1980, **1**, pp.256-261.

7. BOLDEA, I. & NASAR, S.A.: "Linear motion electromagnetic systems", (John Wiley & Sons Inc, 1985, USA).

8. SEIFERT, W.W.: "Technological aspects of high-speed ground transportation", *Proc. Instn. Mech. Engrs.*, 1966-67, **181**, 3G, pp.111-123.

9. POLGREEN, G.R.: "Magnetic suspension", ibid., pp.145-150.

10. BARWELL, F.T. & LAITHWAITE, E.R.: "Application of the linear induction motor to high-speed transport", ibid., pp.83-100.

11. LAITHWAITE, E.R. & BARWELL, F.T.: "Linear induction motors for high-speed railways", *Electronics & Power*, 1964, **10**, (April), pp.100-103.

12. ARMSTRONG, D.S.: "Application of the linear motor to transport", *Railway Gazette*, 17 Feb 1967, **123**, pp.145-150.

13. KOLM, H.H.: "Electromagnetic flight", *IEEE Trans. Magnetics*, 1974, **MAG-10**, (3), pp.397-401.

14. RHODES, R.G., MULHALL, B.E., HOWELL, J.P. & ABEL, E.: "The Wolfson Maglev project", ibid., pp.398-401.

15. URANKAR, L.: "Survey of basic magnetic levitation research in Erlangen", ibid., pp.421-424.

16. BURKE, P.E., TURTON, R.A. & SLEMON, G.R.: "The calculation of eddy losses in guideway conductors and structural members of high-speed vehicles", ibid., pp.462-465.

17. SEN, P.C.: "On linear synchronous motor (LSM) for high-speed propulsion", *IEEE Trans. Magnetics*, 1975, **MAG-11**, (5), pp.1484-1486.

18. OBERRETL, K. & KRATKI, N.: "Transients and oscillations in the repulsive magnetic levitation system", ibid., pp.1493-1494.

19. BURKE, P.E.: "The use of stranded conductors to reduce eddy losses in guideway conductors of high speed vehicles", ibid., pp.1501-1503.

20. RHODES, R.G. & MULHALL, B.E.: "The Wolfson magnetic levitation project", *Cryogenics*, 1975, **15**, (7), pp.403-405.

21. BORCHERTS, R.H.: "Repulsion magnetic suspension research - US progress to date", ibid., pp.385-393.

22. ATHERTON, D.L. & EASTHAM, J.F.: "Superconducting Maglev and LSM development in Canada", *IEEE Trans. Magnetics*, 1975, **MAG-11**, (2), pp.627-632.

23. REITZ, J.R. & BORCHERTS, R.H.: "US Department of Transportation program in magnetic suspension (repulsion concept)", ibid., pp.615-618.

24. SLEMON, G.R.: "The Canadian Maglev project on high-speed interurban transportation", ibid., **MAG-11**, (5), pp.1478-1483.

25. GUTBERLET, H.G.: "The German magnetic transportation program", *IEEE Trans. Magnetics*, 1974, **MAG-10**, (3), pp.417-20.

26. EASTHAM, A.R., DAWSON, G.E., SCHWALM, C.L. & KATZ, R.M.: "The testing of a single-sided linear induction motor with squirrel-cage and solid steel reaction rails", *Proc. Int. Conf. Elec. Mach.*, 1980, Pt. 1, pp.146-153.

27. EL-ANTABLY, A.M.: "Optimum steady state performance characteristics of a linear reluctance motor", ibid., 1982, Pt.3, pp.1046-1048.

28. BAUDON, Y. & IVANES, M.: "Simulation of the control of a linear synchronous motors propelled vehicle", ibid., pp.1038-1041.

29. ISMA'EEL, M.E.: "Supersonic-speed ground transportation and the space launcher", ibid., 1984, Pt.2, pp.1509-1512.

30. HOSNY, W.M. & DODDS, S.J.: "Applied superconductivity developments in Japan", *Power Engineering Journal*, 1993, **7**, (4), pp.170-176.

31. McLEAN, G.W.: "Review of recent progress in linear motors", *IEE Proc. B*, 1988, **135**, (6), pp.380-416.

32. EASTHAM, J.F.: "Novel synchronous machines: linear and disc", *IEE Proc. B*, 1990, **137**, (1), pp.49-58.

33. LAITHWAITE, E.R.: "Induction machines for special purposes", (George Newnes Ltd, 1966, London).

34. SADLER, G.V. & DAVEY, A.W.: "Applications of linear induction motors in industry", *Proc. IEE*, 1971, **118**. (6), pp.765-776.

35. NIX, G.F. & LAITHWAITE, E.R.: "Linear induction motors for low-speed and standstill applications", *Proc. IEE*, 1966, **113**, (6), pp.1044-1056.

36. MENDRELA, E.A. & GIERCZAK, E.: "Performance of rotary-linear induction motor with rotating travelling field", *Elec. Mach. & Pwr Systems*, 1984, **9**, (2-3), pp.171-178.

37. BUDIG, P.K. & TIMMEL, H.: "Helical motor for extremely small steps", *Proc. Int. Conf. Elec. Mach.*, 1986, Pt. 3, pp.1019-1022.

38. AUSTIN, P.R. & EASTHAM, A.R.: "Helically-wound linear induction pump for molten non-ferrous metals", *IEEE Trans. Ind. App.*, 1985, **IA-21**, (4), pp.738-748.

39. MENDRELA, E.A. & KAPLON, A.: "Rotary-linear induction motor with rotating-travelling field", *Proc. Int. Conf. Elec. Mach.*, 1982, Pt. 3, pp.1034-1037.

40. SHEHATA, M.A. & HANITSCH, R.: "Performance of the direct current linear motor with electronic commutation", ibid., 1980, Pt. 1, pp.256-268.

41. FOGGIA, A., OLIVIER, E., CHAPPUIS, F. & SABONNADIERE, J.C.: "A new three degrees of freedom electromagnetic actuator", *Proc. IEEE Conf. Industry Applications Society*, 1988, **1**, pp.137-141.

42. VADHER, V.V.: "Tubular linear induction motors with steel rotors", UPEC, 1986, pp.351-354.

43. LAITHWAITE, E.R.: "Propulsion without wheels", (English Universities Press Ltd, 1970, 2/e, London).

44. LAITHWAITE, E.R.: "Some aspects of electrical machines with open magnetic circuits", *Proc. IEE*, 1968, **115**, (9), pp.1275-1283.

45. LAITHWAITE, E.R., EASTHAM, J.F., BOLTON, H.R. & FELLOWS, T.G.: "Linear motors with transverse flux", *Proc. IEE*, 1971, **118**, (12), pp.1761-1767.

46. LAITHWAITE, E.R.: "The goodness of a machine", *Proc. IEE*, 1965, **112**, (3), pp.538-541.

47. EASTHAM, J.F. & ALWASH, J.H.: "Transverse-flux tubular motors", *Proc. IEE*, 1972, **119**, (12), pp.1709-1718.

48. FREEMAN, E.M.: "Equivalent circuit for the transverse flux tubular induction motor", *Proc. IEE*, 1975, **122**, (7), pp.744-745.

49. EASTHAM, J.F. & LAITHWAITE, E.R.: "Linear motor topology", *Proc. IEE*, 1973, **120**, (3), pp.337-343.

50. YAMAMOTO, Y., YAMADA, H., FUKUNAGA, S., MURASHITA, J., HAMANAKA, Y. & WAKIWAKA, H.: "Artificial heart driver using flat type linear pulse motor", *Proc. Int. Conf. Elec. Mach.*, 1986, Pt 3, pp.1187-1190.

51. ZEHDEN, A.: US Patent 732312, 1905.

52. WILSON, H.W.: "Electrification of railways", *Trans. Liverpool Engng. Soc.*, 1905, **26**, pp.218-229.

53. JAPOLSKY, N.: "Moving magnetic fields in electrical engineering and physics", *Scientific Journal of the Royal College of Science*, 1931, **1**, pp.105-126.

54. VADHER, V.V.: "Theory and design of linear induction motor with steel reaction plates", *IEE Proc. B*, 1982, **129**, (5), pp.271-278.

55. SADLER, G.V.: "Improvements in cranes and lifts", British Patent 967985, 1962.

56. DAVEY, A.W.: "Improvements in drives for cranes, hoists and travelling trolleys", British Patent 1185929, 1970.

57. TROMBETTA, P.: "The electric hammer", *Trans. AIEE*, 1922, **41**, pp.233-241.

58. JAPOLSKY, N.: "Über Magnetfelder mit veränderlicher Bewegungsgeschwindigkeit", *Archiv für Elektrotechnik*, 1924, **XIV**, (1), pp.106-128.

59. JAPOLSKY, N. & KOSTENKO, M.: "Improvements in installations for operating reciprocating electric motors", British Patent 214393, 1924.

60. JAPOLSKY, N.S. & PRESS, S.A.: "The production and use of variable-frequency currents", *Engineering*, 1926, **122**, pp.31-33, 99-100, 158-160.

61. HOLMAN, B.W.: "Recent research in ore dressing — magnetically operated stamps", *S.A. Mining and Engng Journal*, 1925, **36**, (2), pp.81-83.

62. BULLOCK, J.B.: "Some applications of variable frequency currents", *Trans. S.A. IEE*, 1926, **17**, pp.52-62.

63. SHI-KUN, C.: "A linear electric motor driven forging hammer mounted on a rocker-arm", *Proc. Int. Conf. Elec. Mach.*, 1984, Pt. 2, pp.477-480.

64. FUCHS, E.F. & SASAKI, K.: "Design of a resonant electromagnetic pile driver", ibid., pp.497-500.

65. FINCH, J.W.: "Linear doubly-salient magnetic couplers", ibid., 1982, Pt. 3, pp.1021-1024.

66. STRONG, G.H.: "Electromagnetic ball conveyor", *Elec. Engng.*, 1956, **75**, pp.1064-1069.

67. PENMAN, J. & WILLIAMSON, A.C.: "Feasibility of electromagnetic separation of irradiated nuclear reactor fuel-rod components", *IEE Proc. B*, 1980, **127**, (5), pp.277-286.

68. LAITHWAITE, E.R., TIPPING, D. & HESMONDHALGH, D.E.: "The application of linear induction motors to conveyors", *Proc. IEE*, 1960, **107A**, pp.284-294.

69. EBIHARA, D., YOSHIURA, T. & YOKOI, T.: "Design of a PM type linear stepping motor for automatic conveyor system", *IEE 2nd Int. Conf. Elec. Mach.- Design and Applications*, 1985, pp.265-269.

70. WEH, H., MAY, H. & KAUPERT, G.: "The asynchronous linear motor as a drive unit for belt drives", *Proc. Int. Conf. Elec. Mach.*, 1982, Pt. 3, pp.1000-1005.

71. WARD, F.G. & DAVEY, A.W.: "Improvements in drives for conveyors", British Patent 1148497, 1969.

72. SALEH, M.A., ZAHER, F.A. & FAHIM, A.A.: "An approach to the design of tubular actuators with composite secondaries", *Proc. Int. Conf. Elec. Mach.*, 1982, Pt. 3, pp.1053-1056.

73. FAHIM, A.A. & NOVOTNY, D.W.: "Considerations in the design of tubular linear induction motors for variable frequency operation", ibid., 1984, Pt. 2, pp.493-496.

74. DAVEY, A.W.: "Improvements in overhead travelling cranes or lifts driven by linear induction motors", British Patent 1152410, 1969.

75. BLAKE, L.R.: "Conduction and induction pumps for liquid metals", *Proc. IEE*, 1957, **104A**, pp.49-63.

76. KLIMAN, G.B.: "Large electromagnetic pumps", *Elec. Mach. & Electromechanics*, 1979, **3**, pp.129-142.

77. SUNDBERG, Y.: "Magnetic travelling fields for metallurgical processes", *IEEE Spectrum*, 1969, **6**, (5), pp.79-88.

78. SAJDAK, G., BARGLICK, J. & KUREK, K.: "Electromagnetic transport, feeding and stirring of liquid non-ferrous metals in the foundry industry", *Elektrowärme Int. B*, 1985, **43**, (1), pp.38-41.

79. NAMJOSHI, K.V. & BIRINGER, P.P.: "Fourier analysis of linear induction pumps with concentric windings and infinite arrays", *Proc. Int. Conf. Elec. Mach.*, 1980, Pt. 1, pp.109-116.

80. ONUKI, T. & LAITHWAITE, E.R.: "Optimised design of linear induction motor accelerators", *Proc. IEE*, 1971, **118**, (2), pp.349-355.

81. "A wound-rotor motor 1400 feet long", *Westinghouse Engineer*, 1946, **6**, pp.160-161.

82. DESIGN IDEAS: "Test cars propelled by largest ever linear induction motor", *Design Eng. (UK)*, May 1968, pp.117-119.

83. JOHNSON, W., LAITHWAITE, E.R. & SLATER, R.A.C.: "An experimental impact-extrusion machine driven by a linear induction motor", *Proc. Instn. Mech. Engrs.*, 1964-65, Pt. 1, **179**, (1), pp.15-35.

84. BEDFORD, B.D., PEER, L.H.B & TONKS, L.: "The electromagnetic levitator", *General Elec. Review*, 1939, **42**, (6), pp.246-247.

85. FREEMAN, E.M.: "Levitation or attraction due to a travelling field", *Proc. IEE*, 1968, **115**, (6), p.894.

86. RAJANATHAN, C.B., LOWTHER, D.A. & FREEMAN, E.M.: "Study of Xi-core transverse-flux plate levitator", *IEE Proc. B*, 1980, **127**, (3), pp.183-189.

87. HARRIS, M.R. & STEPHAN, S.Y.: "Support of liquid metal surface by alternating magnetic field", *IEEE Trans. Magnetics*, 1975, **MAG-11**, (5), pp.1508-1510.

88. EASTHAM, J.F. & WILLIAMSON, S.: "Experiments on the lateral stabilisation and levitation of linear induction motors", ibid., 1974, **MAG-10**, (3), pp.470-473.

89. REEKS, C.G. & DAVEY, A.W.: "Improvements in mean for automatically operating and controlling reciprocating motion", British Patent 1065562, 1967.

90. BOLTON, H.: "Forces in induction motors with laterally asymmetric sheet secondaries", *Proc. IEE*, 1970, **117**, (12), pp.2241-2248.

91. LAITHWAITE, E.R. & NIX, G.F.: "Further developments of the self-oscillating induction motor", *Proc. IEE*, 1960, **107A**, pp.476-486.

92. LAITHWAITE, E.R.: "Oscillating machines, synchronous and asynchronous", *Proc. IEE*, 1962, **109A**, pp.411-414.

93. LAITHWAITE, E.R. & MAMAK, R.S.: "An oscillating synchronous linear machine", ibid., pp.415-426.

94. WEST, J.C. & JAYAWANT, B.V.: "A new linear oscillating motor", ibid., pp.292-300.

95. ROUBICEK, O. & PEJSEK, Z.: "Oscillatory synchronous linear motor with permanent-magnet excitation", *IEE Proc. B*, 1980, **127**, (1), pp.8-12.

96. ZHI-GANG, D.: "A high performance d.c. linear motor for instrumentation", *Proc. Int. Conf. Elec. Mach.*, 1984, Pt. 2, pp.485-488.

97. KAMINSKI, G., BIERNAT, A. & SZCZYPIOR, J.: "Linear d.c. motor for graphical printer application", ibid., pp.521-522.

98. CAUSTON, J.R. & RICHARDSON, J.: Europe Patent 79300646.1, 1979.

99. BROWN, R. & HORSNELL, T.S.: "The wrong way round", *Elec. Review*, 1969, **184**, (7), pp.235-236.

100. McCARTHY, J.B.: US Patent 1417189, 1922.

101. PRESGRAVE, C.: US Patent 2975897, 1961.

102. WALLACE, D.L. & MARTINA, W.P.: US Patent 4062443, 1977.

103. GLOVER, D. & MINTER, M.J.: US Patent 4077872, 1978.

104. "Test sieve data", (Endecotts Filters Ltd, 1970, London).

105. BRITISH STANDARDS INSTITUTION: "Test sieves", BS410, 1986.

106. CAUSTON, J.R. & RICHARDSON, J.: Europe Patent 79300674.9, 1979.

107. MOSKOWITZ, R. & ROSENSWEIG, R.E.: "Nonmechanical torque-driven flow of a ferromagnetic fluid by an electromagnetic field'', *App. Phys. Letters*, 1967, **11**, (10), pp.301-303.

108. LAITHWAITE, E.R. & HARDY, M.T.: "Rack-and-pinion motors: hybrid of linear and rotary machines", *Proc. IEE*, 1970, **117**, (6), pp.1105-1112.

109. LAITHWAITE, E.R.: "How an experiment with iron filings provided new motor design information", *Elec. Review*, 1973, **192**, (3), pp.93-95.

110. LAITHWAITE, E.R.: "Experiments with a linear induction motor", (Tecquipment Ltd, 1972, Nottingham).

111. SHOBAIR, A.I.A.: "Investigations of some applications of primitive ferrofluids", (PhD Thesis, 1975, University of Sheffield).

112. GALZOV, O.A.: "Entrainment of a ferromagnetic suspension by a travelling magnetic field", Magnetohydrodynamics (USA), 1973, **3**, (July-Sept.), pp.395-396.

113. GLAZOV, O.A.: "Setting a ferromagnetic liquid into motion with a running magnetic field", Magnetohydrodynamics (USA), 1976, **4**, (Oct.-Dec.), pp.400-404.

114. FUJINO, Y., SAKAMOTO, T. & ADACHI, Y.: "Magnetic suspension and guidance using ferromagnetic fluid", *J. Electrical and Electronics Eng.*, Australia, 1989, **9**, (1/2), pp.44-49.

115. BARDSLEY, K.: "Progress report on Davy-Loewy powder cleaners DL66 and DL1000", (Internal report, Davy McKee (Sheffield) Ltd, 1980).

116. MOULD, S.J.: "An investigation into the removal of inclusions from metal powders by the use of a linear motor separator", (ibid., 1980).

117. RIGBY, M.: "Progress report on the development of the linear motor separator", (ibid., 1980).

118. SILVESTER, R.A.: "Progress report on the development of the linear motor separator", (ibid., 1981).

119. HESMONDHALGH, D.E. & TIPPING, D.: "Translational forces on discrete metallic objects in travelling magnetic fields", *IEE Proc. B*, 1981, **128**, (3), pp.137-148.

120. GOPINATH, A.: "An investigation into the uses of magnetic fields to accelerate ferromagnetic particles", (PhD Thesis, 1965, University of Sheffield).

121. HORSNELL, T.S.: "Acceleration of ferromagnetic particles by pulsed magnetic field and rotating magnet systems", (PhD Thesis, 1968, University of Sheffield).

122. OSBORN, J.A.: "Demagnetising factors of the general ellipsoid", *Phys. Rev.*, 1945, **67**, (11/12), pp. 351-357.

3. Preliminary Investigations

In this chapter, a one-dimensional force-expression is first derived, followed by a derivation of the expressions for the two-dimensional forces on a ferromagnetic particle due to a travelling magnetic field. (Although the one-dimensional expression may be obtained from the expressions given by Gopinath[1] and Horsnell[2], it is useful to derive it here using a similar approach to the derivation of the two-dimensional expression thus clarifying the latter derivation). The initial experiments on the powder cleaner (see Chapter 2) provided by Davy McKee (Sheffield) Limited are then described, followed by a discussion of a hypothesis for the motion of ferromagnetic particles under the influence of a travelling magnetic field. Particle motion on the powder cleaner was investigated using high-speed photographic techniques, and the experimental particle velocities and motional characteristics of different ferromagnetic powders are compared with predictions from the hypothesis.

3.1 Derivations of the Forces on a Ferromagnetic Particle

It is shown in Appendix A that for a particle of relative permeability μ_r,

$$M = \frac{(\mu_r - 1)}{1 + (\mu_r - 1)D} \cdot B \qquad (3.1)$$

where M = dipole moment per unit volume (the intensity of magnetisation);
B = magnetic flux density prior to the introduction of the particle;
and D = demagnetising factor[3].

The demagnetising factor for the prolate spheroid[3,4] (a special case of the general ellipsoid with semi-axes a, b, c such that b = c and a > b) along the long axis is given by,

$$D = \left[\frac{1}{e^2} - 1\right]\left\{\frac{1}{2e} \ln \frac{(1 + e)}{(1 - e)} - 1\right\} \qquad (3.2)$$

where e = eccentricity of the ellipse, $\left[1 - \frac{c^2}{a^2}\right]^{\frac{1}{2}}$.

3.1.1 One-dimensional Force

Consider a rod-like magnetic particle of length 2a and diameter 2c, situated in a travelling field such that its centre is at a distance x from some arbitrary origin. At its ends, let it have pole strengths of m_1 and m_2. Since the force on a pole[5] is given by F = H(x).m (i.e. H is a function of x), then the forces on the poles of the particle are:

$$f_1 = m_1 H(x + a) \qquad \text{and} \qquad f_2 = m_2 H (x - a),$$

where H is the magnetic field intensity prior to the introduction of the particle, i.e. (B/μ_0), and the total force is F = f1 + f2. The applied field B travels sinusoidally in the x-direction with

$$B = \hat{B} \sin \left[\omega t - \frac{2\pi}{\lambda} x \right] \tag{3.3}$$

where ω = angular supply frequency;

t = time, and

λ = wavelength = $2\lambda_p$; λ_p = pole-pitch.

Noting that $m_2 = -m_1$ and letting $m = m_1$, then substituting from eqn (3.3) and eqn (3.1) leads to (see Appendix A)

$$F = - \left[\frac{\mu_r - 1}{1 + (\mu_r - 1)D} \right] \left[\frac{\hat{B}^2}{\mu_0} \right] \pi c^2 . \sin \left[\frac{2\pi}{\lambda} a \right] . \sin 2 \left[\omega t - \frac{2\pi}{\lambda} x \right] \tag{3.4}$$

From eqn (3.3), the field travels in the positive x-direction, but eqn (3.4) shows that the force on a particle is directed in the negative x-direction, with the magnitude of the force being dependent upon the size, shape and relative susceptibility of the magnetic particle. With a sinusoidal travelling field, the force also varies sinusoidally but at twice the frequency.

3.1.2 Two-dimensional Forces

Although Gopinath and Horsnell did not do so, the above expression for the one-dimensional force on a particle may be derived using their treatment (see Appendix A). What is lacking, however, is any particle motion in the y-direction; the expression assumes that the particle moves in a line parallel to, and coincident with, the active surface of the linear machine. The force expression may however, be extended to allow the particle to travel in a plane parallel and normal to the plane of the active surface of the LIM (the author is unaware of this having been done previously). In this case, if B_x is the component of the field in the x-direction and B_y in the y-direction then[6],

$$B_x = \hat{B} \exp(-2\pi y/\lambda) \,.\, \sin\left[\omega t - \frac{2\pi}{\lambda} x\right] \tag{3.5}$$

and

$$B_y = \hat{B} \exp(-2\pi y/\lambda) \,.\, \cos\left[\omega t - \frac{2\pi}{\lambda} x\right] \tag{3.6}$$

The demagnetising factor[4] in the y-direction is given by,

$$D_y = \frac{1 - D_x}{2} \tag{3.7}$$

The force on the particle (see Appendix A) may be shown to be

$$F_x = - K_x A_x \frac{\hat{B}^2}{2\mu_0} \{E_1 - E_2 - e_3\} \tag{3.8a}$$

$$F_y = K_y A_y \frac{\hat{B}^2}{2\mu_0} \{E_1 - E_2 + e_3\}$$

$$= - \left[\frac{K_y A_y}{K_x A_x}\right] F_x + K_y A_y \left[\frac{\hat{B}}{\mu_0}\right] . e_3 \qquad (3.8b)$$

$$= \left[\frac{1 + (\mu_r - 1) D_x}{1 + (\mu_r - 1) D_y}\right] \left[\frac{a}{c}\right] F_x + K_y A_y \left[\frac{\hat{B}}{\mu_0}\right] . e_3$$

where $$E_1 = \exp\left(-2\pi Y_1/\lambda\right) . \cos 2 \left[\omega t - \frac{\pi}{\lambda} X_1\right] \qquad (3.9)$$

$$E_2 = \exp\left(-2\pi Y_2/\lambda\right) . \cos 2 \left[\omega t - \frac{\pi}{\lambda} X_2\right] \qquad (3.10)$$

$$e_3 = \left[\exp\left(-2\pi Y_1/\lambda\right) - \exp\left(-2\pi Y_2/\lambda\right)\right] . \cos \left[\frac{2\pi}{\lambda} a . \cos \theta\right] \qquad (3.11)$$

$$K_x = \frac{\mu_r - 1}{1 + (\mu_r - 1) D_x} \qquad (3.12a)$$

$$K_y = \frac{\mu_r - 1}{1 + (\mu_r - 1) D_y} \qquad (3.12b)$$

$$A_x = \pi c^2 \qquad (3.13a)$$

$$A_y = \pi c a \qquad (3.13b)$$

$$X_1 = 2x + a . \cos \theta; \qquad X_2 = 2x - a . \cos \theta \qquad (3.14a)$$

$$Y_1 = 2y + a . \sin \theta \qquad Y_2 = 2y - a . \sin \theta \qquad (3.14b)$$

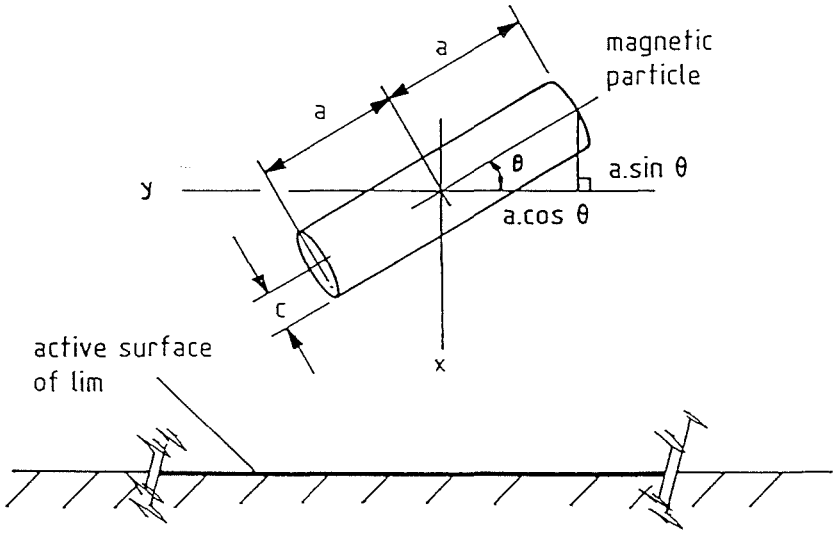

MAGNETIC PARTICLE UNDER THE INFLUENCE
OF A TRAVELLING MAGNETIC FIELD

Figure 3.1

and θ is the angle made by the axis of the particle with the horizontal (see Fig. 3.1).

Consideration of the expressions for the force on a particle shows that F_x and F_y both consist of an exponentially scaled travelling wave E_2 (see eqn (3.10)), subtracted from another, differently exponentially scaled travelling wave E_1 (see eqn (3.9)), both waves travelling in the positive x-direction. The scaling factors and the travelling waves both depend upon the position of the particle with respect to the stator of the linear machine. Both forces (see eqn (3.8)) are further modified by the relative susceptibility of the particle (eqn (3.12)) and the size and shape of the particle (eqn (3.13)). Note again that F_x is directed in the negative x-direction, i.e. in opposition to the travelling magnetic field, and that F_x and F_y both vary at twice the frequency of the impressed travelling field. F_x is greatest when $e_3 \rightarrow 0$ which occurs when $\theta = 0$ (i.e. the particle in Fig 3.1 is parallel to the stator); F_y is greatest when $e_3 \rightarrow$ maximum which occurs when $\theta = \pi/2$ (i.e. the particle in Fig 3.1 is normal to the stator), both as expected from eqn (3.11). The term e_3 (see eqn (3.11) scales the forces F_x and F_y due to the height of the particle above the stator, its orientation and its semi-length (see also eqn (3.15b)). The height of the particle above the stator also modifies the magnitudes of the travelling waves E_1 and E_2 (eqns (3.9) and (3.10)) and the start positions of these travelling waves are shifted due to the orientation of the particle.

It is easily seen that if $\theta = 0$ and $y = 0$ (the constraints of the previous case), by substituting from eqns (3.9) to (3.14), eqn (3.8) simplify to

$$F_x|_{y,\theta=0} = - K_x A_x \frac{\hat{B}^2}{\mu_0} . \sin \left[\frac{2\pi a}{\lambda} \right] . \sin 2 \left[\omega t - \frac{2\pi}{\lambda} x \right] \qquad (3.15a)$$

$$F_y|_{y,\theta=0} = - \left[\frac{K_y A_y}{K_x A_x} \right] F_x|_{y,\theta=0} \qquad (3.15b)$$

If we now substitute for K_x, A_x, K_y and A_y then, as expected, eqn (3.15a) is seen to be the same as equation (3.4) and eqn (3.15b) becomes

$$F_y|_{y,\theta=0} = \left[\frac{(\mu_r - 1)}{1 + (\mu_r - 1)D_y}\right]\left[\frac{\hat{B}^2}{\mu_0}\right]\pi ca \,.\, \sin\left[\frac{2\pi a}{\lambda}\right] \,.\, \sin 2\left[\omega t - \frac{2\pi x}{\lambda}\right] \qquad (3.16)$$

Equation (3.16) shows that the y-directed force, similar to the x-directed force in eqn (3.4), varies sinusoidally at twice the frequency of the impressed field and that its magnitude is also dependent upon the size, shape and relative susceptibility of the magnetic particle. This expression further indicates that at $\omega t = 0$, the force $F_y|_{y,\theta=0}$ is directed in the negative y-direction, i.e. towards the stator of the linear machine, thereby attracting the iron particle. This force is positive, i.e. directed away from the stator thus repelling the particle, when

$$\sin 2\left[\omega t - \frac{2\pi x}{\lambda}\right] > 0 \qquad (3.17a)$$

which occurs when

$$2n\pi < 2\left[\omega t - \frac{2\pi x}{\lambda}\right] < (2n + 1)\pi \qquad (3.17b)$$

where $n = 0, 1, 2, \ldots$

Solving for x (see Appendix A) gives the following limits for x

$$V_s \,.\, t - \left[n + \frac{1}{2}\right]\frac{\lambda}{2} < x < V_s \,.\, t - n\frac{\lambda}{2} \qquad (3.18a)$$

where $V_s = f\lambda$, the speed of the travelling field, and

$\frac{\lambda}{2} = \lambda_p$, the pole-pitch.

Thus, for a given instant of time, particles lying within the limits of eqn (3.18a) will be repelled from the LIM stator because $F_y|_{y,\theta=0}$ becomes positive. Conversely, when

$$V_s . t - \left[n + \frac{1}{2}\right] \frac{\lambda}{2} > x > V_s . t - n\frac{\lambda}{2} \qquad (3.18b)$$

then particles lying within these limits will be attracted to the device, and the particles at the boundaries (i.e. when the inequalities of eqn (3.18) become equalities) will experience a zero net vertical force. Equations (3.18) give values for x over a pole-pitch rather than over two pole-pitches because the force varies at twice the rate of the travelling field as already noted.

3.2 High-Speed Photographs

Modifications to the powder cleaner (see Chapter 2) enabled ciné films to be taken illustrating the motion of powder along the stator of the cleaner. The non-magnetic plate which supported the linear motor, the transparent enclosure and the hoppers (see Fig 2.12) were removed and a new, flat non-magnetic plate was used to support the motor. Two perspex sheets were attached through which the powder could be viewed and, together with a third sheet fixed to the framework transverse to the direction of motion of the powder, prevented particles being thrown clear of the cleaner. Finally, a perspex box was used to collect powder that fell from the cleaner.

Using a Hycam 400 camera[7-9] and intense illumination enabled high-speed, 16 mm filming of the motion of particles along the powder cleaner[10]. Initially coarse, rod-shaped iron filings were used, having the size distribution of Fig 3.2 as found from a standard sieving procedure[11,12]. Photographic stills produced from the films are given in Fig 3.3, where Fig 3.3(a) shows the full length of the cleaner, Fig 3.3(b) how the powder was lifted from the vibratory feeder and Fig 3.3(c) an area at the middle of the cleaner. The last section of the cleaner has a winding separate from the remainder, which is pulsed "on" and "off" to deposit iron powder in a container (see Chapter 2). Figure 3.3(d) shows this section at the instant when power to the winding has just been switched off.

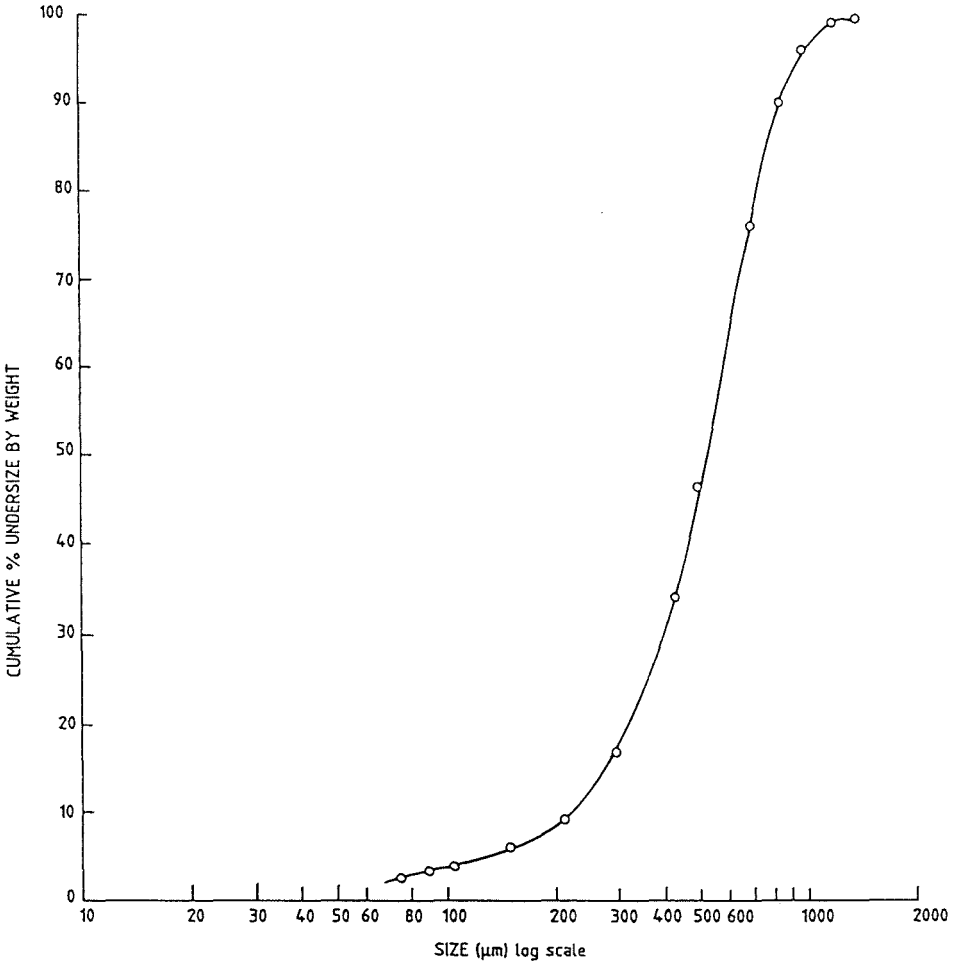

THE SIZE DISTRIBUTION OF IRON FILINGS

Figure 3.2

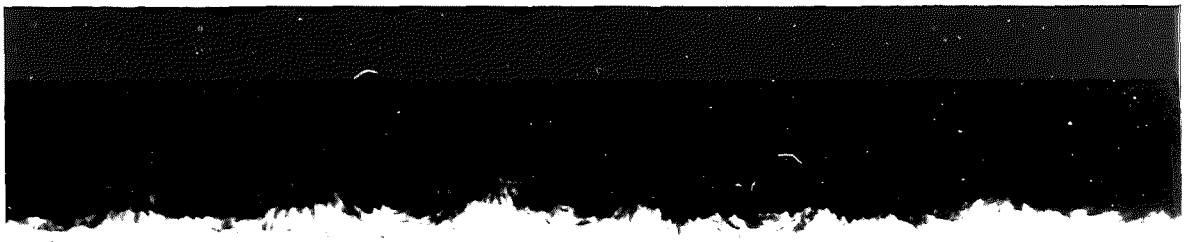

(a) full length of powder cleaner (430mm approx.)

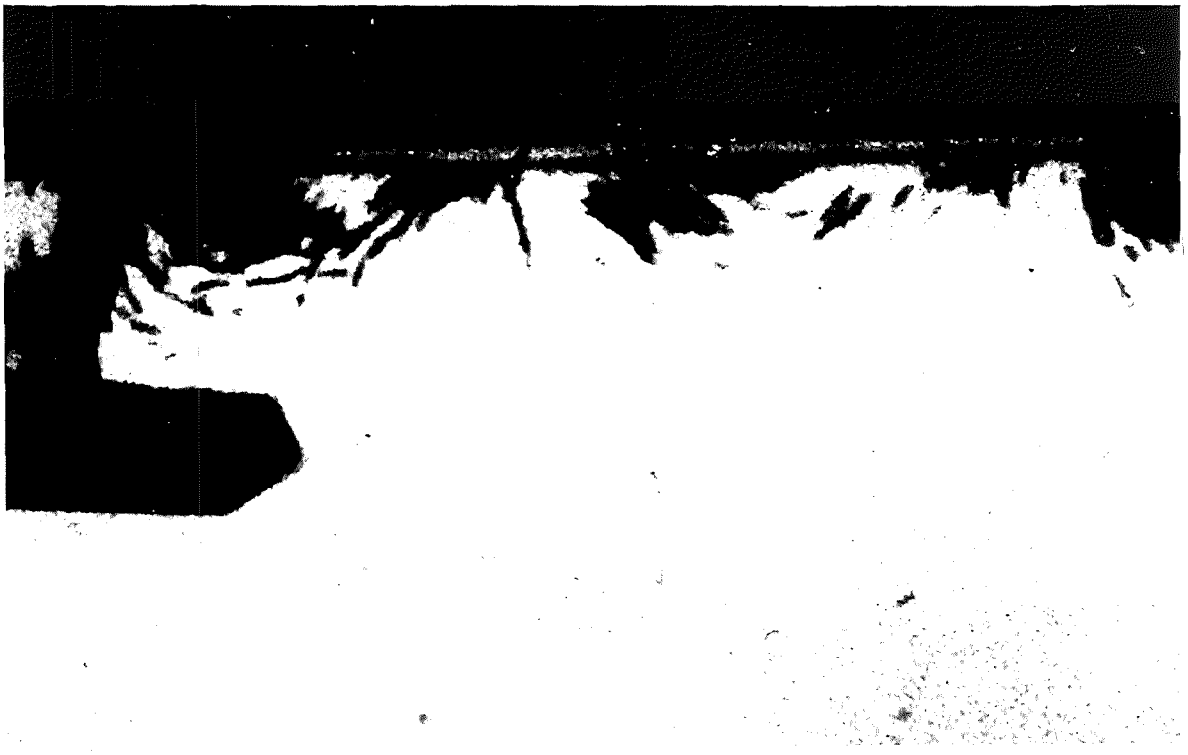

(b) pick-up end of powder cleaner

MOTION OF IRON FILINGS ALONG THE POWDER CLEANER
(continued ...)

Figure 3.3

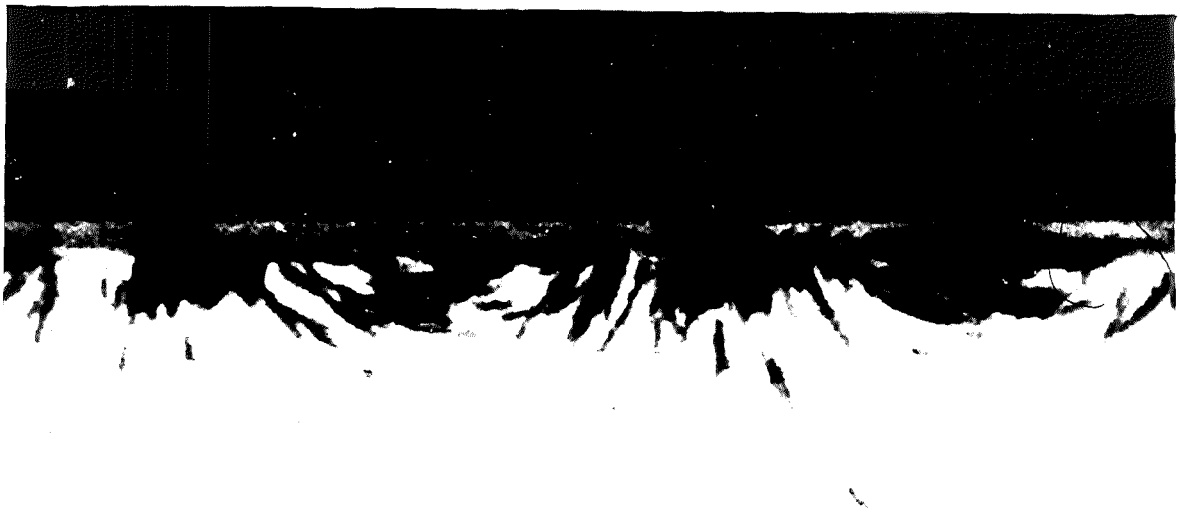

(c) middle section of powder cleaner

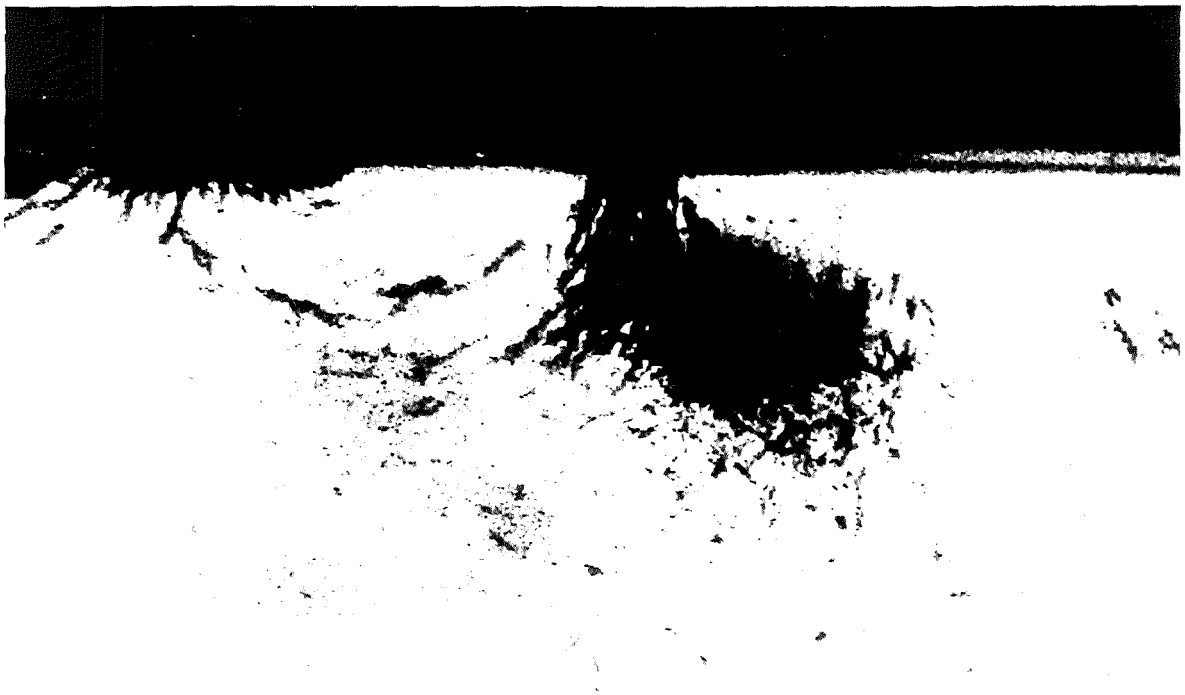

(d) pulsed end of powder cleaner

MOTION OF IRON FILINGS ALONG THE POWDER CLEANER

Figure 3.3

A qualitative description of the powder's motion based on these high-speed photographs is given below.

3.2.1 Particle Motion

It was noticed initially that the particles moved in bunches as can be seen in Fig 3.3(c), with each bunch increasing and decreasing in size as it travelled, giving the appearance of wave-like motion. As a particle-bunch moved to the next part of the linear device, the position it had vacated was taken up by the following particle-bunch. However some particles from the bunch did not remain with the bunch but became part of the succeeding particle-bunch. This motion appeared to be similar to that of sea waves where, as the water bobs up and down, energy is transferred down the wave until it is finally transformed into translational motion near the seashore where the water breaks.

On closer inspection it was evident that particles transported via different modes, with some travelling individually and some in strings, a number of which when close together form a particle-bunch (see Fig 3.3(b) and (c)). During their motion, the particles would leave the motor-face and rotate an integral number of quarter-revolutions before returning either to their previous position or to a position further along the linear motor. Particles that remained close to the motor-face tended to rotate by up to three quarter-revolutions, whereas those that were considerably further away (i.e. 25 mm or more) continued to rotate until they returned to the motor-face having completed a revolution or more. These particles sometimes travelled up to 150 mm before beginning to move back towards the motor and, during their travel, rotated an integral number of half-revolutions. Particles remote from the motor tended to travel with an orientation such that their flat-side faced the motor and to rotate suddenly. Particles close to the motor-face rotated smoothly while in flight (i.e. travelling from one point on the stator to another while not in contact with the stator during their travel) but only by half a revolution during the time of leaving the motor-face and returning to the motor-face.

The particle-strings comprising only two or three particles tended to hold together quite well during their motion, although as they were thrown from the motor-face the strings would break up and new ones would form. It was due to the violent, agitated motion that longer particle-strings were not sufficiently stable to hold together. At times particles

were thrown about 50 mm from the LIM, yet they still continued to follow the field, continuing to rotate as they were brought back to the motor-face. The fact that many particles travelled in strings suggests that they were acting like tiny permanent magnets and, by forming strings, were decreasing the local field (see later).

At the start of the machine (Fig 3.3(a)), a few mostly non-ferromagnetic particles did not travel and could be clearly seen to tumble randomly off the device. Due to the continuous stream of particles fed to the LIM by the vibratory feeder some non-magnetic material was carried with the magnetic particles. The violent and agitated motion caused more non-magnetic material (together with a small amount of magnetic material) to fall off the device. If this material (usually a small fraction of the total) was re-introduced, more magnetic material was seen to transport to the end of the device. Depending upon its size distribution and content, this re-introduction could sometimes be repeated up to three times, thereby drawing out more magnetic powder from the non-magnetic. Not all the magnetic powder was drawn out during the first pass, because of the violent motion and because of adhesion between smaller particles.

3.2.2 Particle Speeds

The powder cleaner was a 3-phase, star-connected device operating at 50 Hz and with a tooth pitch of 18.67 mm. It was $^2/_3$ chorded, wound with one slot per pole per phase and the speed of the travelling wave was 5.6 m/s. The speed of the particles (rotational and linear) may be estimated from the film speed, as shown below. Figure 3.4 shows the path taken by a particle near the entry end of the machine but remote from the motor-face; Fig 3.5(a) shows the corresponding path for a particle in the mid-section of the cleaner; and Fig 3.5(b) attempts to illustrate the motion of a bunch of particles and also of some individual particles. The numbers on the diagrams relate to the film-frame counted from an arbitrary zero.

In Fig 3.4, the particle shown rotates by 90° in 9 frames, 180° in 16 frames, 270° in 22 frames, 360° in 32 frames etc. Since the film speed was 4000 frames/sec, the rotational speed over one revolution was approximately $4000 \div 32 = 125$ revs/sec (7500 rpm), and the average rotational speed over the four time instants was also approximately 7500 rpm. The horizontal distance travelled was approximately 100 mm in 65 frames giving the

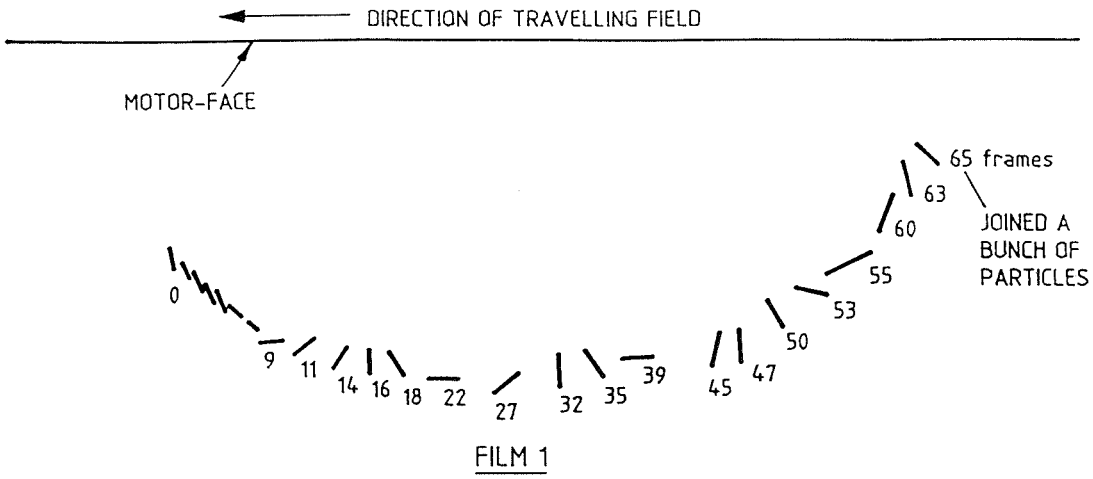

Fig. 3.4 PATH TAKEN BY A PARTICLE NEAR THE ENTRY END OF THE CLEANER

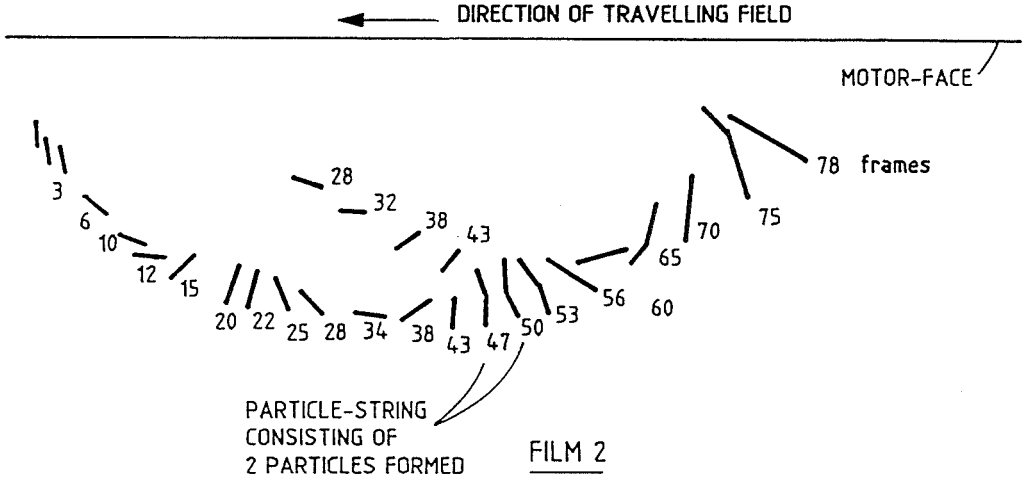

(a) individual particles forming a particle - string

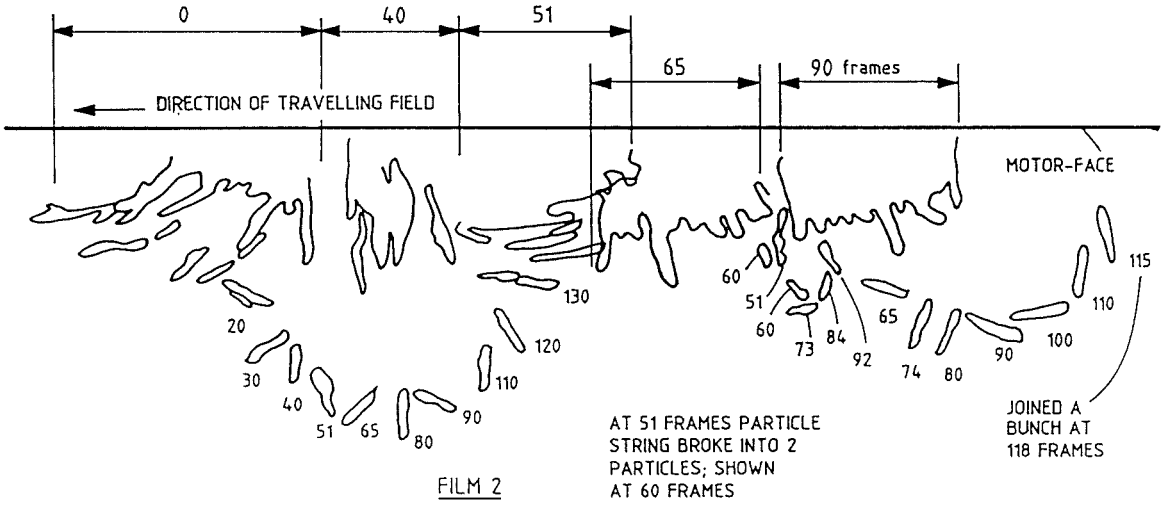

(b) a particle - bunch

Fig. 3.5 PATH TAKEN BY PARTICLES AT THE MID-SECTION OF THE CLEANER

horizontal speed as about 6.2 m/s. As the particle took 32 frames (i.e. 8 ms) to reach the lowest point of its parabolic path, the vertical speed was about 2.5 m/s over one revolution. For the next revolution the vertical speed was greater and in the opposite direction.

Figure 3.5(a) illustrates how two particles came together to form a particle-string. The rotational speed here was about 85 revs/sec (5100 rpm), and the horizontal speed was about 5.3 m/s. It can be seen that, once the particle string had formed, it continued to travel as if it were only one particle still rotating and continuing in the same direction. Figure 3.5(b) shows how the particles near the motor-face travelled. An outline of a bunch of particles was sketched and this particular bunch occupied various positions at various instants of time, as indicated by the frame numbers. The diagram shows how particles left and joined the bunch of moving particles. Note that the individual particle on the left-hand side of the diagram vacated the bunch but made its way back towards the motor-face by frame 130. It did not rejoin the bunch it left but became part of the succeeding bunch, as seen by the fact that, by frame 90, the original bunch had moved on much further than the particle. The rotational speed of the particle was $4000 \div 130 \times 2 = 62$ revs/sec (3700 rpm), and its horizontal speed approximately 1.7 m/s, whereas the average speed of the centre of the bunch of particles was about 4.4 m/s. On the right of Figure 3.5(b) a particle-string separated from a bunch of particles which had already traversed this point on the machine and then the string itself broke. One of these particles then joined, shortly after frame 92, the bunch of particles that had been tracked. This particle completed half a revolution at a rotational speed of $(4000 \times 60) \div (92 - 60) \div 2 = 3750$ rpm with negligible horizontal translation but with vertical motion causing it to return to the motor-face. A third particle on the right side of the diagram (frames 65-115) rotated erratically, i.e. over frames 80-90 it rotated approximately 90°, yet over a similar interval (frames 90-100) it rotated only a few degrees.

These diagrams clearly show the various different paths and methods of transport taken by the particles as they travelled along the inverted LIM, although the particle-speeds given above are not highly reliable. The large variations in the rotational and linear speeds of the different particles given above may be accounted for by a number of factors which may be grouped into particle-related, environment-related or measurement-related factors.

The particle-related factors influencing particle speed are:

i) relative permeability,
ii) demagnetising factor (i.e. shape, since the demagnetising factor is mainly dependent upon shape[3], as may be seen from eqn (3.2)), and
iii) size and length.

The environment-related factors may be sub-divided into:

i) initial position and orientation with respect to the LIM stator,
ii) proximity of other particles (e.g. motion individually, in strings or in a bunch),
iii) collisions with other particles, and
iv) adhesion to other particles;

and, finally, the true film speed must be determined since the camera setting was only a guide to the true film speed. Some of the above factors (i.e. particle-related and the initial position and orientation) have been investigated through the derivation of the force-expressions given earlier, whereas others, such as adhesion, are extremely difficult to quantify. It was possible, however, to remove the uncertainty regarding film speed and the accurate estimation of the frame rate is described below.

3.3 Estimation of Particle Velocity

The Hycam camera[7-9] was fitted with a light-emitting-diode (LED) situated directly behind the film. The LED, which had an integral lens, could be used to produce a focused light beam on an area of the film between the sprocket holes as the film travelled past the shutter and lens mechanism. If the LED was pulsed at a fixed, pre-determined rate an accurate assessment of the film speed could be made. A timing circuit designed and constructed to perform this operation is described below.

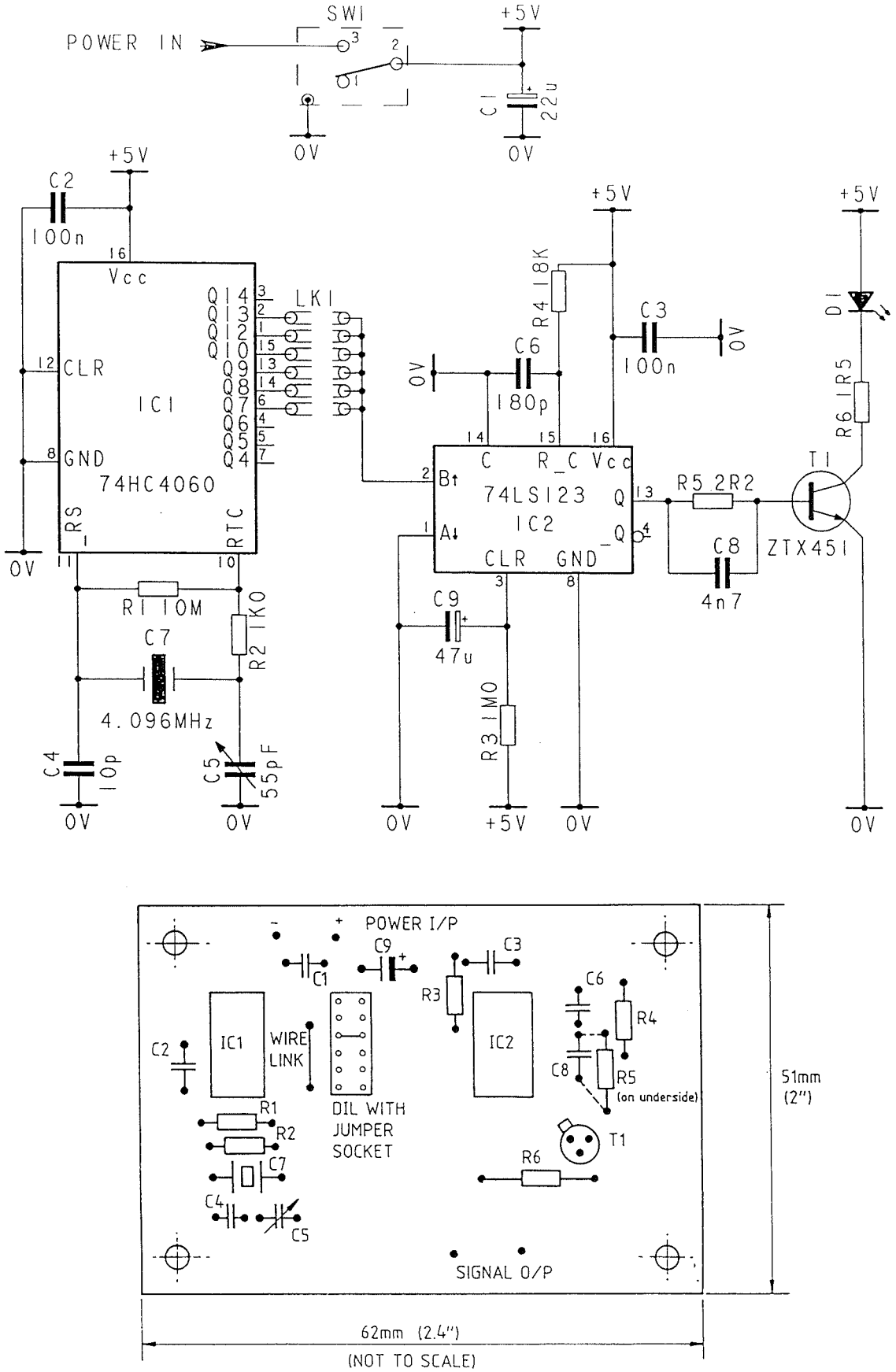
POWER IN
SW1
+5V
C1
22u
0V
C2
100n
Vcc
IC1
74HC4060
CLR
GND
RS
RTC
Q14
Q13
Q12
Q10
Q9
Q8
Q7
Q6
Q5
Q4
LK1
R1 10M
R2 1K0
C7
4.096MHz
C4
10p
C5
55pF
R4 18K
C6
180p
C3
100n
IC2
74LS123
C
R_C
Vcc
B
A
Q
CLR
GND
R5 2R2
C8
4n7
C9
47u
R3 1M0
D1
R6 1R5
T1
ZTX451

POWER I/P
C1
C9
C3
R3
IC1
IC2
WIRE LINK
C2
C6
R4
C8
R5
(on underside)
R1
R2
C7
C4
C5
DIL WITH JUMPER SOCKET
T1
R6
SIGNAL O/P
51mm (2")
62mm (2.4")
(NOT TO SCALE)

Figure 3.6

3.3.1 Determination of Film Speed

The timing circuit (Fig 3.6) was constructed on printed circuit board, powered from four rechargeable batteries and enclosed in a die-cast box, thus producing a light-weight, portable stand alone unit. Pulses were generated at a frequency of 1000 Hz.

An oscillator and divider integrated circuit[13] (IC1) in conjunction with a 4.096 MHz crystal provided square waves at different frequencies all related by powers of two. The divide-by-2^{12} output of the divider thus generated a 1 kHz square wave which was selected by a link and applied to the input of a multivibrator[14] (IC2). On every rising edge of this signal, the multivibrator generated a pulse to drive the LED via a transistor. By trial and error (as no information was available) it was found that applying a pulse of width 20 μs to the LED produced the expected timing marks on the film. Thus, if the film attained a running speed of 4000 frames/sec, a mark would be produced on the film every four frames, corresponding to a pulse rate of 1 kHz.

Before further high-speed photographs were taken, vertical lines having a separation of 50 mm were marked on the perspex sheet through which the powder was viewed. With the film speed providing the time of travel and the markers the distance of travel, the rotational and linear speeds of the particles could be accurately estimated.

3.3.2 Experimental Conditions

With the intention of investigating a reasonable spread of different particle properties, and in order to ascertain particle velocities, further high-speed photographs were taken of four different types of powder. These powders were photographed as they travelled along the mid-section of the LIM and are listed below, referenced by a film number for ease of identification:

i) coarse iron filings (as before), film 11;
ii) powder type AISI 430(2), film 22;
iii) powder type Ni/Fe 50/50, film 23; and
iv) magnetic iron oxide Fe_3O_4, film 26.

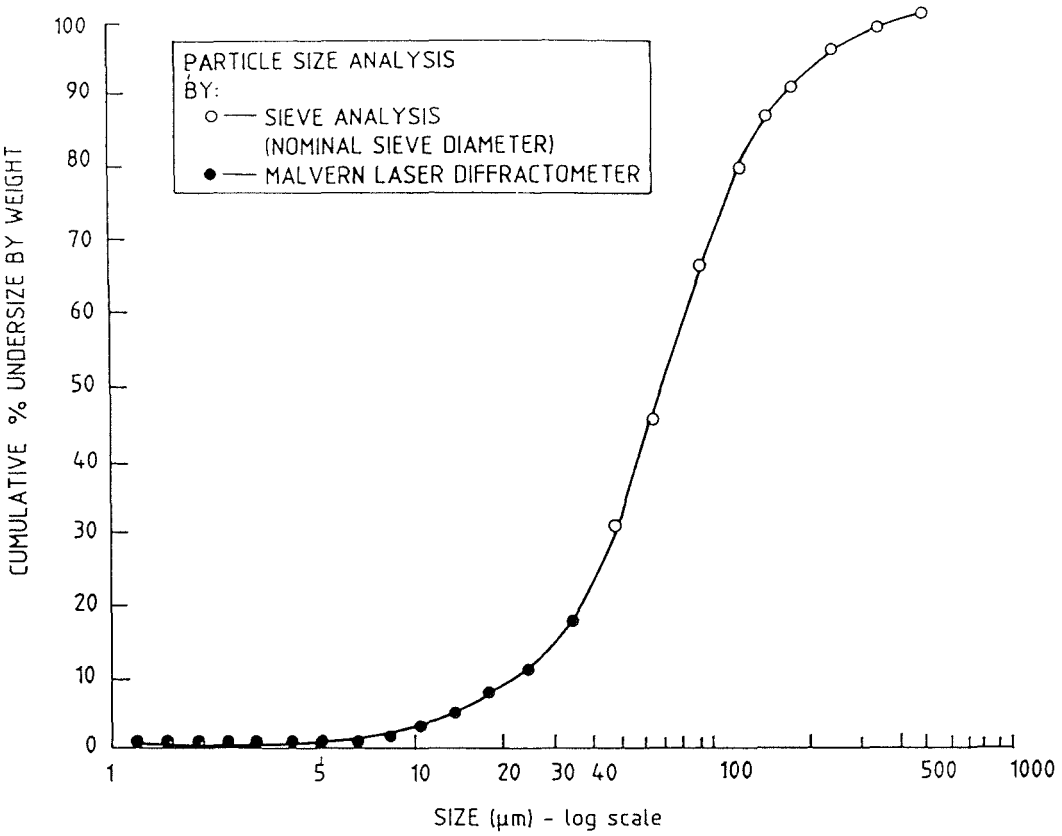

(a) THE SIZE DISTRIBUTION OF SAMPLE AISI 430 (2)

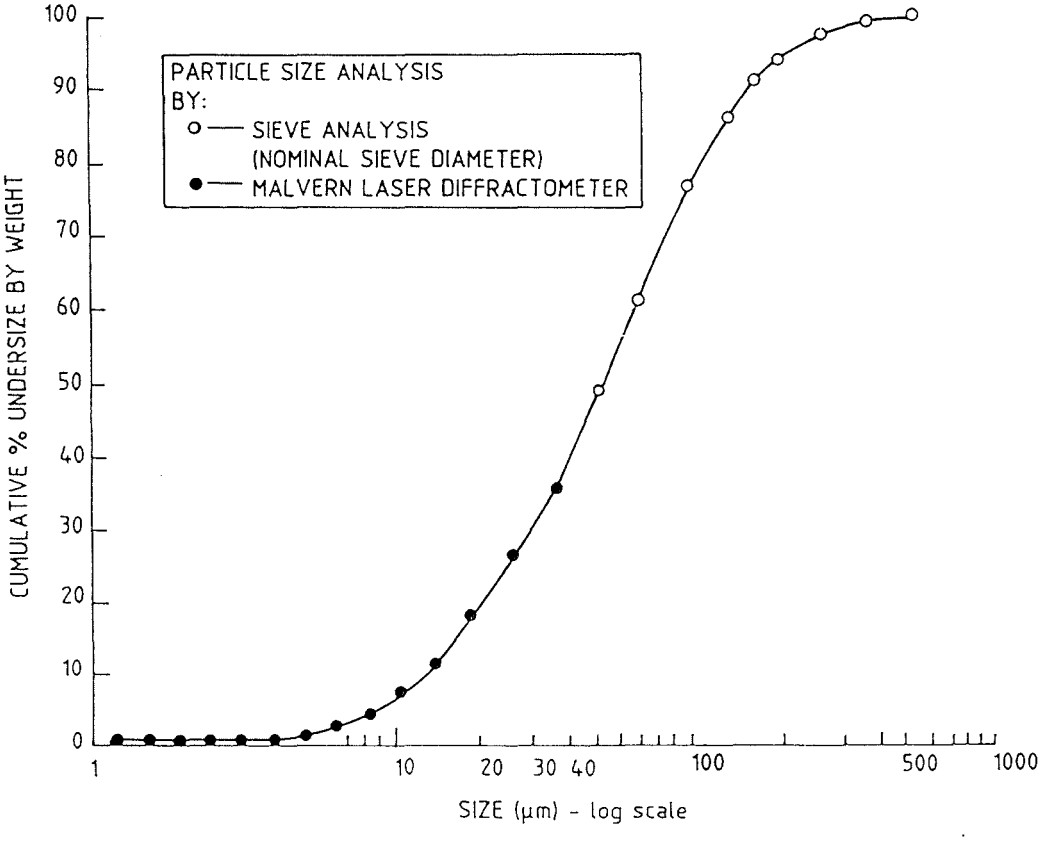

(b) THE SIZE DISTRIBUTION OF SAMPLE 50/50 IRON/NICKEL POWDER

Figure 3.7

continued...

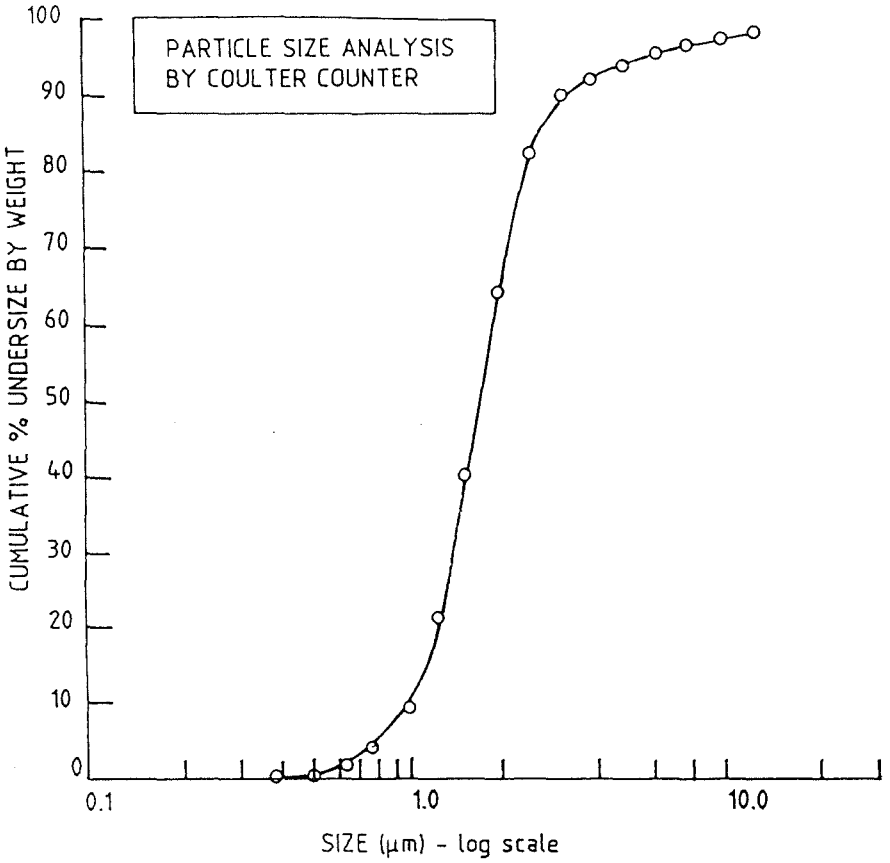

(c) THE SIZE DISTRIBUTION OF MAGNETIC IRON OXIDE

Figure 3.7 PARTICLE SIZE DISTRIBUTIONS

The size distributions (Fig 3.7) of the powders (ii) and (iii) were found via sieving[12,15,16] and Fraunhofer diffraction[11,17-19] using the Malvern Laser Diffractometer[20,21]. Due to the extremely small particle size of the iron oxide, its size distribution was determined via a Coulter counter[22]. These different powders enabled different particle-properties to be studied since powder (i) consisted of magnetically hard, large particles (see Fig 3.2); powder (ii) was also magnetically hard but consisted of smaller particles (see Fig 3.7(a)); powder (iii) was similar in size to powder (ii) but magnetically soft, and powder (iv) was an extremely fine powder. The films, apart from film 26, were taken under the same conditions, with a phase voltage of 175 V and a phase current of 4.4 A. Powder (iv), however, required a phase voltage of 240 V and a phase current of 6.4 A, otherwise the powder was not picked up. This was partly due to its small size, adhesion to the other particles and the distance separating the vibratory feeder from the linear motor.

3.3.3 Experimental Results

For each of the four powders a number of successive photographic stills are presented (see Figs 3.8, 3.10, 3.12 and 3.14) showing the timing marks between the sprocket holes. In order to aid analysis, marks were made by hand on the frame itself corresponding to the timing marks and these can be clearly seen. Additionally, the paths of motion taken by particular particles were plotted together with their frame numbers and respective time instants from an arbitrary zero being noted (see Figs 3.9, 3.11, 3.13 and 3.15).

a) *Film 11; coarse iron filings*

From Figs 3.8 and 3.9 the average film speed may be calculated as approximately 4250 frames/sec. Figure 3.9 shows that the particle of interest separated from another particle after about 2 ms and eventually joined a bunch of particles at the motor-face. During the first 48 ms it completed three revolutions, giving an anticlockwise rotational speed of 3 x 60/0.048 = 3750 rpm. Its average horizontal velocity was 1.2 m/s. Over a period of 52 ms, the particle dropped a distance of 13.3 mm and then climbed this distance, so that its average vertical velocity was 26.6 mm/52 ms = 0.5 m/s.

The motion of the particle was such that it rotated a quarter-revolution in 5 ms (rotational speed = 3000 rpm), yet took only 3 ms to rotate a further 90° (rotational speed = 3750

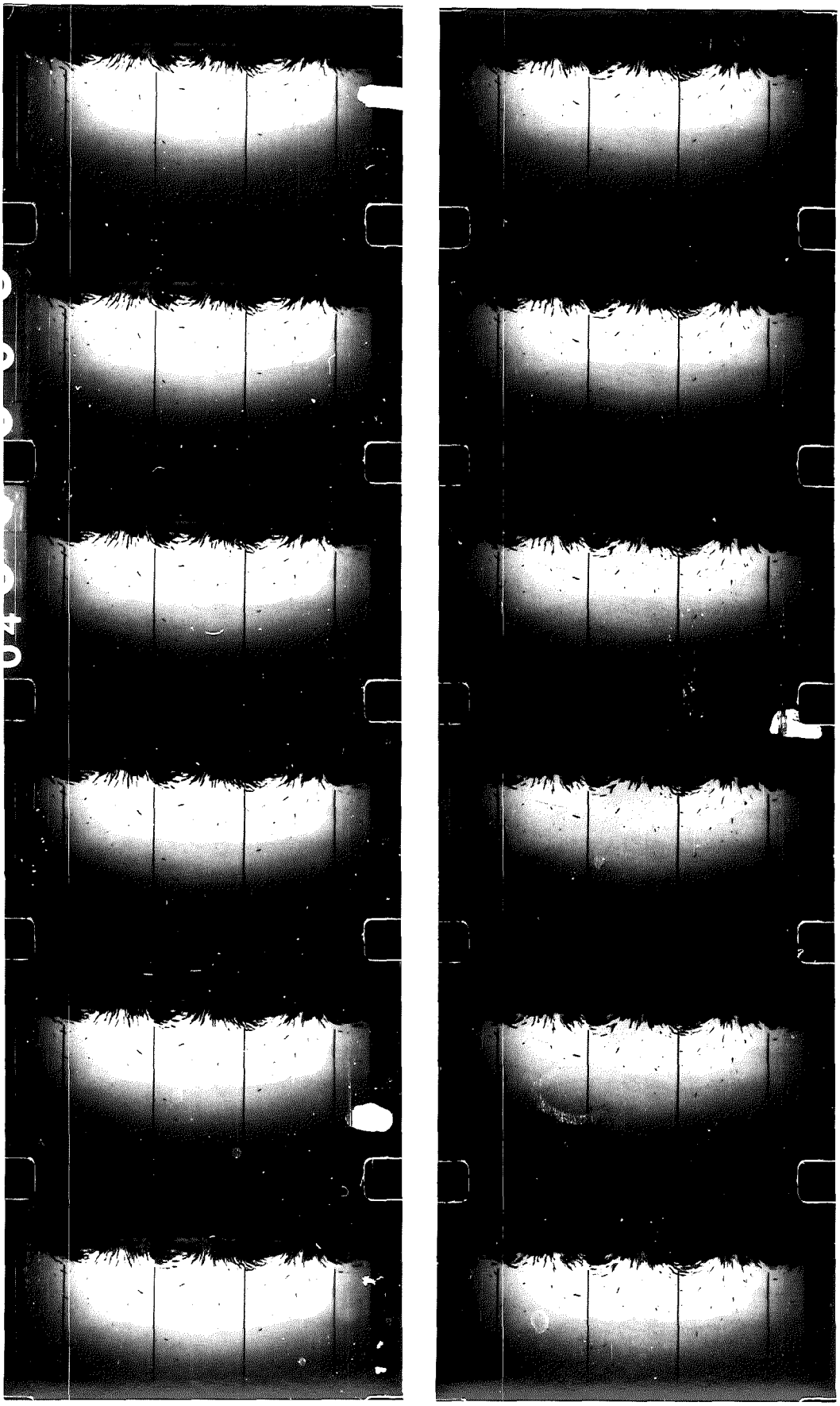

SUCCESSIVE PHOTOGRAPHIC STILLS FROM FILM 11

Figure 3.8

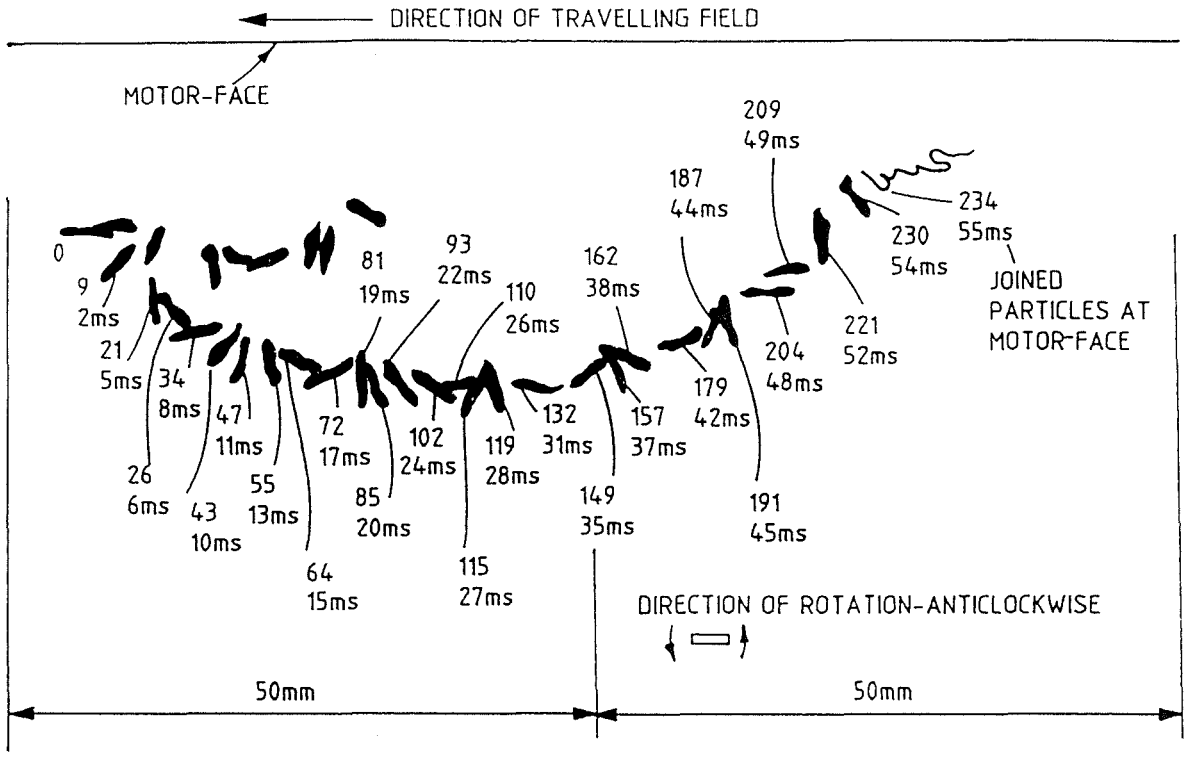

FILM 11

TIMED PATH OF PARTICLES FROM FILM 11 (iron filings)

Figure 3.9

rpm). The particle travelled mainly horizontally, remaining practically stationary in the vertical sense after having reached its lowest point after about 20 ms. During some periods of time the particle's horizontal motion fell almost to zero although it continued to rotate (e.g. frames 110 to 119 and 149 to 162).

Estimates of the linear and rotational speeds of an individual particle travelling closer to the motor-face than the previous particle (and also close to a particle-bunch) were also made and the results for three time instants are given in Table 3.1.

Table 3.1: Linear and rotational speeds of a particle near motor-face for film 11

film speed = 4250 frames/second					
frame number	time (ms)	distance (mm)	linear speed (m/s)	angle of rotation (deg)	rotational speed (rpm)
35	8.24	23.9	2.9	180	3640
58	13.6	38.6	2.84	360	4410
85	20	51.5	2.58	540	4500

Since the above results are concerned with the motion of individual particles, the rotational and linear speeds of two particle-bunches were also estimated. Both were found to rotate half a revolution in 8 ms, giving a rotational speed of 3750 rpm; one particle-bunch travelled 18 mm and the other 19 mm in this time, giving linear speeds of 2.3 m/s and 2.4 m/s respectively. Note that both these distances are approximately a slot-pitch.

b) *Film 22; AISI 430(2)*

The motion of this powder, AISI, had similar characteristics to that of the coarse iron filings described above. Only a small amount of this powder, however, travelled in the air-space, with the vast majority travelling along the motor-face. This made it difficult therefore to follow the motion of individual particles, as can be seen from Fig 3.10, but particle-speeds may be estimated using Fig 3.11 given that the film speed was 39 frames/9 ms = 4330 frames/sec. Particles that did travel in the air-space tended to

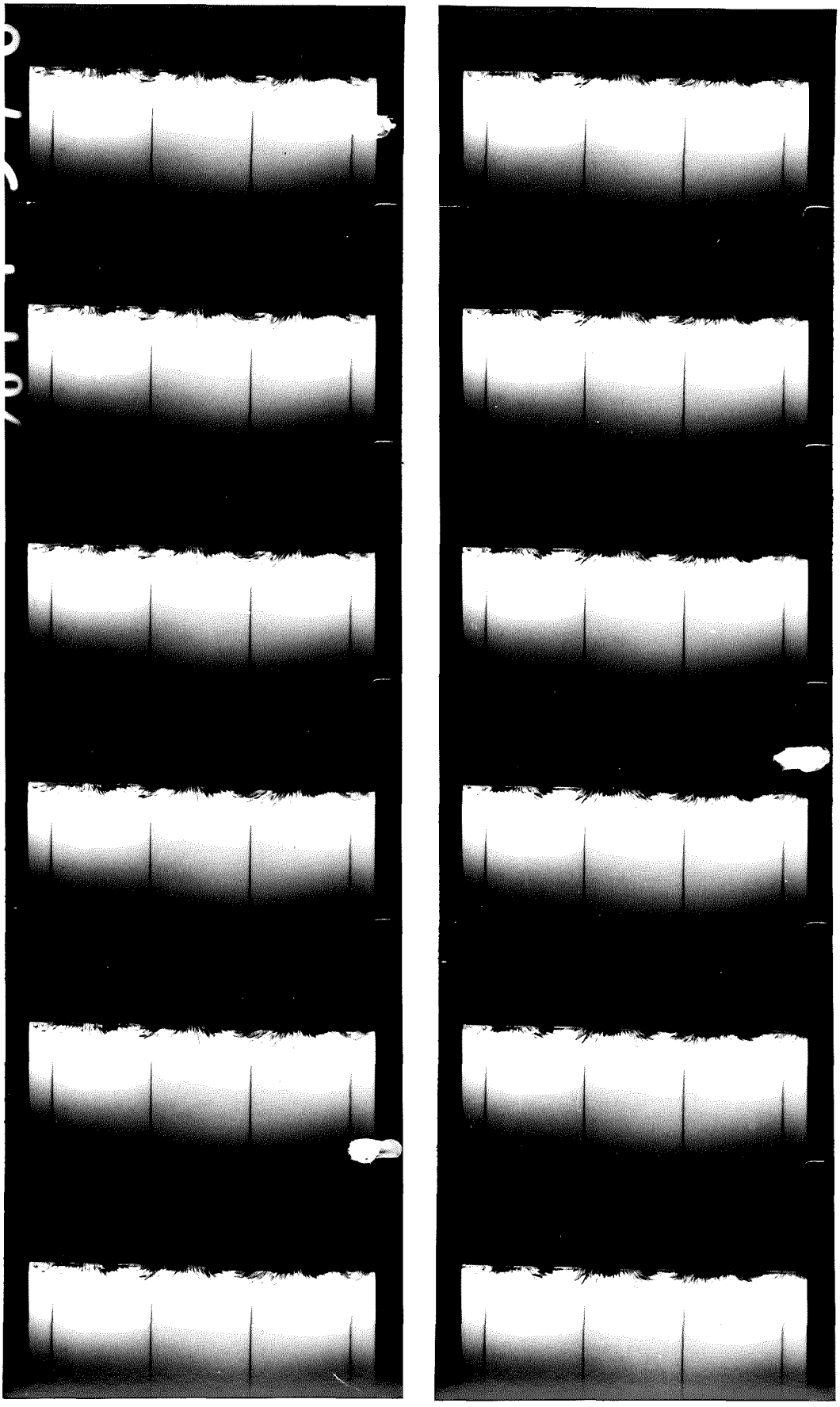

SUCCESSIVE PHOTOGRAPHIC STILLS FROM FILM 22

Figure 3.10

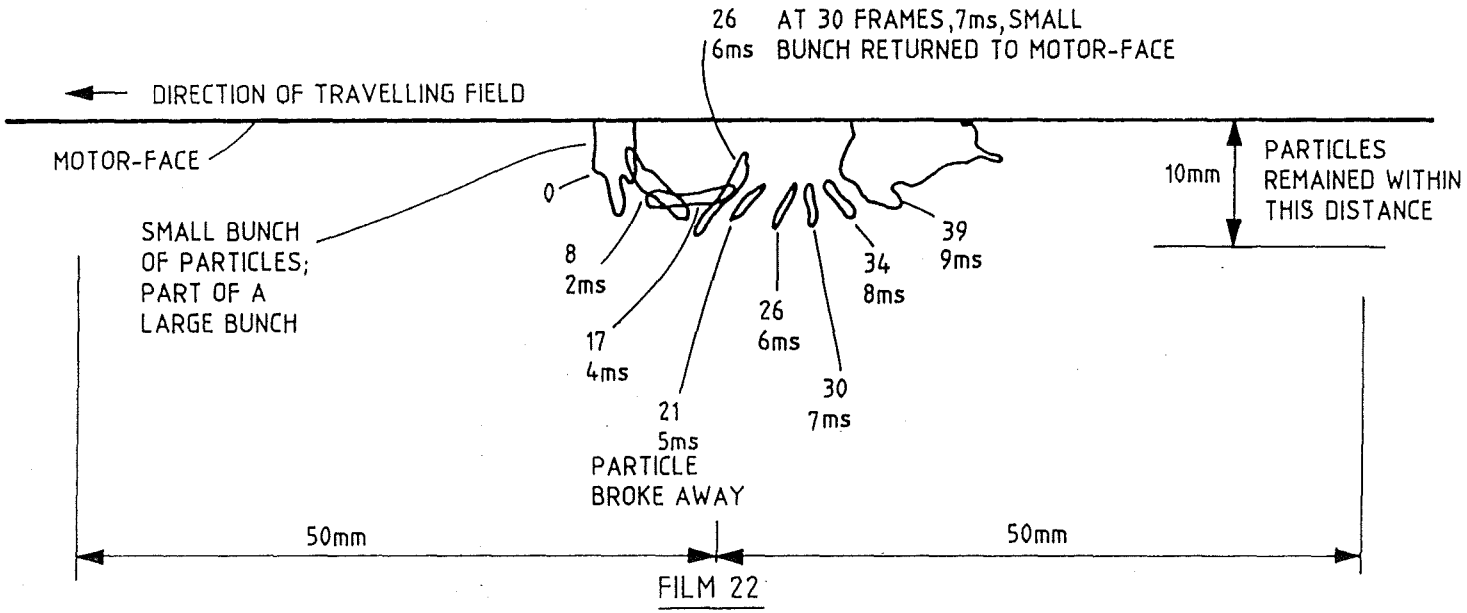

Figure 3.11

TIMED PATH OF PARTICLES FROM FILM 22 (AISI 430)

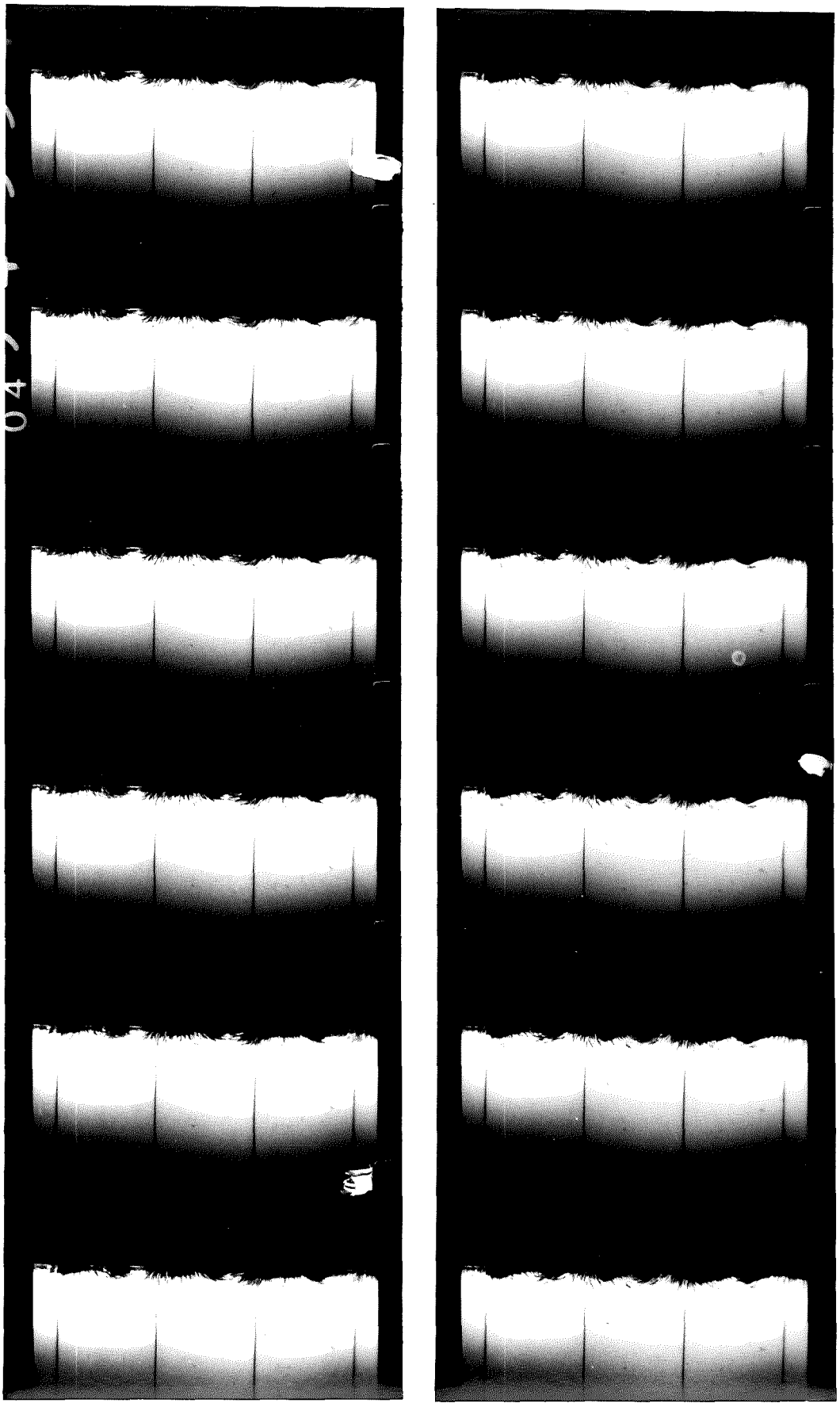

SUCCESSIVE PHOTOGRAPHIC STILLS FROM FILM 23

Figure 3.12

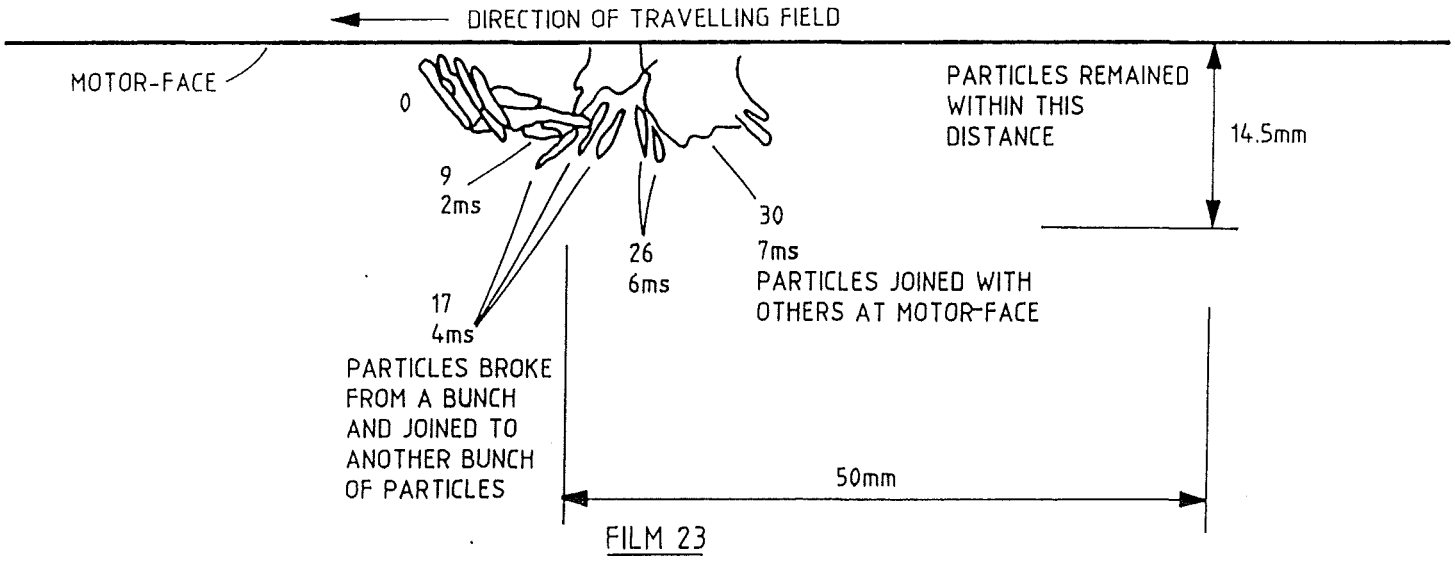

Figure 3.13

TIMED PATH OF PARTICLES FROM FILM 23 (Ni/Fe 50/50)

remain within about 10 mm of the LIM stator, this being in contrast to the coarse iron filings. This is probably due to the powder's size (see Figs 3.2 and 3.7) which is smaller than the iron filings.

Figure 3.11 shows a small particle-bunch separating from a larger particle-bunch and, after completing half a revolution, returning to the motor-face. The rotational speed of this bunch is 4290 rpm and its horizontal velocity is 1.7 m/s. Observations of Fig 3.10 show the particle motion to be agitated and a hint of this may be seen in Fig 3.11. After the small particle-bunch left the stator, an individual particle separated from it at frame 21. The linear speed of this particle was 2.75 m/s, but over the whole period (0 to 39 frames) including its time as part of the particle-bunch its speed was 2.3 m/s, and when travelling individually it rotated at a speed of about 90° in (9-5) ms, i.e. 3750 rpm.

c) *Film 23; Ni/Fe 50/50*

As with the previous powder, AISI, the majority of particles travelled in bunches near the motor-face (see Figs 3.12 and 3.13) but its motion was seen to be considerably more agitated. Figure 3.13 shows that the particles tended to remain within a distance of about 15 mm below the motor and, for the time interval shown, the particles were within 10 mm. After 17 frames the first particle-bunch in Fig 3.13 broke up, with the particles joining another particle-bunch a few frames later. Two of these particles, however, joined with a different bunch at 30 frames. It is interesting to note that more particles tended to return to the same place on the motor-face than with the previous powder. Over the thirty frames, the average rotational speed of the particles was one revolution in 14 ms, i.e. 4290 rpm, and the horizontal speed was 2.5 m/s with the film speed in this case being 4290 frames/sec.

d) *Film 26; Fe_3O_4*

These extremely fine particles were truly "powder-like" as seen by the way they filled the skin pores. The particles tended to stick to the motor-face even after the machine was switched off, probably due to their small size. Even in a jar, the particles tended to agglomerate and stick to the sides.

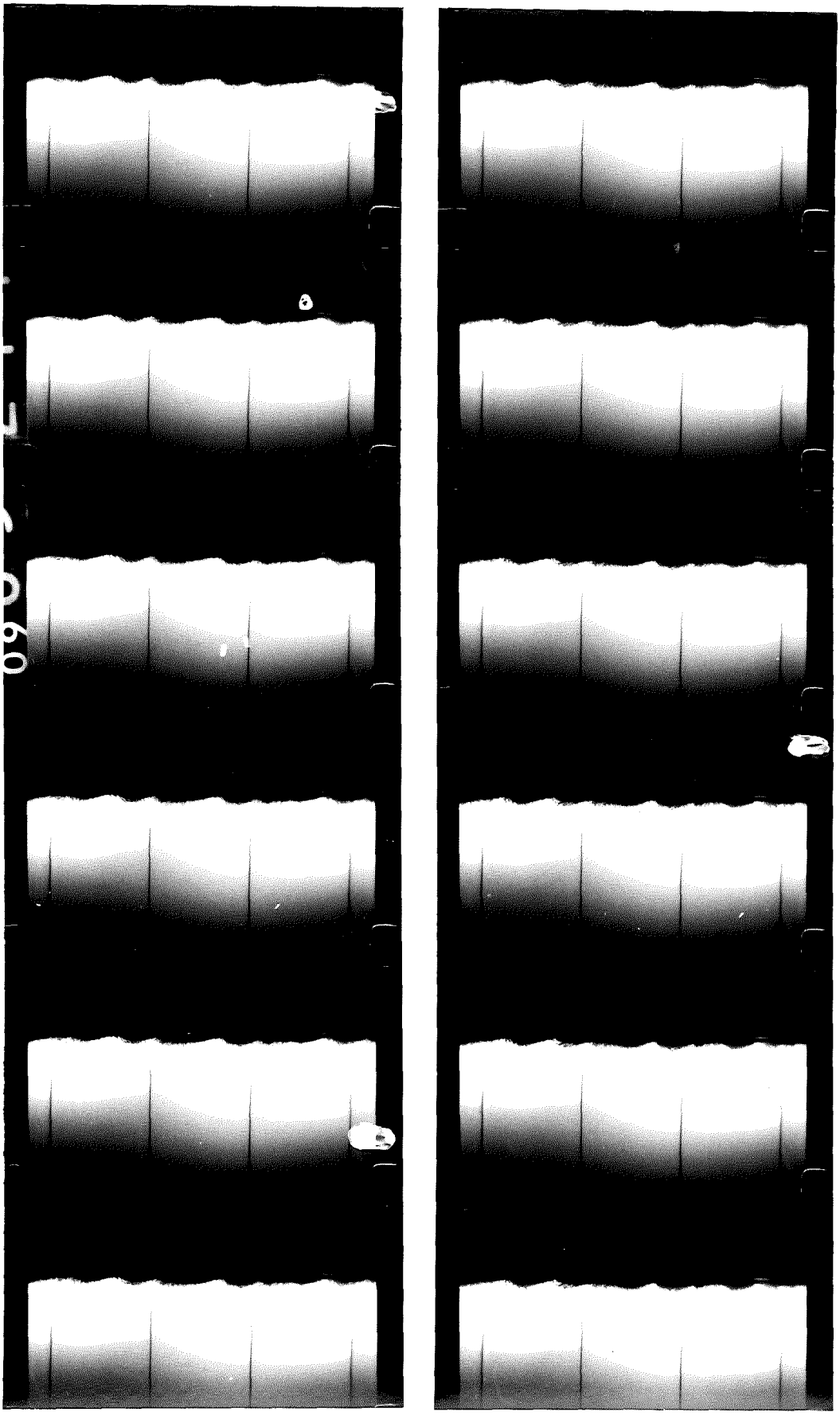

SUCCESSIVE PHOTOGRAPHIC STILLS FROM FILM 26

Figure 3.14

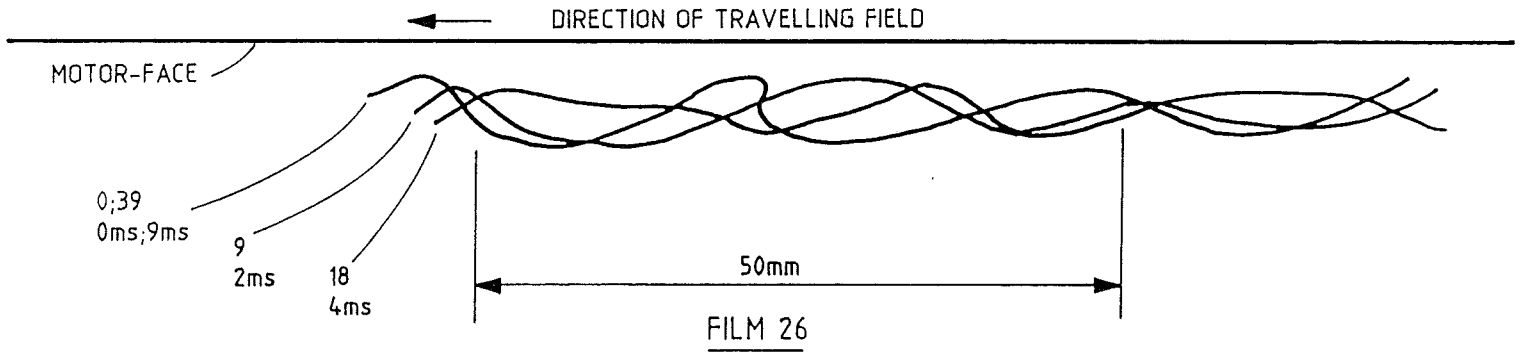

Figure 3.15

TIMED PATH OF PARTICLES FROM FILM 26 (iron oxide)

Due to their size it was difficult to observe the motion of individual particles; they appeared to travel only in bunches at the motor-face (see Figs 3.14 and 3.15). Their motion strongly resembled a wave-like movement, as the particle-bunches continually increased and decreased in size. It was only possible to sketch an outline of the progression of the particles (Fig 3.15) and from this it is difficult to estimate the particle speed. Although identical positions on the outlines were not readily identifiable from Fig 3.15, the linear speed was, however, estimated over two different time intervals to be 1.75 m/s and 1.3 m/s giving an average speed of 1.5 m/s, with the film speed being 4330 frames/sec.

The rotational speed and the manner of rotation could not be determined, due to the difficulty of viewing individual particles. Their rotation may have differed from the other particles, in that they tended to agglomerate and therefore small particle-bunches may have rotated. Otherwise there is nothing to suggest that they rotated any differently.

3.3.4 Summary of Results

The results are summarised below in Table 3.2 with the linear speed of the particles also being expressed as a fraction of the speed of the travelling wave.

Table 3.2: Particle-speeds

Speed of travelling wave = 5.6m/s			
Powder Type	Rotational Speed (rpm)	Linear Speed (m/s)	Fraction of Travelling Wave Speed
Coarse iron filings film 11 4250 frames/sec	Individual particle away from motor-face:		
	3750	1.2	0.21
	Individual particle near motor-face:		
	3640	2.9	0.52
	4410	2.84	0.51
	4500	2.58	0.46
	Particle bunch:		
	3750	2.3	0.41
	3750	2.4	0.43
AISI 430(2) film 22 4330 frames/sec	Individual particle:		
	3750	2.75	0.49
	Particle bunch:		
	4290	1.7	0.3
Ni/Fe 50/50 film 23 4290 frames/sec	4290	2.5	0.45
Fe_3O_4 film 26 4330 frames/sec	—	1.5	0.27

The coarse iron filings travelled mainly as individual particles because of their size, rather than in particle-bunches as did the other powders. This presented a slight difficulty in ascertaining the speed of the smaller powders, as individual particles were less distinct, which accounts partly for the variation in the linear speeds of the different powders. Note that the results in Table 3.2 show that all the particles near the motor-face travelled at about one-half the speed of the travelling wave. Disregarding the result for the powder Fe_3O_4, because of measurement difficulties, the average linear speed of

the particles was approximately 0.42 of the travelling wave speed. All these speeds, however, are low in comparison with the speed of the travelling wave, and it should be noted that the majority of the energy possessed by any particle was due to its rotational speed.

The ratio of rotational energy to linear energy may be expressed as $2r\omega^2/v^2$ with the symbols having their usual meaning. For the coarse iron filings, a typical particle has a radius r of about 1.5 mm. When the particle is near the motor-face measurements gave linear speeds of 2.9 m/s and 2.58 m/s for two different time intervals (see Table 3.2). Thus, for these two different particle speeds, the ratios of rotational to linear energy are:

i) $$\frac{2r\omega^2}{v^2} = \frac{2\times1.5\times10^{-3} \quad (3640\times2\pi/60)^2}{(2.9)^2} = 52$$

ii) $$\frac{2r\omega^2}{v^2} = \frac{2\times1.5\times10^{-3} \quad (4500\times2\pi/60)^2}{(2.58)^2} = 100$$

Clearly the rotational energy possessed by a particle can be 100 times greater than its linear energy and is at least fifty times as great. As the particle size decreases both of these figures obviously decrease. Taking, as rough averages, a rotational speed of 4000rpm and a linear speed of 2 m/s, then the particle radius needs to be of the order of 10 μm before the linear and rotational energies possessed by the particle are equal. Hence, only for very small particles (such as the powder Fe_3O_4) is the rotational energy less than the linear energy.

When filming the powder motion, observations clearly showed that the powder Ni/Fe had a lower mass flow rate than the powder AISI, and Figs 3.11 and 3.13 show that Ni/Fe grew to a depth of about 50% greater than AISI below the motor-face. Both powders have similar size distributions (see Fig 3.7) but differ in that powder Ni/Fe was magnetically soft compared with powder AISI, thus implying that Ni/Fe could be re-magnetised comparatively easily, rather than being forced to follow the pole-centres of the field to the same extent as powder AISI. Similarly, powder Ni/Fe could branch out further before the field became too weak to retain the particles within its influence.

3.4 Hypothesis of Particle Motion

After discussing the effect of the demagnetising factor on the internal field, the particle motion is described followed by predictions of linear and rotational speeds, the time and distance of travel for a ferromagnetic particle close to the motor-face.

3.4.1 Internal Field

It has been shown that the internal field is dependent upon the demagnetising factor[3,4] of the object in question (also see Appendix A), and from eqn (3.2) the demagnetising factor D is 0.109 for a particle of diameter 2c and length 2a such that c/a = $^1/_3$ (i.e. a particle three times longer than its diameter). Assuming an applied flux density of 0.3 T and a relative permeability of 100, the flux density inside the particle B_i (Appendix A) is 2.5 T. The particle obviously saturates before such a high flux density exists, illustrating that, even for low values of applied flux density, the particle is saturated and behaves like a permanent magnet with North and South poles at the two ends.

In the previous description of particle motion it was noted that particles often travel in strings and, for this situation, the demagnetising factor is reduced significantly lending further weight to the permanent-magnet concept. Considering two identical particles that form a string, c/a is now $^1/_6$ and, from eqn (3.2), D = 0.0432. The relative permeability of the string is less than before and will be assumed to be 70 for the combination so that with B = 0.3 T as before, B_i = 5.2 T. As before the particles saturate well before this figure is reached, but this shows again that the particles behave like permanent magnets because it is advantageous for them to form strings; it is well known that permanent magnets, if allowed, will join together, end to end.

It is informative to work the problem in reverse, by assuming that saturation occurs at approximately 1.5 T, so that B_i = 1.5 T. For an individual particle, the applied field needed to produce this value of B_i is only 0.18 T, and for the particle string it only needs to be 0.085 T. Hence saturation can occur at very low values of applied B and, when particles are introduced into the field of the linear motor, they therefore have N and S-poles induced at their ends and are attracted to the motor-face.

3.4.2 Particle Motion

Consider next a single particle held at a point along the motor-face with the field having the pole-pattern shown in Fig 3.16, and assume that at time $t = t_0 = 0$ the N-pole of the particle is attracted to a S-pole of the device. As the field progresses (to the left in the case of Fig 3.16), the pole-centres will move as shown in the diagram and the flux density at the point where the particle is held will sinusoidally (for a sinusoidally travelling field) decay to zero allowing the particle to fall under gravity. While the field at the tooth to which the particle was held is decaying, the field at the teeth on either side is growing; to the left of the particle the flux density is increasing forming a S-pole centre, and to the right a N-pole is growing.

Once the particle starts to fall, it attempts to follow the field trying to keep its N-pole attached to the S-pole to which it was held and this causes the particle to begin rotating. This rotation has the effect of causing the S-pole of the particle to become physically closer to the tooth on its right compared with the distance between its N-pole and the tooth on its left. (This difference in distance will be dependent upon the particle's initial position on the tooth to which it was held.) Since a N-pole is growing to the right of the particle, the particle is attracted to the tooth immediately to its right thus travelling in the opposite direction to the field as illustrated in Fig 3.16. This, however, is not the only possible path the particle can take. Once the S-pole to which the particle was initially held has decayed to zero, a N-pole also commences to grow on this tooth. If during its rotation the particle rotates sufficiently (i.e. more than a quarter-revolution) before travelling linearly past the tooth to which it was held, it may indeed be attracted back to the tooth it just left, since its S-pole is close to the newly-forming N-pole, thereby having no net horizontal motion but rotating a half-revolution. Such particle-motion was observed earlier, but occurred relatively infrequently when compared with the majority of the particle-motion. This kind of motion is less likely because the flux-density of the N-pole immediately to the right of the particle is greater than that of the N-pole on the tooth vacated by the particle (see Fig 3.16).

An assumption in the above discussion is that the particles travel from tooth to tooth and this is probable because the field is concentrated at the teeth, also indicated in the previous chapter and shown in later chapters. Observations of particle-motion clearly

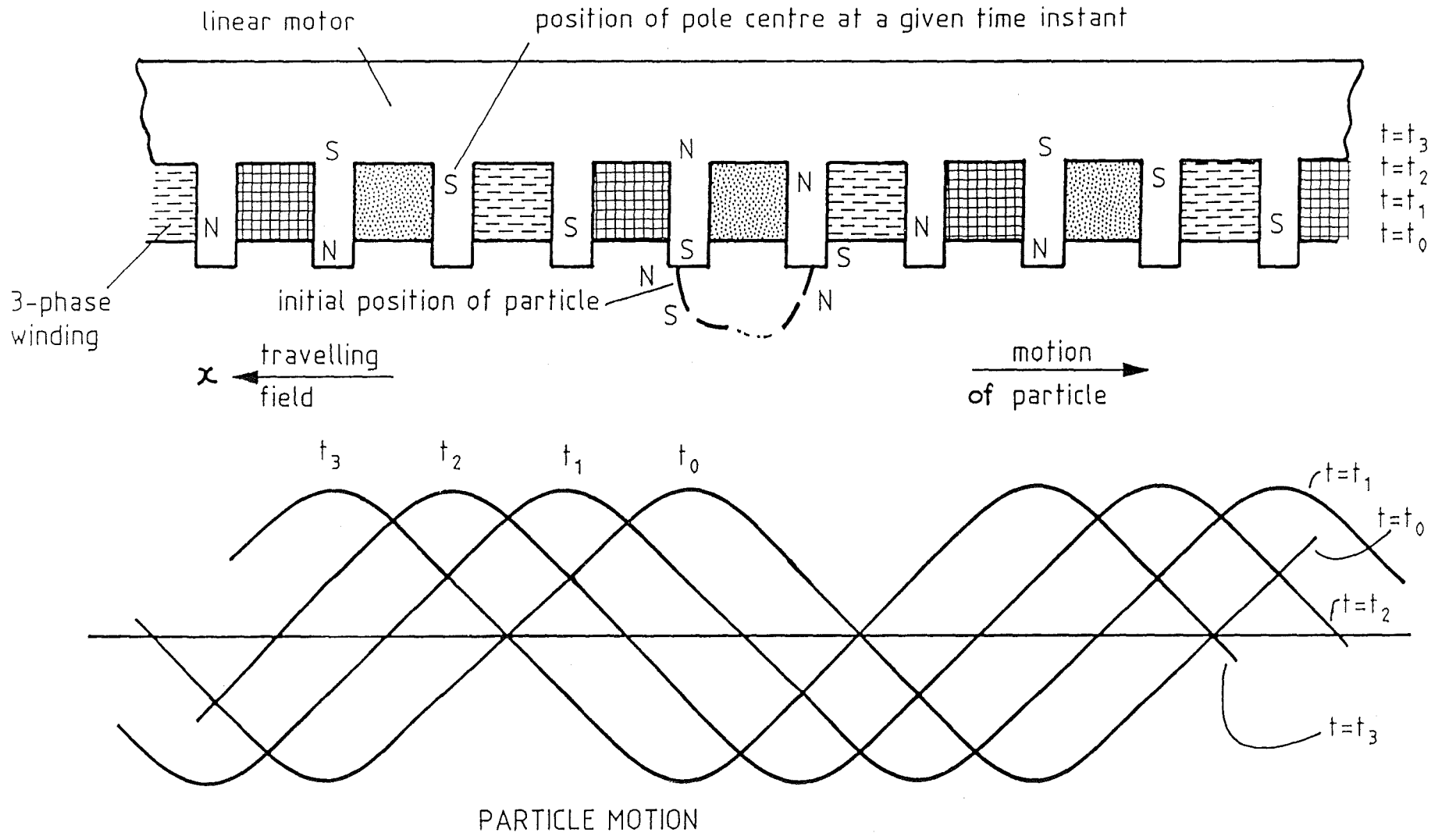
linear motor
position of pole centre at a given time instant
3-phase winding
initial position of particle
travelling field
motion of particle
x
t=t3
t=t2
t=t1
t=t0
PARTICLE MOTION

Figure 3.16

showed a wave-like motion (as mentioned earlier), implying that the particles were not evenly spread across the LIM stator, thus supporting the above discussion since the particles were travelling from and to specific positions on the stator. It was not possible to verify decisively that particles travelled from tooth to tooth on the powder cleaner, since the LIM was encapsulated and the stator further hidden by its supporting non-magnetic plate (see Fig 2.12). Dust patterns on the supporting plate, left by the particles, did however indicate the stator's expected tooth width and pitch.

Observations have also shown that particles sometimes travelled greater distances than a slot-pitch and this may also be explained. Consider again the particle in Fig 3.16 under the initial conditions given above. Although the tooth immediately to the right of the particle has a growing N-pole, while the S-pole to which it was held decays, the second tooth to its right has a N-pole of greater flux density than the adjacent tooth for the 1 slot/pole/phase winding in Fig 3.16. The particle may therefore be attracted to this tooth, thereby travelling 2 slot-pitches in the opposite direction to the field. During its travel it is likely to travel with its flat-side facing the stator and then to rotate as one of its ends is brought back to the motor-face. Other influences (e.g. other particles on the machine) may cause the particle to travel even further, with the local field causing the particle to continue rotating as observations have shown, with the expected distance of travel being an integral number of slot-pitches. Such particle-motion implies that a winding with a large number of slots/pole/phase is likely to produce greater distances of travel for the particles before they return to the stator, because a pole will be spread over a larger number of slots.

This discussion has been concerned with the motion of an individual particle, whereas in practice there are a great many particles travelling at any time. The motion of any particle will be affected by others due to changes in the local field; one such change, for example, being that particles have been seen to travel in strings and that the strings themselves usually travel together in bunches near the motor-face.

3.4.3 Particle Velocity Predictions

It is possible, based on the above hypothesis, to make a theoretical assessment of the linear and rotational speeds of a particle. The equation for the travelling field may be written

$$B = \hat{B} \cos \left[\omega t - \frac{2\pi}{\lambda} x \right] \tag{3.19}$$

If $x = 0$ is the initial position of a particle (such as in Fig 3.16), then at this position at $t = 0$, $B = \hat{B}$ and the time taken for the field to decay to zero at this point is given by $t = \frac{\pi}{2\omega} = 5$ ms. The field one slot pitch to the right is given by

$$B = \hat{B} \cos \left[\frac{\pi}{2} - \frac{2\pi(-18.67)}{2\times3\times18.67} \right] = - \hat{B} \frac{\sqrt{3}}{2}$$

Since the particle has left the motor-face and rotated anticlockwise by the time the field has decayed to zero at $x = 0$, it moves to the right because it is attracted by the build up of the field on the right. The field will be strongest at the teeth of the motor rather than at the slots, causing the particle to travel from tooth to tooth as illustrated in Fig 3.16. It must be remembered that while the particle is moving from one tooth to the next, the field is also travelling, but in the opposite direction. Assuming that the particle reaches the next tooth at the same time the pole-centre does, it is possible to estimate its horizontal speed. Thus,

$$- \hat{B} = \hat{B} \cos \left[\omega t - \frac{2\pi\ (-18.67)}{2\times3\times18.67} \right]$$

$$\therefore\ t = \frac{\pi - \pi/3}{\omega} = 6.67 \text{ ms}$$

Since, on average, the particle has travelled one slot-pitch in this time, its speed is 18.67/6.67 = 2.8 m/s. It is interesting to note that this theoretical figure is one-half the speed of the travelling wave. Although, on average, the particle travels one slot-pitch between leaving and returning to adjacent teeth, it may actually travel anything between 1 slot-width and 1 slot-width plus 2 tooth-widths, i.e. 12.67 mm and 24.67 mm respectively for the powder cleaner. These distances are the dimensions between the corners of adjacent teeth that are either closest or furthest apart since a particle may travel from and to corners of teeth as it is at the corners that the flux density is greatest.

An estimate of the rotational speed of the particles may also be made. It has already been established that the particle travels approximately 1 slot-pitch in 6.67 ms and, from the previous discussion, has rotated by 180°. Its average rotational speed is therefore

$$\frac{1000}{2\times 6.67} \times 60 = 4500 \text{ rpm}$$

A comparison between these figures for linear and rotational speeds for particles close to the motor-face and corresponding experimental results is made below.

3.5 Comparison of Results

The diagrams, Figs 3.8 to 3.13, all show that the particles rotated anticlockwise in line with the hypothesis above. Clearly, if the linear motor had been connected such that the field travelled in the opposite direction to that in Fig 3.16, the particles would have rotated clockwise and still travelled in the opposite direction to the field. This reverse rotation has also been noticed by Brown[23] who attempted to explain the effect via rotating vectors.

a) *Powder AISI 430; film 22*

This powder, AISI (see Figs 3.10 and 3.11) travelled close to the motor-face, representing the situation presented in the hypothesis above. The horizontal speed of the individual particle in Fig 3.11 travelling by itself was 2.75 m/s, which is a discrepancy

of less than 2% from the theoretical average of 2.8 m/s. When it travelled as part of a particle-bunch, its average speed of 2.3 m/s differed by nearly 18% from theory, but the distance of 21 mm that it travelled (see Fig 3.11) is clearly within the expected limits of 12.67 mm and 24.67 mm. It is interesting to note that the particle rotated approximately half a revolution as predicted above. A small particle-bunch was also observed in Fig 3.11 and was found to have travelled only 10 mm, which differs by approximately 20% from the theoretical minimum of 12.67 mm. This, however, is readily explained by the fact that a particle-bunch would agglomerate around a tooth, making it difficult to ascertain which particles would have been in contact with the tooth and therefore not all particles would necessarily travel even one slot-width. In addition, a measurement error of only a few millimetres on the magnified view of Fig 3.11 would considerably affect the discrepancy. (Measurement error and also the fact that particles in a bunch modify the local field also explain the 18% discrepancy in the speed of the particle when it travelled as part of a particle-bunch.) The particle-bunch rotated during its travel at 4290 rpm differing by less than 5% from the expected value of 4500 rpm, and the individual particle had a rotational speed of 3750 rpm differing by 17% from that expected. The measurements, however, were taken over small intervals (see Fig 3.11), making them liable to error.

b) *Powder Ni/Fe 50/50; film 23*

Photographs illustrating the motion of this powder are given in Fig 3.12 and, from Fig 3.13, the horizontal speed has already been estimated as 2.5 m/s, which is nearly 11% below the theoretical average. From their initial position, the particles joined two different bunches (see Fig 3.13), travelling 12 mm and 17.5 mm respectively in the process, both distances being within the expected range. These particles also rotated half a revolution anticlockwise, as predicted by the hypothesis, at a speed of 4290 rpm, which is 5% below expected giving good agreement with theory. Much of this powder tended to return to the same place on the motor-face, more so than the previous powder, AISI. Being magnetically softer than AISI, Ni/Fe is likely to exhibit such motion, because the field is able to magnetise and re-magnetise it more easily. Such motion is also predicted by the hypothesis.

c) *Powder Fe_3O_4; film 26*

As mentioned previously, it was not possible to observe individual particles of Fe_3O_4 due to the lack of magnification available on the camera, and there is no experimental figure for its rotational speed. Its estimated linear speed differs by nearly 50% from the theoretical figure but the experimental figure cannot be relied upon.

d) *Coarse iron filings; film 11*

As noted earlier, the linear speeds of two particle-bunches were measured as 2.3 m/s and 2.4 m/s and their distance of travel as 18 mm and 19 mm respectively. Although the speeds differ by 18% and 14% respectively from the theoretical average of 2.8 m/s, both horizontal distances are very nearly one slot-pitch (18.67 mm) as predicted. The discrepancy in the speed for the particle-bunches is due to the reasons already given above for the powder AISI. As predicted, both particle-bunches also rotated by half a revolution during their horizontal motion at an estimated speed of 3750 rpm which is almost 17% below the expected value of 4500 rpm. It is apparent from the photographs given earlier (see Figs 3.8, 3.10 and 3.12) that individual particles are not identifiable within a bunch, and the hypothesis mostly relates to individual particles. A particle-bunch, however, is expected to rotate at approximately the predicted value since, from earlier discussion, the bunch itself, to an extent, would behave like a permanent-magnet, but it is not possible to identify the centre of the particle-bunch. Coupled with the fact that the measurements had to be taken over small intervals, much of the discrepancy can be attributed to measurement error.

The individual particle tracked in Fig 3.9 travelled away from the motor-face covering a horizontal distance of 68 mm at an average velocity of 1.2 m/s. By extension of the argument presented above, a particle may be expected to travel on average an integral number of slot-pitches with the expected minimum being a tooth-width less and the expected maximum being a tooth-width greater than this average. For the motor, the slot-width is 12.67 mm and the tooth-width 6 mm, implying that the particle almost travelled the minimum expected distance of 4 slot-pitches minus 1 tooth-width, i.e. 68.68 mm, which differed by less than 9% from the expected average of 74.68 mm. The linear speed is, however, in considerable disagreement with that in the discussion above, but

this is not surprising since the hypothesis deals with particles close to the motor-face. From the particle motion in Fig 3.9 it is evident that the horizontal velocity fell almost to zero, which may be explained by the local field, which was likely to be significantly different due to other particles travelling close to the motor-face. A further extension to the hypothesis above predicts that particles will rotate an integral number of half revolutions, and this particle rotated seven half revolutions with an average speed of 3750 rpm which is 17% below that expected. It appears that although local field effects significantly move the linear and rotational speeds of particles remote from the motor-face away from those expected, the motional characteristics remain the same, i.e. the distance travelled and the amount of rotation can be accurately predicted.

Results for an individual particle travelling close to the motor-face were presented in Table 3.1 and these correlate well with the hypothesis. Measurements were taken for three successive time instants when the particle had returned to the motor-face, and it is clear that the particle had rotated by a half revolution on each occasion. The distances of travel all fall within the expected minimum and maximum of an integral number of slot-pitches $\pm$ one tooth-width and, apart from the first measurement of rotational speed, both the linear and rotational speeds are close to the predicted values of 2.8 m/s and 4500 rpm respectively. Discrepancies from theory may partly be explained by measurement error but are also due to localised field effects since this particle was also travelling close to a particle-bunch.

It is clear from the above discussion and the good agreement between the measured and theoretical results that the proposed hypothesis explains reasonably well the motion of ferromagnetic powder along the stator of a linear induction machine.

3.6 Summary

This chapter has described initial experiments conducted on the modified powder cleaner, providing a clearer picture of the way that particles move when under the influence of a travelling magnetic field. After studying these results, accurately timed high-speed photographs were taken of four different types of powder, in order to quantify rotational and linear speeds. Substantiated by information regarding demagnetising factors, a

hypothesis was proposed to explain the complex particle motion. Using the hypothesis, predictions of rotational and linear speeds, the time and distance travelled by a particle between successive instants of contact with the stator and other particle motional characteristics were made. Comparisons between the results from the hypothesis and from experiment showed that the two were in good agreement. Any discrepancies outside the bounds of experimental error were explained.

Two sets of force expressions (one- and two-dimensional) have been derived and these show that the horizontal force is directed in opposition to the field and that both the x- and y-directed forces depend upon the size, shape and relative permeability of the particle. The position, height and orientation of the particle above the stator also modify the forces, and the expressions indicate that both forces vary at twice the rate of the impressed travelling magnetic field. These force-expressions cannot be used to estimate the speed of a particle, since the hypothesis predicts a speed irrespective of particle-size or mass. Both particle-size and mass are important, since they are likely to be limiting factors determining whether the particles will, or will not, move. (In the previous chapter it was mentioned that Davy McKee[24] had found a particle-size that did not transport along a LIM stator.) The force-expressions however provide insight into particle-motion, since they predict a motion that follows the shape of the field and the direction of motion taken by the particles, both of which support the hypothesis. Although the particles experience different magnitudes of force, depending upon a variety of factors, the speed of the particles does not have a straight-forward relationship to the force. Not only does the hypothesis predict linear speed, but the arguments used imply that greater linear speeds will be achieved with winding arrangements consisting of a greater number of slots/pole/phase.

References

1. GOPINATH, A.: "An investigation into the uses of magnetic fields to accelerate ferromagnetic particles", (PhD Thesis, 1965, University of Sheffield).

2. HORSNELL, T.S.: "Acceleration of ferromagnetic particles by pulsed magnetic field and rotating magnet systems", (PhD Thesis, 1968, University of Sheffield).

3. OSBORN, J.A.: "Demagnetising factors of the general ellipsoid", *Phys. Rev.*, 1945, **67**, (11/12), pp. 351-357.

4. BRAILSFORD, F.: "Physical principles of magnetism", (D. Van Nostrand Company Ltd., 1966, London).

5. STARLING, S.G. & WOODALL, A.J.: "Electricity and magnetism for degree students", (Longmans, 1956, 8/e, London).

6. LAITHWAITE, E.R.: "Induction machines for special purposes", (George Newnes Ltd., 1966, London).

7. "Hycam instruction manual", (Red Lake Laboratories, Inc, USA).

8. "Hycam 16 mm high-speed motion-picture camera", (Telford Products Ltd, Form HY-164, USA).

9. "Hycam rotating-prism type 16 mm high-speed motion-picture camera", (Red Lake Laboratories, Form HY-865, USA).

10. GUPTA, D.K., HOBSON, L. & LLOYD, P.J.: "Transportation of powders using a linear motor device", *Applied Energy*, 1987, **28**, (2), pp. 107-122.

11. ALLEN, T.: "Particle size measurement", (Chapman and Hall Ltd, 1981, 3/e, London).

12. LESCHONSKI, K.: "Sieve analysis: the cinderella of particle size analysis methods?", [In: GROVES, M.J. (Ed.): "Particle size analysis", (Heyden & Son Ltd, 1978, pp. 205-217, London)].

13. "Logic databook, Vol. 1", (National Semiconductor Corporation, 1984, USA).

14. "The TTL databook for design engineers", (Texas Instruments, 1982, USA).

15. "Test sieving", BS1796, 1976.

16. "Test sieves", BS410, 1986.

17. CORNILLAULT, J.: "Particle size analyser", *Applied Optics*, 1972, **11**, (2), pp. 265-268.

18. CORNILLAULT, J.: "High resolution and submicronic measurements with a laser particle size analyser", Int Lab, 1987, **17**, (7), pp. 28-36.

19. CORNILLAULT, J. & JOLY, F.: "On line particle size analyser for process monitoring", TIZ, 1986, **110**, (12), pp. 844-847.

20. FELTON, P.G.: "Measurement of particle/droplet size distributions by a laser diffraction technique", *Proc. 2nd European Symp. Particle Characterisation (Nurnberg)*, 1979, pp. 662-680.

21. "2200/3300 Particle sizer handbook, version 1.3", (Malvern Instruments).

22. "Determination of particle size distribution: recommendations for electrical sensing zone method (the Coulter principle)", BS3406, Pt.5, 1983.

23. BROWN, R.: "Travelling magnetic waves in electrical machines described by rotating vectors", *Proc. IEE*, 1969, **116**, (6), pp. 1011-1013.

24. RIGBY, M.: "Progress report on the development of the linear motor separator", (Internal Report, Davy McKee (Sheffield) Ltd., 1980).

4. Tubular Linear Induction Machine

The tubular linear induction machine (TLIM) described previously in Chapter 2 is a topological variation of the standard linear induction motor. formed by 'rolling' the LIM primary winding around an axis parallel to the direction of motion. This enables a greater stator-surface area to be used, without a significant increase in the end-turn losses as compared with the flat LIM, because of the circular coil structure[1]. A TLIM was therefore designed and constructed to investigate powder transport, and it was hoped that the machine would be able to pump powder using the full circumference of its bore.

4.1 Design and Construction of the Tubular Motor

The stator of the experimental machine was constructed from the standard linear motor laminations of length 467 mm shown in Fig 4.1. A number of laminations were arranged in stacks, each stack held together by non-magnetic nuts and bolts. The stator coils were fitted into the 24 lamination-stacks of the motor while they were being positioned around an 80 mm diameter rod. The complete structure was made rigid and, as shown in Fig 4.2, assembled on a wooden base. (Further details of the design and construction are given in Appendix B.) This method of construction has the effect of producing a number (in this case 24) of individual standard linear induction machines all equi-distant from a central axis.

A double-layer winding (an inner and outer coil-side in each of the 24 slots) was used, with the coil-ends brought out to a terminal rail to facilitate ease of connection and the study of different winding arrangements. Since the coils are circular, with like magnetic poles facing each other across the TLIM, the flux travels in an axial direction. Use of the equation

$$E = 4\sqrt{2} \cdot \pi r \lambda_p f k_w N_p \hat{B} \qquad (4.1.)$$

where E = rms value of applied voltage;

r = radius of bore;

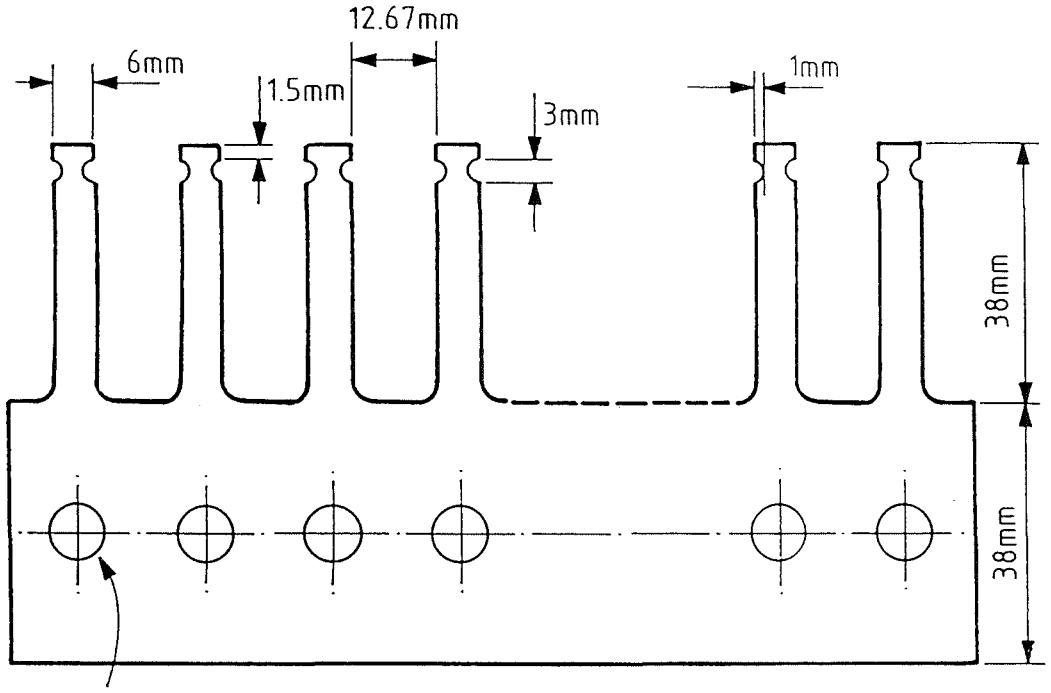

LAMINATION THICKNESS = 0.635mm
STACK: 15 LAMINATIONS
THICKNESS OF STACK = 9.525mm

LINEAR MOTOR LAMINATION

Figure 4.1

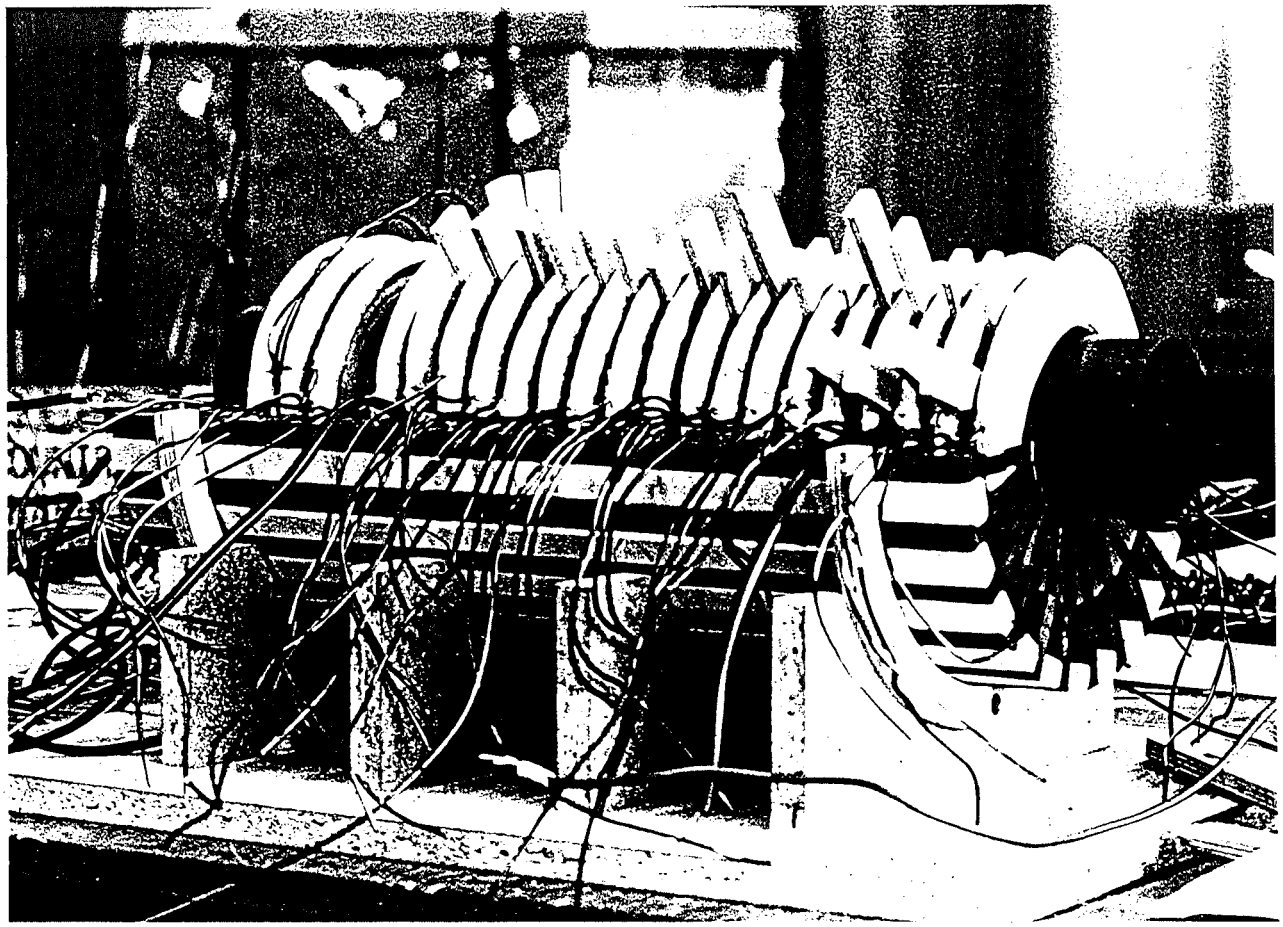

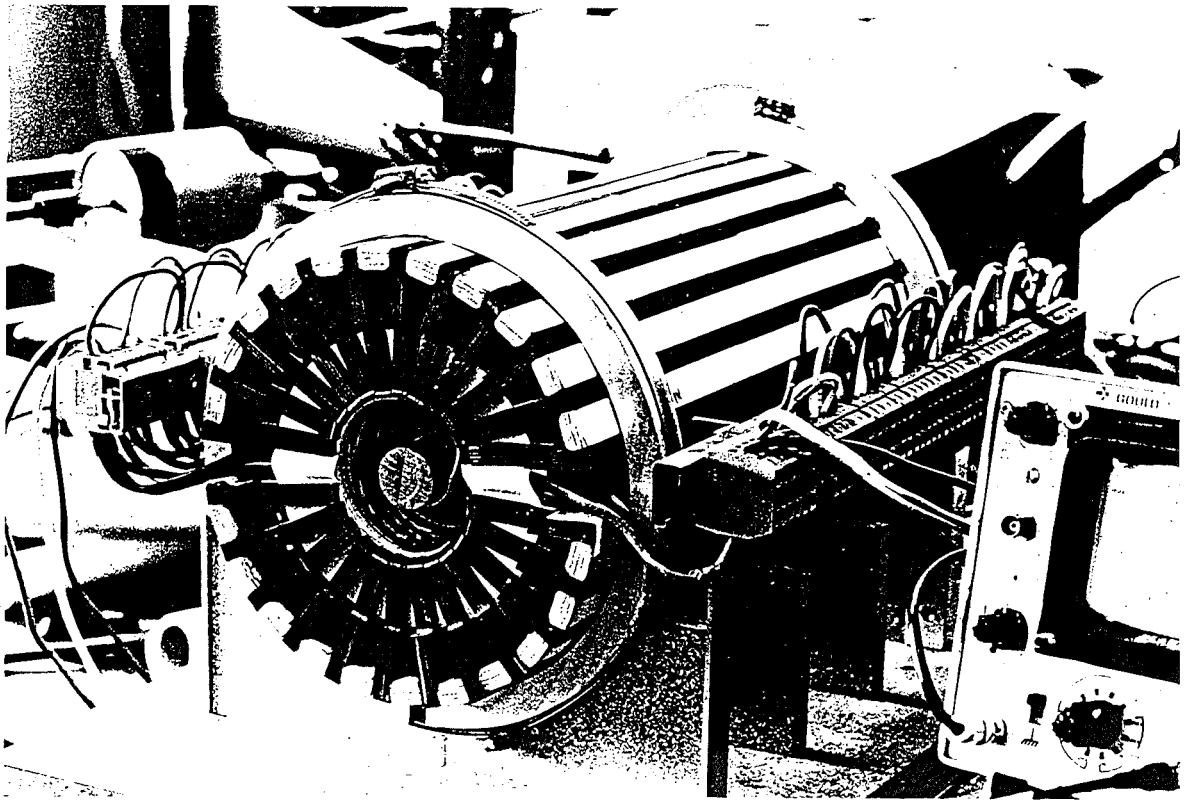

PHOTOGRAPHS OF THE TLIM PARTLY AND FULLY CONSTRUCTED

Figure 4.2

λ_p = pole-pitch;

f = supply frequency;

k_w = winding factor;

N_p = number of turns/phase;

$\hat{B}$ = peak flux density

with an estimate of the available slot area, indicated that each coil should consist of 20 turns of 2.9 mm diameter copper wire (see Appendix B).

In summary, the machine was of length 467 mm with a bore diameter of 80 mm and a double-layer winding with 48 coils.

4.2 Preliminary Investigations

Plastic tubes fitted inside the bore of the TLIM were used for all of the experiments undertaken, with powder placed at one end of the tube. Such an arrangement prevented the powder from falling into the stator.

4.2.1 Powder Motion

It was verified by disconnecting one phase of the winding that ferromagnetic powder does not transport in the absence of a travelling field (see Chapter 2). A travelling field was then generated by connecting all three phases but omitting several coils, chosen at random, to produce an unbalanced machine. Although it was possible to move a 63 mm diameter aluminium rod at a current of approximately 25-30 A/phase, the powder failed to transport near either the laminations or the axial centre of the machine.

The powder did, however, experience a small amount of movement; and near the laminations it vibrated but without any significant horizontal motion. Increasing the current to about 30 A/phase caused vigorous vibration of the powder, with wafer-thin powder ridges as shown in Fig 4.3 beginning to form and the powder slowly spreading along the tube from the small area where it had been initially placed. Although this motion was limited, it still demonstrated powder motion in the expected direction, against

Figure 4.3 SCHEMATIC SHOWING POWDER RIDGES

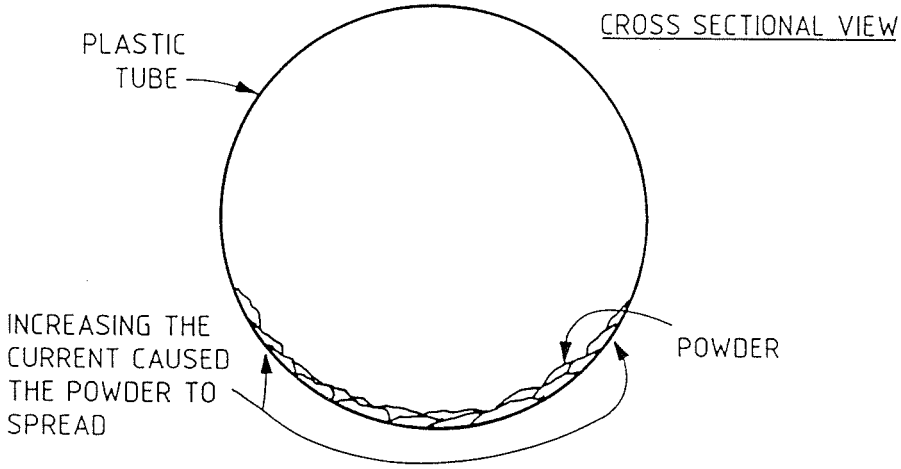

Figure 4.4 POWDER MOTION NEAR THE LAMINATION TEETH

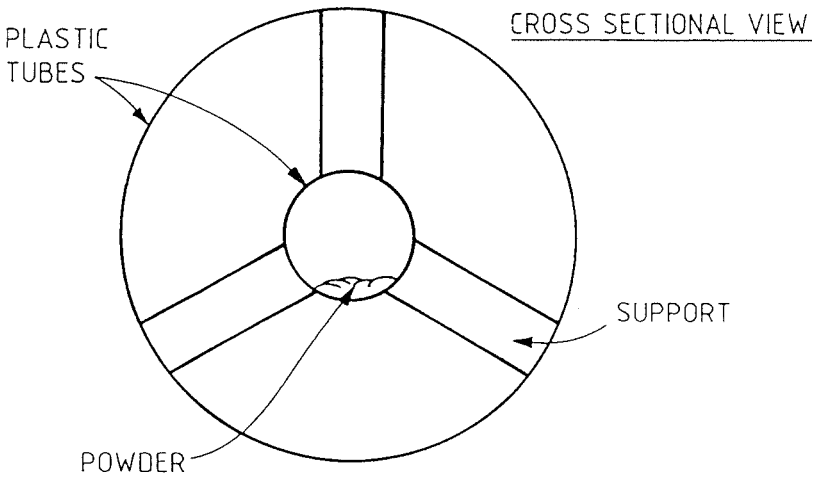

Figure 4.5 POWDER MOTION ALONG THE AXIS OF THE TUBULAR MACHINE

the travelling field. The increased current also caused the powder to spread around the inner circumference of the tube, as indicated in Fig 4.4, suggesting that it may indeed be possible to pump powder through the tubular motor.

Near the axis (Fig 4.5), the unbalanced nature of the machine is not so dominant and the powder motion was observed to be greater than that near the laminations. This is thought to be due to the more nearly sinusoidal travelling field and the increased tangential component over the normal component of flux density despite the overall lower field at the machine centre. Previous effects occurring near the laminations, such as the agitated powder vibration and ridge-formation, also occurred along the axis of the motor, although to a lesser extent, with increasing current.

4.2.2 Powder Motion with a 1 slot/pole/phase Winding

The motion of iron filings was observed with the tubular machine fully wound with 1 slot/pole/phase, and at 50 Hz this produces an axially travelling field at a speed of 5.6 m/s. With the tube shown in Fig 4.4 there was little movement of the iron particles at low currents and approximately 20 A/phase was required for reasonable motion. As expected, this was again in the opposite direction to the travelling field. Introducing the powder into the motor produced a small but noticeable drop in the input current due to the lower reluctance path provided by the particles. Due to the greater flux density at the laminations' surface, the powder travelled considerably faster and more vigorously than along the axis.

With the powder initially placed at the entry end of the tubular motor in the tube shown in Fig 4.4, the powder tended to form ridges as observed previously on other linear machines. Unlike the powder cleaner (an inverted linear motor, see Chapters 2 and 3), however, the powder formed long ridges from one end of the TLIM to the other. Increasing the current caused the ridges to shorten, with their height remaining approximately the same and the particles migrating towards the exit end of the machine. The rear of the powder ridges, i.e. closest to the entry end of the TLIM, tended to collapse and the particles continued to travel towards the exit end of the motor, with some joining other ridges, others traversing the ridges and still others forming new ridges. Placing a steel rod along the machine axis (see Fig 4.6) had the effect of

CROSS SECTIONAL VIEW

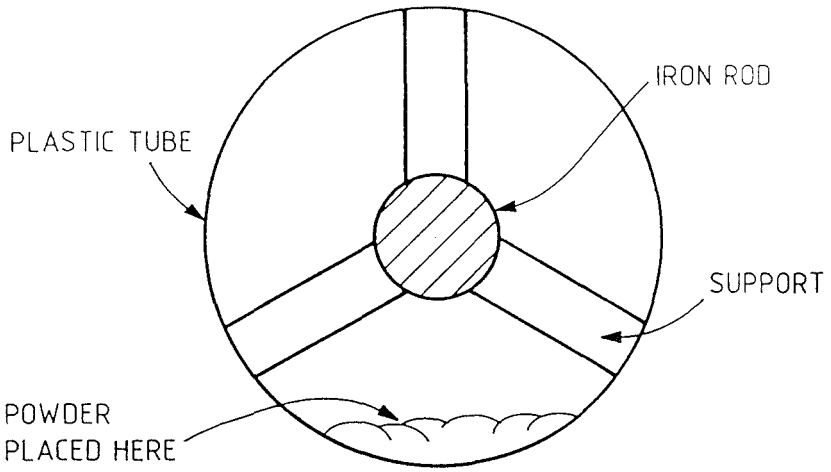

POWDER MOTION WITH INCREASED NORMAL FLUX DENSITY

Figure 4.6

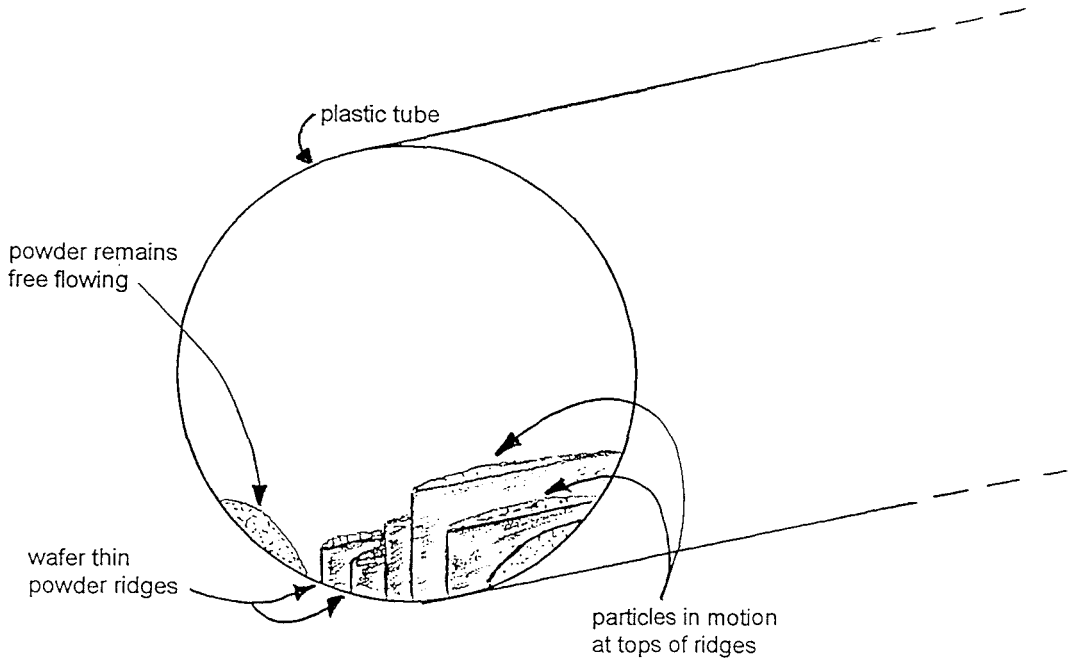

POWDER RIDGES WITHIN THE TLIM

Figure 4.7

increasing the normal component of flux density, which violently agitated the ferromagnetic particles and caused them to vibrate between the laminations and the steel rod as they attempted to move along the field lines. The powder ridges still continued to form, but they were considerably reduced in length due to the particle motion between the stator and the steel rod.

4.2.3 Powder Motion with a 2 slots/pole/phase Winding

Due to the method of construction, it was possible to re-connect the coils of the TLIM at the terminal rails to give a 2 slots/pole/phase winding. With this arrangement, two magnetically hard powders, AISI and coarse iron filings (see Chapter 3), were introduced into the plastic tubes of Figs 4.4 and 4.5, and only limited motion occurred at a phase current of 10 A. Some particles immediately traversed the bore of the motor and formed small ridges. Increasing the phase current to 15 A produced more movement with the powder spreading along the machine bore and forming longer ridges. Eventually two or three ridges grew to the same length as the device. The powder also unsuccessfully attempted to spread around the inner circumference of the tube (Fig 4.4).

At 25 A/phase, the powder initially travelled quickly, forming ridges in a few seconds and spreading considerably along the inner circumference of the tube. At switch-on, with powder placed just outside the machine bore at entry end, significantly more powder was 'pulled in' than with the previous 1 slot/pole/phase winding, with the majority of the powder tending to settle over the first two or three teeth. Although at the exit end of the motor most particles clustered around the last few teeth, some moved beyond the end of the bore, before being attracted back. Most of the powder transported in the first few moments, with the particle-ridges preventing further motion and leaving a large quantity of powder at the entry end of the motor. With a phase current of 35 A, the motional characteristics were similar but increased in degree, with the powder travelling more quickly still and more being 'pulled' into the bore of the machine.

Increasing the current still further (to 40 A/phase) produced further enhancement of the motion characteristics noted at 25 A/phase and 35 A/phase. The powder spread further around the inner circumference of the tube, the ridges formed more quickly, the powder motion was more vigorous and more powder was 'pulled in' to the motor. The powder

ridges grew to a height exceeding 25 mm (see Fig 4.7) and hindered powder motion as with the powder cleaner. Where there were no ridges the powder remained free flowing but, as the majority of the powder was contained in the ridges, there was little powder transport. There was also a little particle motion on the top of the ridges, which tended to keep their shape even after the machine was switched off, again similar to the effects observed on the powder cleaner.

Soft magnetic powder (Ni/Fe — see Chapter 3) was also used and, apart from the fact that larger currents were required, the motional characteristics were similar to those for AISI. Other minor differences were that more movement was observed on the tops of the powder ridges and a few of the outermost ridges tended to break up, with some of the released powder becoming part of other ridges and the remainder travelling to the exit end of the machine.

Powder motion was clearly better with this winding arrangement compared with the 1 slot/pole/phase arrangement since more powder transported more vigorously at lower input currents.

4.3 Flux Density Measurements

Flux density measurements were obtained using search coils of approximately 9 mm outer diameter (see Fig 4.8 and Appendix B). The results are considered below and given in detail in Appendix C.

4.3.1 A 1 slot/pole/phase Winding

Figure 4.9 shows that B_n, the normal component of flux density, is greater above a tooth than above a slot and has a linear variation with current. Above a slot, however, it increases slowly until the current is about 17 A after which it increases linearly. The initial non-linear variation is due to the flux taking the lower reluctance path provided by the laminations, as compared with the higher reluctance path of the slot.

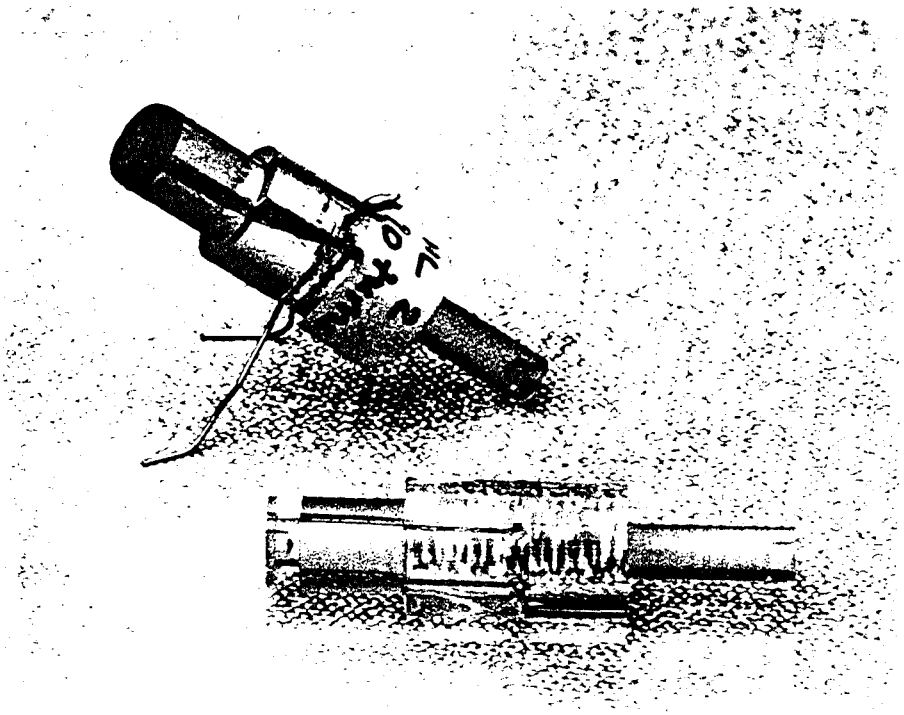

PHOTOGRAPH OF SEARCH COIL USED FOR FLUX DENSITY MEASUREMENTS

Figure 4.8

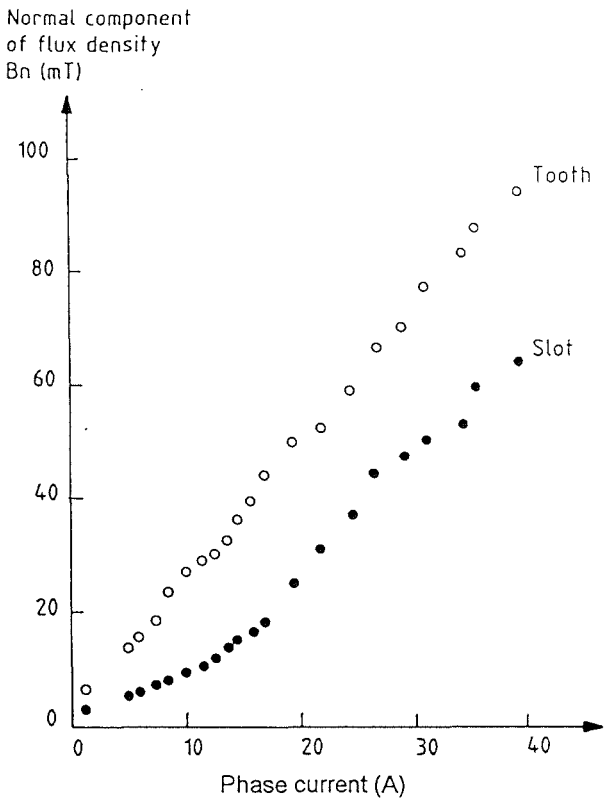

VARIATION OF B_n FOR A SLOT AND TOOTH OF THE TLIM (1 slot/pole/phase)

Figure 4.9

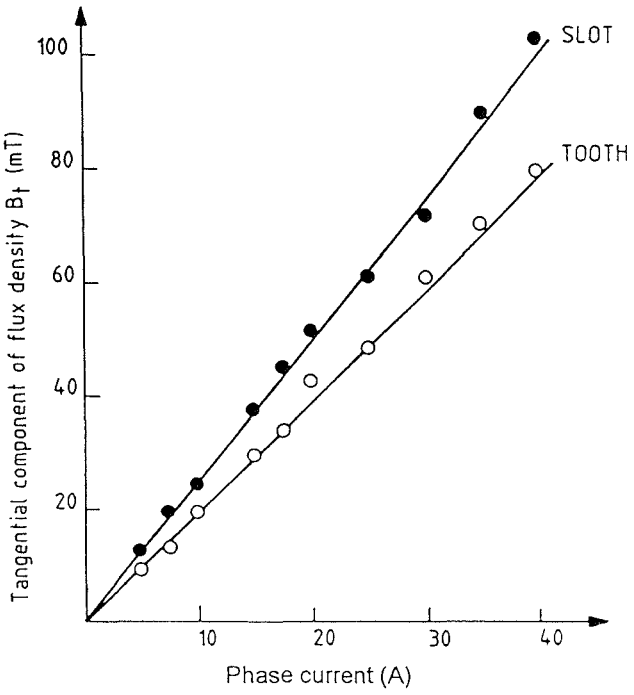

VARIATION OF B_t FOR A SLOT AND TOOTH OF THE TLIM (1 slot/pole/phase)

Figure 4.10

Figure 4.10 shows that B_t, the tangential component of flux density, increases linearly above both tooth and slot but is greater above a slot than above a tooth. The readings of tangential flux density were taken at a height of about 7 mm, due to the physical size of the search coil (Fig 4.8). It will be noted from both Figs 4.9 and 4.10 that the tangential flux density above the slot is approximately equal to the normal component above the tooth and is greater, therefore, than the normal component above the slot, illustrating that the majority of the flux in a tubular motor is tangential. This observation forms the basis of the expectation that a tubular motor might be capable of pumping ferromagnetic powder.

When viewed on an oscilloscope, the flux-density waveshape was sinusoidal at low currents but slightly departed from this at higher currents. Above a tooth the flux density waveshape became slightly "peaky" and above a slot slightly "rounded". Nevertheless, this basically verified the design assumption that the airgap flux density is predominantly sinusoidal, as eqn (4.1) (see also Appendix B) is obtained by considering a sinusoidal travelling field.

4.3.2 A 2 slots/pole/phase Winding

With this winding arrangement, Figs 4.11 and 4.12 show that both the normal and tangential components of flux density vary linearly above tooth and slot. As expected, the normal component is greater above a tooth than above a slot and the tangential component is greater above a slot. The fact that the flux density is mostly tangential in a tubular motor is more marked with this winding arrangement than previously, since the tangential flux density (Fig 4.12) is clearly greater than the normal component (Fig 4.11) whether compared above slots, teeth or slots and teeth. With the previous 1 slot/pole/phase winding, Figs 4.9 and 4.10 show that above a tooth the normal flux density is greater than the tangential component, but since in the present case this is reversed, the implication is that the ratio of tangential to normal flux density has increased. In addition, the normal component has fallen and the tangential component has been increased by changing the winding from 1 slot/pole/phase to 2 slots/pole/phase, indicating an increase in tangential flux density at the expense of the normal flux density (Figs 4.9, 4.10, 4.11 and 4.12).

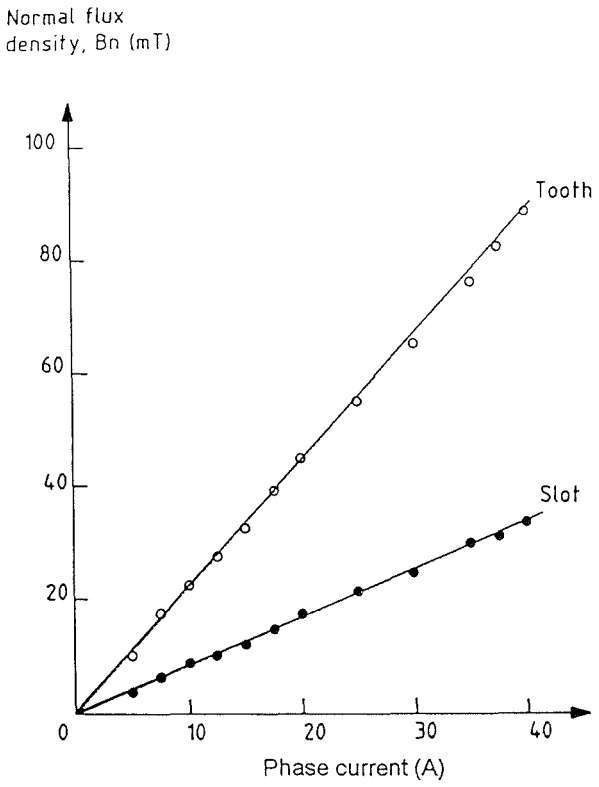

VARIATION OF B_n FOR A SLOT AND TOOTH OF THE TLIM (2 slots/pole/phase)

Figure 4.11

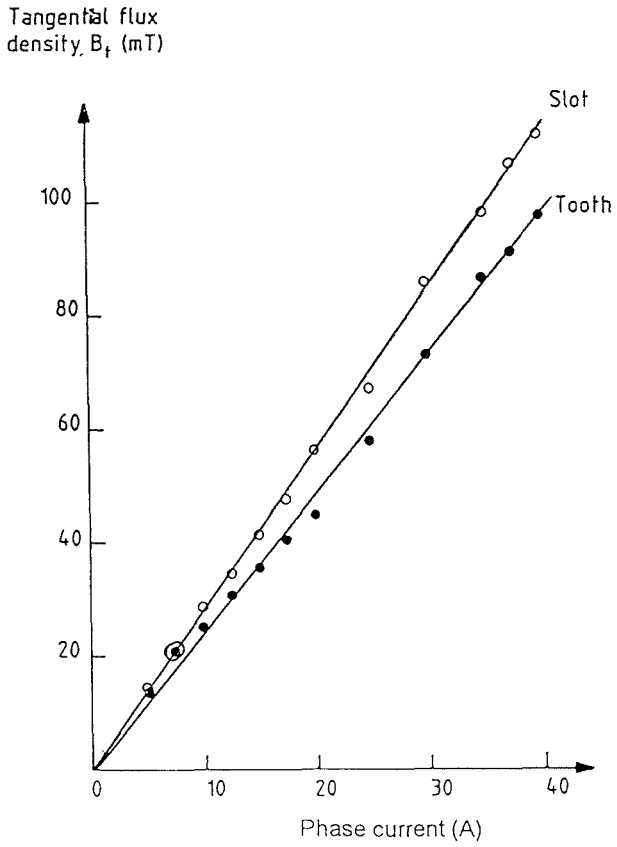

VARIATION OF B_t FOR A SLOT AND TOOTH OF THE TLIM (2 slots/pole/phase)

Figure 4.12

A direct comparison may be made by calculating the gradients of these graphs and the results of this are given in Table 4.1. (The value of the normal component above a slot with 1 slot/pole/phase winding is approximate, since its variation with current is non-linear as shown in Fig 4.9. A straight-line approximation was used to obtain this value which therefore has an influence on some of the ratios in Table 4.1.) This table clearly shows the decrease in the normal component of flux density and the increase in the tangential component when using a 2slots/pole/phase winding arrangement, thus producing a significant increase in the ratio of tangential to normal flux density. Calculation of B_{mod}, the modulus of the flux density per unit current, from Table 4.1 gives values of 3.12 mT/A and 2.92 mT/A respectively for a tooth and slot of the 1 slot/pole/phase winding and 3.26m T/A and 2.93m T/A respectively for a tooth and slot of the 2 slots/pole/phase winding. There is clearly no significant change in the overall levels of flux density but rather an increase in the tangential flux density at the expense of the normal flux density, which may explain the improved powder motion seen with a 2 slots/pole/phase winding arrangement.

Table 4.1: Comparison of flux density values for two different winding arrangements

Slope of the graphs of normal (B_n) and tangential (B_t) flux density against current		**Winding arrangement (slots/pole/phase)**		**2slots/pole/phase values as a fraction of 1slot/pole/phase values**
		1	**2**	
B_n/I (mT/A) (see Figs 4.5 and 4.10)	Tooth	2.4	2.2	0.92
	Slot	~1.5	0.85	~0.57
B_t/I (mT/A) (see Figs 4.6 and 4.11)	Tooth	2.0	2.4	1.2
	Slot	2.5	2.8	1.12
$\left[\frac{B_t}{B_n}\right]$	Tooth	0.83	1.1	1.33
	Slot	~1.7	3.3	~1.94

4.4 Mass Transport Rate Measurements

In order to quantify the powder motion described previously, the mass flow rate of various ferromagnetic powders was measured using the tubes described above. Powder was introduced into the first 80 mm and collected from the last 80 mm, as shown in Fig 4.13. It is clear that, at the entry end, some of the powder is outside the motor while the remainder is under one pole-pitch when using 1 slot/pole/phase. A similar situation occurs at the exit end, with powder being collected from underneath three slot-pitches of the device. Powder within the two extremes of the entry and exit ends was classed as being within the bore of the motor.

Mass flow rate measurements were made by spreading a known mass of powder evenly at the entry end and recording the amount at the entry and exit ends, and along the bore, at successive time instants for a fixed phase current. From these results the cumulative mass flow rate ($\dot{m}_c$) and the powder distribution within the tubular motor may be calculated and the results are presented graphically in Figs 4.14 to 4.17, 4.21 and 4.22 and in tabular form in Appendix C.

4.4.1 A 1 slot/pole/phase Winding

Using a 1 slot/pole/phase winding, 200 g of iron powder were placed at the entry end of the motor and the mass of powder in the three regions described above was measured for a phase current of 25 A. Figure 4.14(a) illustrates that the majority of the transported powder travelled in under 30 s, with the rate of change of the cumulative mass transport rate decreasing with time. (The mass transport rate is also a function of the amount of powder introduced as will be seen later.) The majority of the powder remained within the bore of the machine as shown by Fig 4.14(b), and it may also be seen that the powder was `pulled back' into the bore from the exit end. After 90 s, the increase in the amount of powder along the bore was made up by the decrease at both the entry and exit ends. This could be due to the flux at the ends of the motor returning to the laminations (see Fig 4.13) and, since the powder travels against the field, the end effect causing the powder to be drawn back into the machine-bore.

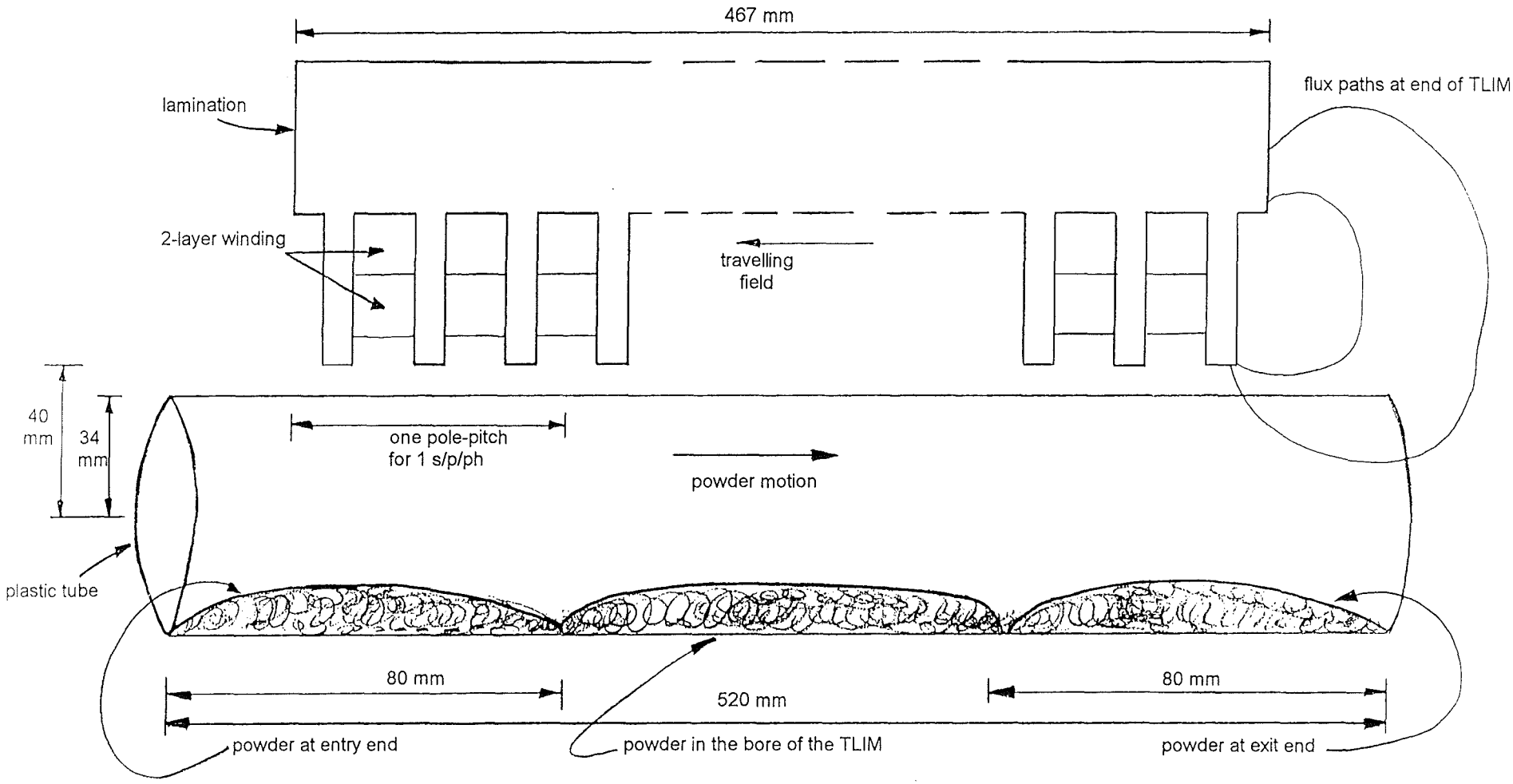

POWDER COLLECTION POINTS ALONG THE TLIM FOR MASS TRANSPORT RATE MEASUREMENTS

Figure 4.13

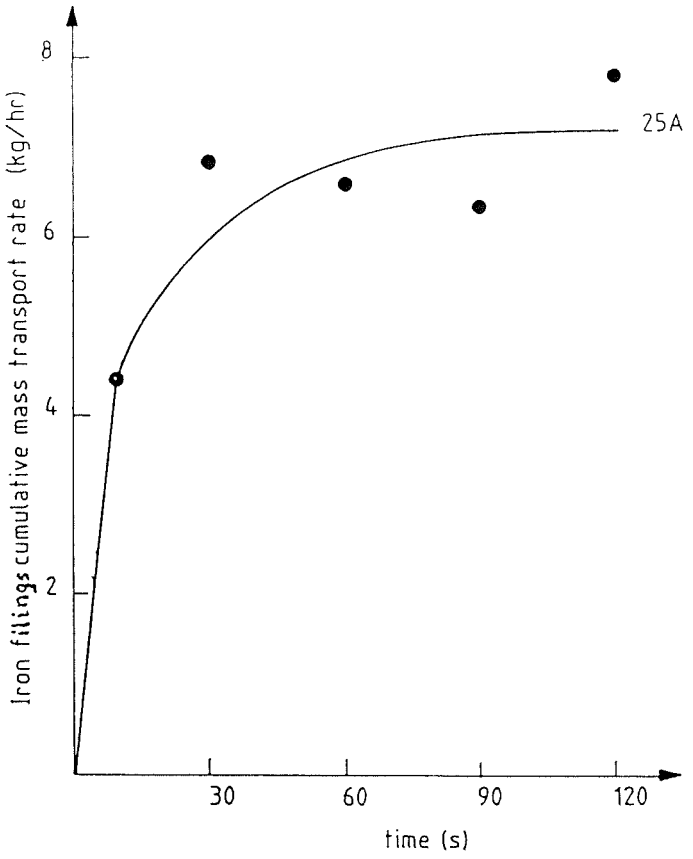

(a) mass transport rate

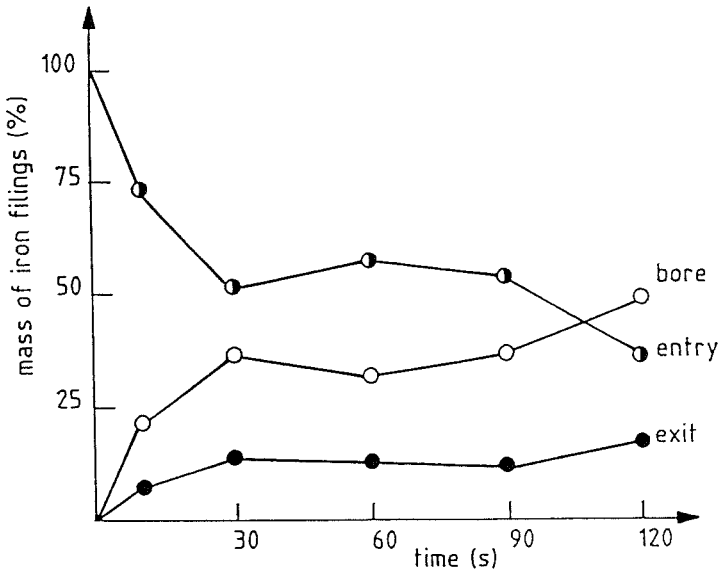

(b) powder distribution

TRANSPORT CHARACTERISTICS OF 200g OF IRON FILINGS WITHIN THE TLIM
(with a 1 slot/pole/phase winding at 25 A/ph)

Figure 4.14

After approximately 30 s (after the majority of powder transport) one or more powder ridges form rapidly and prevent further powder motion. Practically all powder stops flowing after about 60 s, with only a few particles able to free themselves from the stationary ridges which span nearly the full length of the motor and travel on to the end. The powder distribution graph of Fig 4.14(b) shows that not much powder has transported and a large amount has remained within the bore. Between 30 s and 90 s, the influence of the powder ridges is evident in both graphs, with a build up at the entry end and a decrease in the cumulative mass transport rate, implying that powder from the bore and the exit end was returning to the entry end. After 30 s, only about 10% of the powder has travelled to the exit end leaving approximately 50% still at the start. With the initial placement of the powder at the entry end (Fig 4.13), it was found that much of the powder was outside the influence of the present winding arrangement and therefore did not transport. The powder did not leave the machine (as already mentioned and as may be deduced from Fig 4.14) but rather clustered towards the last few teeth of the stator.

4.4.2 A 2 slots/pole/phase Winding

Earlier observations had indicated that powder motion was better with a 2 slots/pole/phase winding than with a 1 slot/pole/phase winding. Several powders were therefore used and their corresponding transport characteristics measured. Mass flow rate measurements were made in a similar fashion to that for the previous winding arrangement, with powder being introduced and collected from the first and last 80 mm of the plastic tube respectively.

a) *Iron filings*

Initially, for comparison with the previous winding arrangement, a test was conducted with 200 g of iron powder at 25 A/phase which, after 60 s, gave the following powder distribution:

at entry	-	35%;
along bore	-	62%;
at exit	-	3%.

Although very little powder travelled to the exit end, these results show that considerably more powder was "pulled" into the bore of the motor than with the previous winding, which had approximately 57% of powder still at the start and only 31% in the bore (see Fig 4.14).

The powder distribution results explain the observed transport characteristics. Immediately after switch-on, a few particles travelled to the exit end and long particle chains were formed rapidly running the length of the motor. These chains quickly grew into ridges which, as already described, first hindered and then prevented further powder motion. The 3% of powder that travelled to the end of the machine arrived in the first few seconds, whilst the remainder was spread evenly along the machine-bore by the travelling field during the majority of the remaining 60 s.

b) *Powder AISI*

Observations in Chapter 3 of comparative powder motion over the powder cleaner indicate that the mass flow rate of AISI is expected to be poorer than that of the previous powder. As mentioned there, the smaller size of powder AISI produces a lower mass flow rate.

Initially 100 g of AISI powder was used and the transport rate and distribution of the powder was measured for various currents. From the graphs of Fig 4.15, it is evident that, whatever the input current, the amount of powder remaining in the bore of the machine is between approximately 70% and 80%. At 20 A/phase, however, the amount of powder in the bore tends to be less than 70% but the amount of powder left at the start of the machine is around 30%, compared with less than 25% at 30 A/phase and less than 10% at 40 A/phase. Clearly most of the powder travelled in the first 30 s for each of the three different currents, with the majority travelling in the first 10 s. Increasing the current caused more powder to reach the exit end, showing a marked improvement between 20 A/phase and 30 A/phase, but only a small increase between 30 A/phase to 40 A/phase. The most notable change was the reduction of powder left at the start of the device with increasing current, as the effect of powder being "pulled" into the machine at switch-on is more pronounced. Figure 4.15(d) shows that at 20 A/phase the amount of powder at the exit end remained the same between 30 s and 60 s, but that in the bore

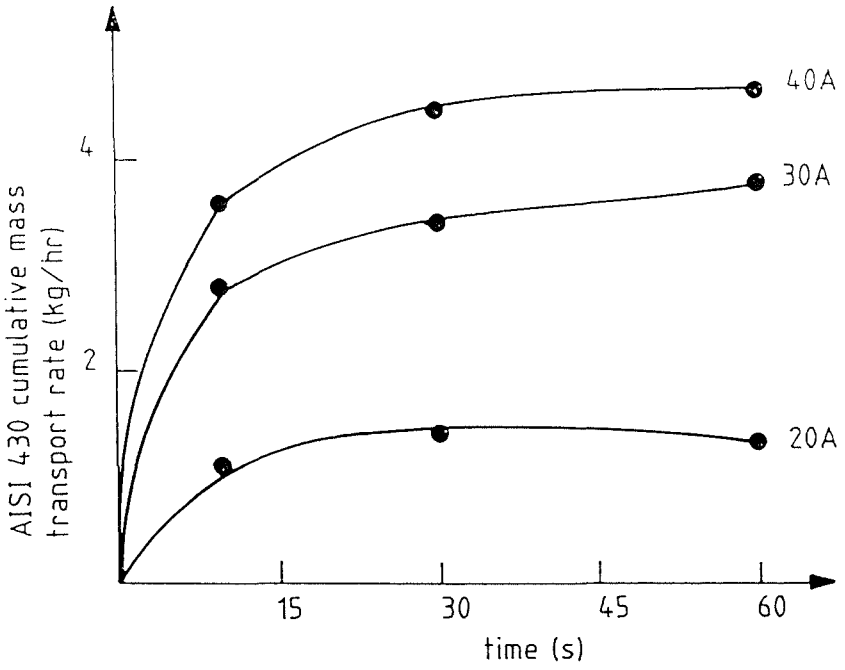

(a) mass transport rate

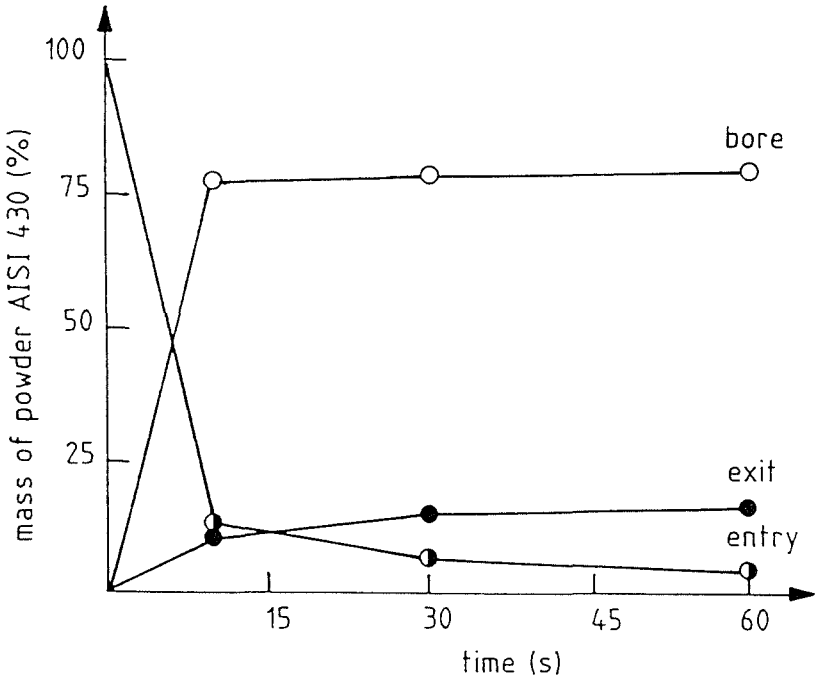

(b) powder distribution at 40 A/phase

TRANSPORT CHARACTERISTICS OF 100g OF AISI WITHIN THE TLIM
(with a 2 slots/pole/phase winding)

Figure 4.15

continued

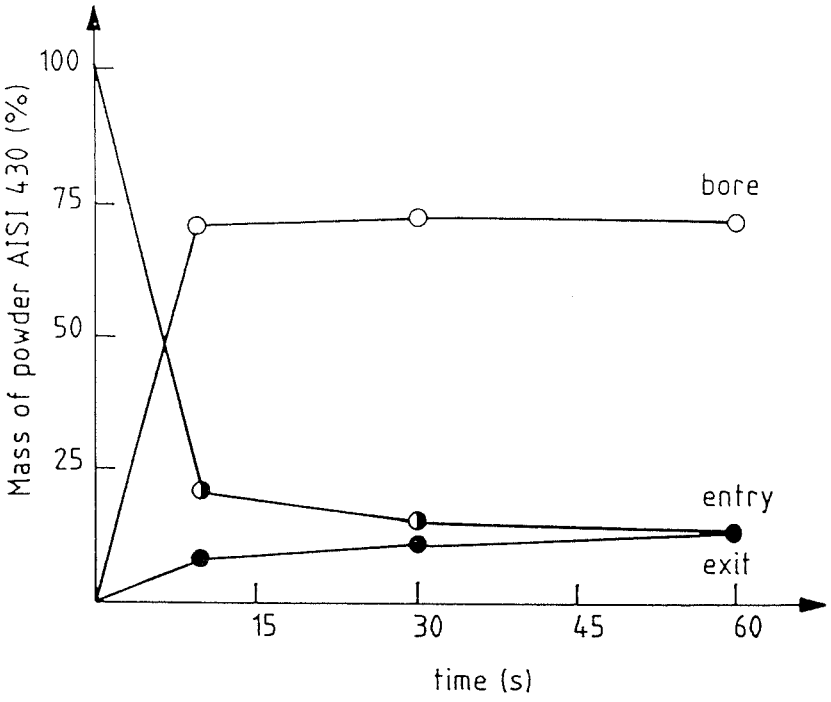

(c) powder distribution at 30 A/phase

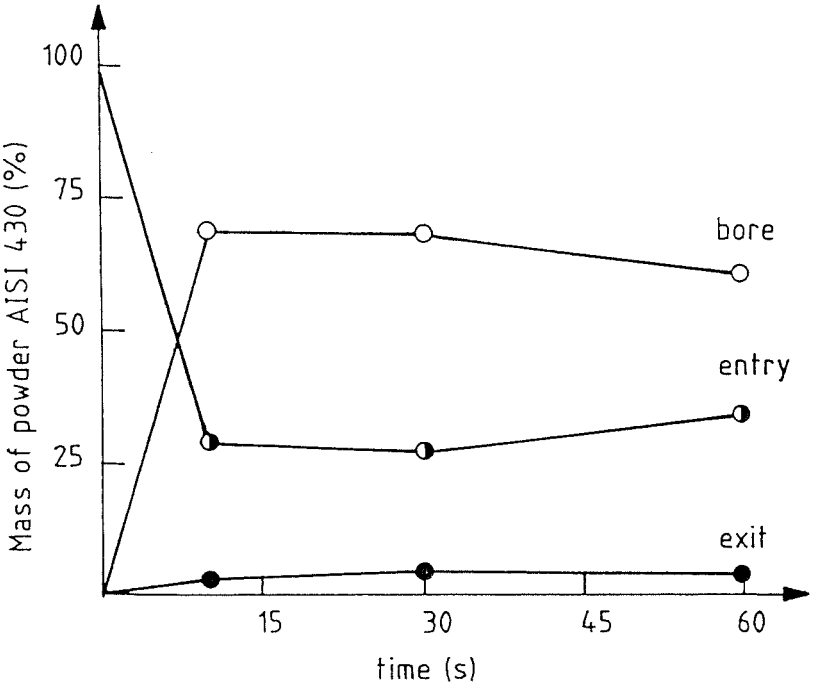

(d) powder distribution at 20 A/phase

TRANSPORT CHARACTERISTICS OF 100g OF AISI WITHIN THE TLIM
(with a 2 slots/pole/phase winding)

Figure 4.15

decreased and that at the entry end increased, showing that small amounts of powder sometimes travelled back due to the powder ridges that formed. Thus, not only did the ridges hinder and sometimes prevent powder transport, but on occasions they channelled powder backwards.

The cumulative mass flow rate graph of Fig 4.15 shows more clearly that the majority of powder transport occurred in the first 30 s. It also shows that the flow rate was more than doubled when the current was increased from 20 A/phase to 30 A/phase, and a further increase of at least 25% was produced at supply current of 40 A/phase.

Consideration of the motion of 200 g of AISI powder at 30 A/phase produced the results in Fig 4.16, which show that 30 s after switch-on, the flow rate was improved by less than 10% compared with that of 100 g of powder. The flow of powder to the exit end started slowly (compared with Fig 4.15), with the flow rate at 10 s being less than that with 100 g of AISI powder. Due to the greater amount of powder introduced, considerably more powder was left at the entry end of the motor and, as explained before, the powder ridges caused some to flow back to the entry end. With this larger amount of powder, only 8% of the total had reached the exit end after 60 s compared with 14% for 100 g of powder (see Fig 4.15) so that the mass of powder arriving in either case was approximately the same.

Increasing the current to 40 A/phase for the introduction of 200 g of AISI, resulted in the following powder distribution after 60 s:

at the entry end	-	11%;
along the bore	-	76%;
at the exit end	-	13%.

These results are similar to the 100 g case at 30 A/phase, with the generally low mass flow rates being due to the tendency of the powder to remain within the machine-bore and, with more powder introduced, the tendency to move back into the device rather than to continue to collect at the exit end.

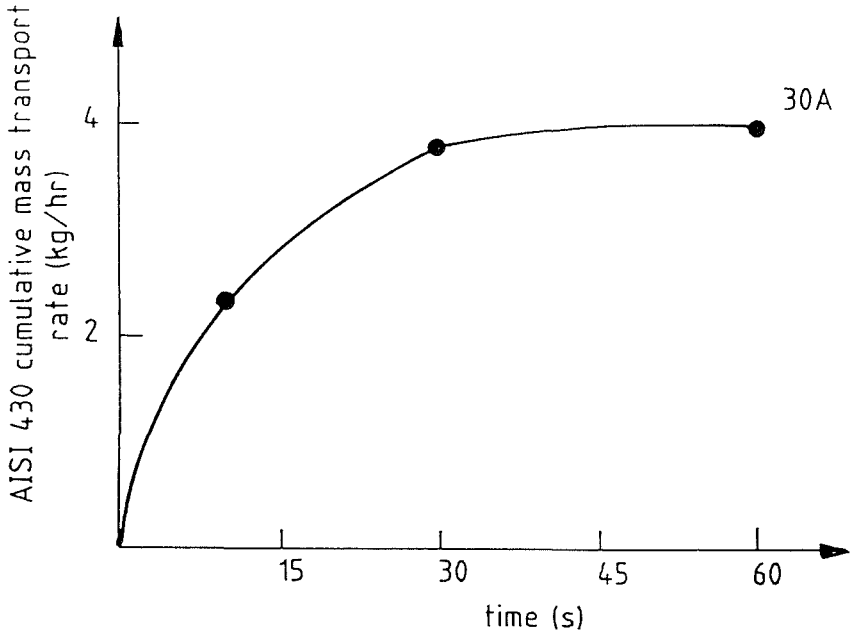

(a) mass transport rate

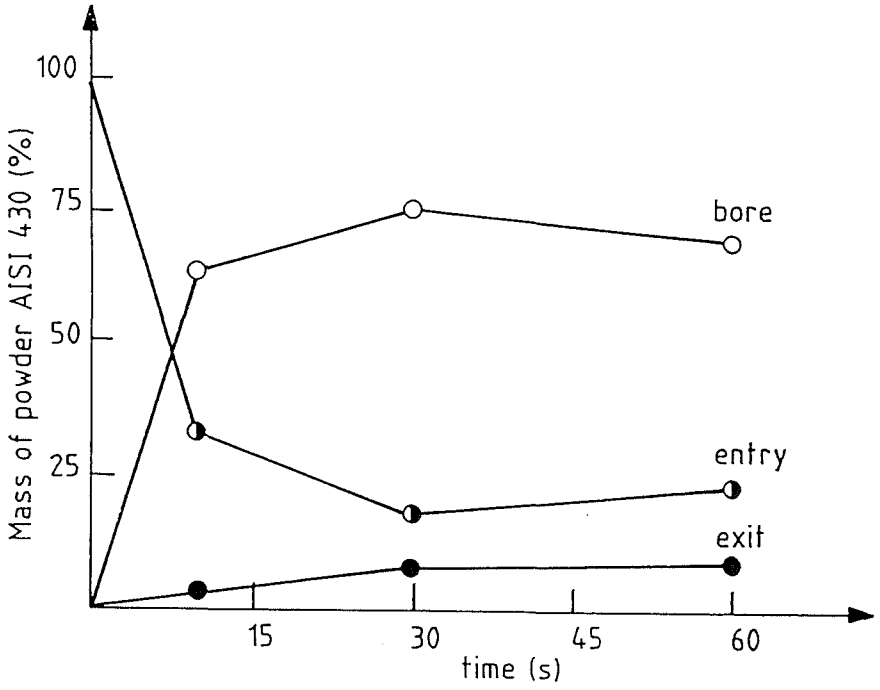

(b) powder distribution

TRANSPORT CHARACTERISTICS OF 200g OF AISI WITHIN THE TLIM
(with a 2 slots/pole/phase winding at 30 A/phase)

Figure 4.16

c) *Powder Ni/Fe*

Since movement was better at higher currents and with less powder, a test was performed at 40 A/phase with 100 g of the magnetically soft Ni/Fe powder. Figure 4.17(a) shows that the cumulative mass flow rate was 0.5 kg/hr greater than with AISI (Fig 4.15(a)) but the powder distributions (Fig 4.17(b) and Fig 4.15(b)) were similar, indicating that the soft powder initially travelled more quickly but soon settled down to a similar mass flow rate. Other motional differences were the greater agitation of Ni/Fe (discussed previously in Chapter 3) and greater movement on the powder ridges, with these ridges growing to a height of at least 25 mm.

4.4.3 An Accelerating Field

For this test, the tubular motor was wound as in Fig 4.18 so as to have an accelerating field[2].

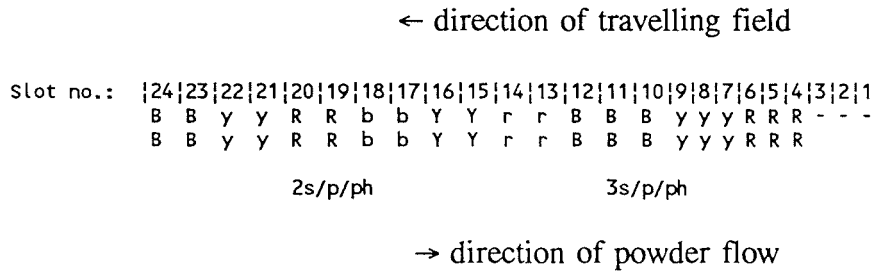

Figure 4.18: The TLIM with an accelerating field

Although with this winding the powder spread further around the inner circumference of the tube in which it travelled (due to the increased flux density within the bore), the results were disappointing. The flow rate was approximately the same as previously and the powder failed to travel to the exit end, but stopped at slot 3 where the windings ended, indicating that even if the last three slots had been wound the powder would not have left the device. This winding was therefore not investigated further, although it did point to possible experimentation with a 4 slots/pole/phase winding because of the increased powder spread.

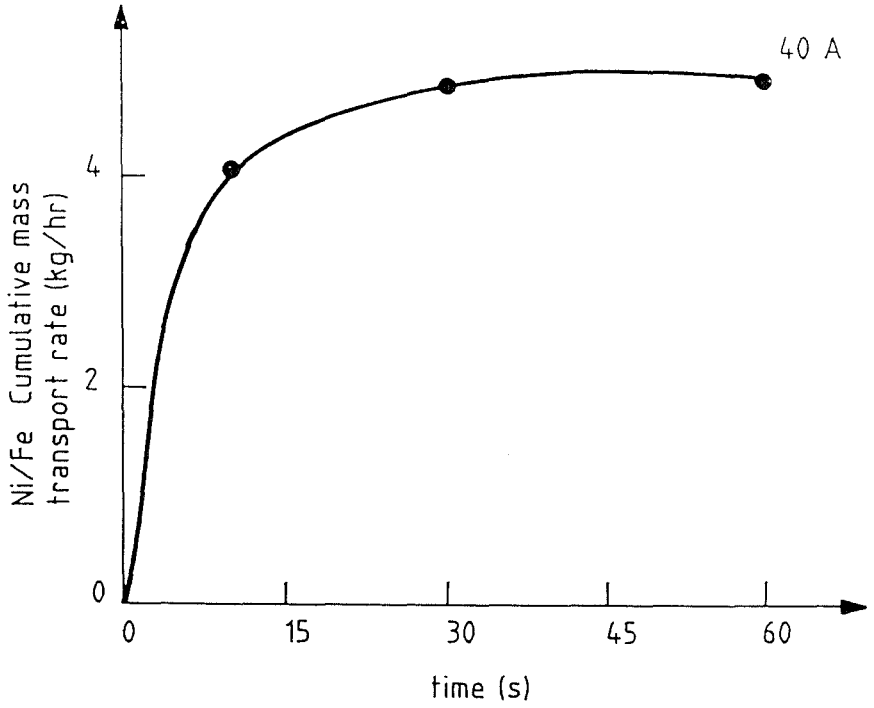

(a) mass transport rate

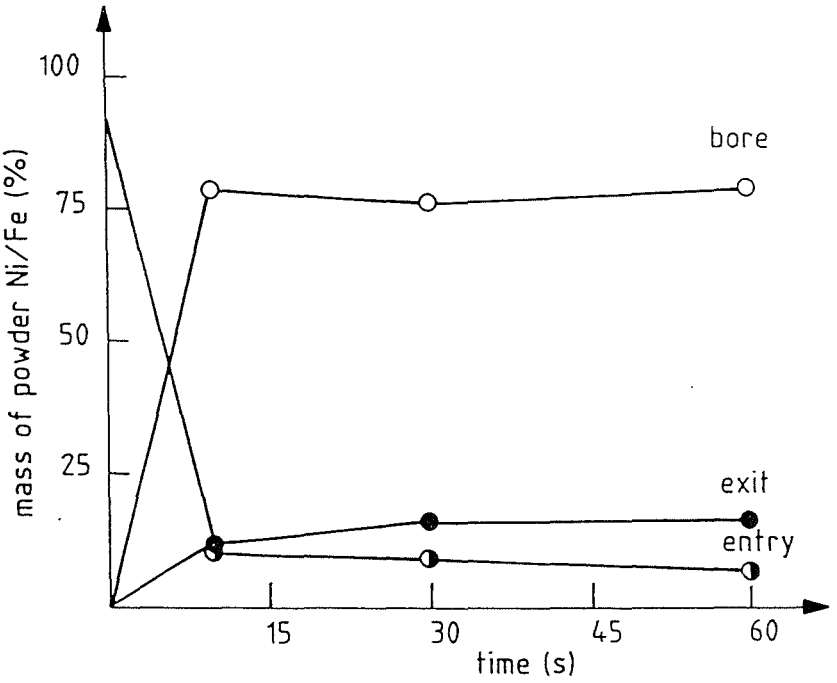

(b) powder distribution

TRANSPORT CHARACTERISTICS OF 100g OF Ni/Fe WITHIN THE TLIM
(with a 2 slots/pole/phase winding at 40 A/phase)

Figure 4.17

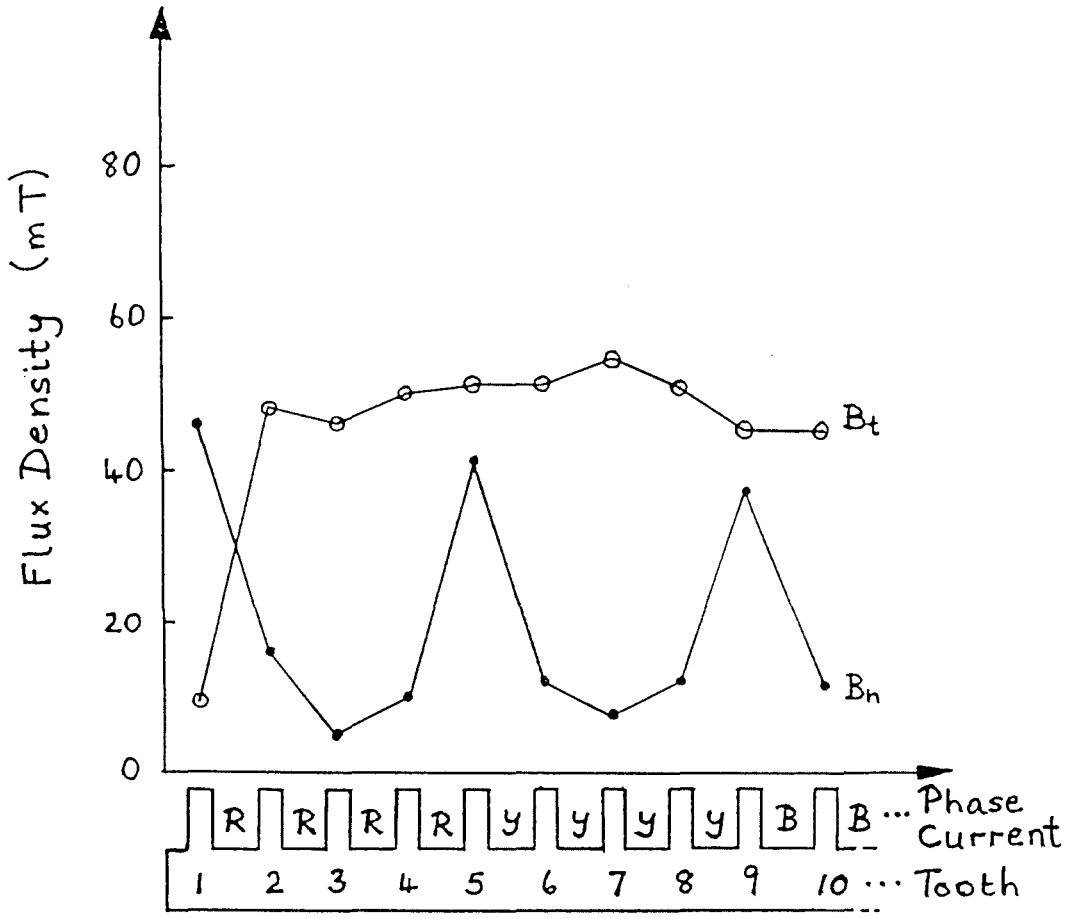

VARIATION OF FLUX DENSITY ALONG THE TLIM
(with a 4 slots/pole/phase winding at 20 A/phase)

Figure 4.19

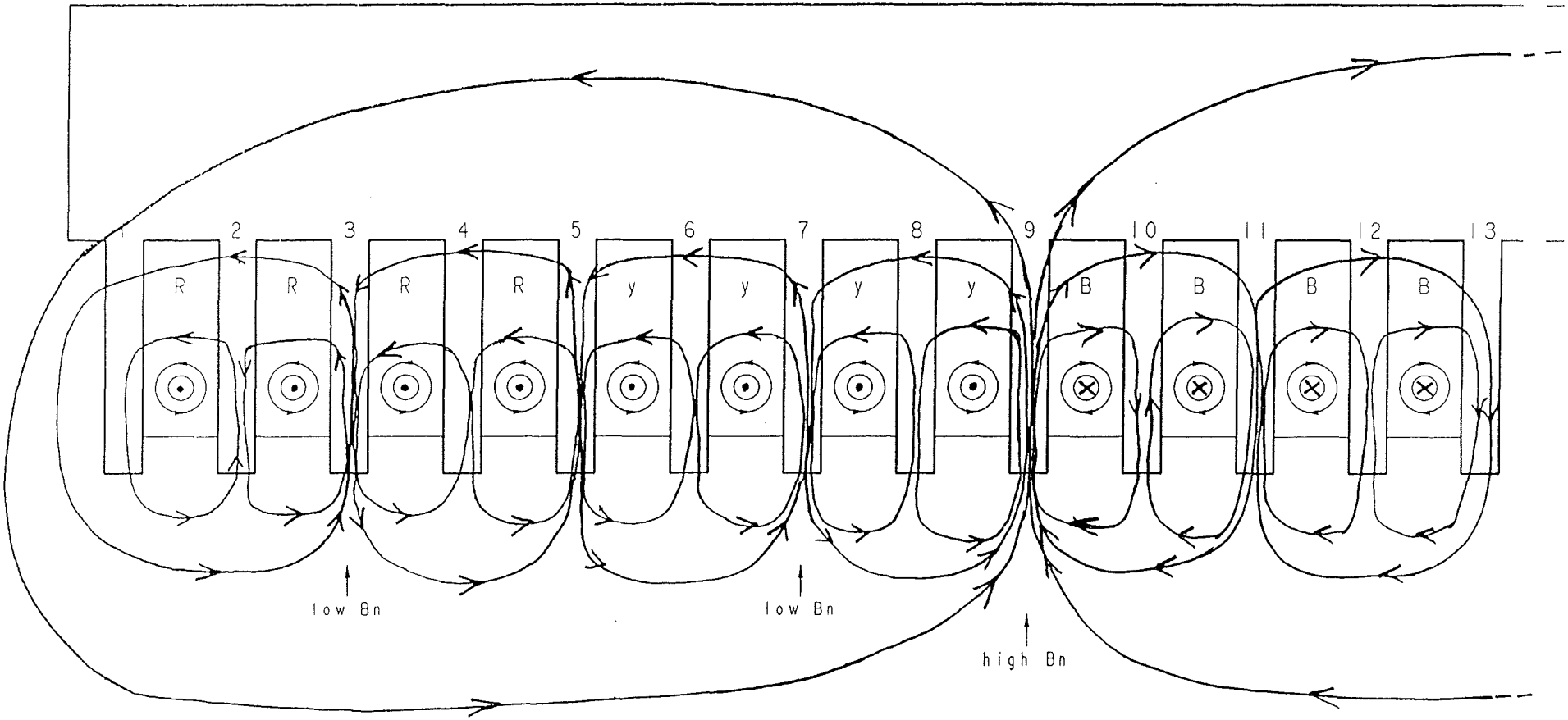

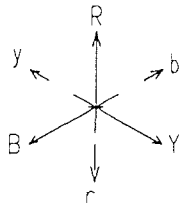

DIAGRAMMATIC REPRESENTATION OF THE FLUX DISTRIBUTION AT 4 slots/pole/phase

Figure 4.20

4.4.4 A 4 slots/pole/phase Winding

Having re-wound the tubular machine as a 2-pole, 4 slots/pole/phase fully-pitched device, flux density measurements and observations of powder transportation were made.

a) *Flux density measurements*

The variation of the normal and tangential components of flux density at 20 A/phase above the teeth of the motor (see Fig 4.19) illustrates that the flux density is predominantly tangential except at the ends of the device, and also that the normal flux density has a peaky shape. Since the pole-pitch is considerably increased over previous winding arrangements, it was expected that the majority of the flux density would be tangential and fairly constant. As expected, the normal flux density was very low at certain teeth due to partial cancellation of the mmf (see Fig 4.20). The diagrammatic lines of flux show that:

i) at teeth 3 and 7, a very low normal flux density is expected;

ii) at teeth 1 and 9, a high normal flux density is expected;

iii) over teeth 3 to 7, a high tangential flux density is expected, having built up over teeth 1 and 2, and decreased over teeth 8 and 9;

iv) a larger normal flux density is expected at tooth 5 compared with teeth 4 and 6 due to the phase relationship in the adjoining slots.

All these are consistent with the experimental results. It was also noted from Fig 4.20 that the tangential flux density varied only slightly along the radius of the motor but that the normal flux density dropped off rapidly.

Within the motor, the normal flux density peaks at approximately 40 mT (see Fig 4.19) compared with 45 mT for the 2 slots/pole/phase winding (see Fig 4.11) and about 50 mT for the 1 slot/pole/phase winding of Fig 4.9. The tangential flux density for the 1 slot/pole/phase winding of Fig 4.10 is about 40 mT, increasing to a little under 50 mT

for a 2 slots/pole/phase winding (see Fig 4.12) and rising to over 50 mT for the present winding as shown in Fig 4.19. Although the absolute changes are small, they amount to approximately 10% of the values of flux density concerned, indicating a shift from normal to tangential flux density. The most notable change however is the almost constant value of tangential flux density throughout the majority of the tubular machine for the present winding (Fig 4.19).

b) *Powder motion*

When AISI powder was introduced into the entry end of the motor there was practically no movement at 10 A/phase, apart from a small amount of powder which was pulled in. At 20 A/phase, two different events were clearly seen: the first was that much of the powder was drawn into the motor; and the second was that the powder transported and spread around the circumference of the tube. At 30 A/phase, the majority of the powder was rapidly pulled into the motor and spread at least 180° around the tube. In one or two places, the powder-spread was a full 360° although this was accomplished by only a few particles. Powder transport was effective with many particles travelling as though flying down the middle of the tube, i.e. travelling from one point on the tube to another while not in contact with the tube during their travel. At the exit end the powder settled in thin well-defined bunches, a few particle diameters thick, and still failed to leave the motor with the last few teeth attracting the powder back into the machine-bore.

Increasing the current further to 40 A/phase had the effect of pulling all the powder into the motor, with much of it transporting. When a relatively small amount of powder was introduced, most was eventually transported, but with a large amount, little further transportation occurred after an initial surge. Instead powder ridges quickly formed at the exit end of the motor, while other powder spreading along the inside of the tube hindered powder transportation and soon prevented it altogether. From about the middle to the exit end, the powder spread a full 360° round the tube, and considerably more powder than at 30 A/phase was seen to travel along the middle of the tube, with some particles flying nearly the length of the motor. Powder ridges and bunches formed, with the latter being less well-defined than previously due to the ridges bridging the gaps between these bunches.

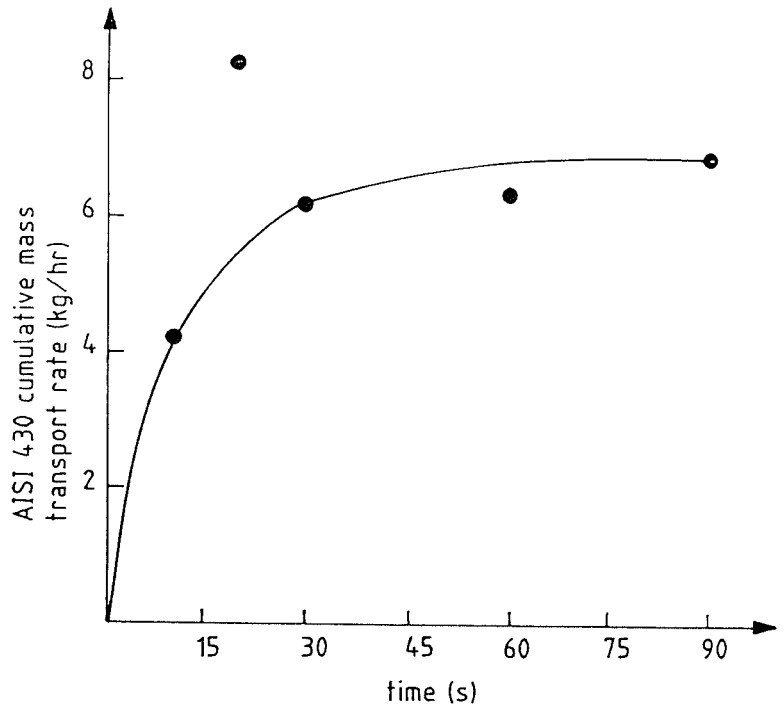

(a) mass transport rate

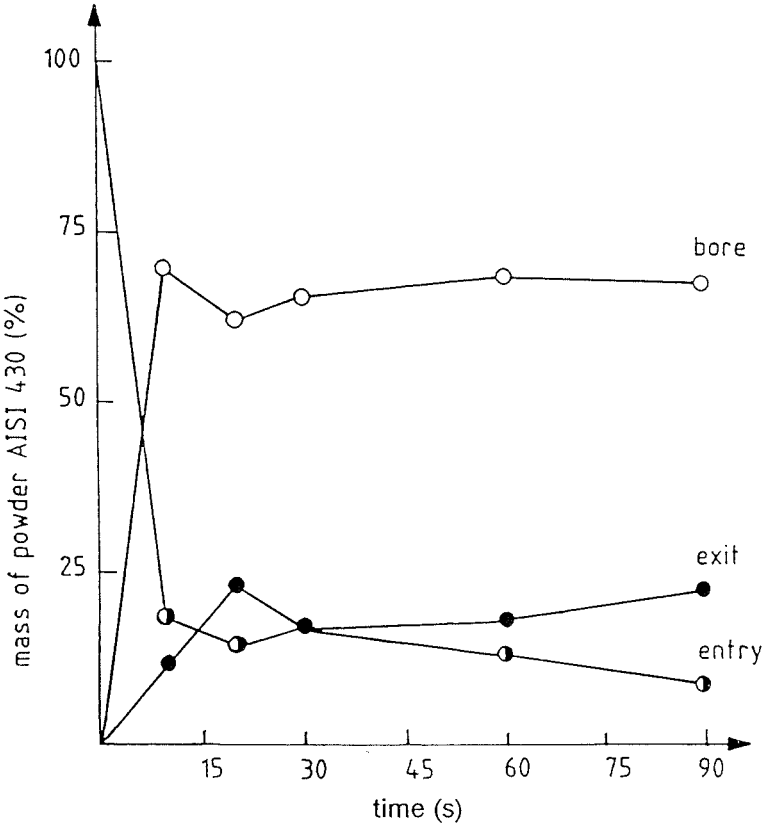

(b) powder distribution

TRANSPORT CHARACTERISTICS OF 100g OF AISI WITHIN THE TLIM
(with a 4 slots/pole/phase winding at 40 A/phase)

Figure 4.21

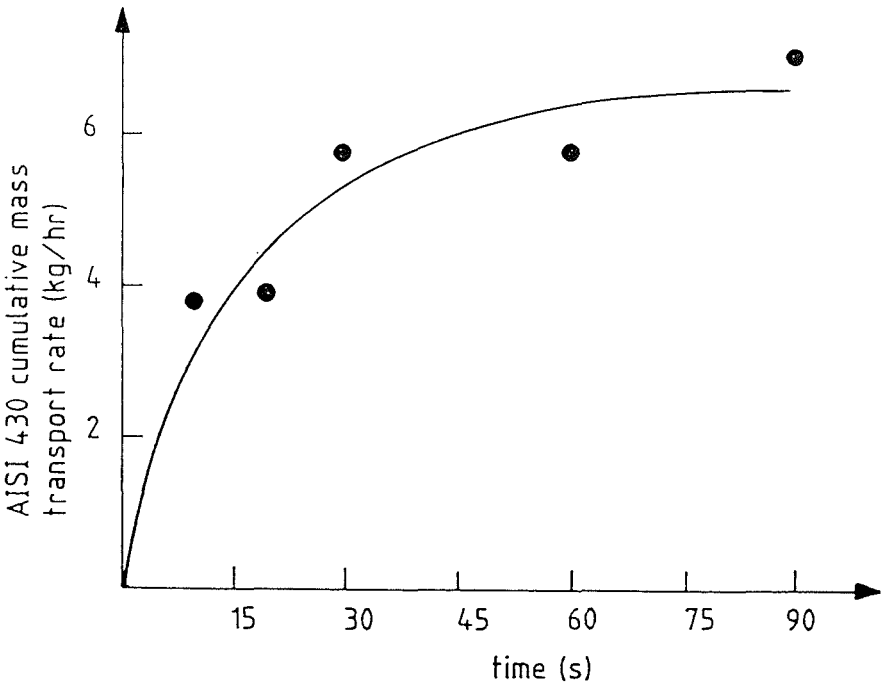

(a) mass transport rate

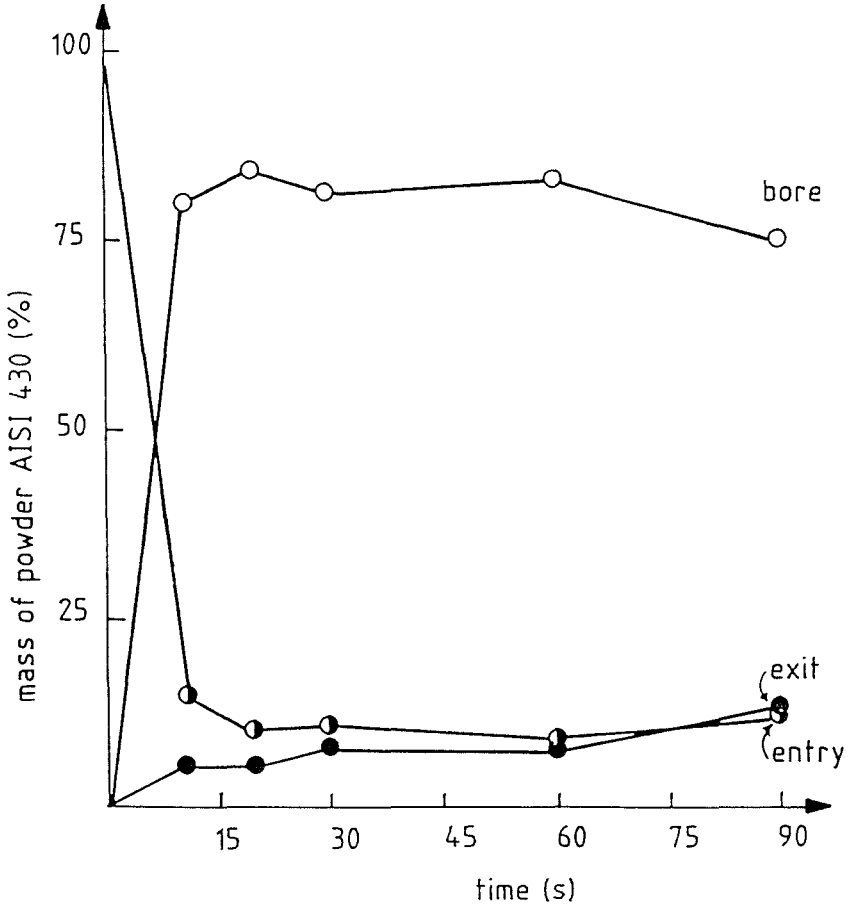

(b) powder distribution

TRANSPORT CHARACTERISTICS OF 200g OF AISI WITHIN THE TLIM
(with a 4 slots/pole/phase winding at 40 A/phase)

Figure 4.22

c) *Mass transport rate measurements*

Mass flow rate experiments were again conducted at 40 A/phase with the AISI-powder. The distribution and cumulative mass transport rate for 100 g are shown in Fig 4.21, and for 200 g in Fig 4.22. For both conditions the cumulative mass transport rate is essentially the same, at approximately 6.6 kg/hr after about 70 s. The cumulative mass transport rate graphs show however that the initial mass flow rate is greater with only 100 g of powder introduced, and from the more detailed results in Appendix C it can also be shown that the successive increases in the flow rate are marginally greater. The result at 20 s for 100 g of AISI (see Fig 4.21(a)) is anomalous rather than erroneous. As already described, powder collects at the end of the machine hindering further powder motion, but this does not always occur in the same way under apparently similar conditions. More powder than previously travelled to the end of the motor, giving a cumulative flow rate of more than 8 kg/hr (Fig 4.21(a)). However, since the powder failed to leave the device, it travelled backwards into the bore and to the entry end along the powder ridges, as shown by the increase in the amount of powder in the bore and at the entry end, at the expense of powder at the exit end, over the interval 20 s to 30 s in Fig 4.21(b). The powder distribution graph for 200 g of powder (Fig 4.22(b)) shows it travelled steadily to the end of the machine. The powder distribution for 100 g (Fig 4.21(b)) was, however, better than for 200 g since, proportionately, more powder travelled to the end of the motor and there was less powder left either in the bore or at the entry end.

A further test was carried out using 400 g of the AISI-powder. Initially the motional characteristics were as before, with an initial surge causing the powder to be distributed reasonably evenly throughout the tube. Soon after this, no further powder transportation took place, but ridges spreading along the inner circumference and some powder activity on the ridges were observed. The powder distribution, measured after 10 s, was:

at the entry end	-	46 g (11.5%);
along the bore	-	332 g (83%);
at the exit end	-	22 g (5.5%),

giving the cumulative mass transport rate as 7.9 kg/hr. Although the initial flow rate is large, the proportionate amount of powder at the exit end (5.5%) is low compared to that with 100 g of powder (see Fig 4.19(b)).

4.5 Comparison of Results

Using Figs 4.23 and 4.24 and the cumulative mass transport rate results above, a measure of the efficiency of the tubular motor for the transportation of powder may be calculated for the different winding arrangements, as shown in Table 4.2.

The result for the iron filings is more than 2½ times better than any other result, as expected from the comparative motional characteristics of this powder and AISI given in Chapter 3. The larger size of the iron filings produced this high efficiency.

Table 4.2: Efficiency of the TLIM for different winding arrangements

Powder type	Winding arrangement (s/p/ph)	Efficiency (kg/kWh)	Phase Current (A/ph)	Mass of powder introduced (g)
Iron filings	1	6.4	25	200
Ni/Fe	2	1.4	40	100
AISI	2	1.9	20	100
		2.3	30	
		1.3	40	
		2.4	30	200
	4	1.9	40	100
		1.9		200
		2.3		400

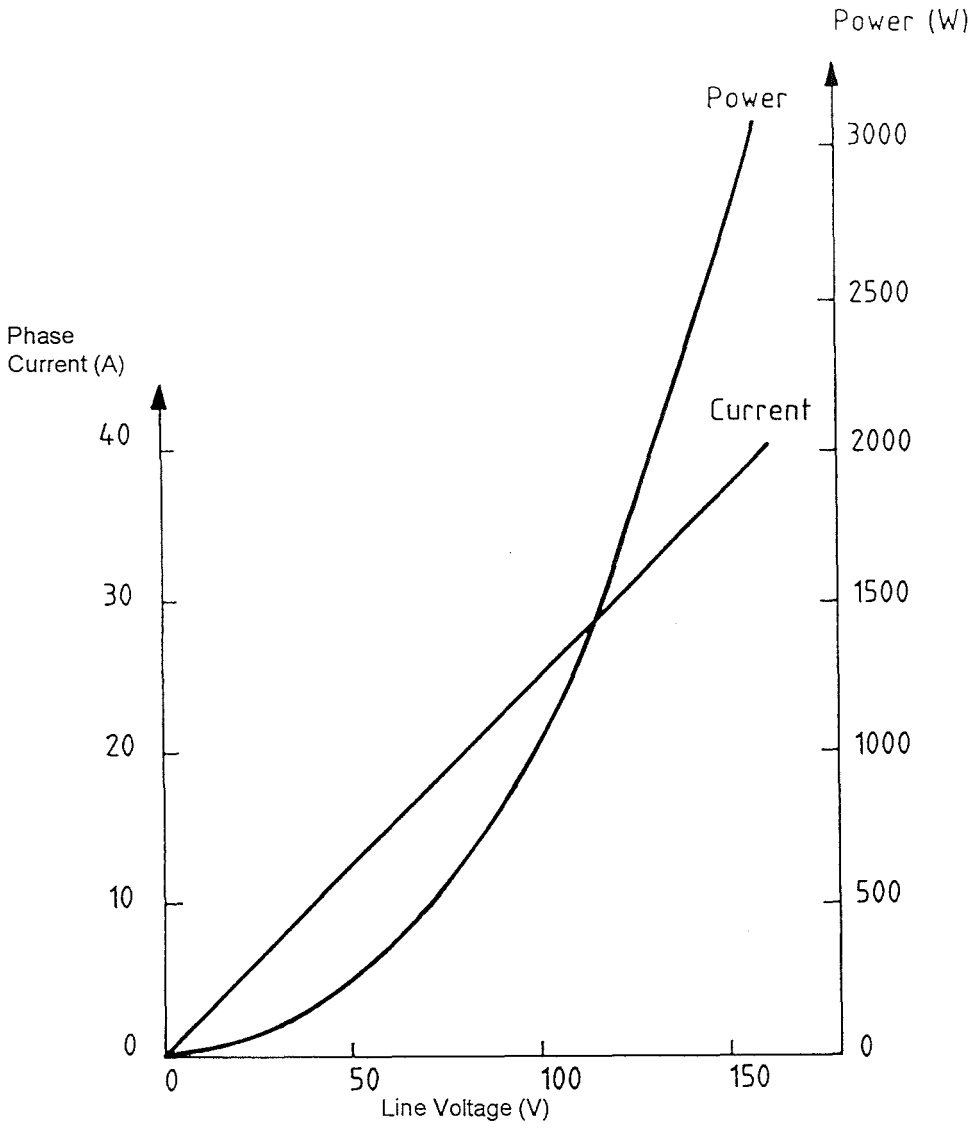

NO - LOAD MEASUREMENTS FOR THE TLIM (with a 1 slot/pole/phase winding)

Figure 4.23

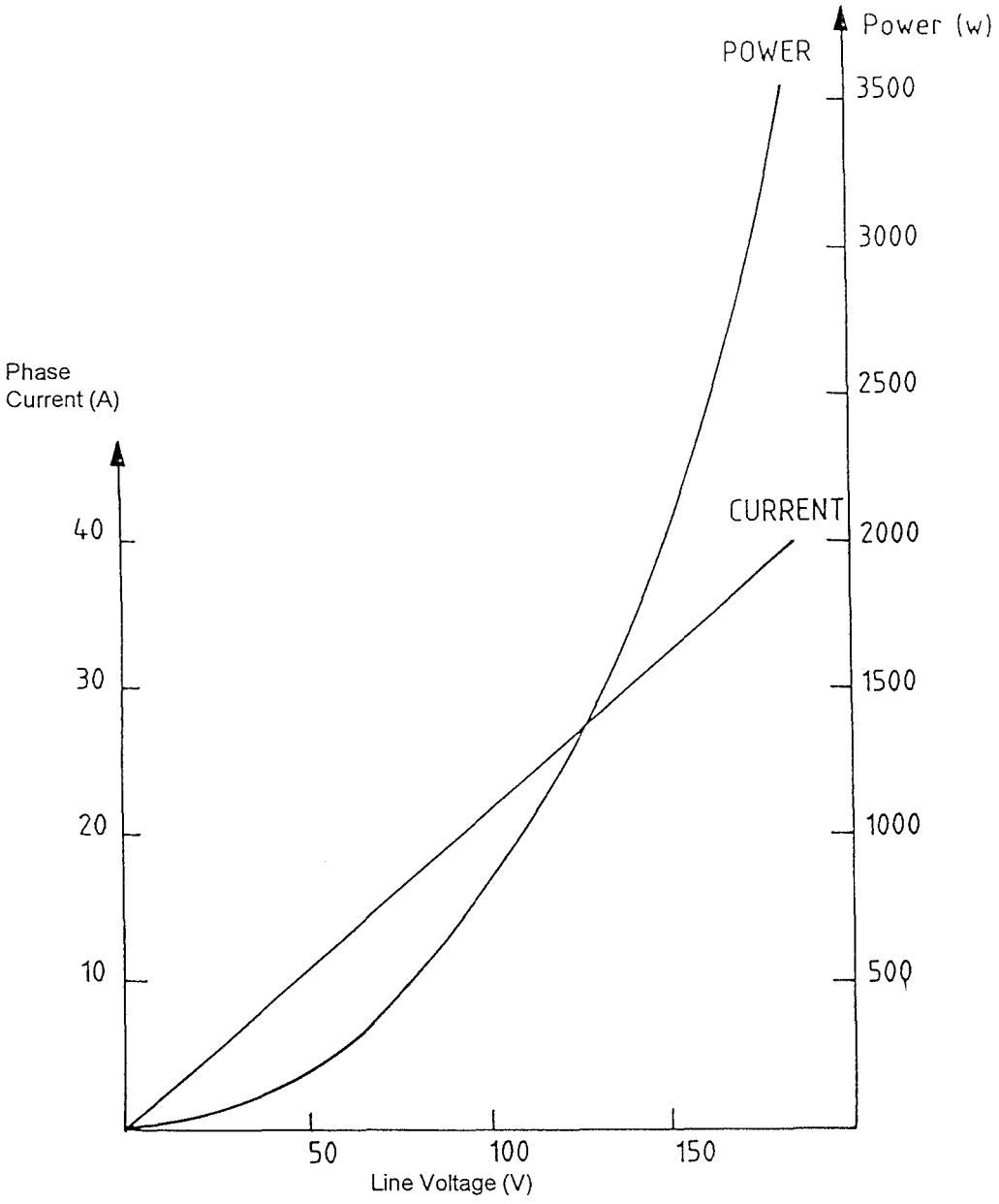

NO - LOAD MEASUREMENTS FOR THE TLIM (with a 2 slots/pole/phase winding)

Figure 4.24

The remainder of the results apparently contradict the previous assertions that powder motion is improved with increased current and a winding arrangement with a large number of slots/pole/phase. Firstly, powder motion was definitely better with increased current, as evidenced by the better powder distribution achieved, with little powder remaining at the entry end but travelling into the bore of the tubular motor. The cumulative mass flow rate, measured at say 30 s (when the majority of the powder travelling to the exit end had reached its destination), was also greater with increased current, improving by nearly 40% from a 2 slots/pole/phase to a 4 slots/pole/phase winding. The results in the table appear to indicate, however, that the improved mass transport rate does not compensate for the increased input power.

Secondly, since the powder did not leave the device, the measuring method favoured winding arrangements with a small number of slots/pole/phase; at the exit end, the powder tended to collect approximately over one pole-pitch, suggesting that the cumulative mass transport rate was improved for these windings. Reference to Fig 4.13 shows that the area designated as the exit end covered a pole for a 1 slot/pole/phase, 50% of a pole for a 2 slots/pole/phase and only 25% of a pole for a 4 slots/pole/phase winding. Considering the powder motion in this way implies that not all the powder was measured for the 2 and 4 slots/pole/phase windings. If measurements had been made in this way then powder still in the middle of the device would have been considered to have reached the exit, which does not appear sensible. The real problem was that powder failed to leave the tubular motor having arrived at the exit end, due to the flux paths at the end of the laminations and to local field effects. It will be recalled that, with an introduction of less powder, proportionately more is transported to the exit end. In addition, the amount of powder at the exit end determined how much more would travel to the exit, since ridges would form due to the local field and the tendency of particles to join together like permanent magnets (see Chapter 3). Thus, the larger the amount introduced, the proportionately greater the amount that would be hindered by the powder ridges, detrimentally affecting the results for the introduction of larger amounts of powder.

4.6 Summary

This chapter has investigated an experimental tubular linear induction motor for powder transportation. The powder motion has been described and results have been presented for flux density and cumulative mass transport rate measurements with different winding arrangements. An accelerating winding was also studied but this, unfortunately, was disappointing. A problem common to all the windings was the tendency of the powder to collect over approximately the last pole of the motor, causing powder ridges to form which hindered further powder transportation. Observations and results have shown that, for good powder transportation, the following are required:

i) a good travelling field;

ii) large input currents, and

iii) a large ratio of tangential to normal flux density, achievable via a winding with a large number of slots/pole/phase.

As expected, the TLIM was able to "pump" ferromagnetic powder through the use of a 4 slots/pole/phase winding at 40 A/phase.

References

1. NIX, G.F. & LAITHWAITE, E.R.: "Linear induction motors for low-speed and standstill application", *Proc. IEE*, 1966, **113**, (6), pp. 1044-1056.

2. ONUKI, T. & LAITHWAITE, E.R.: "Optimised design of linear induction motor accelerators", *Proc. IEE*, 1971, **118**, (2), pp. 349-355.

5. Finite Element Analysis

Several analytical approaches[1-10] have been used to characterize the behaviour of linear machines, including numerical techniques such as the finite-difference[11-13] and finite-element[14-17] (f.e.) methods, with numerous references existing on the theory of the f.e. method[18-26]. Using existing software[27-30], an attempt was made to correlate the flux distribution obtained from this method with the complex motion, incorporating both translational and rotational components, of iron particles above a linear device.

Problems to be solved using finite-element analysis are first modelled by treating a problem as being made up from a number of small, usually triangular, elements. A mesh is generated by fixing the size and location of these elements and their associated nodes, and after defining solution parameters and material properties and data, the mesh is ready for analysis. Setting up the mesh is usually the most time consuming (user and CPU) part of f.e. analysis, followed by viewing and analysing the results (post-processing) and finally by obtaining the actual solution. To obtain the solution, an iterative procedure is applied to the mesh, element by element, until the difference between the result of the present and previous iterations (the "error") is less than a pre-determined tolerance. After obtaining the solution, further software is used to translate the large array of numbers into meaningful results, e.g. plotting graphs of flux density in the areas of interest.

Magnetic field problems are often three-dimensional and open, because no practical material has infinite permeability. Assumptions are therefore necessary in a numerical analysis, in order that the problem may be handled in two dimensions to make the analysis manageable. To analyse a field extending to infinity, an infinitely large number of elements needs to be handled, and this is accommodated by fixing a boundary at points sufficiently distant from the source. The position of this boundary is described below, for both the tubular and linear machines that were modelled using the two-dimensional packages of GEC[27] and Rutherford Laboratories[28-30]. After an initial analysis of the TLIM the work was expanded, firstly by investigating the LIM and later by introducing particles into both the tubular and linear models.

5.1 Initial Study of the Tubular Machine

The tubular machine was modelled using the GEC software, which consists of a suite of three programs: pre- and post-processors and a solver, EARZ (Eddy-current, magnetic vector potential in polar (r,z) co-ordinates).

Using the pre-processor, all the information required by the solver was generated and stored in three data files, which contained information on the mesh, the geometrical outline of the problem and data on the materials modelled (e.g. their relative permeability, magnitude and phase of the exciting currents). The model of the TLIM was then passed to the solver, which calculated the solution data in terms of the magnetic vector potential, with the post-processor being used to present the results in pictorial and graphical form.

5.1.1 The Mesh

A mesh representing the TLIM was generated interactively using the pre-processor. Either straight-lines or arcs were drawn in sections and an appropriate number of equi-distant nodes placed along each section. As the experimental tubular machine (described in Chapter 4) was constructed from standard linear motor laminations (see Fig 4.1), it was these laminations that were modelled. A slot pitch (see Fig 5.1) representing a slot pitch in the actual lamination of Fig 4.1 was therefore drawn, and replicated to produce all twenty four slots of the lamination, and after adding the remaining sides and stamping holes the outline of the lamination was complete. Other areas, such as the copper windings and the air surrounding the lamination and opposite the teeth, were modelled in a similar manner to complete the geometrical and nodal information (see Fig 5.2(a)). Alphanumeric labels, also shown in Fig 5.2(a), were assigned to the different areas of the model (e.g. "I" for the region modelled as the iron lamination, "A" for the regions modelled as air) enabling specific data (e.g. material properties) to refer to particular areas of the model. The mesh was completed (see Fig 5.2(b)) after the triangular elements were automatically generated by the computer using the previously supplied nodal information.

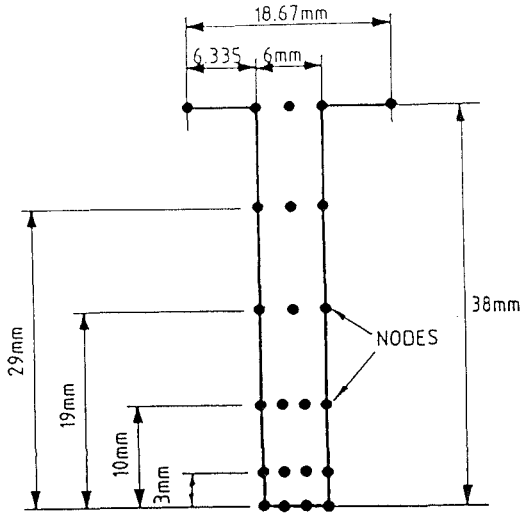

A SLOT PITCH

Figure 5.1

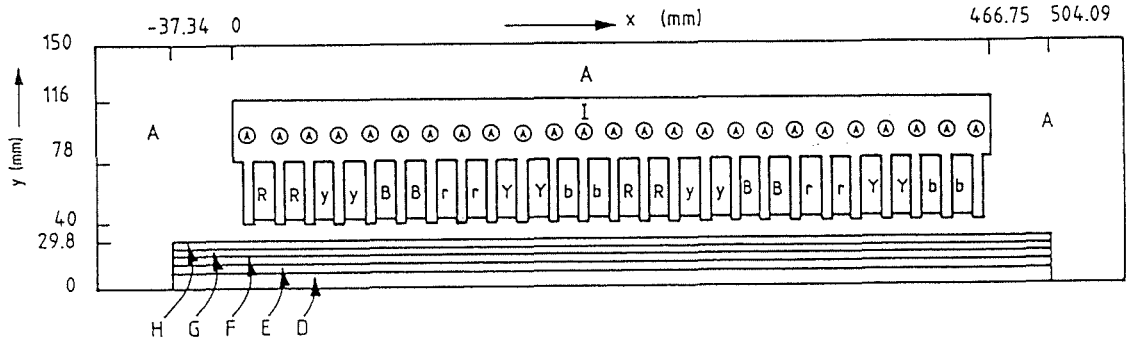

(a) outline

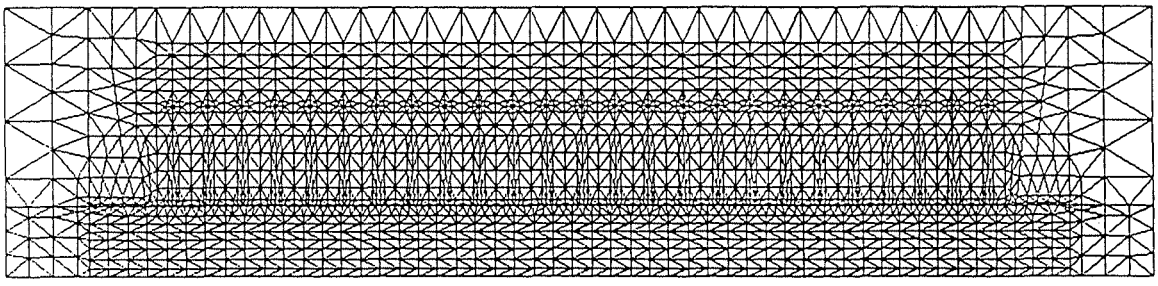

(b) mesh

OUTLINE AND MESH FOR THE TLIM

Figure 5.2

A 2 slots/pole/phase winding with full pitch coils (i.e. RR yy BB rr YY bb etc), 20 turns/coil and an rms current of 40 A/phase was used for the model. The current, entered in real and imaginary parts at time zero, was calculated from,

$$\text{real part} = 20 \times 40\sqrt{2} \cdot \cos\theta$$

$$\text{imaginary part} = 20 \times 40\sqrt{2} \cdot \sin\theta$$

where $\theta = \begin{cases} 0 \text{ for the red phase;} \\ \frac{2\pi}{3} \text{ for the blue phase, and} \\ \frac{4\pi}{3} \text{ for the yellow phase.} \end{cases}$

Hence the balanced phase currents in each slot were:

R → 1131.4 + j0 A
Y → -565.7 - j979.82 A
B → -565.7 + j979.82 A
r → -1131.4 + j0 A
y → 565.7 + j979.82 A
b → 565.7 - j979.82 A

From Fig 5.2(a) it may be seen that the lamination teeth are 40 mm above the lower boundary of the problem, this being the machine axis. The tubular device therefore has an airgap diameter of 80 mm and, along with the winding scheme and currents given above, the model reflects conditions in the experimental tubular machine (see Chapter 4). A current of 40 A/phase was used for the f.e. model corresponding to a current of 20 A/phase for the experimental machine, which had a double layer winding with each coil consisting of 20 turns.

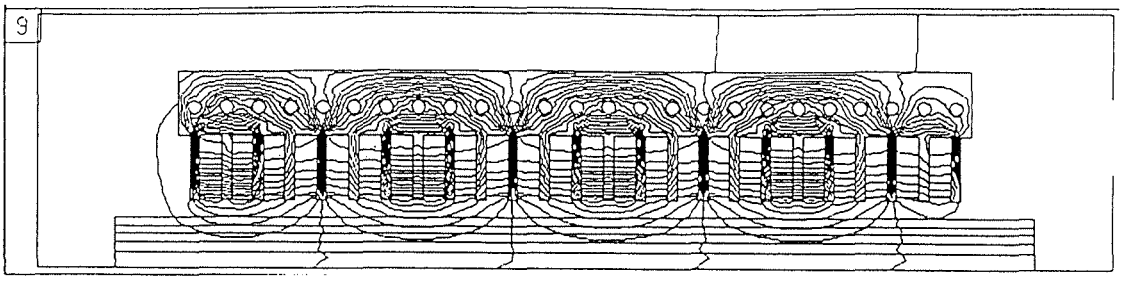

(a) $\omega t = 0$

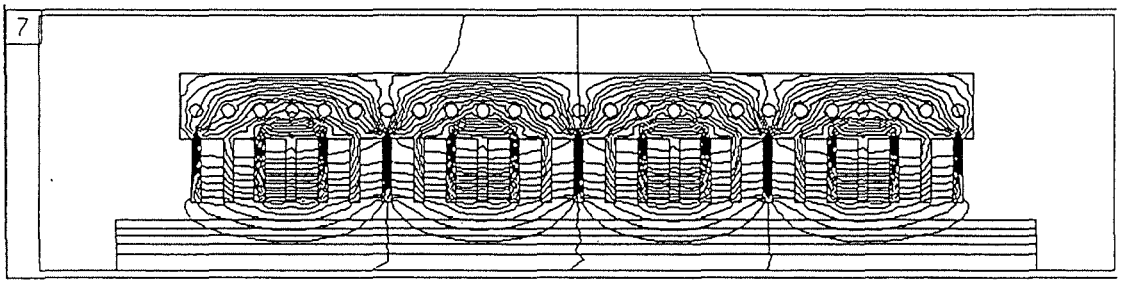

(b) $\omega t = \pi / 3$

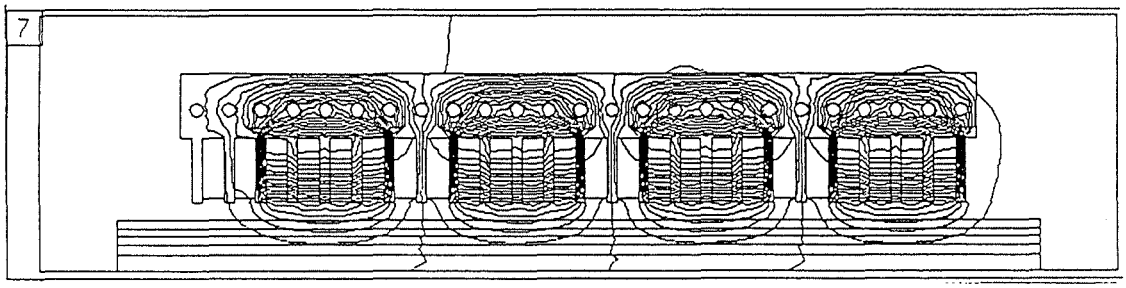

(c) $\omega t = \pi / 2$

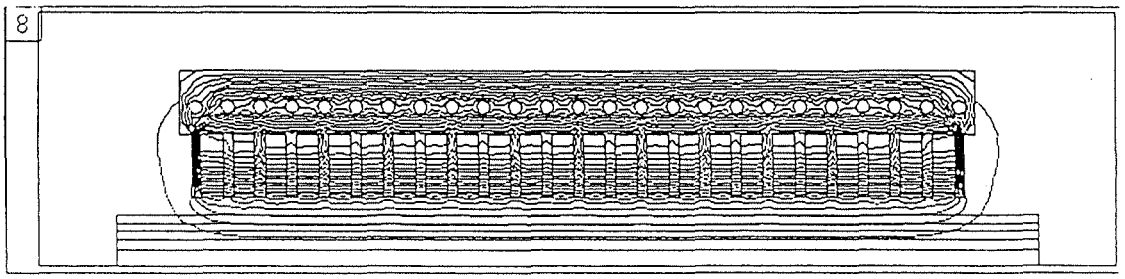

(d) modulus

FLUX DISTRIBUTION OVER THE TLIM

Figure 5.3

As the tubular machine is axisymmetric, the finite-element formulation of the problem may be solved in two dimensions, and the boundary conditions were therefore set along the machine axis (magnetic vector potential = 0).

5.1.2 Results

Figure 5.3 shows the flux distribution over the four poles of the tubular machine, for four different values of ωt. The motion of the travelling field can be clearly seen and, at $\omega t = \pi/3$, the field has moved on from $\omega t = 0$ by the expected two slot-pitches. It is clear that the greater build-up of flux in some of the slots is accompanied by a concentration of flux in the iron behind these slots and, in addition, the flux lines curve round the lamination stamping holes to follow the path of least reluctance. As this process only occurs near the holes, the flux pattern around the tooth tips will be unaffected if the holes were not modelled. The magnetic flux did not extend to any considerable degree into the airgap and there is virtually no flux outside the lamination, except directly below the teeth. This is clear from Fig 5.3(d), which illustrates the time averaged flux pattern, and it is apparent that the majority of the flux travels across the slots. Due to the discontinuity of the tubular linear device, the first and last teeth have to contain more flux than any other tooth or any other part of the iron lamination.

Figure 5.4 shows that the maximum flux density ($\hat{B}$) occurs in the middle of alternate lamination teeth. It can also be seen in Fig 5.4 that these teeth have a greater tooth-tip flux density and a concentration of flux in the iron immediately behind them when compared with adjacent teeth. Close inspection of Fig 5.3(d) also reveals that alternate teeth contain more flux than the intermediate teeth. The flux density in most of the bore of the model is less than 19.5 mT, whereas near the teeth it rises to approximately 30 mT. Near the stamping holes, the flux density is less than 20 mT and elsewhere (e.g. towards the back edge and sides of the lamination) it falls to below 10 mT.

Graphs showing the variation of the normal (B_n) and tangential (B_t) components and the modulus (B_m) of flux density along various lines parallel to the machine axis, where B_n is perpendicular and B_t is parallel to the axis, are presented in Fig 5.5. As the radius of the lines increases, B_n becomes progressively less sinusoidal, finally developing twenty

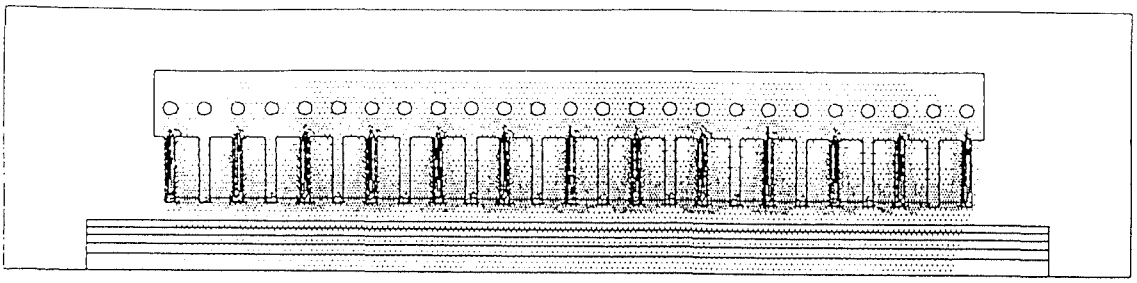

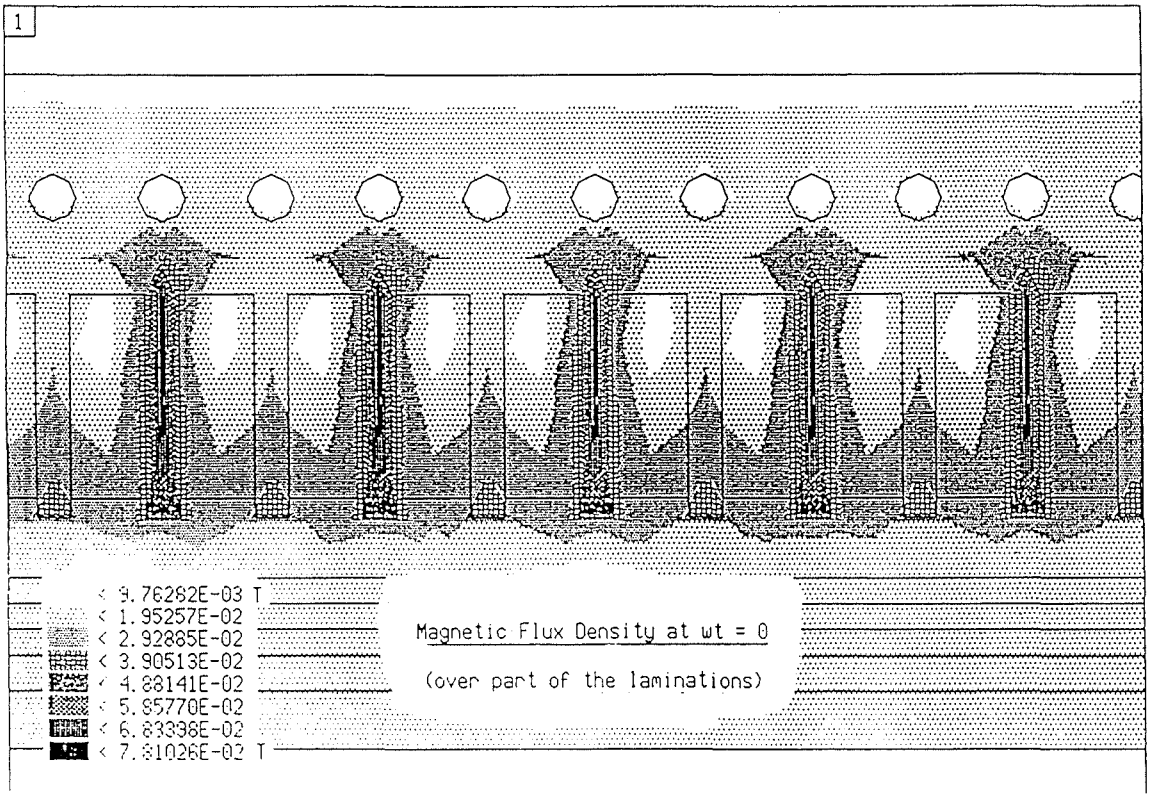

VARIATION OF FLUX DENSITY IN THE TLIM

Figure 5.4

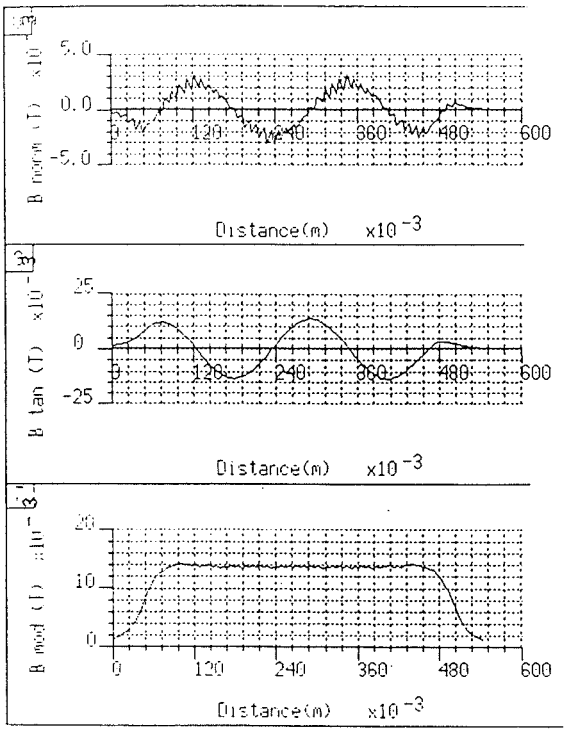

Graphs of Flux Density at radius 12.0mm

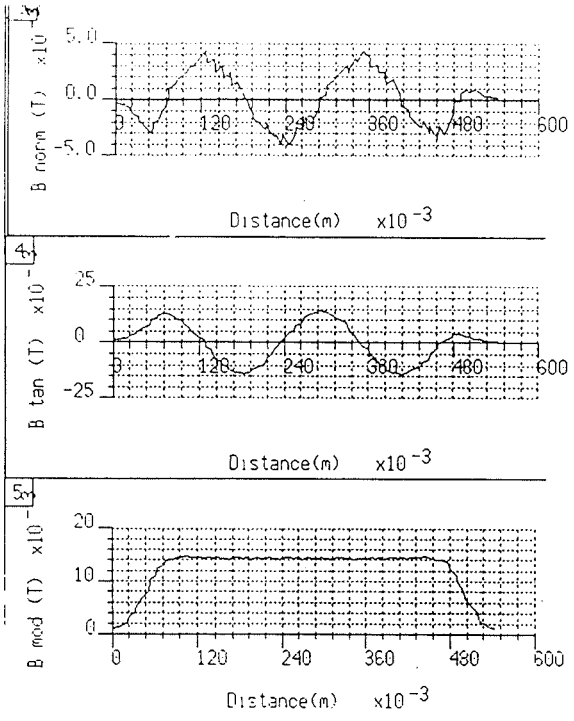

Graphs of Flux Density at radius 20.0mm

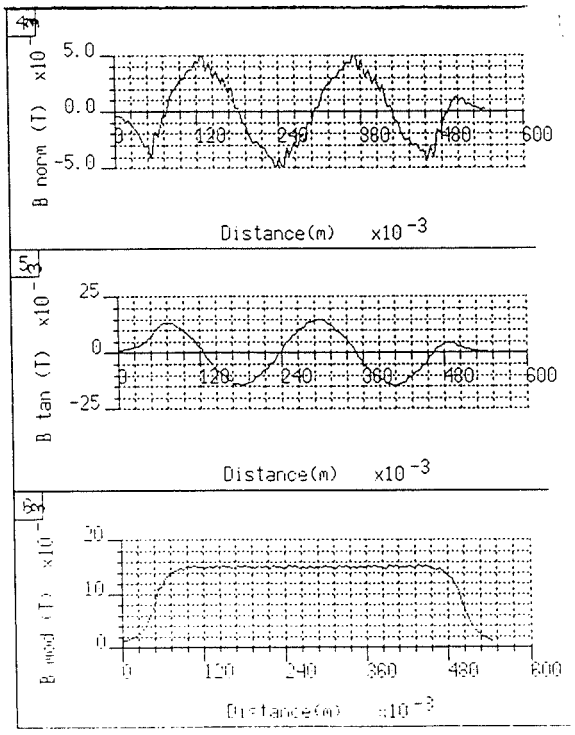

Graphs of Flux Density at radius 22.75mm

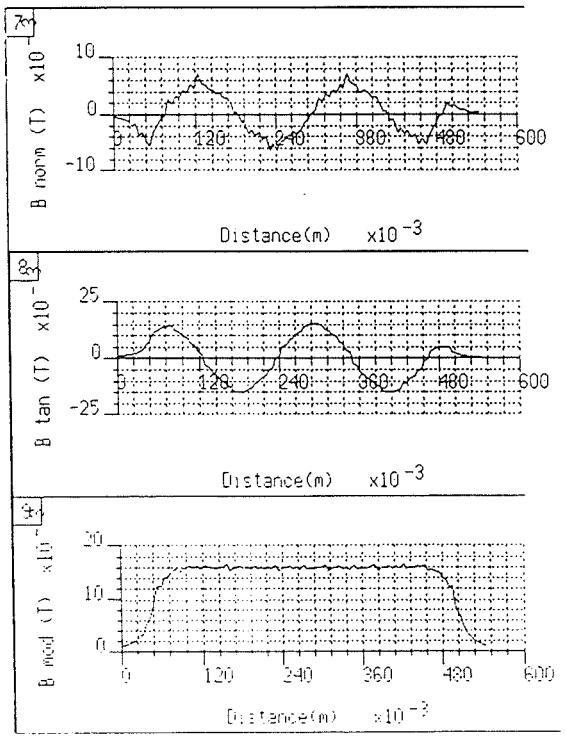

Graphs of Flux Density at radius 28.0mm

VARIATION OF FLUX DENSITY ALONG LINES PARALLEL TO MACHINE - AXIS

continued ...

Figure 5.5

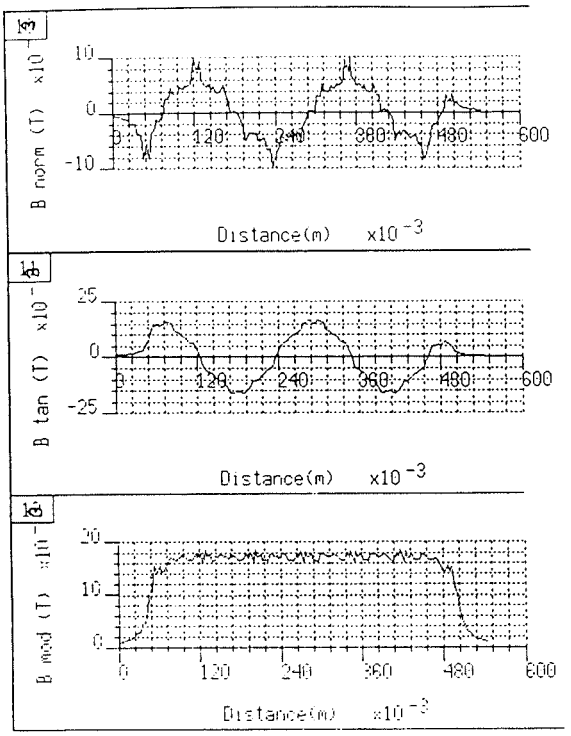

Graphs of Flux Density at radius 32.0mm

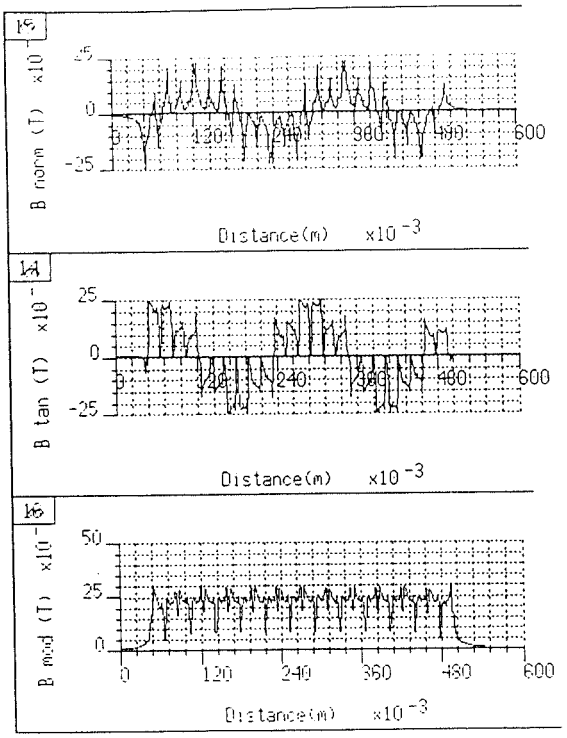

Graphs of Flux Density at radius 39.9mm

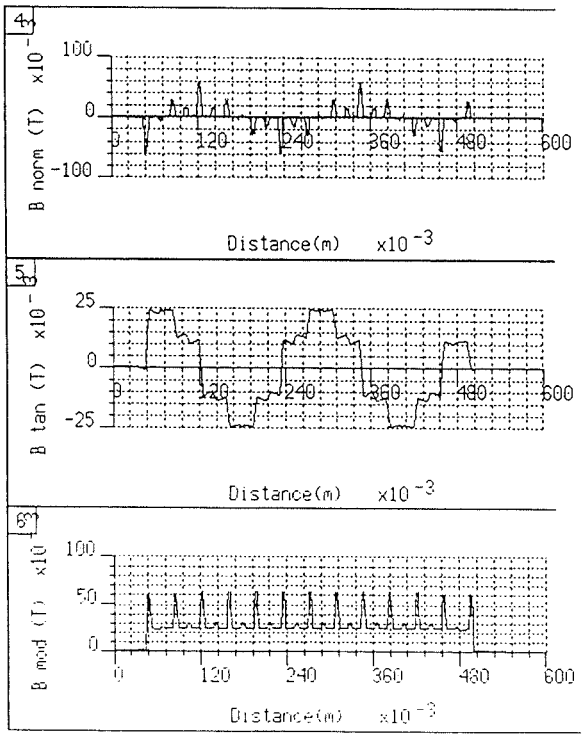

Graphs of Flux Density at radius 46.0mm

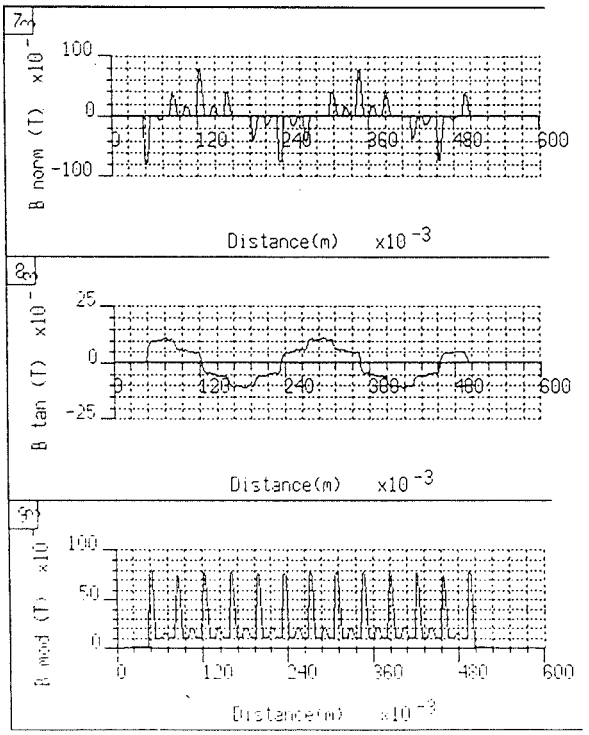

Graphs of Flux Density at radius 62.0mm

VARIATION OF FLUX DENSITY ALONG LINES PARALLEL TO MACHINE - AXIS

continued ...

Figure 5.5

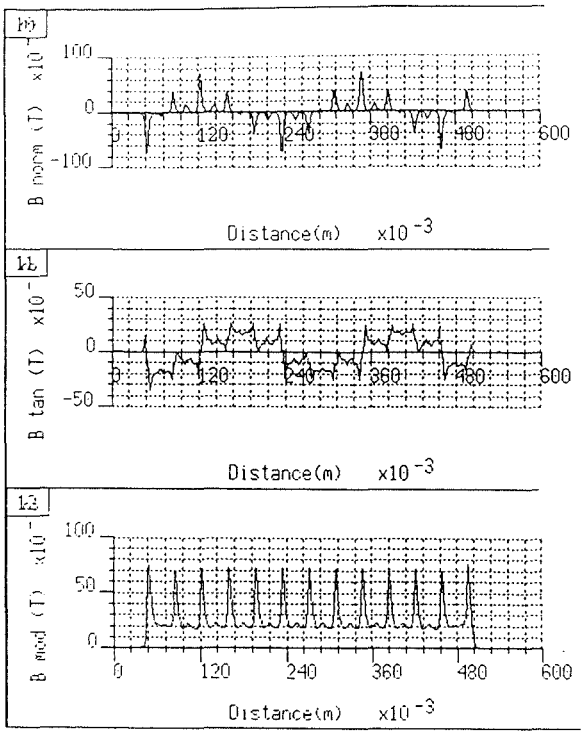

Graphs of Flux Density at radius 80.0mm

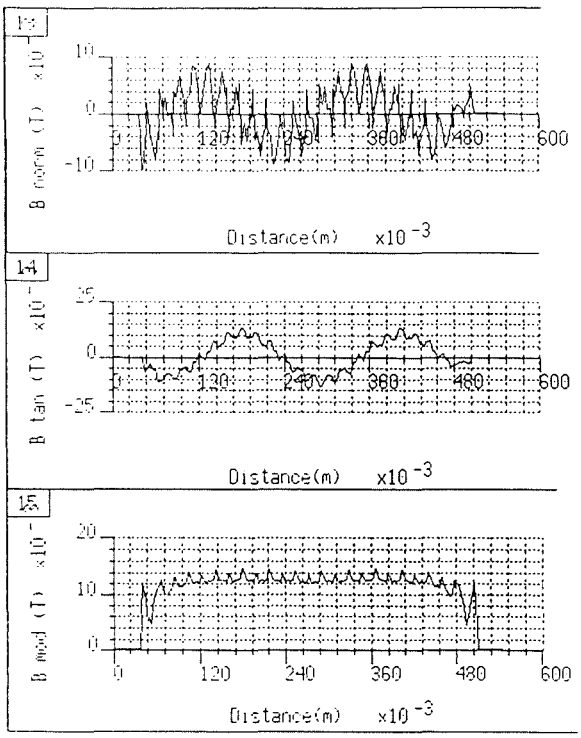

Graphs of Flux Density at radius 100.0mm

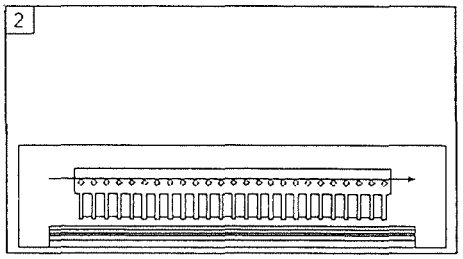

VARIATION OF FLUX DENSITY ALONG LINES PARALLEL TO MACHINE - AXIS

Figure 5.5

five separate peaks at a radius of 39.9 mm corresponding to the twenty five lamination teeth. B_t also becomes less sinusoidal with increasing radius, but develops twenty four plateaux along the surface of the teeth, corresponding to the twenty four slots. The peak value of B_m also increases with radius and, at the surface of the teeth, the graph of B_m illustrates the presence of the teeth and slots of the model by sharp peaks and troughs, which also relate to the distortions in B_n and B_t. An angular separation of 90° is expected between the tangential and normal pole-centres in the graphs of Fig 5.5 and sample calculations (see Appendix D) confirm this.

On entering the lamination teeth, the peak value of B_n increases rapidly, although B_t decreases with an overall increase in B_m (see the graph for a radius of 62 mm). Continuing towards the back of the lamination B_t increases and B_n decreases, with B_m decreasing to less than 15 mT near the stamping holes. (A table listing the abscissa co-ordinates of the teeth, slots and ends of the lamination, together with a table relating the major abscissa divisions of the graphs in Fig 5.5, will be found in Appendix D.)

The diagrams in Fig 5.6 are obtained from the graphs of Fig 5.5 (a table of values is given in Appendix D) to show variations in B_n, B_t and B_m along lines perpendicular to the machine axis. Graphs (a) and (b) highlight respectively the entry and exit ends of the device, whilst the others provide information for various teeth and slots. (The sign of B_n and B_t indicates their change in direction as related to the direction of the lines along which the graphs are plotted.)

From Fig 5.6(b) and Fig 5.3, it is seen that B_n is greatest in teeth one and twenty-five. Rapid changes of flux density occur as the teeth are entered over the interval 40 mm $\leq$ r $\leq$ 46 mm. The graphs for slots seven and sixteen (Fig 5.6(d) and (f)) show that, between the start of the winding (r = 46 mm) and r = 100 mm, only B_t is present (i.e. B_n = 0), which is confirmed by Fig 5.3. Along the edges of the lamination and in the space outside the area below the teeth, B_m is extremely low. Nearly all the flux is confined to the lamination and between the slots, with the airgap flux density being minimal.

It was expected that at the current of 20 A/phase the tubular machine would not transport powder effectively, as there was little field strength in the airgap. Relating this to the

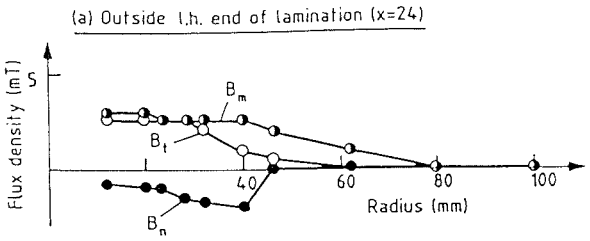

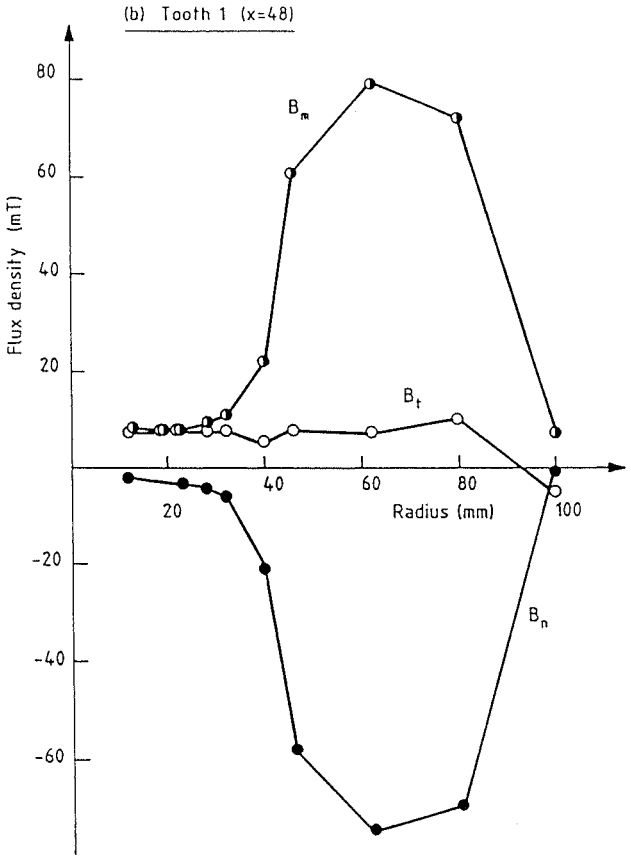

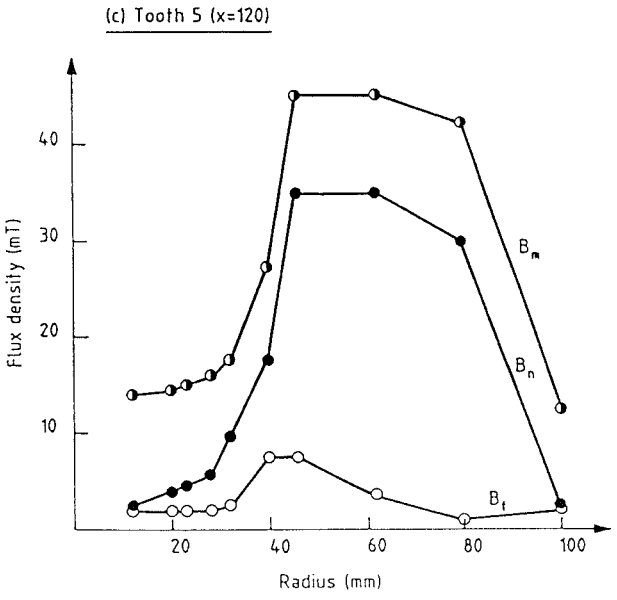

VARIATION OF FLUX DENSITY ALONG LINES PERPENDICULAR TO MACHINE - AXIS

continued ...

Figure 5.6

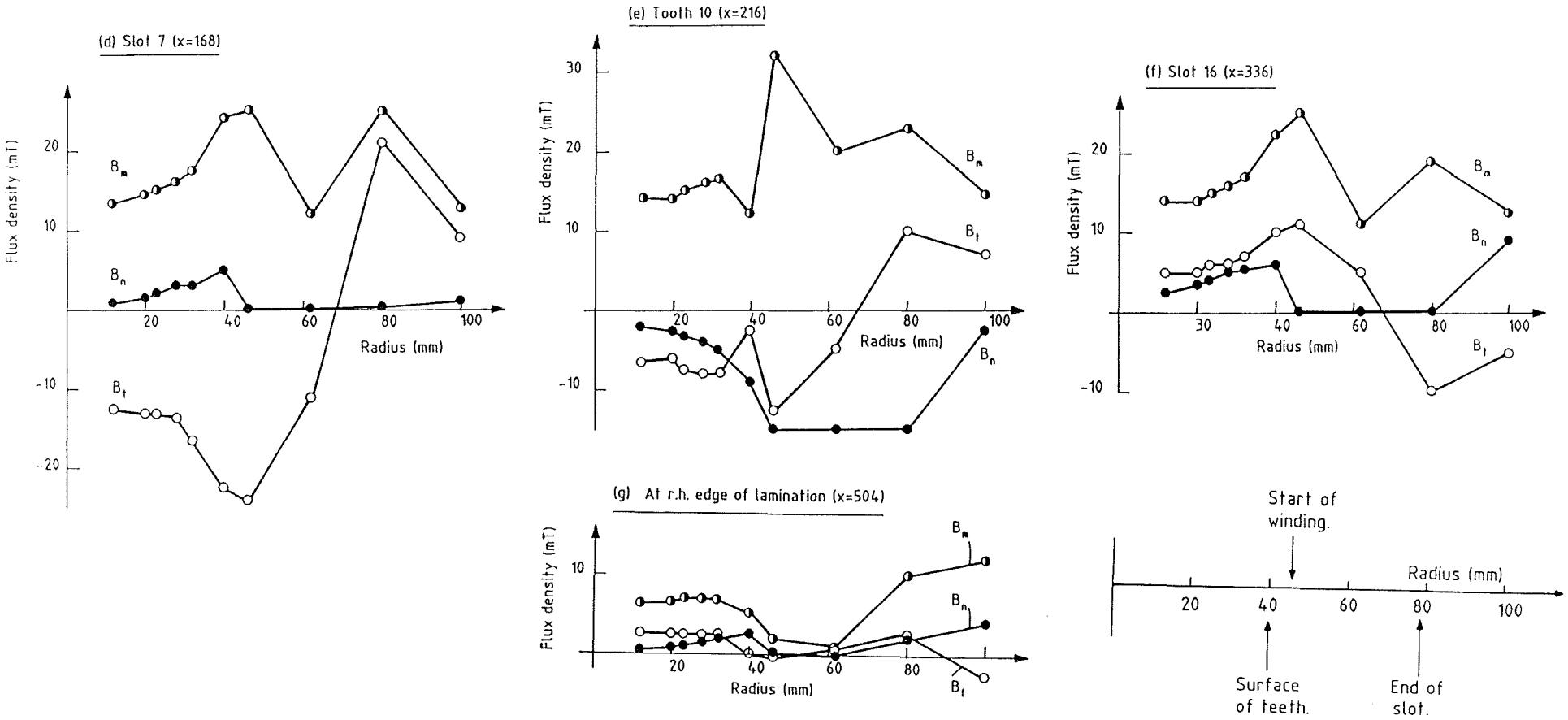

VARIATION OF FLUX DENSITY ALONG LINES PERPENDICULAR TO MACHINE - AXIS

Figure 5.6

initial investigations on the powder cleaner (Chapter 3) means that the field may be insufficient to induce dipoles in the ferromagnetic particles. Other considerations, such as the separate low values of normal and tangential flux density, would decrease the effectiveness of the device; with the low B_n being unable to repel the particles from the machine surface, and the low B_t unable to convey the powder along the bore of the device even if the particles had been sufficiently influenced by B_n.

The finite-element analysis of the tubular device was continued using the Rutherford software via the JANET computer link. During this period the linear machine was also investigated.

5.2 A Further Model

A new mesh was generated using PE2D[29] (the Rutherford software) by splitting the area into quadrilateral (or annular regions), with each region being meshed into finite elements (triangles). The earlier study had established that the stamping holes (see Fig 4.1) made very little difference to the flux distribution either in the airgap or in the lamination, and these were therefore not modelled. In addition, the notches in the lamination teeth were also omitted (as in the previous model), which was expected to make little difference to the actual flux pattern. The program had a limit of two hundred regions and had been set up to solve for a maximum of six thousand elements. Once these limitations were overcome a model was finally produced for the tubular machine and, with some minor changes, the same basic mesh was used for the linear device.

5.2.1 The Tubular Mesh

The lamination was considered as made up of nine parts and hence nine regions as illustrated in Fig 5.7, which shows one end of the lamination with regions R7, R8 and R9 representing a tooth, regions R1 and R4 the iron behind the tooth and regions R2 and R5 the iron behind the slot. Replicating the regions R1, R2, R4, R5, R7, R8 and R9 produced a model for all twenty-four teeth and slots, and a replication of regions R3 and R6 completed the model of the lamination. The lamination teeth were modelled by three regions, because a double-layer winding was to be used with the two equal-sized larger

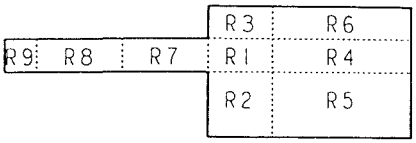

ONE END OF THE LAMINATION SPLIT INTO 9 REGIONS

Figure 5.7

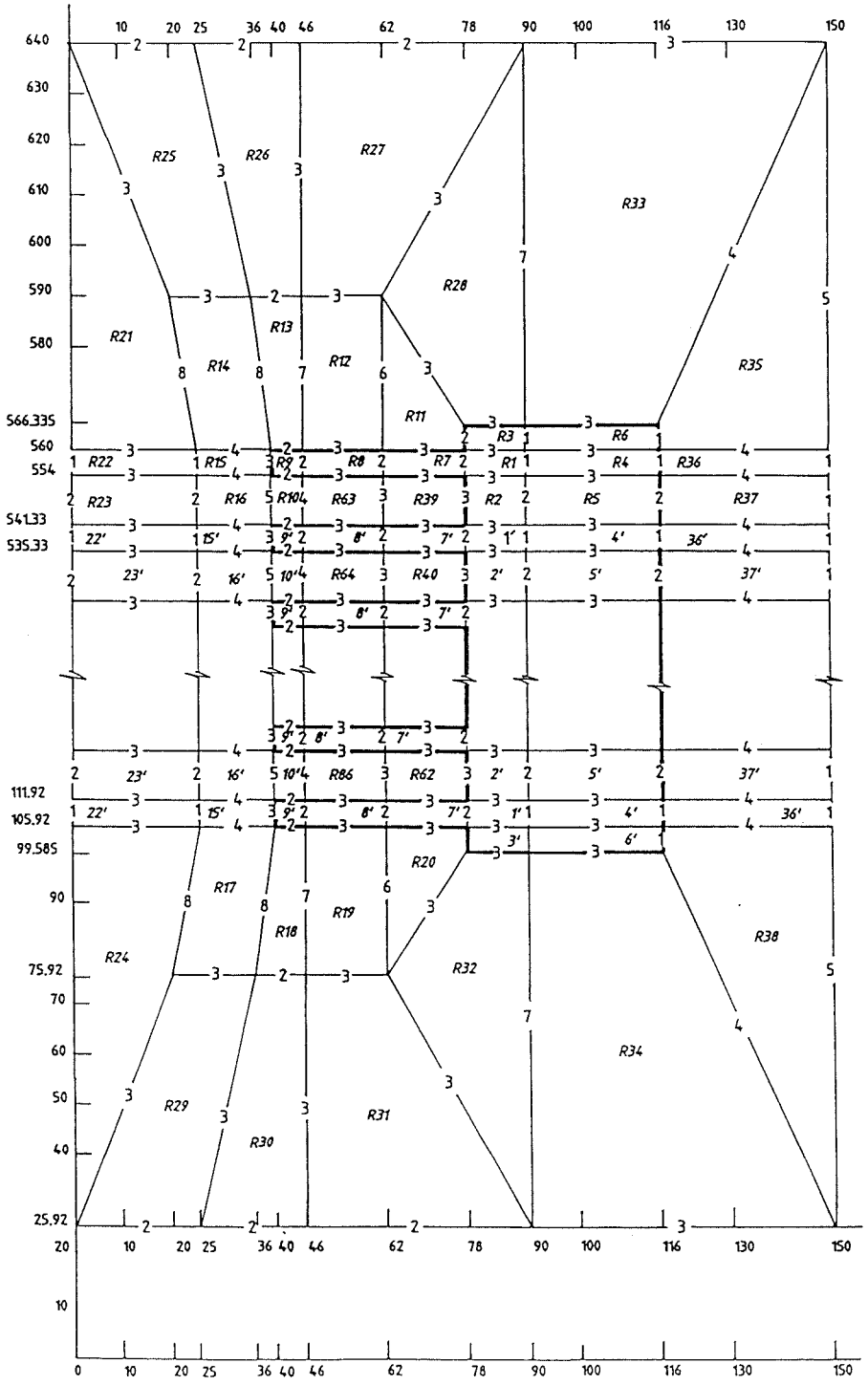

OUTLINE FOR THE TLIM MODEL SHOWING REGIONS

Figure 5.8

regions (R7 and R8 in Fig 5.7) being adjacent to the windings and the remainder of the tooth (region R9) being surrounded by air. Such a scheme also had the advantage of allowing the teeth to have a graded mesh, with more elements near the tooth tip.

Next, the regions surrounding the lamination were drawn and replicated where possible, with the current-carrying regions added to complete the basic model. The number of subdivisions along each face of every quadrilateral region had to be established, which also fixed the number of nodes along the faces (e.g. three subdivisions along a face implied four nodes) and the number of elements. Depending upon the choice of the subdivisions, any region may be given either a symmetrical or an unidirectional graded mesh. Good approximations to the number of elements in each region were obtained and, by judicious choice of the subdivisions, this systematic generation of the mesh ensured that the number of elements did not exceed six thousand.

The completed model used for the tubular machine, and shown in Fig 5.8, contained eighty six regions: nine for the lamination (R1 to R9), twenty nine for the air regions (R10 to R38) and forty eight for the winding regions (R39 to R86), with a total of 5482 elements (Table 5.1). From Fig 5.8, which shows the quadrilateral regions and the subdivisions along their faces and the co-ordinates of the model, various details regarding the model may be deduced. For example, region R34 towards the bottom right of Fig 5.8 has, in clockwise order, subdivisions of 3, 4, 3 and 7 along its faces, implying a total of (7 + 4) x 3 = 33 elements for the region (see Table 5.1). It can also be seen that the line x = 46 marks the extent of the double layer winding and x = 40 the extent of the teeth. The entire lamination is radially bounded by y = 99.585 and y = 566.335, with the model itself bounded by x = 0, y = 640, x = 150 and y = 25.92.

It was expected that the field components would have their greatest rate-of-change in the teeth, in the air gap near the teeth, at the tooth tip and in the slots. These areas were therefore more finely meshed than areas such as the back of the lamination, and the air both behind and further away from the lamination (see Fig 5.9).

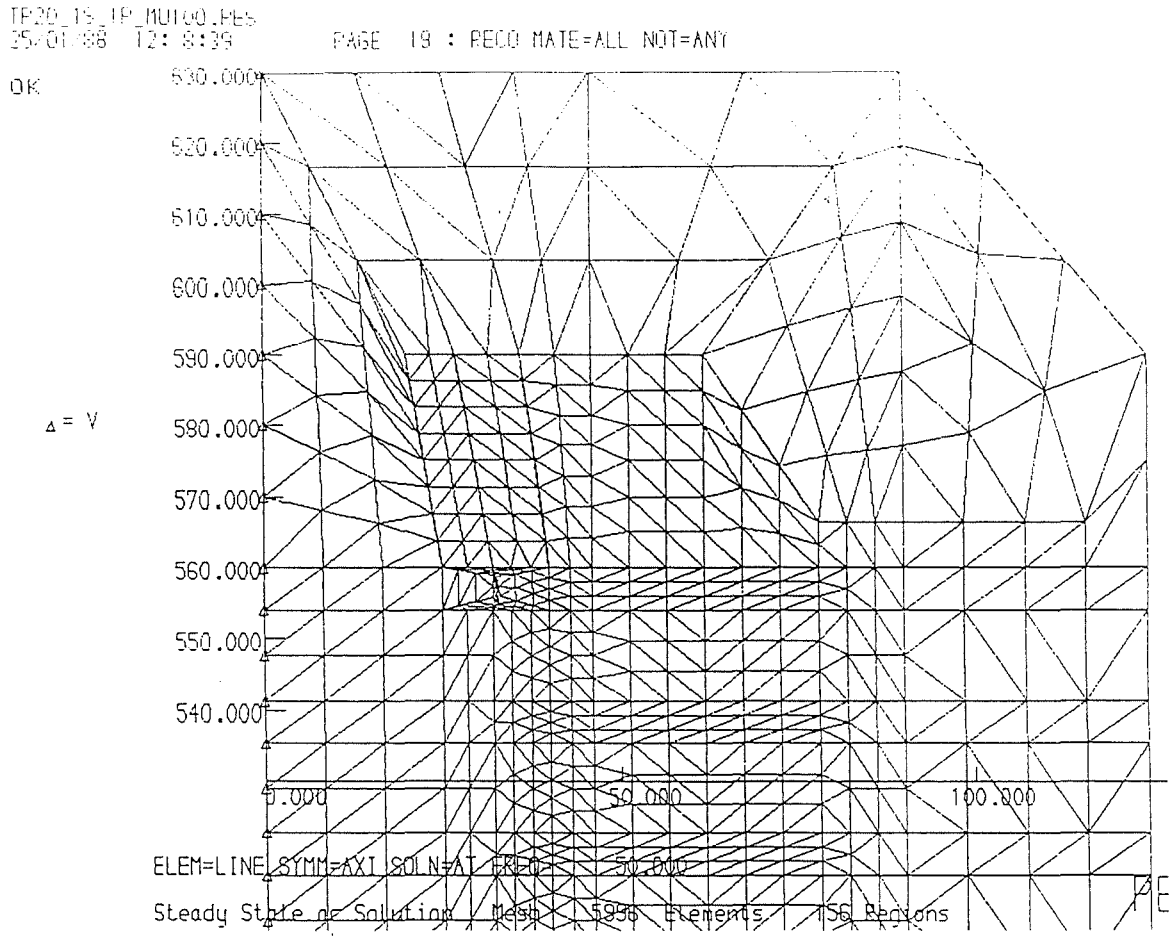

PART OF THE MESH FOR THE TUBULAR AND LINEAR MOTORS

Figure 5.9

Table 5.1: Number of Elements in Each Region

Region	Number of Elements	Cumulative Total	Region	Number of Elements	Cumulative Total
1	175	175	26	13	3958
2	312	487	27	13	3970
3	14	501	28	28	3998
4	150	651	29	13	4011
5	288	939	30	12	4023
6	12	951	31	13	4036
7	300	1251	32	28	4036
8	300	1551	33	33	4067
9	225	1776	34	33	4130
10	408	2184	35	24	4154
11	22	2206	36	200	4354
12	37	2243	37	216	4570
13	29	2272	38	24	4597
14	49	2321	39-62	(24x18) =	
15	350	2671		432	5026
16	600	3271		(1st winding layer)	
17	49	3320	63-86	(24x19) =	
18	29	3349		456	5482
19	37	3386		(2nd winding layer)	
20	22	3408			
21	43	3451			
22	150	3601			
23	288	3889			
24	43	3932			
25	13	3945		TOTAL	5482

Total: 2824 nodes and 5482 elements

The mesh shown in Fig 5.9 is representative of the initial mesh used for the tubular machine, but is actually a part of the mesh used for both the tubular and linear models with particles, which is discussed later. (The dark area opposite a tooth in Fig 5.9 illustrates the position of one of the particles.) When generating the mesh a careful choice of the shape and the number of subdivisions along the faces of the quadrilateral regions is required, since the elements should ideally be equilateral triangles with the same area, although this is nearly always impractical. A compromise is therefore made, such that the number of long thin triangular elements and the change in area from one element to those adjoining it is minimised. Having made these approximations, the effectiveness of the model may be enhanced by allowing departures from the ideal to exist predominantly in less important parts of the model, such as the air behind the lamination in this case.

To complete the finite-element formulation of the problem, the boundary conditions and material properties for the model were set. The tubular machine was modelled as axisymmetric and, because it is an axial flux device (N-pole faces N-pole and S-pole faces S-pole), no flux crosses the machine-axis. A Dirichilet boundary condition was therefore set along this axis, with eighty eight nodes being assigned a potential of zero. To keep the model simple and manageable, the relative permeability of the iron was assumed constant and given a value of 100[32]. A current density of 6.35 A/mm^2, equivalent to 20 A/phase, was allowed for the winding regions, which were assumed to have a 1 slot/pole/phase winding. The remaining regions were modelled as air, by setting their current density to zero and their relative permeability to one. To calculate[31] the current density and phase angle a sinusoidal time variation of current density was assumed, such that

$$j = \hat{J} \sin(wt + \phi) \tag{5.1}$$

where j and $\hat{J}$ are respectively the instantaneous and peak current densities.

The phase angle for the red phase was taken as 0°, for the yellow phase 120° and for the blue phase 240°, and the peak current density was:

$$\hat{J} = \frac{\hat{I}}{A_{cu}} = \frac{I_{rms}\sqrt{2}}{A_{cu}} \tag{5.2}$$

$$\text{and } A_{cu} = \frac{\pi d^2}{4} \tag{5.3}$$

where I_{rms} = rms current,

d, A_{cu} = diameter and area of wire respectively.

In the experimental device under construction, d = 2.38 mm, and therefore at 20 A/phase,

$$\hat{J} = \frac{20\sqrt{2}}{\pi(2.38)^2} \times 4 = 6.35 \text{ A/mm}^2.$$

5.2.2 The Linear Mesh

With the tubular mesh already produced, it was relatively simple to generate the linear mesh needed to model the linear machine. Although not entirely necessary, the tubular mesh was rotated so that the linear model would be visually more acceptable. Other modifications made were to set the solution parameters in Cartesian co-ordinates and to move the boundary conditions. Dirichilet boundary conditions were set behind the lamination with twelve nodes being assigned a potential of zero. As no other changes were made, the problem had the same number of nodes and elements as the tubular model (i.e. 2824 nodes and 5482 elements). The linear model was solved as a two-dimensional problem with the implied assumption that the LIM had infinite width, which is acceptable if the flux outside the width of the lamination stack is relatively small. In other words, the solution will be most accurate along a plane parallel to the direction of motion passing through the middle of the machine.

The linear mesh, having been generated from the tubular model, had a 40 mm air space above its active face, as the axisymmetric model had been modelled with an 80 mm bore. Although not ideal, in that only a small part of the air space above the linear device was modelled, it was considered satisfactory because the particles were transported near the motor face.

5.3 Preliminary Results

Solutions for both the tubular and linear models were obtained, and to avoid confusion the results are referred to by the filenames: T20_1S_1P.RES (T - Tubular; 20 - 20 A/phase; 1S - 1 slot/pole/phase; 1P - fully pitched; .RES - results) and L20_1S_1P.RES (L - Linear; etc).

The variations in the modulus and normal component of flux density along various lines parallel and perpendicular to the machine axis are presented in Fig 5.10. The position of these lines with respect to the TLIM may be determined from Fig 5.8.

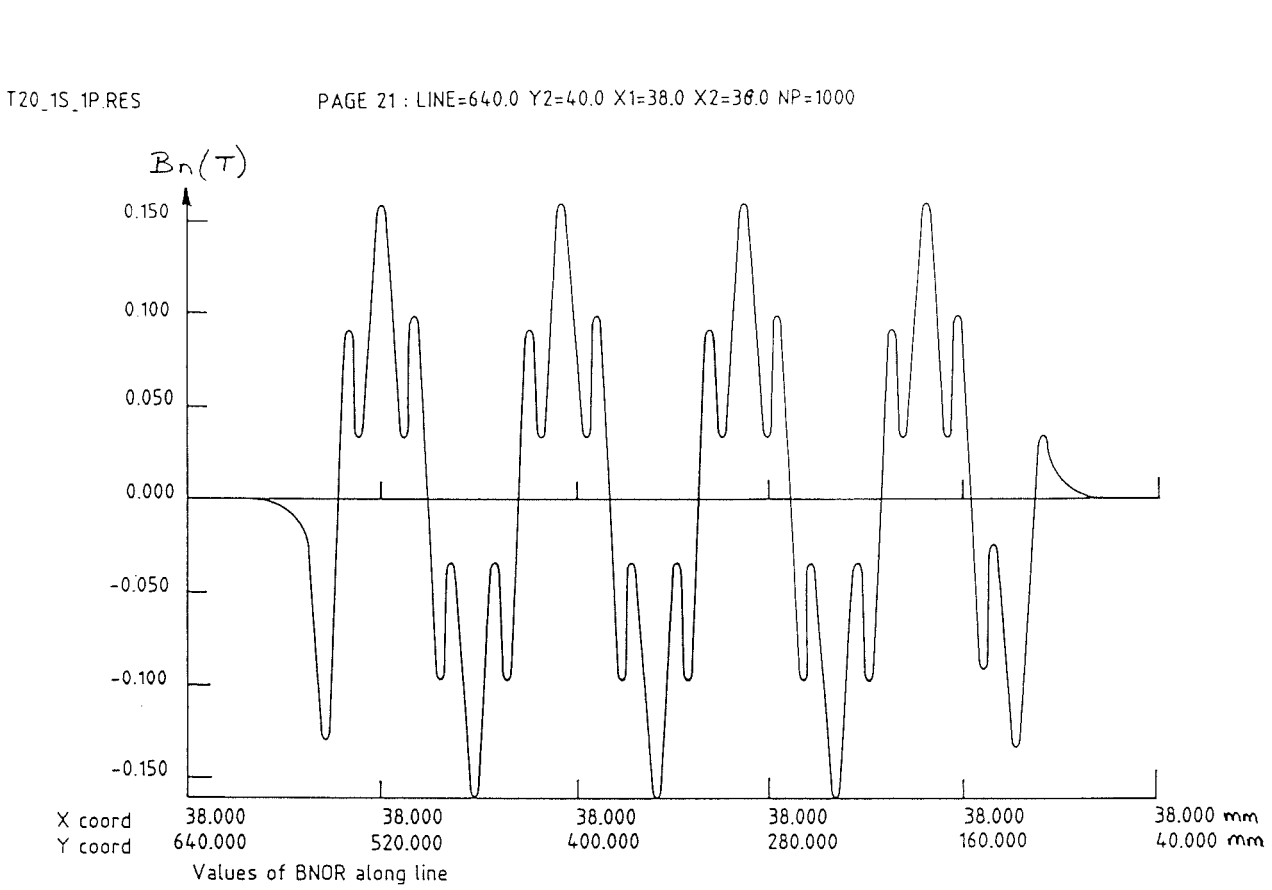

(a) B_n along x = 38

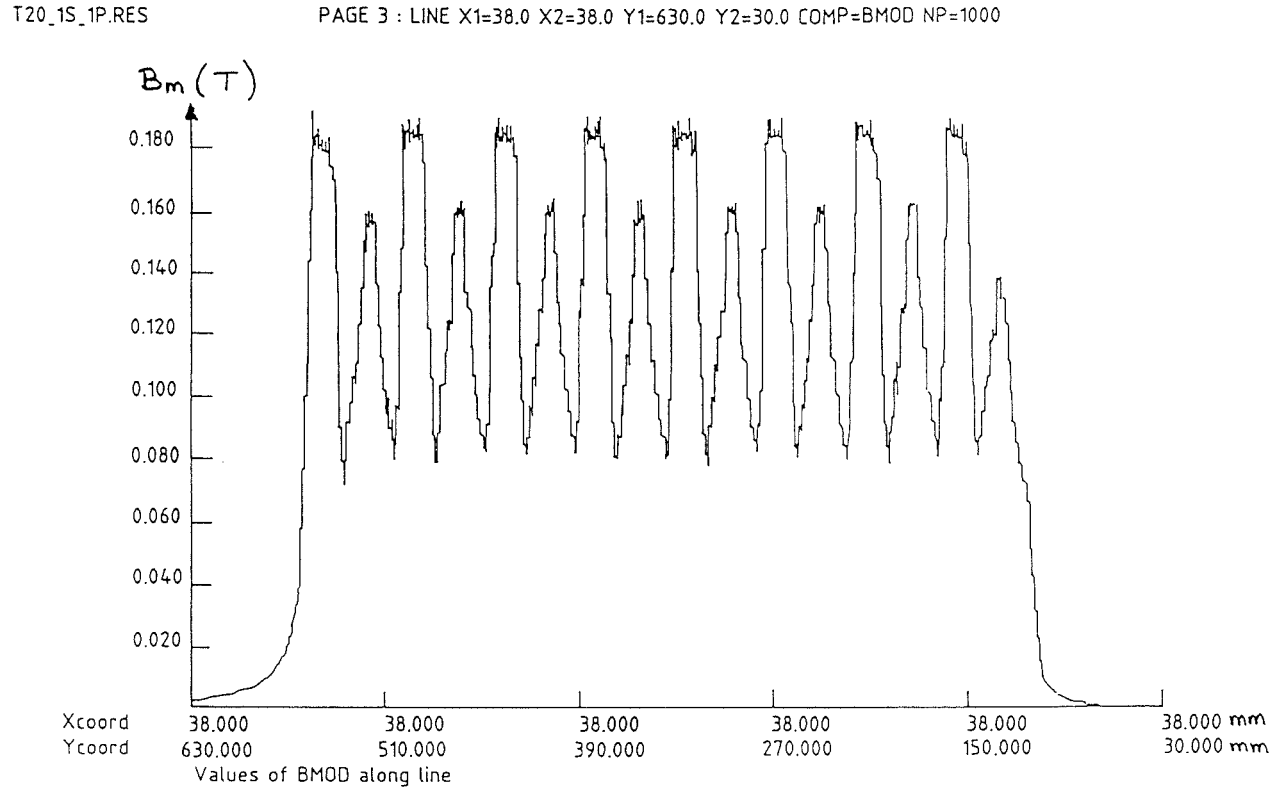

(b) B_m along x = 38

VARIATION OF FLUX DENSITY ALONG LINES PARALLEL AND PERPENDICULAR TO MACHINE - AXIS

continued ...

Figure 5.10

T20_1S_1P.RES PAGE 7 : NP=1000

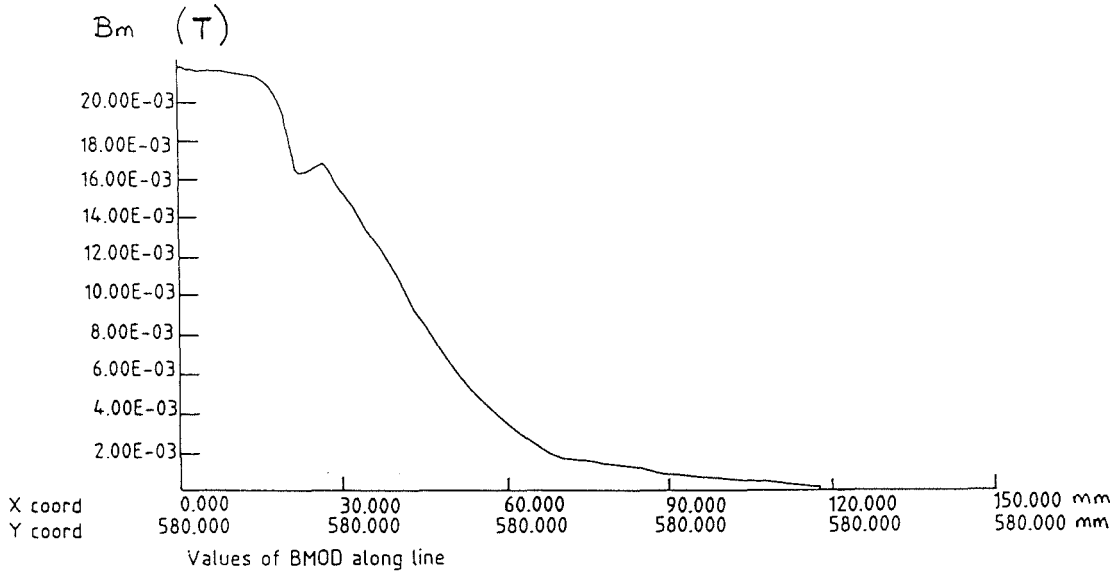

(c) B_m along y = 580

T20_1S_1P.RES PAGE 14 : COMP=BMOD AUTO=YES

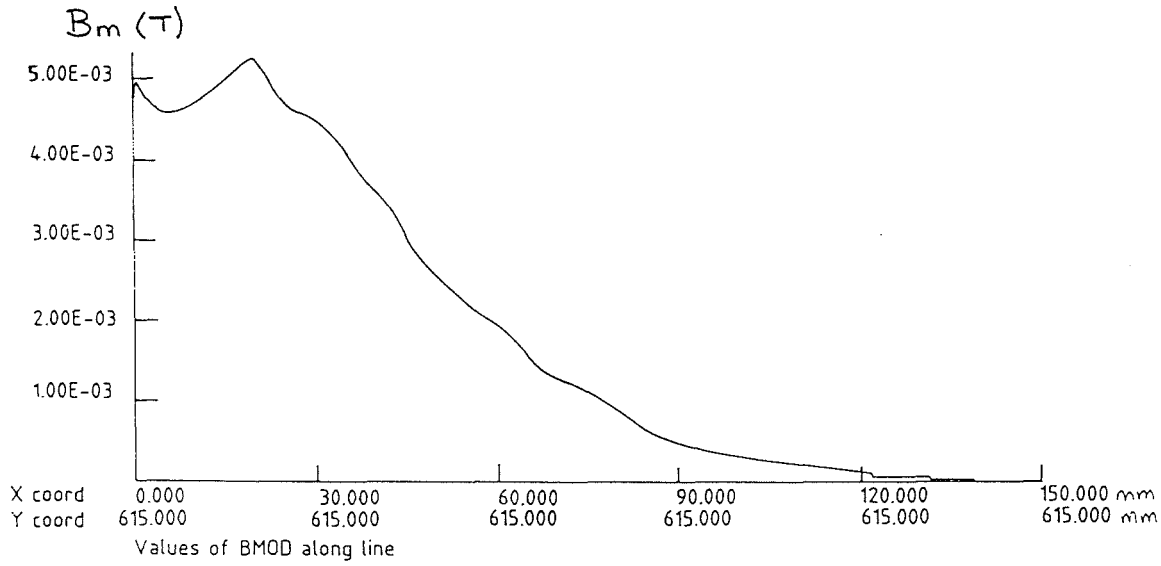

(d) B_m along y = 615

VARIATION OF FLUX DENSITY ALONG LINES PARALLEL AND PERPENDICULAR TO MACHINE - AXIS

continued ...

Figure 5.10

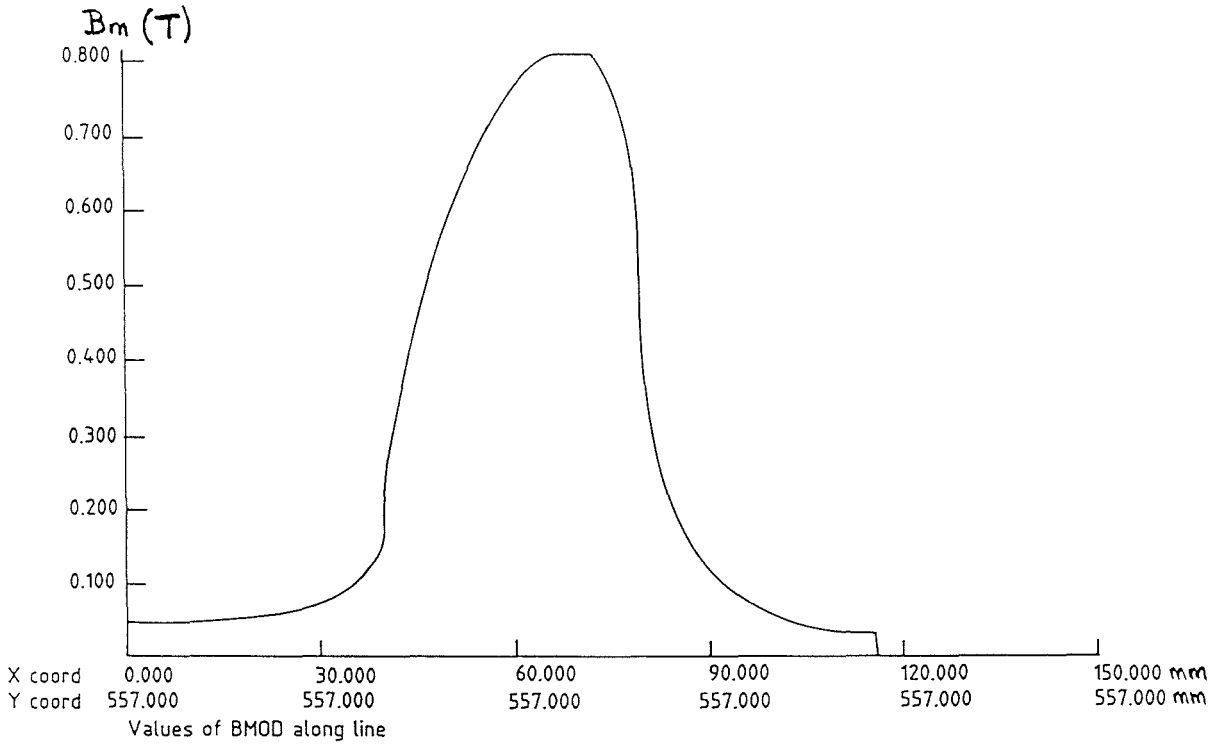

(e) B_m along y = 557

VARIATION OF FLUX DENSITY ALONG LINES PARALLEL AND PERPENDICULAR TO MACHINE - AXIS

Figure 5.10

Along x = 38 (just above the lamination teeth), the waveform of B_n (see Fig 5.10(a)) was "peaky" with a maximum value of about 0.15 T. The eight poles are clearly visible, with the first and last being split into two partial poles. Twenty-five peaks, corresponding to the twenty five teeth, can be seen, with adjacent peaks separated by an integral multiple of the 56 mm pole-pitch. A roughly sinusoidal envelope is traced out by the waveform, with some distortion arising because the plot was obtained close to the lamination teeth. Along the same line, the different magnitudes of B_n and B_t are evident in the graph of B_m (Fig 5.10(b)), with the eight poles of both components being clearly visible.

The graphs of B_m along y = 580 (Fig 5.10(c)) and y = 615 (Fig 5.10(d)) are similar in shape, and show that the field outside the lamination is very small. (The dip at $x \approx 21$ for B_m along y = 580 in Fig 5.10(c) is probably due to the discretisation in this area of the model.) The majority of the flux is confined to the lamination, with there being little flux behind the lamination, which is shown by the graph of B_m along y = 557 in Fig 5.10(e). The value of B_m rises sharply as the lamination is entered via the tooth and it continues to increase steadily, reaching a maximum of approximately 0.8 T in the back half of the tooth and falling to zero at the back of the lamination. The graphs clearly show that there was little flux in the bore of the device.

The results for the linear model had similar characteristics to those for the tubular model, i.e. the majority of the flux was confined to the lamination, with little or no flux behind the lamination. The average value of B_m just above the teeth was approximately the same for both the LIM and the TLIM, implying that the powder motion may be similar for the two devices.

The areas of greatest error in the models were near the teeth tips and just behind the teeth in the lamination (see Fig 5.11), where a greater discretisation is required to reduce the error.

Having obtained these models for the linear and tubular machines, refinements were made and particles added to continue the finite-element investigation.

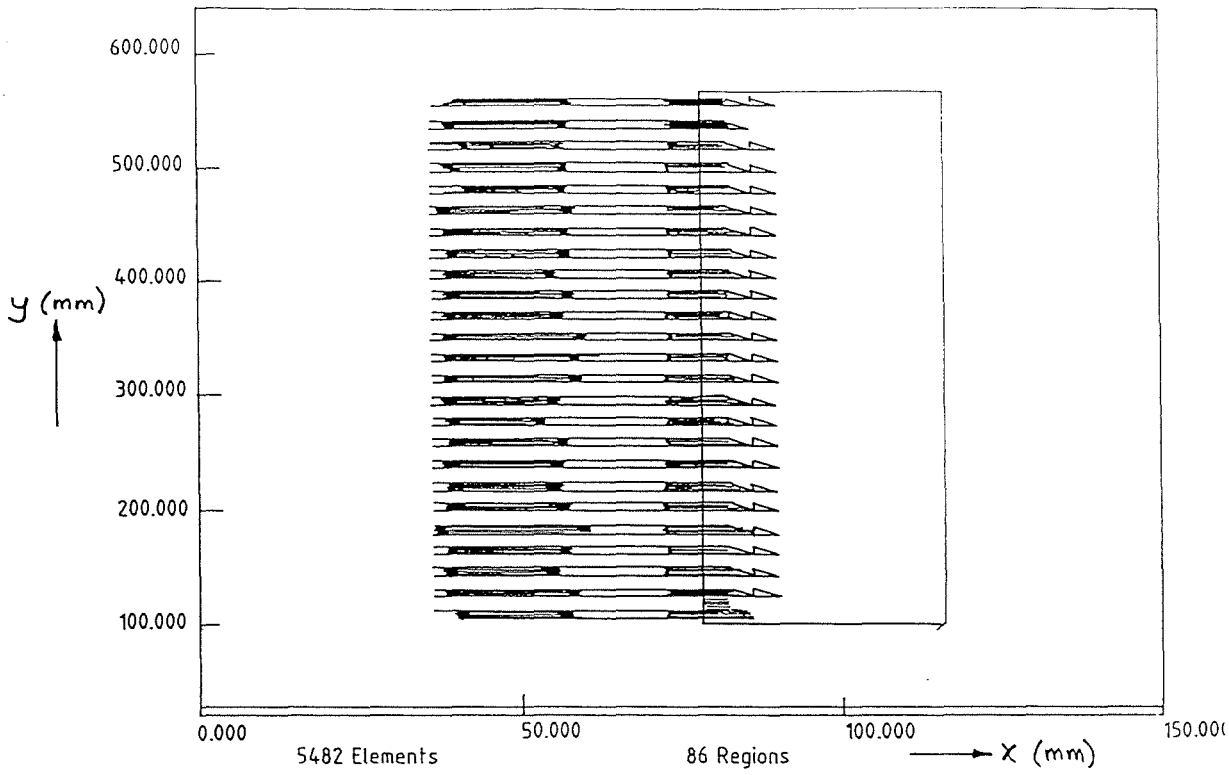

AREAS OF "ERROR" IN THE MODEL

Figure 5.11

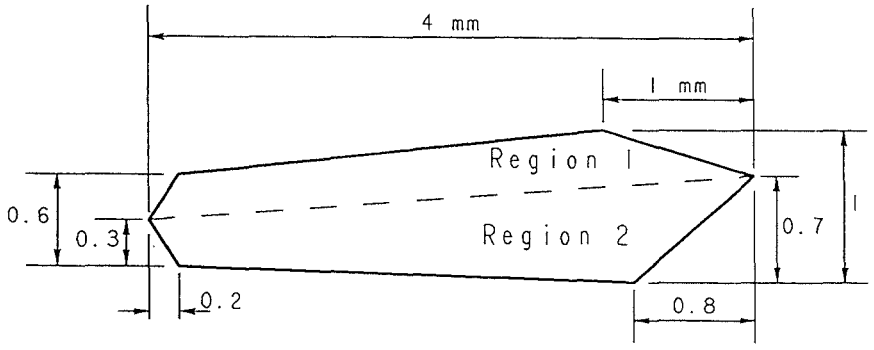

MODELLED PARTICLE CONSISTING OF TWO REGIONS

Figure 5.12

5.4 Refinements and Additions to the Model

The mesh was modified by increasing the number of elements in the areas identified in Fig 5.11, and reducing their number in other, less important areas. A number of particles were also introduced into the mesh and, as the problem was solved in two dimensions, the particles were modelled as thin iron rings in the tubular mesh and as small, infinitely deep layers of iron in the linear mesh.

Six particles were drawn into the tubular and linear models, with each particle (see Fig 5.12) consisting of two regions. For simplicity, the particles all had the same rod-like shape, because the iron particles used in the experimental investigation were also rod-like. The modelled particles were positioned such that they were a minimum of 7 mm from the lamination teeth, as that corresponded to the air gap in the tubular machine under construction.

Changes to the mesh included reducing the air space and number of elements behind and at both ends of the lamination, and increasing the number of elements above the lamination teeth. The new models shown in Fig 5.13 illustrate the position and orientation of the particles and further data is given in Table 5.2, with the part of the mesh in Fig 5.9 showing the discretisation in and around a particle. The particles (as shown in Fig 5.12) opposite teeth 1 and 20 and slot 7 had their flat side parallel to the axis and those opposite teeth 12, 15 and 25 with their flat side perpendicular to the axis. (Tooth 1 and slot 1 starts respectively at y = 554 and y = 541 for the TLIM and respectively at x = 554 and x = 541 for the LIM.) The results files for these two new studies were named in a similar fashion to the previous files: TP20_1S_1P.RES (T - Tubular; P - Particles; 20 - 20 A/phase; 1S - 1 slot/pole/phase; 1P - fully pitched; .RES - results) and LP20_1S_1P.RES (L - Linear; P - Particles etc).

As the particles may be modelled with any desired relative permeability, they can be modelled as air by setting $\mu_r = 1$ or as iron by giving μ_r a more appropriate value. A comparison of the old and new tubular and linear models was made by modelling the particles as air as a simple check.

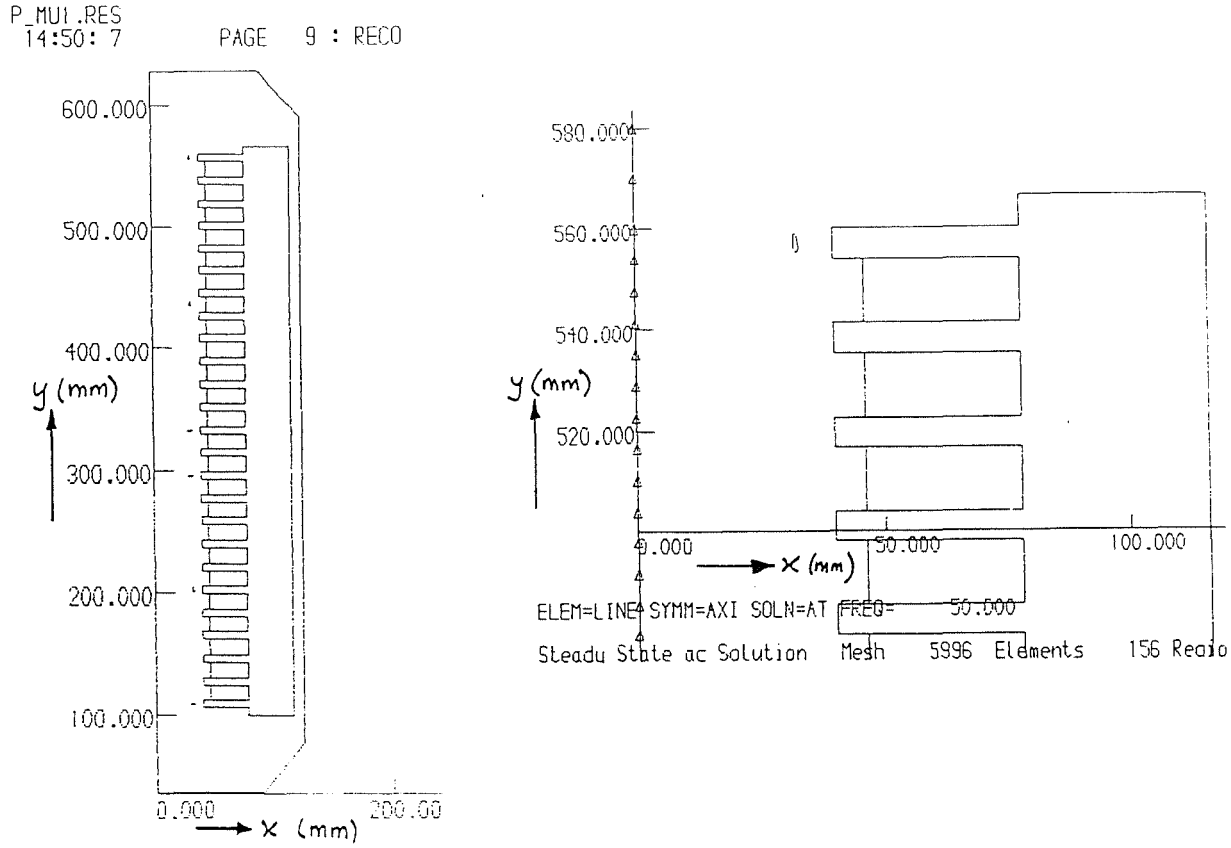

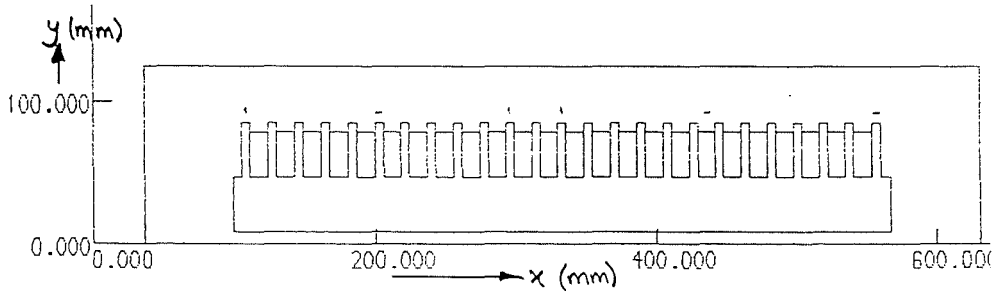

TUBULAR AND LINEAR MODELS WITH PARTICLES

Figure 5.13

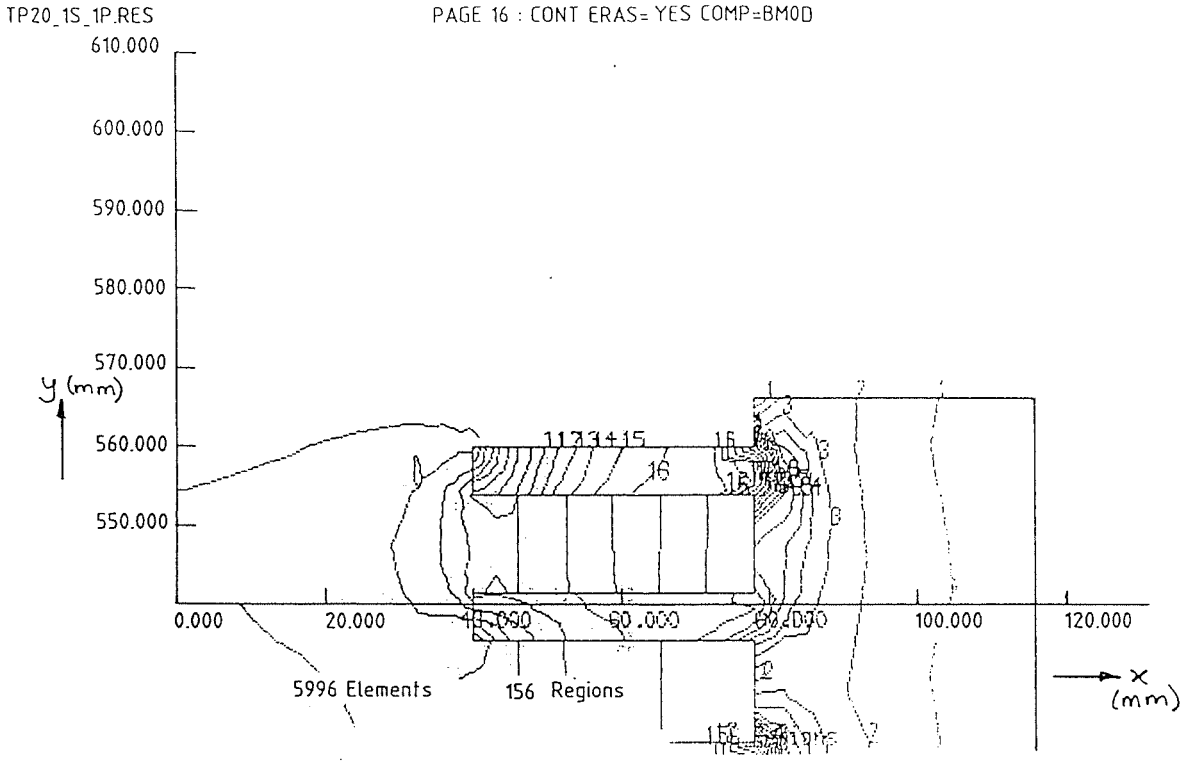

(a)

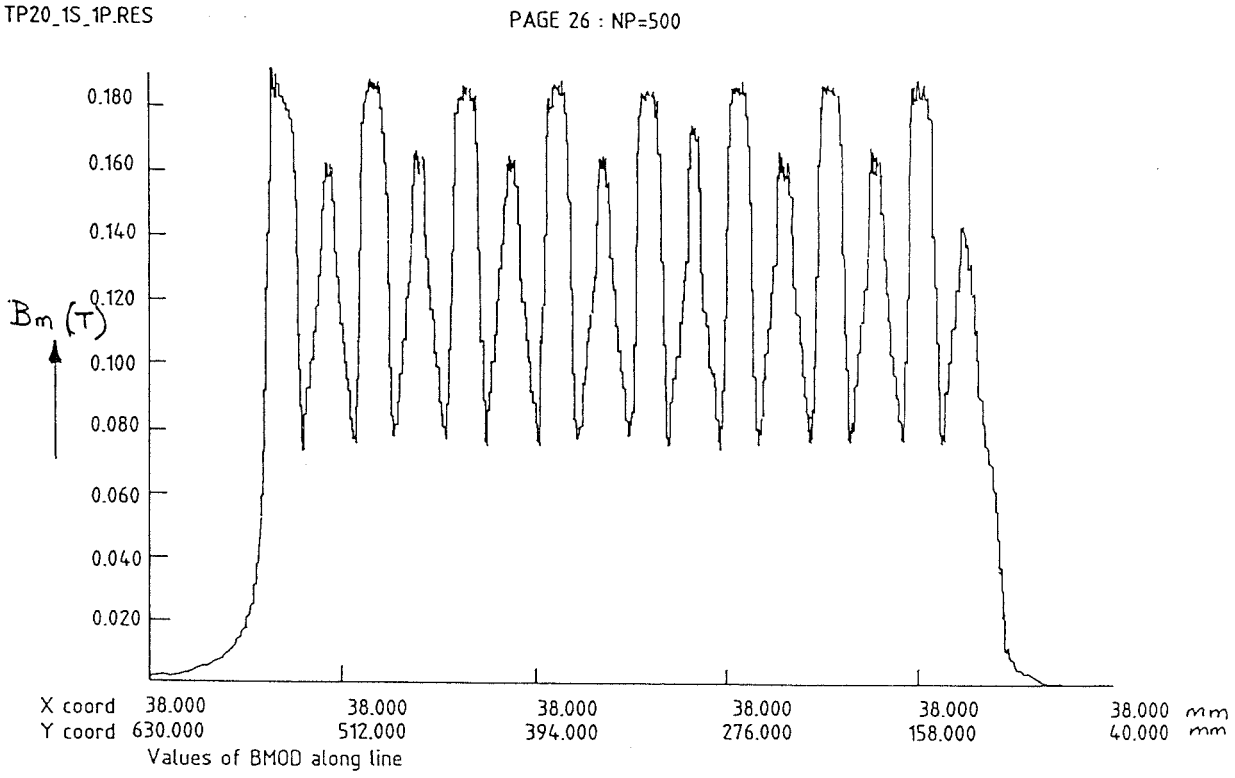

(b)

RESULTS FROM THE STUDY TP20_1S_1P.RES

continued ...

Figure 5.14

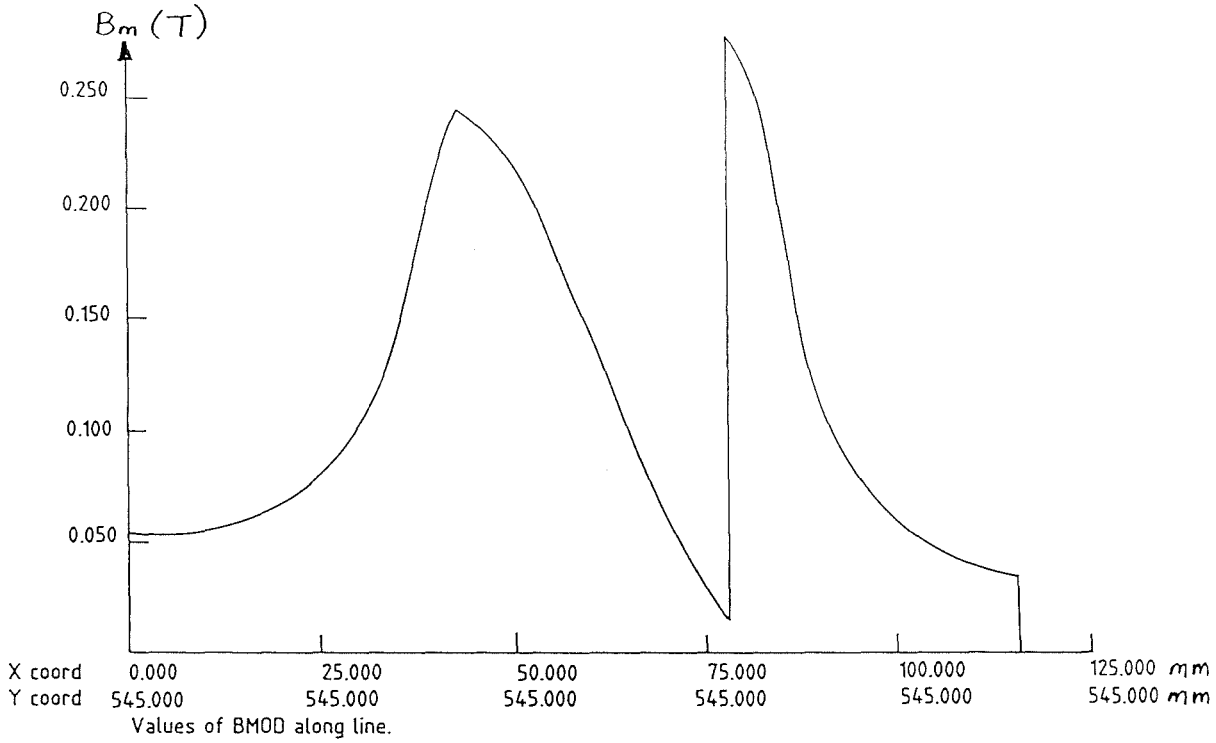

(c)

RESULTS FROM THE STUDY TP20_1S_1P.RES

Figure 5.14

(a) Contours of B_m over one end of the lamination
(b) B_m along x = 38
(c) B_m along y = 545

Table 5.2: Data for Tubular and Linear Models with Particles

File	Number of Regions	Number of Elements
TP20_1S_1P.RES	156 regions consisting of: R1-R9 lamination; R10-R38 air; R39-R86 windings; R87-R98 six particles; R99-R134 air surrounding particles; R135-R156 air	5996
LP20_1S_1P.RES	156 regions consisting of: R1-R9 lamination; R10-R32 air; R33-R44 six particles; R45-R80 air surrounding particles; R81-R108 air; R109-R156 winding	5986

5.5 Comparison of Old and New Models

The diagrams of Fig 5.14 (tubular machine) and Fig 5.15 (linear machine) show that the models containing the particles were consistent with the old models. Contour plots of B_m over one end of the lamination for the tubular machine, with and without particles, were the same, and only that from TP 20_1S_1P.RES is presented. (A particle may be seen directly opposite the first tooth.) The maximum value of B_m occurred directly behind the teeth (as shown by the increased density of contour lines in Fig 5.14), reaching a value of approximately 850 mT as in the results for the previous model (see Fig 5.10). Close comparison of the graphs of B_m along the line x = 38 (for TP20_1S_1P.RES see Fig 5.14 and for T20_1S_1P.RES see Fig 5.10) shows minor differences due to the modifications made to the mesh and may be ignored.

A similar situation occurred for the linear models (see Fig 5.15). The contour plots of B_m were practically the same and only that for LP20_1S_1P.RES is presented. The peak value of B_m occurred directly behind the teeth in the lamination, shown again by the increased number of contour lines, attaining a value of 1.4 T. Graphs of B_m along x = 530 (see Fig 5.13) for both linear models were also identical and that from

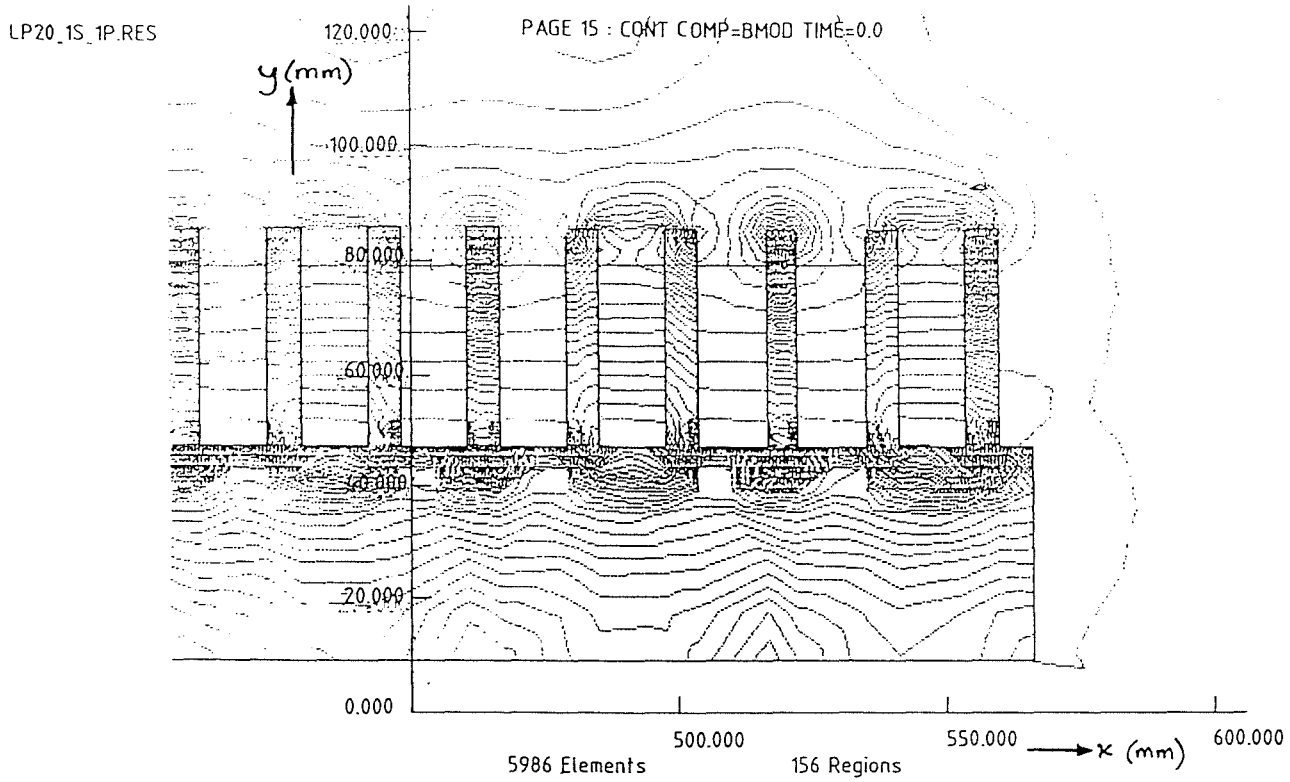

(a) Contours of B_m over one end of the lamination (LP20_1S_1P.RES)

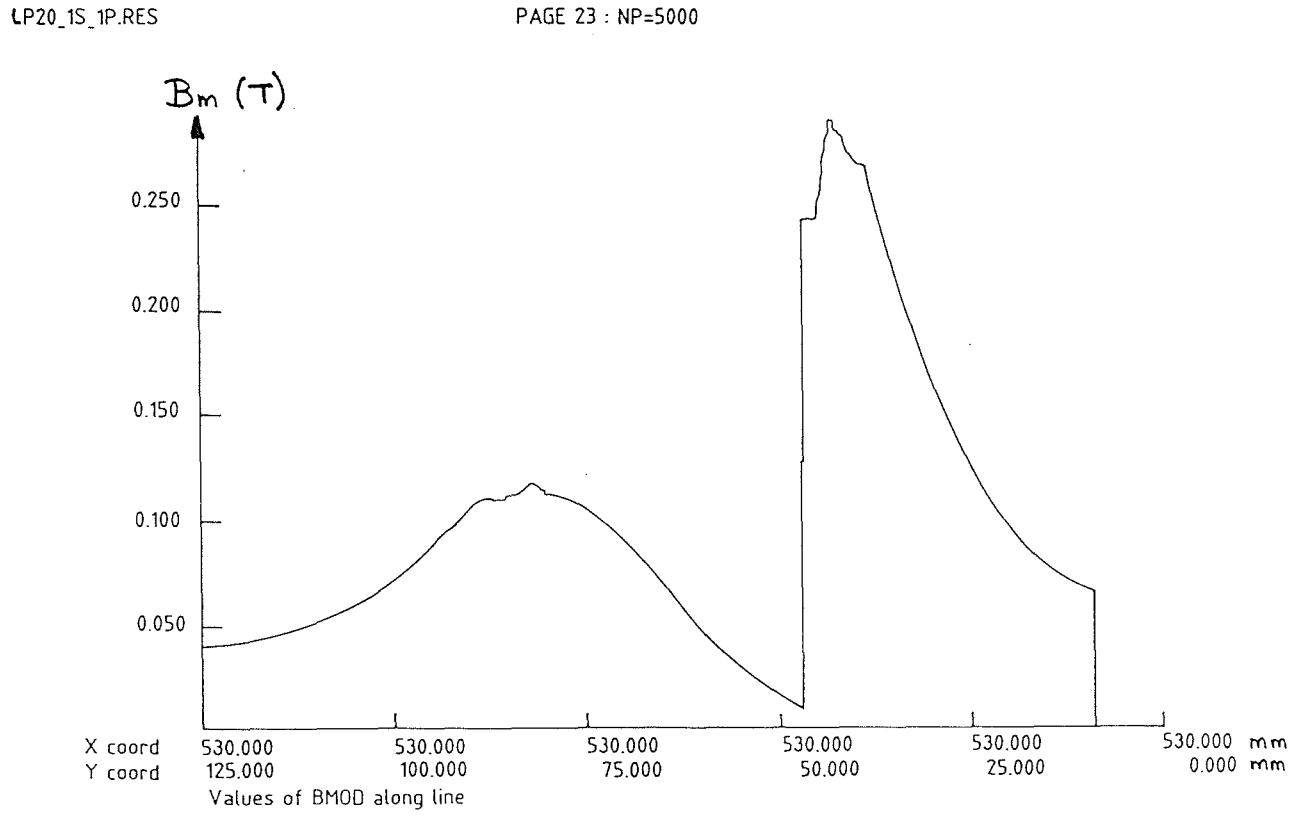

(b) B_m along x = 530.0 (LP20_1S_1P.RES)

COMPARISON OF THE LINEAR MODELS WITH AND WITHOUT PARTICLES
(LP_20_1S_1P and L20_1S_1P)

continued ...

Figure 5.15

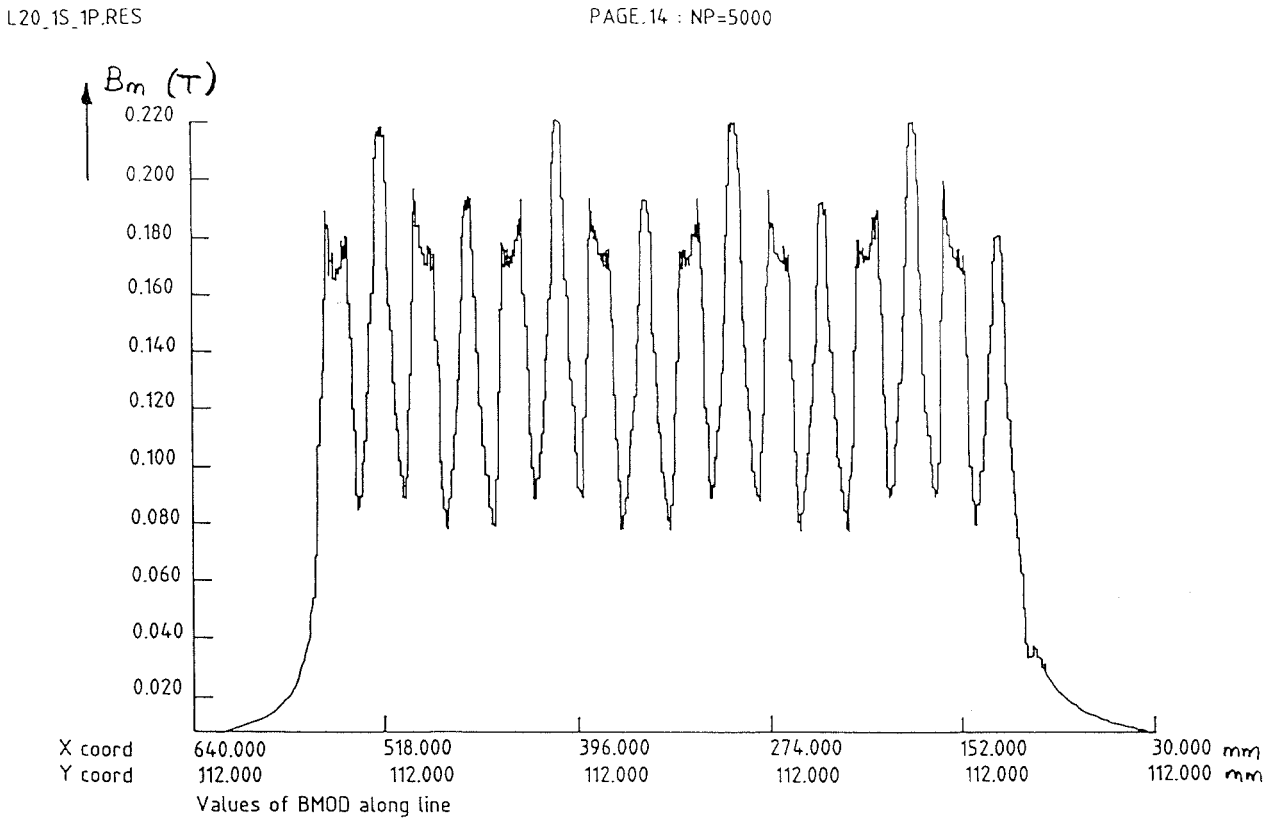

(c) B_m along a line 2 mm above the lamination (y = 112.0) for L20_1S_1P.RES

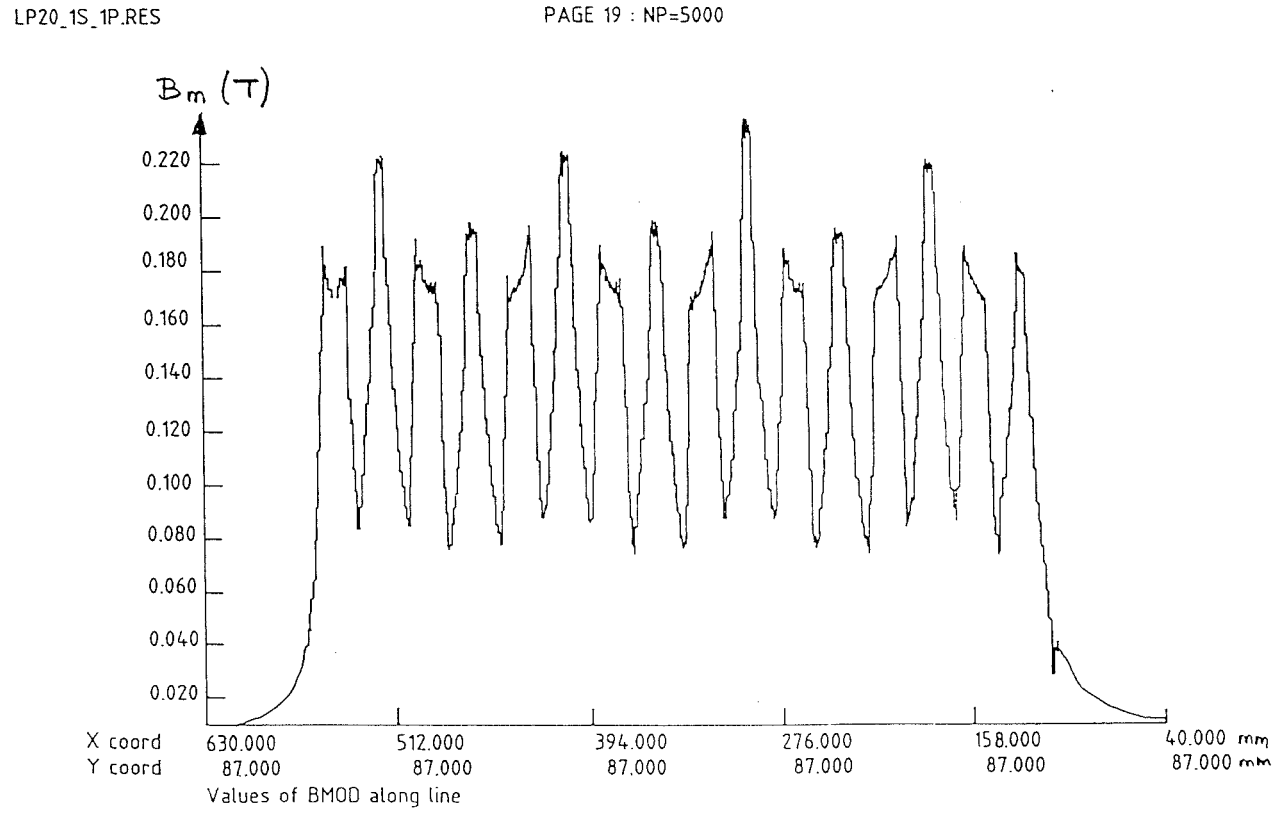

(d) B_m along a line 2 mm above the lamination (y = 87.0) for LP20_1S_1P.RES

COMPARISON OF THE LINEAR MODELS WITH AND WITHOUT PARTICLES
(LP_20_1S_1P and L20_1S_1P)

Figure 5.15

LP20_1S_1P.RES is presented in Fig 5.15. Graphs of B_m at a distance 2 mm above the lamination teeth (i.e. y = 112 for L20_1S_1P.RES and y = 87 for LP20_1S_1P.RES) were plotted and both are given in Fig 5.15. Although close inspection reveals a few minor differences, these too may safely be ignored.

Since the above results show that the refined models were consistent with the previous models, a number of studies were conducted on the two new models.

5.6 Studies on the Tubular and Linear Machines

It is simple to change the data in the meshes in order to perform different studies, such as for different currents or different particle permeabilities. Nine such studies were eventually performed and to avoid confusion each study (Table 5.3) will be referred to by its filename.

Studies with the particles modelled as air were conducted to provide a basis from which it would be possible to determine how the introduction of particles affected the flux distribution over the devices. No study was carried out at 30 A/phase for the linear machine, as it was found that the lamination was already close to saturation at 20 A/phase. For the tubular model three current values and two particle permeabilities were studied: at 30 A/phase the TLIM lamination was near saturation and the study at 6 A/phase (T6_1S_1P) used the old mesh and was performed to compare field values at low currents.

5.6.1 Results for the Tubular Machine

Diagrams showing the results from the model TP20_1S_1P.MU1 (i.e. TLIM at 20 A/phase with particles modelled as air) are presented in Figs 5.16-5.26. Figure 5.16(a) shows the contours of B_m, and the eight poles (seven complete poles and two partial poles at the ends of the device) can be clearly seen. The six small "dots" to the left of the lamination illustrate the position and size of the particles. As the field distribution was regular (except at the ends) only sections of the lamination were examined.

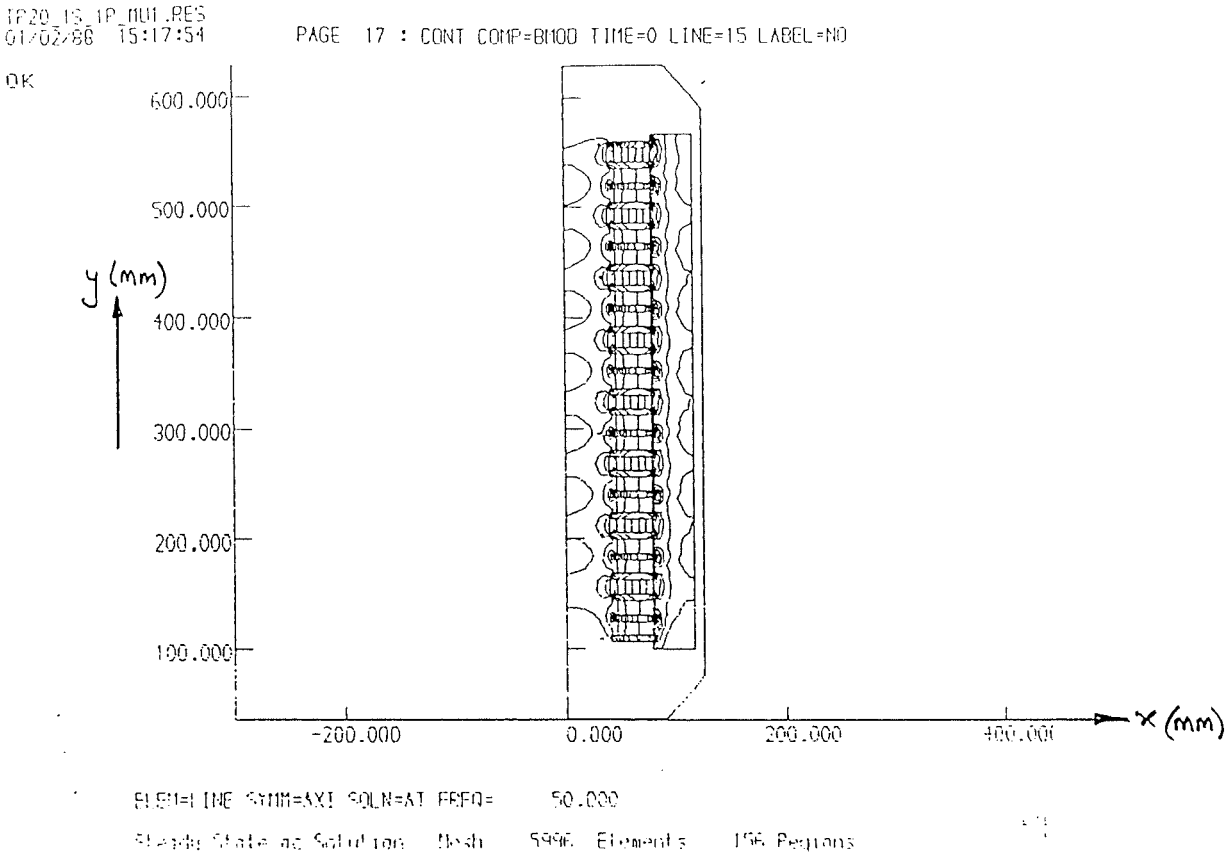

(a) Contours of B_m over the whole lamination

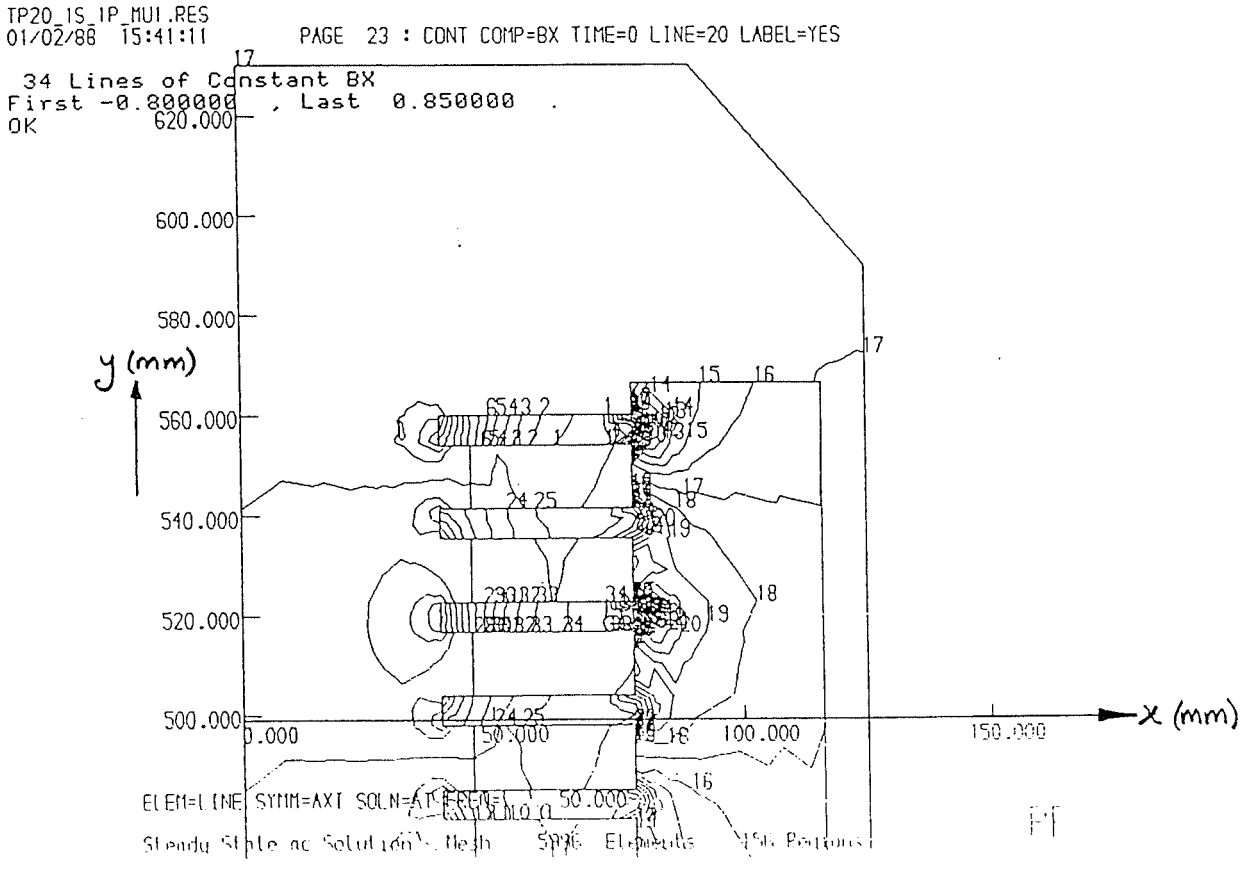

(b) Contours of B_x over one end of the lamination

Figure 5.16 FLUX DENSITY CONTOURS FOR THE TLIM STUDY
TP20_1S_1P_MU1

continued ...

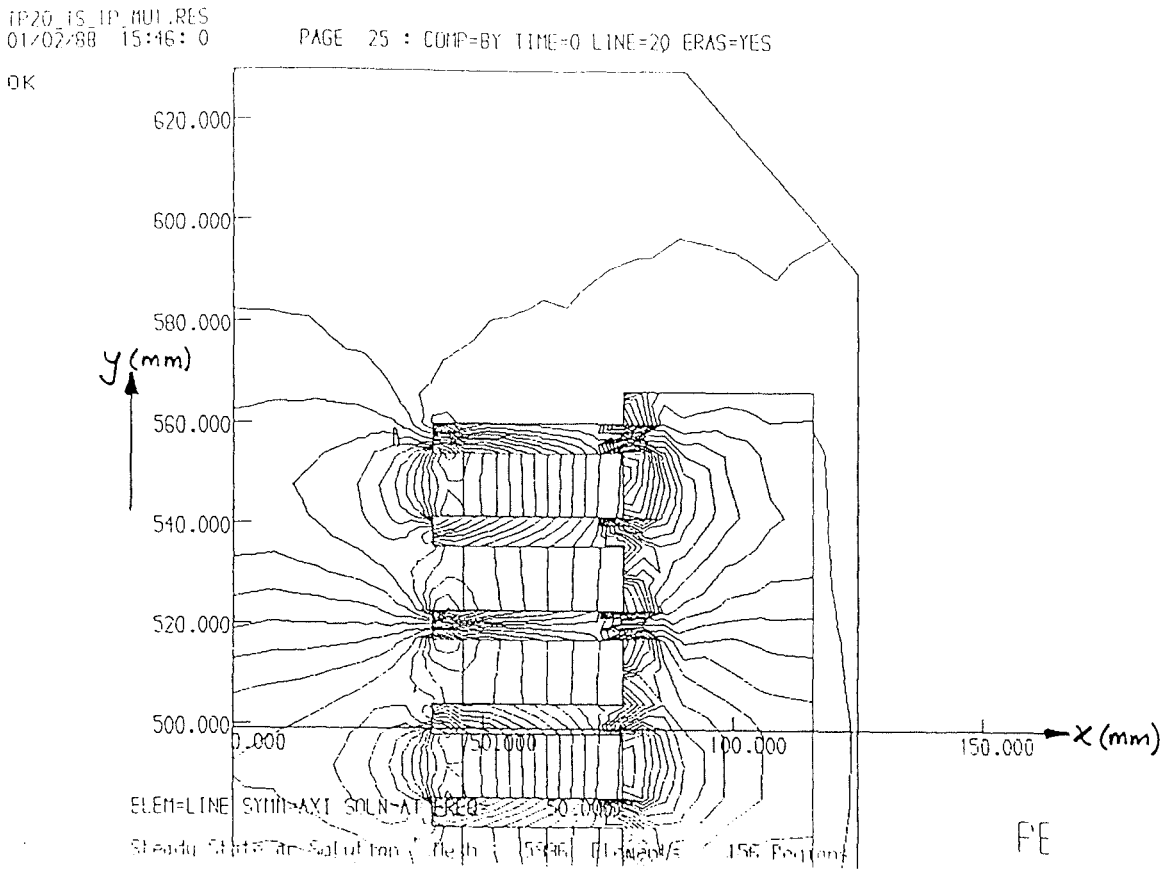

(c) Contours of B_y over one end of the lamination

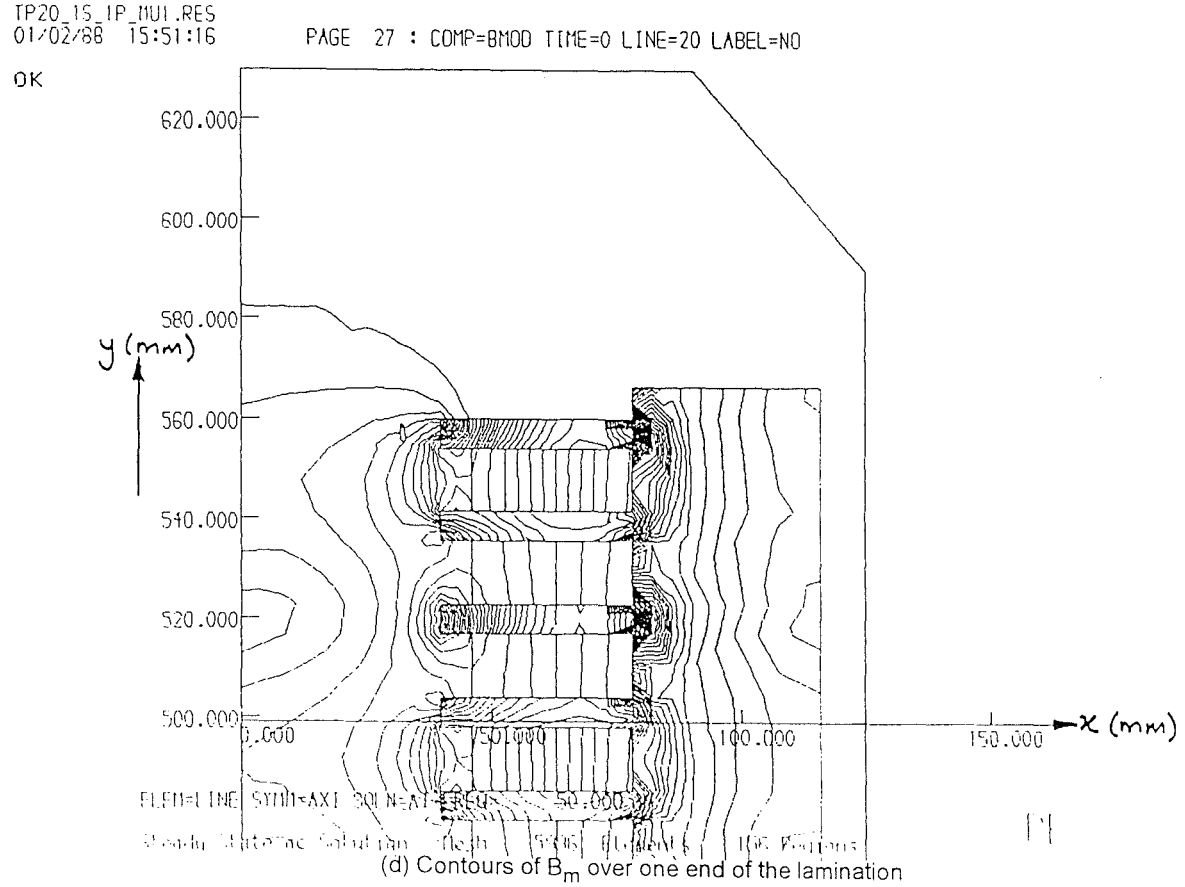

(d) Contours of B_m over one end of the lamination

Figure 5.16 FLUX DENSITY CONTOURS FOR THE TLIM STUDY
TP20_1S_1P_MU1

continued ...

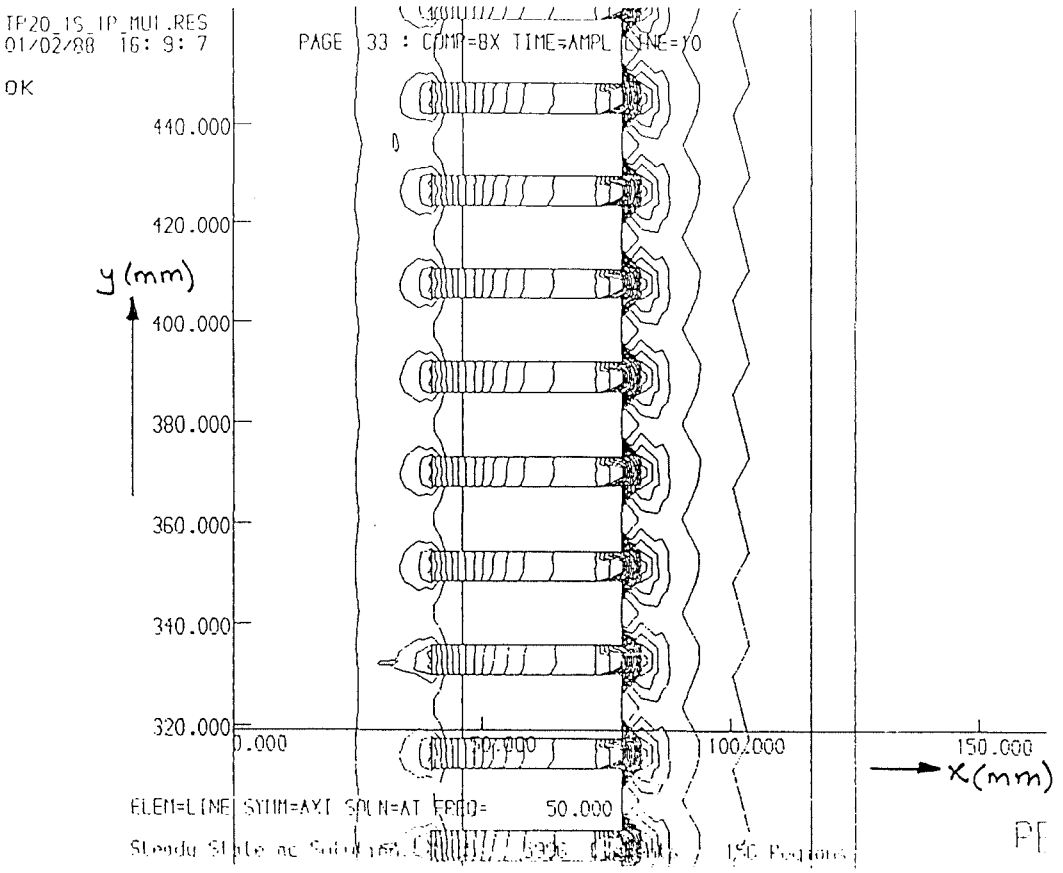

(e) Time-averaged contours of B_x over a central area of the lamination

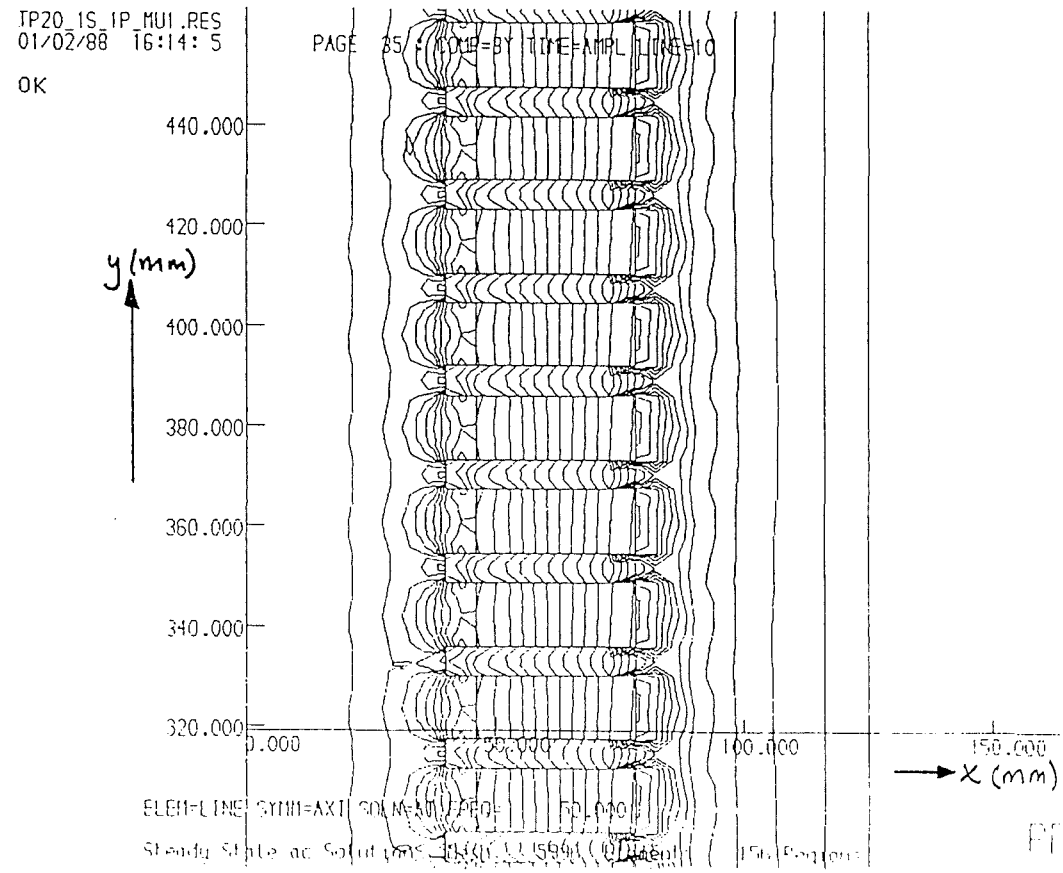

(f) Time-averaged contours of B_y over a central area of the lamination

Figure 5.16 FLUX DENSITY CONTOURS FOR THE TLIM STUDY
TP20_1S_1P_MU1

continued ..

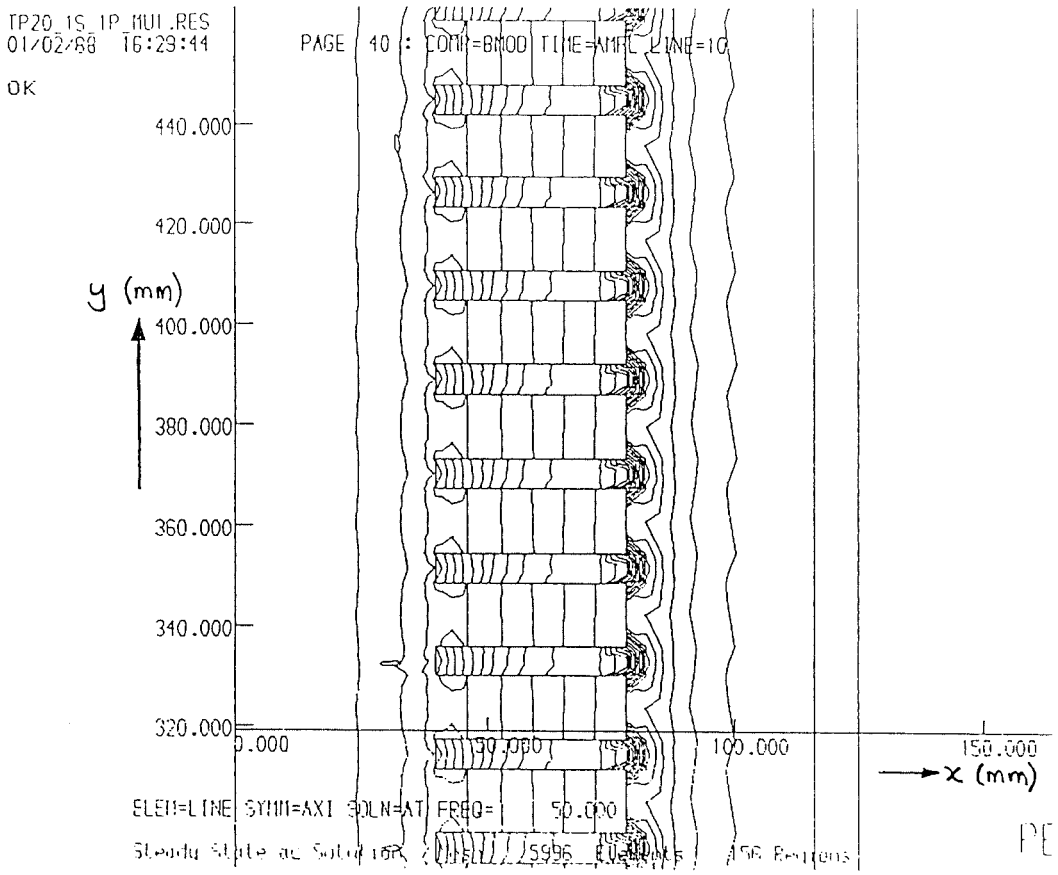

(g) Time-averaged contours of B_m over a central area of the lamination

Figure 5.16 FLUX DENSITY CONTOURS FOR THE TLIM STUDY
TP20_1S_1P_MU1

(a) Contours of B_m over the whole lamination
(b) Contours of B_x over one end of the lamination
(c) Contours of B_y over one end of the lamination
(d) Contours of B_m over one end of the lamination
(e) Time-averaged contours of B_x over a central area of the lamination
(f) Time-averaged contours of B_y over a central area of the lamination
(g) Time-averaged contours of B_m over a central area of the lamination

Table 5.3: Description of Studies

Number	Filename/Study	Explanation
1	LP6_1S_1P_MU1	LP - linear with particles 6 - 6A/ph 1S - 1 slot/pole/phase 1P - fully pitched winding MU1 - μ_r = 1 for the particles (i.e. particles modelled as air)
2	LP20_1S_1P_MU1	As number 1, but with 20A/ph
3	LP20_1S_1P_MU100	As number 2, but MU100 - μ_r = 100 for the particles
4	TP20_1S_1P_MU1	TP - tubular with particles 20 - 20A/ph 1S - 1 slot/pole/phase 1P - fully pitched MU1 - μ_r = 1 for particles (i.e. particles modelled as air)
5	TP20_1S_1P_MU100	As number 4, but MU100 - μ_r = 100 for particles
6	TP20_1S_1P_MU500	As number 4, but MU500 - μ_r = 500 for particles
7	TP30_1S_1P_MU100	As number 5, but 30 - 30A/ph
8	TP30_1S_1P_MU500	As number 6, but 30 - 30A/ph
9	T6_1S_1P	T - tubular (no particles) 6 - 6A/ph 1S - 1 slot/pole/phase 1P - fully pitched

Figure 5.16(b), (c) and (d) show the x-component of the flux density (B_x), y-component of the flux density (B_y) and B_m over one end of the lamination. (In this case B_x is also the radial, or normal, component and B_y the tangential component.) The maximum B_m occurred at the base of the teeth, with a value of approximately 860 mT. From the contours of B_m, it is apparent that the majority of the flux did not travel in the bore of the device. The time average values of B_x, B_y and B_m for a central portion of the tubular lamination are given in Fig 5.16(e), (f) and (g), and the radial and tangential components can both be seen to be concentrated at the base of the teeth. The radial flux density was

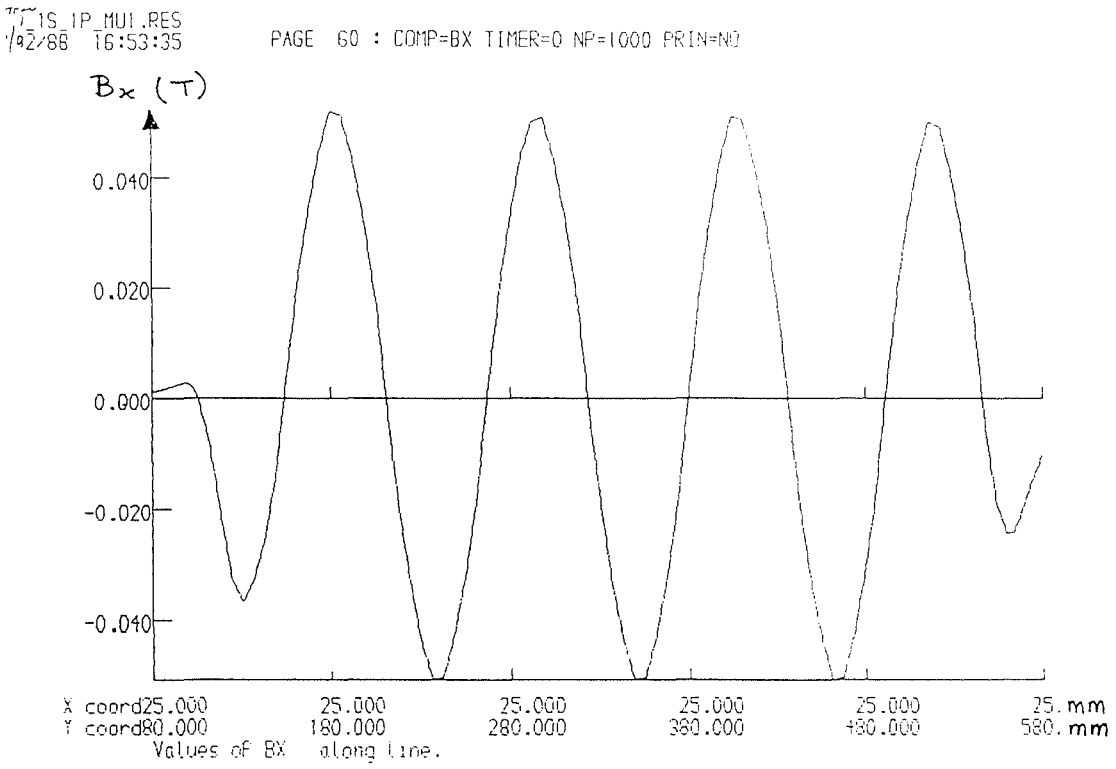

(a) Normal flux density, B_x

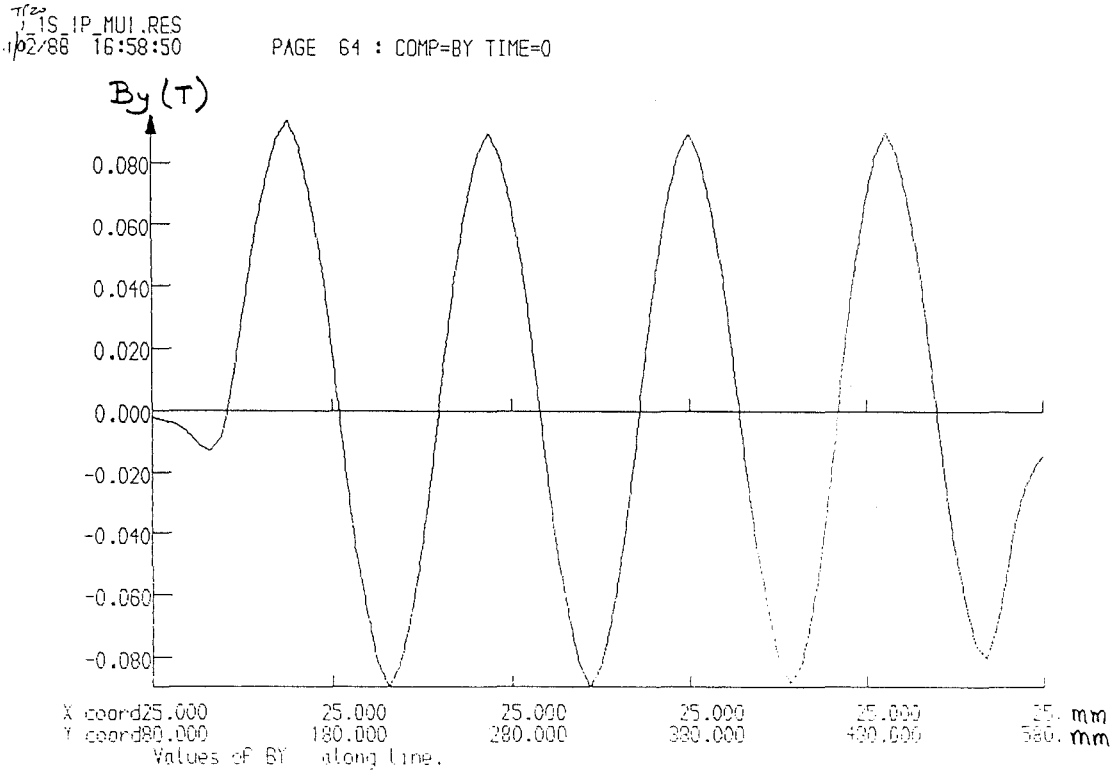

(b) Tangential flux density, B_y

VARIATION OF FLUX DENSITY ALONG x = 25
(TP20_1S_1P_MU1)

continued ...

Figure 5.17

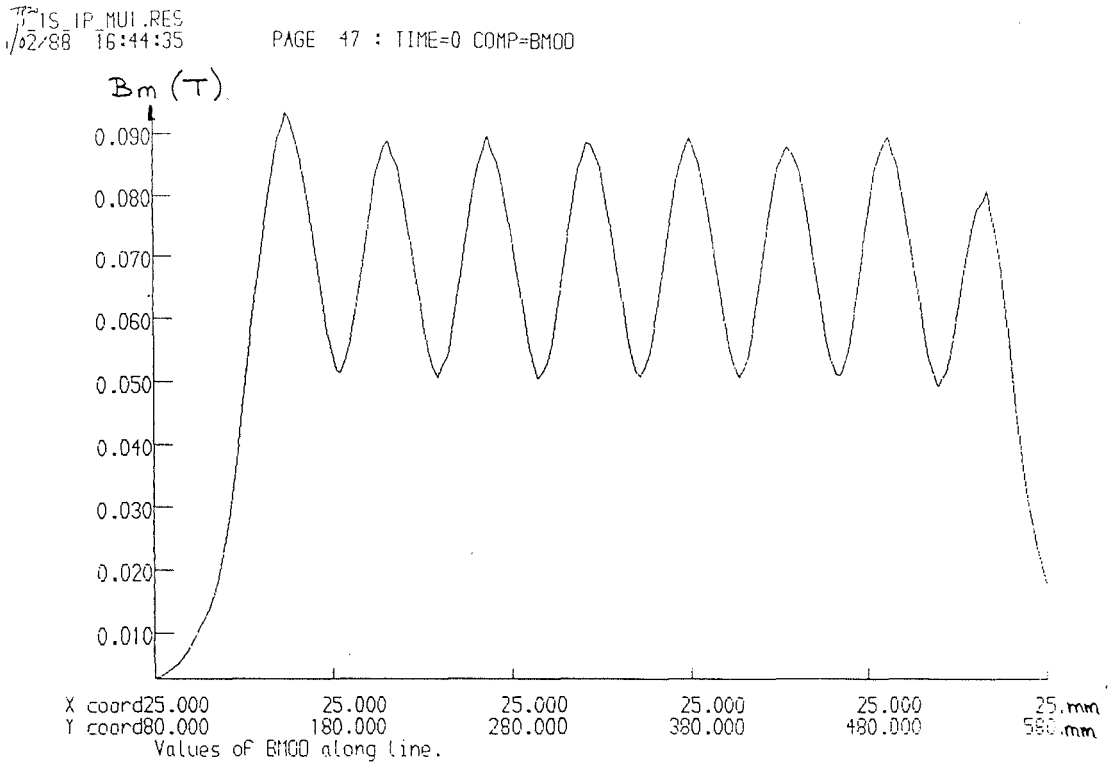

(c) Modulus of flux density, B_m

VARIATION OF FLUX DENSITY ALONG x = 25

(TP20_1S_1P_MU1)

Figure 5.17

(a) Normal flux density, B_x
(b) Tangential flux density, B_y
(c) Modulus of flux density, B_m

very low in both the back of the lamination and the airgap, being concentrated mostly around the teeth tips, and there was no radial component in the winding region (see Fig 5.16(e)). However, the majority of the tangential flux density travelled across the windings and clearly went from tooth tip to tooth tip (Fig 5.16(f)) and there was a greater tangential component (compared to the radial component) in the bore of the TLIM.

In order to investigate the variation in the field, graphs along various lines were plotted. Along x = 25 (see Fig 5.17) corresponding to a line through the bore of the machine and 15 mm from the lamination teeth, the graph of B_m (see Fig 5.17(c)) shows the pole distribution due to the sinusoids B_x (Fig 5.17(a)) and B_y (Fig 5.17(b)) which have their poles displaced by ninety degrees (when B_x reached its peak, B_y is zero etc.). The graph of B_m therefore follows the peaks of both B_x and B_y, as may be seen in Fig 5.17, with B_m attaining a maximum of approximately 90 mT (equivalent to peak B_y) and a minimum of approximately 50 mT (equivalent to peak B_x). Thus, as the contour plots have already indicated, the tangential flux density is greater than the normal within the bore of the tubular machine.

Figure 5.18 shows graphs of the flux density through the position of the particles (x = 32). Both B_x and B_y are less sinusoidal, with their shape being not dissimilar to that from the initial study (see Fig 5.5) after accounting for the difference in the modelled windings. (The components B_n and B_t (Fig 5.5) are equivalent to B_x and B_y (Fig 5.18).)

The spikes on the graphs of B_x, B_y and B_m in Fig 5.18 correspond to the position of the particles and were unexpected, since it was thought that the particles had been modelled as air. It was discovered however that the particles had been modelled as iron with a relative permeability of one, and the spikes were therefore due to boundary changes from air to iron (μ_r = 1) and back to air. Careful inspection of Fig 5.16(e), (f) and (g) shows that, in the vicinity of the particles, the flux density contours were attracted to the particles by either being drawn closer or by modifying their path so as to flow through the particles, implying a lower reluctance path. Although μ_r = 1 for the particles, the analysis software PE2D has assumed the characteristics of iron. The height of these spikes is also misleading, since an expansion of the area of the plot around the largest spike in the graph of B_m (Fig 5.18(c)) given in Fig 5.18(d) shows that the height is less than 110 mT, as opposed to greater than 160 mT, and this inconsistency is thought to be

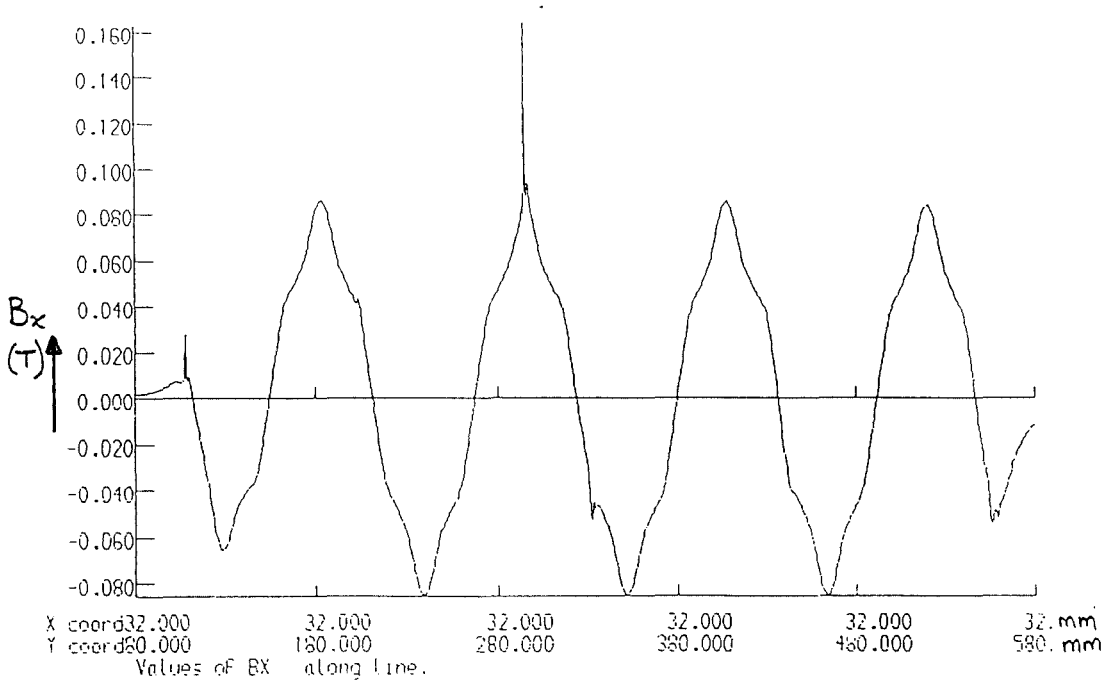

(a) Normal flux density, B_x

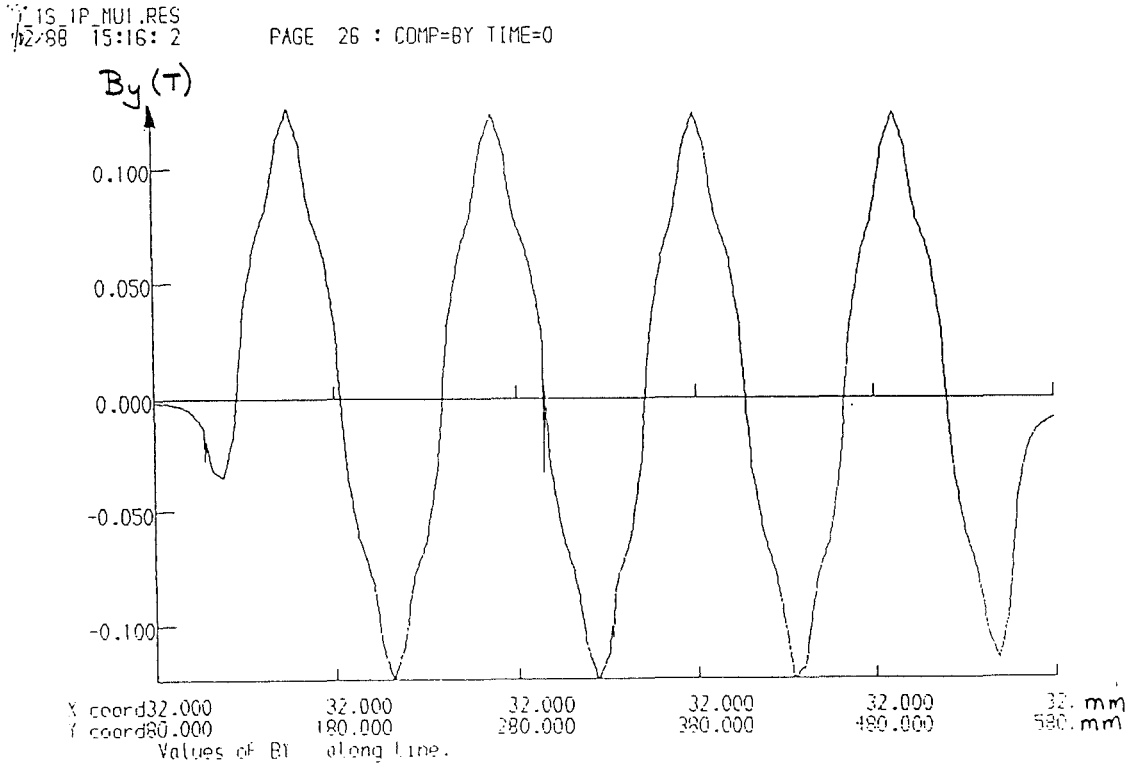

(b) Tangential flux density, B_y

VARIATION OF FLUX DENSITY THROUGH THE PARTICLES (ALONG x = 32)
(TP20_1S_1P_MU1)

continued ...

Figure 5.18

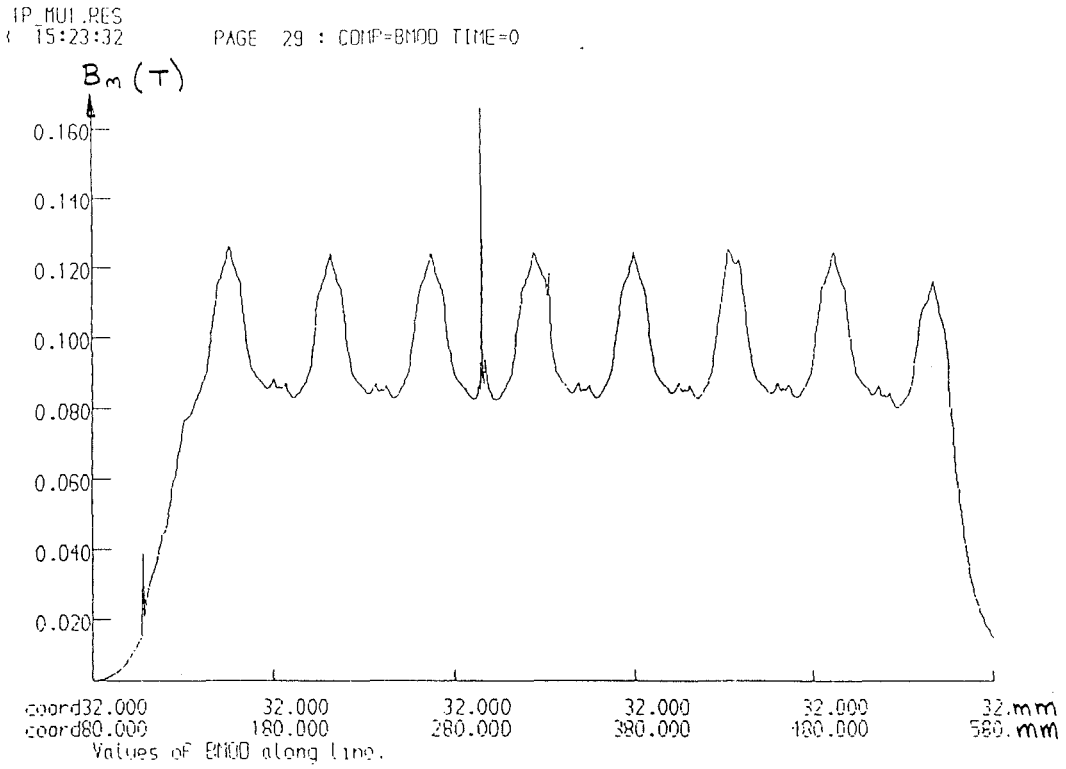

(c) Modulus of flux density, B_m

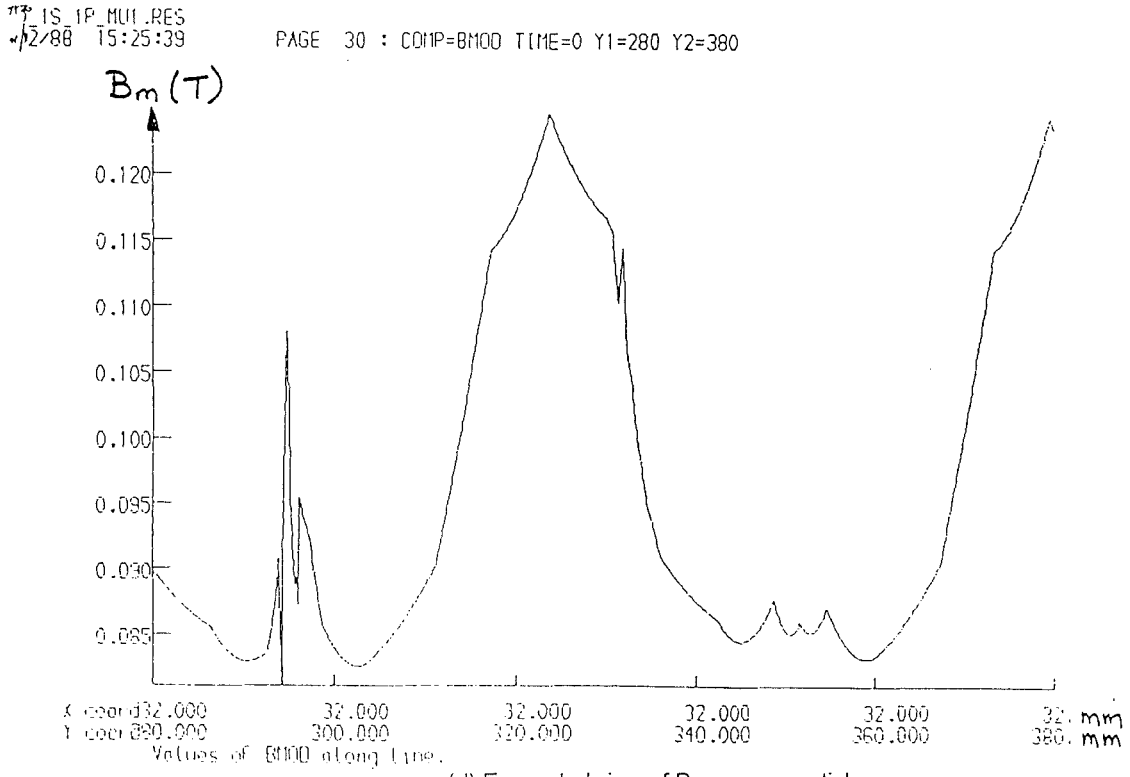

(d) Expanded view of B_m near a particle

VARIATION OF FLUX DENSITY THROUGH THE PARTICLES (ALONG x = 32)
(TP20_1S_1P_MU1)

Figure 5.18

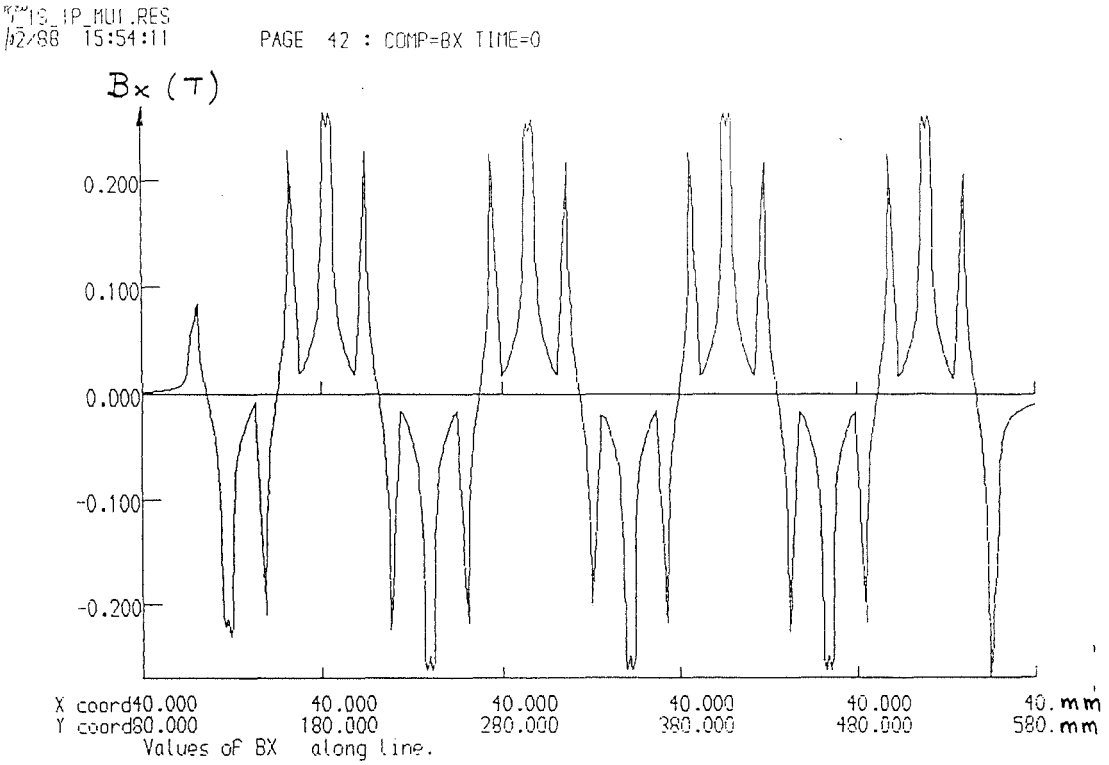

(a) Normal flux density, B_x

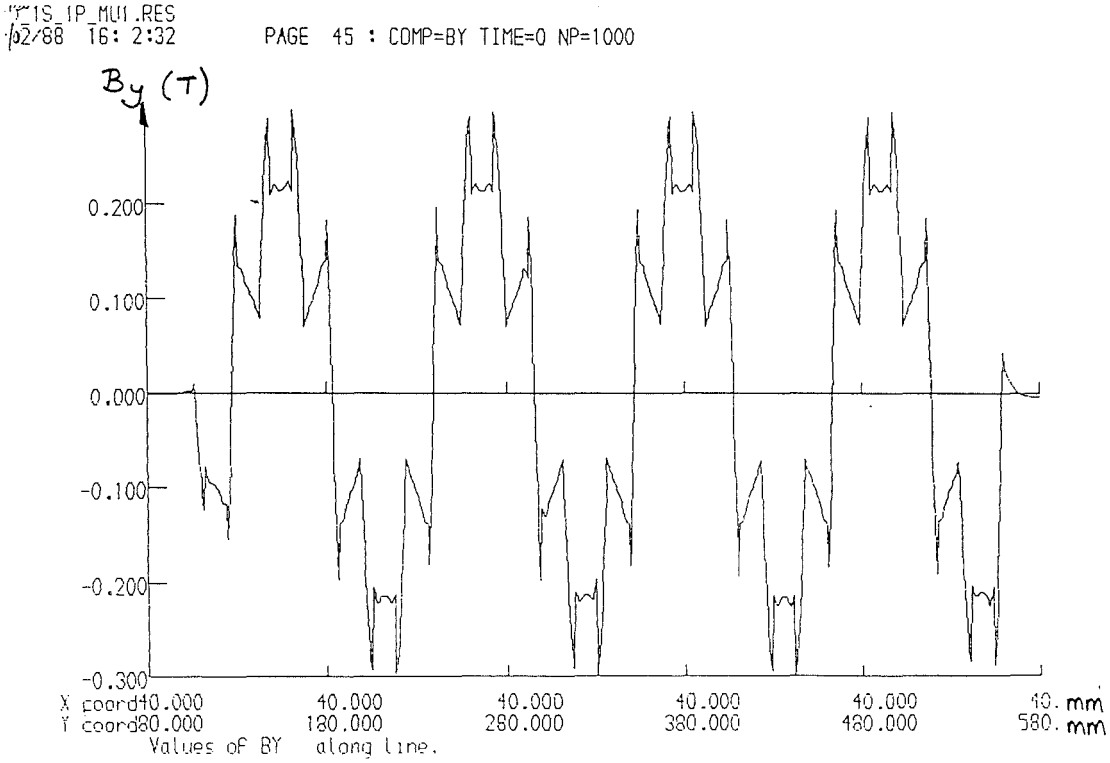

(b) Tangential flux density, B_y

VARIATION OF FLUX DENSITY ALONG THE TOOTH SURFACE (x = 40)
(TP20_1S_1P_MU1)

continued ...

Figure 5.19

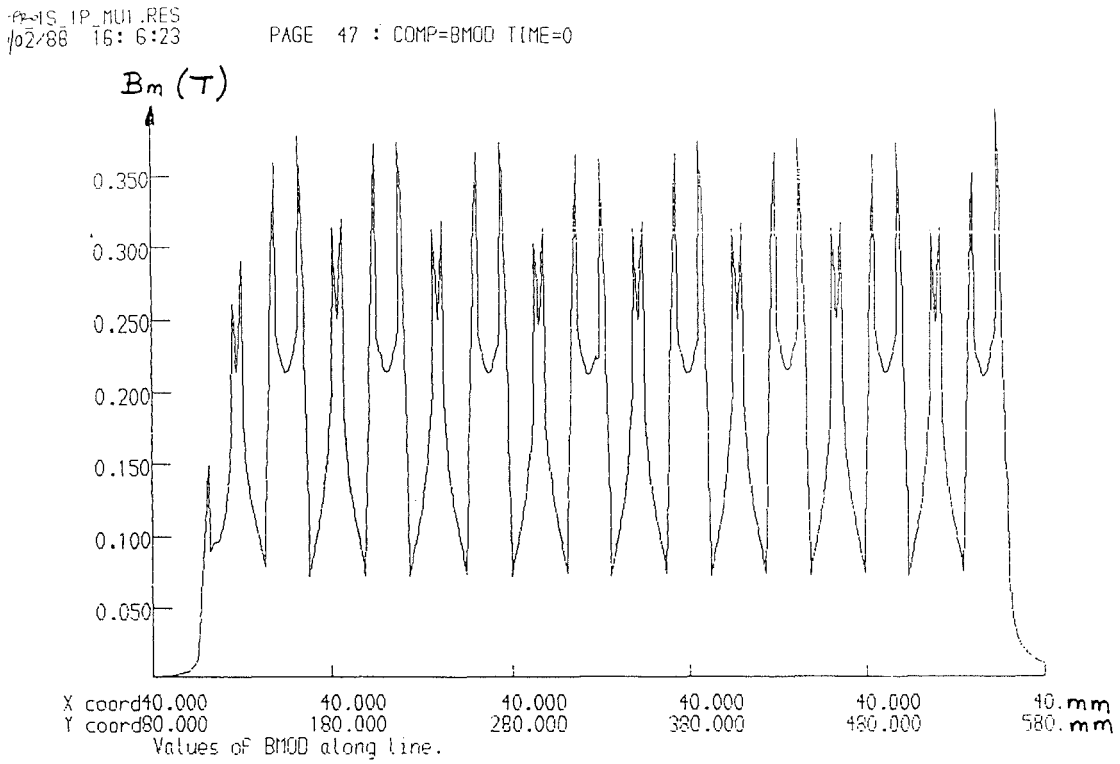

(c) Modulus of flux density, B_m

VARIATION OF FLUX DENSITY ALONG THE TOOTH SURFACE (x = 40)
(TP20_1S_1P_MU1)

Figure 5.19

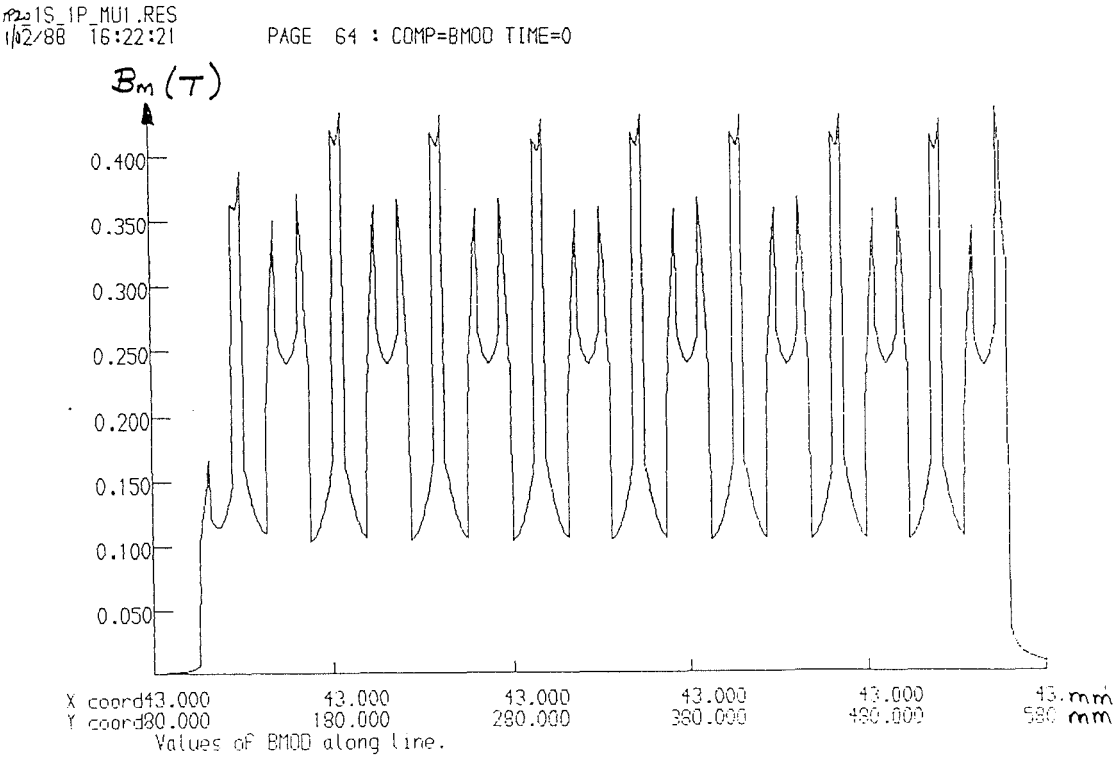

VARIATION OF FLUX DENSITY ALONG x = 43
(TP20_1S_1P_MU1)

Figure 5.20

due to quantisation effects. Each graph along a line (such as those in Fig 5.18) is plotted over a finite number of points and, for the same number of points, the point-to-point separation in Fig 5.18(c) is five times greater than that in Fig 5.18(d), thereby implying that the expanded view is more accurate, as would be expected. For both these reasons, i.e. a modelling oversight and a quantisation error, the spikes may be ignored. It is when the particles have a relative permeability much greater than unity that changes in the field become of interest, and such effects are seen later.

Along the surface of the teeth (x = 40), the graphs are far from sinusoidal (see Fig 5.19), but eight poles can be clearly seen in the graphs of B_x and B_y, the pole-pitch being 56 mm. The spikes in the graph of B_x are due to the twenty five teeth and the flux density between successive teeth was predominantly tangential (see also Fig 5.16). Obviously the slots occurred between the spikes and all twenty four can be identified from the graphs of B_x and B_y; the position of the teeth and slots may be verified from the data in Appendix D.

Plateaux can be seen in the graph for B_y (see Fig 5.19(b)) corresponding to the position of the slots. Superimposed on these is the influence of the teeth, and the fifty spikes (convex and concave) mark the start and end positions of each tooth. The graph of the modulus of B_x and B_y (B_m in Fig 5.19(c)) shows the eight poles of B_x and B_y, giving a total of sixteen. On the surface of the teeth B_x and B_y (normal and tangential components respectively) are approximately equal, and this is also true just inside the teeth where they had both slightly increased (see Fig 5.20). Continuing further into the teeth the flux density was predominantly normal, with the maximum B_x approximately equal to 800 mT and maximum B_y approximately equal to 120 mT (see Fig 5.21). The position of the teeth and slots is again evident, and as expected B_x is greatest in the teeth and B_y is greatest in the slots. Each of the steps in the graph of B_y (Fig 5.21(b)), which resembles an mmf waveform, occurred at the start of a slot; B_y remained constant along the slot and then increased (or decreased) linearly along adjacent teeth as determined by the current flowing in the next slot.

Directly behind the teeth, along the line x = 80, the graph of B_m in Fig 5.22(a) correlates well with the contour plot presented in Fig 5.16(a). A build up of flux occurs behind every tooth, and B_m can be seen to peak in those areas, with the troughs illustrating the

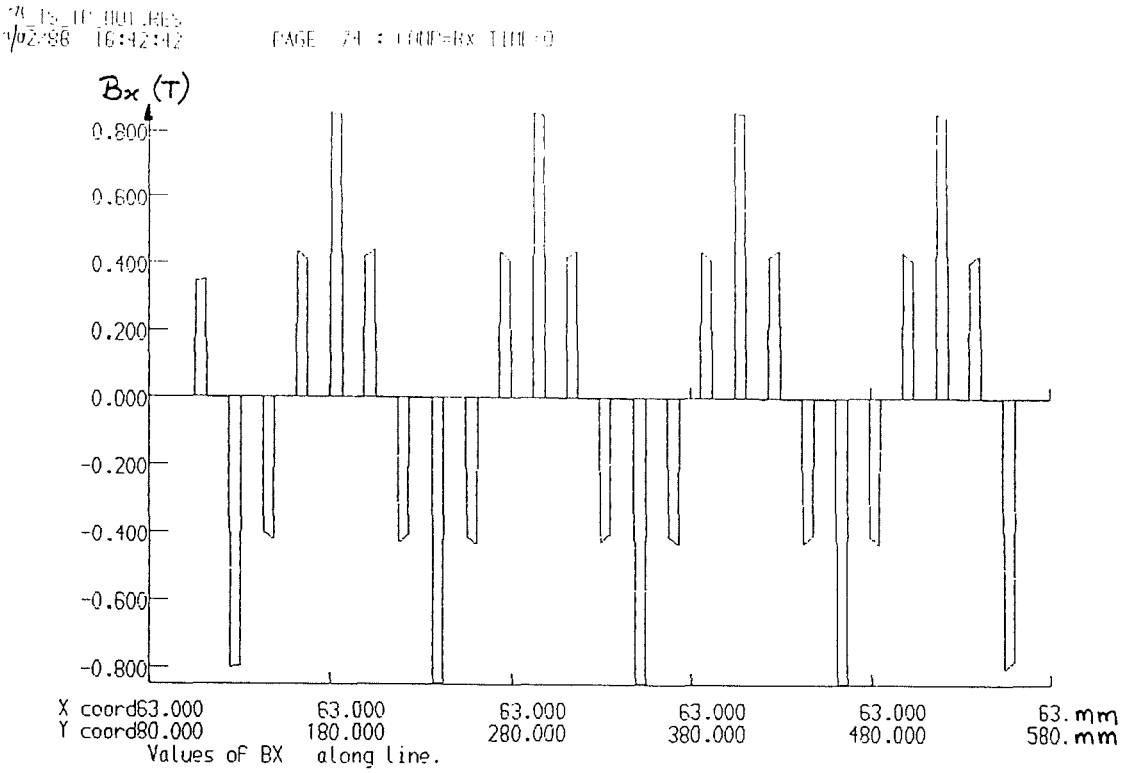

(a) Normal flux density, B_x

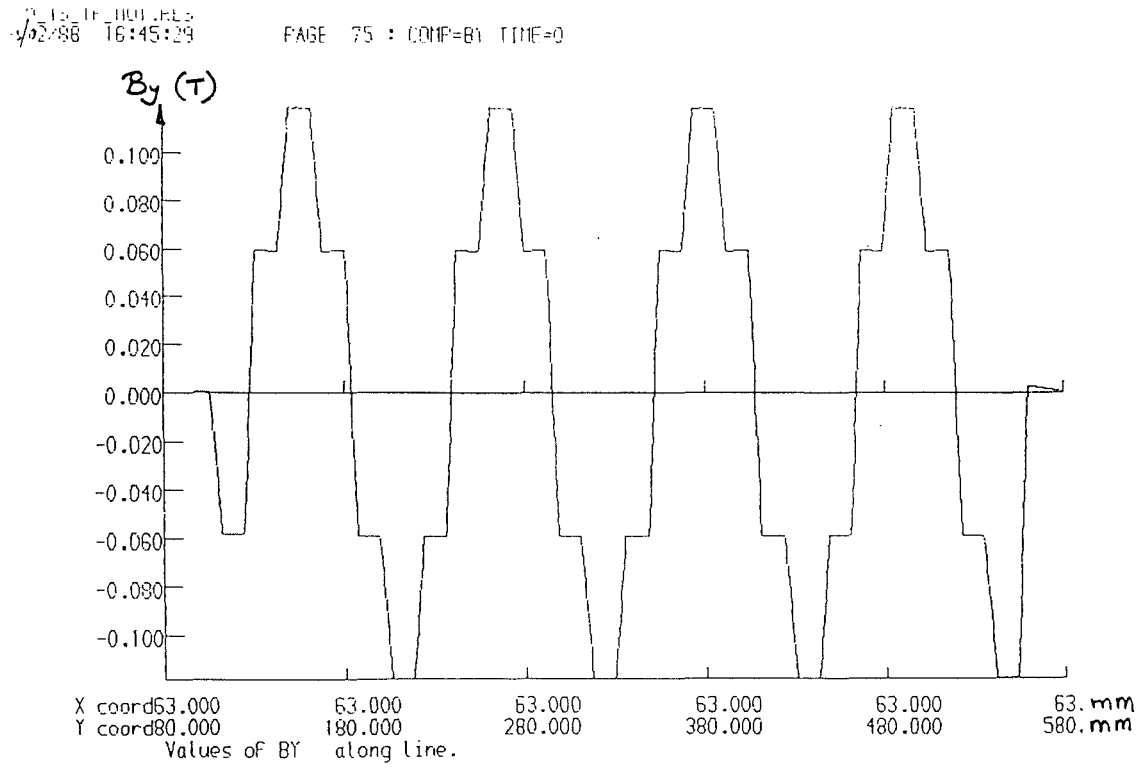

(b) Tangential flux density, B_y

VARIATION OF FLUX DENSITY ALONG x = 63
(TP20_1S_1P_MU1)

Figure 5.21

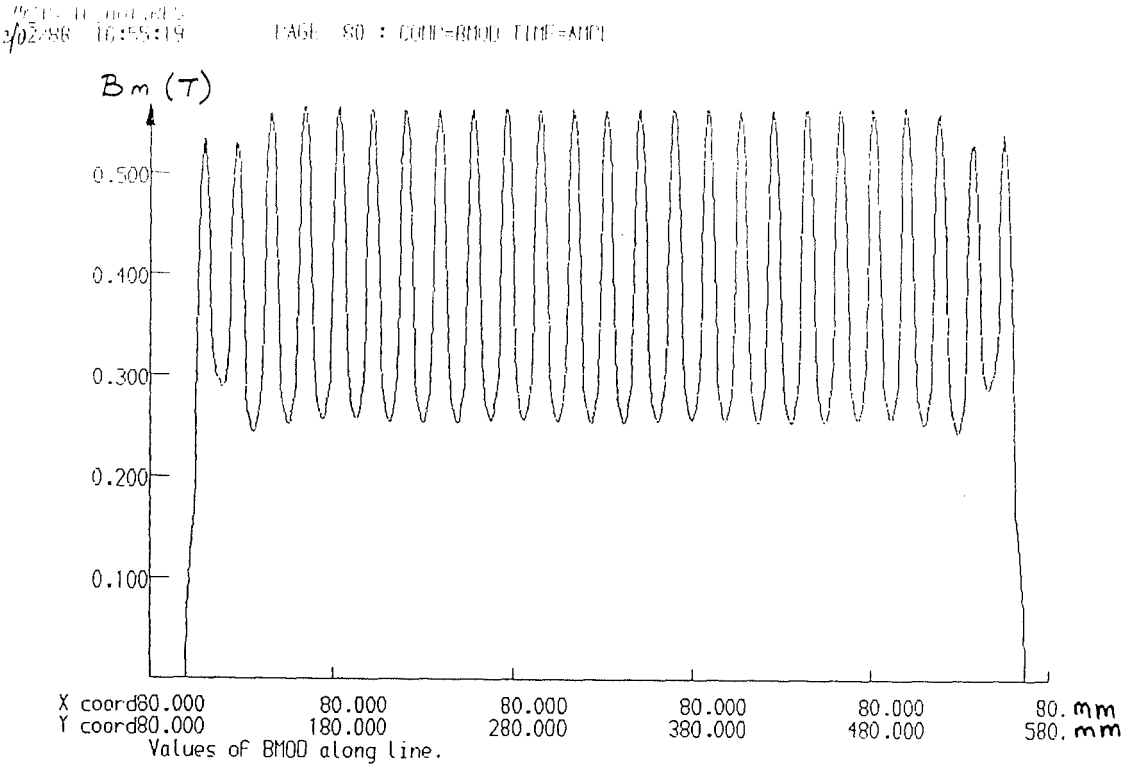

(a) Modulus of flux density, B_m

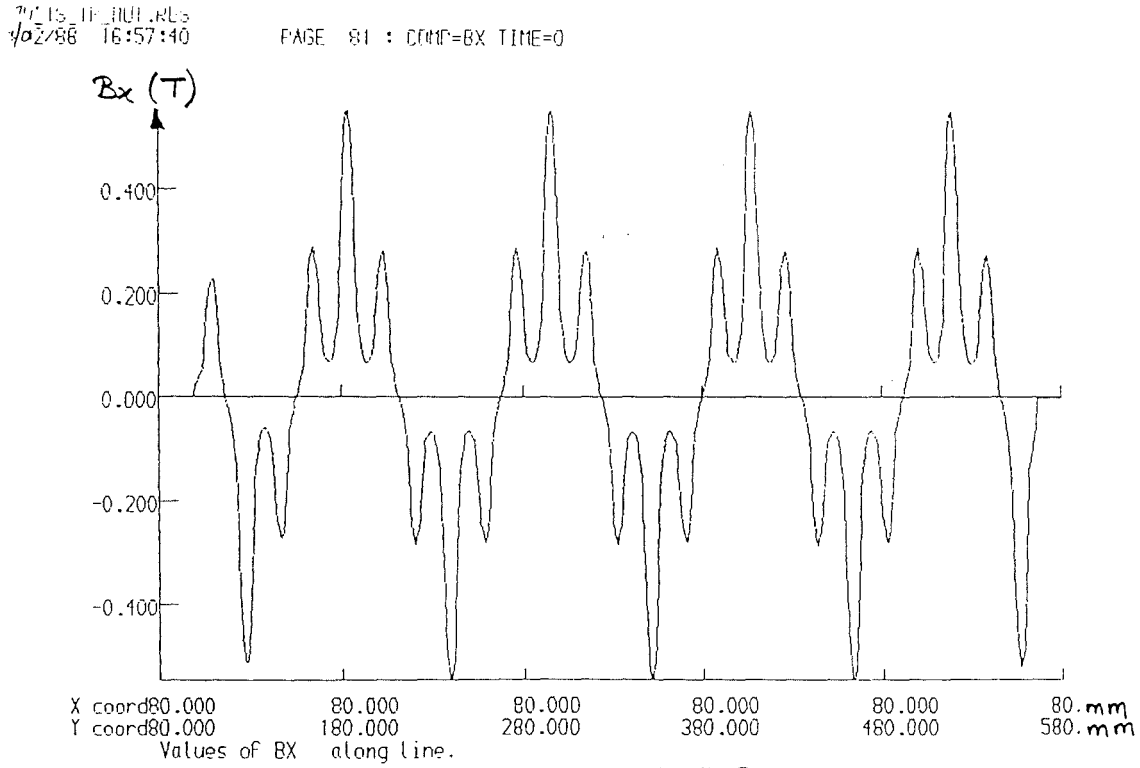

(b) Normal flux density, B_x

VARIATION OF FLUX DENSITY DIRECTLY BEHIND THE TEETH (x = 80)
(TP20_1S_1P_MU1)

continued ...

Figure 5.22

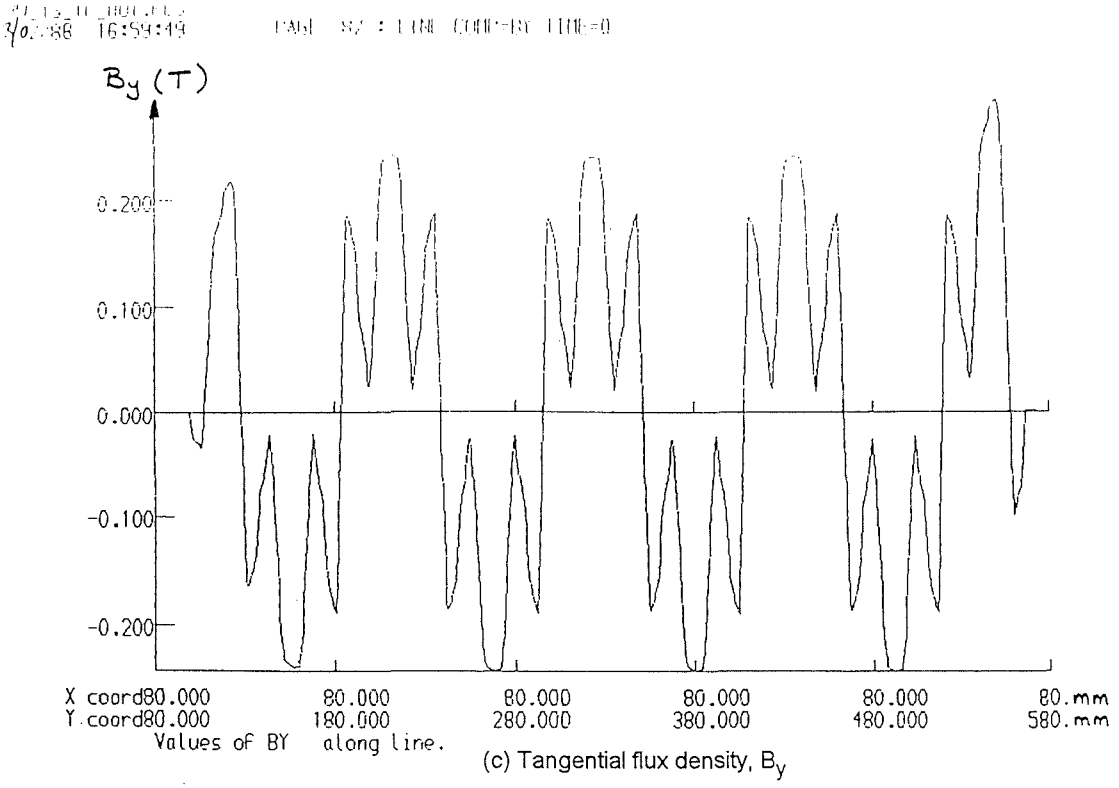

(c) Tangential flux density, B_y

VARIATION OF FLUX DENSITY DIRECTLY BEHIND THE TEETH (x = 80)
(TP20_1S_1P_MU1)

Figure 5.22

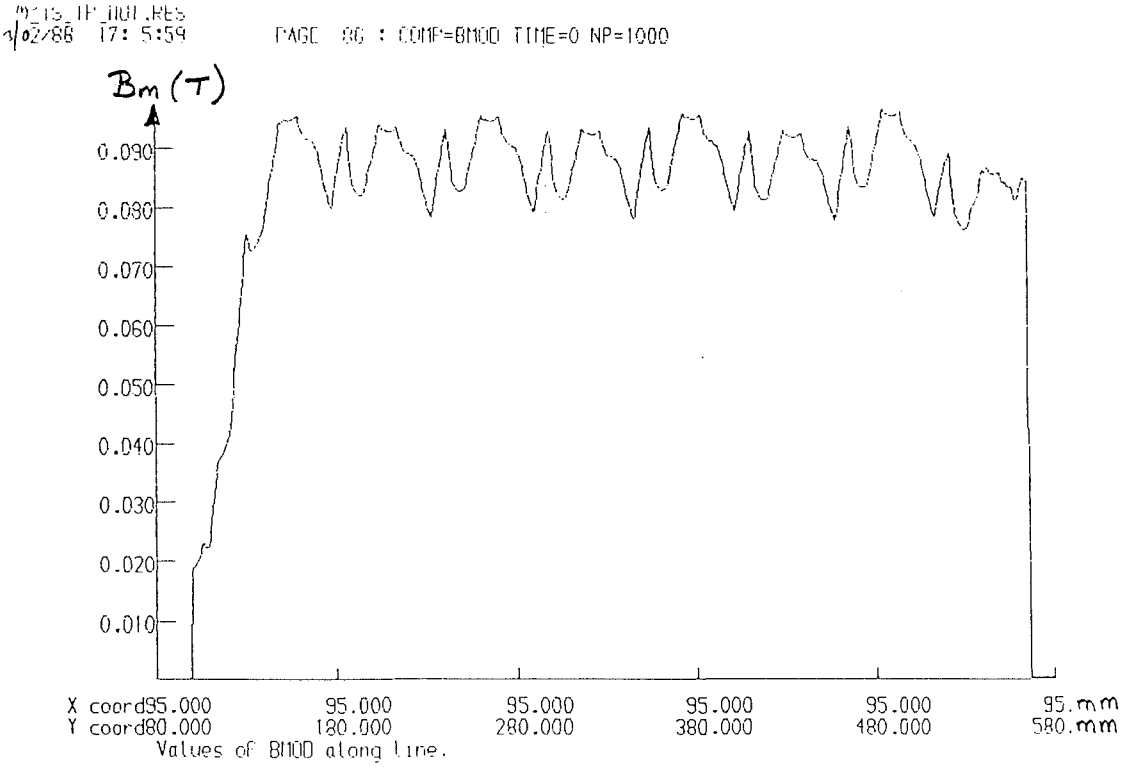

VARIATION OF FLUX DENSITY ALONG x = 95
(TP20_1S_1P_MU1)

Figure 5.23

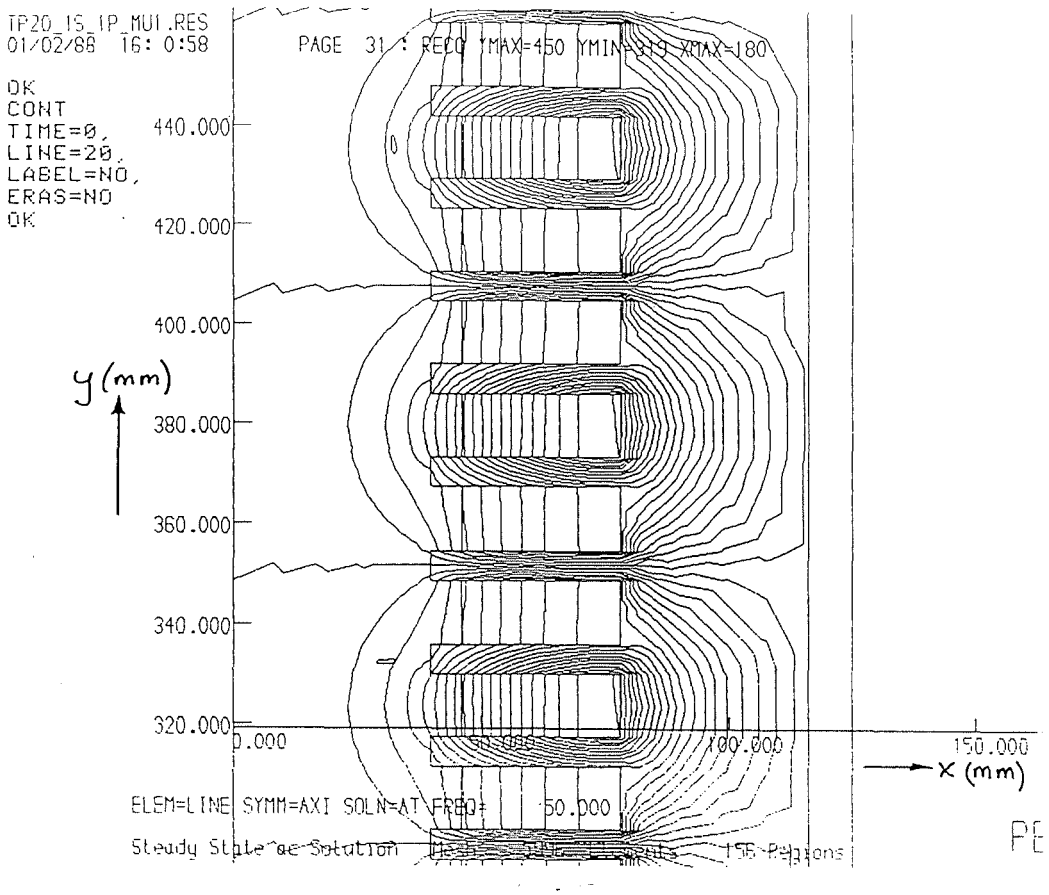

PARTICLE POSITION AND ORIENTATION

OPPOSITE THE SLOT AT y = 436 AND THE TOOTH AT y = 332.5

Figure 5.24

slots of the device. B_x along the same line was no longer zero behind the slots (see Fig 5.22(b)), but was still predominant with a peak value approximately twice that of B_y (Fig 5.22(c)). Further in the lamination (along x = 95) B_x and B_y were approximately equal, as implied by Fig 5.23 which also shows that B_m had dropped to approximately 90 mT.

Field values through a slot and tooth are plotted in Figs 5.25 and 5.26, both of which had a particle opposite them as illustrated by Fig 5.24 which clearly shows the two particles. The slot at y = 436 contained a red-phase winding and the tooth at y = 332.5 had a blue-phase winding one side and a red-phase winding on the other (see Appendix D for the co-ordinates). From Figs 5.25(a) and (b), the graphs of B_x and B_y through the particle and slot along the line y = 436, it is clear that the majority of the flux was tangential. The absolute value of B_y (Fig 5.25(b)) increases from about 60 mT at the axis to a maximum of approximately 240 mT at the top of the winding, and decreases linearly through the winding in the slot until the back of the lamination was entered. At this point B_y changed sign, rising to another maximum of approximately 250 mT and finally decreasing smoothly through the lamination. Outside the back of the lamination there is neither tangential nor normal flux density, as shown clearly in Figs 5.25(a) and (b). There is a small disturbance in the field at x = 32, which marks the exact position of the particle and may be seen in the graph of B_x (Fig 5.25(a)). (Reasons for this field variation were discussed earlier.)

For the particle and tooth along y = 332.5 shown in Fig 5.24, it was found that B_m peaked part of the way through the tooth, attaining a value of about 810 mT. The normal flux density B_x (see Fig 5.26(a)) peaked at the same position and with a similar shape to that of B_m (which is not presented for this reason), implying that the majority of the flux was normal; B_x was low in the bore of the device and was concentrated mostly in the lamination, as expected. Although greater than B_x in the airgap, B_y (Figure 5.26(b)) was comparatively low. However, the absolute value of B_y experienced a sudden increase at the start of the tooth to about 240 mT before decreasing rapidly along the tooth, until a position directly next to the winding was reached (at x = 46). It then decreased less rapidly, becoming zero just before the base of the tooth where B_y changed sign, before rising to another maximum and finally decreasing through the remainder of the lamination. Both the graphs of B_x and B_y (Fig 5.26) show again that outside the back of the lamination there is neither normal nor tangential flux.

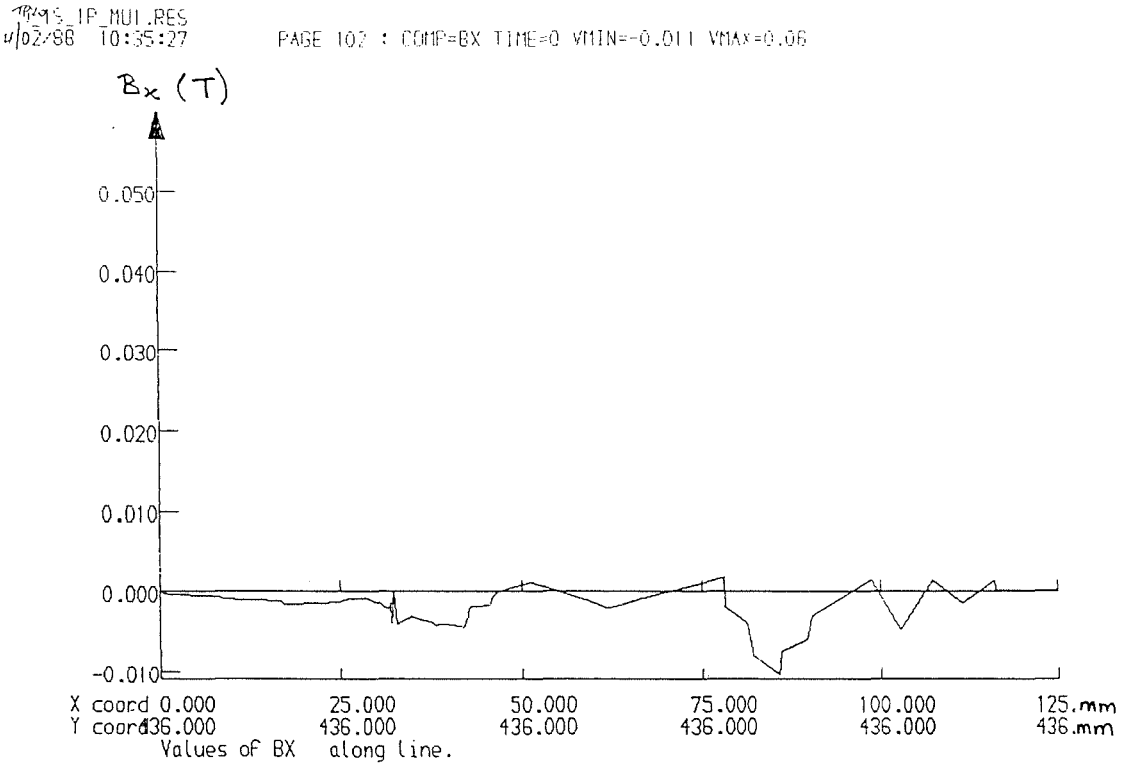

(a) Normal flux density, B_x

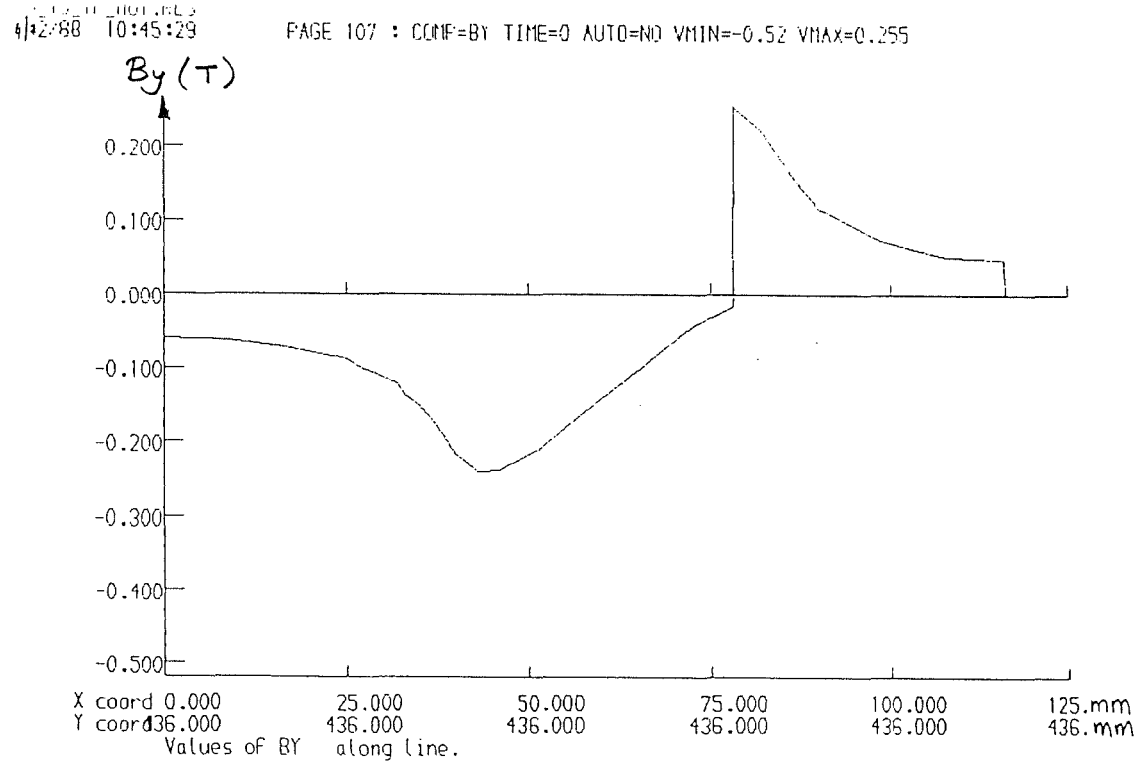

(b) Tangential flux density, B_y

VARIATION OF FLUX DENSITY THROUGH THE PARTICLE AND SLOT ALONG y = 436
(TP20_1S_1P_MU1)

Figure 5.25

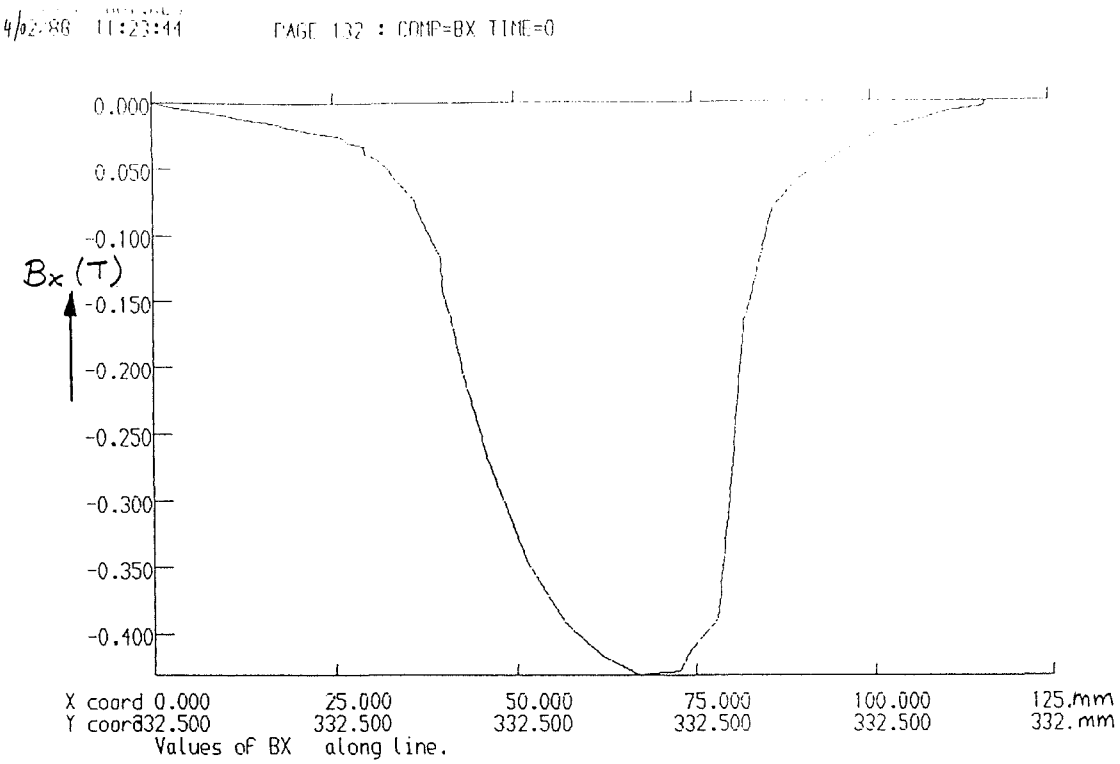

(a) Normal flux density, B_x

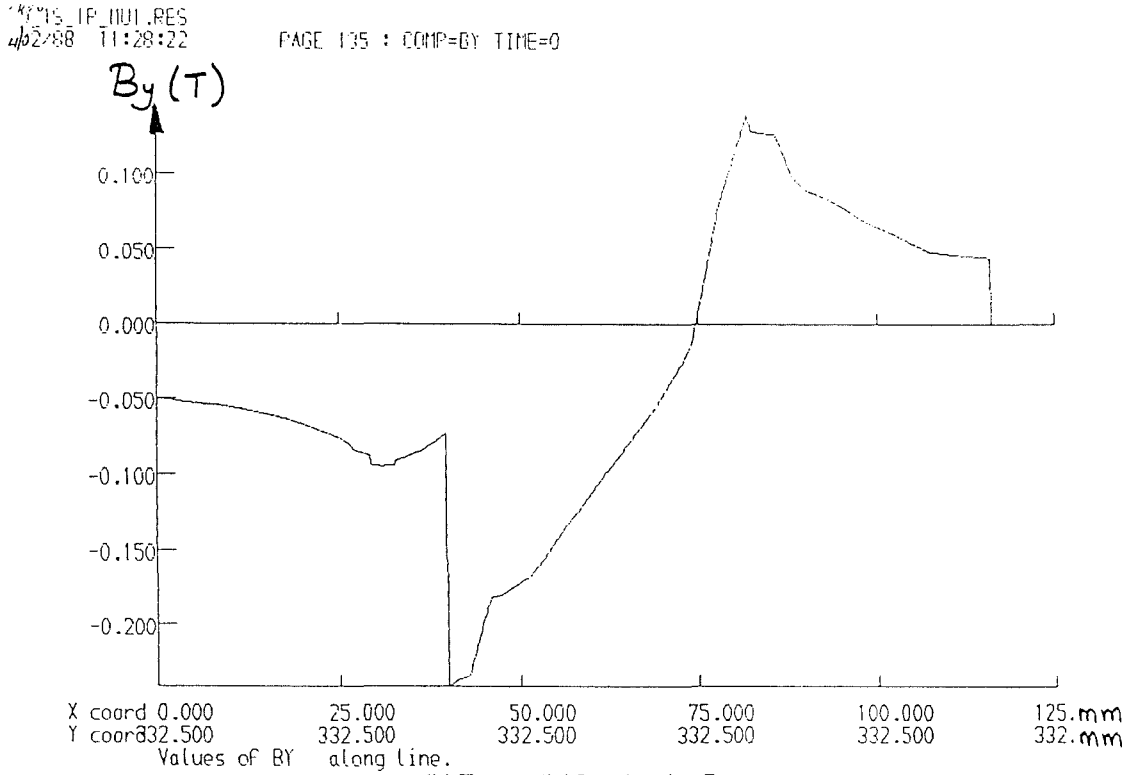

(b) Tangential flux density, B_y

VARIATION OF FLUX DENSITY THROUGH THE PARTICLE AND TOOTH ALONG y = 332.5 (TP20_1S_1P_MU1)

Figure 5.26

5.6.2 Results for the Linear Machine

Results from the model LP20_1S_1P.MU1 (i.e. linear machine at 20 A/phase with particles modelled as air) are presented in Figs 5.27-5.30. Figures 5.27(a), (b) and (c) shows contours of B_m, B_x and B_y over one end of the lamination, Figs 5.27(d), (e) and (f) the same contours over a central portion of the lamination and Fig 5.27(g) the time-averaged contours of B_m. (For the linear machine, B_y is the normal component and B_x the tangential component of flux density.) The diagrams show that a concentration of flux density occurs at the base of the teeth. The poles may be identified in Figs 5.27(d), (e) and (f), with the B_x poles shifted by 1½ slot-pitches (i.e. 90°) with respect to the B_y poles. As in the tubular machine, the majority of the flux travels across the teeth and windings of the device but, in this case, the airgap flux density and the flux density inside the lamination are greater, with B_m attaining a maximum value of 1.45 T at the base of the lamination teeth (see Fig 5.27(g)). Although the particles have been modelled with $\mu_r = 1$, it may be noted that they still affect the local field, as seen by the modified path taken by the flux density contours in Figs 5.27(d), (e), (f) and (g).

As for the tubular device, graphs were plotted along lines perpendicular and parallel to the lamination. In Fig 5.28 the variation of B_x, B_y and B_m is plotted along a line which passes through all the modelled particles (y = 93). The time-average graph of B_x in Fig 5.28(a) contains spikes corresponding to the teeth of the device, with B_x having a mean value of about 0.1 T. The time-average mean value of B_m in Fig 5.28(c) is approximately 0.14 T which is some 30 mT greater than that for the same conditions in the TLIM study (see Fig 5.18). Note that for the reason mentioned previously, the particles have shown up as very large spikes.

Figure 5.29 (i.e. through the particle and slot along x = 436) and Fig 5.30 (i.e. through the particle and tooth along x = 332.5) both show that outside the back of the lamination there is no flux. Instead, both figures show an immediate increase to a finite value of flux density for both B_x and B_y as soon as the lamination is entered. Further inside the lamination, the flux density continues to increase to a peak at the base of both slots (Fig 5.29) and teeth (Fig 5.30). Through the slot, the flux density (which is predominantly tangential, as expected) can be seen to increase in Fig 5.29 until about the end of the winding, after which it begins to decrease in the airgap; the flux density is mostly

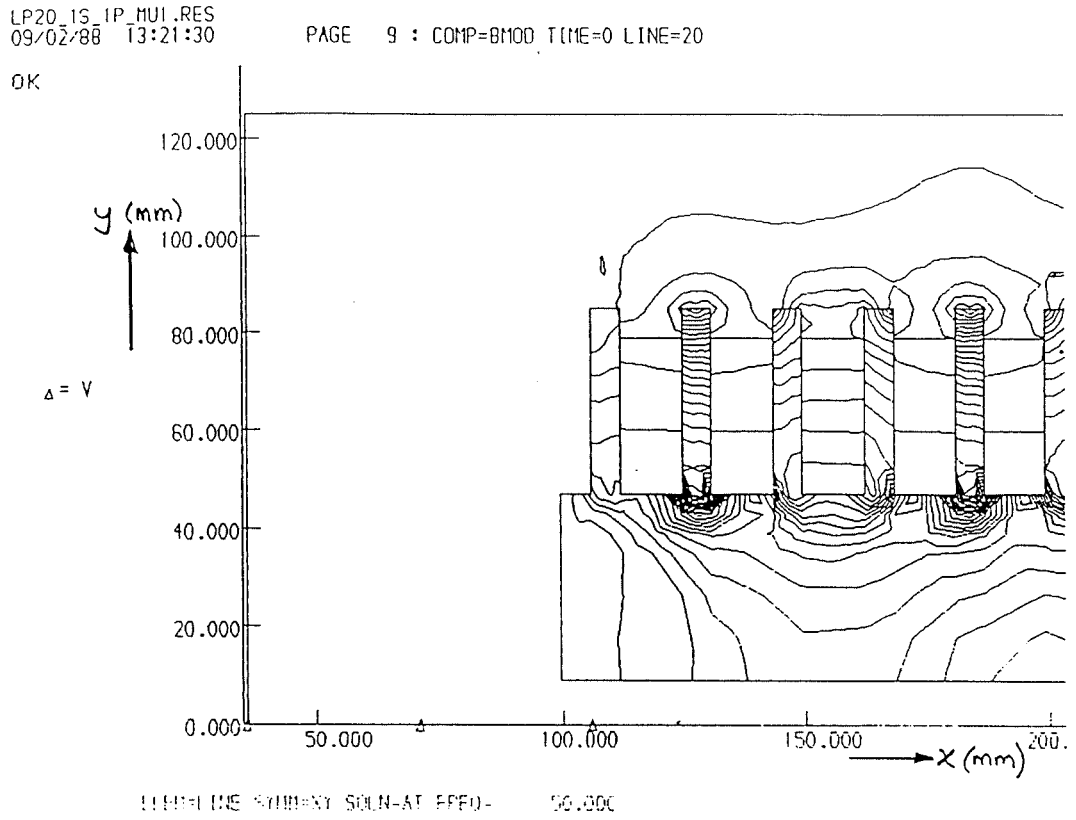

(a) Contours of B_m over one end of the lamination

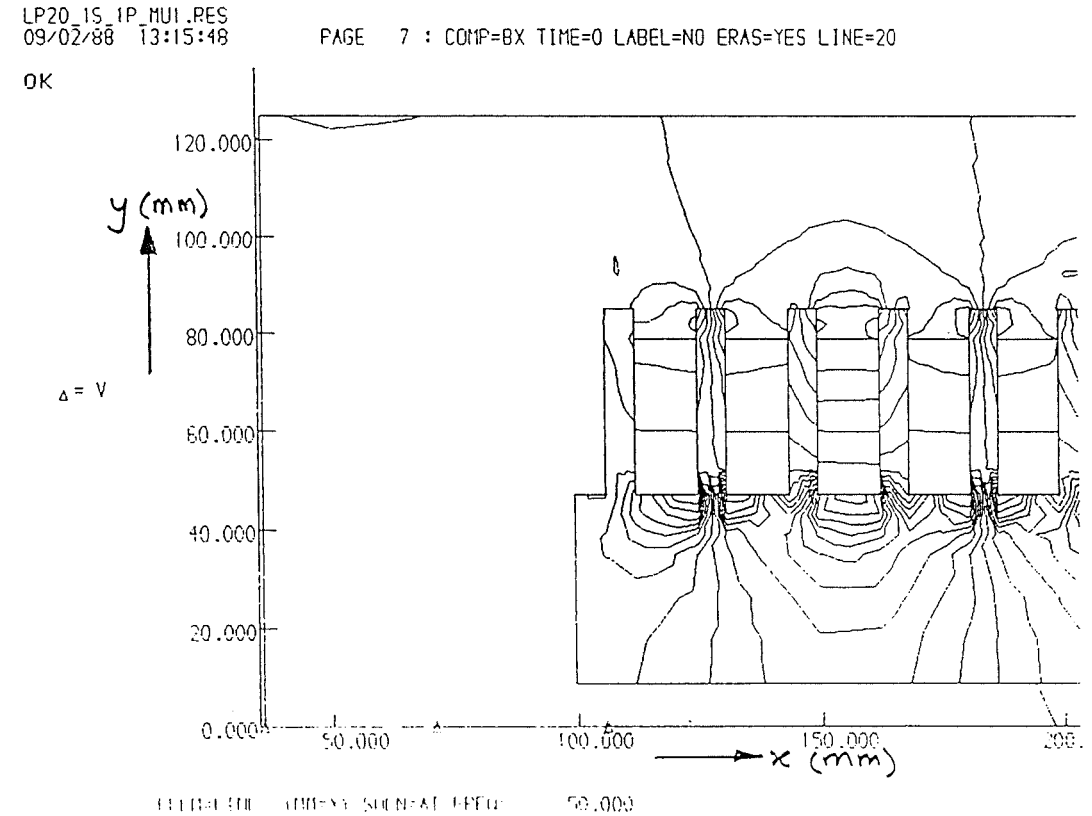

(b) Contours of B_x over one end of the lamination

Figure 5.27 FLUX DENSITY CONTOURS FOR THE LIM STUDY
LP20_1S_1P_MU1

continued ...

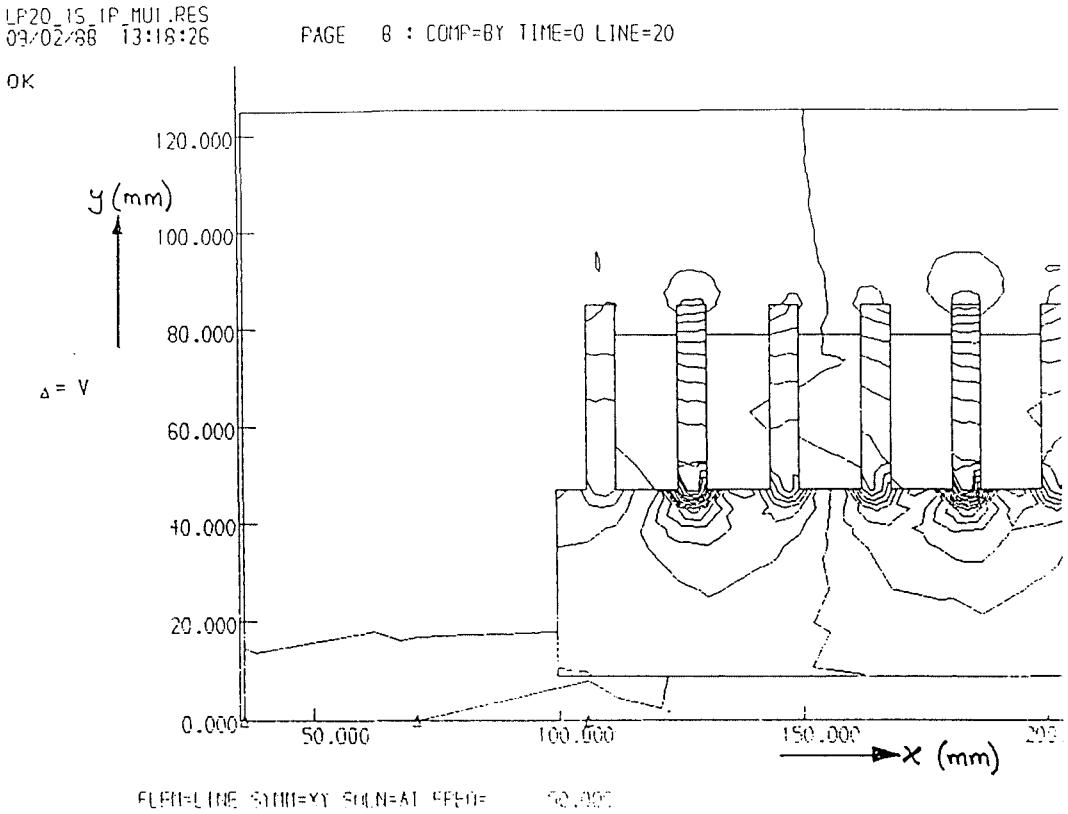

(c) Contours of B_y over one end of the lamination

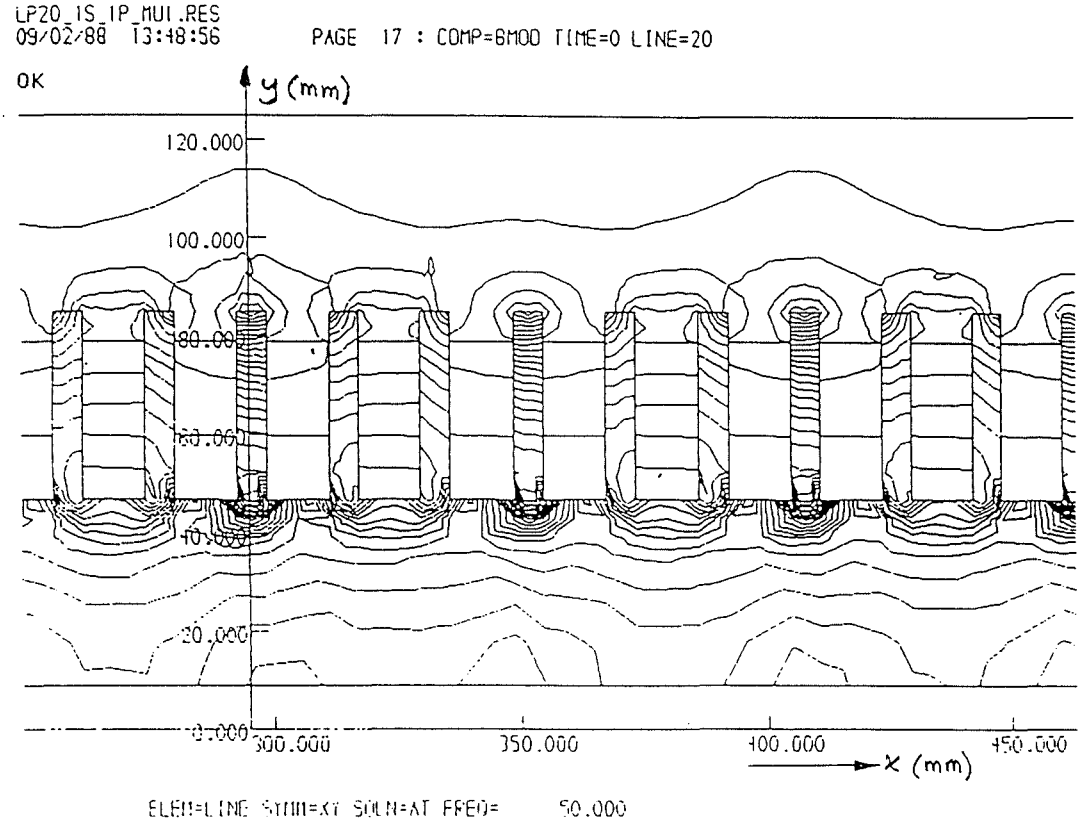

(d) Contours of B_m over a central area of the lamination

Figure 5.27 FLUX DENSITY CONTOURS FOR THE LIM STUDY
LP20_1S_1P_MU1

continued ...

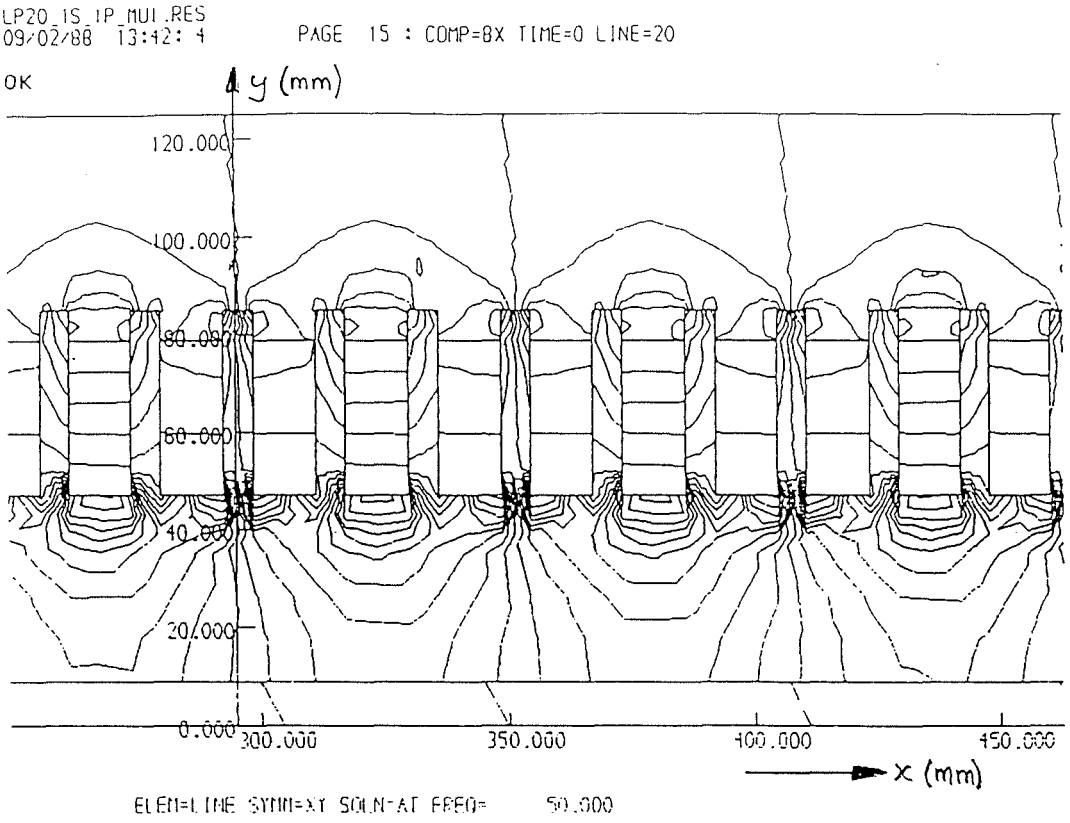

(e) Contours of B_x over a central area of the lamination

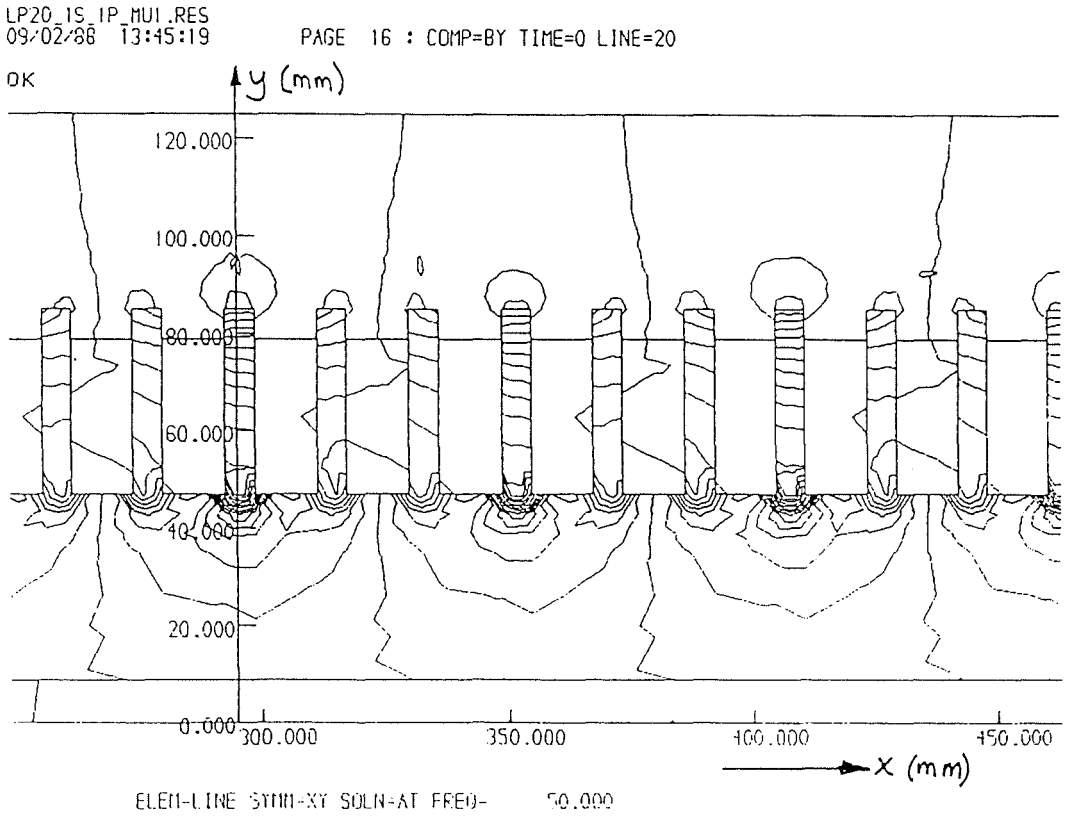

(f) Contours of B_y over a central area of the lamination

Figure 5.27 FLUX DENSITY CONTOURS FOR THE LIM STUDY
LP20_1S_1P_MU1

continued ...

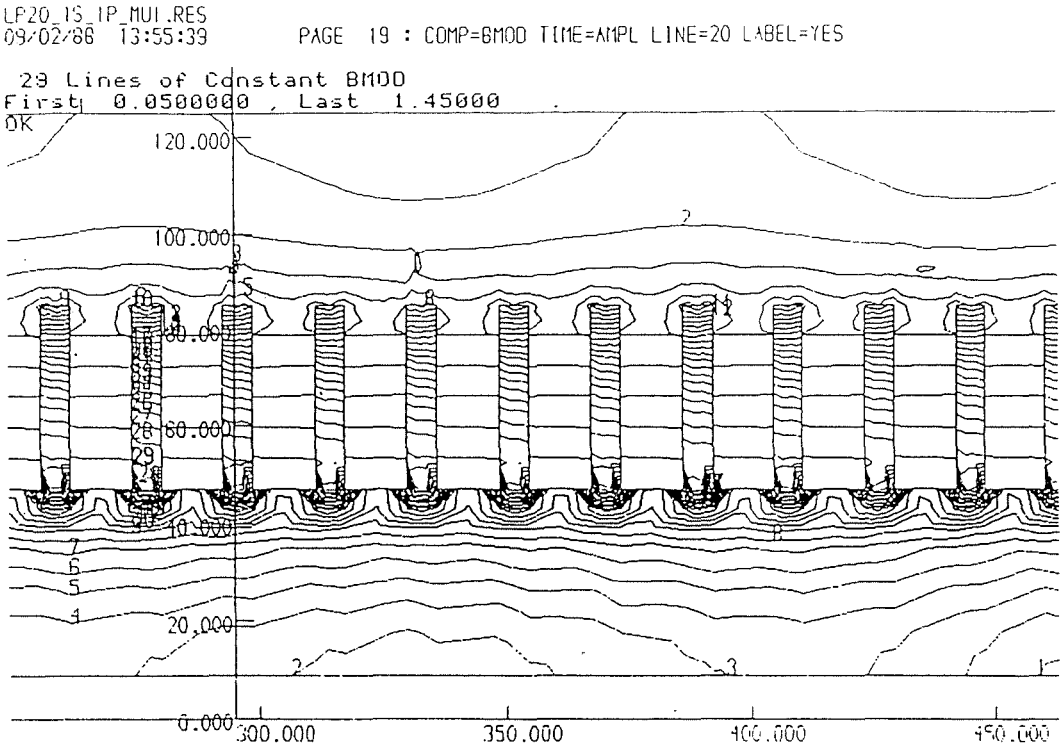

(g) Time-averaged contours of B_m over a central area of the lamination

Figure 5.27 FLUX DENSITY CONTOURS FOR THE LIM STUDY
LP20_1S_1P_MU1

(a) Contours of B_m over one end of the lamination
(b) Contours of B_x over one end of the lamination
(c) Contours of B_y over one end of the lamination
(d) Contours of B_m over a central area of the lamination
(e) Contours of B_x over a central area of the lamination
(f) Contours of B_y over a central area of the lamination
(g) Time-averaged contours of B_m over a central area of the lamination

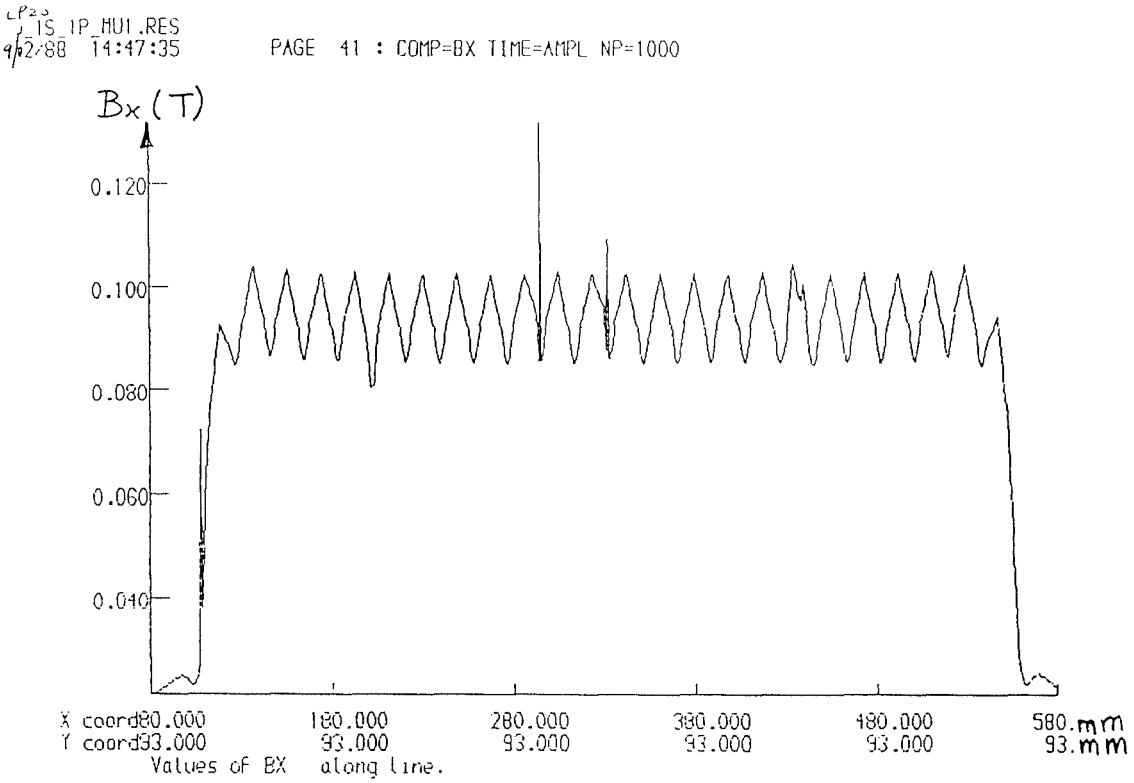

(a) Time-averaged tangential flux density, B_x

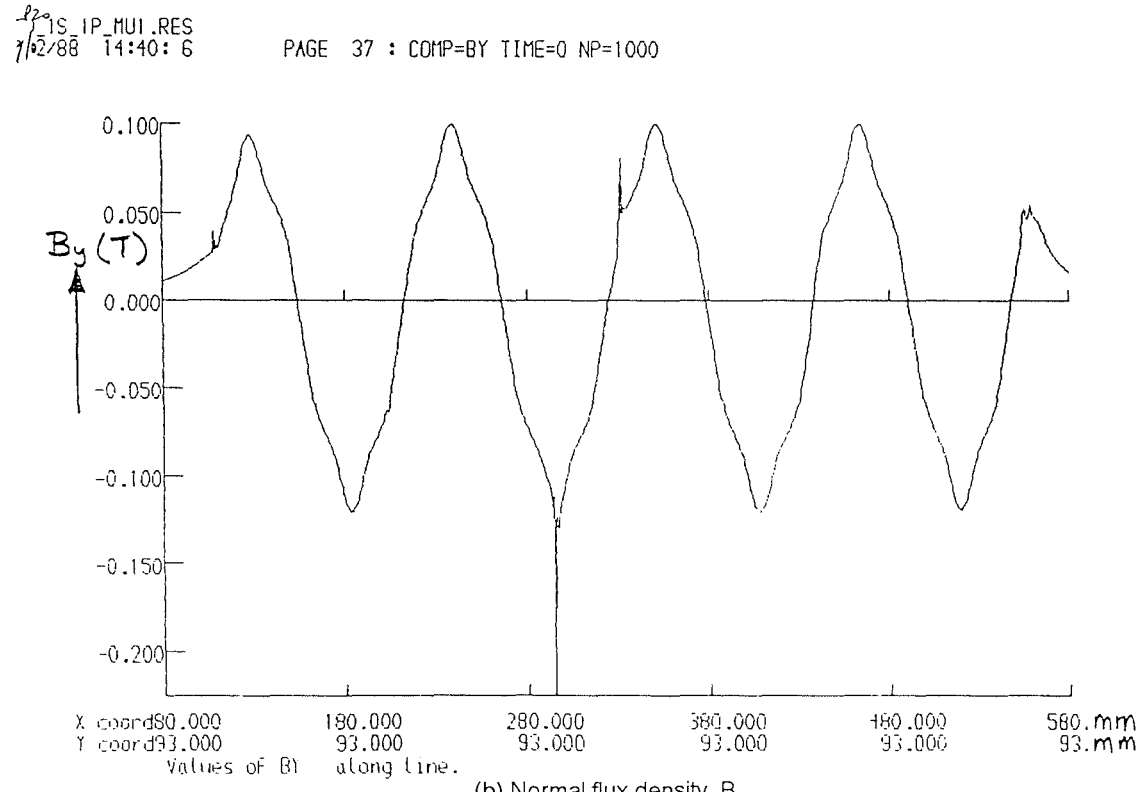

(b) Normal flux density, B_y

VARIATION OF FLUX DENSITY THROUGH THE PARTICLES (y = 93)
(LP20_1S_1P_MU1)

continued ...

Figure 5.28

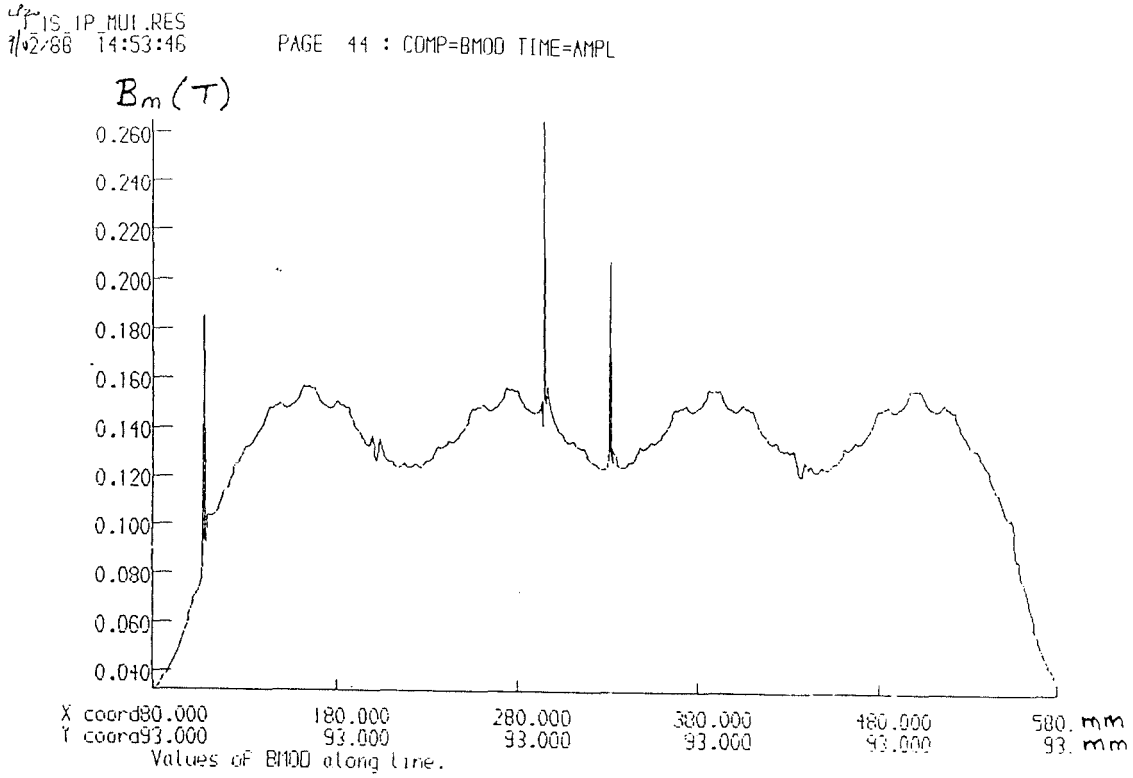

(c) Time-averaged modulus of flux density, B_m

VARIATION OF FLUX DENSITY THROUGH THE PARTICLES (y = 93)
(LP20_1S_1P_MU1)

Figure 5.28

(a) Time-averaged tangential flux density, B_x
(b) Normal flux density, B_y
(c) Time-averaged modulus of flux density, B_m

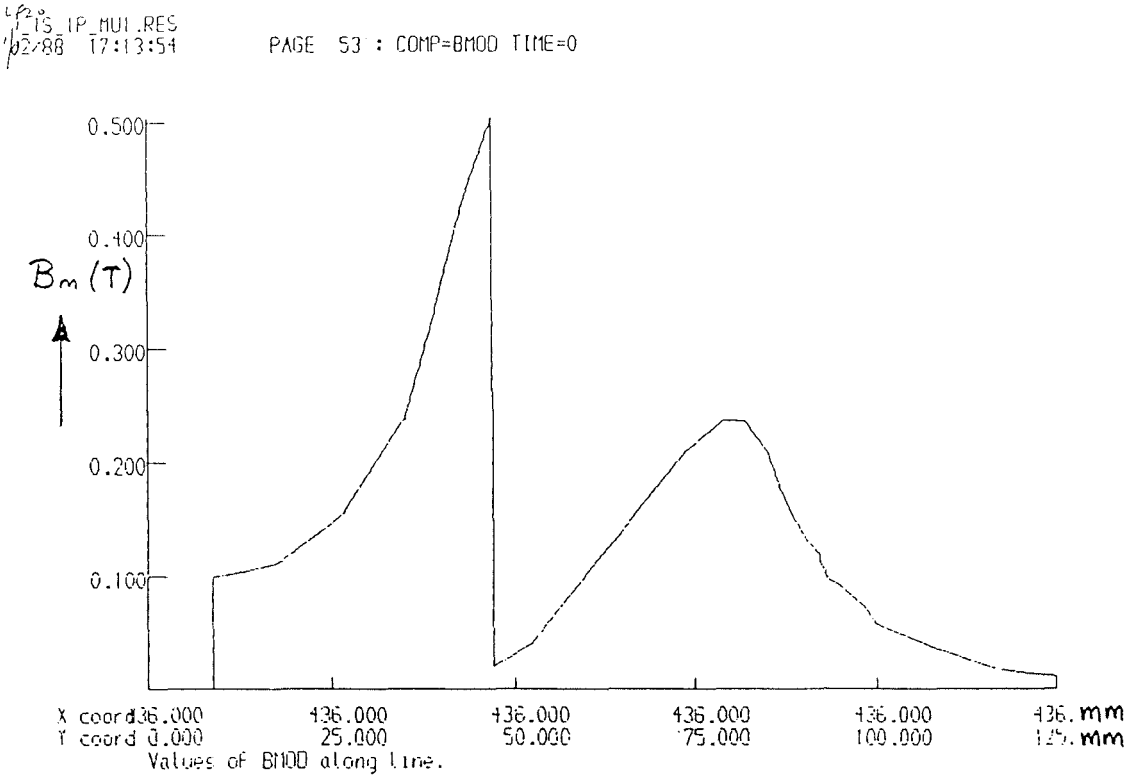

(a) Modulus of flux density, B_m

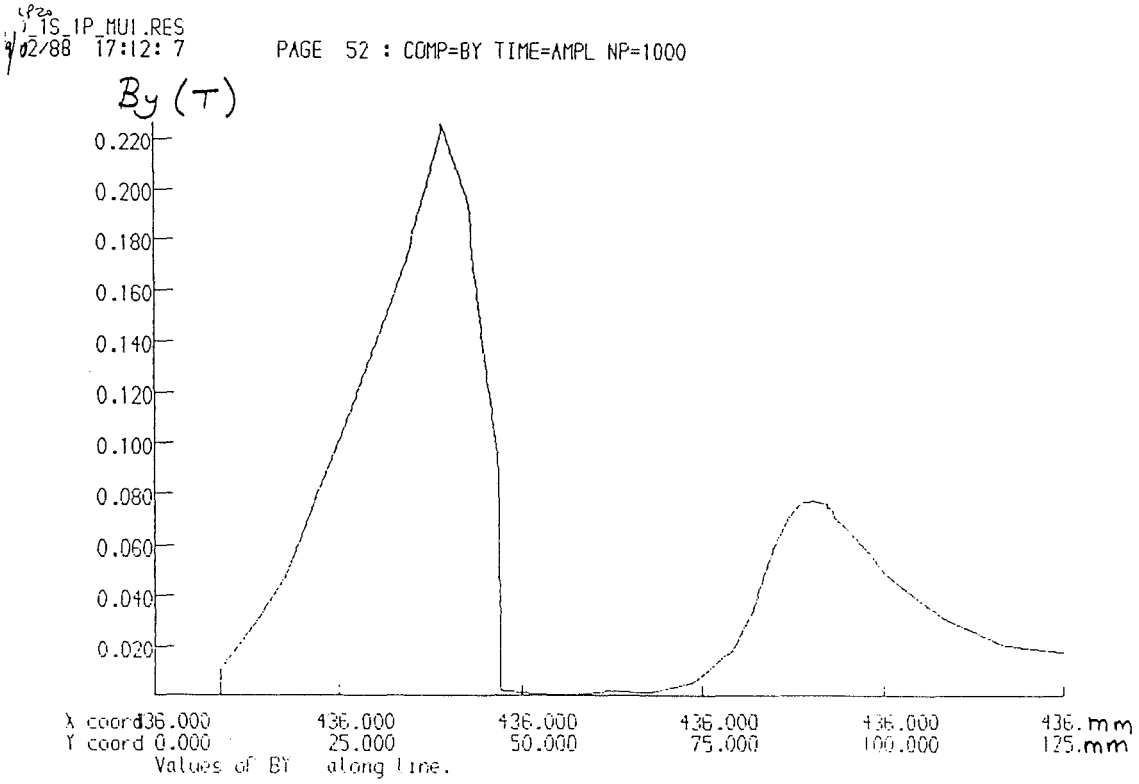

(b) Normal flux density, B_y

VARIATION OF FLUX DENSITY THROUGH THE PARTICLE AND SLOT ALONG x = 436
(LP20_1S_1P_MU1)

Figure 5.29

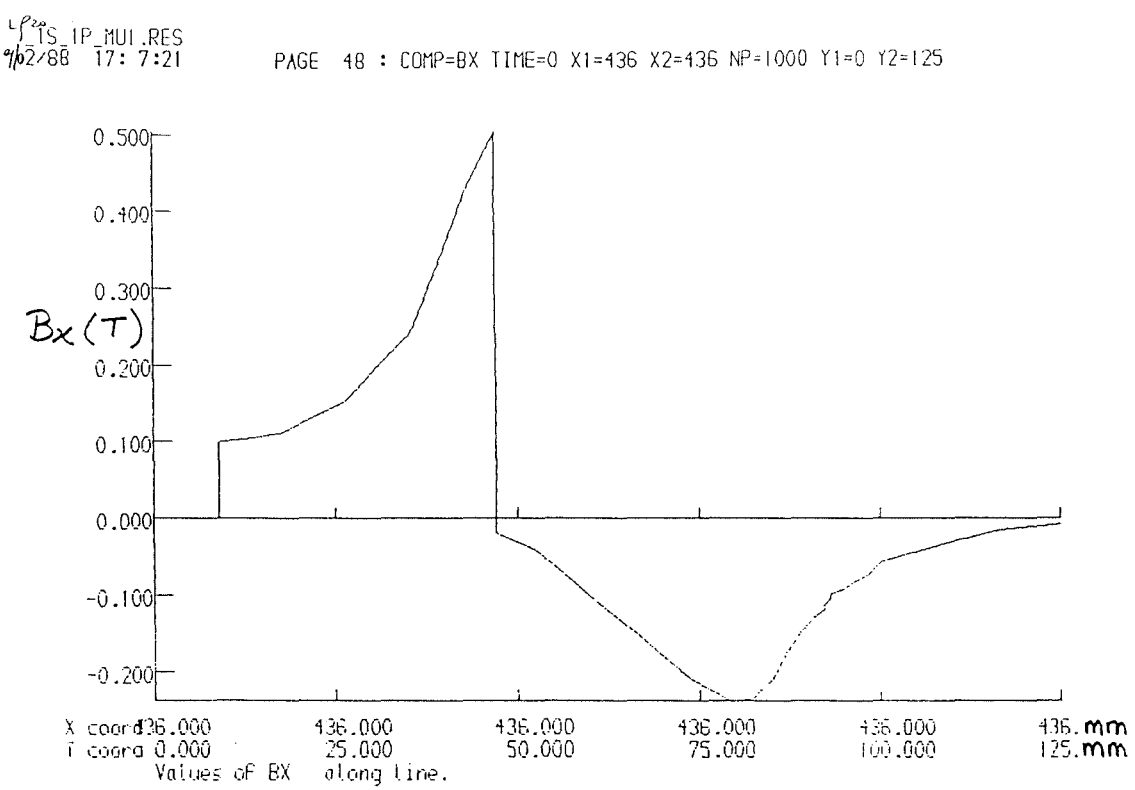

(c) Tangential flux density, B_x

VARIATION OF FLUX DENSITY THROUGH THE PARTICLE AND SLOT ALONG x = 436
(LP20_1S_1P_MU1)

Figure 5.29

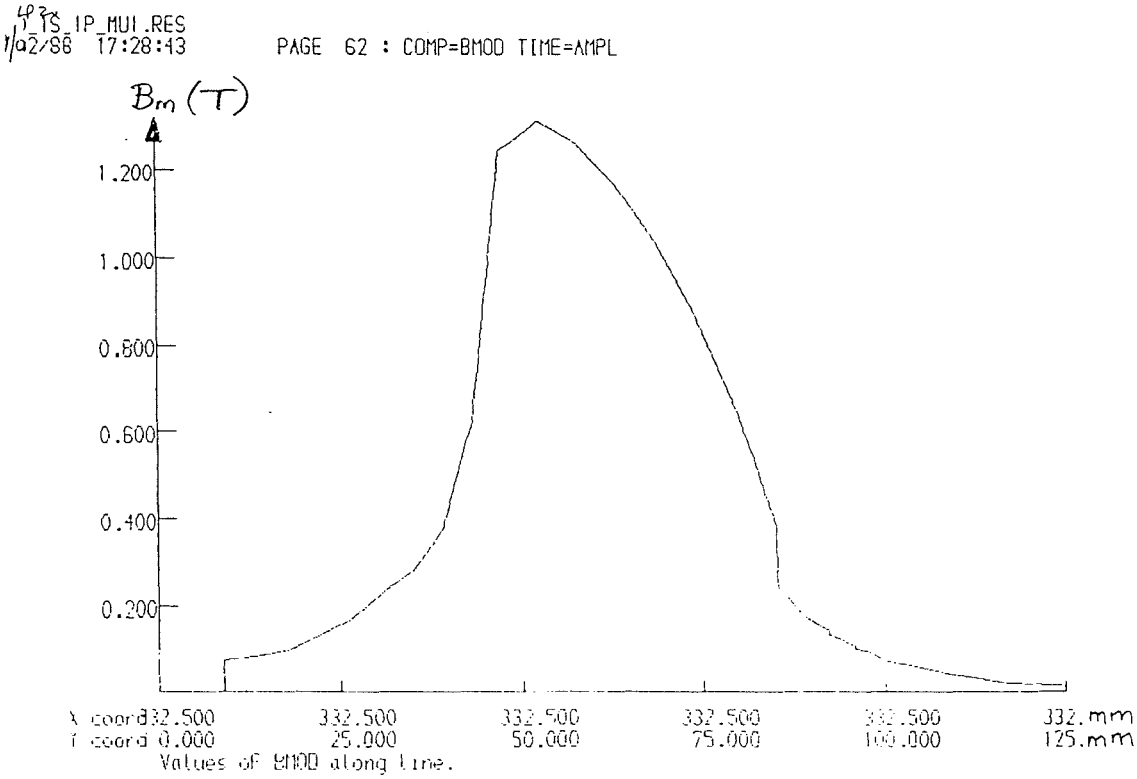

(a) Time-averaged modulus of flux density, B_m

VARIATION OF FLUX DENSITY THROUGH THE PARTICLE AND TOOTH ALONG x = 332.5
(LP20_1S_1P_MU1)

continued ...

Figure 5.30

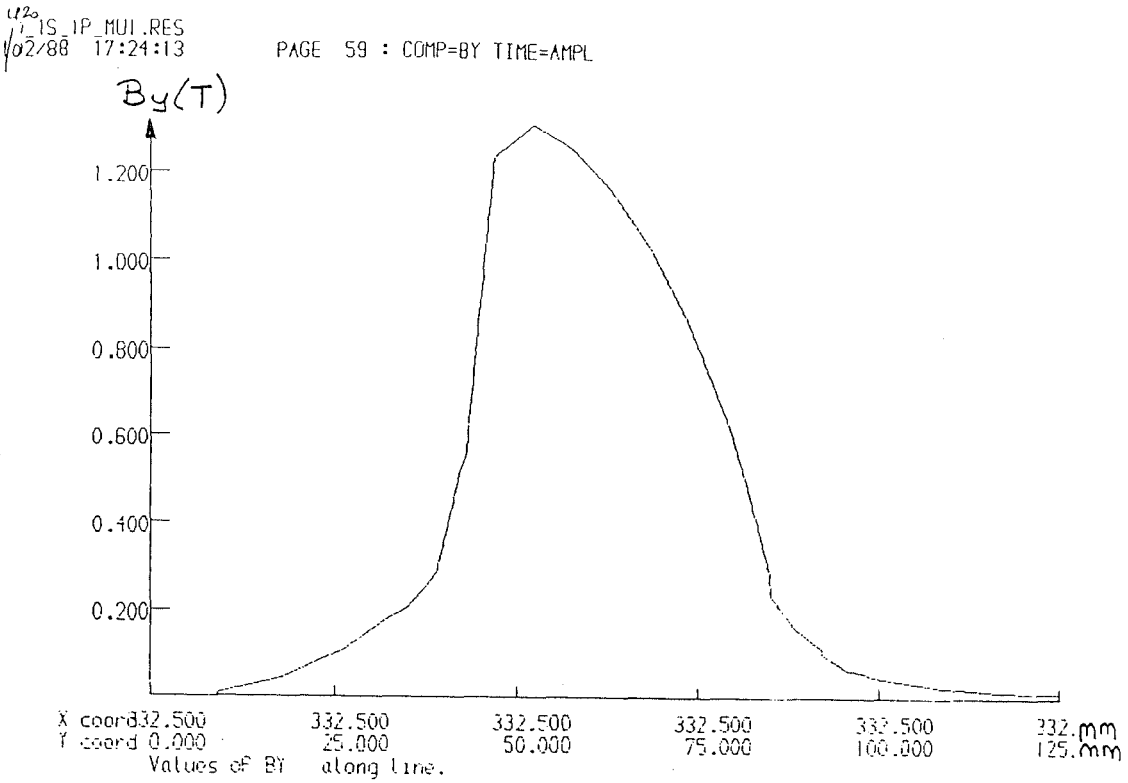

(b) Time-averaged normal flux density, B_y

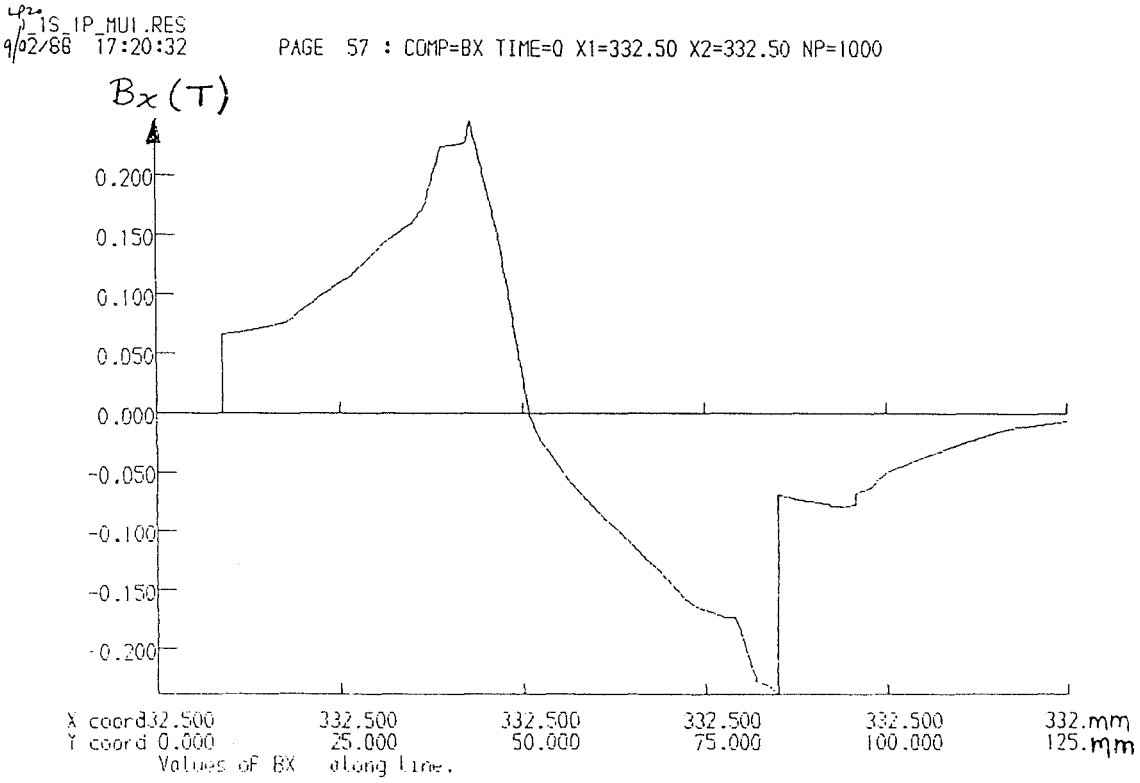

(c) Tangential flux density, B_x

VARIATION OF FLUX DENSITY THROUGH THE PARTICLE AND TOOTH ALONG x = 332.5 (LP20_1S_1P_MU1)

Figure 5.30

tangential, as can be seen from the similarity of the graphs of B_x and B_m. The normal flux density (B_y in Fig 5.29(b)) variation is similar to the tangential variation (B_x in Fig 5.29(c)) but with a reduced magnitude and, in particular, with a value of almost zero in the slot. Note the plateau which occurs in all three graphs of Fig 5.29 but predominantly in the graphs of B_x and B_m which indicates initially the end of the winding and then the end of the slot. At y = 93, the position of the particle, there is a small disturbance to both the tangential and normal flux density components: B_x is reduced in the particle and B_y reaches a maximum just prior to, through and just after the particle (see Fig 5.29(b) and (c)). Figure 5.30 shows that the flux density rises more rapidly behind the tooth than a slot (Fig 5.29) and is predominantly normal (i.e. B_y) as seen by the similarity of the curves of B_y and B_m. (In both Figs 5.29 and 5.30 the change in sign of B_x is only indicative of a change of direction of the vector.)

Once the lamination is entered, the normal flux density (Fig 5.30(b)) rises steadily and then extremely rapidly as the base of the tooth is approached, contrasting dramatically with the rapid decrease of tangential flux density (Fig 5.30(c)) in this area. B_y then decreased through the tooth whereas B_x increased with reversed sign. Upon emerging from the tooth B_y and B_x both experience a sudden decrease (also seen for B_m in Fig 5.30(a)), with B_y and B_m continuing to decrease steadily through the airgap. The tangential flux density increased slightly as the particle was approached, remained constant through the particle, dropped suddenly upon leaving the particle and then continued to decrease through the airgap. Close examination of the normal flux density (B_y) reveals that it experienced a small, sudden drop inside the particle at y = 93 (Fig 5.30(b)). (This again shows iron particles with $\mu_r = 1$ are affecting the local field.) Both Figs 5.29 and 5.30 clearly show that at y = 125, the extent of the airgap, the flux density is low, so that the error in modelling a much larger airspace above the linear machine is negligible.

Comparing Figs 5.29 and 5.30 with Figs 5.25 and 5.26 shows that, at the particle-position, the tangential flux density is greater for the TLIM case; i.e. tangential flux density for the tubular machine is some 25 mT greater opposite a tooth and about 50 mT greater opposite a slot, but the shapes of the curves are similar. As the absolute flux density within the lamination is greater in the LIM than the TLIM, the lower airgap density may be due to saturation in the LIM laminations.

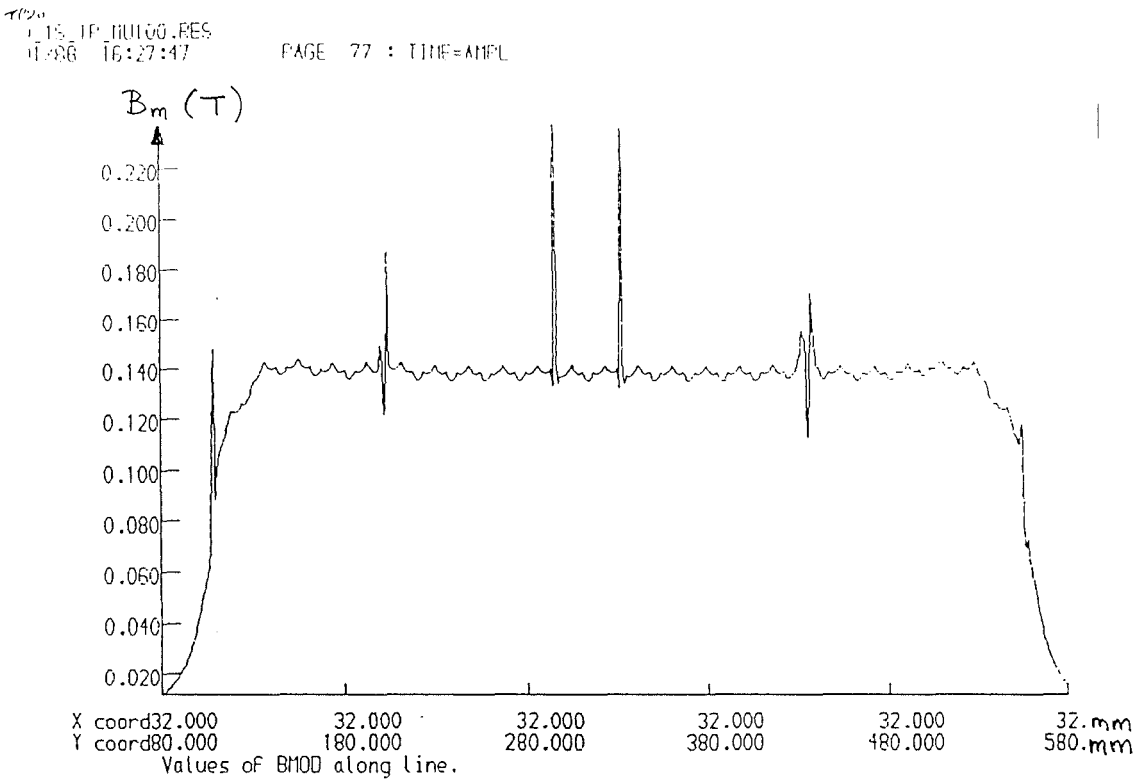

(a) Modulus of flux density, B_m

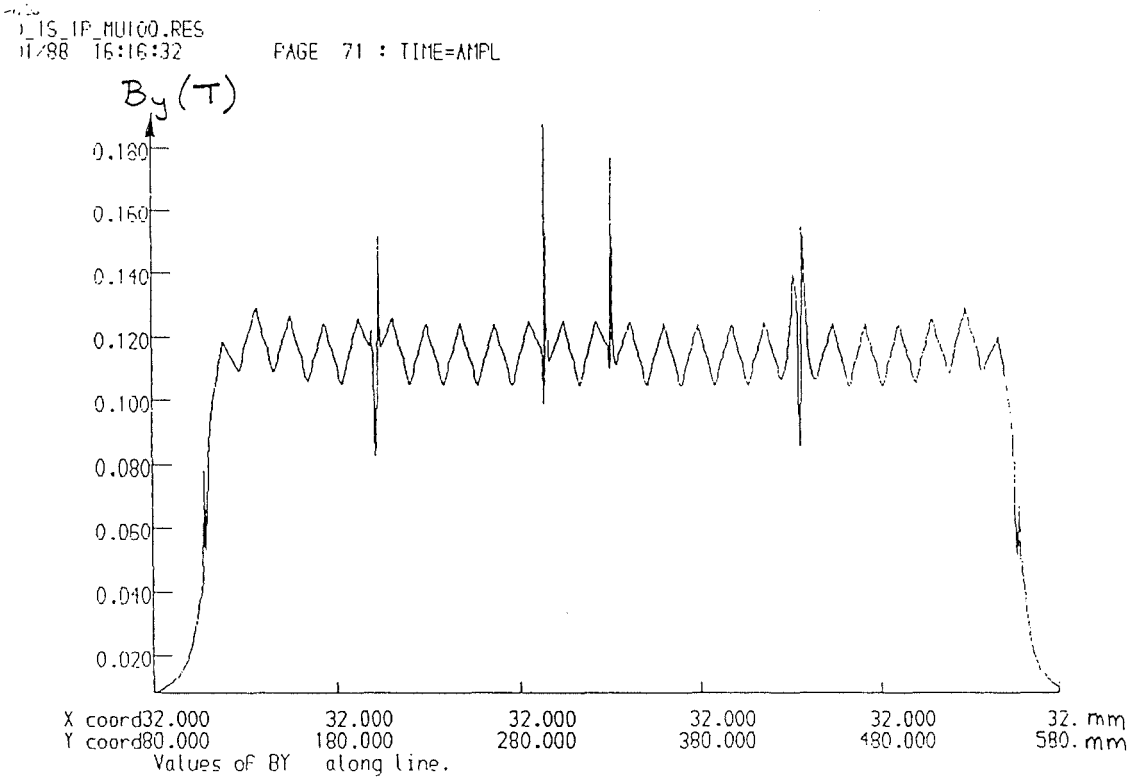

(b) Tangential flux density, B_y

VARIATION OF FLUX DENSITY THROUGH THE PARTICLES (ALONG x = 32)
(TP20_1S_1P_MU100)

continued ...

Figure 5.31

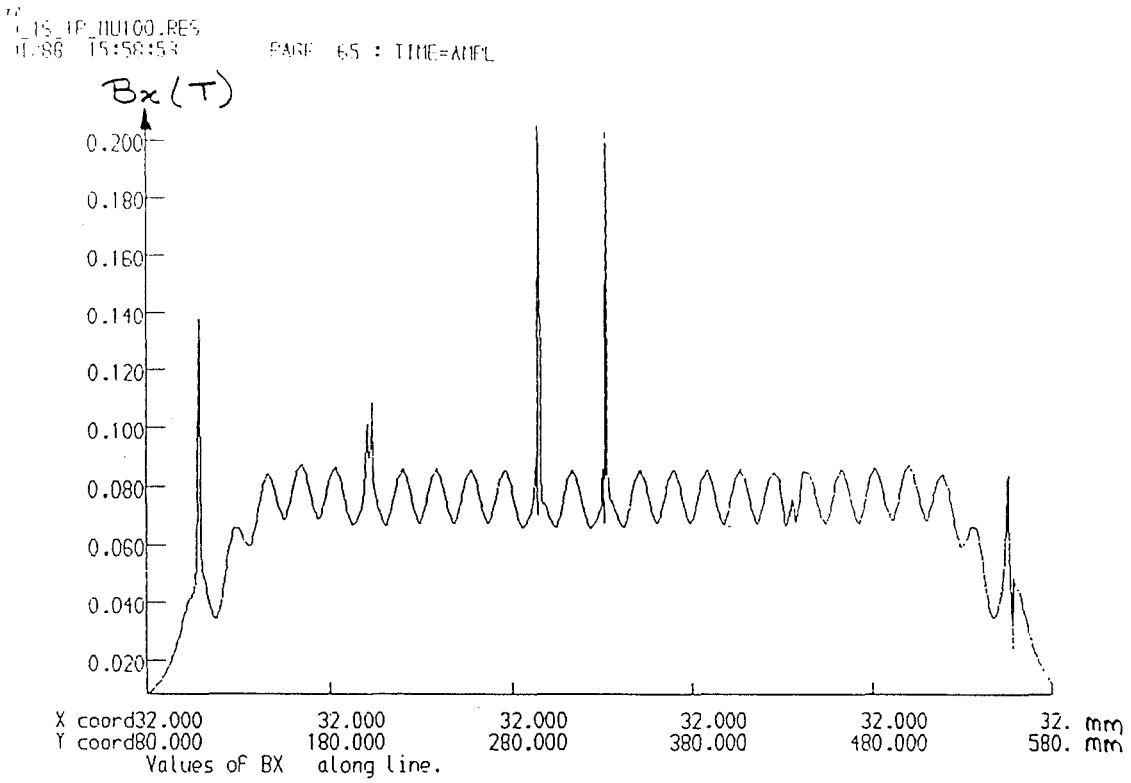

(c) Normal flux density, B_x

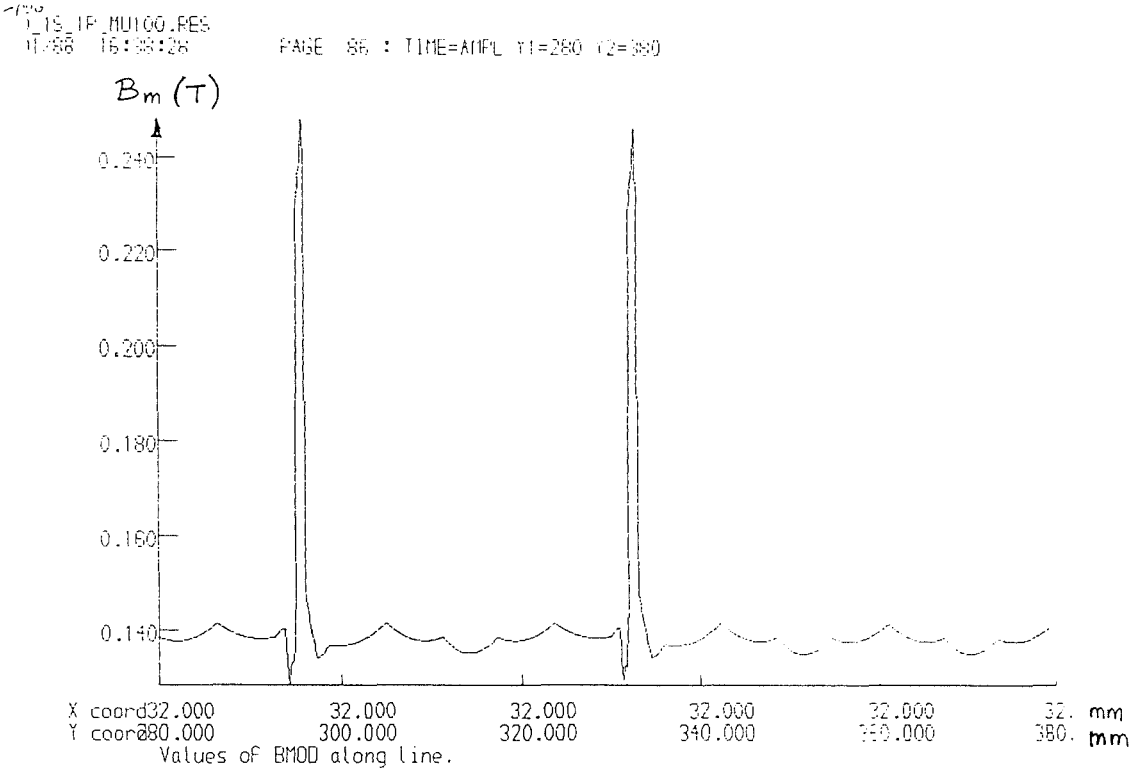

(d) Expanded view of B_m near a particle

VARIATION OF FLUX DENSITY THROUGH THE PARTICLES (ALONG x = 32)
(TP20_1S_1P_MU100)

Figure 5.31

5.6.3 Introducing Particles in the Tubular Model

Four studies with iron particles were performed:

a) with a current of 20 A/phase and the relative permeability of the particles set to 100 (TP20_1S_1P_MU100);

b) as for (a) but with the relative permeability of the particles set to 500 (TP20_1S_1P_MU500);

c) as for (a) but with a current of 30 A/phase (TP30_1S_1P_MU100), and

d) as for (b) but with a current of 30 A/phase (TP30_1S_1P_MU500).

Figure 5.31 shows time-averaged graphs of B_m, B_y and B_x for TP20_1S_1P_MU100 along a line through the particles (x = 32), with the effect of these on the field being clearly visible. Neglecting for the moment the field disturbance due to the particles, it may be noted that the peaks in the graph of B_y (Fig 5.31(b)) and the peaks in the graph of B_x (Fig 5.31(c)) correspond respectively to the slots and teeth of the tubular machine. It can also be seen that, at the position of the particles, the tangential flux density B_y is greater than the normal flux density B_x whether compared above teeth, slots or teeth and slots, with B_x attaining a maximum value of about 90 mT, B_y a minimum value of about 105 mT and B_m a maximum value of about 140 mT (Fig 5.31(a)). Comparing these graphs to those in Fig 5.18 (where the particles had $\mu_r = 1$) it is seen that, apart from the disturbance in the field near the particles, the field values are the same. In previous graphs with μ_r set to unity, close inspection showed that the field disturbance due to the particles, if present, was small (see Fig 5.18). In Fig 5.31(d), however, the field variation with μ_r set to 100 is significant and B_m attains a value of approximately 0.24 T inside the particles.

Increasing the particle relative permeability to 500 (i.e. study TP20_1S_1P_MU500) produced graphs, shown in Fig 5.32, practically identical to those in Fig 5.31 (study TP20_1S_1P_MU100). Graphs were also plotted along lines y = 436 and y = 332.5, i.e. through particles opposite a slot and tooth respectively (see Fig 5.24), and these are

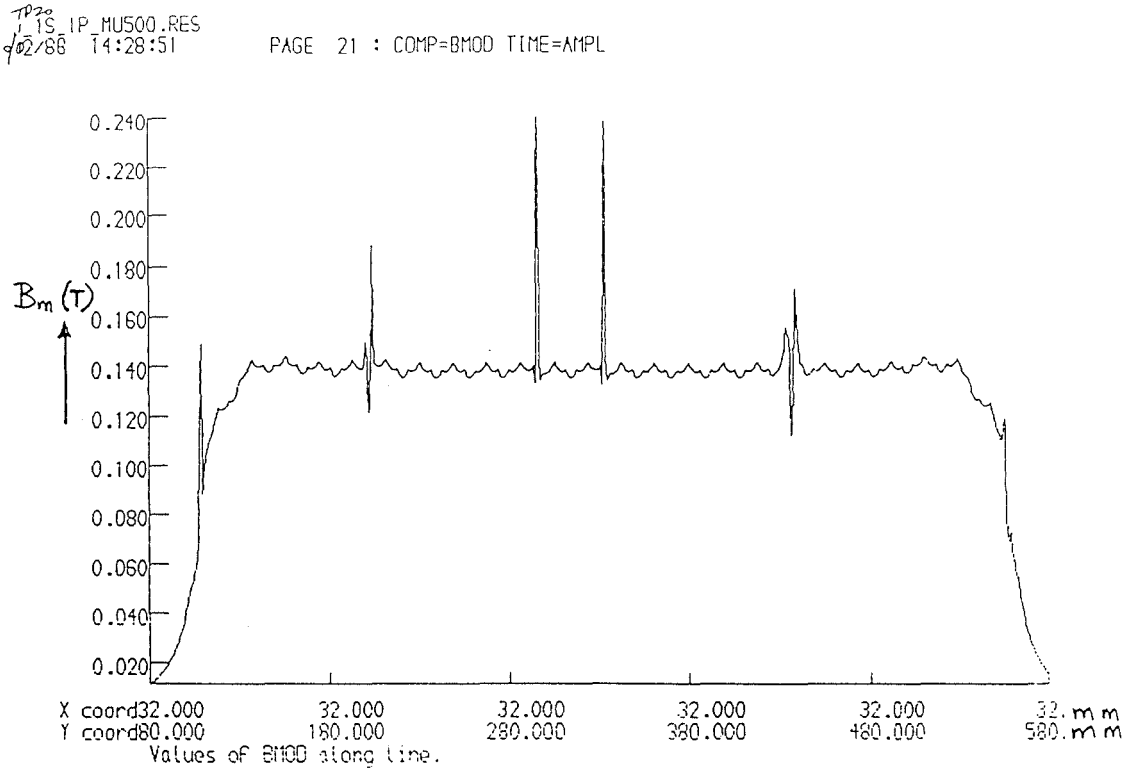

(a) Modulus of flux density, B_m

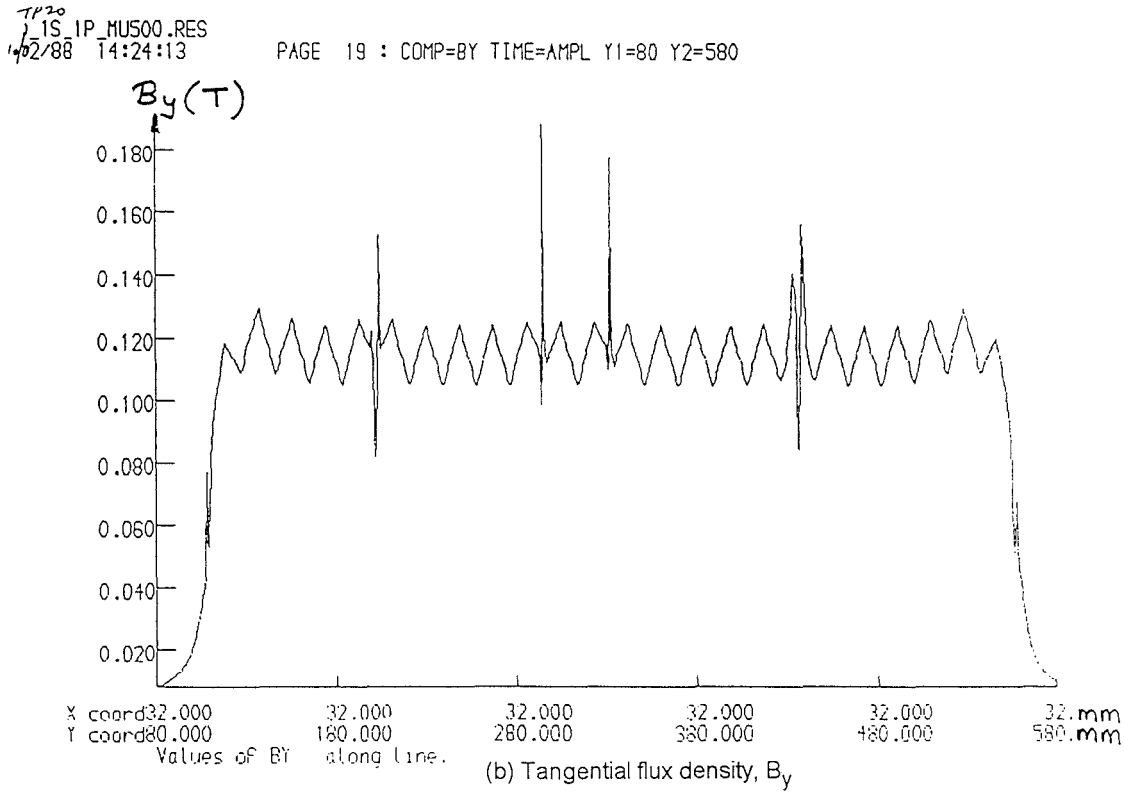

(b) Tangential flux density, B_y

VARIATION OF FLUX DENSITY THROUGH THE PARTICLES (ALONG x = 32)
(TP20_1S_1P_MU500)

continued ...

Figure 5.32

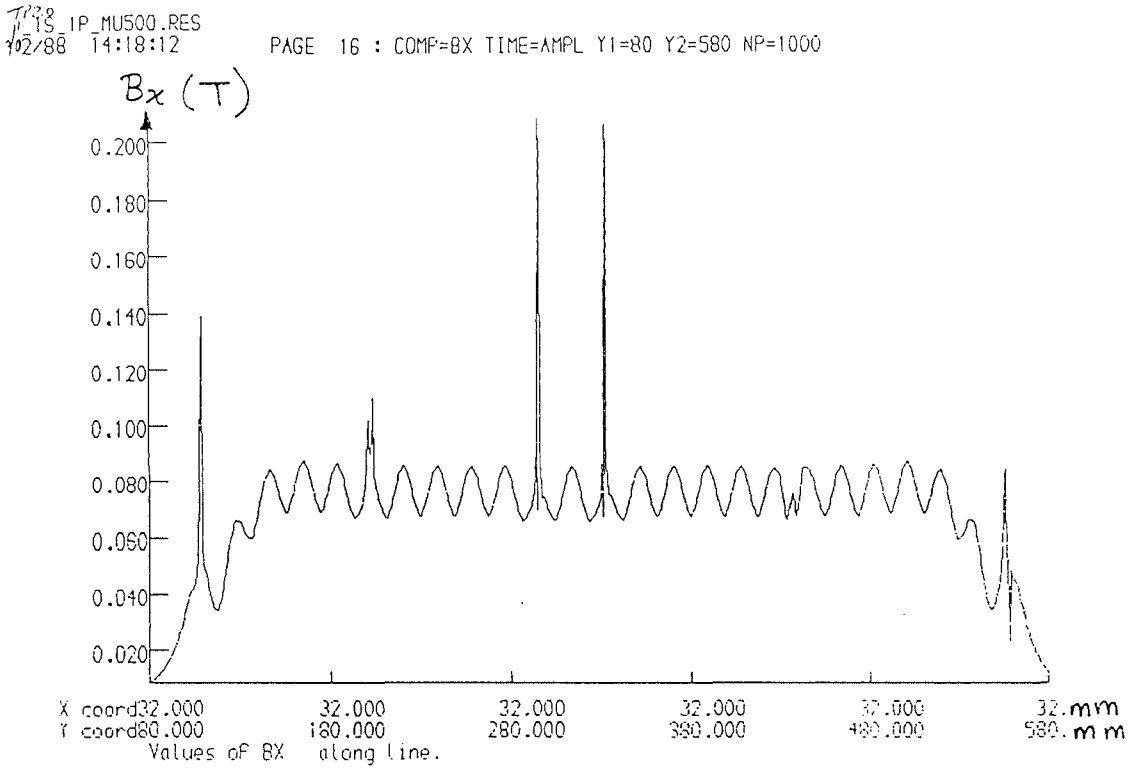

(c) Normal flux density, B_x

VARIATION OF FLUX DENSITY THROUGH THE PARTICLES (ALONG x = 32)

(TP20_1S_1P_MU500)

Figure 5.32

(a) Time - averaged modulus of flux density, B_m
(b) Time - averaged tangential flux density, B_y
(c) Time - averaged normal flux density, B_x

given in Figs 5.33 and 5.34. Comparison with similar graphs for particles modelled as air (Figs 5.25 and 5.26) showed that the field disturbance due to the particles is again present. The graphs in Fig 5.33 suggest that the modulus of the flux density had a peak value of approximately 0.54 T (i.e. along y = 436) and, for the particle opposite the tooth (y = 332.5 in Fig 5.34), the time-averaged peak value of B_m in the particle was approximately 0.24 T, as also seen in Figure 5.32. Two apparent inconsistencies need explanation: (i) the disagreement between Fig 5.32 and Fig 5.33; and (ii) the different values of B_m inside the two particles at y = 436 and y = 332.5.

In explaining the above, note that the particle at y = 436 was opposite a slot and that at y = 332.5 was opposite a tooth (see Fig 5.24). The first problem is due to the resolution provided in the graphical plots by the PE2D software. The number of data points (fixed to the maximum allowable) gave a point-to-point separation which was four times greater in the case of Figs 5.33 and 5.34 than in Fig 5.32, due to the length of line along which the graphs were plotted. By omitting these points not all the field values are shown. Also, since the solution is discrete (i.e. on an element-by-element basis) there is an uncertainty in each solution value for every element and, given that the number of elements per modelled particle was small, the truth lies somewhere between the values in Fig 5.32 and Figs 5.33 and 5.34. The time-averaged values of B_x and B_y in Fig 5.33 give confidence in the solution, as they are as expected, namely B_y is likely to be significantly greater than B_x opposite a slot and for a particle opposite a slot.

Opposite a tooth (i.e. along y = 332.5 in Fig 5.34) the field inside the particle was approximately 0.24 T compared with about 0.5 T opposite a slot. Remembering that the particles were some 7 mm away from the tooth surface and that the flux takes the path of least reluctance, then the normal flux density, B_x, (which will be greater than the tangential, B_y) opposite a tooth does not extend far into the airgap. Thus, the field inside the particle will be correspondingly less (see Fig 5.34). Referring to Figs 5.32, 5.33 and 5.34 shows that the field was increased by a factor of about 1.7 inside the particle at y = 332.5 and by at least 4 for the particle at y = 436.

Results for a similar study at 30 A/phase (i.e. TP30_1S_1P_MU100) are presented in Fig 5.35 which shows the time-averaged graphs of B_m, B_y and B_x. Figure 5.35 and Fig 5.31 (i.e. results for TP20_1S_1P_MU100) clearly have similar shapes, with those for the

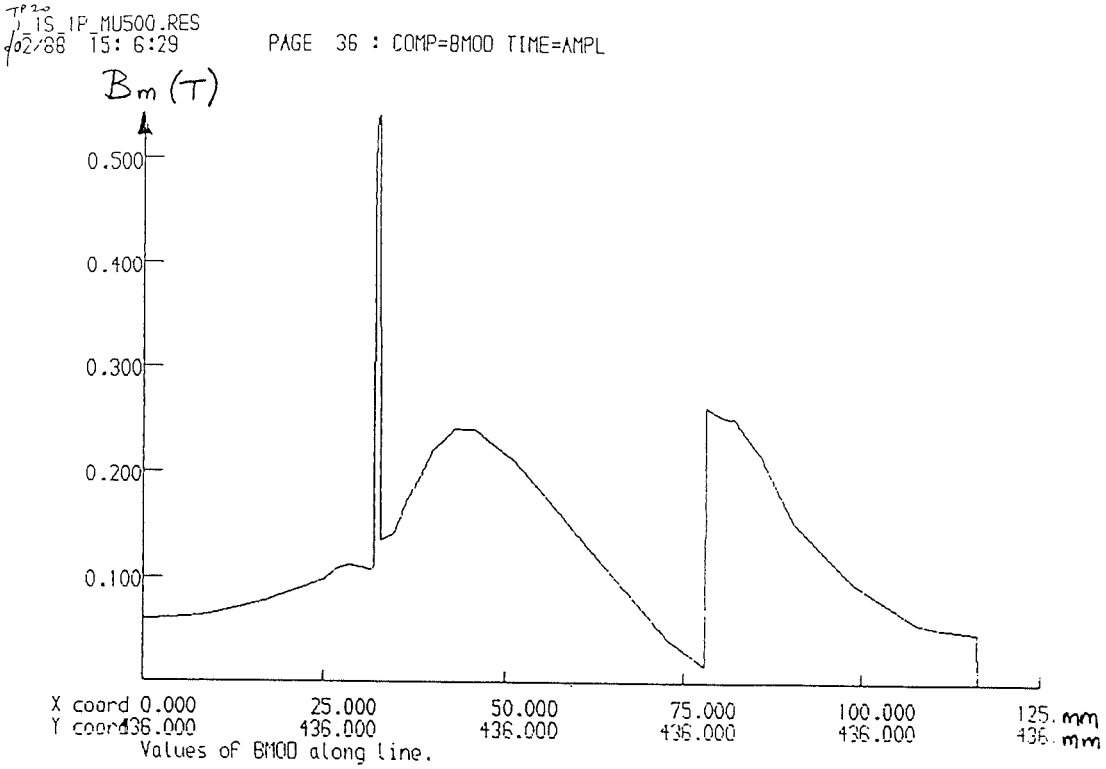

(a) Modulus of flux density, B_m

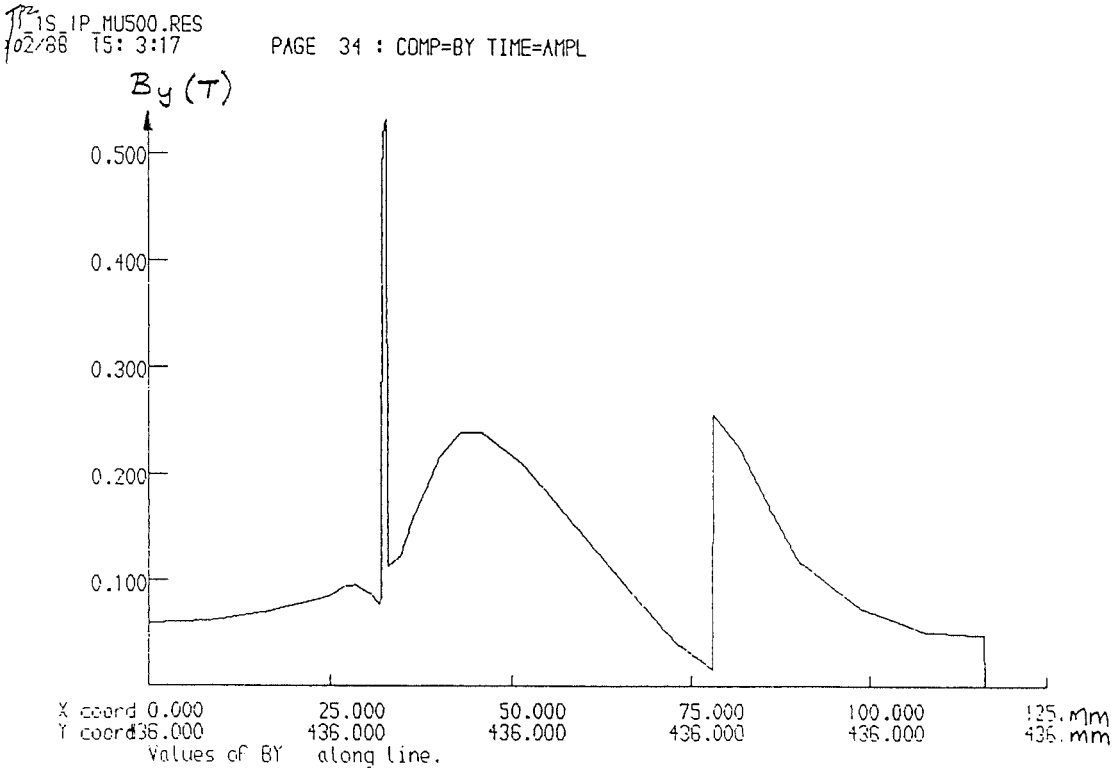

(b) Tangential flux density, B_y

VARIATION OF FLUX DENSITY THROUGH THE PARTICLE AND SLOT ALONG y = 436
(TP20_1S_1P_MU500)

continued ...

Figure 5.33

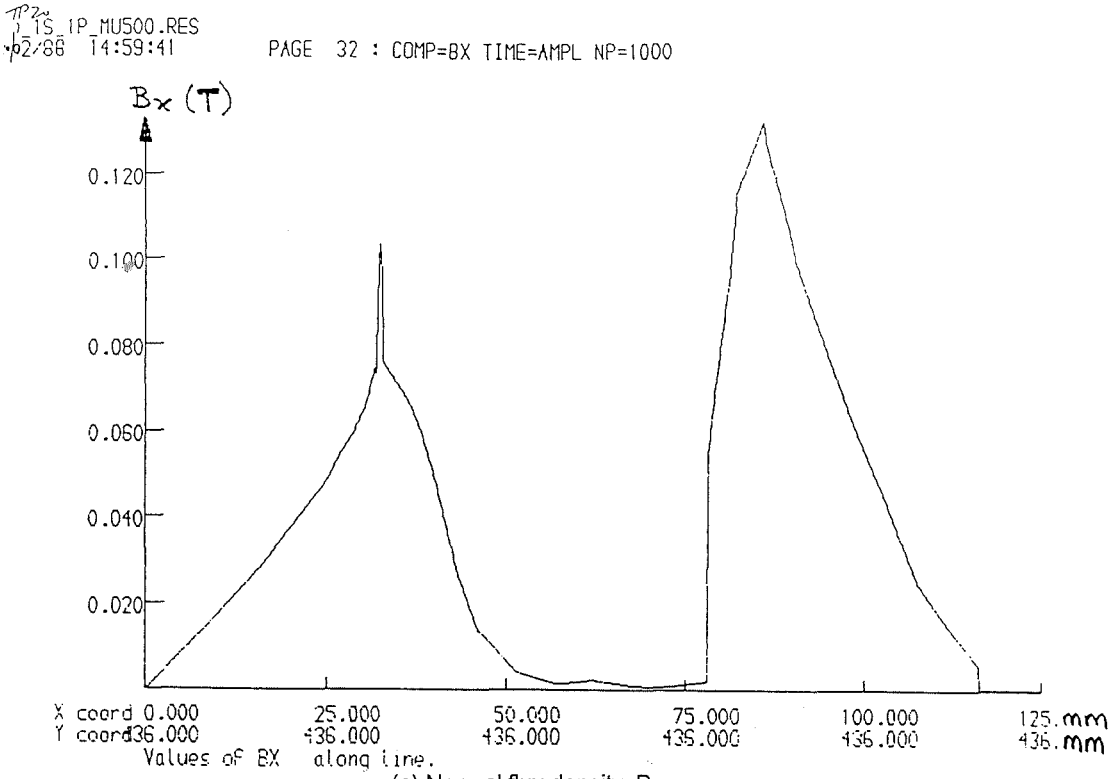

(c) Normal flux density, B_x

VARIATION OF FLUX DENSITY THROUGH THE PARTICLE AND SLOT ALONG y = 436
(TP20_1S_1P_MU500)

Figure 5.33

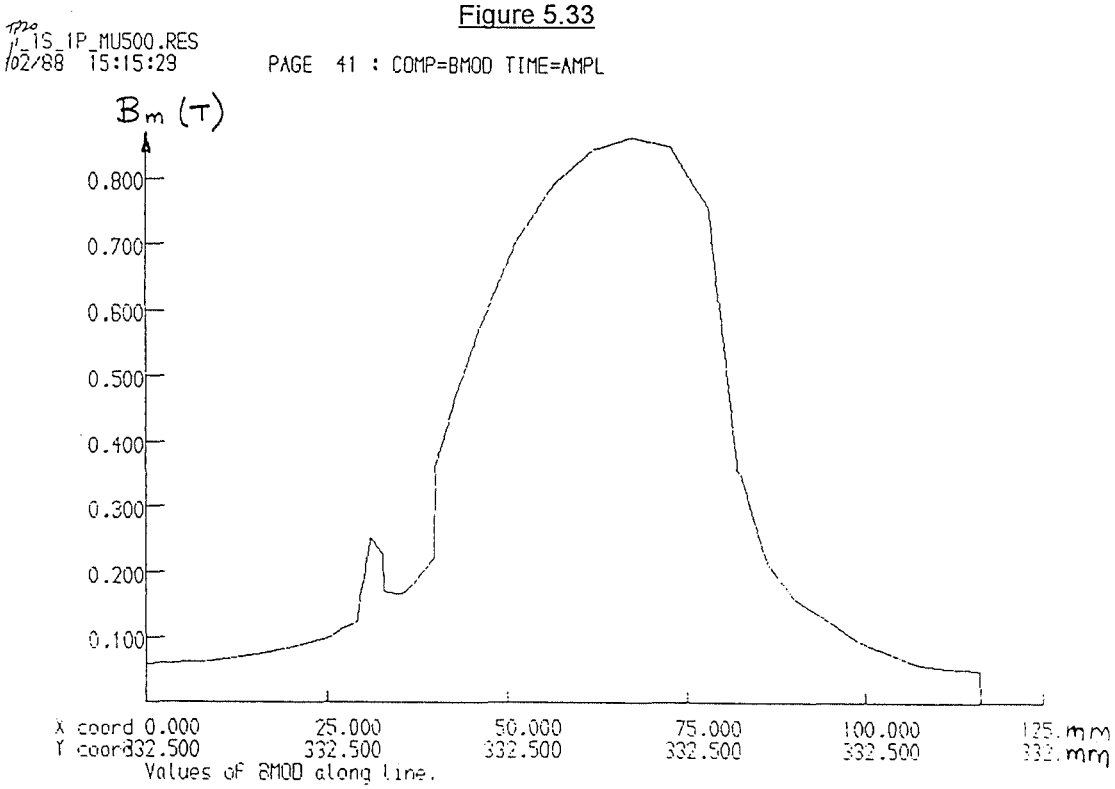

(a) Modulus of flux density, B_m

VARIATION OF FLUX DENSITY THROUGH THE PARTICLE AND TOOTH ALONG y = 332.5
(TP20_1S_1P_MU500)

continued ...

Figure 5.34

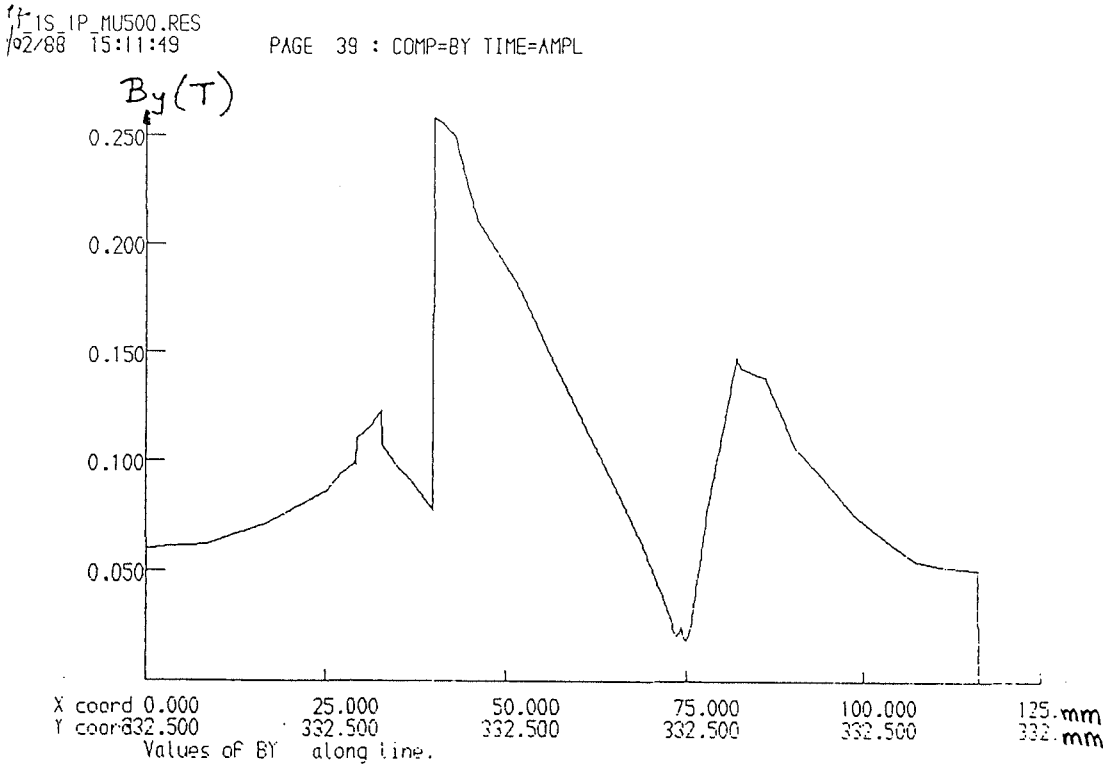

(b) Tangential flux density, B_y

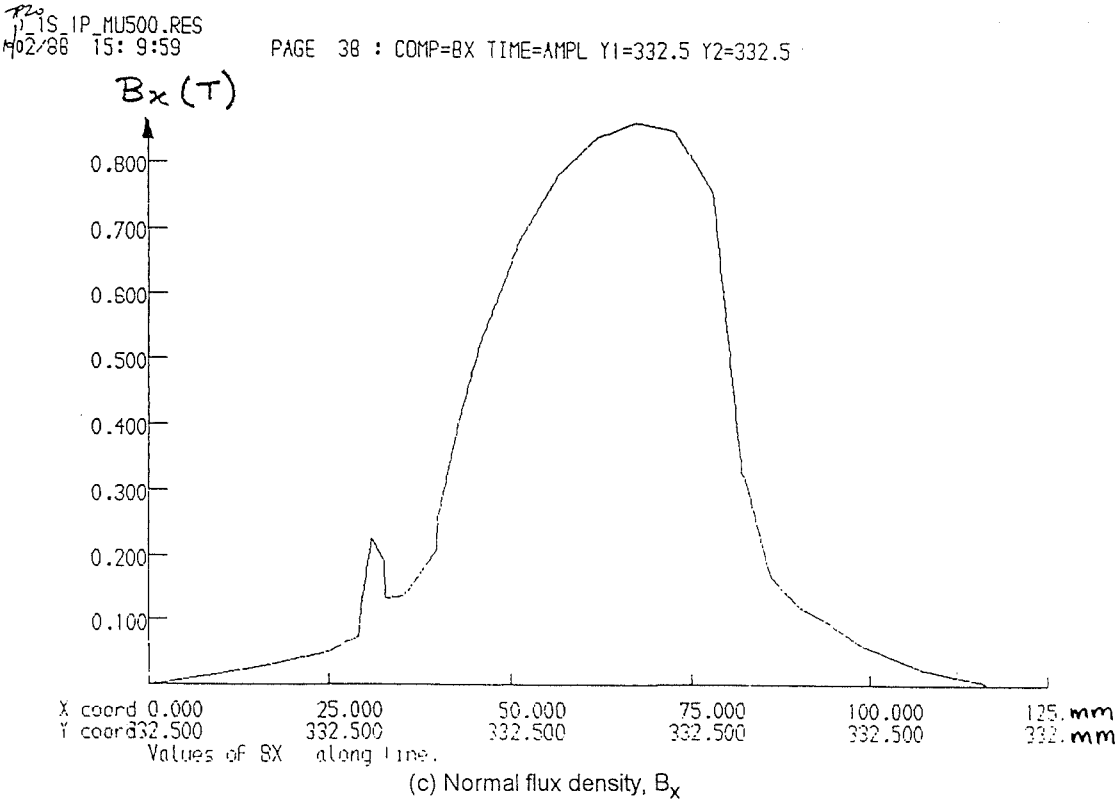

(c) Normal flux density, B_x

VARIATION OF FLUX DENSITY THROUGH THE PARTICLE AND TOOTH ALONG y = 332.5
(TP20_1S_1P_MU500)

Figure 5.34

study at 30 A/phase having greater values of flux density because of the increased phase current. The study TP30_1S_1P_MU100 shows B_m having an average value of approximately 0.21 T compared with 0.14 T in Fig 5.31. The flux density values within the particles are also greater; for the particles near the middle of the TLIM the flux density was increased by about 110 mT.

The diagrams for study TP30_1S_1P_MU500 (i.e. 30 A/phase and a particle permeability of 500) given in Figs 5.36, 5.37 and 5.38, are the same as those for TP20_1S_1P_MU500 shown in Figs 5.32, 5.33 and 5.34 except for the absolute values. Again, the only difference between the two studies was that, at 30 A/phase, the flux density was increased and behind the lamination teeth rose to about 1.3 T, implying that the lamination would saturate if the current was much further increased. Table 5.4 summarises the main findings for the TLIM studies with particles. It shows that increasing the current increased the flux density above the lamination by nearly 50% and in the particles by approximately 46%, closely matching the 50% increase in current. The 50% increase is maintained in the majority of the flux density values throughout the lamination. It may also be seen that the flux density is greatest behind the teeth rather than behind the slots, and that it is respectively mostly normal or mostly tangential. Table 5.4 also shows that the increased particle permeability makes little difference to the flux density, either in the particles themselves or in the airgap. Since the flux density in the particles, airgap and the lamination increased linearly with current, the ratio of the flux density inside the particles to that outside, but nearby, did not appreciably change. Essentially, if a particle is opposite a tooth then, at the height considered (i.e. about 7 mm above the lamination teeth), the f.e. model indicates that the flux density inside the particle is nearly twice as great as that outside. For similar conditions, a particle opposite a slot has a flux density more than four times inside it compared with that outside.

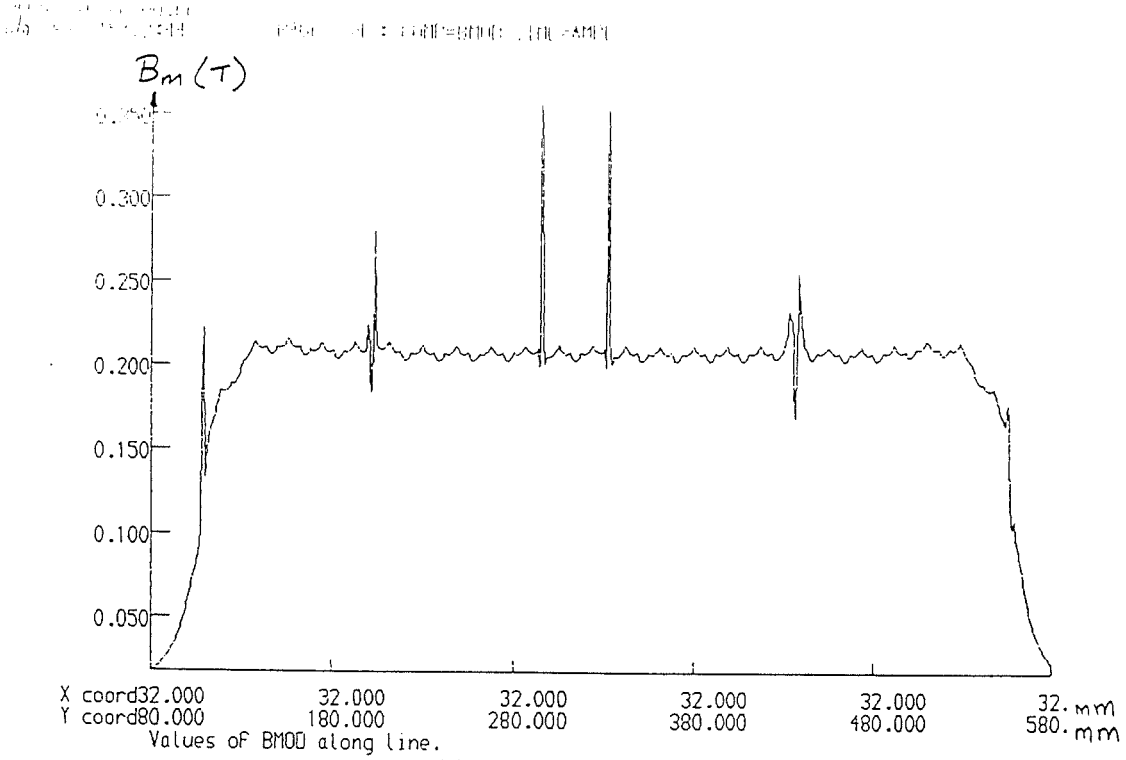

(a) Modulus of flux density, B_m

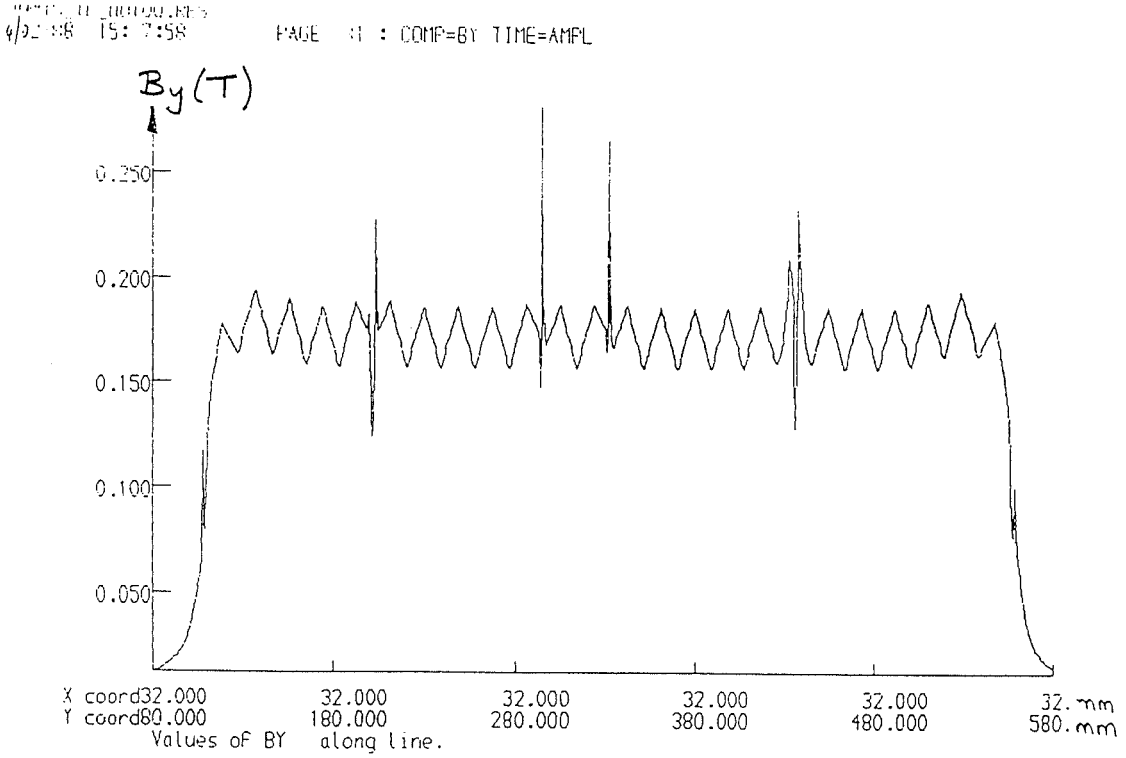

(b) Tangential flux density, B_y

VARIATION OF FLUX DENSITY THROUGH THE PARTICLES (ALONG x = 32)
(TP30_1S_1P_MU100)

continued ...

Figure 5.35

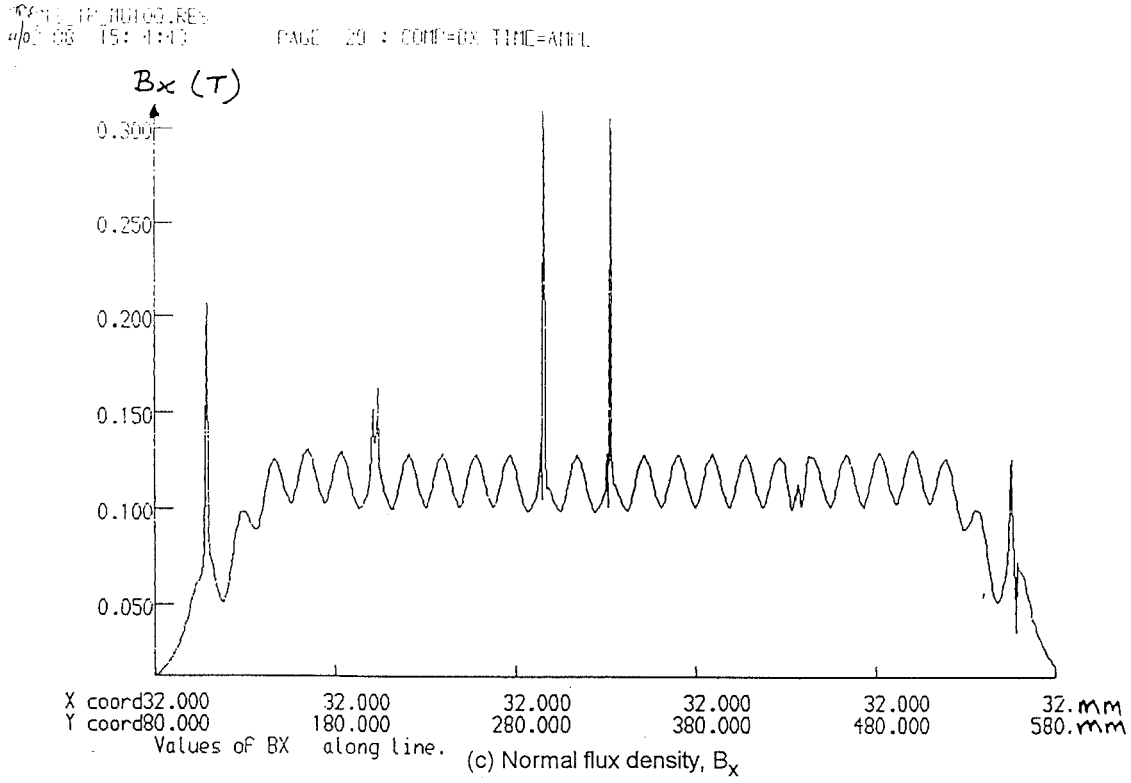

(c) Normal flux density, B_x

VARIATION OF FLUX DENSITY THROUGH THE PARTICLES (ALONG x = 32)
(TP30_1S_1P_MU100)

Figure 5.35

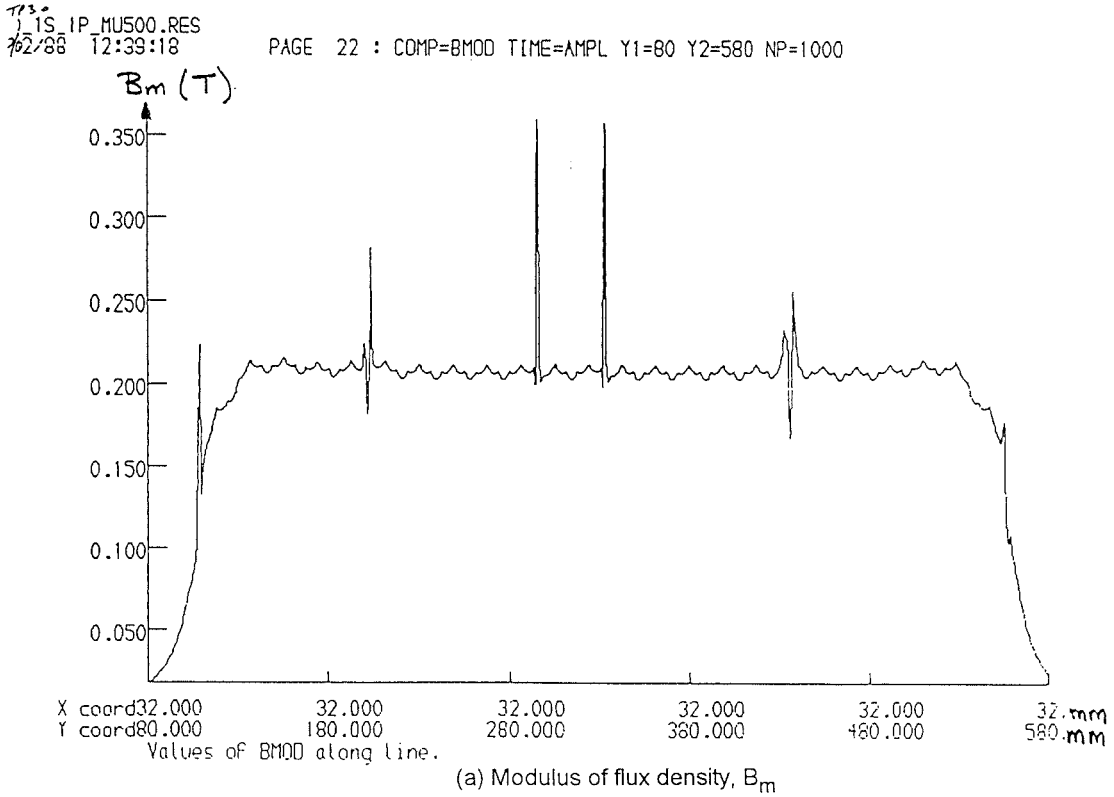

(a) Modulus of flux density, B_m

VARIATION OF FLUX DENSITY THROUGH THE PARTICLES (ALONG x = 32)
(TP30_1S_1P_MU500)

continued

Figure 5.36

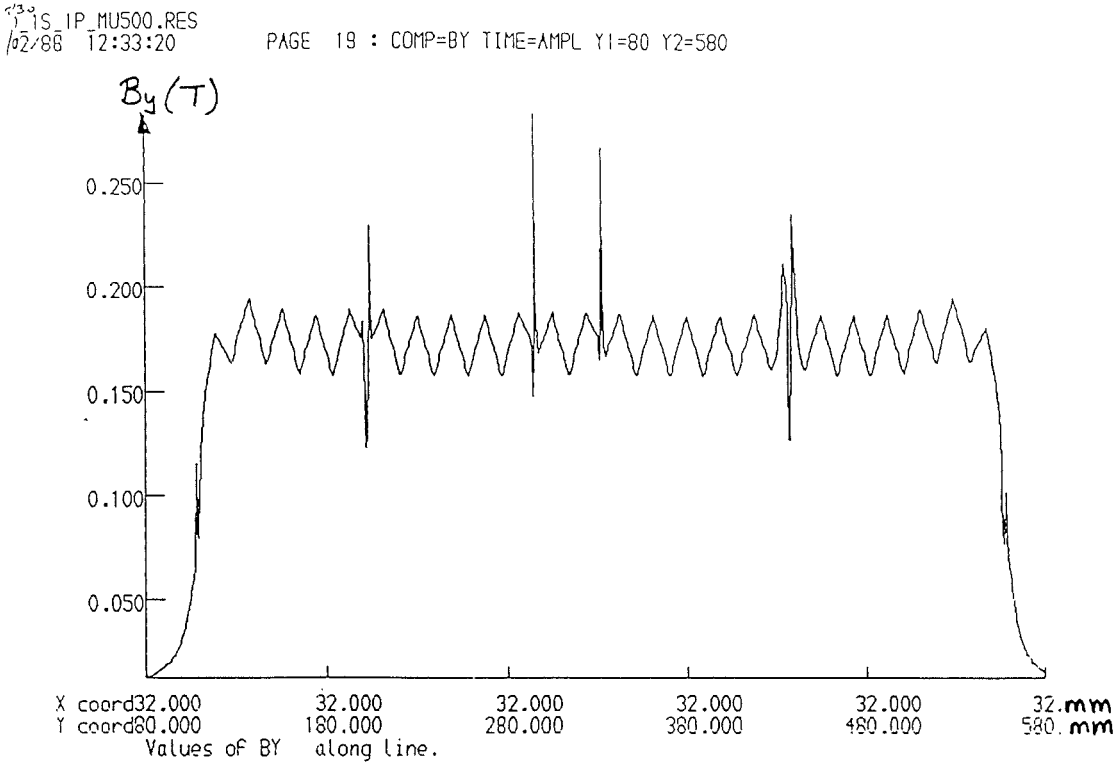

(b) Tangential flux density, B_y

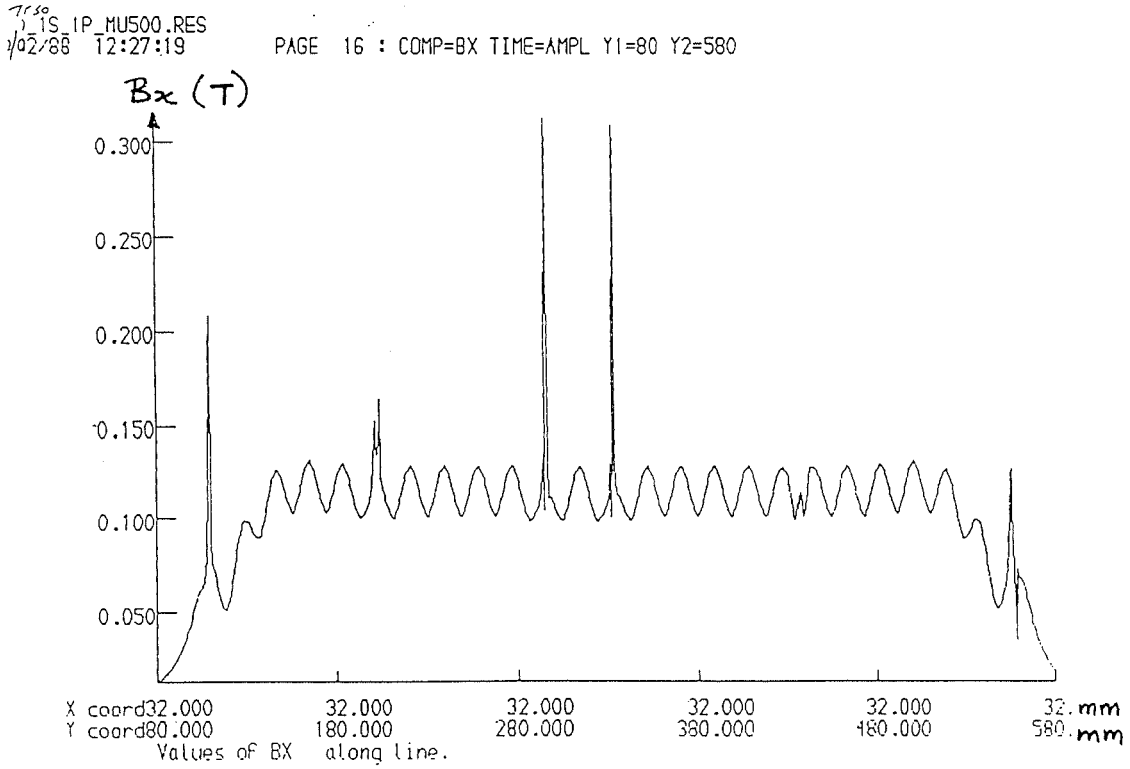

(c) Normal flux density, B_x

VARIATION OF FLUX DENSITY THROUGH THE PARTICLES (ALONG x = 32)
(TP30_1S_1P_MU500)

Figure 5.36

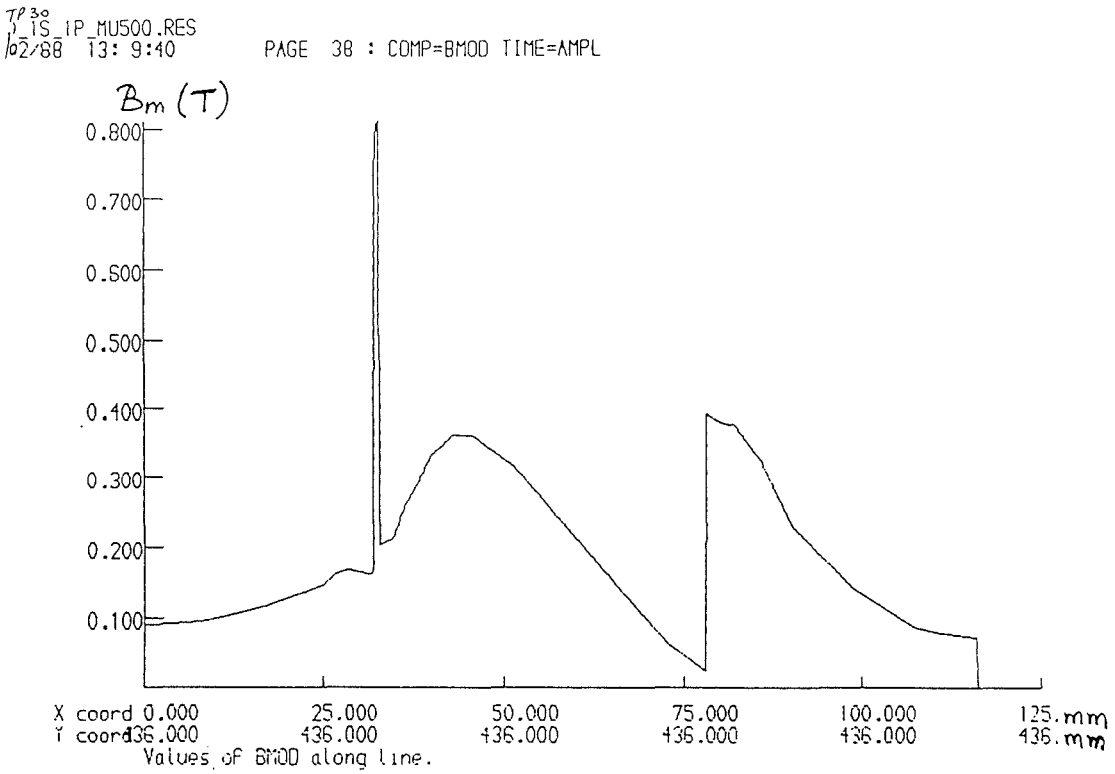

(a) Modulus of flux density, B_m

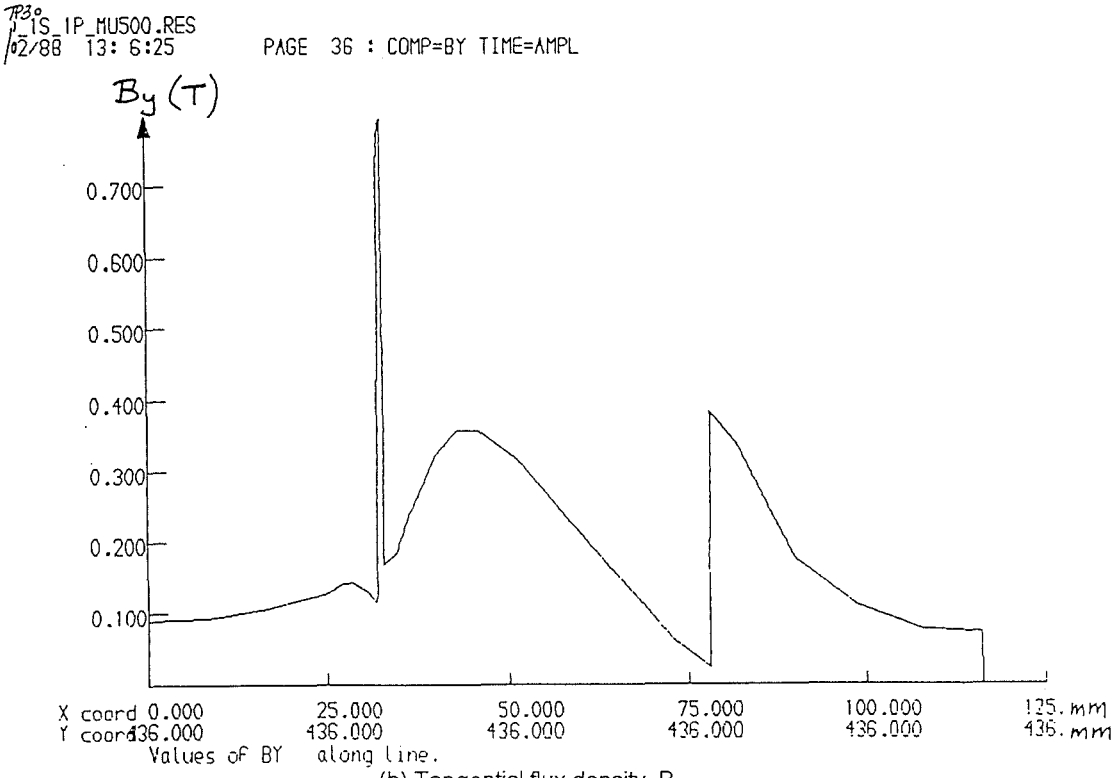

(b) Tangential flux density, B_y

VARIATION OF FLUX DENSITY THROUGH THE PARTICLE AND SLOT ALONG y = 436
(TP30_1S_1P_MU500)

continued ...

Figure 5.37

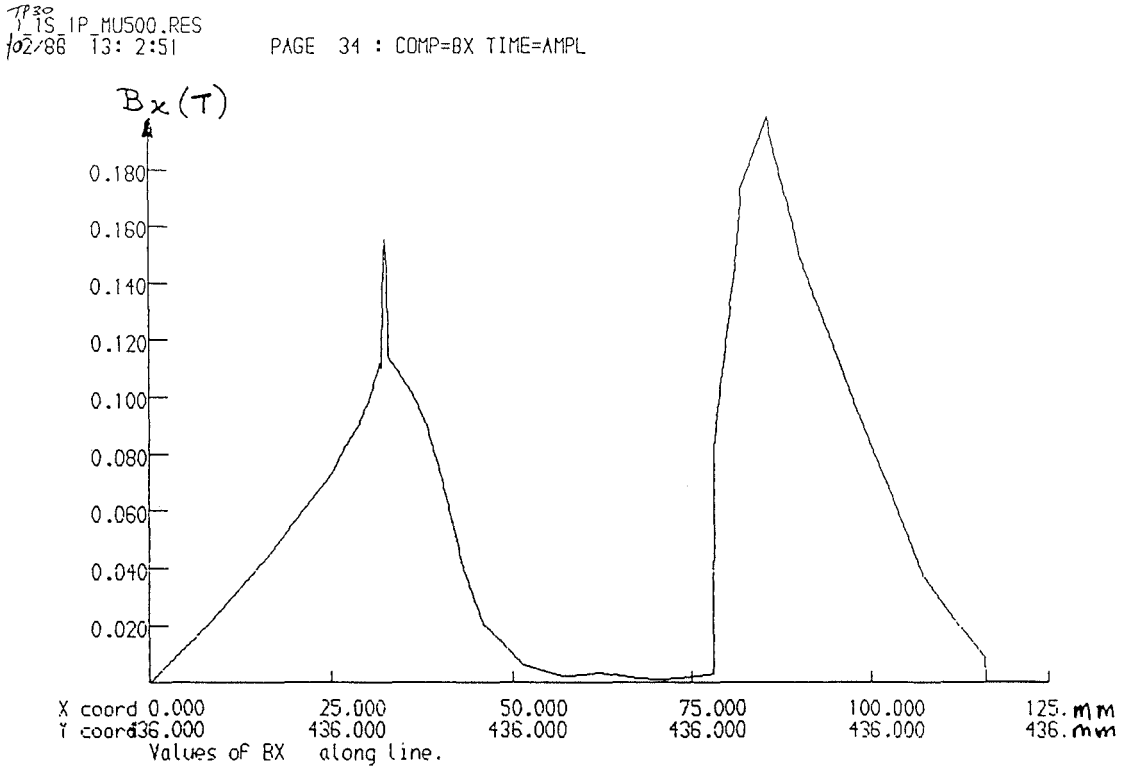

(c) Normal flux density, B_x

VARIATION OF FLUX DENSITY THROUGH THE PARTICLE AND SLOT ALONG y = 436
(TP30_1S_1P_MU500)

Figure 5.37

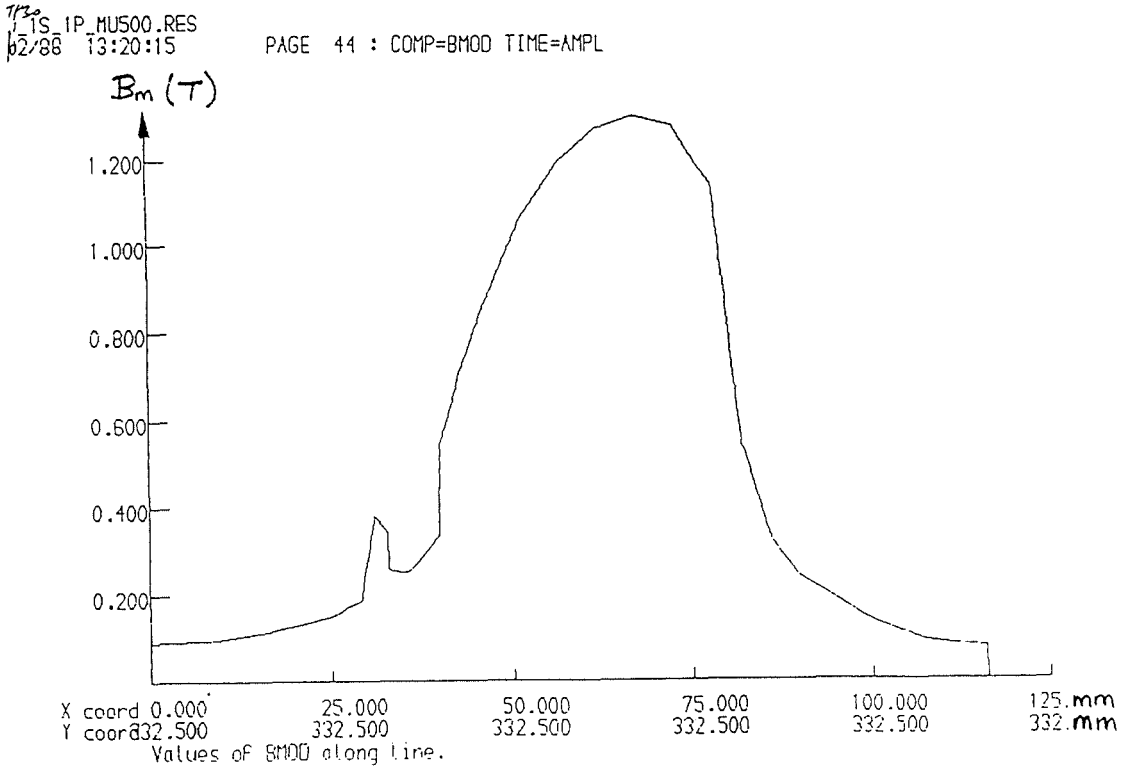

(a) Modulus of flux density, B_m

VARIATION OF FLUX DENSITY THROUGH THE PARTICLE AND TOOTH ALONG y = 332.5
(TP30_1S_1P_MU500)

continued ...

Figure 5.38

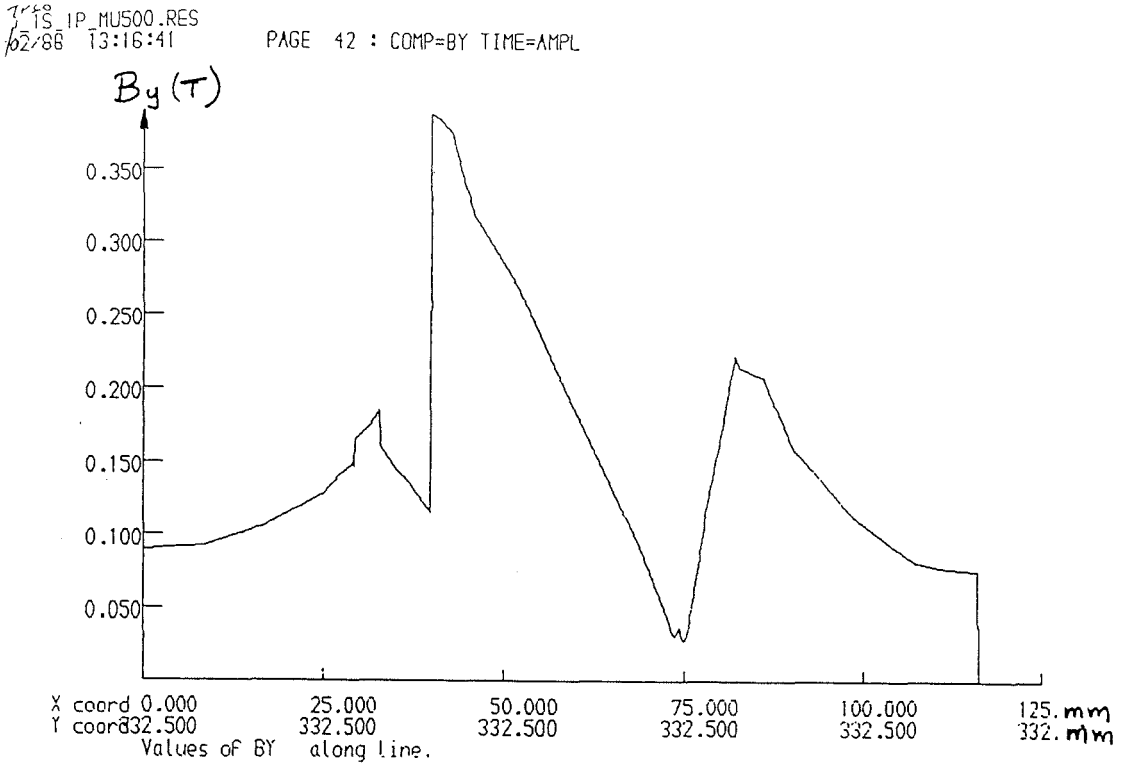

(b) Tangential flux density, B_y

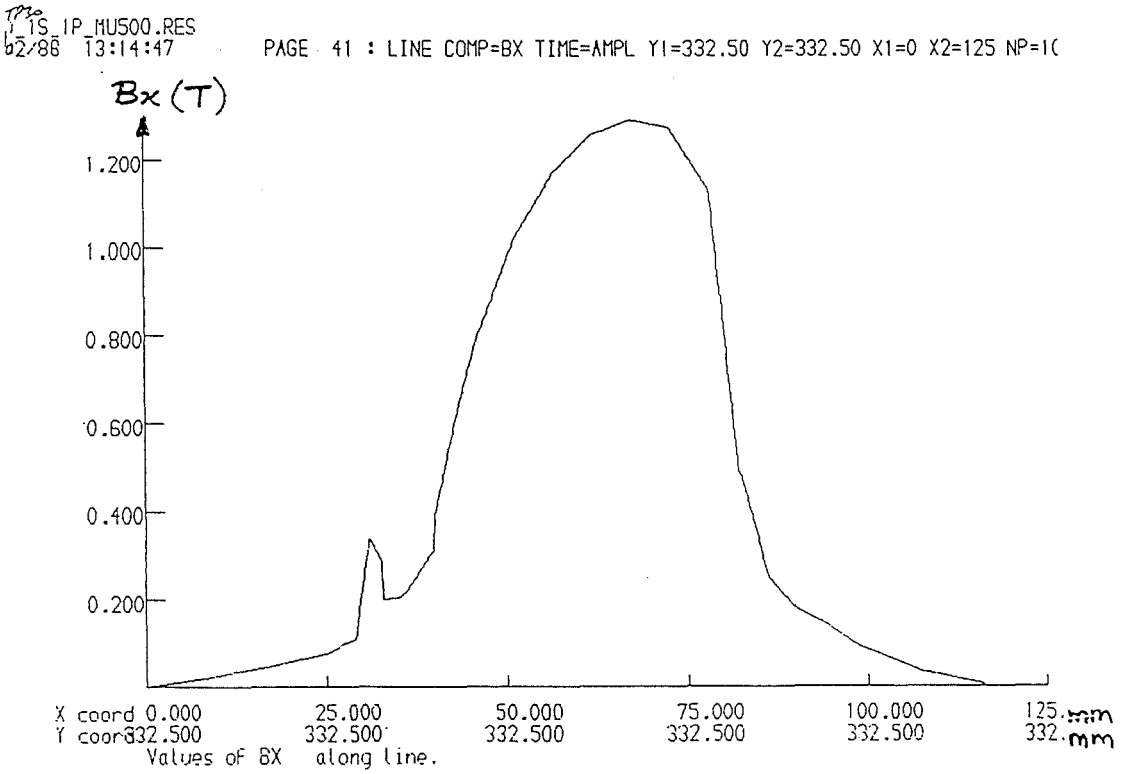

(c) Normal flux density, B_x

VARIATION OF FLUX DENSITY THROUGH THE PARTICLE AND TOOTH ALONG y = 332.5 (TP30_1S_1P_MU500)

Figure 5.38

Table 5.4: Flux Density Values for the Tubular Studies

Study	Component of flux density (T)	Along x=32 (through particles) at:					Along y=332.5 (particle opposite tooth) at:				Along y=436 (particle opposite slot) at:			
		y=332.5	y=436	over central part of lamination	Ratio A		x=32	x=40	x=68	Ratio A	x=32	x=43	x=78	Ratio A
					y=332.5	y=436								
TP20_1S_1P_MU100	B_m	0.24	0.175	0.14	1.71	1.25	-	-	-	-	-	-	-	-
	B_y	0.18	0.155	0.115	1.62	1.45	-	-	-	-	-	-	-	-
	B_x	0.2	0.075	0.08	2.4	1.11	-	-	-	-	-	-	-	-
TP20_1S_1P_MU500	B_m	0.24	0.175	0.14	1.71	1.25	0.25	0.37	0.85	1.64	0.54	0.25	0.27	4.43
	B_y	0.18	0.155	0.115	1.60	1.41	0.12	0.26	0.075	1.14	0.53	0.24	0.25	5.3
	B_x	0.205	0.075	0.08	2.36	1.12	0.23	0.27	0.85	2.3	0.12	0.03	0.06	1.6
TP30_1S_1P_MU100	B_m	0.35	0.26	0.21	1.67	1.24	-	-	-	-	-	-	-	-
	B_y	0.26	0.23	0.175	1.56	1.44	-	-	-	-	-	-	-	-
	B_x	0.305	0.12	0.125	2.35	1.18	-	-	-	-	-	-	-	-
TP30_1S_1P_MU500	B_m	0.355	0.255	0.21	1.69	1.21	0.38	0.55	1.3	1.75	0.81	0.36	0.4	4.28
	B_y	0.265	0.235	0.175	1.56	1.44	0.18	0.39	0.1	1.32	0.8	0.36	0.39	5.58
	B_x	0.31	0.12	0.125	2.38	1.2	0.33	0.4	1.3	2.1	0.155	0.04	0.08	1.37

$$\text{Ratio A} = \frac{\text{component of flux density in particle}}{\text{component of flux density outside but near particle}}$$

5.6.4 Introducing Particles in the Linear Model

From the previous study, LP20_1S_1P_MU1 (see Figs 5.28, 5.29 and 5.30), it was noted that the modelled LIM was close to saturation, so that only a single study at 20 A/phase was made. It has also been seen that the permeability of the particles made little difference to the results for the tubular machine, and the particles were therefore only modelled with a permeability of 100. Results for this study (LP20_1S_1P_MU100), given in Figs 5.39, 5.40 and 5.41, are similar to those in Figs 5.28, 5.29 and 5.30, i.e. study LP20_1S_1P_MU1.

Similar to the tubular studies, the graphs in both sets of figures are practically identical apart from the flux density values in the particles. Table 5.5 shows the flux density at selected points for the present study, and the greatest flux density occurs near the base of the lamination teeth, being primarily due to the normal component of flux density. As for the previous results, the discrepancy between the values of flux density in the particle opposite a tooth and opposite a slot is explained by similar reasoning to that given for the tubular studies. Calculation of the same ratio as in Table 4.4 shows that, at the same height of 7 mm, the flux density inside is almost twice to that outside, for a particle opposite a tooth. For the particle opposite a slot, this ratio clearly shows that the flux density inside is more than five times the value outside.

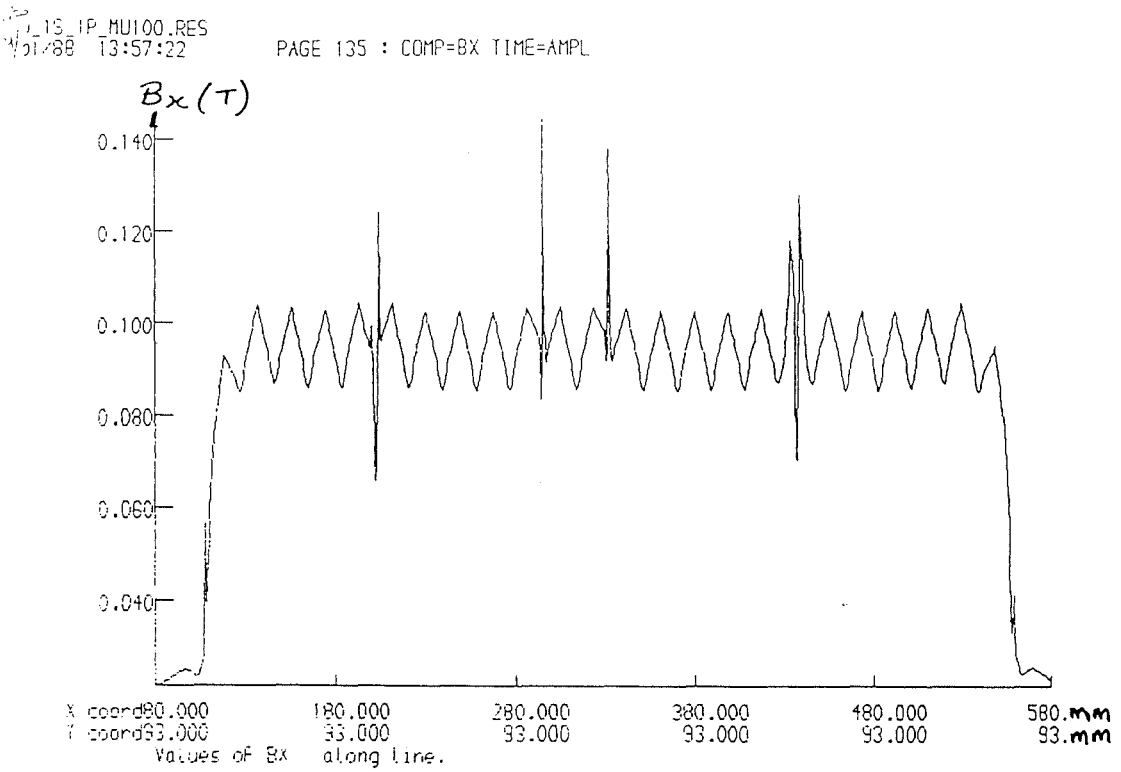

(a) Time-averaged tangential flux density, B_x

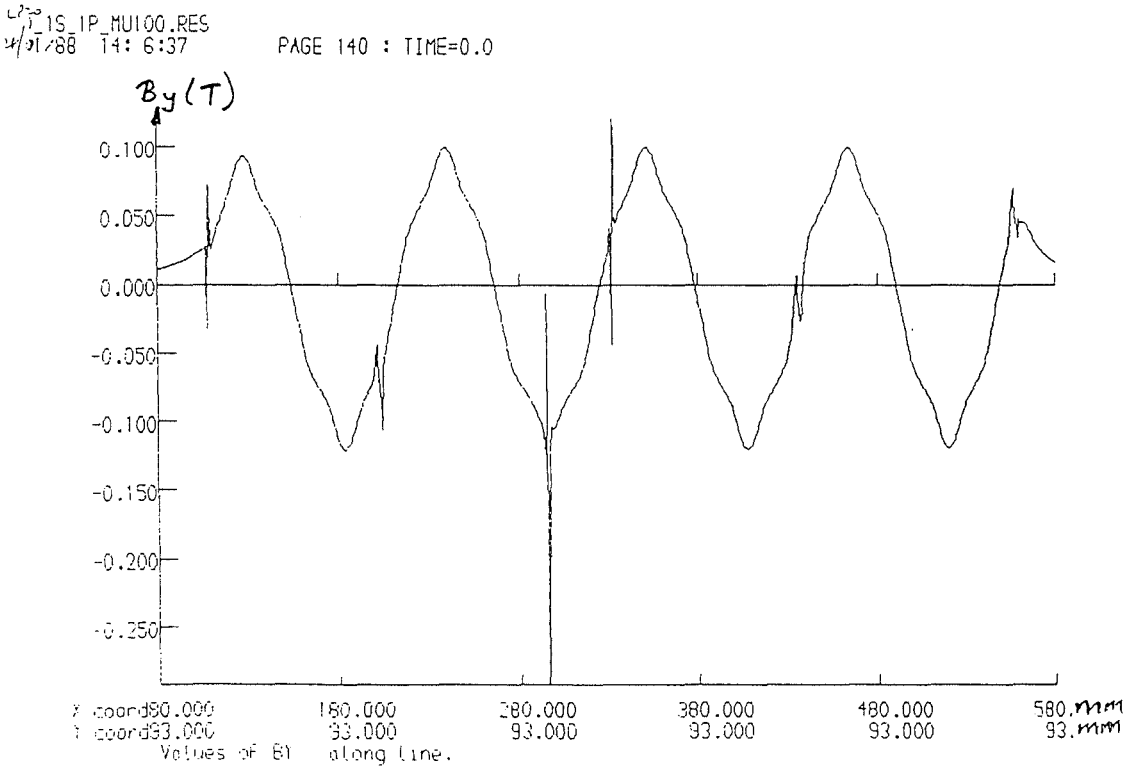

(b) Normal flux density, B_y

VARIATION OF FLUX DENSITY THROUGH THE PARTICLES (y = 93)
(LP20_1S_1P_MU100)

continued ...

Figure 5.39

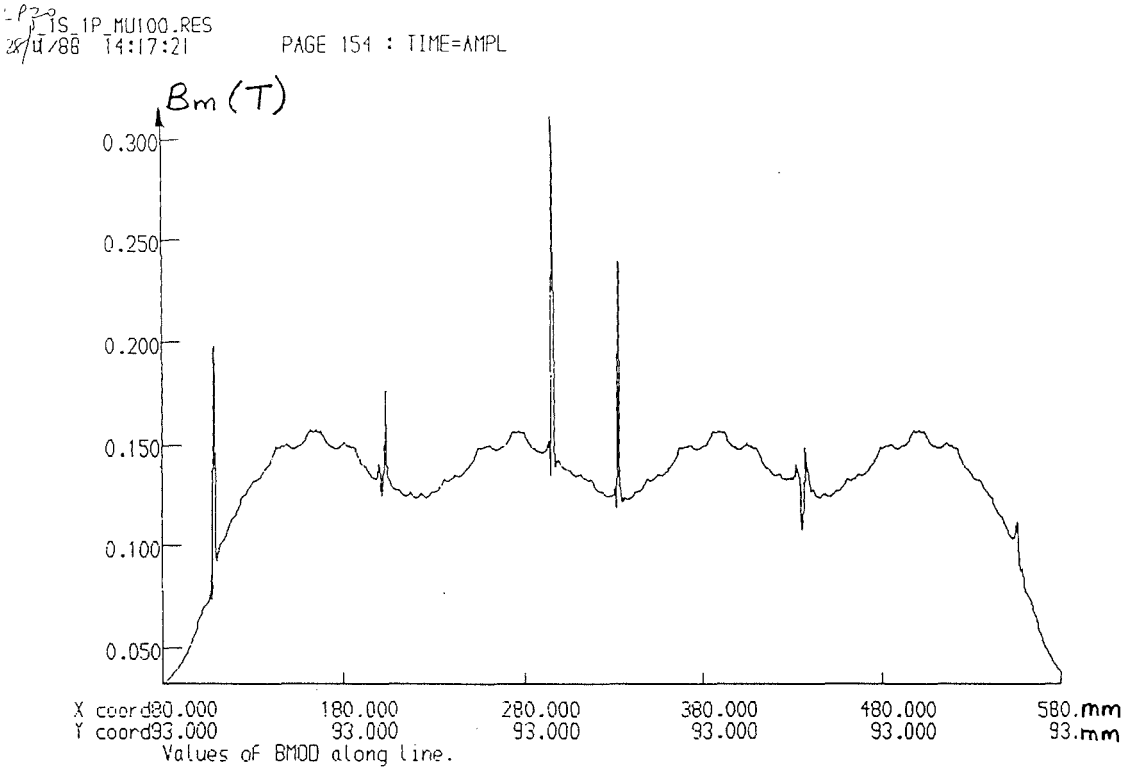

(c) Time-averaged modulus of flux density, B_m

VARIATION OF FLUX DENSITY THROUGH THE PARTICLES (y = 93)
(LP20_1S_1P_MU100)

Figure 5.39

(a) Time-averaged tangential flux density, B_x
(b) Normal flux density, B_y
(c) Time-averaged modulus of flux density, B_m

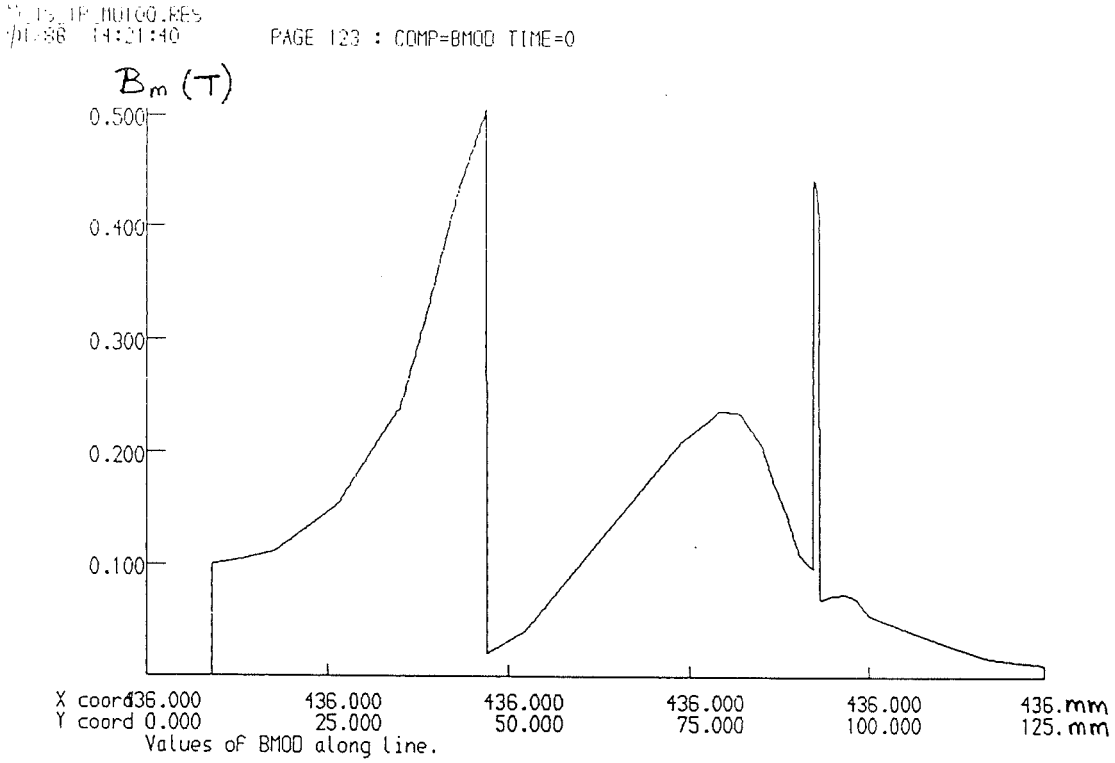

(a) Modulus of flux density, B_m

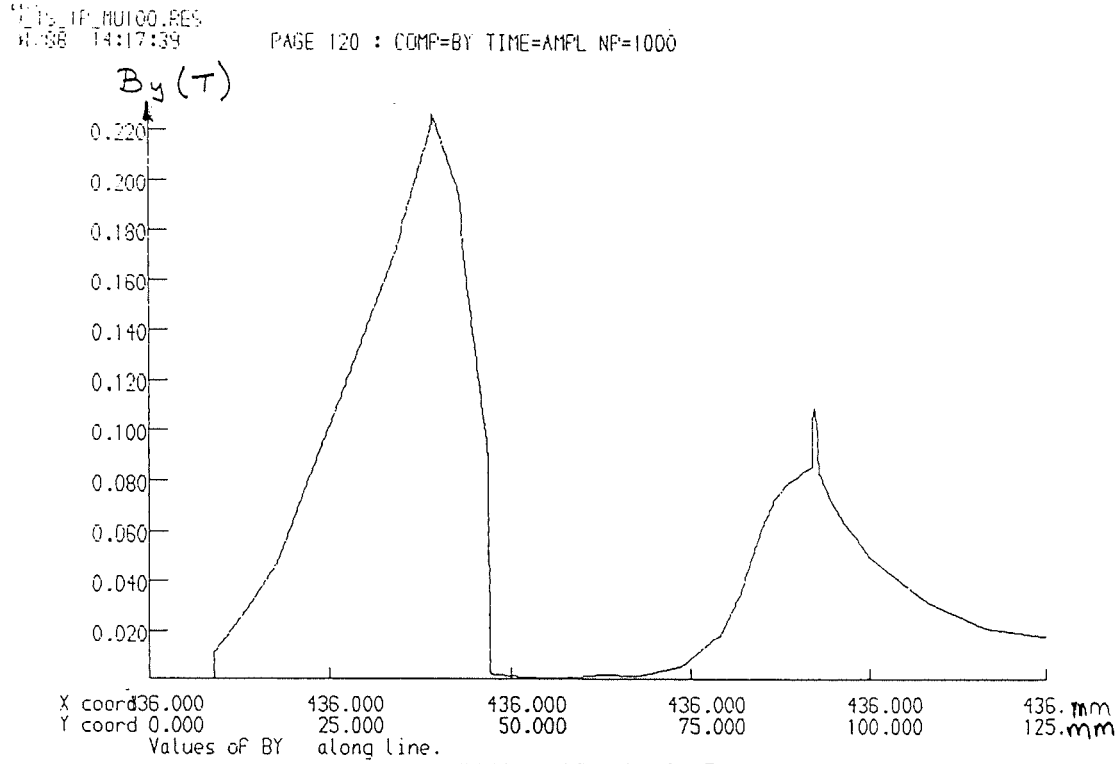

(b) Normal flux density, B_y

VARIATION OF FLUX DENSITY THROUGH THE PARTICLE AND SLOT ALONG x = 436
(LP20_1S_1P_MU100)

continued ...

Figure 5.40

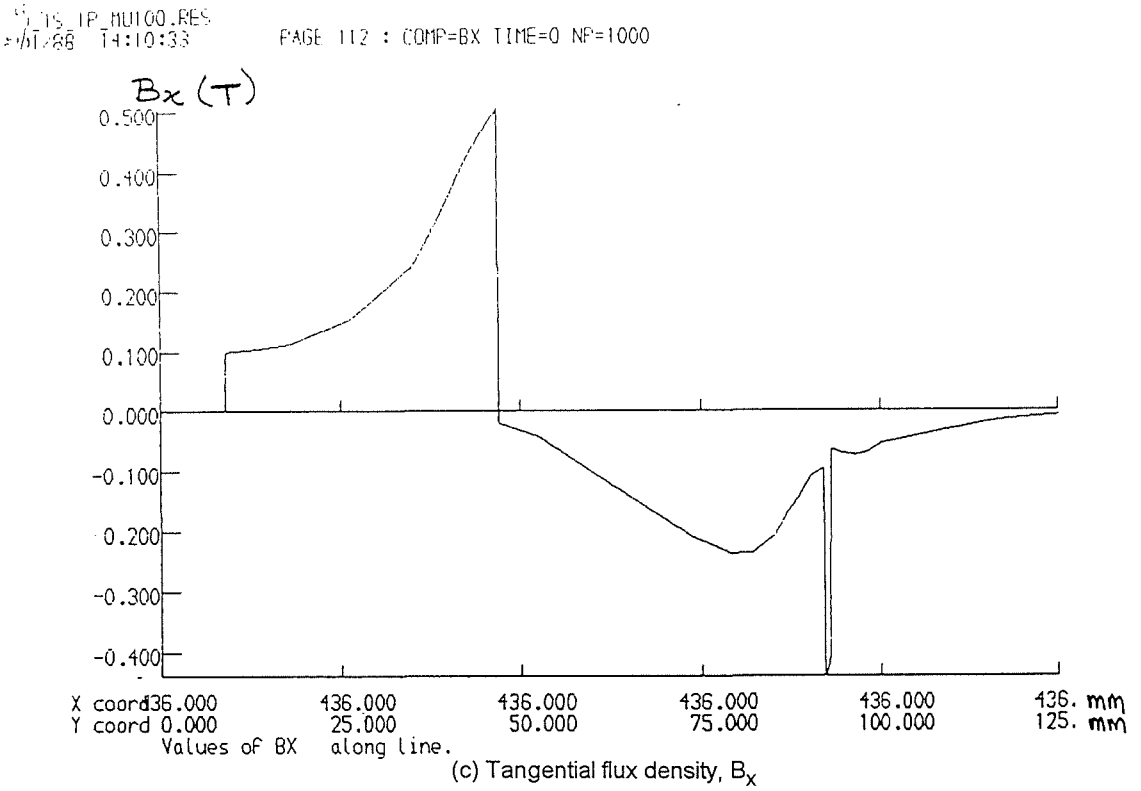

(c) Tangential flux density, B_x

VARIATION OF FLUX DENSITY THROUGH THE PARTICLE AND SLOT ALONG x = 436
(LP20_1S_1P_MU100)

Figure 5.40

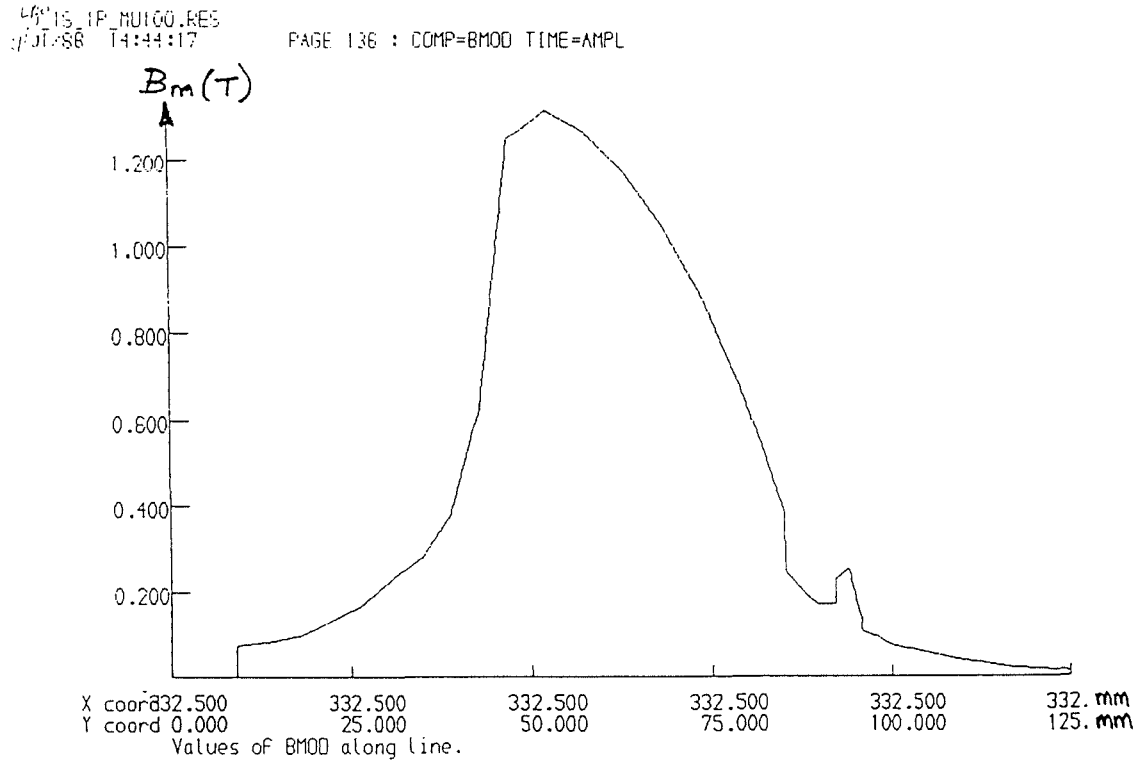

(a) Time-averaged modulus of flux density, B_m

VARIATION OF FLUX DENSITY THROUGH THE PARTICLE AND TOOTH ALONG x = 332.5
(LP20_1S_1P_MU100)

continued ...

Figure 5.41

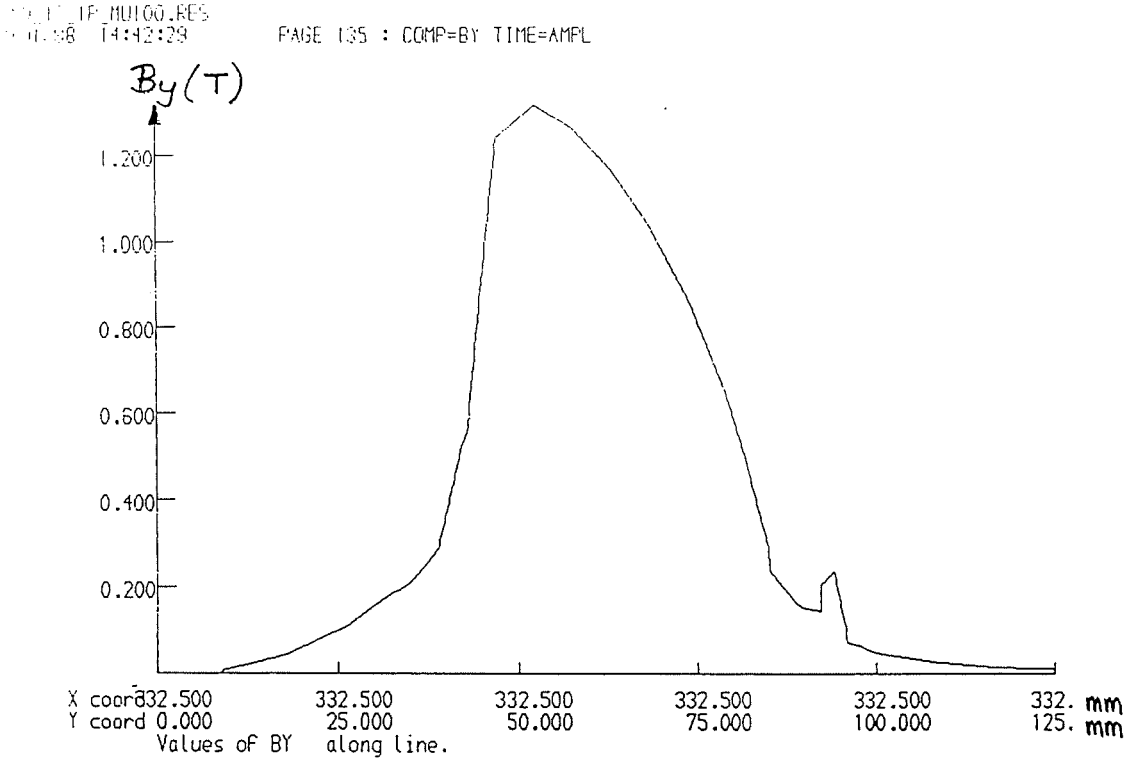

(b) Time-averaged normal flux density, B_y

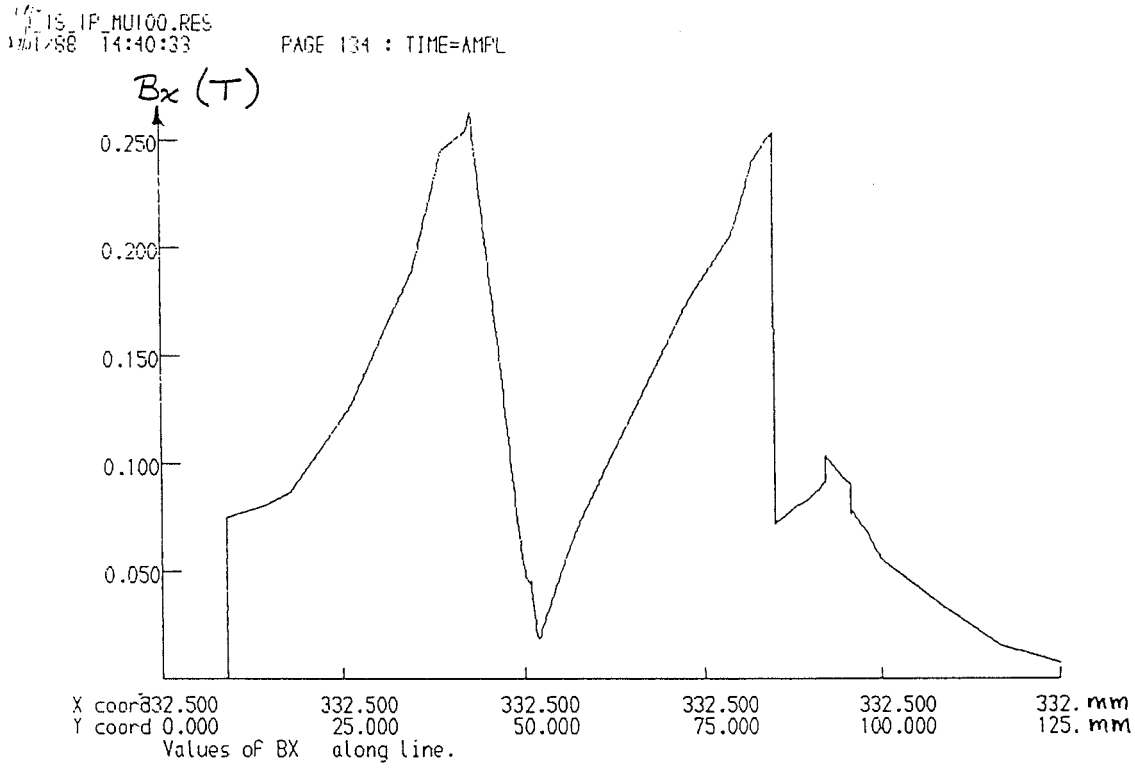

(c) Time-averaged tangential flux density, B_x

VARIATION OF FLUX DENSITY THROUGH THE PARTICLE AND TOOTH ALONG x = 332.5
(LP20_1S_1P_MU100)

Figure 5.41

Table 5.5: Flux Density Values for the Linear Machine

Component of flux density (T)		Along y=93 (through particles) at:					Along x=332.5 (particle opposite tooth) at:				Along x=436 (particle opposite slot) at:			
		x=332.5	x=436	over central part of lami nation	Ratio A		y=93	y=85	y=53	Ratio A	y=93	y=82	y=47	Ratio A
					x=332.5	x=436								
LP20_1S_1P_MU100	B_m	0.24	0.15	0.14	1.95	1.2	0.25	0.4	1.32	1.67	0.44	0.24	0.51	5.3
	B_y	0.22	0.085	0.1	2.4	1.13	0.23	0.32	1.32	2.0	0.11	0.035	0.14	1.3
	B_x	0.138	0.128	0.095	1.5	1.25	0.1	0.25	0.03	1.2	0.44	0.23	0.51	5.3

$$\text{Ratio A} = \frac{\text{component of flux density in particle}}{\text{component of flux density outside but near particle}}$$

5.6.5 Comparison Between the TLIM and LIM

In the graphs presented for the TLIM and LIM in the previous sections, there is considerable similarity between the flux density values in the airgap near the particles (the area of interest) for the two models, and this is also seen when entries in Table 5.5 are compared with their respective counterparts in Table 5.4. (When comparing the two tables, B_x for the TLIM must be compared with B_y for the LIM, because the normal components of flux density are then being compared. Similarly, B_y for the TLIM should be compared with B_x for the LIM, this being the tangential flux density for the respective models.) It is not entirely surprising that, at the position of the particles, the results for both the linear and tubular machines are similar. With the particles relatively close to the laminations, the tubular machine appears to the particles as a linear machine.

The tables show that the ratio of B_n inside the particles to that outside is greater in the case of the TLIM than the LIM. This may be explained by noting that for the linear machine the flux density may, in the limit, spread to infinity above the lamination, but the axial symmetry of the tubular machine contains the flux within its bore and increases the flux density inside the particles to that existing outside. This increase however is small, and caution must be exercised in the interpretation of all these results as they are only as good as the models to which they relate. It may also be seen that the flux density values and ratios for the particle opposite the tooth (i.e. along $y = 332.5$ and along $x = 332.5$ respectively for the TLIM and LIM) are practically identical, but, for the particle opposite the slot (i.e. along $y = 436$ and along $x = 436$), B_m and B_t are clearly larger for the tubular machine. This is due to the expected increase in tangential with respect to normal flux density in the airgap of the tubular machine compared with the linear machine, which was found to be the case.

Considering the transport of powder the tubular machine is likely to be the better choice because it will begin to saturate at much higher currents than the linear machine, as indicated by the flux density values in the lamination in Tables 5.4 and 5.5. Since the airgap flux density in the region of interest is similar for both machines for the same exciting current, the TLIM is better in this respect as the higher currents will produce an increased airgap flux density. Table 5.4 adds support to this, in that the flux density

ratios at 30 A/phase are practically the same as those at 20 A/phase, indicating a linear variation.

5.7 Summary

In this chapter finite-element models of the LIM and the tubular LIM were developed. After the initial simulation of basic models, particles were added to the mesh and a number of studies were carried out by varying the magnitude of the exciting currents and the permeability of the particles. The results of these investigations have been presented in graphical form, with tables, where this is appropriate.

The LIM and TLIM models have shown that the particle permeability is of little importance. However, it must be remembered that, in the real case, there will not be merely six particles traversing the LIM or TLIM but "sheets" of particles and, in that case, the permeability is likely to have a significant effect. It has also been seen that the airgap flux density ratios are similar for both the linear and tubular machines. The tubular machine gains however in that, for the same exciting current, it is further from saturation than the linear machine, allowing greater flux densities to be achieved both in the airgap and in the particles. (The increased excitation has been shown to produce greater movement as discussed in Chapter 4.)

These flux density ratios are of interest however for they support the theory given in Chapter 3, which discussed how iron particles in a field tend to have a considerably increased internal field causing them to act as tiny permanent magnets.

References

1. OGAWA, K., SABONNADIERE, J.C., and SILVESTER, P.: "Finite element solution of saturated travelling magnetic field problems", *IEEE Trans. Power Apparatus and Systems*, 1975, **PAS-94**, (3), pp.866-871.

2. YOSHIDA, K.: "Three dimensional analysis of short primary linear induction machines with finite iron length, width and depth using new transfer-matrix method" *Proc. Int. Conf. Elec. Mach.*, 1980, Pt.I, pp.20-27.

3. ISMA'EEL, M.E., and SALEH, M.A.: "Finite iron and secondary width effects in linear induction motors", *Proc. Int. Conf. Elec. Mach.*, 1980, Pt.I, pp.35-42.

4. BRAMER, D. and MOSEBACH, H.: "Field and force distribution in the linear induction motor - analysis and measurements", *Proc. Int. Conf. Elec. Mach.*, 1980, Pt.I, pp.43-49.

5. BOLTE, E., and OBERRETL, K.: "Three dimensional analysis of linear motor with solid iron secondary", *Proc. Int. Conf. Elec. Mach.*, 1980, Pt.I, pp.68-75.

6. NANAKA, S., YOSHIDA, K. and OGAWA, K.: "Magnetic fields in high-speed linear induction motors taking into account finite length of primary cores", *Proc. Int. Conf. Elec. Mach.*, 1980, Pt.I, pp.76-83.

7. NAMJOSHI, K.V. and BIRINGER, P.P.: "Fourier analysis of linear induction pumps with concentric windings and infinite arrays", *Proc. Int. Conf. Elec. Mach.*, 1980, Pt.I, pp.116-169.

8. ALWASH, J.H.H. and AL-RIKABI, J.A.H.: "Finite-element analysis of linear induction machines", *Proc. IEE*, 1979, **126**, (7), pp.677-682.

9. POLOUJADOFF, M. and BOLOPION, A.: "A comparison of two and three dimensional analysis of linear induction machines", *Energy Convers. Mgmt*, 1982, **22**, (2), pp.85-94.

10. EASTHAM, J.F., BALCHIN, M.J. and RODGER, D.: "Measurement and calculation of rotor-core flux densities in axial flux linear induction motors", *IEE Proc. B*, 1981, **128**, (6), pp.326-332.

11. AL-MAAYOUF, M.A. and VAN BUEREN, J.: "Three dimensional analysis of a linear induction motor represented by homogeneous anisotropic/isotropic models", *Proc. Int. Conf. Elec. Mach.*, 1982, **3**, pp.972-975.

12. SHARPLES, K.O. and Van BUEREN, J.: "Surface impedance models for 3-D field computations in linear induction machines", *Proc. Int. Conf. Elec. Mach.*, 1980, Pt.I, pp.14-19.

13. RAJANATHAN, C.B., LOWTHER, D.A. and FREEMAN, E.M.: "Study of Xi-core transverse-flux plate levitator", *IEE Proc. B*, 1980, **127**, (3), pp.183-189.

14. ONUKI, T., YOSHINO, K. and RYU, S.: "Reduction of finite element region on semi-infinite two media problem by finite-boundary element method", *Elec. Eng. Japan* (USA), 1985, **105**, (1), pp.27-35.

15. FAHIM, A.A. and SALEH, M.A.: "Finite element analysis of a linear tubular motor with composite rotor", *Proc. IMACs Int. Symp. Elec. Mach. and Conv.*, 1984, pp.167-173.

16. Van LEUVEN, J.: "Analysis of the double-sided linear induction motor by finite elements", *Proc. Int. Conf. Elec. Mach.*, 1980, Pt.I, pp.3-13.

17. BAUDON, Y., ELZAWAWI, A. and IVANES, M.: "Numerical study with a finite elements method of a homopolar linear synchronous motor and experimental verification", *Proc. Int. Conf. Elec. Mach.*, 1980, Pt.I, pp.202-209.

18. DAVIES, A.J.: "The finite element method: a first approach", (OUP, 1980, Oxford).

19. HUEBNER, K.H. and THORNTON, E.A.: "The finite element method for engineers", (John Wiley and Sons, Inc., 1982, 2/e, USA).

20. RAO, S.S.: "The finite element method in engineering", (Pergamon Press Ltd, 1982, Oxford).

21. BURNETT, D.S.: "Finite element analysis: from concepts to applications", (Addison-Wesley Publishing Company, 1987, USA).

22. ZIENKIEWICZ, O.C.: "The finite element method", (McGraw Hill, 1977, 3/e, England).

23. CHARI, M.V.K. and SILVESTER, P.P. (Editors): "Finite elements in electrical and magnetic field problems", (John Wiley and Sons Ltd, 1980, New York).

24. SILVESTER, P. and CHARI, M.V.K.: "Finite element solution of saturable magnetic field problems", *IEEE Trans. Power Apparatus and Systems*, 1970, **PAS-80**, (7), pp. 1642-1648.

25. DONEA, J., GIULIANI, S. and PHILLIPPE, A.: "Finite elements in the solution of electromagnetic induction problems", *Int. J. Numer. Methods Engng.*, 1974, **8**, pp.359-367.

26. FOGGIA, A., SABONNADIERE, J.C. and SILVESTER, P.: "Finite element solution of saturated travelling magnetic field problems", *IEEE Trans. Power Apparatus and Systems*, 1975, **PAS-94**, (3), pp.866-871.

27. PRESTON, T.W. and REECE, A.B.J.: "The contribution of the finite-element method to the design of electrical machines: an industrial viewpoint", *IEEE Trans. on Magnetics*, 1983, **MAG-19**, (6), pp.2375-2380.

28. SIMKIN, J. and TROWBRIDGE, C.W.: "On the use of the total scalar potential in the numerical solution of field problems in electromagnetics", *Int. J. Numer. Methods Engng.*, 1979, **14**, pp.423-440.

29. BIDDLECOMBE, C.S., DISERENS, N.J., RILEY, C.P. and SIMKIN, J.: "PE2D user guide: 2d- axisymmetric static and dynamic electromagnetic analysis package", (Rutherford Laboratory, 1985, RL-81-089, Oxford).

30. BIDDLECOMBE, C.S. and SIMKIN, J.: "Electromagnetics software course - program theory", (Rutherford Laboratory, 1980, CAG 80-22, Oxford).

31. EMSON, C.R.I.: *Private communication*, September 1987, Rutherford-Appleton Laboratories, Chilton, Didcot, Oxon OX11 0QX.

32. PRESTON, T.W.: *Private communication*, 1987, GEC Research.

33. VADHER, V.V.: *Private communication*, 1987, University of Technology, Loughborough.

6. Transverse Flux Linear Induction Machines

As described in Chapter 2, the transverse flux linear induction machine[1] (TFLIM) is a device which has flux paths perpendicular to the direction of its motion. The principal advantage of this arrangement is that the pole-pitch may be increased without the disadvantage, prevalent in other forms of linear induction machine, of saturating the core. Transverse flux machines may be constructed using either C- or E-cores, with various winding arrangements being possible. With C-cores, the windings may be placed either on the two limbs opposite to each other or on the centre limb connecting the two outer limbs. With E-cores, the windings may be placed on the three projecting limbs, the two side or outer projecting limbs, the two limbs connecting the three projecting limbs or the centre-limb alone.

Readily available E-shaped laminations (as shown in Fig 6.1) were employed in the construction of an experimental TFLIM used to investigate powder transportation. Windings were placed only on the centre limb, which has the advantage that the end-windings rest inside the slots making up the E-shaped lamination (as shown in Figs 6.2 and 6.5) unlike a longitudinal LIM. They are therefore not wasted, in that they do not consume power without aiding the generation of the magnetic field. This feature enables large pole-pitches to be investigated, without a detrimental effect on the power consumption. Also, energising only the centre limb causes the magnetic flux to leave this limb, divide equally and return via the two outer limbs, which was expected to aid in the containment of the powder. Previous observations of the powder motion on a longitudinal linear induction machine have shown that the powder spreads the full width of the core, often further onto the end connections and, sometimes, off the sides of the device. Since the powder travels in the opposite direction to the flux, a winding on the centre limb of an E-core should tend to cause the powder to travel down the centre of the device.

This chapter describes the design, construction and investigation of an experimental transverse flux linear induction machine.

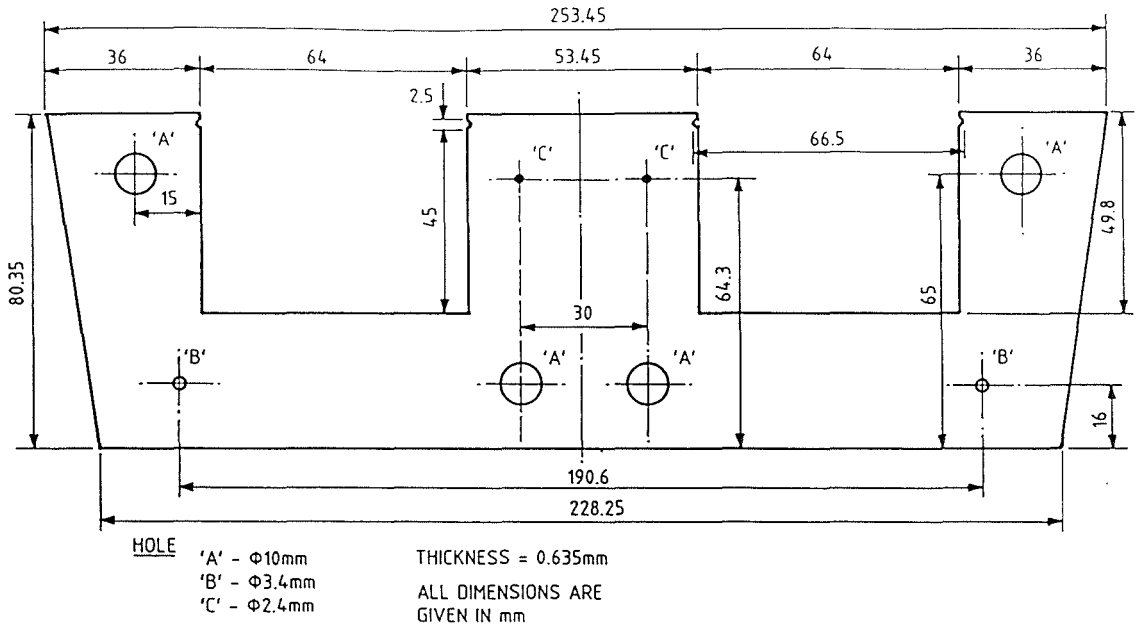

E - SHAPED LAMINATION

Figure 6.1

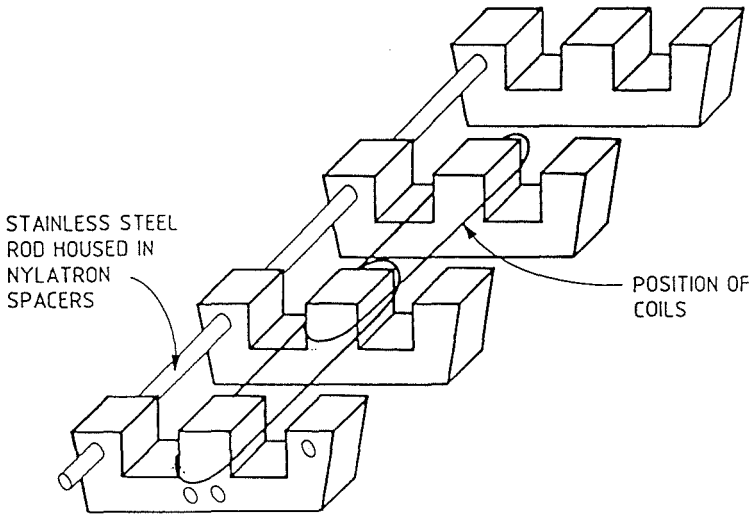

RELATIVE POSITIONS OF LAMINATION STACKS, COILS and STAINLESS STEEL RODS (only one shown)

Figure 6.2

6.1 Design and Construction

The E-shaped laminations of Fig 6.1 were assembled in stacks of fifteen giving a stack thickness of 9.525 mm, and the stacks were positioned in a hardwood, slotted base a fixed distance apart. Nylatron spacers positioned between each stack with stainless-steel rods threaded through the spacers and the four holes marked A in Fig 6.1 were fixed in position using stainless-steel nuts, thereby keeping the structure rigid and the lamination stacks in place (see Fig 6.2). Coils were placed round the centre limb of each stack, with the coil-ends being brought out to a terminal rail to allow some flexibility in the study of different winding arrangements.

6.1.1 First Transverse Flux Device

Fifty-five lamination stacks were positioned at 10 mm intervals in the wooden base thus producing a machine of overall length 1.064 m, with a 1 slot/pole/phase, $^2/_3$-chorded winding arrangement giving an eighteen pole field.

Coil Design

The number of turns per coil may be estimated from (see Appendix B),

$$E = 4\ W\ \lambda_p\ f\ k_w\ N_p\ B \qquad (6.1)$$

where E = rms voltage (240 V);
W = width of centre tooth (approximately 54 mm);
λ_p = pole-pitch (3 x (9.525 + 10) $\simeq$ 60 mm);
f = supply frequency (50 Hz);
k_w = winding factor (0.866);
N_p = number of turns/phase, and
B = flux density.

Assuming a peak airgap flux density[2] of 0.4 T, then

$$N_p = 240 / (4 \times 54 \times 60 \times 10^{-6} \times 50 \times 0.866 \times 0.4/\sqrt{2})$$

$$\simeq 1512 \text{ turns per phase or approximately 84 turns/coil in 18 coils/phase.}$$

Practical difficulties at this stage, such as winding the coils with wire of a suitable diameter and accommodating the coils in the slots meant that coils consisting of only 54 turns and the 1½ slots/pole/phase, $^4/_9$-chorded winding shown in Fig 6.3 was in fact used.

Initial Results

The motor performance was adversely affected by the modifications detailed above, but initial tests described below were promising, and a re-design was considered worthwhile.

Although the motor moved both aluminium and copper plate reasonably well, the amount of powder movement was limited. With the aid of a search coil, it was found that the flux travelled from one lamination stack to the next without being thrown sufficiently far upwards to interact effectively with either metal plate or iron powder. As Fig 6.4 shows, the transverse flux path was more than six times the length of the longitudinal flux path because the inter-stack separation was 10 mm (64:10) and the flux therefore took the latter lower reluctance path. In order to increase the longitudinal to transverse airgap ratio, every other lamination stack was removed, thereby giving a twenty seven slot device and reducing the ratio to approximately 2:1.

6.1.2 Second Transverse Flux Device

After removing the old coils and alternate lamination stacks the machine was re-wound as a 1 slot/pole/phase, $^2/_3$-chorded device, with the coil ends brought out to the terminal rail.

Coil Design

Assuming an approximate 40% increase in the area of the pole-face due to the coil width and fringing effects[3], and using eqn (6.1),

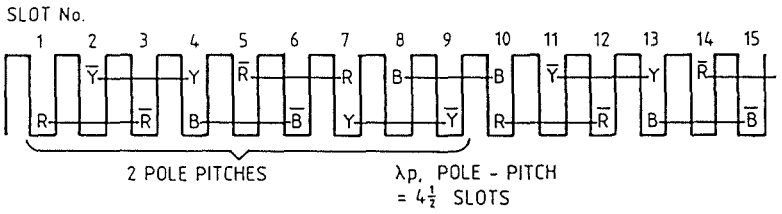

INITIAL WINDING SCHEME

Figure 6.3

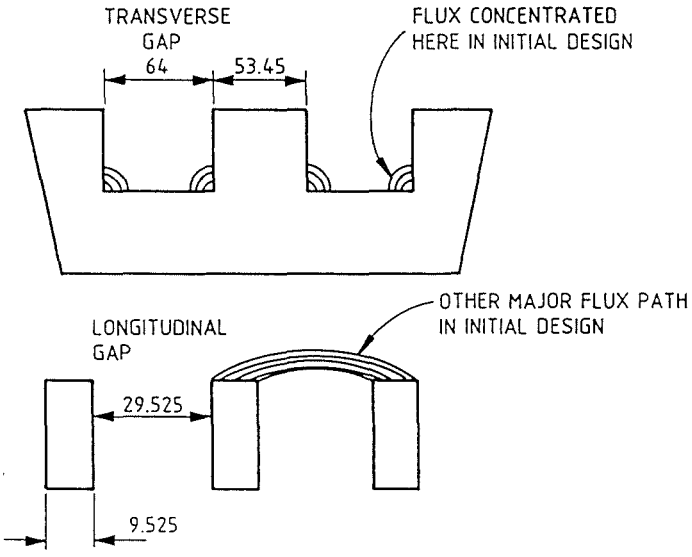

AIRGAP LENGTHS

Figure 6.4

$$N_p \approx \frac{240}{4 \times 54 \times 120 \times 10^{-6} \times 1.4 \times 50 \times 0.866 \times 0.283}$$

$$\approx 540 \text{ turns/phase}$$

and for this eight pole, twenty four slot device the number of turns per coil is approximately sixty seven.

To ease the coil-winding process multi-strand wire, consisting of a number of small diameter parallel-connected wires, was used to wind the coils using a specially designed former (details are given in Appendix E). A realistic estimate of the number of strands required may be made by considering the manner in which wires pack together into a rectangular cross-section, and this approach leads to an expression for the best achievable packing factor (see Appendix E). Twenty-nine coils, each with fifty turns comprising seven strands of 0.96 mm diameter wire were wound and fitted into the slots of the transverse flux machine. When connected 1 slot/pole/phase, $^2/_3$-chorded, the machine had four half-filled slots and twenty two fully-filled slots, thus producing an eight pole field. The photographs in Fig 6.5 clearly show the coils and the terminal rail to which they are connected, along with plastic inserts used to hold the coils in place, and Fig 6.6 illustrates the under-pitched winding arrangement.

6.2 Preliminary Investigations

To confirm the direction of the travelling magnetic field, an aluminium plate was placed on the motor initially in position A as shown in Fig 6.6 and, with the motor connected to a 3-phase 415 V 50 Hz supply, the plate moved in the direction of the travelling field at a current of about 8 A/phase. The plate's lateral stability was enhanced by placing it in position B (Fig 6.6) because it then covered complete lamination stacks and travelled the length of the motor rather, than attempting to leave the motor-face from either side, as it did when in position A. A copper plate also travelled in the direction of the field, but a steel plate was strongly attracted to the stator and did not move even with large input currents. All three plates experienced eddy-current heating, with the area directly above the centre tooth heating most rapidly.

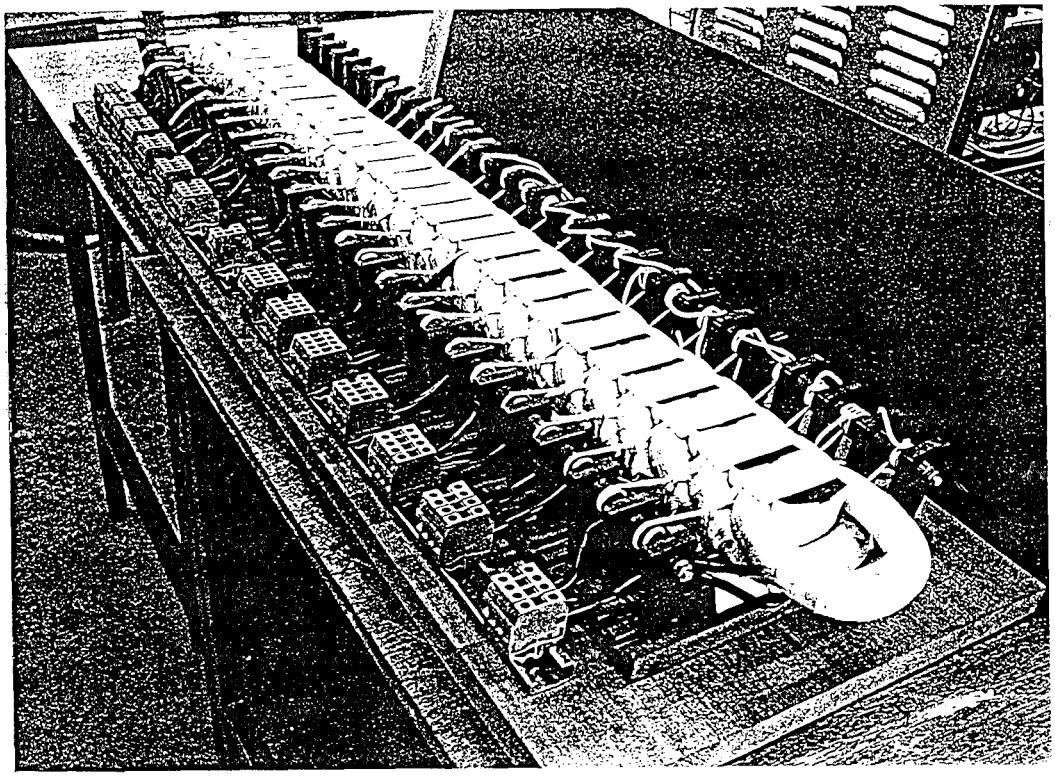

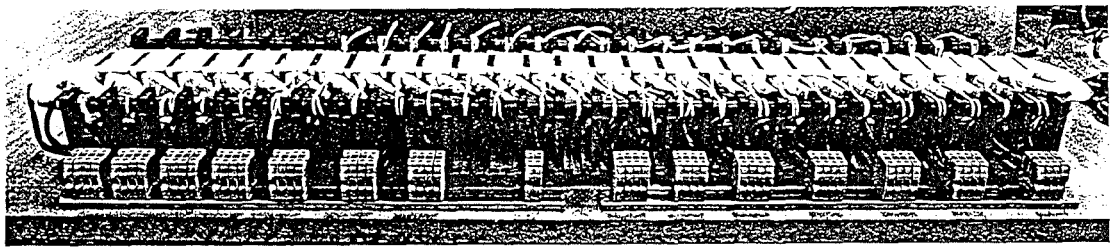

Fig. 6.5. Photographs of the TFLIM

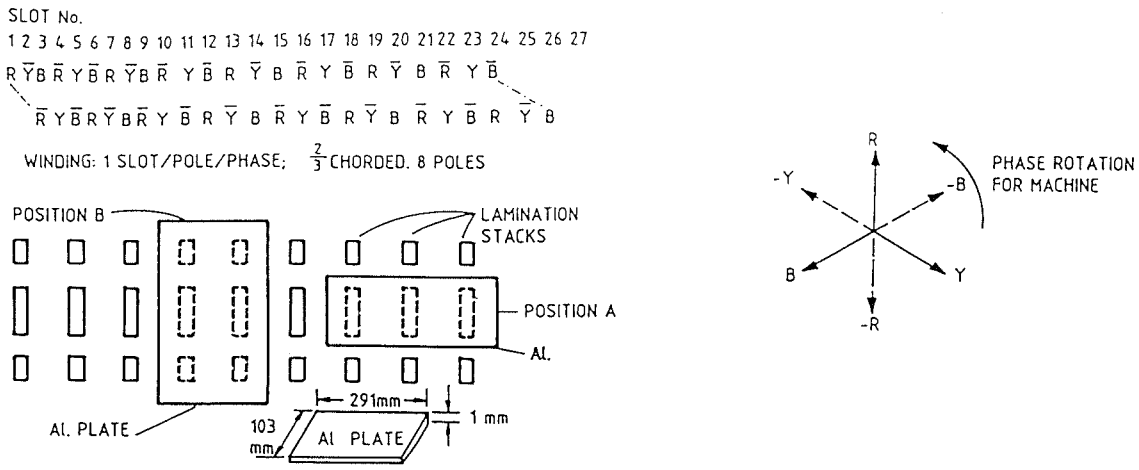

INITIAL EXPERIMENTS ON THE TFLIM

Figure 6.6

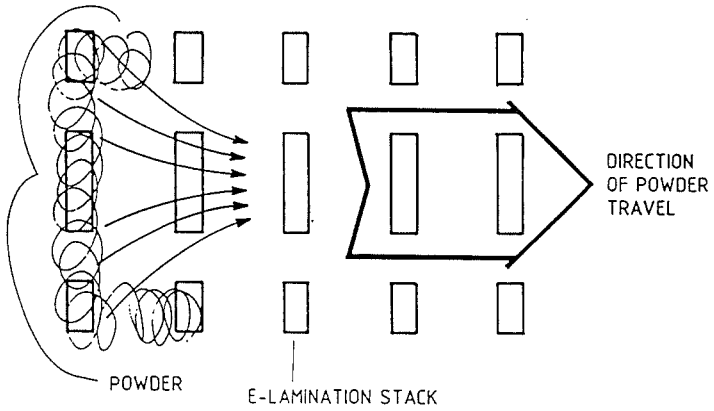

Figure 6.7 POWDER MOVEMENT OVER THE TFLIM

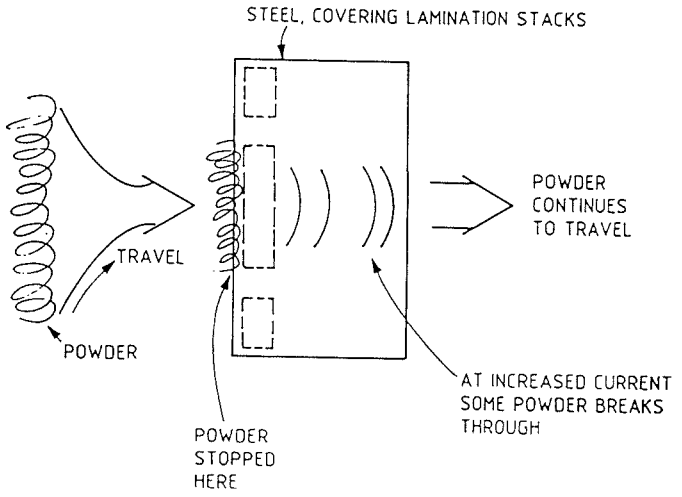

SHEET STEEL CAUSING DISRUPTION OF POWDER MOVEMENT

Figure 6.8

Powder Motion

The powder motion had the same characteristics as over a standard linear motor and the powder cleaning device described in Chapter 3. Iron powder, in a perspex box, placed on top of the transverse flux motor as shown in Fig 6.7 travelled in the opposite direction to the travelling field. The iron particles could be seen to travel individually, in particle-strings and in bunches (a collection of particle-strings). They were seen to "hop" and "jump" along and over the motor, and they clearly moved from tooth to tooth. Restricting the powder flow caused it to form thin wafer-like ridges, as on the powder cleaner and tubular motor (see Chapter 4). As noted previously, movement continued at the back of the ridges and also along their outermost edges. Once formed the ridges splayed out from neighbouring ones, thereby describing the flux pattern over the machine.

A simple experiment to illustrate that the powder followed flux paths was performed by placing a steel plate underneath the box containing the powder. The flux was short-circuited by the low reluctance path provided by the steel, and over the confines of the plate no powder movement took place. Upon reaching the steel plate, the powder did not travel past the plate as there was insufficient flux density, and instead it attempted to move between the plate and the stator (see Fig 6.8). Increasing the current to approximately 30 A/phase saturated the plate allowing a weak travelling field to transport the powder above it. Over the plate, the powder moved slowly as at low currents but was considerably agitated, vibrating and hopping from point to point, but past the plate the normal powder movement was resumed (Fig 6.8).

At currents below about 5 A/phase, very fine dust-like particles move slowly (that is, they have a low mass flow rate) from tooth to tooth, travelling mainly as individual particles along the motor-face. With currents between 5 A/phase and 10 A/phase, the powder began to transport and powder along the machine sides was slowly drawn in, and at 10 A/phase the powder became agitated, with particle strings beginning to form from the outer to the centre limbs. If powder was placed in a heap ridges would form, and powder laid flat was clearly transported. Increasing the current further continued the trend, with the powder movement becoming more vigorous and transporting more quickly.

Between 15 and 20 A/phase particle strings continually formed and re-formed as the violent and agitated motion broke existing strings due to the powder jumping and hopping from tooth to tooth, spending little time in the slots. Powder transportation was along the centre limbs of the E-laminations, with powder above the outer limbs being drawn onto the centre ones (Fig 6.7). Since the flux leaves the centre limbs and divides equally before returning via the outer limbs, the powder moved from the outer to the centre limbs because of its characteristic tendency to travel in the opposite direction. Motion in particle bunches occurred mostly above the outer limbs as powder was drawn onto the centre limbs, and also at the end of the motor when powder had started to build-up.

At approximately 20 A/phase, nearly all the powder transported from the start to the end of the device, with the powder being quickly and effectively drawn in from the machine sides. As the powder built-up, ridges formed, with much activity on the ridges. Adding the powder caused a current drop of approximately 5% due to the lower reluctance path provided for the flux.

The TFLIM tended to "sprinkle" powder onto the sides of the device, just outside the influence of the travelling field. A further increase in the current to above 25 A/phase considerably increased the powder transport rate and drew powder in from the outer limbs, without it being "sprinkled" back onto the outer limbs. Although powder transportation was improved at high currents, there was less tendency for the powder to leave the device and the powder build-up at the end of the machine hindered powder flow. Ridges then formed, which further hindered the transport of powder.

6.3 Flux Density Measurements

Measurements made on the transverse flux linear induction machine are recorded in detail in Appendix F.

6.3.1 A 1 slot/pole/phase Winding

Search coil measurements (see Appendix B for details of the search coil) of the flux density at the centre and edge of a tooth and slot showed an expected trend, with the flux

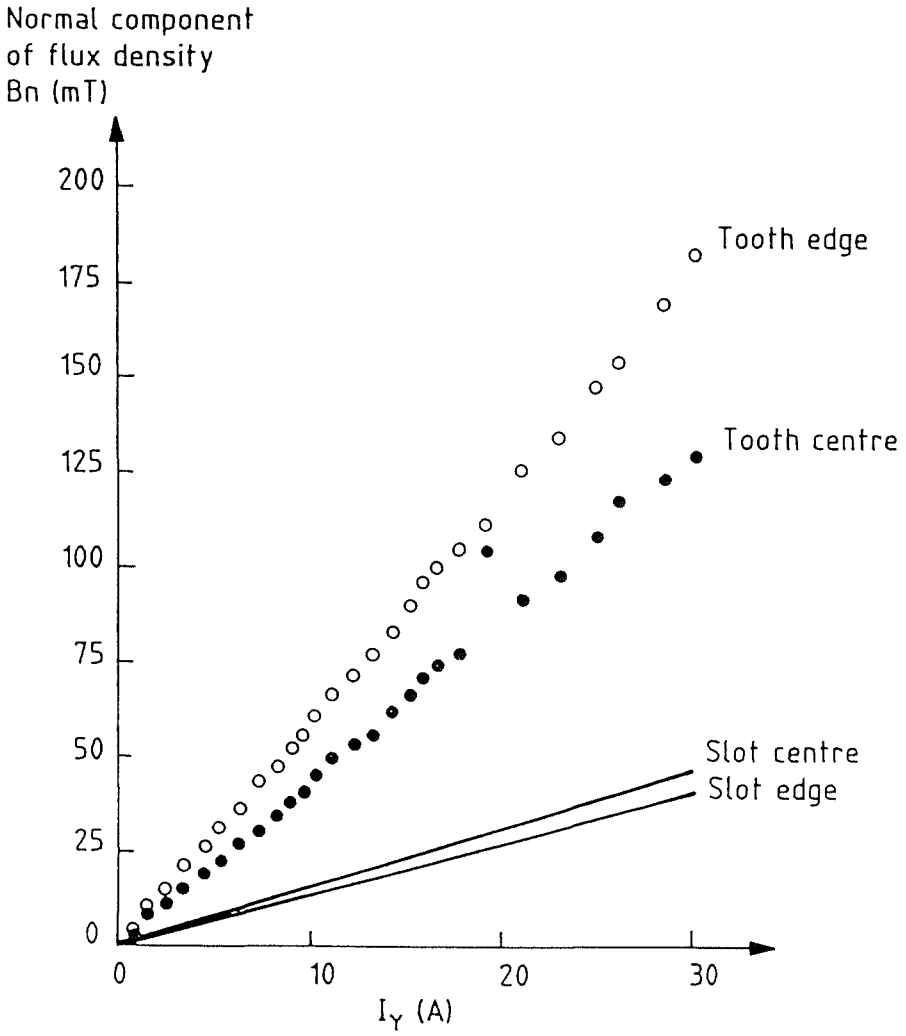

FLUX DENSITY MEASUREMENTS ALONG A TOOTH AND SLOT FOR THE TFLIM

Figure 6.9

density being greatest at the teeth rather than at the slots. The linear nature of Fig 6.9 shows that the machine in its main central portion, where the measurements were made, was unsaturated, even at 30 A/phase. The tangential flux density (B_t) along a centre-limb (see Fig 6.10) was about 25% of the normal flux density (B_n) at the tooth centre and constant. (Due to the width of the search coil, B_t was not measured at the tooth surface as B_n had been but about 5 mm above this surface.) Clearly B_n was constant along approximately half of the tooth centre, with peaking at the two ends causing more powder to transport along the teeth edges than to flow along the centre of the motor. Flux concentration at the teeth edges was considerable, as B_n was 30% greater at the edges than at the teeth centre.

Figure 6.11 illustrates that, in the central region of a slot, B_n was about 70% of B_t. The normal flux density, however, increased rapidly at the start of each tooth, rising to a maximum at the centre. Conversely, the tangential flux density dropped at the leading edge of each tooth, decreasing further to a minimum at the centre. Such a flux pattern aids powder transport from tooth to tooth. The tangential to normal flux density ratios plotted in Fig 6.12 illustrate that, along the length of a tooth, the ratio remains reasonably constant. Between teeth however, it increases dramatically, assisting powder flow because the particles behave like tiny permanent magnets allowing the travelling field to carry them from tooth to tooth, as discussed in the hypothesis in Chapter 3.

A plot of flux density along one half of the motor width is given in Fig 6.13, and the ratio (B_t/B_n) is plotted in Fig 6.14. Comparing Figs 6.11 and 6.13 shows that the flux density was greater between centre limbs rather than between the centre and outer limbs, thus aiding powder flow along the centre of the device. Although the flux density was low between the centre and outer limbs, B_t rose to more than double B_n. It has already been noted that, at sufficiently high currents, powder was pulled in from above the outer limbs towards the centre limb, and this large ratio caused powder flow in that direction.

The variation of flux density with height given in Fig 6.15 may be expressed approximately by

$$B_n = \exp(5.75)\, h^{-1.02} = 314\, h^{-1.02} \qquad (6.2)$$

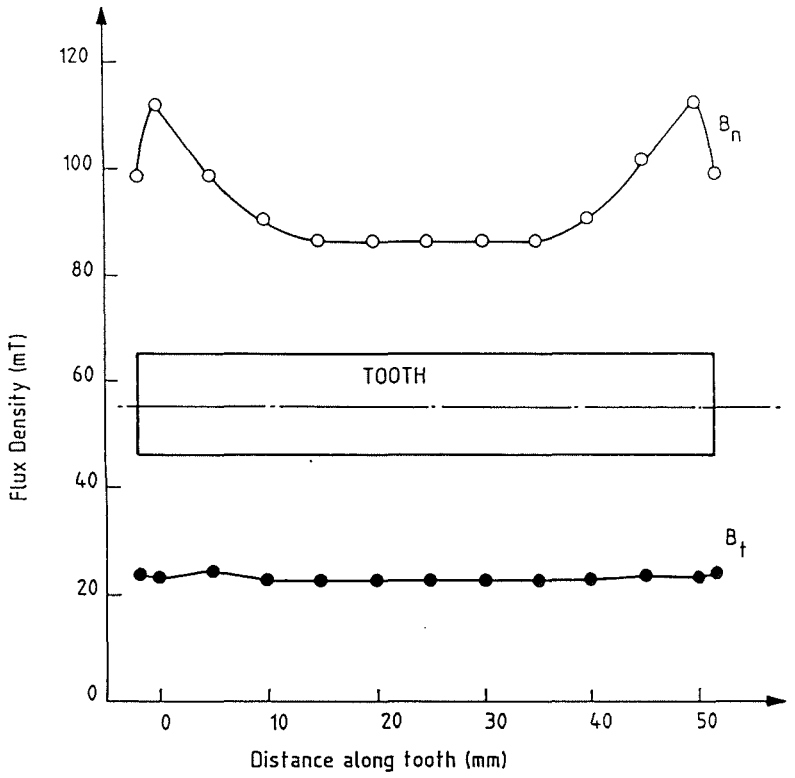

VARIATION OF FLUX DENSITY ALONG A CENTRE TOOTH OF THE TFLIM AT 20 A/phase

Figure 6.10

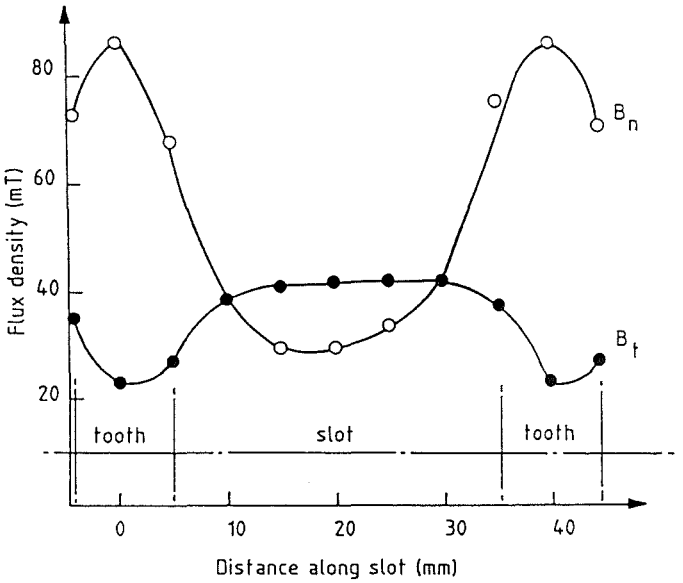

VARIATION OF FLUX DENSITY ALONG A CENTRE SLOT OF THE TFLIM AT 20 A/phase

Figure 6.11

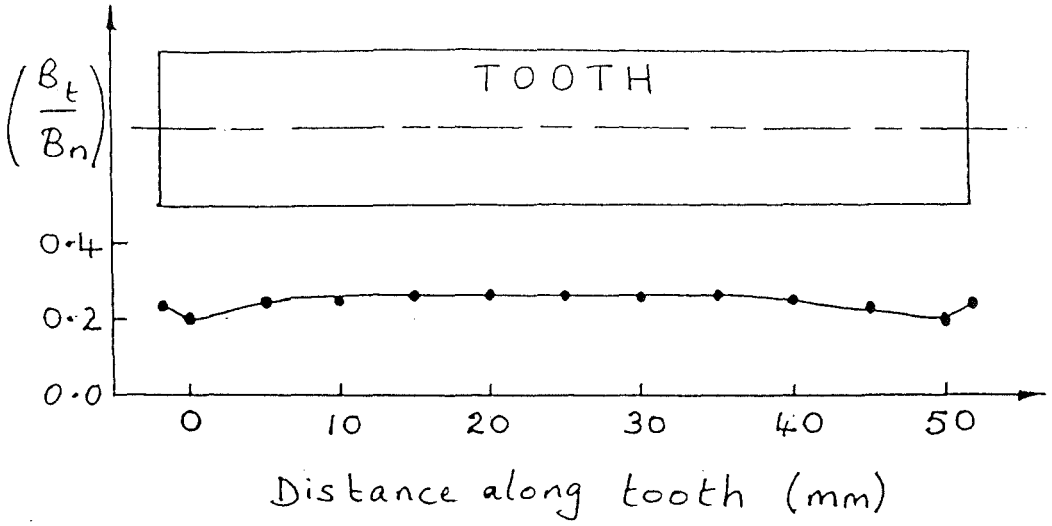

(a)

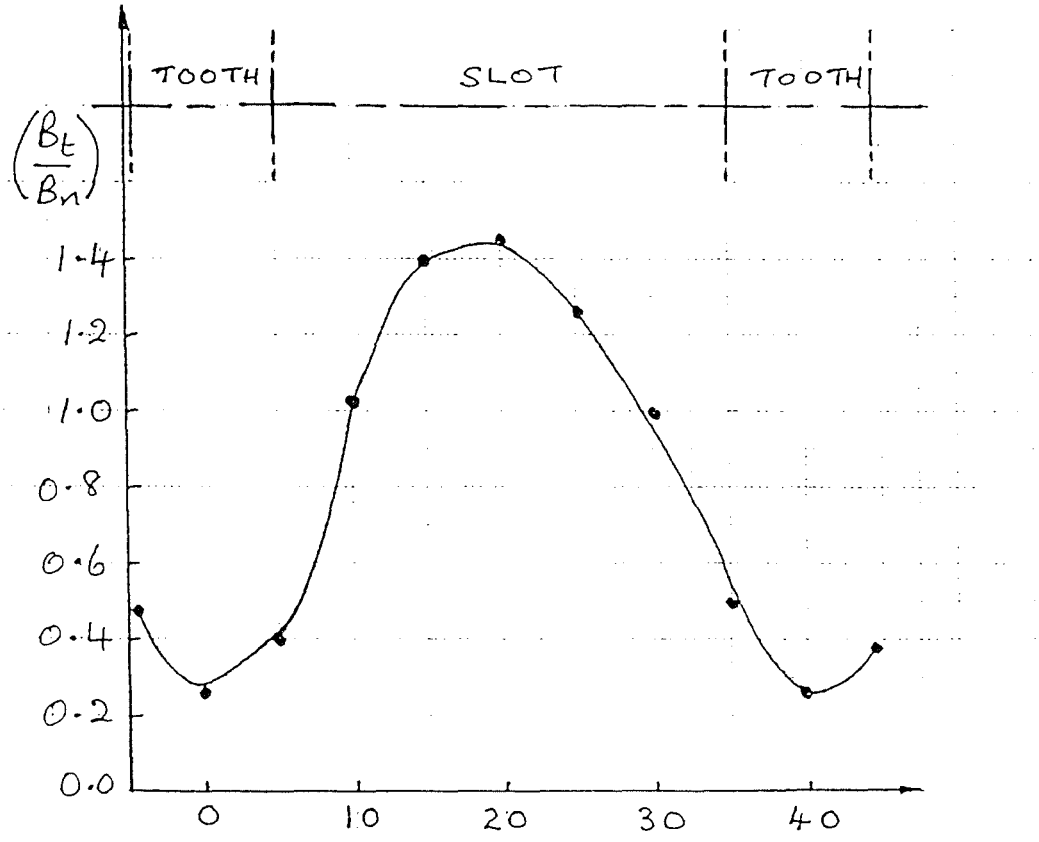

(b)

VARIATION OF THE (B_t / B_n) RATIO ALONG A CENTRE TOOTH AND SLOT OF THE TFLIM AT 20 A/phase

Figure 6.12

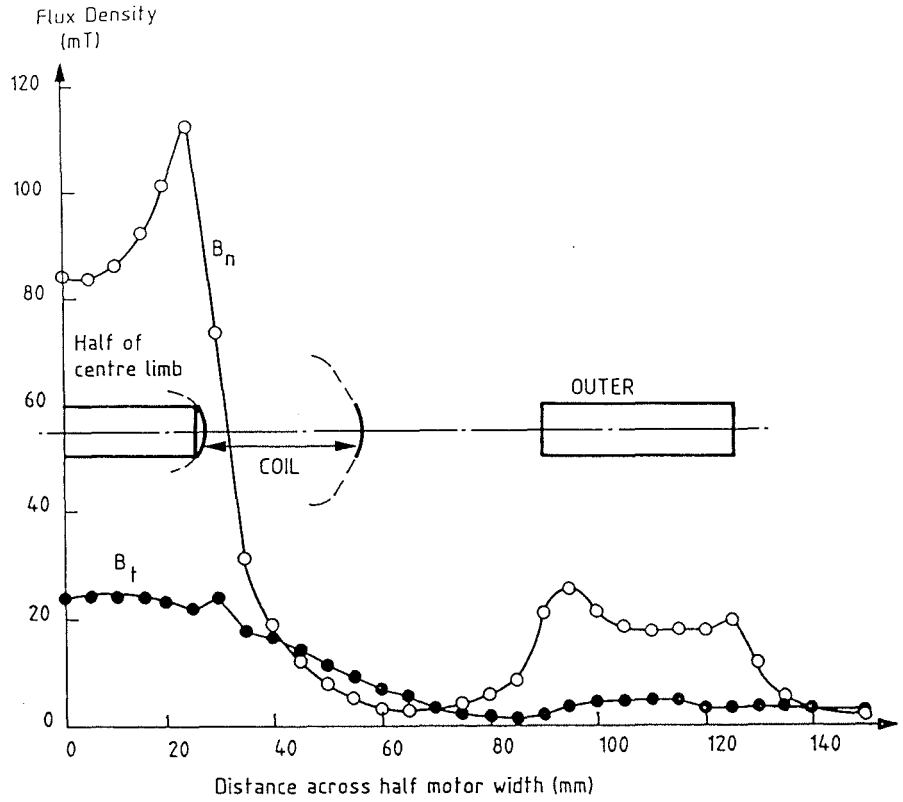

VARIATION OF FLUX DENSITY ACROSS HALF THE TFLIM MOTOR WIDTH AT 20 A/phase

Figure 6.13

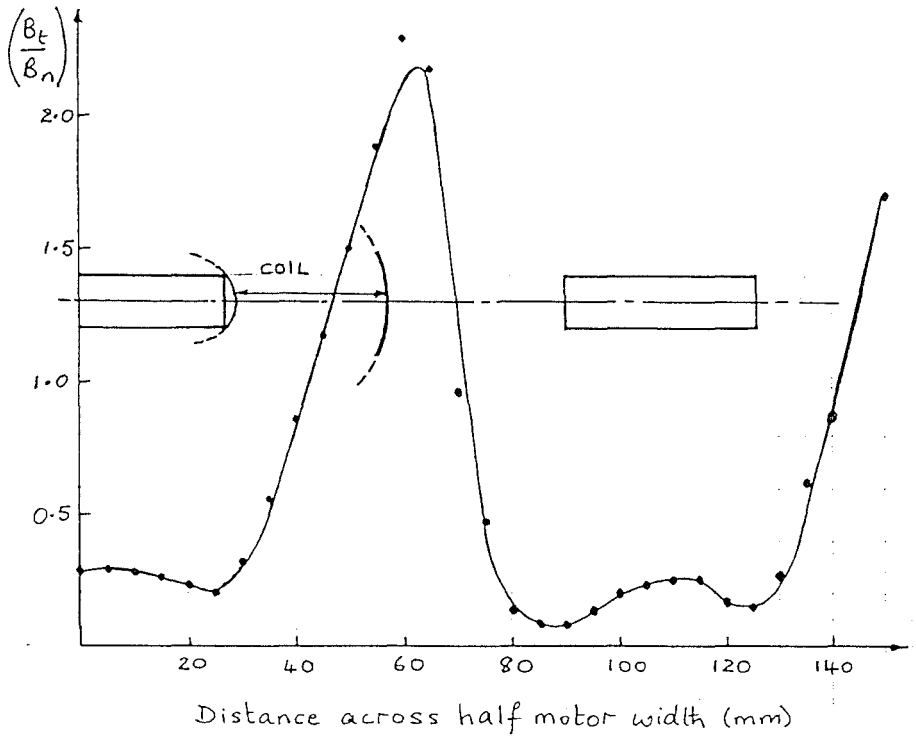

VARIATION OF THE (B_t / B_n) RATIO ACROSS HALF THE TFLIM MOTOR WIDTH AT 20 A/phase

Figure 6.14

implying that B_n, for the TFLIM, is inversely proportional to the height above the motor-face.

Flux density measurements at various heights at the edge and centre of a tooth and slot (Figs 6.16, 6.17 and 6.18) illustrate that the flux density falls off rapidly with increasing height, as also seen in Fig 6.15. They further show a mostly linear variation of both normal and tangential flux density with current. The waveforms of both B_n and B_t became progressively less sinusoidal and more triangular as the current increased, and as the current was increased further they became more nearly square. This trend was irrespective of the height at which the observations were made, although the distortion began at higher currents for both B_n and B_t at a greater height. The value of B_t at the surface of a slot was greater than B_n at the same position (see Figs 6.11, 6.12 and 6.16), but this changed with increasing height, as seen from Figs 6.17 and 6.18. At a height of 10 mm (Fig 6.17) B_n at a tooth centre is greater than at a tooth edge, because the flux at the edge of a centre-tooth has a low reluctance path to the sides of the tooth and therefore does not need to extend far into the airspace to complete a circuit. The flux from the centre of the tooth has, however, to extend further than the flux from the edge of the tooth to complete a circuit. At a height of 25 mm, B_n at a slot centre was greater than B_n at a tooth edge (see Fig 6.18) for reasons similar to that given above. (Line A in Fig 6.18 represents three graphs, as indicated on the diagram, which were all within ± 2 mT of each other.) The decrease in B_t with height is less marked than that of B_n, and the values of B_t were similar in magnitude except at the surface of the tooth and slot where the spread was about 30 mT at 50 A (Fig 6.16).

6.3.2 A 2 slots/pole/phase Winding

Further flux density measurements were made with the transverse flux motor wound as a 2 slot/pole/phase device, achieved by reconnecting the coils appropriately at the terminal rail to give:

```
R  R  y  y  B  B  r  r  Y  Y  b  b  R  R  y  .  .  .
      r  r  Y  Y  b  b  R  R  y  y  B  B  r  r  Y  .  .  .
```

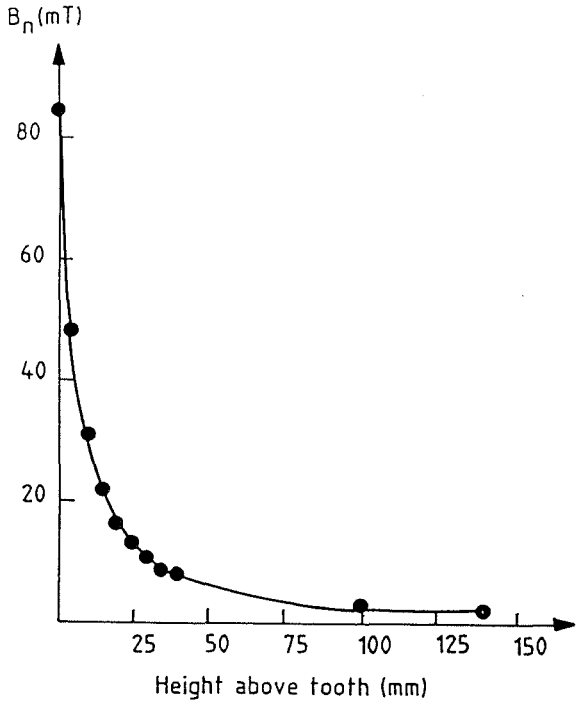

(a)

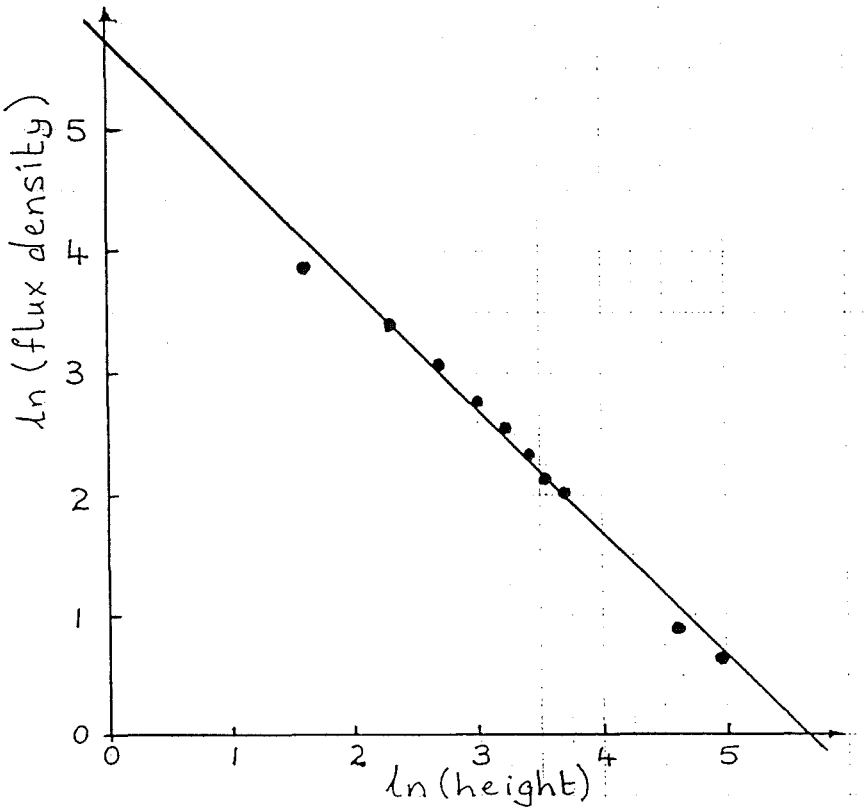

(b)

VARIATION OF B_n WITH HEIGHT ABOVE A TOOTH FOR THE TFLIM AT 20 A/phase

Figure 6.15

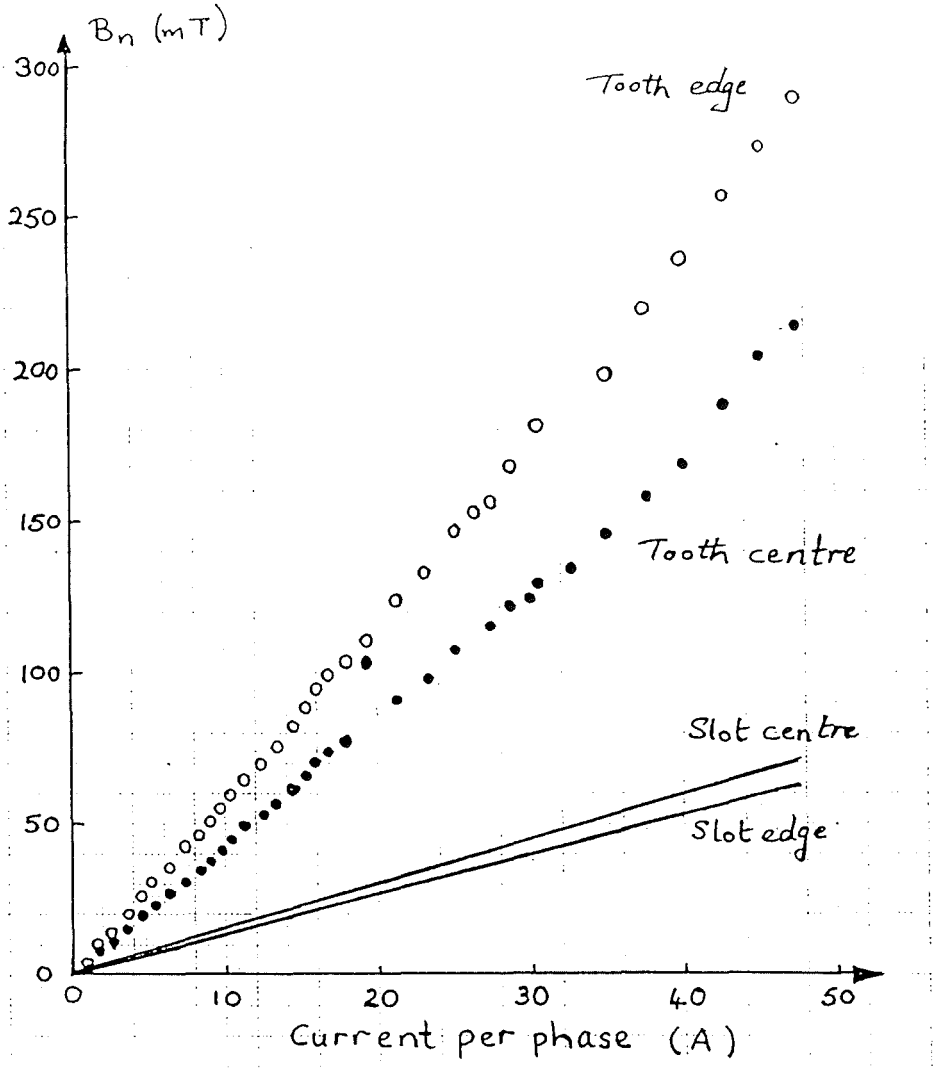

(a)

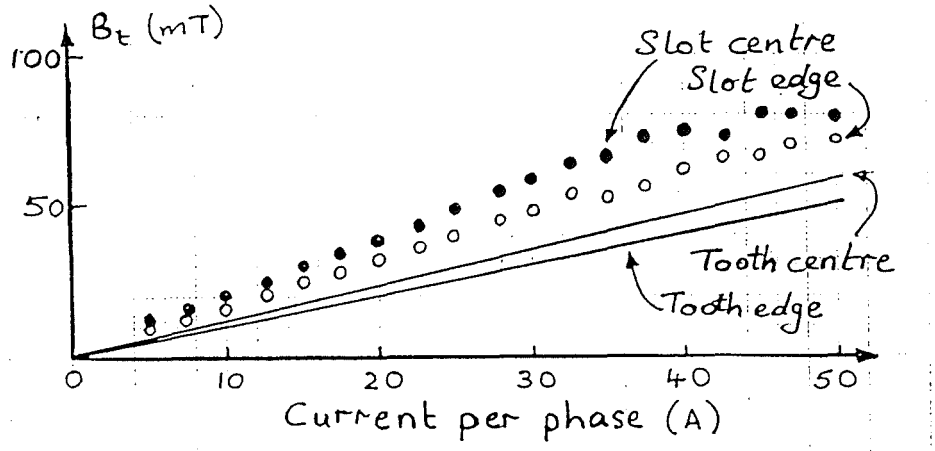

(b)

VARIATION OF FLUX DENSITY ALONG A TOOTH AND SLOT OF THE TFLIM AT ZERO HEIGHT

Figure 6.16

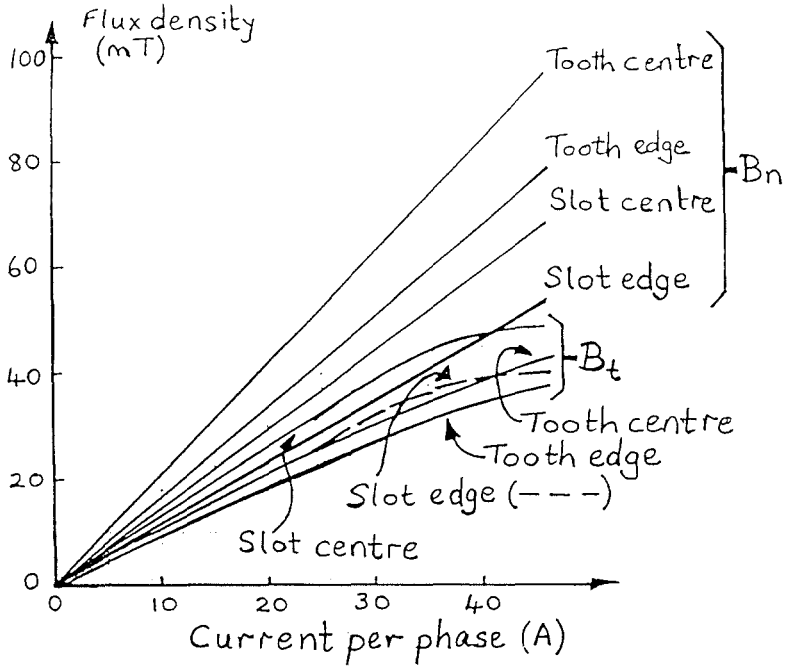

VARIATION OF FLUX DENSITY ALONG A TOOTH AND SLOT OF THE TFLIM AT A HEIGHT OF 10 mm

Figure 6.17

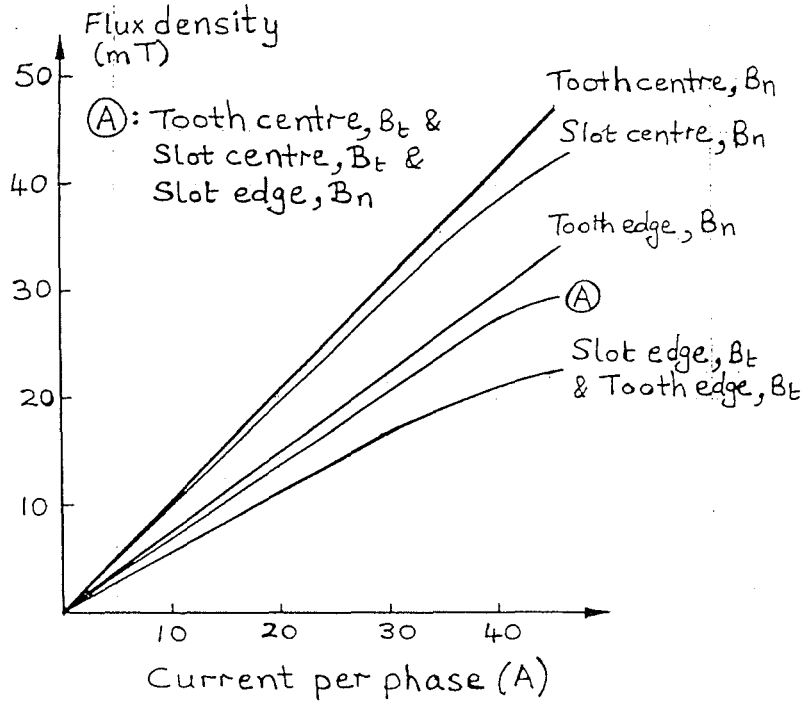

VARIATION OF FLUX DENSITY ALONG A TOOTH AND SLOT OF THE TFLIM AT A HEIGHT OF 25 mm

Figure 6.18

where each coil still spans two slots, but there are now 6 slots/pole and a winding factor of $^1/_3$.

Figures 6.19 and 6.20 show the decrease in flux density as the measurement height was increased. The approximately linear variation with current indicates that, at the currents involved, there was no saturation. Just as in the previous winding arrangement, the waveshape of B_n and B_t became progressively less sinusoidal as the current increased, which explains the scattering of the points on the graph of B_t at zero height for the tooth centre (Fig 6.19(b)). A closer study of these points reveals that the points upto 20 A lie on a straight line, and those from 25 A to 40 A lie on a second straight line. Between 20 A and 25 A, the waveshape of B_t became noticeably triangular and between 40 A and 45 A, it became almost square. The values plotted, however, were calculated assuming perfect sinusoidal waveshapes. At a height of 10 mm (Fig 6.20) the distortion was reduced and the assumption of a sinusoidal waveshape produced little error in any of the graphs.

As with the previous winding arrangement, at a height of 10 mm B_n at the tooth centre is greater than B_n at an edge, with this situation being reversed at zero height (see Figs 6.19(a), 6.20, 6.16(a) and 6.17). Changing the winding from 1 slot/pole/phase to 2 slot/pole/phase reduced the flux density by approximately 20%, and it was expected therefore that the powder flow would be reduced (that is, a reduced mass flow rate and less vigorous powder motion).

A plot of normal and tangential flux density and the ratio (B_t/B_n) for the teeth and slots is given in Fig 6.21 at zero height, 20 A/phase and at the centre of the teeth and slots. After the first few teeth and slots, when end effects are negligible, B_n at the slot centres is fairly constant at about 28 mT and alternates between approximately 73 mT and 54 mT for the teeth, with the larger value occurring at the odd-numbered teeth. The tangential flux density however, alternated between approximately 25 mT at the slot centres and 17 mT at the teeth centres. Of greater interest is a comparison of the tangential to normal flux density ratios for the 2 slots/pole/phase winding with those for the 1 slot/pole/phase winding. At the teeth the ratio is almost constant along the tooth for a 1 slot/pole/phase winding (see Fig 6.12), whereas it alternates for the 2 slot/pole/phase winding (see Fig 6.21) because of the change in the value of B_n between successive teeth. The (B_t/B_n)

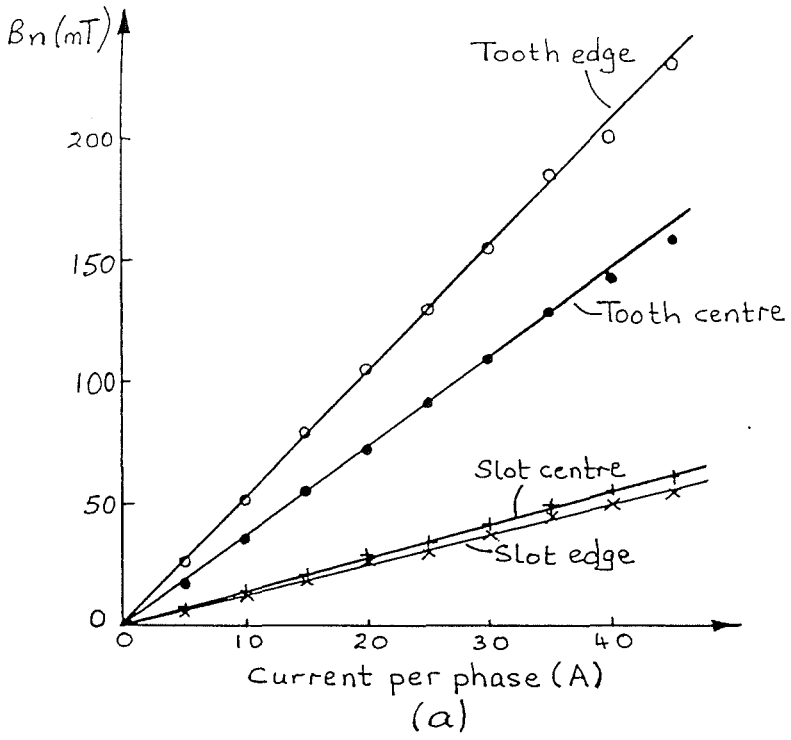

(a)

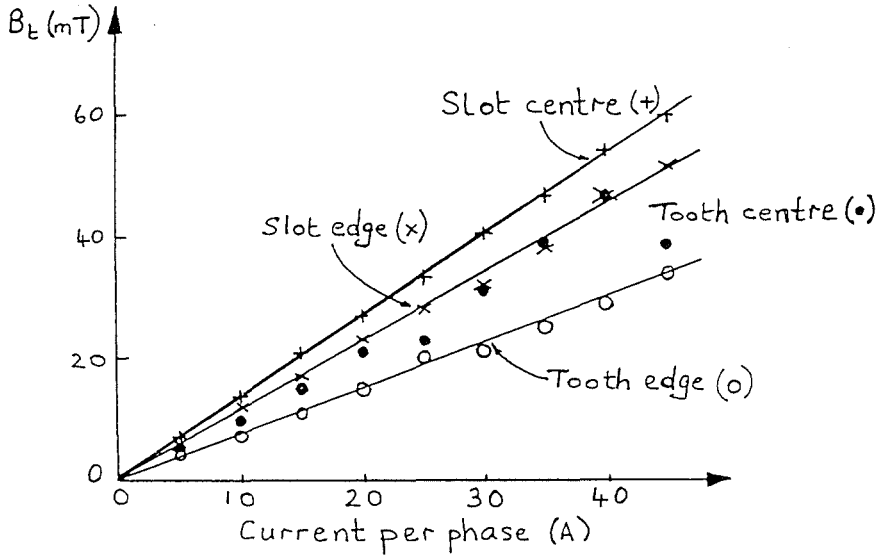

(b)

VARIATION OF FLUX DENSITY ALONG A TOOTH AND SLOT OF THE TFLIM WITH a 2 slot/pole/phase, $^1/_3$ - chorded WINDING AT ZERO HEIGHT

Figure 6.19

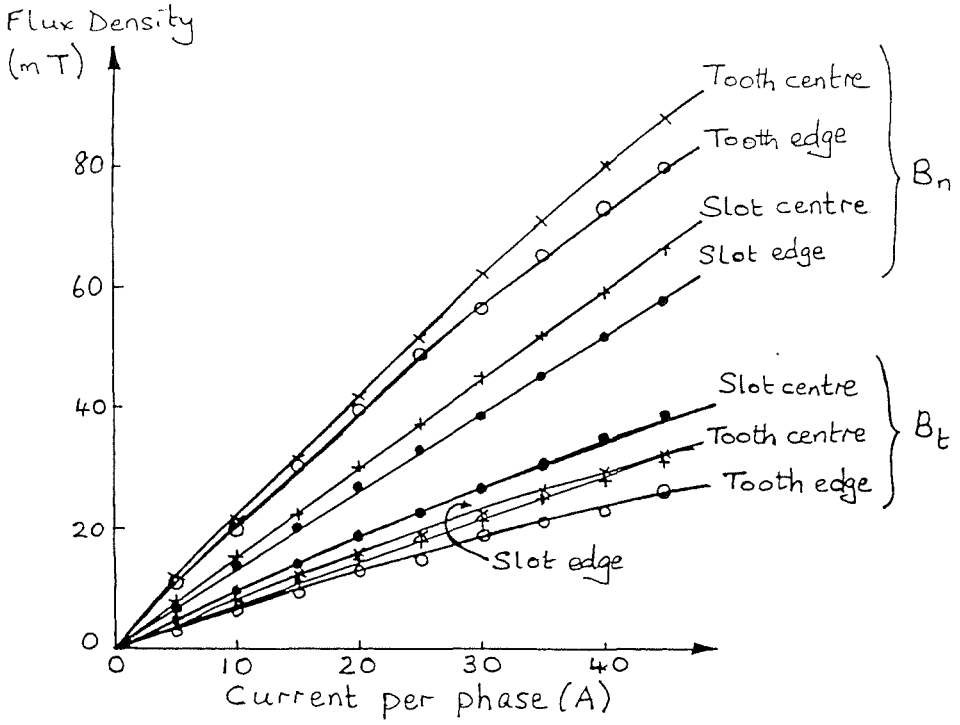

VARIATION OF FLUX DENSITY ALONG A TOOTH AND SLOT OF THE TFLIM WITH a 2 slot/pole/phase, $^1/_3$ - chorded WINDING AT A HEIGHT OF 10 mm

Figure 6.20

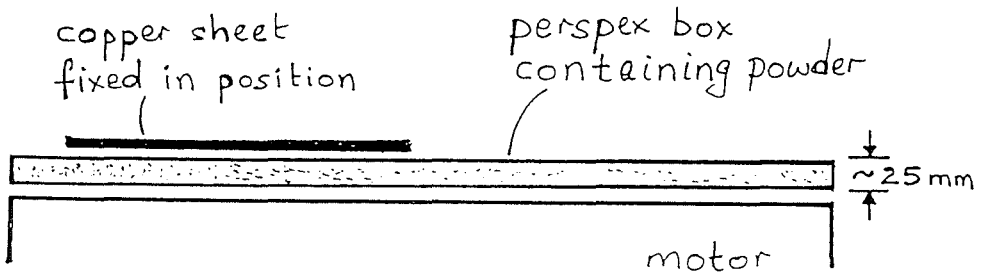

ATTEMPT TO INCREASE THE (B_t / B_n) RATIO

Figure 6.22

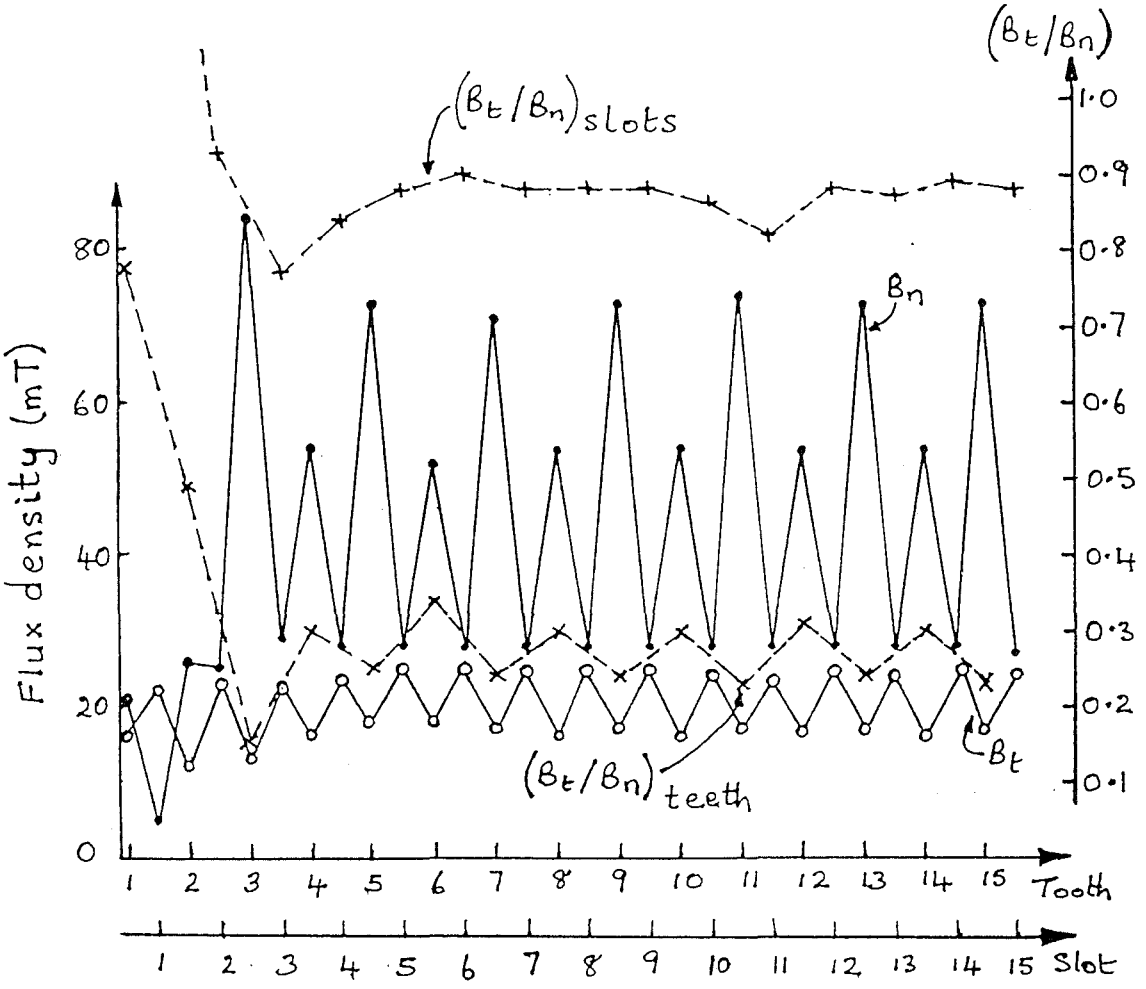

VARIATION OF FLUX DENSITY ALONG THE TFLIM WITH a 2 slot/pole/phase, $^1/_3$ - chorded WINDING AT 20 A/phase AND ZERO HEIGHT

Figure 6.21

ratio for the slots is nearly constant along the majority of the device, but it is considerably lower than the ratio for the 1 slot/pole/phase winding. These results suggest that the powder transport may be less good than the previous winding arrangement, since it is likely that the reduced (B_t/B_n) ratio for the slot would fail to convey the powder as effectively from tooth to tooth.

6.4 Mass Transport Rate Measurements

Powder motion over the transverse flux motor has already been described, and it was noted that as the current increased the powder travelled more vigorously. An attempt to increase B_t with respect to B_n was made by placing a copper sheet directly above a perspex box which contained the moving powder (Fig 6.22). (The eddy currents induced in the copper tend to decrease B_n and thereby to increase (B_t/B_n) for the particles.) The result was however inconclusive, as there was no significant change in the powder motion. It was thought that the copper sheet produced no significant difference in the ratio (B_t/B_n).

Several mass transport rate measurements were made in a similar way to those for the tubular motor (see Chapter 4), with an area of the transverse flux motor designated as the start of the device consisting of the first three teeth and slots. Powder was placed over the centre limb of the first tooth and the adjacent slot, and for the next two teeth and slots powder was spread across the whole motor-width such that it was above the two outer limbs and the adjacent slots. (Powder motion from the outer to the centre limbs takes place as previously described.) The powder was, therefore, above the first two half-filled slots and above the first fully-filled slot, that is, above a pole-pitch for the 1 slot/pole/phase winding (see Fig 6.6). Similarly, an area of the motor designated the exit end of the device was considered to start at tooth twenty two and to continue to the end, and therefore consisted of almost two pole-pitches (Fig 6.6). The remainder of the motor, that is, the area between these two extremes, was taken to be the middle of the device, where the powder was still considered to be in transit.

Once the experimental set-up was defined, mass transport rate measurements were made by spreading evenly a known mass of powder at the entry end, and recording the amount

at the entry and exit ends and along the middle of the device at successive time instants for a fixed phase current. Measurements were made with different powders at varying heights, mostly at 40 A/phase since observations had already shown that higher currents produced more vigorous, faster and greater powder motion. From these results the cumulative mass flow rate ($\dot{m}_c$) and the powder distribution over the motor may be calculated, and the results are given in detail in Appendix F.

6.4.1 A 1 slot/pole/phase Winding

Using a 1 slot/pole/phase winding, 250 g of iron powder (the Fe filings of Chapter 3) were placed at the entry end of the TFLIM (as described above) and their mass transport rate was measured at heights of zero, 10 mm and 25 mm. Powder was collected from the three designated collection areas at different times, and the results are given in Fig 6.23.

At zero height, it was observed that virtually all the powder had travelled to the end of the device after 45 s, with over 90% having travelled after the first 30 s. The results for a height of 10 mm were similar, as highlighted by Fig 6.23(d), showing that the cumulative mass transport rates for heights of zero and 10 mm were practically identical, with both attaining a maximum of approximately 140 kg/hr and the majority of the powder travelling in the first few seconds. At a height of 25 mm, Fig 6.23(c) shows that the powder transported linearly with time and after about 15 s the amount of powder along the central portion of the motor was not depleted. All three graphs (Fig 6.23(d)) are similar in shape, with a straight section before the cumulative rate begins to fall. This levelling off is due primarily to the depletion of powder at the start of the device. At a height of 25 mm, the amount of powder along the middle of the machine remained approximately the same, while powder at the start of the motor transferred to the end. Compared to the heights of zero and 10 mm, less powder travelled at any given time but it transferred steadily, whereas at the lower heights the vast majority transported in the first few seconds, with a net flow from both the start and middle of the motor after the first few seconds. At 25 mm height, the cumulative mass flow rate began levelling off at approximately 112 kg/hr and several seconds later compared to both 0 mm and 10

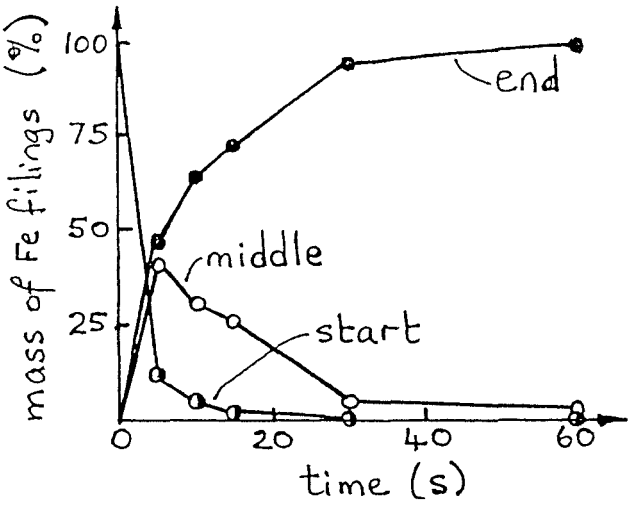

(a) h = 0 mm

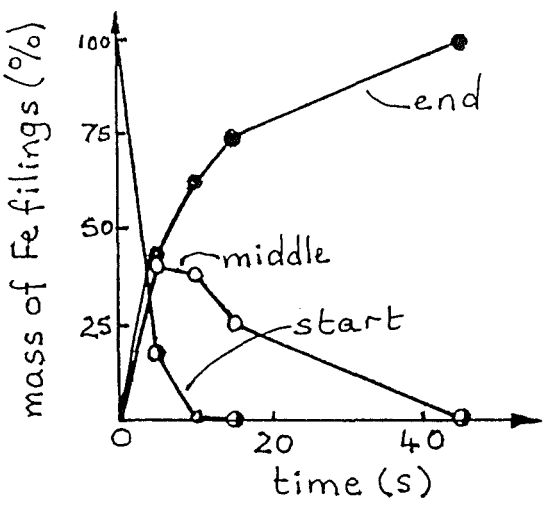

(b) h = 10 mm

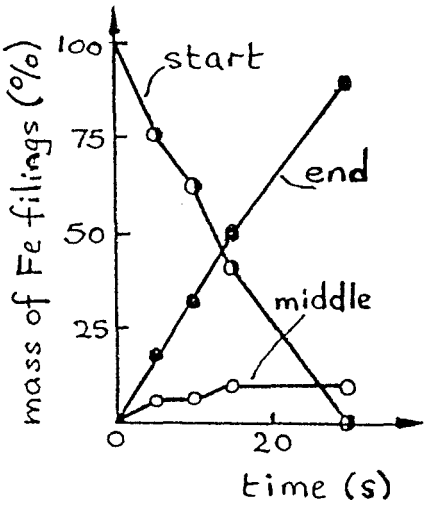

(c) h = 25 mm

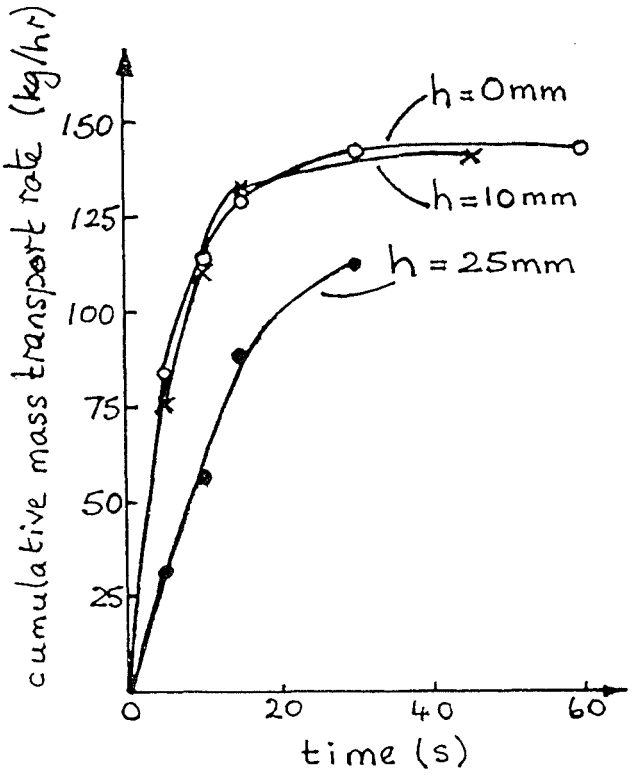

(d)

TRANSPORT CHARACTERISTICS OF Fe FILINGS ON THE TFLIM
WITH a 1 slot/pole/phase WINDING AT 40 A/phase AND VARIOUS HEIGHTS

Figure 6.23

mm, which began levelling off at approximately 130 kg/hr and about 15 s after switch-on.

Powder AISI 430

Motion of AISI 430 powder also improved with increasing current, but it blocked more easily than the iron filings, that is, it formed ridges which hindered the powder transport. Frantic particle activity was seen at the back and along the outermost edges of the ridges. It was also observed that the AISI particles were better contained within the magnetic field when compared with the iron filings which tended to be thrown to the sides of the device. As before, measurements of the transport characteristics were taken for heights of zero and 10 mm (see Fig 6.24), since at 25 mm the powder motion was observed to be poor.

The transport of AISI at 0 mm and 10 mm was similar, with all graphs (Fig 6.24) having a similar shape but varying by about 10% for the two heights. In both cases, approximately 50% of the powder reached the end of the device after about 15 s. The mass flow rate then levelled off, with powder at the end of the motor building up and that in the middle of the motor depleting, linearly with time for both heights, and after about 20 s little powder was left at the start. At a height of 10 mm, the powder at the start of the device rose slightly at 30 s compared to 20 s, due to some being drawn back from the middle area of the motor. Compared to the flow of iron filings, AISI travelled more slowly (over an interval of 20 s, the iron filings at 25 mm height progressed better than AISI at zero height) and were spread more evenly over the motor than the iron filings at any given time, and a greater quantity of the iron filings reached the end of the machine.

Powder Ni/Fe 50/50

This soft magnetic powder did not transport well, having a cumulative mass transport rate of about one-third that of the iron filings (see Fig 6.25). Ridge formation occurred more easily and quickly than with AISI powder, which reduced the mass transport rate (Fig 6.25(b)). Due to this only 200 g of powder was used when making the measurements, as opposed to 250 g for the previous two powders. The transport rate is low because this powder is magnetically soft; the travelling field of the TFLIM was able to magnetise and

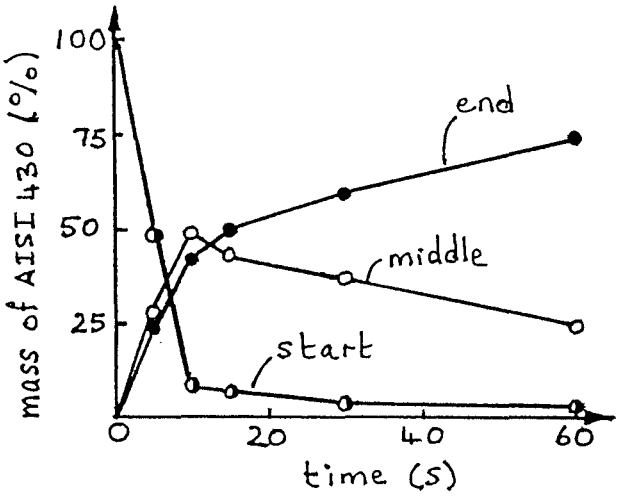

(a) h = 0 mm

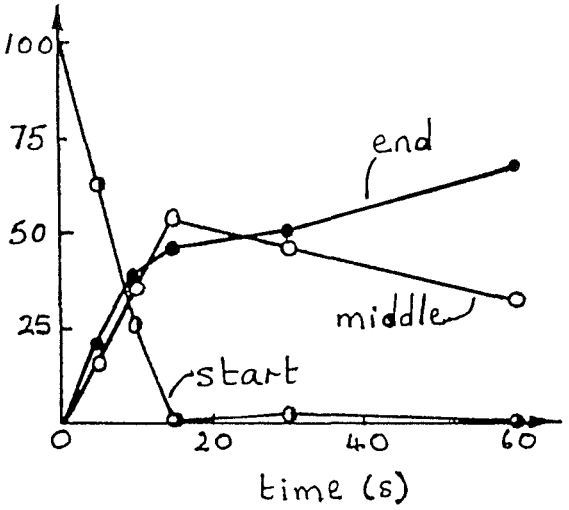

(b) h = 10 mm

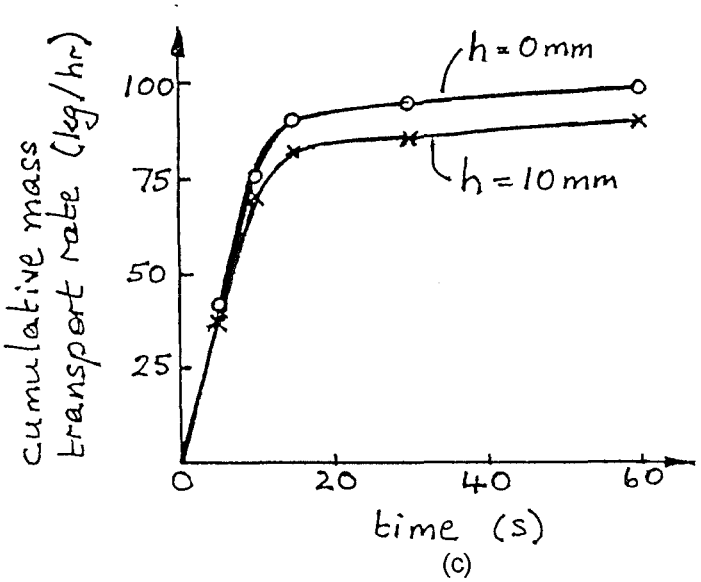

(c)

TRANSPORT CHARACTERISTICS OF AISI 430 POWDER ON THE TFLIM WITH a 1 slot/pole/phase WINDING AT 40 A/phase AND VARIOUS HEIGHTS

Figure 6.24

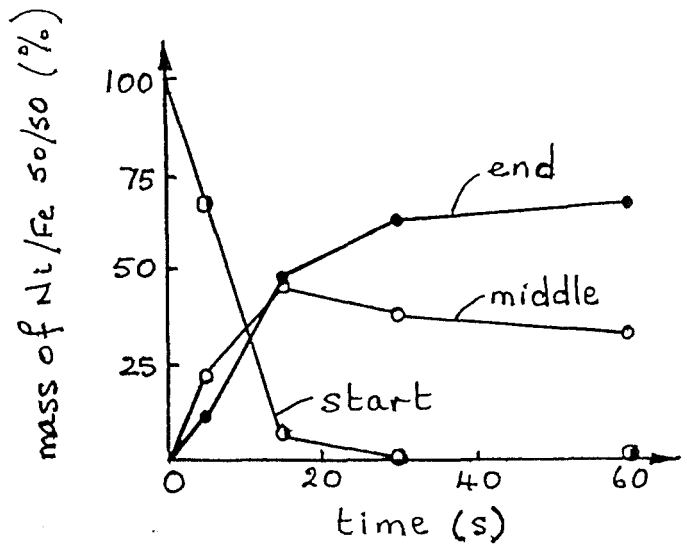

(a) h = 10 mm

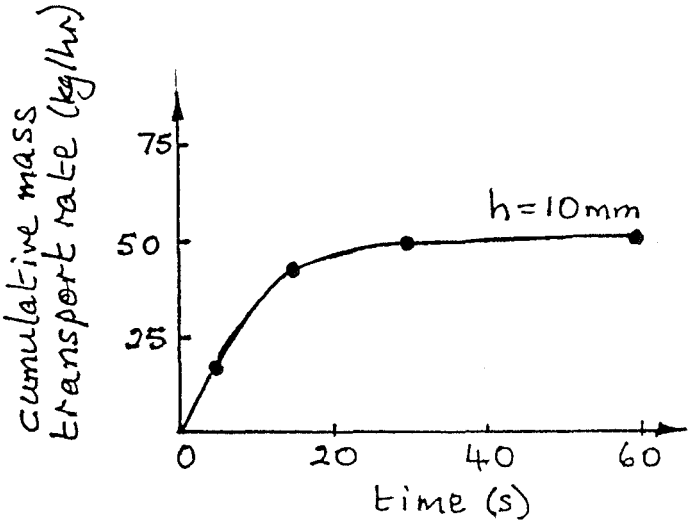

(b)

TRANSPORT CHARACTERISTICS OF Ni/Fe 50/50 POWDER ON THE TFLIM WITH a 1 slot/pole/phase WINDING AT 40 A/phase AND 10 mm HEIGHT

Figure 6.25

re-magnetise the particles more easily causing them to "stick" to each other and to the motor.

The cleaning application of linear machines was demonstrated on the transverse flux motor by placing "dirty" ferromagnetic powder at the start of the device. After only a few seconds a significant amount of sand was left, with the majority of the iron powder at the end of the device. An inverted TFLIM would be better suited to cleaning ferromagnetic powder, since there would be less likelihood of impurities being carried along with the iron particles, indeed they would fall under gravity away from the influence of the travelling field (as already discussed in Chapter 3).

6.4.2 A 2 slots/pole/phase Winding

With the TFLIM wound with 2 slots/pole/phase, the device had four poles, 6 slots/pole, 8 coils/phase and a winding factor of $^1/_3$.

AISI 430 powder at zero height and 40 A/phase transported in a similar manner to the previous 1 slot/pole/phase, $^2/_3$-chorded winding arrangement, although the ridge formation appeared to be worse. In the middle of the transverse flux device, powder tended to bunch on alternate lamination teeth (see Fig 6.26) which may be explained by reference to Fig 6.21 which illustrates the alternating nature of the flux density for the teeth.

At a height of 5 mm the powder transport was reduced below that at zero height, and the powder no longer tended to congregate on alternate teeth. Instead a new effect was observed at the end of the device where ridges formed and spread across the centre teeth and slots to the outer teeth and slots of the motor. A powder build up at the end of the machine, which spanned the gap between the centre and outer teeth, travelled backwards (i.e. against the main powder flow) in sheets for a distance of a few slots and then rotated back into the influence of the centre teeth before continuing to transport once more to the end of the device (see Fig 6.27). At the end, the flux leaves the last few lamination stacks and returns via stacks just prior to these, and the powder which has built up and formed ridges extending to the outer teeth follows this path to produce the motion just described.

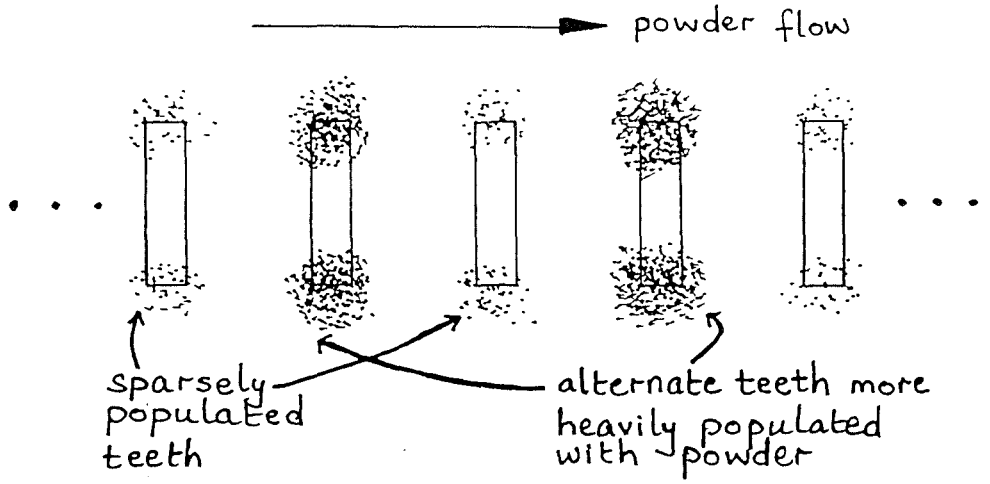

PARTICLE BUNCHING ON THE TFLIM WITH a 2 slots/pole/phase WINDING

Figure 6.26

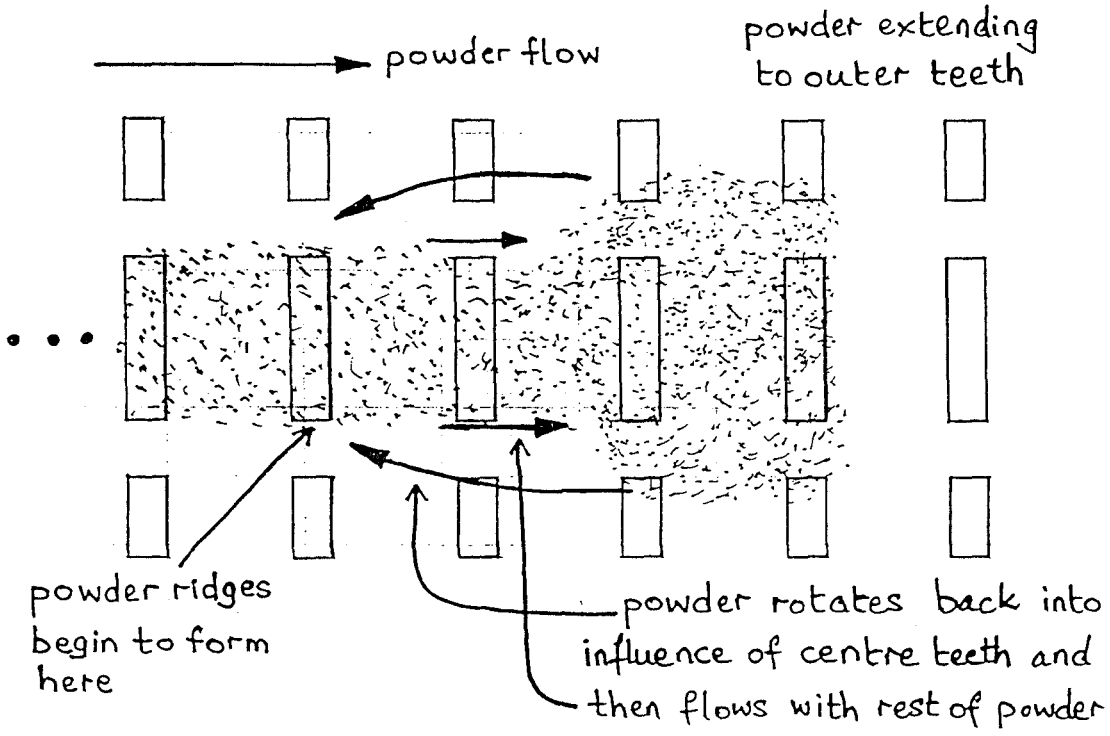

POWDER MOTION ON THE TFLIM WITH a 2 slots/pole/phase WINDING AT 40 A/phase AND 5 mm HEIGHT

Figure 6.27

Increasing the height to 10 mm significantly reduced the powder flow rate and neither of the above motion effects (particle-bunching or the motion end-effect) were seen. Ridges, however, still continued to form.

Mass transport rate measurements conducted at 40 A/phase and heights of zero and 10 mm with AISI powder exhibited similar transport characteristics (see Fig 6.28) to the previous measurements. Comparing the motion of AISI powder at 2 slots/pole/phase with its motion at 1 slot/pole/phase (Fig 6.24) shows little difference in the cumulative flow rate for zero height, but considerable difference in the powder distribution. In both cases approximately 75% of the powder reached the end of the device after 60 s, but at 2 slots/pole/phase (Fig 6.28(a)) there was an equal amount of powder (about 10%) at the start and in the middle of the motor, whereas at 1 slot/pole/phase (Fig 6.24(a)), there was virtually no powder left at the start. At 2 slots/pole/phase, the cumulative mass transport rate was about 20% greater at approximately 120 kg/hr than that at 1 slot/pole/phase after 60 s.

Differences between the transport characteristics at a height of 10 mm were more marked: with 2 slots/pole/phase, the mass transport rate was less than half that at zero height and only two-thirds that with 1 slot/pole/phase. Figure 6.28(b) shows clearly that less than half the powder reached the end of the device, with the majority still not having left the start. This transport graph is different to the others as it shows very little powder in transit at any instant, with the mass of powder in the middle of the device never being more than 4% of the total. The other graphs illustrate that powder built up at the end and in the middle quickly, and that the amount of powder in the middle depleted as the powder at the start also depleted. At this height of 10 mm, virtually no powder was transported to the end of the motor after about 15 s, as shown by Fig 6.28(c).

From the flux density graphs in Figs 6.21, 6.10 and 6.11, the flux density values are reduced for the 2 slots/pole/phase compared to the 1 slot/pole/phase winding, but with the (B_t/B_n) ratio above the teeth increasing by approximately 20% and above the slots decreasing by over 33% (see Figs 6.12 and 6.21). The improved powder motion at zero height with a 2 slots/pole/phase winding follows since, even though the flux density values were reduced, they remained sufficient to magnetise the particles, and the increased pole-pitch carried the particles further in less time than with a 1 slot/pole/phase

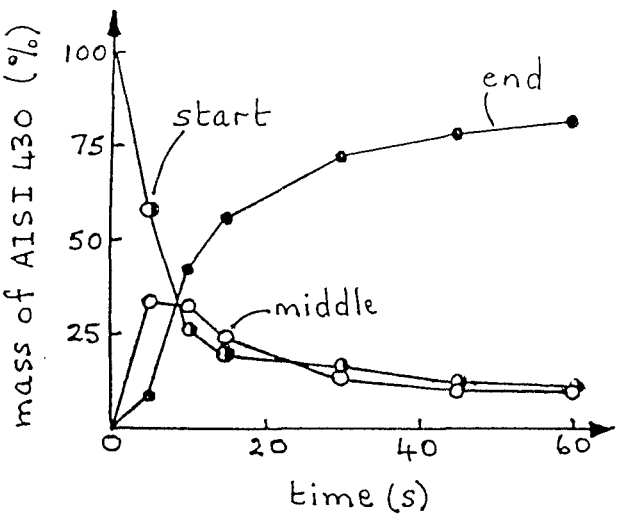

(a) h = 0 mm

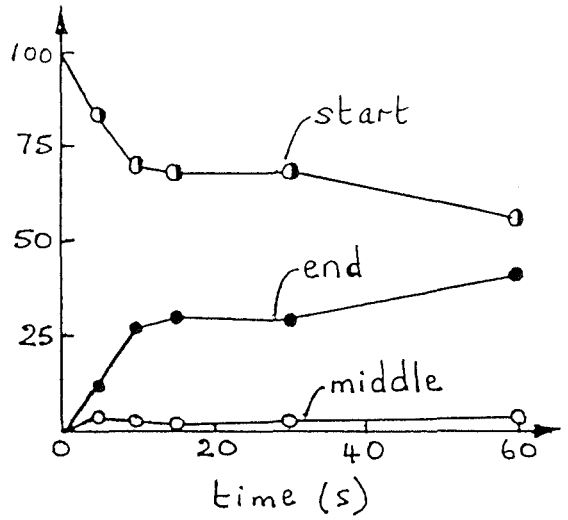

(b) h = 10 mm

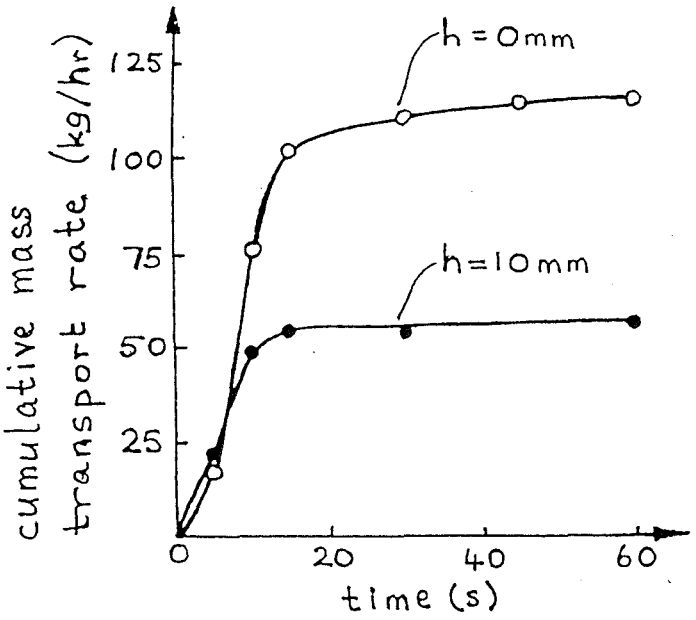

(c)

TRANSPORT CHARACTERISTICS OF AISI 430 POWDER ON THE TFLIM WITH a 2 slots/pole/phase WINDING AT 40 A/phase AND VARIOUS HEIGHTS

Figure 6.28

winding. Since the (B_t/B_n) ratio above the slots is high for both winding arrangements, a decrease in this is likely to have little effect on powder transportation, but the increase in the ratio above the teeth gives an improvement in powder flow. The reduced mass flow rate at 10 mm height with a 2 slots/pole/phase winding is because the flux density was insufficient to magnetise many particles at any one time. It is normally expected that a greater pole-pitch throws flux further into the airgap, but in this case the chording factor was only $^1/_3$ (rather than $^5/_6$ or full-pitched as is usual for this winding). Additionally, the flux density values had dropped by some 15 to 30% over the previous 1 slot/pole/phase winding, thereby significantly reducing the airgap flux density with increasing height.

6.5 An Inverted Transverse Flux Machine

It was noted earlier that an inverted transverse flux machine may have a better performance for transporting ferromagnetic powder than a standard machine. A second transverse flux machine was therefore constructed with the same winding scheme, that is, 1 slot/pole/phase and $^2/_3$-chorded. A frame to support the device was mounted on threaded steel rods such that the device could be raised or lowered to enable the effect of different airgaps to be studied. A sheet of bakelite spanning the entire length and width of the machine was fixed to the active face of the device, thus retaining the coils in the slots. Mass transport rate measurements were made as before at two different initial airgaps, 56 mm and 32 mm, with the powder placed in a perspex box of appropriate height.

Figure 6.29 shows that the initial mass transport rate for the two different airgaps was approximately the same. With an initial airgap of 56 mm (Fig 6.29(a)), it was expected that the flow rate would decrease considerably, because after 30 s little powder was transported from the start to the middle of the device. In both cases, the powder was attracted to the inverted transverse flux machine and transported along the lid of the box containing the powder, as for the powder cleaner (Chapter 3). Although the initial airgaps were different, the airgap during powder transport was the same at approximately 6 mm (due to the bakelite sheet and construction necessary for the inverted machine). At 56 mm, the flux density was insufficient to draw powder in from the sides of the box

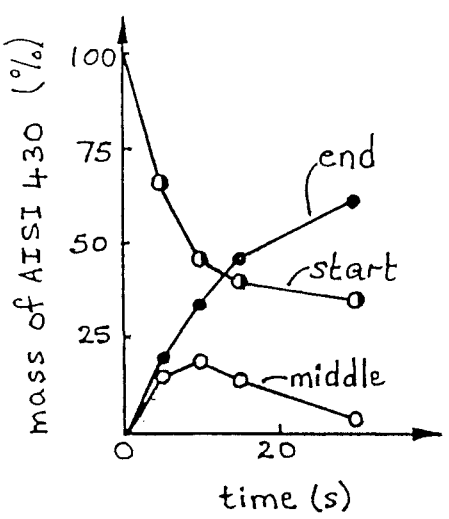

(a) initial airgap = 56 mm

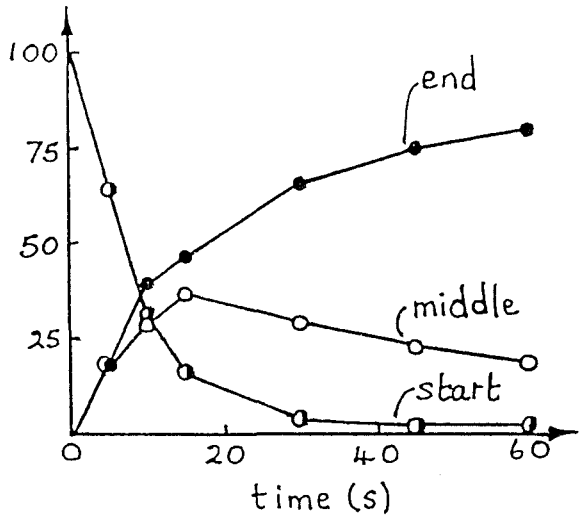

(b) initial airgap = 32 mm

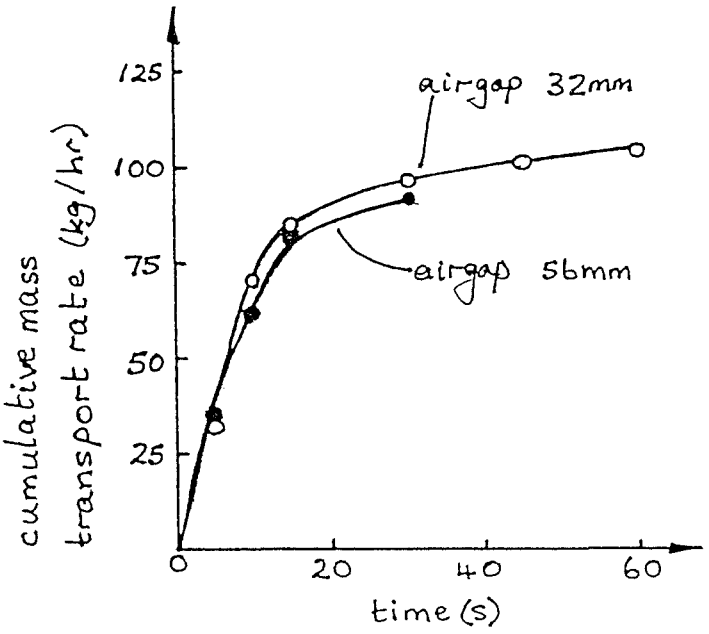

(c)

TRANSPORT CHARACTERISTICS OF AISI 430 POWDER ON THE INVERTED TFLIM WITH a 1 slot/pole/phase WINDING AT 40 A/phase

Figure 6.29

(such motion was described earlier) although it was sufficient at 32 mm. This explains the larger mass flow rate at 32 mm and also the powder distribution, which shows that after 30 s there was less than 5% of the original mass of powder left at the start of the device.

For both experiments, ridges formed and hindered powder transport. For the 32 mm container, the powder ridges attempted to grow beyond the depth of the container and, being unable to do so, increased in length along the motor, thereby considerably hindering the powder flow. It was evident that, if the ridges had been free to grow in height, the mass transport rate would have been greater than that measured. Ridge formation was less severe for the 56 mm container due to its larger depth, which allowed the ridges to grow in height so that they did not significantly increase in length. This suggests that an arrangement similar to that for the powder cleaner (see Chapter 3) could be very effective, since powder at the "exit" end could be removed from the transverse flux motor and powder at the "entry" end could be introduced at a suitable height to aid the powder flow.

Comparison of Figs 6.29 and 6.24 shows that the mass flow rate for the inverted machine was initially less than that of the non-inverted machine, reaching a value of 70 kg/hr compared with 76 kg/hr after 10 s. The flow rate however continued to increase for both machines, but at a greater rate for the inverted than for the non-inverted machine, achieving a cumulative flow rate of approximately 106 kg/hr compared with approximately 96 kg/hr. The airgap during powder transport has already been noted to be about 6 mm longer than for the non-inverted motor, but an improved construction to reduce this and a more suitable airgap for introducing powder into the motor's influence would increase the mass transport rate for the inverted TFLIM. Such changes would aid the powder flow from the start to the middle of the motor and, powder ridges permitting, increase the flow from the middle to the end of the machine.

6.6 The Double-sided Transverse Flux Machine

It was straight-forward to make a double-sided transverse flux linear induction machine (DSTFLIM) by placing the inverted TFLIM above the non-inverted TFLIM. The two machines were series connected with the teeth of one device directly opposite those of the other. Both machines were wound with 1 slot/pole/phase, $^2/_3$-chorded and, initially, N-poles faced S-poles, which was expected to result in a poor powder flow. A second experiment was conducted with N-pole facing N-pole and S-pole facing S-pole, thus producing an axial flux DSTFLIM, when powder transport was expected to be better than for both the standard DSTFLIM and the single-sided TFLIM, whether inverted or not. The experimental scheme used for both the standard and axial flux double-sided transverse flux motors is shown in Fig 6.30.

6.6.1 The Standard DSTFLIM

A box height of 26 mm was initially used for observing the powder motion. The powder did not transport well, traversing only approximately one-fifth of the machine length and quickly bridging the airgap between opposing poles of the two transverse flux motors by forming pillars (see Fig 6.31) on the teeth of the DSTFLIM. The airgap between the two motors was closed almost immediately at switch-on by a small number of particles. Other particles then added to those that had already closed the gap, producing a number of pillars along a small section of the machine. The travelling field did not transport the powder to any great extent as the powder was strongly attracted to the teeth; in other words the tangential flux density was insufficient to cause the powder to flow along the length of the machine.

Powder transport was a little better with the 50 mm box (see Fig 6.30), since some powder did transport the length of the machine. Ridges however quickly formed, slowing down the powder transport and, as these grew in height, the particles were able to bridge the airgap between the two motors. As for the other transverse flux machines, the powder that did transport travelled along the centre limb of the machine.

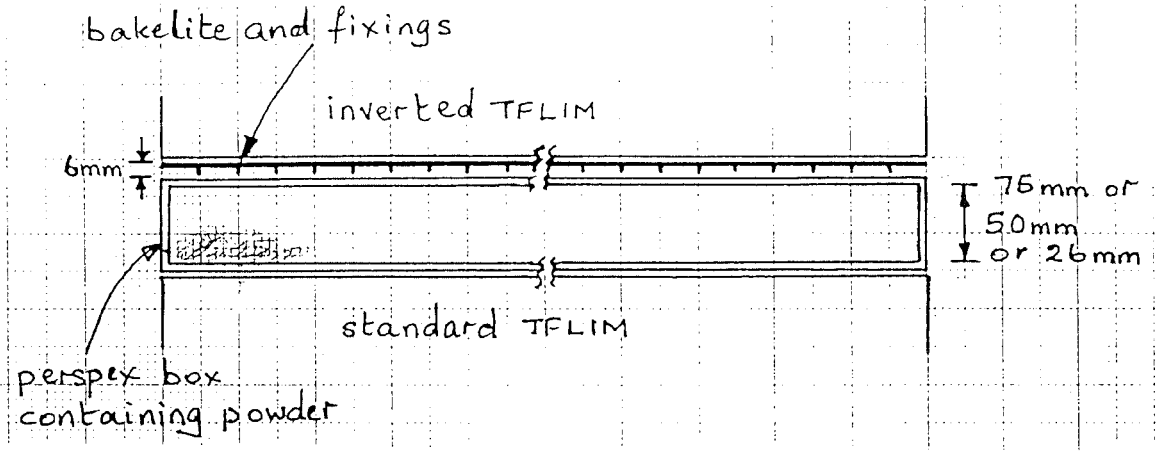

THE EXPERIMENTAL DSTFLIM

Figure 6.30

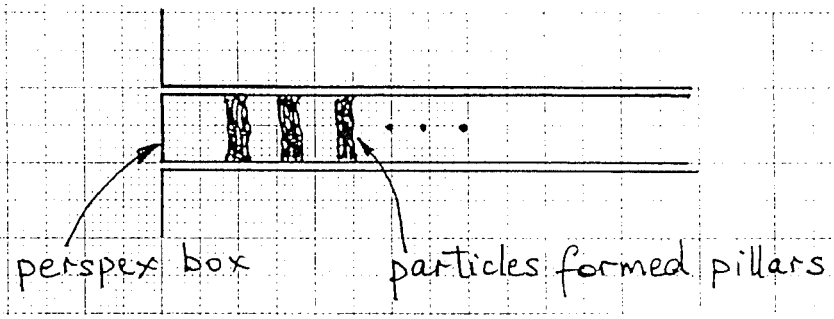

POWDER MOTION IN THE 26 mm BOX FOR THE STANDARD DSTFLIM

Figure 6.31

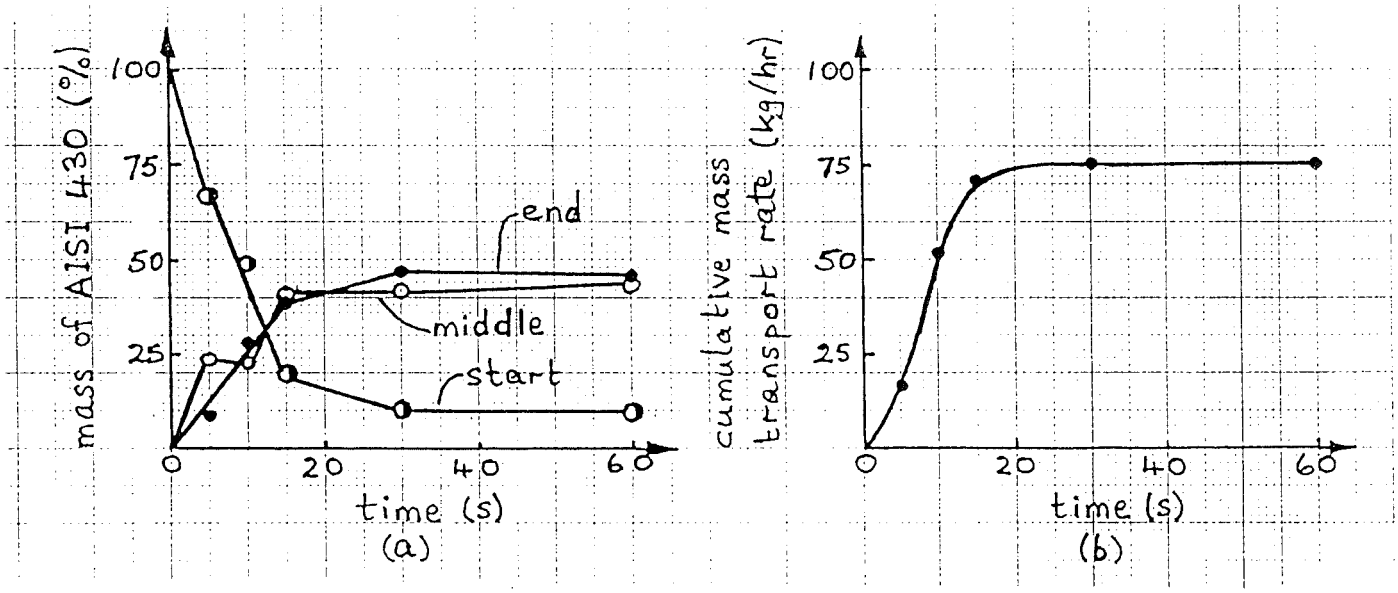

TRANSPORT CHARACTERISTICS OF AISI 430 POWDER ON THE STANDARD DSTFLIM
WITH a 1 slot/pole/phase WINDING AT 35 A/phase

Figure 6.32

Finally a box height of 75 mm was used, and information on the powder transport readings is presented in Fig 6.32 and Appendix F. Despite the poor mass flow rate, the powder motion had similar characteristics to those in the previous TFLIM arrangements, with most of the powder that transported doing so in the first few seconds. Figure 6.32(a) illustrates that the powder was spread across most of the length of the machine, with less than 50% reaching the end. Comparison of Fig 6.32 with Figs 6.29, 6.28 and 6.24 shows that, in this case, once a certain amount of powder had reached the end, no more powder travelled from either the start or the middle of the machine. This is clearly seen by the plateau of the cumulative mass transport rate graph (Fig 6.32(b)), whereas previously the mass transport rate continued to rise steadily, albeit slowly. With this connection of the transverse flux motors the powder transport with a 75 mm box height was better than expected, which is explained by the particles being mostly transported by the lower non-inverted TFLIM and the travelling field of the inverted TFLIM having considerably less effect. Some powder did however travel on the underside of the lid of the perspex box, due to the field of the inverted motor. The effect of the inverted TFLIM with this box height cannot be considered negligible, because ridge formation was clearly worse than with a single TFLIM and pillars of powder, similar to those with the smaller box height, attempted to form. They finally did so at the end of the device, where the usual ridge formation aided the pillar formation since the ridges had already partly bridged the airgap between the two motors.

The mass flow rate in Fig 6.32(b) would have been improved if the power supply had been able to provide 40 A/phase, as in the previous cases. Although the flow rate was better than expected, the powder distribution was less good than before (see Figs 6.32, 6.29, 6.28 and 6.24), because large amounts of powder remained at the start and middle of the machine. The powder transport characteristics of the standard DSTFLIM do however resemble those for the single-sided arrangement with a 2 slots/pole/phase winding at 10 mm height (Fig 6.28). Approximately similar amounts of powder travelled to the end, and the initial mass flow rates are almost identical over the first 10 seconds. The graph at 10 mm heigh of Fig 6.28(c) also has a plateau for the same reason given above, even though powder clearly transported from the start to the end during the last 30 s, as shown in Fig 6.28(b). This powder transport however does not significantly affect the mass transport rate because only a relatively small amount of powder is transported during a relatively long interval. With the DSTFLIM (Fig 6.32), the powder

continued to transfer to the end at a greater rate than in Fig 6.28(b) after the first 10 s, attaining a cumulative flow rate of approximately 75 kg/hr compared with about 57 kg/hr for the non-inverted TFLIM at 2 slots/pole/phase. This is again explained by the particles travelling mostly due to the lower TFLIM, with an airgap therefore of zero.

6.6.2 The Axial Flux DSTFLIM

With the double-sided device connected such that N-pole faced N-pole and S-pole faced S-pole, an axial field (similar to that produced by the tubular machine discussed in Chapter 4) was produced and a 1 slot/pole/phase, $^{2}/_{3}$-chorded winding arrangement was used. This was an attempt to increase the tangential component of flux density with respect to the normal component. A preliminary test with the different box heights (see Fig 6.30) showed that powder motion was best with the 50 mm box, and this was accordingly used for the experiment.

As the powder was closer to the non-inverted transverse flux motor, the powder travelled predominantly along the centre-teeth of this motor. Ridges again formed but they were not so large or as quick to form as on the single-sided TFLIM. Pillars of powder did not form, as the field did not aid such powder flow. Powder transport readings with a 50 mm box and at 39 A/phase are presented in Fig 6.33 and Appendix F.

Figure 6.33(a) shows a steady increase of powder reaching the end of the device over a 60 s interval, with sharp decreases in the powder distribution both along the middle and at the start of the device. The mass flow rate (see Fig 6.33(b)) exhibits a similar shape to the other cumulative mass transport rate graphs, except that it is less steep at the start and does not have a distinct knee at about 20 to 30 s.

When Fig 6.33 is compared with the other experimental schemes (see Figs 6.24, 6.28, 6.29 and 6.32) it can be seen that the powder distribution is improved, since nearly all the powder reaches the end of the device and very little is spread out along the middle and at the start. The experiment with the non-inverted TFLIM at 2 slots/pole/phase (Fig 6.28) and zero height had a fairly good powder distribution, but after 60 s 20% of the powder had still failed to travel to the end of the device compared with less than 10% for the axial flux DSTFLIM. Powder flow to the end is mostly linear for the non-inverted

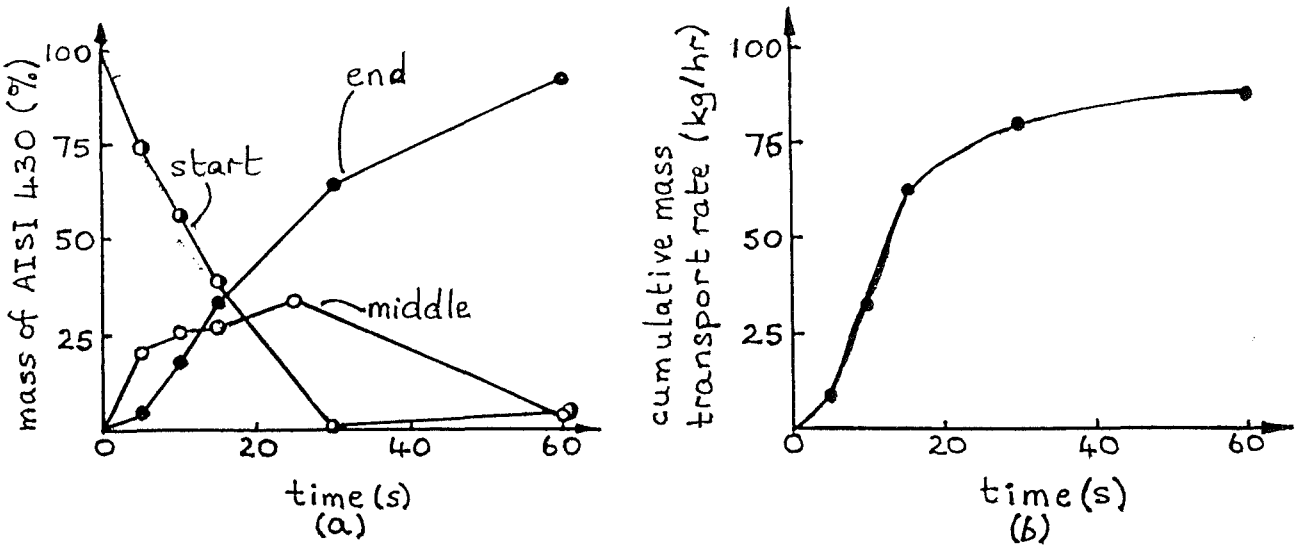

TRANSPORT CHARACTERISTICS OF AISI 430 POWDER ON THE AXIAL FLUX DSTFLIM WITH a 1 slot/pole/phase WINDING AT 39 A/phase

Figure 6.33

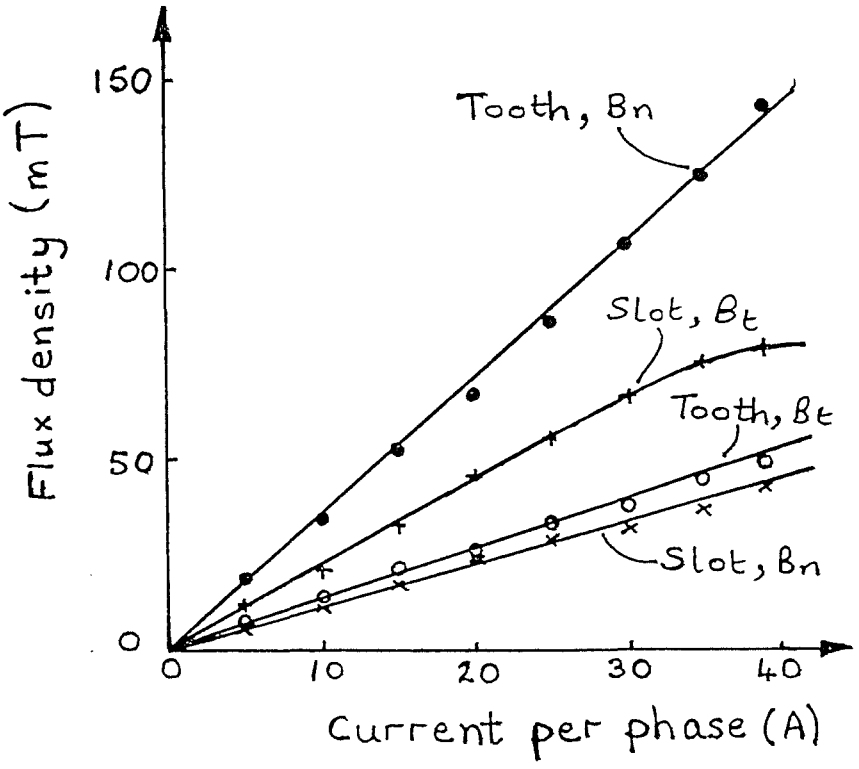

VARIATION OF FLUX DENSITY ON A TOOTH AND SLOT OF THE AXIAL FLUX DSTFLIM

Figure 6.34

TFLIM at 1 slot/pole/phase (Fig 6.24), but appears as if it may be asymptotic for the non-inverted TFLIM at 2 slots/pole/phase and zero height (Fig 6.28(a)), the inverted TFLIM (Fig 6.29) and the axial flux DSTFLIM (Fig 6.33). The mass flow rate for the axial flux DSTFLIM rose more smoothly with time (see Fig 6.33) compared with the other flow rate graphs, attaining a final value of approximately 88 kg/hr comparable to the non-inverted TFLIM figure of 90 kg/hr at 10 mm height (see Fig 6.24). The smooth increase follows from the steady travel of powder to the end whereas, in the other cases, after a certain time very little powder flows to the end. Although less marked, the powder also flowed steadily in the inverted TFLIM experiment (see Fig 6.29), and the graph indicates that powder in the middle of the device would continue to decrease steadily after the 60 s measurement interval.

Graphs of flux density for the axial flux DSTFLIM are presented in Figs 6.34 and 6.35. Figure 6.34 shows that, in the main, the flux density increased linearly with current. The normal flux density on the tooth surface was greatest, with the tangential flux density on the slot surface being greater than the tangential flux density on the tooth. Figure 6.35 shows that along the axis of the DSTFLIM with a 50 mm separation (as defined by the box height (see Fig 6.30)) B_t above a slot fell by about 35% whereas above a tooth it remained virtually the same, giving a greater B_t with respect to B_n away from the surface of either of the transverse flux motors making up the DSTFLIM.

6.7 Comparison of Transverse Flux Machines

Table 6.1 summarises the transportation of powder performance of the transverse flux machines that were investigated. The last column giving the final cumulative mass flow rate per kW has been obtained using Fig 6.36, the graphs of which have the expected shape with the current-voltage relationship being linear for both machines and the slope of the curve for the axial flux DSTFLIM being twice that for the single-sided TFLIM. The single-sided TFLIM with a 2 slot/pole/phase winding had the best performance (i.e. it transported the greatest amount of powder per unit input power) closely followed by the inverted and then the non-inverted transverse flux motors, both with a 1 slot/pole/phase winding. The axial flux DSTFLIM performed less well, because of the large input power and the generally lower mass flow-rate compared to the non-inverted

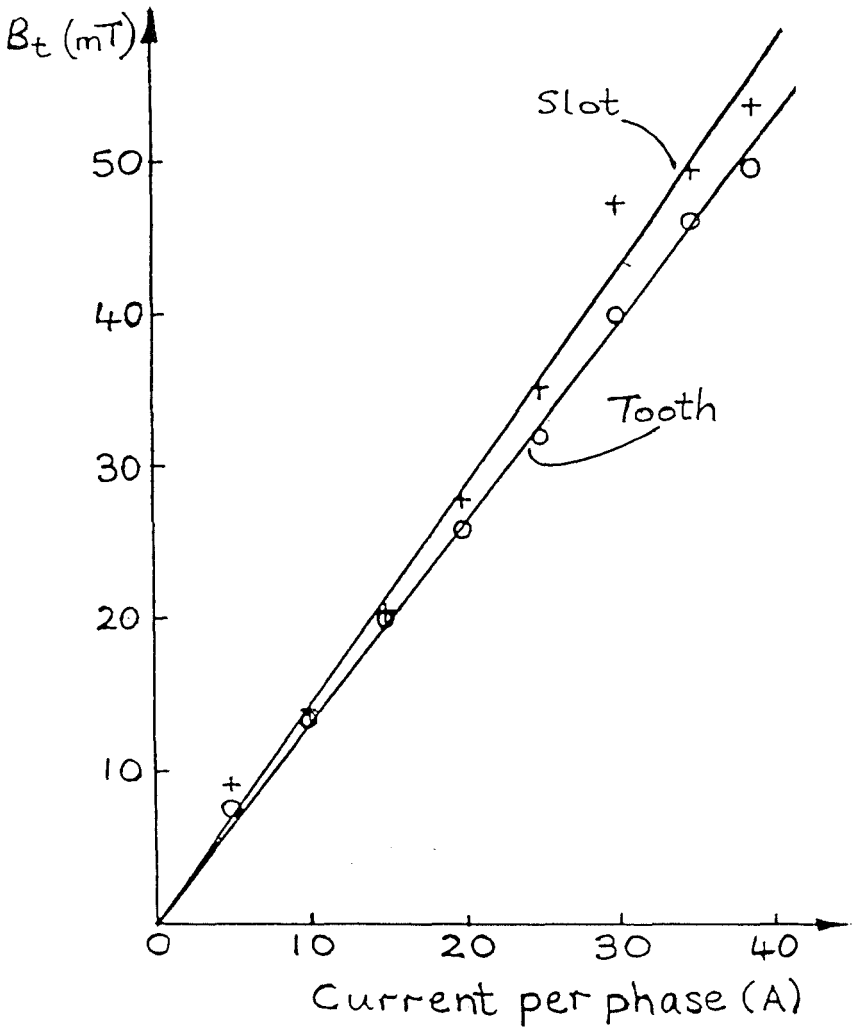

VARIATION OF TANGENTIAL FLUX DENSITY ABOVE A TOOTH AND SLOT ALONG THE AXIS OF THE AXIAL FLUX DSTFLIM

Figure 6.35

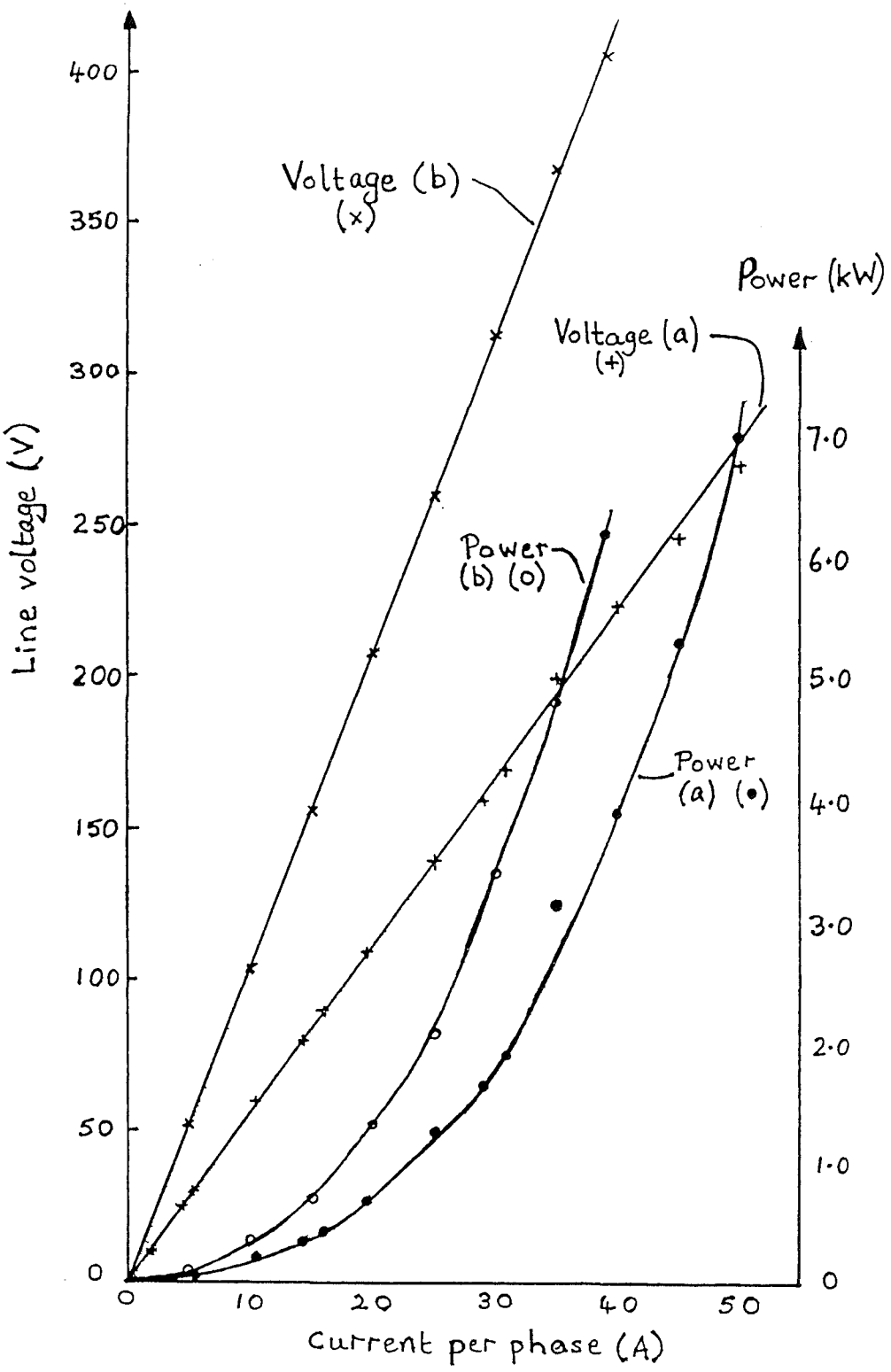

NO LOAD MEASUREMENTS

(a) the standard TFLIM
(b) the axial flux DSTFLIM

Figure 6.36

and inverted transverse flux motors. There is clearly scope for improvement, for example, by experimentation with long pole-pitch winding arrangements.

Table 6.1: Transverse Flux Device Performance for the Transportation of Powder

Experimental Scheme		Cumulative mass flow rate, $\dot{m}$ (kg/hr)		Final cumulative mass flow rate per kW, (kg/kW-hr)
		At knee of graph	Final	
Standard TFLIM 1s/p/ph; 40A/ph (Fig 6.24)	0mm	90	100	25.6
	10mm	82	90	23.1
Standard TFLIM 2s/p/ph; 40A/ph (Fig 6.28)	0mm	102	116	29.7
	10mm	55	57	14.6
Inverted TFLIM 1s/p/ph; 40A/ph (Fig 6.29)	32mm	86	106	27.2
	56mm	80	92	23.6
Standard DSTFLIM 1s/p/ph; 35A/ph (Fig 6.32)		70	75	15.6*
Axial flux DSTFLIM 1s/p/ph; 39A/ph (Fig 6.33)		70	88	14.2

For the axial flux DSTFLIM, the normal flux density (Fig 6.34) is reduced by approximately 20% above a tooth and by approximately 25% above a slot compared to the single-sided TFLIM at 1 slot/pole/phase (Fig 6.16). However the tangential flux density for the double-sided machine is increased by about 15% above both tooth and slot. A comparison of the single-sided TFLIM at 2 slots/pole/phase (Fig 6.19) with it at 1 slot/pole/phase (Fig 6.16) shows that at 2 slots/pole/phase the normal component of flux density is about 15 to 20% less above a tooth and about 10 to 15% less above a slot, and the tangential component is similarly reduced by nearly 20% and 30% respectively. When comparing the axial flux DSTFLIM with the single-sided TFLIM at 2 slots/pole/phase, there is little difference in the normal flux density above a tooth, but

*This figure is based on the power readings for the axial flux DSTFLIM and is therefore merely an indication of the actual value. The input power into the standard DSTFLIM is expected to be lower than for the axial flux DSTFLIM due to the lower reluctance flux paths in the standard DSTFLIM.

above a slot it is almost 20% less for the DSTFLIM. There is however a dramatic difference in the tangential flux density values, with it being greater by approximately 40% above a tooth and by approximately 60% above a slot for the axial flux DSTFLIM.

Table 6.2 summarises the tangential to normal flux density (B_t/B_n) ratios for the different transverse flux machines. The ratios for the axial flux DSTFLIM are large compared to those for the single-sided transverse flux motors, which it was hoped would increase the rate of powder transport. Powder flow was however not improved, since:

(i) the increase in the (B_t/B_n) ratio on the surface of one of the transverse flux motors making up the axial flux DSTFLIM did not cause the already saturated iron particles to experience any significantly greater force when they were close to one of the active surfaces of the device;

(ii) the axial flux device hindered powder transport, in that particles moved from the influence of one transverse flux motor to the other often losing some linear velocity, and

(iii) few particles travelled along the axis of the machine where the (B_t/B_n) ratio was large above both tooth and slot, because of the method of introduction of the powder.

The powder distribution was considerably better with the axial flux DSTFLIM than with the other devices and this was achieved by the inverted transverse flux motor of the pair continuing to transport powder even after ridges had formed at the exit end. It is thought that the flow rate could be improved by the introduction of powder along the axis of the machine and by using a winding with a larger pole-pitch.

Tables 6.1 and 6.2 show that although a high (B_t/B_n) ratio is a factor in good powder transport, it is not all that needs to be considered. Obviously the airgap flux density must be sufficient to magnetise the iron particles, and then to allow an adequate value of tangential flux density to cause the powder to transport. In the standard DSTFLIM,

Table 6.2: Ratio of B_t to B_n for the Various Transverse Flux Devices

Experimental Scheme		B_t/B_n			
		Tooth		Slot	
		Centre	Edge	Centre	Edge
Single-sided TFLIM 1s/p/ph (Figs 6.16; 6.17; 6.18)	height 0mm	0.28	0.16	1.3	1.2
	height 10mm	0.46	0.51	0.85	0.89
	height 25mm	0.65	0.7	0.71	0.76
Single-sided TFLIM 2s/p/ph (Figs 6.19; 6.20)	height 0mm	0.31	0.14	1.02	0.92
	height 10mm	0.36	0.33	0.59	0.58
Axial flux DSTFLIM 1s/p/ph (Figs 6.34; 6.35; 6.18)	surface of one TFLIM	0.38	-	1.91	-
	axis**	1.25	-	1.48	-

where opposing poles faced each other, there was little B_t at certain separations and the powder merely bridged the gap between the two transverse flux motors.

At 10 mm height, the non-inverted single-sided transverse flux motor with 1 slot/pole/phase winding still has a reasonable mass flow rate (Table 6.1), even though (B_t/B_n) for the slots was reduced. Part of its success however is due to the significantly increased (B_t/B_n) above the teeth. Although, as Table 6.2 shows, the (B_t/B_n) ratios continued the same trend, mass flow rate measurements were not made at 25 mm height because observations had previously shown that the powder transportation was poor. As mentioned above, the airgap flux density still needs to be sufficient to magnetise the iron particles and this was not the case at this height. Increasing the pole-pitch noticeably improved the powder transport rate despite reducing this ratio, thereby introducing another factor influencing the mass flow rate, as predicted by the hypothesis of Chapter 3.

**These figures have been calculated using values of B_n from Fig 6.18; theoretically B_n at the axis of an axial flux device is zero.

The inverted TFLIM produced a better result than the non-inverted TFLIM (Table 6.1) even though the (B_t/B_n) ratios are identical. Gravity aids the powder flow, as already described in Chapter 3, and the effect of this may be viewed as a decrease in B_n as seen by the particles, thereby increasing the apparent (B_t/B_n) ratio. The mass flow rate for the inverted transverse flux motor would be increased with improved introduction of powder into its field and the use of larger pole-pitches.

6.8 Summary

This chapter has described the design and construction of a transverse flux linear induction machine using E-laminations and the experiments performed on various physical and winding arrangements. Flux density and mass flow rate measurements were made at different heights and for different winding schemes, and it was discovered that the non-inverted TFLIM with a 2 slot/pole/phase winding had the best performance in terms of both overall mass flow rate and mass flow rate per unit input power. It was also found that the tangential to normal flux density ratio is a useful comparative parameter, with a high figure implying good powder transportation. Care must however be taken when interpreting this figure along with the other conditions of the device, such as the powder entry and the flow; thus although the axial flux DSTFLIM had a large (B_t/B_n) ratio, the powder flow was lower than expected as the powder travelled mostly under the influence of one of the two transverse flux motors making up the device due to the method used to introduce the powder into the influence of the axial flux DSTFLIM.

The axial flux DSTFLIM provides a better powder distribution than the other devices and this connection, along with the inverted transverse flux motor, using large pole-pitches and more suitable powder entry methods merit further investigation. It is however expected that the inverted TFLIM will be the superior device, as the axial flux DSTFLIM requires considerably more input power. This implies an arrangement similar to the powder cleaner (see Chapters 2 and 3) replacing the two inverted linear motors by two inverted transverse flux motors.

The type of powder used also affects its own mass flow rate, as previously discussed in Chapter 3. Of the powders investigated, the iron filings had the greatest flow rate,

followed by AISI 430 and lastly Ni/Fe 50/50. Particle characteristics affecting flow rate are the particle size and shape and its coercivity. If the particles are too small, they tend to stick to each other and the linear machine (as in the case of the magnetic iron oxide powder described in Chapter 3); if they are magnetically soft, they are easily re-magnetised and therefore fail to transport adequately, as in the case of powder Ni/Fe.

Since observations of the powder motion on the various transverse flux machines clearly agree with those made for the other linear devices and especially the powder cleaner, the proposed hypothesis in Chapter 3 describing the mechanism of particle motion is therefore still valid. This further implies that the expressions derived in Chapter 3 are also likely to hold for the transverse flux devices. The use of large pole-pitches to improve powder transportation is one of the predictions of the hypothesis and this has been verified.

References

1. LAITHWAITE, E.R., EASTHAM, J.F., BOLTON, H.R., and FELLOWS, T.G.: "Linear motors with transverse flux", *Proc. IEE*, 1971, **118**, (12), pp.1761-1767.

2. VADHER, V.V.: *Private communication*, University of Technology, Loughborough, 1986.

3. KETTLEBOROUGH, G.: *Private communication*, University of Technology, Loughborough, 1986.

7. Conclusions

Expressions for the forces acting on ferromagnetic particles were derived in Chapter 3 followed by the discussion of an hypothesis explaining the transportation of powder. Design details and the results of the experimental investigation of the tubular and various transverse flux linear induction machines were described in Chapters 4 and 6, with Chapter 5 presenting a finite-element analysis of the standard linear and tubular machines. A discussion of the main conclusions is given in this chapter.

Hypothesis and force-expressions

Previous discussion in Chapter 3 has shown that the force-expressions are able to provide considerable insight into the motion of ferromagnetic particles when under the influence of a travelling magnetic field. They clearly predict that the horizontal motion is directed in opposition to the field, and that both the normal and tangential forces vary at twice the rate of the impressed travelling field. Both components of the force depend upon the size, shape and relative permeability of the particle, with its initial position, including height and orientation, modifying these forces.

In deriving the force-expressions, only one particle was considered and the effect of all others neglected. An ideal cylindrical particle-shape was assumed because the particles used were rod-like, but other shapes which could have been considered would have suitably modified the force-expressions. Consideration of the mode of transport of an individual particle (as determined by the high-speed photographs of Chapter 3) led to the formulation of the hypothesis.

Using information about demagnetising factors, the hypothesis shows that the particles behave like tiny permanent magnets having N and S poles induced at their ends by the travelling field and, in the same way, join together end to end. This explains why the particles often travelled in strings and smaller size particles in bunches, which is a collection of particle-strings. The path taken by an individual moving particle was described and the hypothetical predictions of linear and rotational speed were found to have good agreement with the experimental results. On average, the theoretical linear

speed is one-half the speed of the travelling wave and the rotational speed is 4500 rpm. Extensions to the hypothesis explained why the particles further from the stator took longer paths of travel. Although the linear and rotational speeds of these particles differed from theory, the distance and amount of rotation may be predicted for all particles irrespective of their position. The distance of travel of a particle between contacts with the stator is a theoretical average of an integral number of slot-pitches, with the expected minimum being a tooth-width less than, and the expected maximum a tooth-width greater than this average. The expected rotation during this period of linear travel is an integral number of half-revolutions.

Since the hypothesis predicts that the linear particle-speed is directly proportional to the speed of the travelling wave, it is expected that winding arrangements with a large number of slots/pole/phase (i.e. long pole-pitches) will perform better (i.e. produce a greater throughput of powder) than those with a small number of slots/pole/phase. This is supported by the experimental work on the tubular and transverse flux motors, as described below. Although the hypothesis was based upon an individual particle travelling close to the motor-face, the motional characteristics such as the distance of travel and the amount of rotation can be accurately predicted for nearly all particles.

Experimental tubular motor

From the investigations conducted on the experimental tubular motor in Chapter 4, it was concluded that large input currents and a large ratio of tangential to normal flux density is required for good powder transportation. The latter is achievable by using a winding arrangement having a large number of slots/pole/phase, with the best mass flow rate results obtained at 40 A/phase with 4 slots/pole/phase. This is in good agreement with the hypothesis discussed above.

The main problem with the tubular motor was the tendency of the powder to remain within the machine-bore, causing a powder build-up and ridge formation. Such effects hindered and often prevented powder transportation, thereby decreasing the mass flow rate.

A winding arrangement producing an accelerating field was investigated with disappointing results, since no improvement occurred in the flow rate. The results, however, were approximately similar to previous winding arrangements and there is scope for further testing. To obtain improved transportation with accelerating winding configurations requires a longer tubular motor, since it has already been established that windings with a large number of slots/pole/phase produce improved mass flow rates. Since it was found that the powder tended to collect over one pole-pitch, a winding which decelerates the field at the exit end may improve transportation. Thus, if the last pole was wound with 1 slot/pole/phase, the powder may collect over only this pole-pitch.

Finite-element investigation

The finite-element study of the tubular and linear motors with particles in Chapter 5 showed that the particles have an increased internal field, thereby supporting the permanent magnet concept of Chapter 3. Results indicate however that the internal field is not increased by as large a factor as implied by the formulae of Chapter 3 and Appendix A, and the following reasons help to explain why. Both finite-element studies were two dimensional and therefore in the linear motor study the particles were modelled as small, infinitely deep iron rods and in the tubular motor study as thin iron rings. In both studies the cross-sectional shape of the particles was therefore defined (as described in Chapter 5), rather than the more accurate three dimensional representation. Further reasons explaining the discrepancy between the internal field are that the demagnetising factor equation in Chapter 3 is an approximation to the shape of the actual and modelled particles and, in the evaluation of the demagnetising factor, it was tacitly assumed that the relative permeability remained constant. It is believed however that the finite-element software assumes an S-shaped B-H curve and therefore does not use a constant value for the relative permeability. Even so it is noteworthy that although the multiplication factors differ, the internal field is significantly increased thereby supporting the hypothesis.

Comparison of the flux density values from the experimental tubular motor and that modelled using the finite-element software of GEC shows considerable discrepancy. The normal flux density varies between approximately 15 mT and 45 mT, depending on whether measured above slots or teeth, in contrast to the finite-element results of about

5 mT and 20 mT for apparently the same conditions. Similarly, the experimental tangential flux density has a peak value of approximately 55 mT above a slot in comparison with about 15 mT for the GEC model. Similar comparisons with the finite-element software of Rutherford Laboratories also shows some discrepancies. Where the experimental motor had a peak normal flux density of approximately 50 mT, the model has a peak of about 90 mT, and for the tangential flux density the values are respectively approximately 55 mT and 120 mT. One set of finite-element results has therefore underestimated and the other overestimated the flux densities, leading to a particular cause for concern in that the independent finite-element results do not even closely agree. In both cases the two separate finite-element models would have assumed a perfectly continuous lamination comprising the tubular motor, rather than individual stacks of laminations as used in the experimental motor. Such an assumption would imply increased, rather than decreased, flux densities, as was obtained by the Rutherford finite-element package. To ascertain any sources of error, further investigation into both finite-element packages is required.

Irrespective of the discrepancies between experimental and finite-element models, similar trends have been observed (such as the increased internal field within the particles, tangential flux density being greater than normal flux density in the same areas) thereby implying that the conclusions drawn still have some validity.

Transverse flux machines

The results of Chapter 6 show that the non-inverted transverse flux motor with a 2 slots/pole/phase winding had the best powder transportation performance in terms of both overall mass flow rate and mass flow rate per unit input power, with the inverted transverse flux motor with a 1 slot/pole/phase arrangement coming a close second. Other results have shown that increasing the pole-pitch improves the powder transportation and one of the reasons given is the increase in tangential flux density at the expense of normal flux density, that is increasing the ratio (B_t/B_n). When increasing the pole-pitch for the transverse flux motor, this ratio reduced by 20% above the slots but increased by 10% above the teeth, and it is thought that this aided the improved powder flow. It was expected that the ratio would increase above both teeth and slots but, because of the

construction of the device, the winding factor was only $^1/_3$ at 2 slots/pole/phase. If new coils were manufactured to produce the more usual winding factor of $^5/_6$ or unity, it is expected that both the ratios and the mass transport rate would increase still further.

The inverted transverse flux machine produced a good result, with gravity helping to increase the apparent tangential to normal flux density ratio. Apart from investigations with larger pole-pitches, there is also scope for experimenting with powder entry positions and with a similar arrangement to the powder cleaner, where the last few teeth are pulsed on and off.

The double-sided transverse flux motors appear to be about 50% as efficient as a single-sided scheme, which is expected because there are now two equivalent machines requiring excitation. An alternative measure is the actual mass flow rate which, for the axial flux DSTFLIM, is some 78% to 88% of an equivalent single-sided arrangement. It is thought that larger pole-pitch winding configurations and improved powder entry may close the gap with equivalent single-sided arrangements. An important feature of the axial flux motor was the improved powder distribution compared with the other arrangements with practically no powder being left either at the start or in the middle of the machine.

Powder transportation

Observations of particle motion, whether on the powder cleaner, tubular motor or any one of the transverse flux machines, clearly showed similar motional characteristics, as already described. Powder motion is generally from tooth to tooth through both rotational and translational modes in particle-strings, bunches or as individual particles depending upon a variety of factors including distance from the stator, the pole-pitch, particle-size and the powder coercivity. In all cases the larger powders transported move quicker than the smaller ones and the soft magnetic powder was only able to match, and not exceed, the mass flow rate of the harder magnetic powder. Both the rotation and translation of the particles is predicted by the hypothesis.

Using the mass flow rate per unit input power as a measure of efficiency for powder transportation, it is clear that the single-sided transverse flux motor arrangements are at least an order of magnitude better than the tubular motor. If actual mass flow rates are compared, all the transverse flux motors, including the double-sided arrangements, achieve this figure.

Common to all the linear motors investigated is the tendency of the powder to form ridges when sufficient powder has collected at the exit end. Windings with increased pole-pitch improve powder transportation for both the tubular and transverse flux motors along with large input currents, because of the increased (B_t/B_n) ratio and the increased flux density. Interestingly, the axial flux DSTFLIM did not suffer as greatly as the tubular motor from powder-ridges and the former therefore had the effect of producing a better powder distribution and flow rate. This is probably due to the different separations of the stator for the two motors from their respective central axis, and it may be instructive to investigate a tubular motor with a smaller bore than the one in Chapter 4.

Applications of powder transportation

A number of possible applications were discussed briefly in Chapter 1 and a somewhat greater assessment of their viability can now be attempted.

The cleaning or separation of powder (i.e. the removal of iron powder from impurities or the removal of iron impurities from other powder) by transporting the iron powder has already been demonstrated using a standard linear motor. The use of inverted transverse flux motors in a similar arrangement to the powder cleaner in Chapter 2 is likely to give improved results. Firstly, the powder will be contained within the confines of the width of the centre limb of the E-core making up the transverse flux motor rather than some of it escaping from the sides of the motor as in the case of the powder cleaner; and secondly the powder flow rate is better.

Although expensive in terms of power input when compared with the single-sided machine, the double-sided, axial flux TFLIM is a good choice for the general

transportation of iron powder because of its good powder distribution. The single-sided transverse flux motor, especially with long pole-pitches, would be less costly to operate if the decrease in effectiveness of the powder distribution can be tolerated. Metal recovery from industrial waste could be carried out using such a motor or as above, that is, a separation process, if the waste is dry.

Since physical and magnetic properties of powdered material affect its transportation, there is scope for its sizing and classification into either magnetically soft or magnetically hard. (Investigations which consider other shapes of powdered material are necessary before it is possible to separate out one particle shape from another.) The tubular motor was found to give similar flow rates for both the soft and hard powders and would therefore be unsuitable for this application. Particle sizing could however be carried out through the use of any of the motors since they all had significantly different flow rates for the particle sizes considered although the flow rate for the tubular motor was generally very low. Since the transverse flux machines have the higher flow rate and more marked flow rate differences between powders, they would be the better choice for both sizing and magnetic classification.

A number of different linear devices may be used for enhancing powder circulation and mixing within fluidised beds. In this case it is unnecessary to have high powder flow rates but rather to have much particle agitation, thereby producing a good mixing of chemical agents. Since the tubular motor has similar flow rates for similar-size ferromagnetic particles, the increased mixing produced by this device could, after experiment, be predicted. This is a significant advantage, since reaction times may then be reasonably accurately predicted. Large input currents and long-pole pitches may be needed, but these will depend upon the bore diameter of the tubular motor required for the particular application. Other schemes using standard double-sided arrangements of the linear and transverse flux motor may be useful, but it was observed that, in the main, the particles stayed close to the stator and would therefore not aid mixing in the middle of the fluidised bed. Experimentation with two single-sided motors excited such that their travelling fields are in opposition and positioned at diametrically opposite sides of the fluidised bed may improve mixing, but again the limitation would be the distance the iron particles separated from the stators. Better mixing is more likely by using a tubular

motor, and with one in which the ferromagnetic particles are forced to travel against the air jets producing the fluidised bed.

Recommendations for further work

The hypothesis predicts particle-speeds as half the speed of the travelling magnetic field and results have shown that the mass flow rate is improved with large pole-pitch winding arrangements. Varying the supply frequency will modify the speed of the travelling field and high-speed photographic techniques could be used, as previously, to determine the effect on individual particles.

It was found that a large ratio of tangential to normal flux density aids powder transportation. Extension to the theory in Chapter 3 and Appendix A would show how the tangential and normal forces relate to these flux density components. Investigation of the flux density distribution in three dimensions could then make the advantages of using a TFLIM over a LIM for powder transportation apparent.

As mentioned in Chapter 2, there are a great variety of linear machines and investigations of powder transportation on some of these may be fruitful, e.g. LIMs for helical motion, the d.c. LIM, transverse flux tubular motors and herringbone motors. The latter two different types have the advantage of respectively producing only axial-force and inward-travelling fields (see Chapter 2). The absence of radial-force may improve the powder throughput and the inward-travelling fields may be useful in channelling powder.

Results from both the tubular and transverse flux motors and the hypothesis strongly suggest that powder transportation would be improved through the use of motors with a large pole-pitch. With the construction of new coils for the transverse flux motors, this could then be investigated. Investigations on a physically larger tubular motor with large pole-pitch, accelerating and decelerating windings are also considered worthwhile, as discussed earlier.

Further study is also required on many more different ferromagnetic powders to determine whether there are optimum sizes and shapes for transportation. There will be a certain

size of particle that will no longer transport in the manner described and a particle with diameter 5 mm was mentioned in Chapter 2. More detail is however required, as the hypothesis appears to suggest that the size is related to either the slot or tooth pitch, and that a rod-like particle shape may be better at transporting than a spherically-shaped particle. If this is discovered to be the case then particle sorting by shape may be feasible.

Summary

This chapter has presented the conclusions that may be drawn from this work on powder transportation. The effectiveness or otherwise of various linear motors has been discussed and findings from the experimental work have supported the hypothesis. Various linear motors have been identified as suitable for a number of different powder transportation applications and areas of further work have been suggested.

Factors of importance for powder transportation include large values of flux density, an increased tangential to normal flux density ratio and large pole-pitch winding arrangements. Experimental results, the hypothesis and the finite-element investigation tend to support each other at appropriate points and therefore confirm the mechanisms of powder transportation previously described. The hypothesis is able to predict both linear and rotational particle speeds, the expected minimum and maximum distance travelled and the rotation experienced by the particles.

8. Appendices

Appendix A: Forces on Ferromagnetic Particles

A1 Demagnetising Factor

The field inside any ellipsoid is given by[1],

$$H_i = H - D\frac{M}{\mu_0} \qquad (a.1)$$

where H_i = intensity of magnetic field inside the ellipsoid,
H = intensity of applied magnetic field,
M = dipole moment per unit volume (the intensity of magnetisation), and
D = demagnetising factor[1,2].

Osborn has given a number of complex formulae[1] for evaluating demagnetising factors for a general ellipsoid, but here relationships are given for M and B_i, the flux density inside the ellipsoid, in terms of B, the applied magnetic flux density, using algebraic manipulation.

Substituting in equation (a.1) for magnetic flux density and re-arranging gives,

$$DM = B - \frac{B_i}{\mu_r} \qquad (a.2)$$

But since $M = \mu_0 k_r H_i$ where k_r = relative susceptibility = $(\mu_r - 1)$ (refs 2 and 3),

$$M = (\mu_r - 1)\frac{B_i}{\mu_r} \qquad (a.3)$$

Substituting for B_i from equation (a.3) into equation (a.2), and re-arranging, gives

$$M = \frac{(\mu_r - 1)}{1 + (\mu_r - 1)D} \cdot B \qquad (a.4)$$

To obtain the flux density produced inside the particle by the applied field, M from equation (a3.) is substituted into equation (a.2), to yield

$$B_i = \frac{\mu_r}{1 + (\mu_r - 1)D} \cdot B \qquad (a.5)$$

A2 One-dimensional Force on a Particle

Using the previous results, the one-dimensional force on a ferromagnetic particle under the influence of a travelling magnetic field can be derived. If a rod-like magnetic particle of length 2a and diameter 2c is situated in a travelling field, with its centre a distance x from some arbitrary origin, the force on each magnetic pole[3] m is given by

$$F = m.\ H(x) \qquad (a.6)$$

(i.e. H is a function of x), so that the total force on the poles of the particle is

$$F = m_1.H(x + a) + m_2.H(x - a) \qquad (a.7)$$

where m_1 and m_2 are the pole-strengths at the two ends. If the applied field B travels sinusoidally in the x-direction, with

$$B = \hat{B} \sin \left[\omega t - \frac{2\pi}{\lambda} x \right]$$

where ω = angular supply frequency;

t = time, and

λ = wavelength = $2\lambda_p$, with λ_p being the pole-pitch,

then, after substituting for H in terms of B, noting that $m_2 = -m_1$ and letting $m = m_1$, equation (a.7) becomes

$$F = m\frac{\hat{B}}{\mu_0}.\sin\left[\omega t - \frac{2\pi}{\lambda}(x + a)\right] - m\frac{\hat{B}}{\mu_0}.\sin\left[\omega t - \frac{2\pi}{\lambda}(x - a)\right].$$

Simplifying,

$$F = \frac{m\hat{B}}{\mu_0}\left\{\sin\left[\omega t - \frac{2\pi}{\lambda}(x + a)\right] - \sin\left[\omega t - \frac{2\pi}{\lambda}(x - a)\right]\right\},$$

thus,

$$F = -\frac{2m\hat{B}}{\mu_0}.\cos\left[\omega t - \frac{2\pi}{\lambda}x\right].\sin\left[\frac{2\pi}{\lambda}a\right] \qquad (a.8)$$

Since magnetic moment[3] is equal to pole strength times length, m (pole strength) can be substituted in terms of M (magnetic moment/unit volume) as

$$m = \frac{M.\,\text{volume}}{\text{length}} = M.\frac{\pi c^2.2a}{2a} \qquad (a.9)$$

So, from eqn (a.4),

$$m = \frac{\mu_r - 1}{1 + (\mu_r - 1)D}.B.\pi c^2 \qquad (a.10)$$

Substituting for B and incorporating into equation (a.8),

$$F = -\frac{2\hat{B}}{\mu_0}.\frac{(\mu_r - 1)}{1 + (\mu_r - 1)D}.\pi c^2.\hat{B}\sin\left[\omega t - \frac{2\pi}{\lambda}x\right].\cos\left[\omega t - \frac{2\pi}{\lambda}x\right].\sin\left[\frac{2\pi}{\lambda}a\right]$$

Simplifying and re-arranging,

$$F = - \left[\frac{\mu_r - 1}{1 + (\mu_r - 1) D} \right] \left[\frac{\hat{B}^2}{\mu_0} \right] \pi c^2 . \sin \left[\frac{2\pi}{\lambda} a \right] . \sin 2 \left[\omega t - \frac{2\pi}{\lambda} x \right] \qquad (a.11)$$

With the field travelling in the positive x-direction, eqn (a.11) clearly shows that the force is directed in the opposite direction and has twice the frequency of the travelling field.

This force expression may be obtained from Gopinath[5] and Horsnell[6] as shown below. By extending Gopinath's work, Horsnell gave the following expression for the force in one-dimension:

$$F_z = 4\pi r^3 . B . \frac{\partial H}{\partial z}$$

where $4\pi r^3$ is the dipole moment. Equation (a.4) gives the dipole moment per unit volume and by substituting this into Horsnell's force expression, it becomes

$$\frac{F_z}{\text{volume}} = \frac{(\mu_r - 1)}{1 + (\mu_r - 1) D} \cdot \frac{B}{\mu_0} \cdot \frac{\partial B}{\partial z}$$

Substituting for the flux density gives

$$\frac{F_z}{\text{volume}} = - \left[\frac{\mu_r - 1}{1 + (\mu_r - 1) D} \right] \left[\frac{\hat{B}^2}{\mu_0} \right] \frac{\pi}{\lambda} . \sin 2 \left[\omega t - \frac{2\pi}{\lambda} z \right]$$

and assuming the same rod-like particle as before, which has a volume of $2\pi c^2 a$, the force becomes,

$$F_z = - \left[\frac{\mu_r - 1}{1 + (\mu_r - 1) D} \right] \left[\frac{\hat{B}^2}{\mu_0} \right] \pi c^2 . \left[\frac{2\pi a}{\lambda} \right] . \sin 2 \left[\omega t - \frac{2\pi}{\lambda} z \right] .$$

For small magnetic particles $a << \lambda$ then, with $2\pi a/\lambda \approx \sin(2\pi a/\lambda)$, the above force expression is a close approximation to eqn (a.11).

A3 Two-dimensional Forces on a Particle

The expression in equation (a.11) may be extended by allowing the particle to move also in the y-direction. With the same cylindrical particle (see Fig a.1), and the field[4] given by,

$$B_x = \hat{B} \exp(-2\pi y/\lambda) \sin\left[\omega t - \frac{2\pi}{\lambda} x\right] \tag{a.12a}$$

$$B_y = \hat{B} \exp(-2\pi y/\lambda) \cos\left[\omega t - \frac{2\pi}{\lambda} x\right] \tag{a.12b}$$

equation (a.7) gives

$$F_x = m_x \frac{\hat{B}}{\mu_0} \left\{ \exp\left[-\frac{2\pi}{\lambda}(y + a\sin\theta)\right] . \sin\left[\omega t - \frac{2\pi}{\lambda}(x + a\cos\theta)\right] \right. \tag{a.13a}$$
$$\left. - \exp\left[-\frac{2\pi}{\lambda}(y - a\sin\theta)\right] . \sin\left[\omega t - \frac{2\pi}{\lambda}(x - a\cos\theta)\right] \right\}$$

$$F_y = m_y \frac{\hat{B}}{\mu_0} \left\{ \exp\left[-\frac{2\pi}{\lambda}(y + a\sin\theta)\right] . \cos\left[\omega t - \frac{2\pi}{\lambda}(x + a\cos\theta)\right] \right. \tag{a.13b}$$
$$\left. - \exp\left[-\frac{2\pi}{\lambda}(y - a\sin\theta)\right] . \cos\left[\omega t - \frac{2\pi}{\lambda}(x - a\cos\theta)\right] \right\}$$

where m_x and m_y are the pole strengths, and F_x and F_y the forces in the x and y directions respectively.

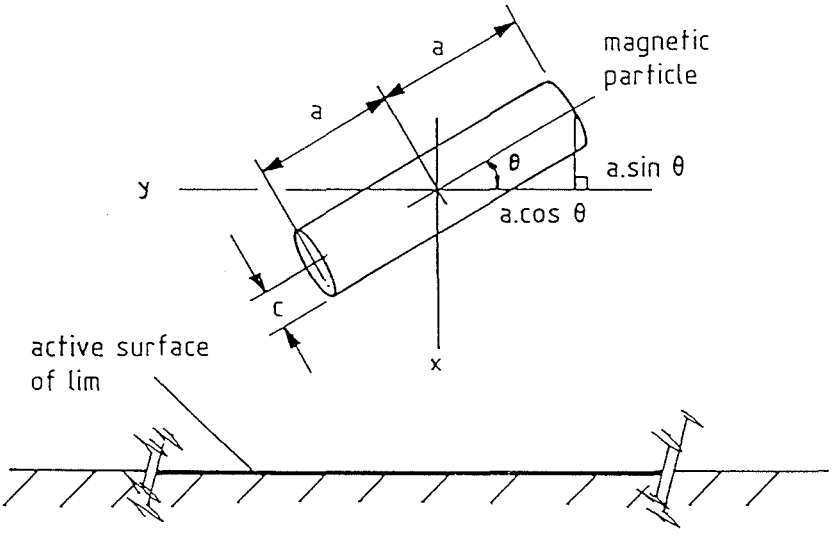

MAGNETIC PARTICLE UNDER THE INFLUENCE
OF A TRAVELLING MAGNETIC FIELD

Figure a1

From equation (a.10),

$$m_x = \frac{(\mu_r - 1)}{1 + (\mu_r - 1)D_x} \pi c^2 B_x = \pi c^2 K_x B_x \qquad (a.14)$$

and similarly,

$$m_y = \frac{(\mu_r - 1)}{1 + (\mu_r - 1)D_y} \cdot \frac{\pi c^2 (2a)}{2c} B_y = \pi c a K_y B_y \qquad (a.15)$$

where D_x and D_y are respectively the demagnetising factors[2] in the x and y directions.

Let

$$\left.\begin{aligned} X_1 &= 2x + a\cos\theta; & Y_1 &= 2y + a\sin\theta \\ X_2 &= 2x - a\cos\theta; & Y_2 &= 2y - a\sin\theta \end{aligned}\right\} \qquad (a.16)$$

Substituting equations (a.12),(a.14), (a.15) and (a.16) into (a.13) gives:

$$F_x = \pi c^2 K_x \frac{\hat{B}^2}{\mu_0} \exp(-2\pi y/\lambda) . \sin\left(\omega t - \frac{2\pi}{\lambda} x\right) . \{\} \qquad (a.17a)$$

$$F_y = \pi c a K_y \frac{\hat{B}^2}{\mu_0} \exp(-2\pi y/\lambda) . \cos\left(\omega t - \frac{2\pi}{\lambda} x\right) . \{\} \qquad (a.17b)$$

where { } contain the same expressions as in equations (a.13).

Using trigonometric identities, equations (a.17) simpliy to:

$$F_x = \pi c^2 K_x \frac{\hat{B}^2}{\mu_0} \exp\left(-2\pi y/\lambda\right).$$

$$\left\{ \exp\left[-\frac{2\pi}{\lambda}\left(y + a.\sin\theta\right)\right] . \frac{1}{2}\left[\cos\left(\frac{2\pi}{\lambda} a.\cos\theta\right) - \cos 2\left(\omega t - \frac{\pi}{\lambda} X_1\right)\right]\right.$$

$$\left. - \exp\left[-\frac{2\pi}{\lambda}\left(y - a.\sin\theta\right)\right] . \frac{1}{2}\left[\cos\left(\frac{2\pi}{\lambda} a.\cos\theta\right) - \cos 2\left(\omega t - \frac{\pi}{\lambda} X_2\right)\right]\right\}$$

and

$$F_y = \pi c a K_y \frac{\hat{B}^2}{\mu_0} \exp\left(-2\pi y/\lambda\right).$$

$$\left\{ \exp\left[-\frac{2\pi}{\lambda}\left(y + a.\sin\theta\right)\right] . \frac{1}{2}\left[\cos\left(\frac{2\pi}{\lambda} a.\cos\theta\right) - \cos 2\left(\omega t - \frac{\pi}{\lambda} X_1\right)\right]\right.$$

$$\left. - \exp\left[-\frac{2\pi}{\lambda}\left(y - a.\sin\theta\right)\right] . \frac{1}{2}\left[\cos\left(\frac{2\pi}{\lambda} a.\cos\theta\right) + \cos 2\left(\omega t - \frac{\pi}{\lambda} X_2\right)\right]\right\}$$

which further reduce to:

$$F_x = -\pi c^2 K_x \frac{\hat{B}^2}{2\mu_0} \left\{ \exp\left(-2\pi Y_1/\lambda\right) . \cos 2\left(\omega t - \frac{\pi}{\lambda} X_1\right)\right.$$

$$- \exp\left(-2\pi Y_2/\lambda\right) . \cos 2\left(\omega t - \frac{\pi}{\lambda} X_2\right) \qquad \text{(a.18a)}$$

$$\left. - \left[\exp\left(-2\pi Y_1/\lambda\right) - \exp\left(-2\pi Y_2/\lambda\right)\right] . \cos\left(\frac{2\pi}{\lambda} a.\cos\theta\right)\right\}$$

and,

$$F_y = \pi c a K_y \frac{\hat{B}^2}{2\mu_0} \left\{ \exp(-2\pi Y_1/\lambda) \cdot \cos 2 \left[\omega t - \frac{\pi}{\lambda} X_1 \right] \right.$$

$$- \exp(-2\pi Y_2/\lambda) \cdot \cos 2 \left[\omega t - \frac{\pi}{\lambda} X_2 \right] \qquad \text{(a.18b)}$$

$$\left. + \left[\exp(-2\pi Y_1/\lambda) - \exp(-2\pi Y_2/\lambda) \right] \cdot \cos \left[\frac{2\pi}{\lambda} a \cdot \cos\theta \right] \right\}$$

When

$$\theta = 0, \; X_1 = (2x + a); \qquad X_2 = (2x - a);$$

$$Y_1 = Y_2 = 2y; \qquad \cos\theta = 1 \text{ and } \sin\theta = 0$$

and substituting into equations (a.18) gives:

$$F_x|_{\theta=0} = -K_x A_x \frac{\hat{B}^2}{2\mu_0} \exp(-4\pi y/\lambda) \left\{ \cos 2 \left[\omega t - \frac{\pi}{\lambda} (2x + a) \right] \right.$$

$$\left. - \cos 2 \left[\omega t - \frac{\pi}{\lambda} (2x - a) \right] \right\}$$

and,

$$F_y|_{\theta=0} = K_y A_y \frac{\hat{B}^2}{2\mu_0} \exp(-4\pi y/\lambda) \left\{ \cos 2 \left[\omega t - \frac{\pi}{\lambda} (2x + a) \right] \right.$$

$$\left. - \cos 2 \left[\omega t - \frac{\pi}{\lambda} (2x - a) \right] \right\}$$

where $A_x = \pi c^2$ and $A_y = \pi ca$. (a.19)

Hence,

$$F_x|_{\theta=0} = -K_x A_x \frac{\hat{B}^2}{\mu_0} \exp\left(-4\pi y/\lambda\right) . \sin\left[\frac{2\pi a}{\lambda}\right] . \sin 2\left[\omega t - \frac{2\pi}{\lambda} x\right] \quad \text{(a.20a)}$$

and,

$$F_y|_{\theta=0} = K_y A_y \frac{\hat{B}^2}{\mu_0} \exp\left(-4\pi y/\lambda\right) . \sin\left[\frac{2\pi a}{\lambda}\right] . \sin 2\left[\omega t - \frac{2\pi}{\lambda} x\right] \quad \text{(a.20b)}$$

$$= -\left[\frac{K_y A_y}{K_x A_x}\right] . F_x|_{\theta=0}$$

Now, setting $y = 0$,

$$F_x|_{y,\theta=0} = K_x A_x \frac{\hat{B}^2}{\mu_0} \sin\left[\frac{2\pi a}{\lambda}\right] . \sin 2\left[\omega t - \frac{2\pi}{\lambda} x\right] \quad \text{(a.21a)}$$

and,

$$F_y|_{y,\theta=0} = K_y A_y \frac{\hat{B}^2}{\mu_0} \sin\left[\frac{2\pi a}{\lambda}\right] . \sin 2\left[\omega t - \frac{2\pi}{\lambda} x\right] \quad \text{(a.21b)}$$

Note that the expression for $F_x|_{y,\theta=0}$ is the same as that previously derived in equation (a.11) as expected.

The above results may be summarised by writing:

$$E_1 = \exp\left(-2\pi Y_1/\lambda\right) . \cos 2\left[\omega t - \frac{\pi}{\lambda} X_1\right] \quad \text{(a.22)}$$

$$E_2 = \exp\left(-2\pi Y_2/\lambda\right).\cos 2\left(\omega t - \frac{\pi}{\lambda} X_2\right) \qquad \text{(a.23)}$$

and

$$e_3 = \left[\exp\left(-2\pi Y_1/\lambda\right) - \exp\left(-2\pi Y_2/\lambda\right)\right].\cos\left(\frac{2\pi}{\lambda} a\,.\cos\theta\right) \qquad \text{(a.24)}$$

Using equations (a.14), (a.15), (a.16) and (a.19), equations (a.18) simplify to:

$$F_x = -K_x A_x \frac{\hat{B}^2}{2\mu_0}\left\{E_1 - E_2 - e_3\right\} \qquad \text{(a.25a)}$$

$$F_y = K_y A_y \frac{\hat{B}^2}{2\mu_0}\left\{E_1 - E_2 + e_3\right\}$$

$$= -\left(\frac{K_y A_y}{K_x A_x}\right) F_x + K_y A_y \frac{\hat{B}}{\mu_0}.e_3 \qquad \text{(a.25b)}$$

$$= -\left[\frac{1 + (\mu_r - 1)D_x}{1 + (\mu_r - 1)D_y}\right]\left(\frac{a}{c}\right) F_x + K_y A_y \frac{\hat{B}}{\mu_0} e_3$$

A4 The Vertical Force on a Particle

Substituting for K_y and A_y from equations (a.15) and (a.19) into equation (a.21b) gives the y-directed force as

$$F_y\big|_{y,\theta=0} = \left[\frac{\mu_r - 1}{1 + (\mu_r - 1)D_y}\right]\left(\frac{\hat{B}^2}{\mu_0}\right)\pi ca\,.\sin\left(\frac{2\pi a}{\lambda}\right).\sin 2\left(\omega t - \frac{2\pi}{\lambda} x\right) \qquad \text{(a.26)}$$

Assuming $x = 0$ at the start of the linear machine, then at $\omega t = 0$ the last sinusoidal term makes the force $F_y\big|_{y,\theta=0}$ negative, indicating that the particles are attracted to the

stator. $F_y|_{y,\theta=0}$ is positive (i.e. repelling particles from the stator) when the sinusoidal term is positive, i.e.

$$\sin 2\left[\omega t - \frac{2\pi x}{\lambda}\right] > 0 \qquad \text{(a.27)}$$

which occurs when

$$2n\pi < 2(\omega t - 2\pi x/\lambda) < (2n+1)\pi \qquad \text{(a.28)}$$

where $n = 0, 1, 2, \ldots$

Considering the inequalities separately, limits for x may be obtained as

$$n\pi < \omega t - \frac{2\pi x}{\lambda}; \qquad (2n+1)\frac{\pi}{2} > \omega t - \frac{2\pi x}{\lambda} \qquad \text{(a.29)}$$

$$\frac{2x}{\lambda} < 2ft - n; \qquad \frac{2x}{\lambda} > 2ft - \frac{2n+1}{2} \qquad \text{(a.30)}$$

$$\therefore \quad x < f\lambda t - \frac{n\lambda}{2}; \qquad x > f\lambda t - \left[n + \frac{1}{2}\right]\frac{\lambda}{2} \qquad \text{(a.31)}$$

Hence,

$$V_s.t - \left[n + \frac{1}{2}\right]\lambda_p < x < V_s.t - n\lambda_p \qquad \text{(a.32)}$$

where $V_s = f\lambda$, the speed of the travelling wave and

$\lambda_p = \frac{\lambda}{2}$, the pole-pitch.

Thus particles within the limits given by equation (a.32) will be repelled and those outside of the limits will be attracted by the stator.

References

1. OSBORN, J.A.: "Demagnetising factors of the general ellipsoid", *Phys. Rev.*, 1945, **67**, (11/12), pp. 351-357.

2. BRAILSFORD, F.: "Physical principles of magnetism", (D. Van Nostrand Company Ltd, 1966, London).

3. STARLING, S.G. & WOODALL, A.J.: "Electricity and magnetism for degree students", (Longmans, 1956, 8/e, London).

4. LAITHWAITE, E.R.: "Induction machines for special purposes", (George Newnes Ltd, 1966, London).

5. GOPINATH, A.: "An investigation into the uses of magnetic fields to accelerate ferromagnetic particles", (PhD Thesis, 1965, University of Sheffield).

6. HORSNELL, T.S.: "Acceleration of ferromagnetic particles by pulsed magnetic field and rotating magnet systems", (PhD Thesis, 1968, University of Sheffield).

Appendix B: Tubular Motor Design Details

B1 Design and Construction of the TLIM

The stator of the experimental machine was built using the standard linear motor laminations shown in Fig 4.1. Fifteen laminations per stack were used to give a stack thickness of approximately 10 mm (theoretically 9.525 mm), and the stacks were held together by nylatron spacers fitted in the holes of the lamination and non-magnetic nuts and bolts. During construction, some of the stacks were positioned around a cylindrical former and the coils for the device were fitted into the slots while the unit was supported on a wooden base. Spacers were used to hold the stacks in position while further lamination stacks were built around the coils. At the circumference of the bore of the TLIM, the stacks touch each other with each stack being at a different radius. For a bore diameter of 80 mm, twenty six stacks were required. Only twenty four stacks were however used, to enable the coil ends to be brought out to two terminal rails, one on each side of the motor, to facilitate the investigation of different winding arrangements.

In order to construct the spacers, an estimate of their size was made by considering the angle subtended by the thickness of a lamination stack, which is 9.525/40, or 0.24 radian. Since the height of a lamination is 76 mm (see Fig 4.1), the width of each spacer was

$$0.24 \times (76 + 40) - 9.525 \approx 18 \text{ mm},$$

and the length was the 467 mm of a lamination. Semi-circular wooden rings enclosing the whole structure kept the spacers in place and helped to strengthen the structure.

B2 Coil Design

The physical dimensions of the coil are determined by the size of the lamination slots, shown in Fig 4.1, and the bore diameter of the TLIM.

Assuming the flux density B is sinusoidally distributed along the machine-bore (see Fig b1), then

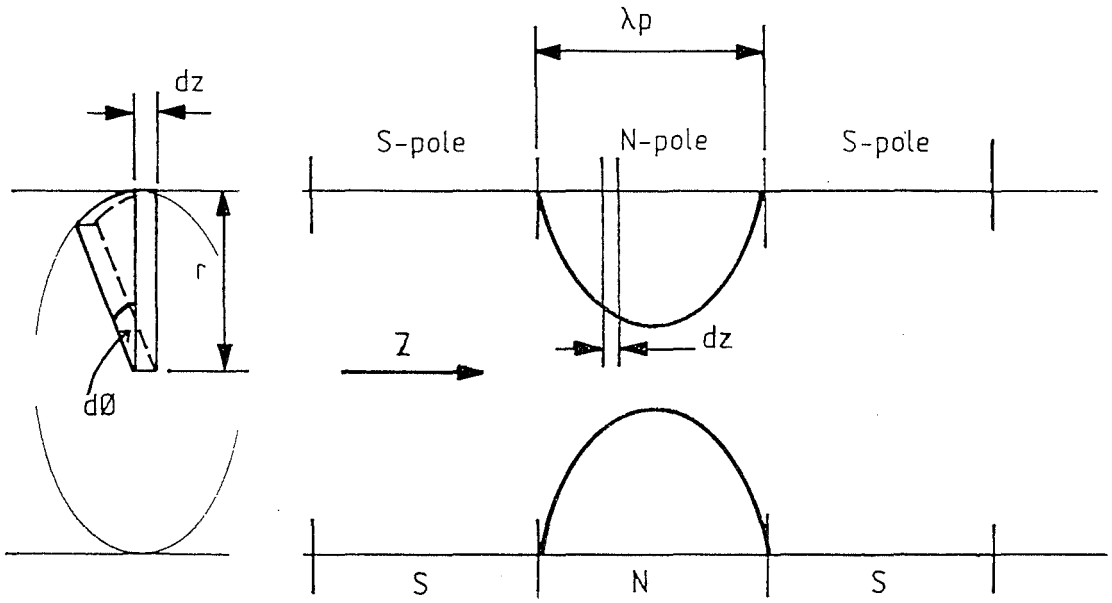

Travelling wave of flux density,

$$B = Bp \cos \left(\frac{\pi}{\lambda p} z - \omega t \right)$$

SINUSOIDALLY DISTRIBUTED FLUX DENSITY

Figure b1

$$\phi = \int B.dA$$

$$= \int_{-\lambda_p/2}^{+\lambda_p/2} \int_{-\pi}^{\pi} \hat{B} \cos \left[\frac{\pi}{\lambda_p} z - \omega t \right] r \, d\theta \, dz$$

$$\therefore \phi = \frac{2\lambda_p}{\pi} (2\pi r) \hat{B} \cos \omega t \qquad \text{(b1)}$$

where λ_p = pole-pitch;

r = radius;

ω = angular frequency;

ϕ = flux per pole,

So that the induced emf e is

$$e = k_w N_p \frac{2\lambda_p}{\pi} (2\pi r) \hat{B} \, 2\pi f \, . \sin 2\pi f t \qquad \text{(b2)}$$

where k_w = winding factor;

N_p = number of turns/phase;

f = supply frequency, and

t = time.

Both this emf and the voltage drop due to the coil resistance oppose the impressed voltage. However, with the latter neglected, equation (b2) may be rewritten,

$$E = 4\sqrt{2} \, \pi r \, \lambda_p f \, k_w \, N_p \, \hat{B} \qquad \text{(b3)}$$

where E is the rms value of the applied voltage.

The device consisted of twenty four slots and had a radius of 40 mm. For a fully-pitched winding with 1 slot/pole/phase, the pole pitch was equivalent to three slot pitches, or λ_p = 56 mm (see Fig 4.1). With a 50 Hz, 240 V supply and assuming a peak airgap flux density[1] of 0.4 T, N_p = 301.4 turns/phase. The assumed winding has eight coils/phase giving the number of turns/coil as approximately forty. The machine was wound with a double-layer winding, with each coil containing twenty turns and all the coil ends brought out to terminal rails.

B3 Coil Construction

For the double layer winding, 48 coils were required and two coil formers were designed for the inner and outer coils (Figs b2 and b3). Each former was securely held to its cheeks by nuts and bolts threaded through equi-spaced holes. The centre of the formers and cheeks were slotted, so that a keyway (see Fig b4) could be used to provide a firm drive from the winding machine to the former. Chamfering the coil former, as shown in Figs b2 and b3, enabled the coil to be easily slipped off the former, and the slots in the circumference of the formers allowed fibre-glass tape to be threaded underneath the fully-wound coil thus retaining its shape.

To protect the coils from the sharp lamination edges, the stator slots were lined with Nomex paper and protection was provided by a layer of fibre-glass tape covering the whole coil. Taking into account this extra space requirement reduces the available slot area to 17.6 x 11.0 = 193.6 mm^2 for each coil (Fig 4.1). Assuming a wire packing factor of approximately 0.7 gives a wire diameter of

$$d = \sqrt{\frac{4 \times 193.6}{20\pi} \times 0.7} = 2.94 \text{ mm} \qquad \text{(b5)}$$

and wire of diameter 2.9 mm was available for use.

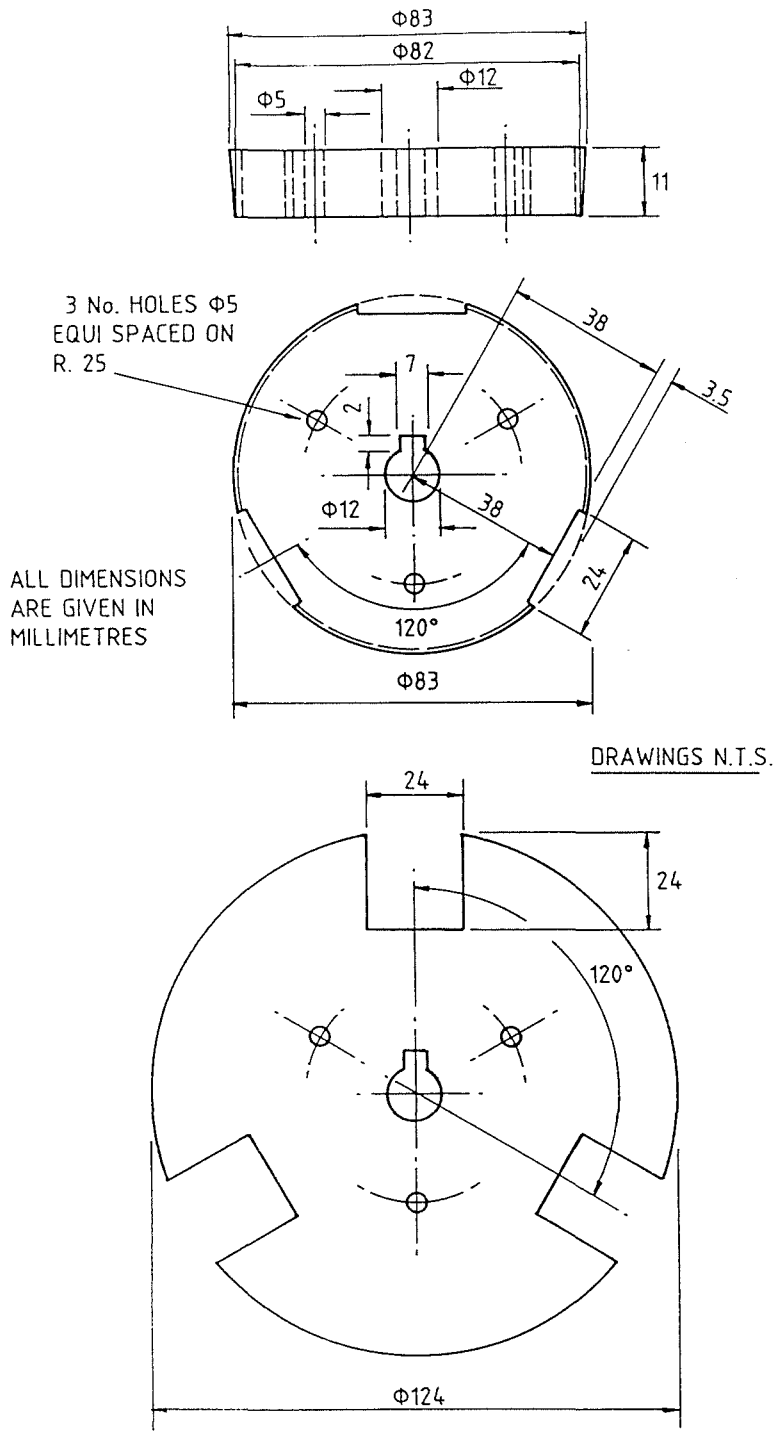

COIL FORMER FOR THE INNER COILS OF THE TLIM

Figure b2

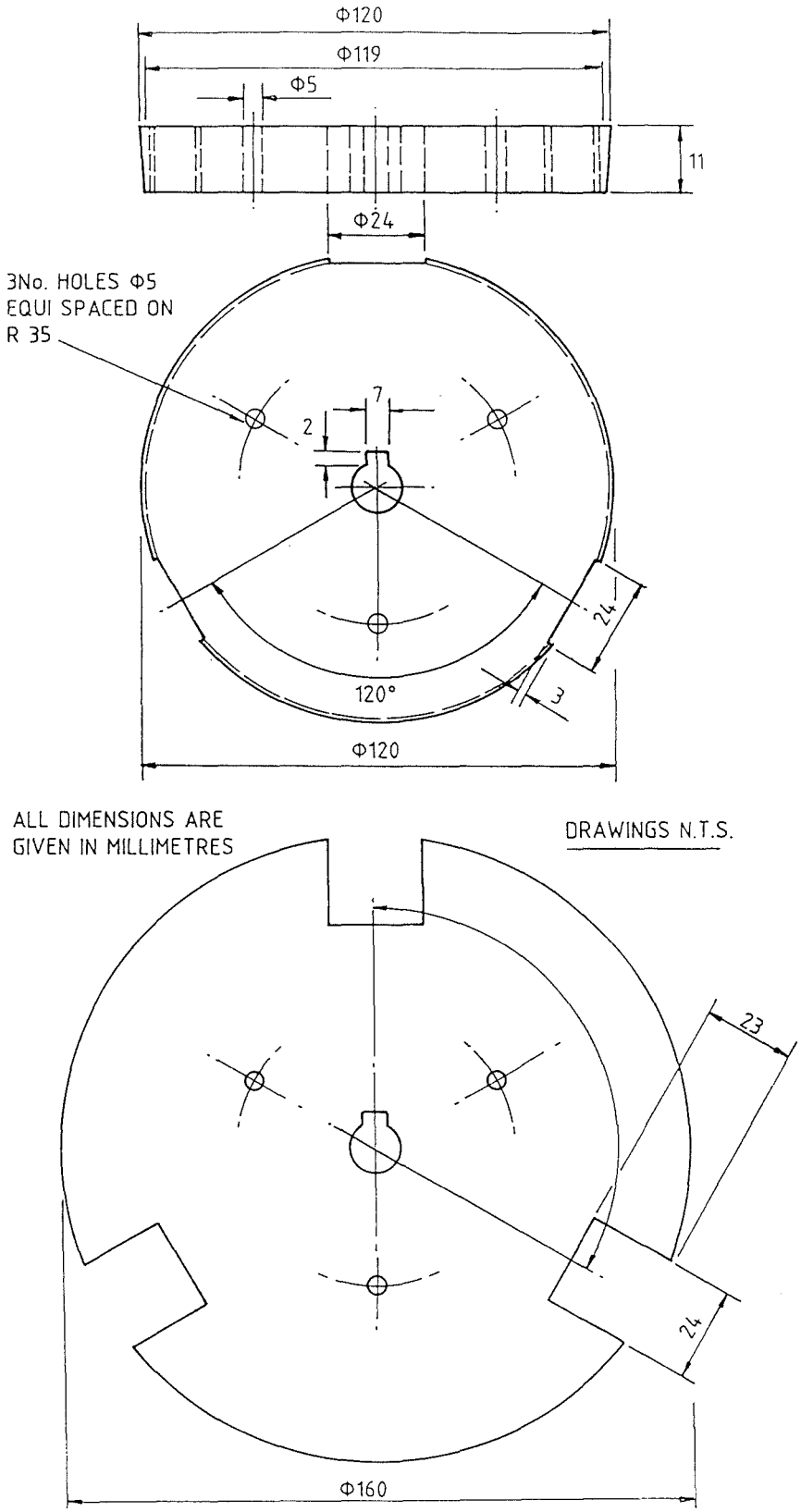

COIL FORMER FOR THE OUTER COILS OF THE TLIM

Figure b3

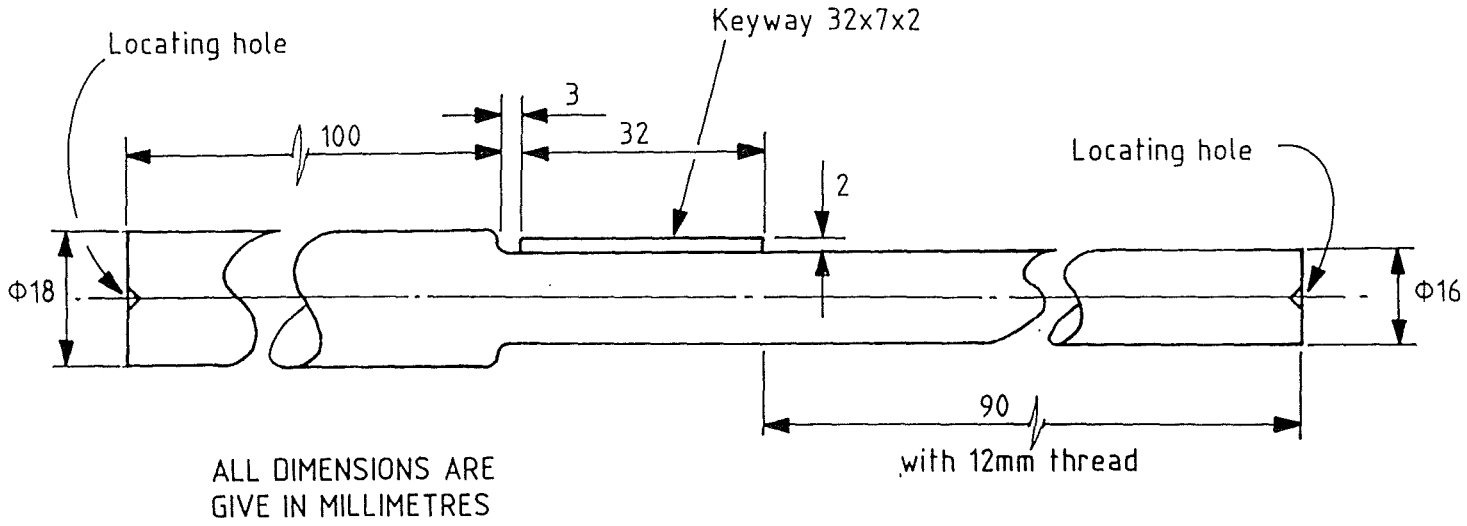

KEYWAY TO ASSIST COIL WINDING

Figure b4

B4 Search Coils

A cylindrical piece of perspex was machined such that one end was approximately 9 mm in diameter (see Fig 4.8), and a slot with a 2 mm square cross-section was cut into this end to contain the search coil. The search coil was therefore sufficiently large to just cover a tooth in the TLIM lamination stack. The slot was filled with fine, enamelled copper wire, with the coil ends brought out through slots only slightly wider than the wire diameter. Two holes drilled into the perspex at the slot end provided access to the coil ends. Both slots and holes may be identified in the photograph of Fig 4.8.

Two search coils were constructed in this manner and, using a CROPICO flux probe, the search coils were calibrated to enable accurate measurements of induced voltage to be made, using either an ac voltmeter or an oscilloscope.

References

1. VADHER, V.V.: *Private communication*, University of Technology, Loughborough, 1986.

Appendix C: Results for the Tubular Motor

Tables C1 and C2 give results for the TLIM with a 1 slot/pole/phase winding using iron filings, and tables C3 to C6 using 100 g of AISI with a 2 slots/pole/phase winding at various phase currents. Tables C7 and C8 give results when 200 g of AISI is introduced into the motor. Tables C9 and C10 record the measurements for 100 g of Ni/Fe powder with a 2 slots/pole/phase winding. Results for 100 g and 200 g AISI powder with a 4 slots/pole/phase winding are given in Tables C11, C12 and C13. Finally, Tables C14 to C17 give various no-load and flux density measurements with various winding arrangements.

The mass transport rate may be evaluated from

$$\dot{m} = \frac{\text{mass of powder}}{\text{time}}$$

and, using Table C1, after 10 s, $\dot{m}_{10} = \dfrac{12 \times 10^{-3}}{10/3600} = 4.3$ kg/hr; and after 30 s, $\dot{m}_{30} = 3.1$ kg/hr. These rates (see Table C2) are the average over the time interval for which they are calculated and the cumulative rate may be evaluated from

$$\dot{m}_c = \frac{\Delta m}{\Delta t}.$$

Thus, after 30s

$$\dot{m}_c = \dot{m}_{10} + \frac{(26 - 12) \times 3.6}{(30 - 10)} = 4.3 + 2.5 = 6.8 \text{ kg/hr}$$

as shown in Table C2.

Table C1: Transport of iron filings with a 1 slot/pole/phase winding at 25 A/phase

Time (s)	Start of device		Along bore		End of device	
	(g)	(%)	(g)	(%)	(g)	(%)
0	200	100	0	0	0	0
10	145	73	42	21	12	6.0
30	102	51	72	36	26	13
60	114	57	63	32	24	12
90	107	54	71	36	22	11
120	71	36	96	48	33	17

Table C2: Mass transport rates for iron filings with a 1 slot/pole/phase winding at 25 A/phase

Time (s)	Average mass transport rate (kg/hr)	Cumulative mass transport rate (kg/hr)
0	0	0
10	4.3	4.3
30	3.1	6.8
60	1.4	6.6
90	0.9	6.4
120	1.0	7.7

Table C3: Transport of 100 g of AISI 430 with a 2 slots/pole/phase winding at 20 A/phase

Time (s)	Start of device		Along bore		End of device	
	(g)	(%)	(g)	(%)	(g)	(%)
0	100	100	0	0	0	0
10	29	29	69	69	3.0	3.0
30	27	27	69	69	4.8	4.8
60	35	35	61	61	4.0	4.0

Table C4: **Transport of 100 g of AISI 430 with a 2 slots/pole/phase winding at 30 A/phase**

Time (s)	Start of device		Along bore		End of device	
	(g)	(%)	(g)	(%)	(g)	(%)
0	100	100	0	0	0	0
10	21	21	71	71	7.9	7.9
30	16	16	74	74	11	11
60	14	14	72	72	14	14

Table C5: **Transport of 100 g of AISI 430 with a 2 slots/pole/phase winding at 40 A/phase**

Time (s)	Start of device		Along bore		End of device	
	(g)	(%)	(g)	(%)	(g)	(%)
0	100	100	0	0	0	0
10	13	13	77	77	10	10
30	7.4	7.4	78	78	15	15
60	4.6	4.6	80	80	16	16

Table C6: **Mass transport rates for 100 g of AISI 430 with a 2 slots/pole/phase winding at 20, 30 and 40 A/phase**

Time (s)	Average mass transport rate (kg/hr)			Cumulative mass transport rate (kg/hr)		
	20 A/ph	30 A/ph	40 A/ph	20 A/ph	30 A/ph	40 A/ph
0	0	0	0	0	0	0
10	1.1	2.8	3.6	1.1	2.8	3.6
30	0.6	1.3	1.8	1.4	3.4	4.5
60	0.2	0.8	1.0	1.3	3.7	4.6

Table C7: **Transport of 200 g of AISI 430 with a 2 slots/pole/phase winding at 30 A/phase**

Time (s)	Start of device		Along bore		End of device	
	(g)	(%)	(g)	(%)	(g)	(%)
0	200	100	0	0	0	0
10	67	34	127	64	6.4	3.2
30	36	18	150	75	15	7.5
60	47	24	138	69	16	8.0

Table C8: **Mass transport rates for 200 g of AISI 430 with a 2 slots/pole/phase winding at 30 A/phase**

Time (s)	Average mass transport rate (kg/hr)	Cumulative mass transport rate (kg/hr)
0	0	0
10	2.3	2.3
30	1.8	3.8
60	1.0	3.9

Table C9: **Transport of 100 g of Ni/Fe at 40 A/phase**

Time (s)	Start of device		Along bore		End of device	
	(g)	(%)	(g)	(%)	(g)	(%)
0	100	100	0	0	0	0
10	10	10	79	79	11	11
30	8.5	8.5	76	76	16	16
60	5.8	5.8	79	79	16	16

Table C10: Mass transport rates for 100 g of Ni/Fe with a 2 slots/pole/phase winding at 40 A/phase

Time (s)	Average mass transport rate (kg/hr)	Cumulative mass transport rate (kg/hr)
0	0	0
10	4.0	4.0
30	1.9	4.9
60	1.0	4.9

Table C11: Transport of 100 g of AISI 430 with a 4 slots/pole/phase winding at 40 A/phase

Time (s)	Start of device		Along bore		End of device	
	(g)	(%)	(g)	(%)	(g)	(%)
0	100	100	0	0	0	0
10	19	19	70	70	12	12
20	15	15	62	62	23	23
30	17	17	66	66	17	17
60	13	13	69	69	18	18
90	9.2	9.2	68	68	23	23

Table C12: Transport of 200 g of AISI 430 with a 4 slots/pole/phase winding at 40 A/phase

Time (s)	Start of device		Along bore		End of device	
	(g)	(%)	(g)	(%)	(g)	(%)
0	200	100	0	0	0	0
10	30	15	160	80	11	5.5
20	21	11	169	85	11	5.5
30	22	11	162	81	16	8.0
60	18	9.0	166	83	16	8.0
90	24	12	150	75	26	13

Table C13: **Mass transport rates of 100 g and 200 g of AISI 430 with a 4 slots/pole/phase winding at 40 A/phase**

Time (s)	Average mass transport rate (kg/hr)		Cumulative mass transport rate (kg/hr)	
	100 g	**200 g**	**100 g**	**200 g**
0	0	0	0	0
10	4.3	4.0	4.3	4.0
20	4.1	2.0	8.3	4.0
30	2.0	1.9	6.1	5.8
60	1.1	1.0	6.2	5.8
90	0.9	1.0	6.8	7.0

Table C14: No-load results for the tubular device with a 1 slot/pole/phase winding

Phase Current (A)	Line Voltage (V)	Power (W)	Normal flux density B_n (mT)	
			Slot	Tooth
1.25	10	12.5	3.33	6.67
5.0	20	50	5.01	13.3
6.0	25	75	5.73	15.7
7.25	30	106	7.31	18.4
8.63	35	137	8.25	23.3
10.0	40	181	9.3	27.3
11.5	45	238	10.7	29.0
12.63	50	284	12.0	29.9
13.75	54.7	331	14.0	33.0
14.63	60	375	15.3	36.0
15.88	65	456	16.6	38.8
17.0	70	519	18.0	44.4
19.5	80	675	25.3	50.1
22.0	90	875	31.3	52.7
24.5	100	1094	37.3	58.8
26.8	110	1350	44.4	66.7
29.3	120	1650	47.5	70.4
31.5	130	1975	50.1	77.2
34.5	141	2300	53.9	83.2
35.5	146	2475	59.9	88.5
39.5	160	3038	64.0	94.5

Table C15: Tangential flux density results for the tubular device with a 1 slot/pole/phase winding

Phase Current (A)	Tangential flux density B_t (mT)	
	Slot	Tooth
0	0	0
5.0	12.3	9.12
7.5	19.3	12.9
10.0	24.1	19.3
15.0	37.6	29.5
17.5	44.9	33.3
20.0	51.5	42.7
25.0	61.2	48.2
30.0	71.8	61.2
35.0	90.0	70.6
40.0	103	79.4

Table C16: No-load results for the tubular device with a 2 slots/pole/phase winding

Phase Current (A)	Line Voltage (V)	Power (W)	Normal flux density B_n (mT)		Tangential flux density B_t (mT)	
			Tooth	Slot	Tooth	Slot
5.0	24.0	37.5	10.0	3.75	13.9	14.5
7.5	36.0	100	17.5	6.26	20.4	20.4
10.0	46.5	163	22.5	8.74	25.2	28.4
12.5	57.5	263	27.5	10.0	30.6	34.3
15.0	69.5	388	32.5	11.9	35.5	41.2
17.5	81.0	538	39.3	15.0	40.3	47.3
20.0	91.5	713	44.9	17.5	44.9	56.4
25.0	114.5	1125	55.2	21.3	57.9	67.0
30.0	138.0	1588	65.1	25.0	73.0	85.8
35.0	162.0	2425	76.4	30.0	86.7	98.5
37.5	174.0	2963	82.4	31.2	91.2	107
40.0	185.0	3550	88.8	33.8	97.6	112

Table C17: Flux density values for a 4 slots/pole/phase fully-pitched winding at 20 A/phase

Tooth number	Phase of current in adjoining slot	B_n (mT)	B_t (mT)	B_t/B_n
1	R	46.3	9.64	0.21
2	R	16.3	48.2	2.96
3	R	4.99	46.1	9.24
4	R	10.0	50.3	5.03
5	y	40.7	51.5	1.27
6	y	11.9	51.5	4.33
7	y	7.5	54.6	7.28
8	y	11.9	50.3	4.23
9	B	36.8	44.9	1.22
10	B	11.9	44.9	3.77

Appendix D: Finite Element Details for the LIM and TLIM

D1 Separation Between Tangential and Normal Pole-Centres

The position occupied by the magnetic poles produced by a 2 slots/pole/phase winding may be seen in Fig 5.3. It is evident that the normal and tangential pole-centres are mutually displaced by three slot-pitches, corresponding to an angle of $^{3}/_{12}$ x 360 = 90°.

It is possible to calculate the angular separation that occurred between the normal and tangential pole-centres in the GEC finite element model for the tubular device. Measurements from near the middle of the computer-drawn graphs in Fig 5.5 show the existence of a tangential pole-centre at x = 294, and of normal pole-centres on either side of this at x = 233 and x = 346. Thus, the first normal pole-centre occurred at an angle of

$$\frac{(294 - 233)}{12 \times 18.67} \times 360° = 98°$$

before the tangential pole centre, and the second at an angle of

$$\frac{(346 - 294)}{12 \times 18.67} \times 360° = 84°$$

after the same tangential pole-centre. (The slot pitch was 18.67 mm and there were 12 slot-pitches per cycle.) Both of the results above are within 10% of the expected value of 90°. Note that one pole-pitch is given by

$$\frac{(346 - 233)}{12 \times 18.67} \times 360° = 182° \simeq 180°.$$

D2 Co-ordinates for the Linear and Tubular Motor Models

Table D1 lists the abscissa co-ordinates of the lamination modelled in the finite element study undertaken at GEC, so that particular teeth or slots may be pinpointed in the graphical plots given for this study in Chapter 5. (Inspection of the outline of the tubular

model will show that the x co-ordinates for the outline have been offset by 37.34 mm compared both to Table D1 and to the graphical plots because of the method used by the GEC software when generating the graphs.) Alongside the slot number is given the phase of the current in that slot for a 2 slots/pole/phase winding, as used in the model. Interpretation of the table shows that, for example, tooth 13 starts at x = 267.715 and finishes at x = 273.715 (i.e. a tooth pitch of 6 mm) followed by slot 13 which has a pitch of 12.67 mm and contains a red phase winding. Table D2 shows to which approximate points the major abscissa divisions refer in the graphical results obtained from the GEC study. Thus, the abscissa x = 240 will give results part-way through slot 11 which, from Table D1, contains a blue phase winding.

Similar information to that in Table D1 is given in Table D3 for the study of the tubular and linear models using PE2D, the two-dimensional finite-element package of Rutherford Laboratories. The co-ordinates given can be used to fix the position of the teeth and slots in the diagrams pertaining to this study.

D3 Results Perpendicular to the Tubular Machine Axis

Table D4 shows the variation of the flux density with radius for the tubular model studied using the GEC finite-element package.

Table D1: Co-ordinates for the GEC Tubular Model

Left-hand end of bore; x - co-ordinate = 0
Left-hand end of lamination; x - co-ordinate = 37.74

Tooth No.	x - Co-ordinate		Slot No.	x - Co-ordinate	
	Start of tooth	End of tooth		Start of slot	End of slot
1	43.675	49.675	1(R)	49.675	62.345
2	62.345	68.345	2(R)	68.345	81.015
3	81.015	87.015	3(y)	87.015	99.685
4	99.685	105.685	4(y)	105.685	118.355
5	118.355	124.355	5(B)	124.355	137.025
6	137.025	143.025	6(B)	143.025	155.695
7	155.695	161.695	7(r)	161.695	174.365
8	174.365	180.365	8(r)	180.365	193.035
9	193.035	199.035	9(Y)	199.035	211.705
10	211.705	217.705	10(Y)	217.705	230.375
11	230.375	236.375	11(b)	236.375	249.045
12	249.045	255.045	12(b)	255.045	267.715
13	267.715	273.715	13(R)	273.715	286.385
14	286.385	292.385	14(R)	292.385	305.055
15	305.055	311.055	15(y)	311.055	323.725
16	323.725	329.725	16(y)	329.725	342.395
17	342.395	348.395	17(B)	348.395	361.065
18	361.065	367.065	18(B)	367.065	379.735
19	379.735	385.735	19(r)	385.735	398.405
20	398.405	404.405	20(r)	404.405	417.075
21	417.075	423.075	21(Y)	423.075	435.745
22	435.745	441.745	22(Y)	441.745	454.415
23	454.415	460.415	23(b)	460.415	473.085
24	473.085	479.085	24(b)	479.085	491.755
25	491.755	497.755	-	-	-

Right-hand end of lamination; x - co-ordinate = 504.09
Right-hand end of bore; x - co-ordinate = 541.43

Table D2: Areas of Lamination Referred to by the Abscissa Divisions in the Results from the GEC Study

No. of Divisions	x - Co-ordinate	Approximate position in lamination
0	0	Left-hand end of bore
1	24	Outside left-hand end of lamination
2	48	3/4 inside tooth 1
3	72	1/3 inside slot 2
4	96	3/4 inside slot 3
5	120	1/3 inside tooth 5
6	144	1/12 inside slot 6
7	168	1/2 inside slot 7
8	192	11/12 inside slot 8
9	216	2/3 inside tooth 10
10	240	1/3 inside slot 11
11	264	3/4 inside slot 12
12	288	1/12 inside tooth 14
13	312	1/12 inside slot 15
14	336	1/2 inside slot 16
15	360	11/12 inside slot 17
16	384	2/3 inside tooth 19
17	408	1/4 inside slot 20
18	432	3/4 inside slot 21
19	456	1/3 inside tooth 23
20	480	1/12 inside slot 24
21	504	Right-hand end of lamination
22	528	Outside right-hand end of lamination
23	552	Outside right-hand end of bore
24	576	Outside right-hand end of bore
25	600	Outside of computer model

Model finishes at x - co-ordinate $\simeq$ 586

Table D3: Co-ordinates for the PE2D Linear and Tubular Models

Start of lamination; y - co-ord (TLIM), x - co-ord (LIM) = 566.335

Tooth No.	y - co-ord (TLIM) x - co-ord (LIM)		Slot No.	y - co-ord (TLIM) x - co-ord (LIM)	
	Start of tooth	End of tooth		Start of slot	End of slot
1	560	554	1(R)	554	541.33
2	541.33	535.33	2(R)	535.33	522.66
3	522.66	516.66	3(y)	516.66	503.99
4	503.99	497.99	4(y)	497.990	485.32
5	485.32	479.32	5(B)	429.32	466.65
6	466.65	460.65	6(B)	460.65	447.98
7	447.98	441.98	7(r)	441.980	429.31
8	429.31	423.31	8(r)	423.31	410.64
9	410.64	404.64	9(Y)	404.64	391.97
10	391.97	385.97	10(Y)	385.97	373.3
11	373.3	367.3	11(b)	367.3	354.63
12	354.63	348.63	12(b)	348.63	335.96
13	335.96	329.96	13(R)	329.96	317.29
14	317.29	311.29	14(R)	311.29	298.62
15	298.62	292.62	15(y)	292.62	279.95
16	279.95	273.95	16(y)	273.95	261.28
17	261.28	255.28	17(B)	255.28	242.61
18	242.61	236.61	18(B)	236.61	223.94
19	223.94	217.94	19(r)	217.94	205.27
20	205.27	199.27	20(r)	199.27	186.6
21	186.6	180.6	21(Y)	180.6	167.93
22	167.93	161.93	22(Y)	161.93	149.26
23	149.26	143.26	23(b)	143.26	130.59
24	130.59	124.59	24(b)	124.59	111.92
25	111.92	105.92	-	-	-

End of lamination; y - co-ord (TLIM), x - co-ord (LIM) = 99.585

Table D4: Variation of Flux Density for the GEC Tubular Model

Position in the tubular model.	Radius (mm)	FLUX DENSITY (mT)																				
		Outside l.h. end of lamination (x=24)			Tooth 1 (x = 48)			Tooth 5 (x=120)			Slot 7 (x=168)			Tooth 10 (x=216)			Slot 16 (x=336)			At r.h. edge of lamination (x=504)		
		B_n	B_t	B_m	B_n	B_t	B_m	B_n	B_t	B_m	B_n	B_t	B_m	B_n	B_t	B_m	B_n	B_t	B_m	B_n	B_t	B_m
Bore of the tubular device	12	-0.8	2.5	3.0	-2.0	7.5	8.5	2.5	2.0	14	0.8	-12.5	13.5	-2.0	-6.5	14	2.5	5.0	14	0.5	2.5	6.5
	20	-1.0	2.5	3.0	-3.0	7.5	7.5	4.0	2.0	14.5	1.5	-13	14.5	-2.5	-6.0	14	3.5	5.0	14	0.8	2.5	6.5
	22.75	-1.0	2.5	2.5	-3.5	7.5	8.0	4.5	2.0	15	2.0	-13	15	-3.2	-7.5	15	4.0	6.0	15	1.0	2.5	7.0
	28	-1.5	2.5	2.5	-4.5	7.5	9.0	5.5	2.0	16	3.0	-13.5	16	-4.0	-8.0	16	5.0	6.0	16	1.5	2.5	7.0
	32	-1.8	2.0	2.5	-6.0	7.5	10.5	9.5	2.5	17.5	3.0	-16.5	17.5	-5.0	-8.0	16.5	5.5	7.0	17	2.0	2.5	7.0
Surface of teeth	39.9	-2.0	1.0	2.5	-21	5.0	22	17.5	7.5	27.5	5.0	-22.5	24	-9.0	-2.5	12	6.0	10	22.5	2.5	0	5.0
Bottom of windings	46	0	0.5	2.0	-58	7.5	61	35	7.5	45	0	-24	25	-15	-12.5	32	0	11	25	0	-0.5	2.0
Halfway thro' windings	62	0	0	1.0	-75	7.0	79	35	3.5	45	0	-11	12	-15	-5.0	20	0	5.0	11	0	0	1.0
Directly behind teeth	80	0	0	0	-70	10	72	30	1.0	42	0	21	25	-15	10	23	0	-10	19	2.0	2.5	10
Directly behind stamping holes	100	0	0	0	-1.0	-5.5	7.0	3.0	2.5	12.5	1.0	9.0	12.5	-2.5	7.0	14.5	9.0	-5.0	12.5	4.0	-2.5	12

Appendix E: Transverse Flux Motor Design Details

E1 Coil Former for the TFLIM

To fit a coil slant-wise into the slots, the inside coil depth must be at least the width of the centre-teeth. To protect the coils, fibre-glass tape was wound around them and Nomex paper placed around the teeth. These additions made a greater inside coil depth necessary and, after constructing a trial coil, the former was made to a width of 60 mm. The height of the former was simply one-third of the available slot-depth (i.e. 15 mm) because the 1 slot/pole/phase winding scheme required three coil-sides in a slot. The width and height fix the distance x (see Fig E1) and the length of the former was determined from

$$z = \sqrt{x^2 + y^2} = \sqrt{30^2 + 48.575^2}$$

$$\therefore \quad z = 57 \text{ mm}.$$

The schematic of the coil former can be seen in Fig E.2 and the coils were wound to a depth of 28 mm. A keyway was cut into the former to prevent it slipping in the winding machine and to provide a firm drive. The inside corners of the former-cheeks were chamfered to guide wire onto the former, and a mark scribed on the inside edge indicated the maximum allowable coil size, so that the coil size could be monitored during winding.

Prior to winding a coil, a thin copper sheet was placed around the former to prevent the highly tensioned wire cutting into the former. This sheet together with the chamfer on the former (see Fig E.2) aided considerably in removing the wound coils; without the chamfer it proved difficult to remove the coils undamaged. Once a coil had been wound, fibre-glass tape was threaded through 2 mm deep slots in the former and cheeks to hold the coil together. The bolts holding the former and cheeks together could then be removed and the coil slipped easily off the former. Fibre-glass tape was used to cover the remainder of the coil, providing a protective layer.

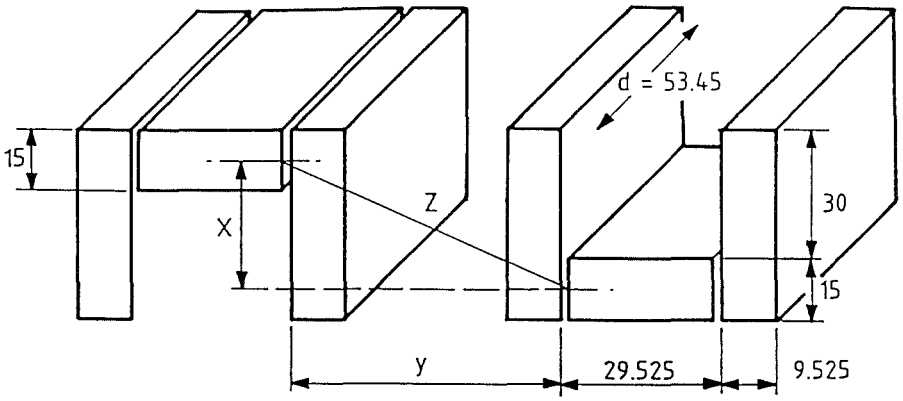

ALL DIMENSIONS ARE
GIVEN IN mm

DETERMINATION OF FORMER LENGTH

Figure E1

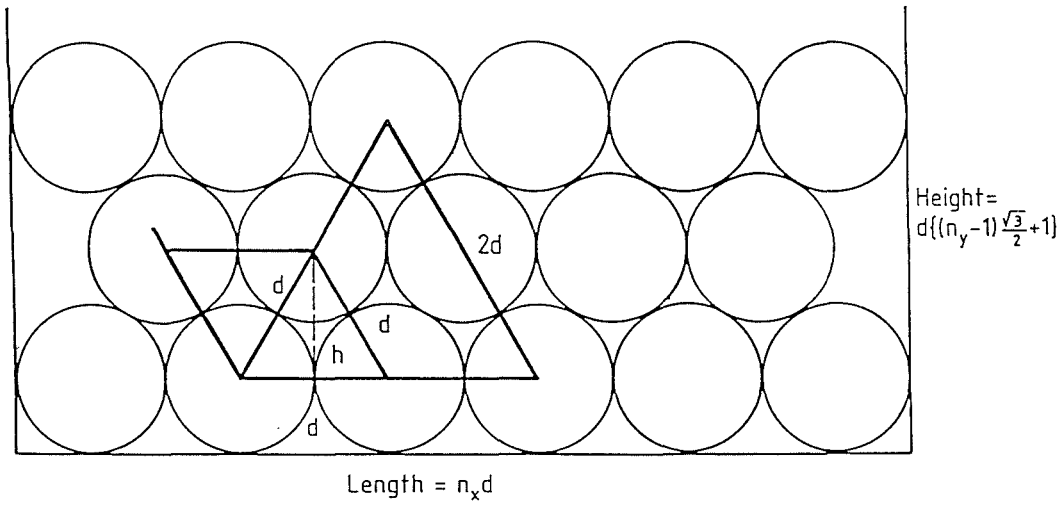

BOX LENGTH AND HEIGHT BASED UPON WIRE DIAMETER

Figure E3

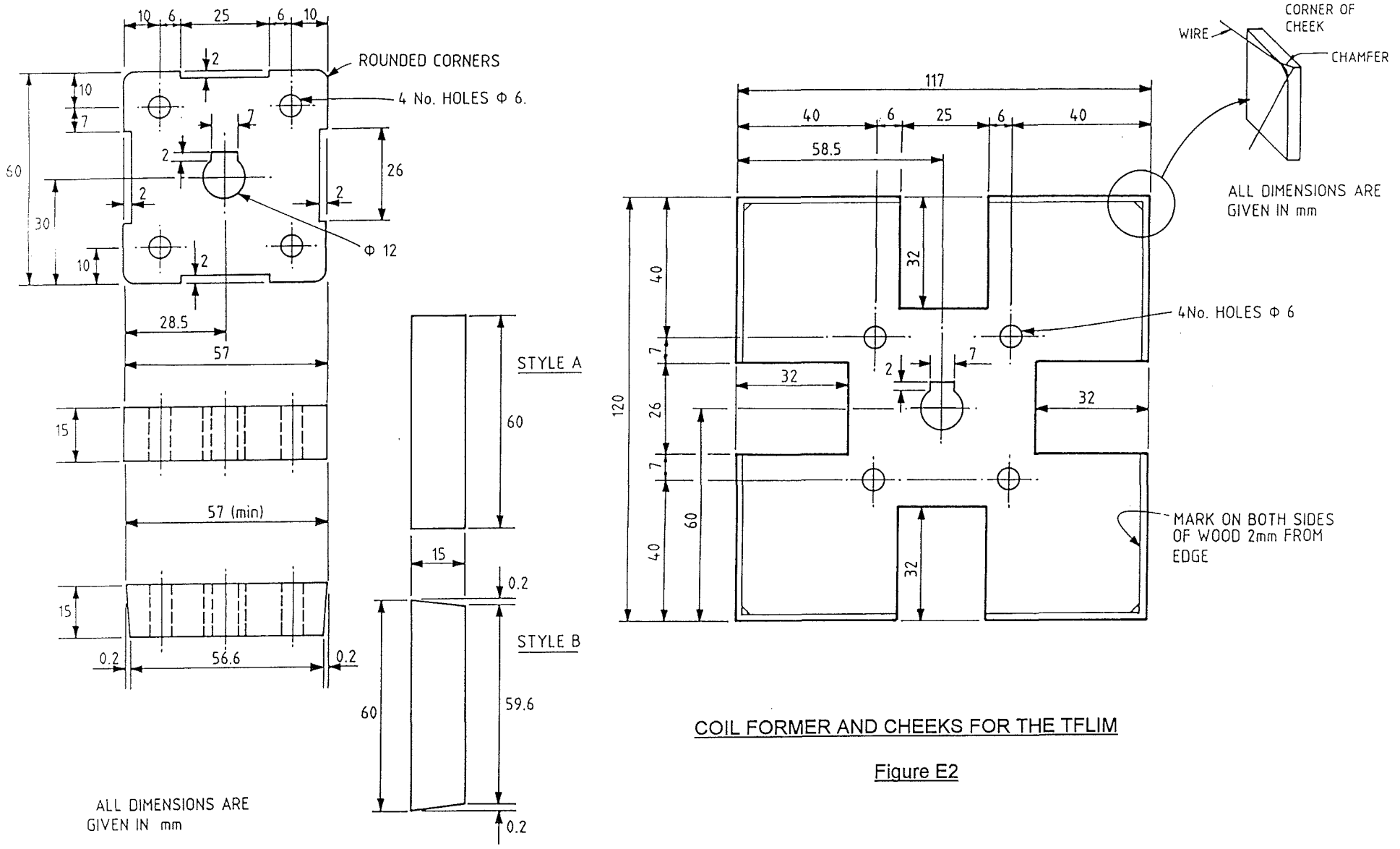

COIL FORMER AND CHEEKS FOR THE TFLIM

Figure E2

E2 Determination of Packing Factor

Wires of circular cross-section cannot fill completely the available area in a rectangular box. The ratio of the area of the wires to the available area is often termed the packing fraction or packing factor, and an expression for the best achievable packing factor may be obtained by considering the required number of turns and the wire diameter.

If the wire diameter d produces a row which spans the total length of a rectangular box, with each wire meeting the next at a perpendicular tangent (as shown by the first row of wires in Fig E.3), the box-length is given by

$$l = n_x\, d$$

where n_x is the number of columns of wires in the first row.

If n_y is the number of rows of wires, then the box-height is

$$h = (n_y - 1)d\frac{\sqrt{3}}{2} + d = d\left\{(n_y - 1)\frac{\sqrt{3}}{2} + 1\right\}$$

(Both n_x and n_y are integers.)

Hence, the box area occupied by the wires is

$$A_B = lh = \frac{n_x d^2}{2}\left\{(n_y - 1)\sqrt{3} + 2\right\}$$

In the first row, there are n_x wires; in the second, $(n_x - 1)$; in the third, n_x; in the fourth, $(n_x - 1)$ etc ... For odd n_y the maximum number of wires is

$$N_o = n_x\frac{(n_y + 1)}{2} + (n_x - 1)\frac{(n_y - 1)}{2}$$

i.e., $N_o = \dfrac{2n_x\, n_y - n_y + 1}{2}$,

and for even n_y, it is

$$N_e = n_x \frac{n_y}{2} + (n_x - 1)\frac{n_y}{2} = \frac{(2n_x - 1)n_y}{2} \approx N_o$$

Either N_o or N_e may be used to estimate the number of wires (or turns) as $N_o \rightarrow N_e$ when $(2n_x - 1)\, n_y >> 1$, which is often the case.

Using N_e, the area occupied by all of the wire including its enamel coating is

$$A_w = \frac{(2n_x - 1)\, n_y}{2} \frac{\pi d^2}{4}$$

If d_{cu} is the diameter of the copper part of the wire, the area of the copper fill is

$$A_{cu} = \frac{(2n_x - 1)n_y}{2} \frac{\pi d_{cu}^2}{4}$$

Thus, the best achievable packing factor based on the total wire area is

$$F_p = \frac{A_w}{A_B} = \frac{(2n_x - 1)\, n_y\, \pi}{4n_x\left\{(n_y - 1)\sqrt{3} + 2\right\}} = \frac{N_e \pi}{2n_x\left\{(n_y - 1)\sqrt{3} + 2\right\}}$$

As $n_x \rightarrow \infty$ and $n_y \rightarrow \infty$, $F_p \rightarrow \dfrac{\pi}{2\sqrt{3}} = 0.907$

Thus, even with an infinite number of turns, a rectangular cross-section cannot be filled using identical diameter cylinders. Obviously the smaller are n_x and n_y, the lower is the packing factor.

The copper fill packing fraction is less than F_p by the ratio of the square of the copper to the wire diameter,

i.e. $$F_p' = F_p \left(\frac{d_{cu}}{d} \right)^2 .$$

E3 Coil Details for the Transverse Flux Machine

The maximum available winding window of 29.525 x 17 mm^2 was reduced to 28 x 15 mm^2, after taking into account the thickness of the fibre-glass tape and the slot liner used to protect the coils. A rectangular cross-sectional former was designed as described earlier, and enamelled copper wire of outside diameter 0.96 mm was used. Using the above expressions and the window dimensions,

$$n_x = \frac{l}{d} = = \frac{15}{0.96} = 15$$

and

$$n_y = \frac{h}{d\frac{\sqrt{3}}{2}} + \left[1 - \frac{2}{\sqrt{3}} \right] \approx \frac{h}{d\frac{\sqrt{3}}{2}} = \frac{28}{0.96\frac{\sqrt{3}}{2}} = 33.$$

(For a perfect fit d needs to be a factor of l, and with the wire chosen it is 4% away from an ideal value.)

Thus, the total number of turns that may theoretically be accommodated is

$$N = \frac{(2 \times 15 - 1) \times 33}{2} = 478 \text{ turns},$$

which, since 67 total turns per coil are required, implies that a 7-stranded cable is required. The total number of wires in a coil wound from such a cable is 67 x 7 = 469, and with $n_x = 15$ and $n_y = 33$ the best achievable packing factor is $F_p = 0.86$, and the best copper fill is $F_p' = 0.76$. In practice it was only possible to accommodate 50 turns of the 7-stranded cable in the slots, giving an average packing factor of approximately 0.6 and a copper fill of approximately 0.53.

Appendix F: Results for the Transverse Flux Machines

Tables F1 to F9 give results for the TFLIM with a 1 slot/pole/phase, $^2/_3$-chorded winding. Tables F10 to F12 give results for the TFLIM with a 2 slots/pole/phase, $^1/_3$-chorded winding and Tables F13 to F15 for the inverted TFLIM with a 1 slot/pole/phase, $^2/_3$-chorded winding. Tables F16 and F17 give results for the standard DSTFLIM with a 1 slot/pole/phase, $^2/_3$-chorded winding using a box height of 75 mm. Tables F18 and F19 give results for the axial flux DSTFLIM at 39 A, with a 1 slot/pole/phase, $^2/_3$-chorded winding using a 50 mm box. Finally, Tables F20 and F21 give the no-load measurements made on the axial flux DSTFLIM and the standard TFLIM respectively.

The mass transport rate, $\dot{m}$, may be calculated from,

$$\dot{m} = \frac{\text{mass of powder}}{\text{time}}. \qquad \text{(F1)}$$

Hence, using Table F1 after 5 s, $\dot{m}_5 = \dfrac{117 \times 10^{-3}}{5/3600} = 84$ kg/hr at zero height; and after 10 s for the same height, $\dot{m}_{10} = \dfrac{159 \times 3.6}{10} = 57$ kg/hr. These rates are the average mass transport rates over the time interval for which they are calculated, and the cumulative mass transport rate may be calculated from,

$$\dot{m}_c = \frac{\Delta m}{\Delta t}.$$

At zero height and after 10 s

$$\dot{m}_c = \dot{m}_5 + \frac{(159 - 117) \times 3.6}{(10 - 5)} = 84 + 30.24 \simeq 114 \text{ kg/hr}.$$

Table F1: Transport of Fe Filings at Zero Height and 40 A/phase

Time (s)	Start of device		Middle of device		End of device	
	(g)	(%)	(g)	(%)	(g)	(%)
0	250	100	0	0	0	0
5	30	12	102	41	117	47
10	14	5.6	77	31	159	64
15	6.3	2.5	64	26	180	72
30	0.7	0.3	14	5.6	235	94
60	0.4	0.2	5.5	2.2	244	98

Table F2: Transport of Fe Filings at Height 10 mm and 40 A/phase

Time (s)	Start of device		Middle of device		End of device	
	(g)	(%)	(g)	(%)	(g)	(%)
0	250	100	0	0	0	0
5	45	18	100	40	105	42
10	0.5	0.2	95	38	154	62
15	0	0	65	26	185	74
45	0	0	0.5	0.2	249	100

Table F3: Transport of Fe Filings at Height 25 mm and 40 A/phase

Time (s)	Start of device		Middle of device		End of device	
	(g)	(%)	(g)	(%)	(g)	(%)
0	250	100	0	0	0	0
5	190	76	15	6	45	18
10	154	62	17	7	79	32
15	102	41	25	10	123	49
30	0.6	0.2	26	10	223	89

Table F4: Mass Transport Rates for Fe Filings at 40 A/phase and Heights 0, 10 and 25 mm

Time (s)	Average mass transport rate (kg/hr)			Cumulative mass transport rate (kg/hr)		
	0mm	10mm	25mm	0mm	10mm	25mm
0	0	0	0	0	0	0
5	84	76	32	84	76	32
10	57	55	28	114	111	57
15	43	44	30	129	133	89
30	28	-	27	142	-	113
45	-	20	-	-	141	-
60	15	-	-	143	-	-

Table F5: Transport of AISI 430 at Zero Height and 40 A/phase

Time (s)	Start of device		Middle of Device		End of Device	
	(g)	(%)	(g)	(%)	(g)	(%)
0	250	100	0	0	0	0
5	122	49	69	28	59	24
10	22	8.8	122	49	106	42
15	17	6.8	107	43	126	50
30	10	4	93	37	147	59
60	7.6	3	59	24	184	74

Table F6: Transport of AISI 430 at Height 10 mm and 40 A/phase

Time (s)	Start of device		Middle of Device		End of Device	
	(g)	(%)	(g)	(%)	(g)	(%)
0	250	100	0	0	0	0
5	157	63	40	16	53	21
10	64	26	89	36	97	39
15	1.9	0.8	134	54	114	46
30	6	2.4	116	46	128	51
60	0	0	81	32	169	68

Table F7: Mass Transport Rates for AISI 430 at 40 A/phase and Heights 0 mm and 10 mm

Time (s)	Average mass transport rate (kg/hr)		Cumulative mass transport rate (kg/hr)	
	Height 0mm	Height 10mm	Height 0mm	Height 10mm
0	0	0	0	0
5	42	38	42	38
10	38	35	76	70
15	30	27	90	82
30	18	15	95	85
60	11	10	99	90

Table F8: Transport of Ni/Fe 50/50 at Height 10 mm and 40 A/phase

Time (s)	Start of device		Middle of Device		End of Device	
	(g)	(%)	(g)	(%)	(g)	(%)
0	200	100	0	0	0	0
5	133	67	43	22	24	12
15	13	6.5	91	46	96	48
30	0	0	75	38	125	63
60	0	0	66	33	134	67

Table F9: Mass Transport Rates for Ni/Fe 50/50 at 40 A/phase and at Height 10 mm

Time (s)	Average mass transport rate (kg/hr)	Cumulative mass transport rate (kg/hr)
0	0	0
5	17	17
15	23	43
30	15	50
60	8	51

Table F10: Transport of AISI 430 at Zero Height and 40 A/phase

Time (s)	Start of device		Middle of Device		End of Device	
	(g)	(%)	(g)	(%)	(g)	(%)
0	250	100	0	0	0	0
5	144	58	82.5	33	23	9
10	65	26	80	32	105	42
15	49	20	60	24	141	56
30	39	16	32	13	179	72
45	28	11	26	10	196	78
60	24	10	24	10	202	81

Table F11: Transport of AISI 430 at Height 10 mm and 40 A/phase

Time (s)	Start of device		Middle of Device		End of Device	
	(g)	(%)	(g)	(%)	(g)	(%)
0	250	100	0	0	0	0
5	208	83	11	4	30	12
10	174	70	8	3	68	27
15	170	68	4	2	76	30
30	160	68	8	3	73	29
60	140	56	9	4	102	41

Table F12: Mass Transport Rates for AISI 430 at 40 A/phase and Heights 0 mm and 10 mm

Time (s)	Average mass transport rate (kg/hr)		Cumulative mass transport rate (kg/hr)	
	Height 0mm	Height 10mm	Height 0mm	Height 10mm
0	0	0	0	0
5	17	22	17	22
10	38	24	76	49
15	34	18	102	55
30	21	9	111	54
45	16	-	115	-
60	12	6	116	57

Table F13: **Transport of AISI 430 at 40 A/phase with Initial Airgap of 56 mm over the Inverted TFLIM**

Time (s)	Start of device		Middle of Device		End of Device	
	(g)	(%)	(g)	(%)	(g)	(%)
0	250	100	0	0	0	0
5	164	66	37	15	49	20
10	116	46	48	19	86	34
15	100	40	35	14	115	46
30	87	35	11	4	152	61

Table F14: **Transport of AISI 430 at 40 A/phase with Initial Airgap of 32 mm over the Inverted TFLIM**

Time (s)	Start of device		Middle of Device		End of Device	
	(g)	(%)	(g)	(%)	(g)	(%)
0	250	100	0	0	0	0
5	161	64	44	18	45	18
10	78	31	73	29	99	40
15	40	16	92	37	118	47
30	11	4	73	29	166	66
45	4	2	57	23	188	75
60	4	2	47	19	199	80

Table F15: **Mass Transport Rates for AISI 430 at 40 A/phase over the Inverted TFLIM**

Time (s)	Average mass transport rate kg/hr)		Cumulative mass transport rate (kg/hr)	
	initial airgap 56mm	initial airgap 32mm	initial airgap 56mm	initial airgap 32mm
0	0	0	0	0
5	35	32	35	32
10	31	36	62	71
15	28	28	83	85
30	18	20	92	97
45	-	15	-	102
60	-	12	-	105

Table F16: **Transport of AISI 430 at 35 A/phase using a Box Height of 75 mm on the Standard DSTFLIM**

Time (s)	Start of device		Middle of Device		End of Device	
	(g)	(%)	(g)	(%)	(g)	(%)
0	250	100	0	0	0	0
5	167	67	60	24	23	9
10	122	49	57	23	71	28
15	51	20	101	40	98	39
30	26	10	106	42	118	47
60	25	10	109	44	116	46

Table F17: **Mass Transport Rates for AISI 430 at 35 A/phase on the Standard DSTFLIM**

Time (s)	Average mass transport rate (kg/hr)	Cumulative mass transport rate (kg/hr)
0	0	0
5	17	17
10	26	52
15	24	71
30	14	76
60	7	76

Table F18: **Transport of AISI 430 at 39 A/phase using a 50 mm Box on the Axial Flux DSTFLIM**

Time (s)	Start of device		Middle of Device		End of Device	
	(g)	(%)	(g)	(%)	(g)	(%)
0	250	100	0	0	0	0
5	186	74	51	20	13	5
10	139	56	65	26	46	18
15	97	39	67	27	86	34
30	3	1	86	34	161	64
60	10	4	10	4	230	92

Table F19: Mass Transport Rates for AISI 430 at 39 A/phase on the Axial Flux DSTFLIM

Time (s)	Average mass transport rate (kg/hr)	Cumulative mass transport rate (kg/hr)
0	0	0
5	9	9
10	17	33
15	21	62
30	19	80
60	14	88

Table F20: No-load Results for the Axial Flux DSTFLIM

Phase Current (A/ph)	Line Voltage (V)	Power (kW)
0	0	0
5	52	0.1
10	104	0.35
15	156	0.7
20	208	1.3
25	260	2.05
30	313	3.4
35	368	4.8
39	405	6.2

Table F21: No-load Results for the Transverse Flux Device

Phase Current (A)	Line Voltage (V)	Power (W)	Normal component of flux density (B_n) on and near tooth 13 (mT)			
			Tooth edge	Tooth centre	Slot edge	Slot centre
0.8	5	3.5	5.03	3.64	1.24	1.45
1.95	10	10	10.9	7.97	2.33	2.79
2.65	15	15	14.9	11.0	3.58	3.97
3.60	20	25	20.7	15.2	4.85	5.46
4.50	25	40	26.2	19.2	6.43	7.0
5.30	30	50	31.3	22.9	6.85	7.82
6.50	35	75	36.7	27.0	9.09	9.70
7.08	40	100	41.8	30.6	9.70	11.2
8.20	45	130	46.7	34.6	11.8	13.0
9.0	50	160	51.5	37.9	13.2	15.5
9.70	55	175	55.5	41.2	13.9	16.7
10.6	60	200	61.2	45.5	13.9	16.1
11.4	65	240	67.6	49.4	13.9	17.7
12.3	70	260	71.8	53.7	16.1	19.8
13.2	75	300	76.1	56.7	17.2	20.4
14.3	80	340	81.8	62.1	19.3	22.5
15.2	85	375	90.0	66.4	21.4	24.1
15.9	90	425	96.4	70.6	22.5	24.6
16.8	95	475	99.7	72.7	25.2	26.8
18.0	100	550	105	77.3	25.7	27.9
19.5	110	675	112	105	27.9	30.6
21.2	120	830	125	91.2	30.6	33.3
23.1	130	1000	134	98.5	33.3	36.4
25.0	140	1250	147	108	35.8	38.2
26.9	150	1450	154	117	38.5	43.3
28.8	160	1650	168	122	38.5	44.9
30.7	170	1900	182	129	41.8	46.1
35	200	3150	198	146	46.1	50.3
40	224	3900	236	169	52.4	56.7
42	-	4200	-	-	-	-

Phase Current (A)	Line Voltage (V)	Power (W)	Normal component of flux density (B_n) on and near tooth 13 (mT)			
			Tooth edge	Tooth centre	Slot edge	Slot centre
45	247	5300	273	204	55.8	64.3
50	271	7000	257	198	50	57

Appendix G: Published Papers

1. GUPTA, D.K., HOBSON, L., and LLOYD, P.J.: "Transportation of Powders Using a Linear Motor Device", *Applied Energy*, 1987, **28**, pp.107-122

2. GUPTA, D.K., and HOBSON, L.: "Design and Analysis of Prototype Linear Motor Devices for Powder Transportation", UPEC-23, 20-22 September 1988, pp.300-303